BEHAVIOR OF TURBULENT STRUCTURES WITHIN A MACH 5 MECHANICALLY DISTORTED BOUNDARY LAYER

A Dissertation

by

SCOTT JACOB PELTIER

Submitted to the Office of Graduate Studies of
Texas A&M University
in partial fulfillment of the requirements for the degree of

DOCTOR OF PHILOSOPHY

Chair of Committee,	Rodney D. W. Bowersox
Committee Members,	Edward B. White
	Othon Rediniotis
	Simon North
Head of Department,	Rodney D. W. Bowersox

August 2013

Major Subject: Aerospace Engineering

ABSTRACT

High-resolution particle image velocimetry (PIV) is employed to resolve the velocity fields within a Mach 4.9 mechanically distorted turbulent boundary layer ($Re_\theta \approx 40{,}000$). The goal of this study is to directly observe the mechanisms responsible for the modified turbulent stresses present in mechanically distorted boundary layers. This is achieved by measuring the effects of the mechanical distortions upon the distribution, population, size, orientation, and energy content of the turbulent structures, and how the perturbed state of these structures is manifested within the ensemble-averaged turbulent stresses. The two mechanical distortions under investigation are 1) streamline curvature-induced favorable pressure gradients (I_p = {-0.08; -0.49}), and 2) periodic arrays of diamond roughness elements ($k/\delta \approx 0.07$). A smooth-wall, flat-plate boundary layer is also included to establish the unperturbed state of the turbulent structures. The response of the mean turbulence statistics is investigated through ensemble-averaged profiles of Reynolds stresses, indicating the respective influences of pressure gradient effects and surface roughness upon the turbulent statistics. The distortion and reorientation of the large-scale coherent motions is quantified through the determination of the integral length scale and local structure angle from two-point correlations. Detection of individual vortices through the swirling strength criterion λ_{ci} allows the population distribution of the turbulent eddies to be examined, along with the conditionally averaged hairpin structure.

The baseline and rough-wall stresses showed good agreement when scaled by the smooth-wall friction velocity. Two-point correlations indicate that the reorientation of the large-scale [i.e. O(δ)] coherent structures, coupled with the modified wall-normal fluctuations, is primarily responsible for the modification of the rough-wall Reynolds stresses. The reduced Reynolds stresses observed in the favorable pressure gradients is partially due to the attenuation of the local flowfield around the near-wall hairpin

structures, mitigating the mechanism for “producing” turbulence. The rotational rate of the hairpin vortices, measured through the mean prograde swirling strength, was reduced for the favorable pressure gradient models.

ACKNOWLEDGEMENTS

I would like to thank my advisor, Dr. Rodney Bowersox, for his endless encouragement and boundless optimism throughout this project, and for granting me the freedom to expand the scope of my research into new and exciting areas. I would also like to thank Dr. John Schmisseur of the Air Force Office of Scientific Research (AFOSR) for financially supporting this endeavor.

I appreciate the technical assistance of Jorge Martinez, John Kochan, and the rest of the staff at the Oran W. Nicks Low Speed Wind Tunnel. Additionally, I would like to thank Will Seward for his machining expertise and general advice.

I would like to thank Dr. Isaac Ekoto, who was responsible for the design and construction of the facilities used during my Ph.D. program, and whose research inspired much of the work in this dissertation. I also appreciate the assistance of all the students at the National Aerothermochemistry Laboratory. Keeping the lab running is definitely a team effort, and I couldn't have completed my research without their assistance.

Finally, I would like to thank Dr. Raymond Humble for his technical and scientific assistance, including the many spirited discussions that encouraged me to push the boundaries of my dissertation.

TABLE OF CONTENTS

Page

Page

Page

Page

Page

LIST OF FIGURES

Page

Page

Page

Page

Page

Page

Page

Page

Page

Page

Page

Page

Page

Page

Page

LIST OF TABLES

Page

1. INTRODUCTION

1.1. Motivation

On October 14, 1947, Captain Charles "Chuck" Yeager became the first human being to pilot a supersonic aircraft (all previous supersonic craft were unmanned rockets). This groundbreaking feat set the stage for repeated aeronautical discoveries in the second half of the 20th century. While the pace of these discoveries has waxed and waned in phase with public interest and funding availability, the desire to achieve ever-greater speeds has remained. Over sixty years after Capt. Yeager's historic flight, these same desires motivate the current efforts in developing a hypersonic (Mach > 5) air-breathing vehicle. Potential applications include military (global strike and high-speed interceptors), commercial (fast-response international cargo transportation), and space-launch (reusable first stage) customers.

The stresses, both mechanical and thermal, experienced by a high-Mach number vehicle can prove instrumental in defining the performance envelope of the aircraft. The advanced propulsion systems necessary to accelerate a vehicle to high Mach numbers, which primarily include ramjets and scramjets, have much lower efficiencies than turbofan engines. For example, a hydrocarbon-fueled ramjet operating at Mach 5 will perform at approximately 25% of the efficiency of a subsonic turbojet engine (Fry 2004). It is not uncommon for such vehicles to be designed to operate near the thrust margin. Therefore, it is essential that the stresses acting upon the vehicle be accurately predicted. For a slender-bodied vehicle, such as the X-43 or X-51, the majority of these stresses are due to viscous effects caused by the turbulent boundary layer (TBL) over the vehicle surface. It is this feature that will be the focus of this dissertation.

The mere presence of a high-Mach number turbulent boundary layer does not present a great challenge to the current suite of predictive tools available to aerodynamicists. This is due primarily to the findings of Morkovin (1961), who showed that the behavior of a compressible turbulent boundary layer, up to and including the second-order statistics,

can be modeled as an incompressible boundary layer, when the density stratification of the flow is taken into account. However, this notion, labeled succinctly as Morkovin's hypothesis, is predicated on the stipulation that the flowfield is canonical, i.e. a smooth-wall, flat-plate boundary layer. It is over such surfaces that a majority of the current knowledge on supersonic boundary layers was developed, which will be discussed in §2. In reality, these flowfields are rarely found in practical aeronautical applications. While modeling a vehicle as a collection of flat plates would simplify the efforts needed for predicting the stresses exerted by the turbulent boundary layer, this ignores many key physical phenomena that may adversely (or favorably) affect the performance and survivability of the aircraft.

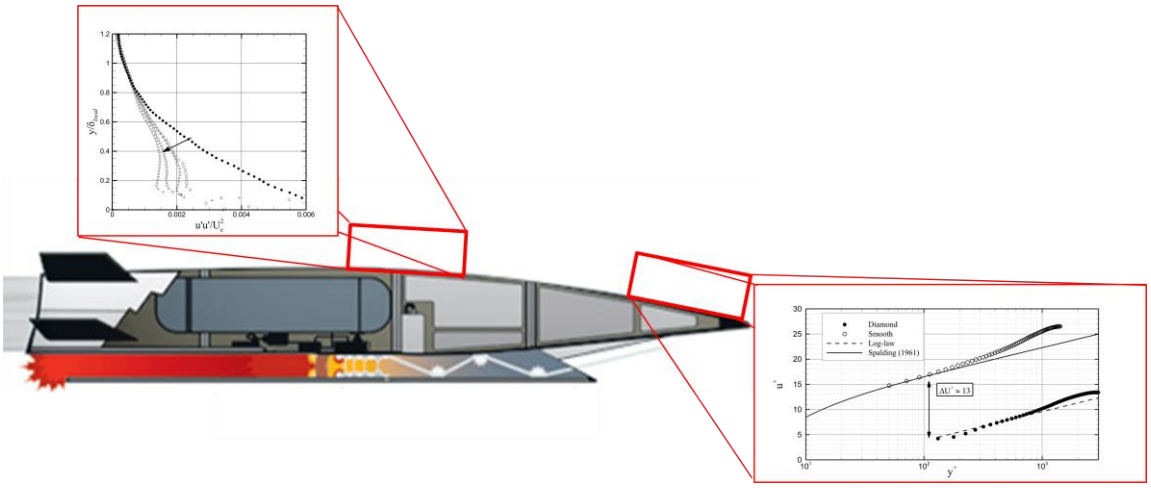

Figure 1.1 Schematic of a typical hypersonic vehicle, indicating potential areas for mechanical distortions. Image taken from Pratt and Whitney.

Visualizing a prototypical high-Mach number vehicle (Fig. 1.1), several key features become apparent. Every supersonic vehicle (excepting reentry vehicles) utilizes a lifting surface, whether that is a traditional wing, a blended wing-body, or simply a control surface. Regardless the type of surface, the pressure distribution across this area will not be uniform, whether due to boundary layer growth or viscous-inviscid interactions,

thereby inducing a pressure gradient within the boundary layer. Pressure gradients also exist in regions near shock boundary layer interactions, and along surface curvature (e.g. cambered airfoils). Given that pressure gradients exist in such mission-critical areas, it is essential to understand the effects of these distortions on the boundary layer, including the distribution of turbulent stresses, which affect both the overall drag and heat transfer rate. Another departure from the canonical smooth-wall, flat-plate boundary layer occurs due to surface roughness. While the majority of the surface area of most aircraft is hydraulically smooth, any aircraft will contain isolated roughness (e.g. rivets, seams, machining imperfections). However, distributed roughness is commonly found on high-Mach number vehicles, leading to large distortions of the boundary layer structure. This prevalence of organized roughness patterns is due to the necessity of thermal protection systems (TPS), owing to the high surface temperatures experienced in flight. Two common forms of TPS are *tiled* and *ablative*. In the former configuration, insulating tiles (composed of metallic, ceramic, or carbon/carbon components) are arrayed along the windward surface of the vehicle in a square, diamond, or hexagonal grid. Consequently, the seams between the tiles can manifest themselves within the turbulent boundary layer as periodic roughness. This effect can be amplified by metallic tiles, which may bow outward due to temperature gradients within the TPS material (Berry *et al.* 1999). Ablative TPS, while initially smooth, may also develop a periodic roughness pattern, due to the naturally occurring phenomenon of cross-hatching. The ablative material is designed to react endothermically, extracting energy that would otherwise be conducted into the vehicle. However, researchers discovered in the 1960s that the surface material receded at a non-uniform rate, producing a diamond pattern of streamwise grooves (Larson & Mateer 1968). This transient process is observed in supersonic TBLs, and was initially believed to be a result of differential ablation caused by heat-transfer perturbations over a wavy surface (Laganelli & Nestler 1969), though later experiments showed that cross-hatching would naturally occur in the surface layer of viscoelastic solids and liquid films [Gold & Probstein 1970; White & Grabow 1973; Stock 1975],

absent any ablative mass transfer. Figure 1.2 offers examples of these roughness patterns.

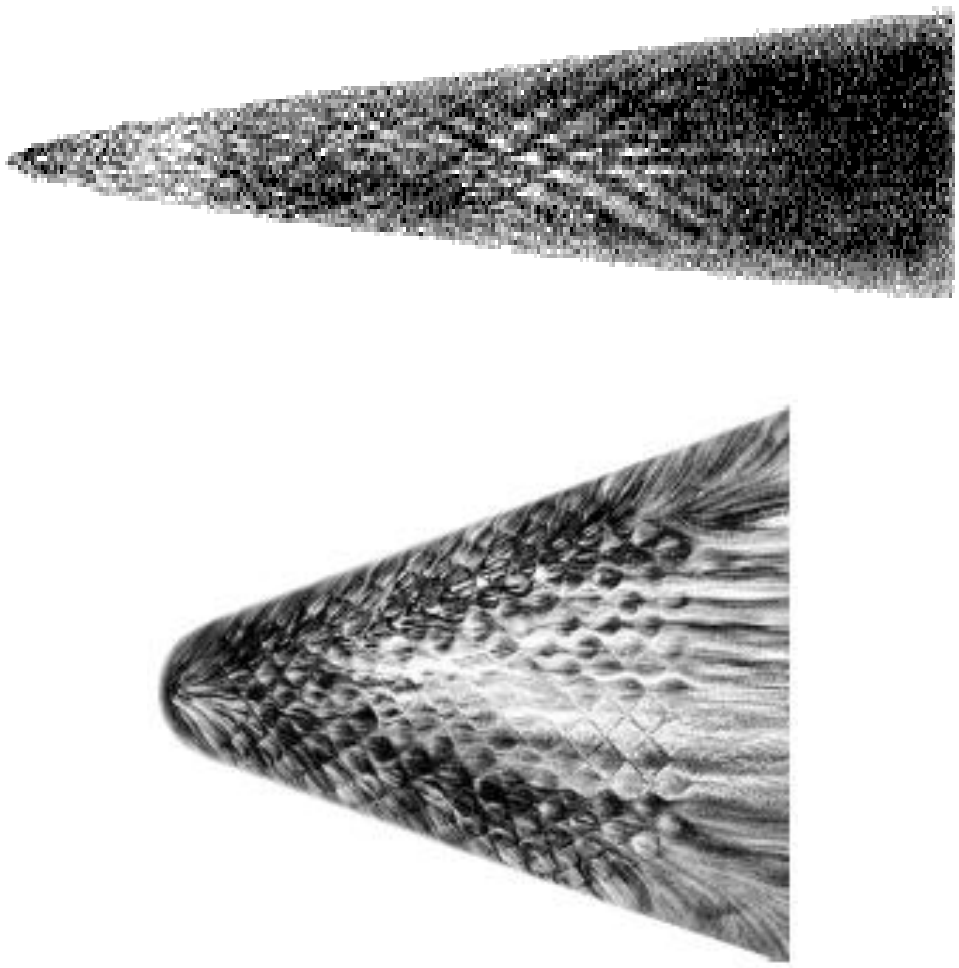

Figure 1.2 Examples of distributed roughness. Top: Cross-hatching of Teflon (White & Grabow 1973). Bottom: Streaklines over bowed metallic tiles (Berry *et al.* 1999)

1.2. Overview of Mechanically Distorted Supersonic TBLs

The features described above are labeled collectively as *mechanical distortions*, and their presence within a flowfield can influence key parameters such as shear stress, heat

transfer, and boundary layer growth. A detailed understanding of these features remains a necessary prerequisite for the accurate design of the most promising aeronautical applications. Given the difficulties associated with the numerical modeling of these phenomena, there is a strong motivation to experimentally investigate and quantify these effects. In the current study, *periodic surface roughness* and *curvature-induced favorable pressure gradients* (FPGs) have been selected for further examination. Adverse pressure gradients (APGs) are also a promising field of study, generating considerable interest due to their association with ramp flows and shock boundary layer interactions. However, these areas have received increasing attention over the past decade. Therefore, APGs will not be included in this study.

In order to establish what technical and scientific challenges lie ahead, it will prove useful to take a brief historical detour, reviewing the studies that have lead to the current state of knowledge concerning mechanically distorted TBLs. The following sub-sections will separately discuss surface roughness and favorable pressure gradient effects within turbulent boundary layers. This should not be considered an exhaustive review, but merely an introduction to the challenges associated with these distortions, as well as describing the central role they occupy in determining the evolution of the boundary layer.

1.2.1. Surface Roughness

A wealth of data exists for incompressible rough-wall boundary layers, summarized by Nikuradse (1933), Perry, Schofield & Joubert (1969), Grass (1971), Perry, Lim & Henbest (1987), Raupach (1991), Jiménez (2004), and Schultz & Flack (2007), among many others. Delving into the salient features of these reviews is beyond the scope of this dissertation. In this sub-section, the discussion will be confined to studies performed within compressible boundary layers, in order to justify the chosen flowfields for this

dissertation. General aspects of rough-wall boundary layers, including the effects on classical scaling, will be discussed more thoroughly in §2.

While studies of rough-wall boundary layers in the incompressible regime have been conducted for nearly a century, investigations into the effects of surface roughness within supersonic boundary layers began in the 1950s. Many of these earliest studies, beginning with Liepmann & Goddard (1957) and Goddard (1959), focused upon the response of the compressible skin-friction coefficient, due to its critical importance in the design process. They found that the skin-friction is solely a function of the roughness Reynolds number $k^+ = ku_\tau/\nu$, where k is the roughness height, u_τ is the friction velocity, and ν is the fluid viscosity. Additionally, Goddard (1959) also found that the shift in the velocity profile $\Delta(u/u_\tau)$ is a function of k^+ only, when the scaling given by Van Driest (1951) is used to account for the density stratification of the compressible boundary layer. These findings are consistent with the incompressible results of Nikuradse (1933).

The next 50 years of research into supersonic rough-wall flows continued in this fashion, addressing the effects of roughness height and topology on the skin-friction and mean velocity scaling. These effects are discussed in §2. It was not until the year 2000 that turbulence measurements were added to the growing database of experimental data. Latin & Bowersox (2000) used laser Doppler velocimetry (LDV) and hot-film anemometry to measure the mean velocity and density, kinematic turbulence intensities, mass flux turbulence intensities, and kinematic Reynolds shear stress over sand-grain and two-dimensional machine roughness elements ($k_s^+ = 100 - 570$) at Mach 2.9. The mean velocity, when scaled by Van Driest II theory, followed the trends of incompressible rough-wall flows, in agreement with Goddard (1959). Kinematic turbulence statistics of each roughness topology (excepting the two-dimensional plate) showed similar behavior when scaled with outer variables, collapsing onto a single curve. However, turbulence intensities (ρu), (ρv), and (ρw) did not collapse in a similar manner, instead showing a dependence upon k_s^+. Also, flow visualizations performed using schlieren photography showed that when the roughness elements protruded into

the supersonic region of the flow, shock waves and expansions fans were produced that persisted through the boundary layer thickness. Such features are not found in incompressible flows, suggesting that sufficiently large roughness elements in a supersonic boundary layer may behave differently than their low-speed counterparts. Additional analysis of this same data set by Latin & Bowersox (2002) showed that surface roughness increased the size of the small-scale structures, and decreased the size of the large-scale structures, as inferred from the autocorrelation curves. Using cross-correlations traces, the average structure orientation was unchanged by the sand-grain roughness, while the two-dimensional roughness indicated a lower angle in the outer region of the boundary layer.

Ekoto *et al.* (2009) used PIV to measure the kinematic turbulence stresses and strain rates over square and diamond roughness at Mach 2.87. Similar to Latin & Bowersox (2000), schlieren photography showed that shock waves and expansions fans were generated by the diamond roughness elements, extending into the outer region of the boundary layer. The elongated nature of the diamond elements resulted in attached waves that were strong enough to induce periodic oscillations in the strain rates and Reynolds shear stress. Measurements using pressure sensitive paint (PSP) showed that these waves generated locally adverse and favorable pressure gradients, corresponding to the attached shock waves and expansion fans, respectively. The stabilizing influence of the local FPG resulted in negative turbulence production over the aft half of each diamond element. The resulting Reynolds shear stress, when averaged over the entire diamond element length, was only 30% larger than the smooth-wall value. Conversely, the square elements increased the Reynolds shear stress by approximately 140%, and exhibited minimal local variations. Measurements of the kinematic stresses, with Morkovin scaling, "for the smooth and square models collapsed onto the expected trend" (Ekoto *et al.* 2009); the diamond roughness did not scale in a similar manner.

The most recent investigation into high-Mach number rough-wall flows was conducted by Sahoo, Papageorge & Smits (2010), using PIV to interrogate the flow over diamond

mesh and square bar elements. The mean velocity showed similar behavior to the incompressible case when scaled with van Driest II theory, again confirming the findings of Goddard (1959). Scaling the turbulence stresses by the local density ratio $(\rho/\rho_w)^{1/2}$ did not successfully collapse the data onto a single curve. The scaled rough-wall stresses are *lower* than the smooth-wall values, which is in disagreement with the data of Latin & Bowersox (2000). It should be noted that the study by Sahoo *et al.* (2010) was conducted at Mach 7.3, which is a significantly higher Mach number than that studied by Latin & Bowersox (2000) and Ekoto *et al.* (2009). This suggests a possible compressibility effect.

These studies, while limited in number, strongly suggest that van Driest II scaling is appropriate for transforming the mean velocity, as per the findings of Goddard (1959). However, Morkovin scaling has shown limited success in supersonic rough-wall boundary layers. The applicability of this scaling appears to be confined to sand-grain roughness (Latin & Bowersox 2000) and square elements (Ekoto *et al.* 2009), showing good agreement in these cases. For roughness topologies that create persistent distortions through the boundary layer (i.e. shock waves and expansion fans), Morkovin scaling is unsuccessful in collapsing the data. The results of Ekoto *et al.* (2009) suggest that localized variations in the strain-rates may be responsible, though this has not been confirmed in other studies. Additionally, no explanation is available for the *reduced* stresses observed by Sahoo *et al.* (2010). Further investigations into the local flowfield near roughness-induced distortions may prove fruitful in explaining these behaviors.

1.2.2. Curvature-Driven Favorable Pressure Gradients (FPGs)

The prevalence of curvature-driven FPGs on high-speed vehicles has directly motivated the increased research activity in this area over the last 40 years. Following the format given in the previous sub-section, only the most recent studies into supersonic FPGs will be described here. A more thorough discussion of the fundamental fluid response,

including the effects on classical scaling, will be included in §2. The experiments described in the following paragraphs are included to illustrate the importance of this flow phenomenon, and justify its inclusion into the current study.

It has been shown by many researchers that favorable pressure gradients exert a stabilizing influence upon the turbulent boundary layer Bradshaw (1974); Dussauge & Gaviglio (1987); Smith & Smits (1991); Smith & Smits (1994); Arnette, Samimy & Elliott (1998)), possibly reverting the flow to a quasi-laminar state if the gradient is of sufficient strength and duration [Narasimha & Sreenivasan (1973)]. Bradshaw (1974) noted that the effect of the FPG upon the turbulence stresses is approximately an order of magnitude larger than predicted by the Reynolds stress transport equation. Using Rapid Distortion Theory (RDT), Smith & Smits (1991) and Dussauge & Gaviglio (1987) found that a majority of the Reynolds stress evolution can be attributed to the role of bulk dilatation.

Velocimetry measurements by Luker, Bowersox & Buter (2000) in a Mach 2.9 curvature-driven FPG boundary layer extended the earlier experimental results, by examining both the turbulence stresses and strain rates. The pressure gradient produced by the curved-wall model was classified as "strong", based upon Bradshaw's (1974) distortion parameter d, defined as the ratio of the largest 'extra strain rate' over the primary strain rate dU/dy. The FPG produced reductions in the near-wall axial and shear stresses of 70% and 75%, respectively. In the outer region, $u'v'$ experienced a sign reversal, indicating negative turbulence production in this area of the boundary layer. Additionally, measurements at the boundary layer edge suggested an increase in intermittency.

Ekoto *et al.* (2009) employed PIV to interrogate the boundary layer response over two gradual expansions, $d \approx 0.1$ and $d \approx 0.3 - 0.4$, at Mach 2.87. These models, labeled as 'weak' and 'strong' pressure gradients, reduced the near-wall shear stress by 20% and 40%, respectively. The largest 'extra' strain rate was dV/dy, due to the expansion of the boundary layer, leading to a significant change in the bulk dilatation for the strong FPG

case. The bulk dilatation for this case was approximately 30% - 50% of the principal strain rate. The axial normal stress production was negative at $y/\delta = 0.4$, indicating that energy is flowing from the turbulent fluctuations into the mean flow.

The most recent study into supersonic curvature-driven FPGs was conducted at Mach 4.9 by Tichenor, Humble & Bowersox (2013). Using the same smooth-wall experimental models as Ekoto *et al.* (2009), they investigated the coupling between the strain-rates and kinematic stresses, finding that the observed sign reversal of the shear stress occurred where the dilatation was larger than the xy-strain. It was shown that the Reynolds stress transport models, specifically the model proposed by Launder, Reece & Rodi (1975), naturally capture the observed trends in the Reynolds shear stress. Additionally, the statistical size of the large-scale structures was estimated using two-point correlations of the fluctuating velocity, finding that the structures decreased in size through the expansion.

The studies described above confirm the expected trend in FPG boundary layers, showing reduced shear and normal stresses. These trends appear to be driven by the response of the strain rates, including the relative magnitudes of the dilatation and xy-strain. It has been suggested (Luker *et al.* 2000) and shown [Tichenor *et al.* (2013)] that the boundary layer structures are reduced in size by the FPG, potentially increasing the amount of energy available for dissipation, and thus contributing to the overall stabilization of the flow. However, RDT analyses by Smith & Smits (1991) and Dussauge & Gaviglio (1987) showed that bulk dilatation is the primary contributor to the response of the boundary layer. Intuitively, it is expected that the turbulent structures would expand with the mean flow, instead of decreasing in scale. To date, no mechanism has been found to explain the disintegration or contraction of the turbulent structures within a favorable pressure gradient. This necessitates a detailed investigation into the response of the boundary layer structures through an expanding flow, focusing upon the deformation of the turbulent eddies.

1.3. Research Framework

As shown above, the current knowledge of supersonic distorted TBLs relies almost exclusively upon a limited set of experimental data. While these studies have been instrumental in establishing the effects of mechanical distortions upon the boundary layer structure, a commonality between these analyses is apparent, namely the reliance upon statistical measurements, e.g. turbulent stresses $u'u'$ and $u'v'$. This provides useful data concerning the Reynolds stress response of the fluid, which supports the ultimate goal of predicting the stresses produced by a distorted TBL. However, two questions remain unanswered by these measurements: "why" and "how". Specifically, *why* do the turbulent stresses exhibit the measured trends, and *how* do the distortions interact with the fluid to produce these trends?

A turbulent boundary layer is composed of organized structures (described more thoroughly in §2), ranging in size from the boundary layer thickness δ to the Kolmogorov scale η, whose coherent motions comprise a majority of the turbulent stresses generated within the boundary layer (Adrian, Meinhart & Tomkins 2000). The boundary conditions of the flowfield (e.g. mechanical distortions) are introduced through the large-scale structures. As energy is transferred to successively smaller scales through the *energy cascade* (Richardson 1922), the influence of these distortions will spread beyond the initial large eddies, affecting both the scale and energy content of the resultant structures. It is through this mechanism that mechanical distortions affect the turbulent kinetic energy (TKE), and therefore the turbulent stresses.

From the studies described in the previous section, it is clear that researchers have attempted to use the measured statistics to infer the effects of mechanical distortions upon the turbulent structures. Single-point measurements, including those produced by spatially averaging two-dimensional data, "are ideal for determining the statistical properties of turbulence, [but] are much less satisfactory for revealing the existence of organized flow structures" (Head & Bandyopadhyay 1981). In order to determine how these distortions produce the observed changes in the turbulent stresses, it is necessary to

visualize the behavior of the instantaneous eddies under both undistorted and distorted conditions. Unfortunately, resolving the structures responsible for the production and redistribution of TKE is technically challenging, owing to the small scales responsible for these processes.

The rationale for the current study is inspired by the argument of Clauser (1956), who in turn invoked the analogy given by Maxwell, which is adapted here for the current study. Any complex system may be simplified as a self-contained mechanism, whose output is determined solely by external influences. This “black box” analogy essentially states that by varying the input to this system, and observing the output, the inner workings of the system may be deduced. To illustrate this point, Clauser (1956) suggested that any system can be imagined as a “complicated machine”, contained within a windowless room. The machine is controlled by a series of levers, and the output is presented as a collection of lights. The internal workings of the machine are unknown to the operator. If the levers are actuated in a systematic manner, and if the colors of the lights are correlated with the positions of the levers, then it is possible for the operator to deduce the inner workings of this machine. While this approach may seem simplistic, it is commonly used throughout our daily lives. For example, it is trivial to draw a crude circuit diagram of a light switch, simply by flipping the switch and observing the result. No knowledge of electrical engineering is necessary.

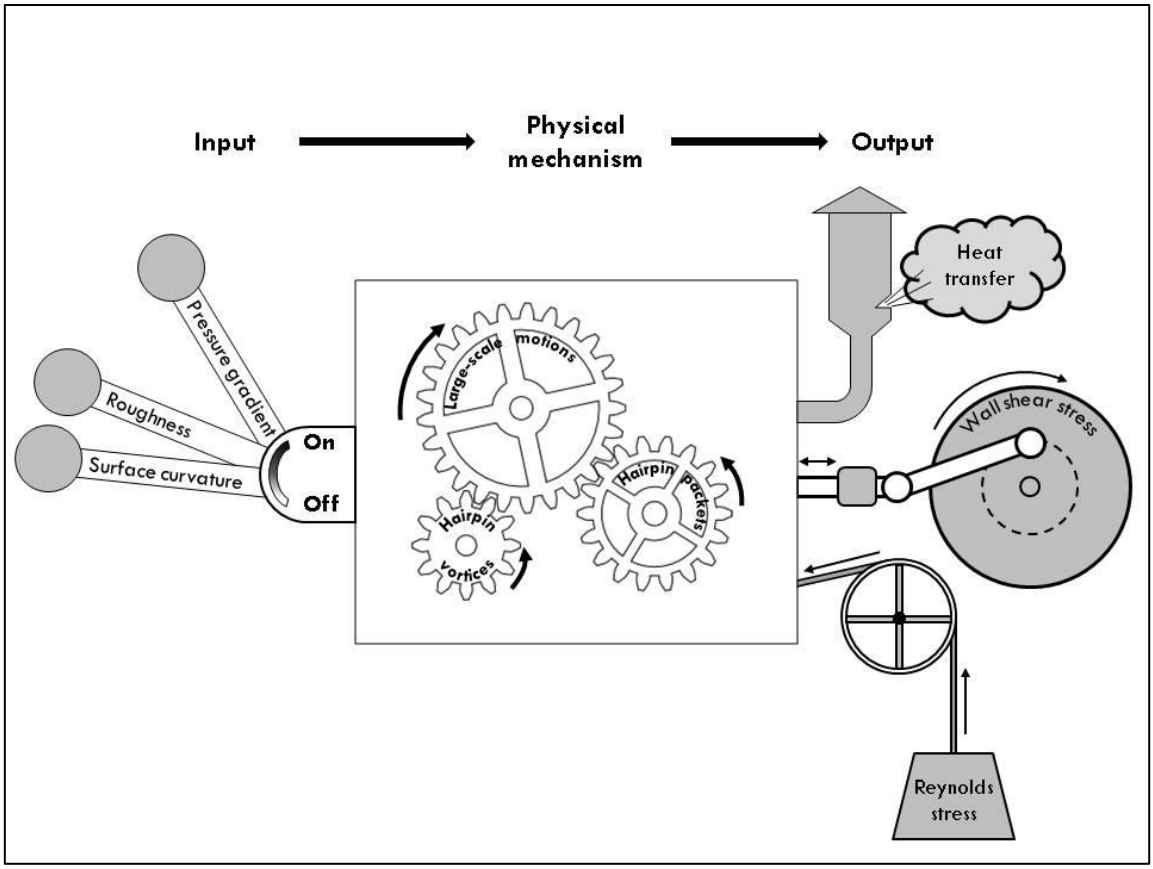

Figure 1.3 Cartoon describing "black box" analysis method for a turbulent boundary layer

This same "black box" analysis has been used to study mechanical distortions in supersonic TBLs (see Fig. 1.3). Surface curvature, roughness topology, and pressure gradients are the "input", and the measured turbulence statistics are the "outputs." By changing the surface orientation or the roughness height, and observing the change in turbulence statistics, researchers have attempted to discern the response of the turbulent eddies within the boundary layer. For example, Luker *et al.* (2000) suggested that the measured reduction in shear stress $u'v'$, coupled with the increase in intermittency, indicated that FPGs are responsible for breaking up the large-scale eddies, though no visualization of these structures was obtained. This approach to scientific research can be very successful, and is commonly used in many disciplines. However, there is a potential

weakness with this approach, not with the analyses per se, but with the application of the conclusions.

Referring back to the motivation described in §1.1, the objective of this study is to provide insight into the fluid dynamics governing high-Mach number distorted TBLs, supporting the ultimate goal of predicting the flowfield over a supersonic vehicle. Practically, this requires the development and refinement of predictive turbulence models. Using the "black box" analysis described above, model developers are only given the time-averaged turbulence statistics. This necessitates a *trial-and-error* approach, adjusting the model constants to produce the desired result. The added disadvantage is that the resulting model is now narrowly optimized for the given conditions and geometries. This laborious approach could be mitigated if researchers were aware of what processes produced the observed results, which could guide the developers in refining the model. For example, instead of attempting to match the reduced shear stress produced by a FPG, turbulence modelers would also know that the observed stress levels are caused by a near-cessation of turbulence production within the logarithmic region. Revisiting the light switch analogy described previously, the scientific framework advocated in this study is akin to asking someone with no electrical engineering knowledge to create a model describing a complicated circuit, based only upon observation of the inputs and outputs of the circuit (i.e. "black box" analysis), and then providing that person with a list of the pertinent components and their functions (e.g. capacitors, inductors, batteries). In essence, the current study attempts to *remove the lid* from the "black box."

1.4. Scientific Approach

The goal of the current study is to experimentally determine the principal processes governing the behavior of a high-Mach number, mechanically distorted TBL. This is performed by measuring the two-dimensional velocity field within the boundary layer,

focusing upon the distribution and deformation of the turbulent structures. High-resolution particle image velocimetry (PIV) is the primary diagnostic used in this study. All experiments are performed at Mach 5, such that the effects of density stratification can be included in the study, while avoiding the thermal non-equilibrium and rarified gas effects associated with the hypersonic regime. The three flowfields under investigation are[1]:

1) periodic surface roughness
2) curvature-driven favorable pressure gradients
3) a flat-plate, smooth-wall TBL

Details of the three geometries selected above will be described further in §3.2. The final case of an undistorted TBL is included not only for comparing to a baseline flowfield, but to lend insight into the behavior of highly compressible TBLs, motivated by the dearth of experimental data at high Mach numbers. This lack of data is due to the difficulty of resolving the velocity field within the high-shear near-wall region. The low density encountered in this region of compressible boundary layers is a direct obstacle to particle-based velocimetry methods (see §4.2). In general, the seeding density is proportional to the fluid density. Hence, the near-wall region, which is the most active region in turbulence production, and is therefore of greatest interest to the scientific community, also suffers greatly from low signal-to-noise levels. The current study addresses this issue through careful implementation of the PIV diagnostic, including the design and construction of a high-flow seeder (Appendix D), as well as minimization of noise generated by laser reflection (see §4.2). The resulting data sets not only support turbulence model development (as described in the previous section), but also aid in the validation of higher-order simulations (e.g. LES and DES).

Using this high-resolution data, the objective of the current study is to extend the existing knowledge of Mach 5 TBLs, under both distorted and undistorted conditions, by

[1] In the current study, the mechanical distortions are studied separately. Data have been collected for the case of rough-wall convex curvature models, but any investigation in the non-linear interaction of these distortions will not be included in this dissertation.

examining the response of the turbulent structures. The application of advanced post-processing algorithms allows for the population, distribution, orientation, and intensity of these structures to be directly computed from the experimental data (see §5 for a complete description of the analysis techniques). With this insight, coupled with "traditional" measurements of turbulence statistics, this study will answer the following:

1) How do mechanical distortions modify the turbulent structures in a Mach 5 turbulent boundary layer?
2) How does the modification of these structures manifest itself in the turbulence statistics?

The dissertation is laid out in the following manner. In §2, the fundamentals of turbulent boundary layers, including scaling and compressibility effects, are discussed. This section also includes an overview of pertinent studies of turbulent structures, and introduces key concepts used throughout the discussion of the results. Section 3 describes the wind tunnel facility used in this study, along with the experimental models. Experimental diagnostics are described in §4, and vortex identification techniques are discussed in §5. Results from the baseline undistorted TBL are given in §6, and FPG and rough-wall results are discussed in §7 and §8, respectively. Finally, key conclusions from each of the three flowfields are summarized in §9. This final section also includes recommendations for future analyses of the current results, as well as potential experiments to complement these data sets.

2. BACKGROUND REVIEW

The following section provides an overview of the key studies that have contributed to the current understanding of distorted turbulent boundary layers. Unless otherwise noted, the review will focus primarily upon the behavior of compressible boundary layers, and their response to favorable pressure gradients and surface roughness.

2.1. Turbulent Boundary Layer Fundamentals

2.1.1. Coherent Structures in Turbulent Boundary Layers

The dynamics of turbulent boundary layer structures has been the subject of countless studies over the past half-century. As such, this summary is not intended to be an exhaustive review of turbulent structures [for an excellent overview of coherent structures in turbulent boundary layers, see Cantwell (1981); Robinson (1991); Panton (2001); Adrian (2007); Adrian & Marusic (2012) and others]. Instead, the following sections will briefly review the turbulent structure taxonomy, and the contributions of each element to the cycle of Reynolds shear stress production. The technical challenge of experimentally probing highly-compressible boundary layers has largely limited this overview to incompressible boundary layers.

During the earliest years of boundary layer research, turbulence was generally regarded as a purely stochastic process, which could be described by random fluctuations u' imposed upon a mean flow U [Reynolds (1895)]. While coherent structures and vortices were known to exist, these were regarded as merely passive actors, and were not considered to be a primary component in the production of Reynolds shear stress. However, this paradigm slowly began to evolve in the mid-20th century, originating with the hairpin vortex model proposed by Theodorsen (1952). He suggested that the turbulent fluctuations, and primarily the generation of Reynolds shear stress, within a sheared flow may stem from the passage of an inclined vortex loop, which has been described as a “horseshoe vortex.” The origin of this horseshoe vortex structure was

attributed to the wall-normal perturbation of a spanwise vortex filament, causing a segment of the vortex to be momentarily lifted away from the wall. Using a purely kinematic argument, it was suggested that the higher mean velocity experienced by the vortex "head" would stretch the structure in the streamwise direction, while the remnants of the vortex filament within the lower parts of the boundary layer (referred to as the "legs") would be drawn toward each other. With continued stretching, the initially spanwise-oriented vortex would resemble a horseshoe or hairpin. It was believed that the rotating fluid within the vortices would induce a local flowfield of anti-correlated *u'* and *v'* fluctuations, hence producing Reynolds shear stress (see Fig. 2.1). Due to the sense of rotation, the hairpin vortex would "eject" low-momentum fluid away from the wall, while drawing in high-momentum fluid from higher in the boundary layer, a behavior which was later integral to explaining the bursting process observed by Kline *et al.* (1967).

The significance of the hairpin vortex model can not be overstated, as it provided a framework by which the seemingly random behavior of the turbulent boundary layer could be described as the result of quasi-deterministic vortex loops. Initially, the implication of these coherent vortex structures was not immediately embraced by the scientific community. In comparison to the early view of a turbulent boundary layer as a chaotic collection of fluctuating velocities, the notion of these macroscopic effects being the manifestation of organized structures was quite unexpected. This reaction was summarized well by Head & Bandyopadhyay (1981):

"At the outset, nothing could have seemed more implausible than that the boundary layer should consist almost exclusively of vortex loops or hairpins originating in the wall region, with dimensions here scaling on wall variables, and that some at least of these same vortex loops or hairpins should extend right through the boundary layer even at high Reynolds numbers ($Re_\theta \approx 10000$), but this is the conclusion we have now come to accept."

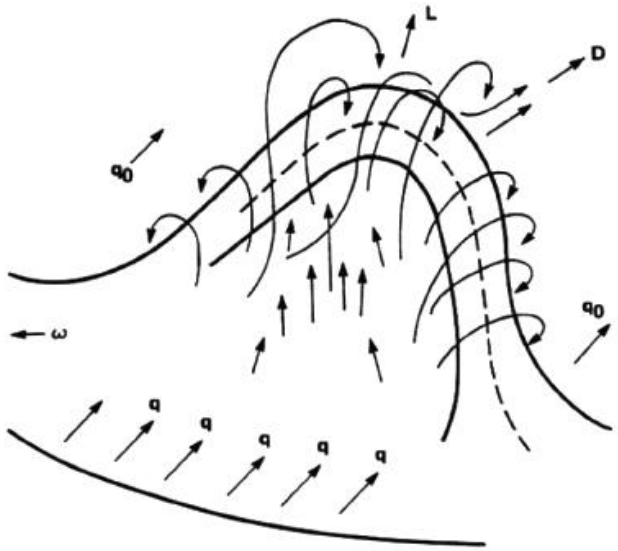

Figure 2.1 Conceptual drawing of a horseshoe or "hairpin" vortex. From Theodorsen (1952)

However, support for a phenomenological approach to turbulent boundary layer behavior grew with the experimental study of Kline *et al.* (1967), who used H_2 bubble visualization to explore the near-wall structural features of a turbulent boundary layer (Fig. 2.2). Long, meandering streamwise streaks were detected within the buffer layer, corresponding to regions of low-velocity fluid (compared to the surrounding mean flow). The spanwise separation between these structures was approximately 100 viscous units, "one of the more reliable physical constants in the study of turbulence" [Adrian (2007)]. The spaces between these low-momentum regions were filled by high-velocity fluid, creating an alternating pattern of high- and low-momentum streaks. Additionally, it was shown that the near-wall low-momentum streaks would occasionally undergo "bursting." This process was characterized by the increasingly violent oscillation of the streaks, followed by a large eruption of fluid away from the wall. Years later, it was shown that the bursting process is actually a series of individual ejection events, and that these ejections increased in intensity through the duration of the burst.

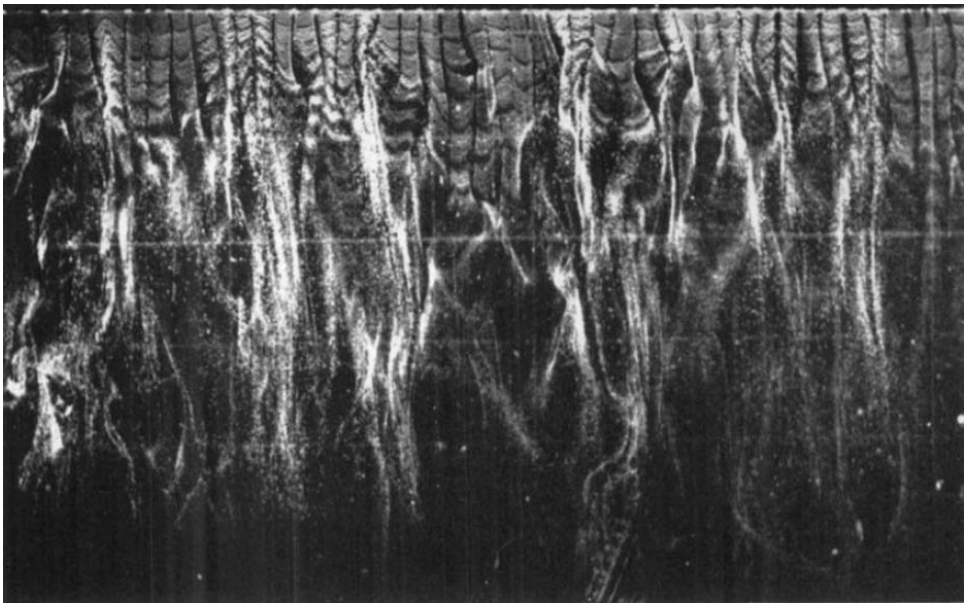

Figure 2.2 H_2 bubble visualization of near-wall "streaky" structures, collected at $y^+ = 9.6$. From Kline *et al.* (1967)

The discovery of the "streaky structures" within the turbulent boundary layer prompted a flurry of theoretical and experimental studies, all with the purpose of characterizing the coherent structures present within the boundary layer. Using smoke visualization inclined at 45 degrees to the flow axis, Head & Bandyopadhyay (1981) showed that the turbulent boundary layer is populated by inclined structures matching the description provided by Theodorsen (1952), arrayed at angles of approximately 45 degrees relative to the wall. Additionally, they noted that these vortex structures would occasionally be detected as small groups of hairpins, with the outer boundary of this group forming a small angle relative to the inclination of the individual vortices. The growth of these structures into the outer region of the flow was consistent with the "large-scale bulges" seen along the intermittent edge of a turbulent boundary layer. Perry & Chong (1982) successfully showed that a random distribution of hairpin vortex structures could replicate the mean velocity, Reynolds stress, and spectra of a turbulent boundary layer. However, their model represented these vortices as independent structures, and did not

account for any grouping of the hairpins, as was observed by Head & Bandyopadhyay (1981).

Up to this point, the existence of three-dimensional vortex loops had been based solely upon two-dimensional measurements of the boundary layer. This was addressed by the large-eddy simulations of Moin & Kim (1982), Moin & Kim (1985), and Kim & Moin (1986), providing direct evidence of hairpin vortices within low-Reynolds number channel flows. By reviewing the available numerical simulations, Robinson (1991) formulated a hierarchy of structures commonly observed within low-Reynolds number boundary layers, consisting of streamwise vortices, hairpin structures, and large-scale arches. It was suggested by Robinson (1991) that the hairpin vortices were formed due to instabilities within the near-wall vorticity layer, consistent with the explanation of Theodorsen (1952). Additionally, he postulated that the streamwise low-momentum streaks are produced by quasi-streamwise vortices within the buffer layer, which lift low-velocity fluid away from the wall.

The ability to experimentally probe the coherent structure behavior was greatly aided by the improvement of the particle image velocimetry (PIV) technique in the 1990's. The most significant of these studies was the work of Adrian *et al.* (2000). Prior to this study, it had been shown that individual hairpin vortices directly contribute to the sweep (Q4) and ejection (Q2) events, using the terminology of Lu & Willmarth (1973). The vortices were typically inclined at a 45-degree angle, and they were found throughout the logarithmic and outer regions of the boundary layer [Robinson (1991)]. The ejection of low-momentum fluid between the hairpin legs contributed to local region of low-momentum fluid, as shown in Fig. 2.3. This model of a single vortex, while successful in describing the statistics of the boundary layer [Perry & Chong (1982)], did not accurately capture the dynamics of the shear stress production, namely the bursting process.

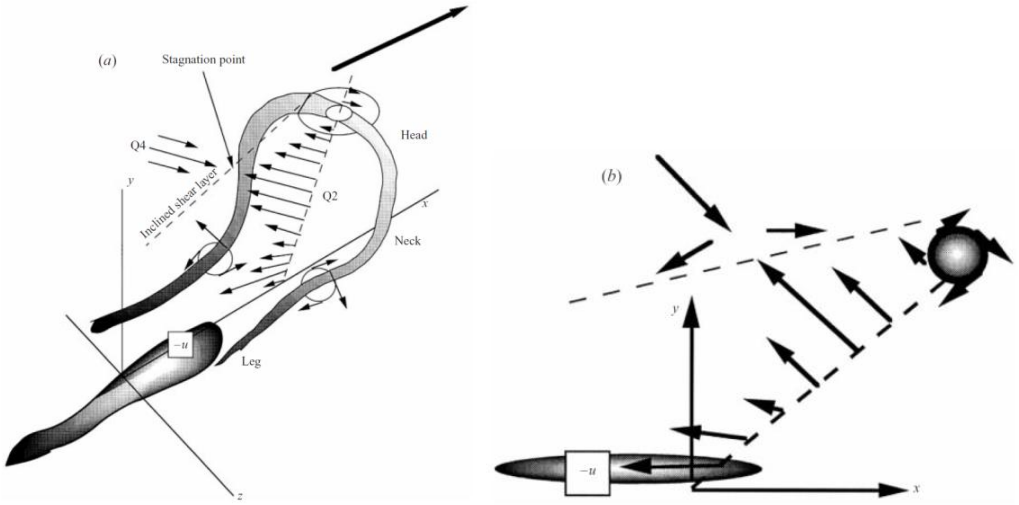

Figure 2.3 Conceptual drawing of a hairpin vortex, showing the a) locally induced flowfield, along with a low-momentum region beneath the vortex; b) The hairpin vortex signature, as seen in the *x-y* plane. Images takes from Adrian *et al.* (2000)

Adrian *et al.* (2000) used PIV to show that individual hairpin vortices do not act in isolation, but are typically streamwise-aligned into packets. This was consistent with the simulations of Zhou *et al.* (1999), who showed that hairpin vortices of sufficient strength could produce younger vortices through auto-generation, and that these vortices convected at a similar velocity. By viewing the hairpin packets as groups of vortices, with the oldest hairpins typically at the downstream edge, it was possible to provide a physical mechanism for the bursting process. Recall that "bursts" were actually composed of multiple ejections of increasing amplitude. This phenomenon agrees well with the passage of a hairpin vortex packet, as the smaller/younger vortices generally produce more energetic ejections. Due to the collective ejections of the hairpin vortices within the packet, these structures are also typically associated with long regions of low-momentum fluid, similar to the streaks observed by Kline *et al.* (1967).

The structural components of a turbulent boundary layer consist of two main "ingredients": low- and high-speed streaks, and hairpin vortices. Both features are integral to the near-wall cycle of turbulence production. While the causal relation

between these structures remains largely unknown, the prevailing theory suggests that the mutual induction between the hairpin legs (i.e. Q2 event) leads to a region of low-momentum fluid beneath the vortex. Within a hairpin vortex packet, the collective action of the vortices will lead to a long streak, similar to those observed by Kline *et al.* (1967). In essence, the hairpin vortex packets can be viewed as streamwise-aligned low-velocity streaks, that are straddled by multiple vortices. Consequently, this theory also supports the creation of the high-momentum regions, as the fluid outboard of the hairpin vortices is swept down toward the wall. Experimental evidence for this behavior was provided by Acarlar & Smith (1987a) and Acarlar & Smith (1987b). When dye was injected into a laminar boundary layer, the interaction between the injected fluid and the boundary layer shear caused the fluid to roll-up into a single hairpin vortex. Additionally, the passage of the vortex created a low-speed streak, suggesting that hairpin vortices may contribute to the creation of the streamwise-oriented streaks.

The behavior of the turbulent structures within an incompressible boundary layer has received considerable attention, as stated above. However, the technical challenge of experimentally probing compressible boundary layers has severely limited the available data in this regime. Neglecting flow visualization studies, the most notable example of the turbulent structure in a supersonic flowfield is the Mach 2 tomographic PIV study of Elsinga *et al.* (2010). They show excellent agreement with the incompressible studies listed above, including the streamwise-alignment of vortices, as well as the characteristic growth angle of the packets. The current study aims to extend these findings, by examining the effects of large wall-normal density gradients (approximately 3 times larger than observed by Elsinga *et al.* (2010)) upon the turbulence structure.

2.1.2. Nomenclature of Coherent Structures

Recalling §1.4, the objective of this study is to explain the behavior of mechanically distorted TBLs, through the examination of the turbulent structures within the boundary

layer. However, the definition of a "turbulent structure" is rather vague, denoting an entire hierarchy of motions, spanning a wide range of length and time scales. Before continuing with the discussion of this study in the following sections, it is imperative that the nomenclature be clarified, so that the reader can appreciate the relative contributions of the analysis methods described herein (§4.4 and §5). In this paper, the following naming conventions will be used: "large-scale motions/structures" and "vortices." *Large-scale motions/structures* refer to motions with scales greater than $\mathcal{O}(0.1\delta)$, and identified as "correlated mass(es) of fluid" (Arnette, Samimy & Elliott 1995). Therefore, two-point correlations will be the primary means of detection for these motions. From the overview provided in previous sections, it is apparent that these large-scale structures are similar to, if not synonymous with, the hairpin packets proposed by Adrian *et al.* (2000). The *vortices* that constitute these *large-scale structures* manifest themselves in the current study as regions of spiraling fluid in a reference frame that is convecting with the flow. Therefore, the vortices detected in this study correspond to the "heads" of hairpins, along with detached vortices in the outer region. However, the description of a vortex is unclear, and often varies with the detection scheme being implemented. This dilemma has been the subject of much research, including Jeong & Hussain (1995), Chakraborty, Balachandar & Adrian (2005), and Haller (2005). An overview of vortex identification techniques is provided in §5, along with a description of the method employed in this study. Before continuing, the reader is cautioned that the above nomenclature of *large-scale structures* and *vortices* may not be entirely consistent within existing literature, owing to the constantly evolving paradigm of organized motions within turbulent boundary layers.

2.2. Favorable Pressure Gradient Effects

The following overview of favorable pressure gradient (FPG) effects in turbulent boundary layers will focus primarily on highly compressible (i.e. supersonic) flowfields. While the inclusion of incompressible boundary layers in this review would provide a

more comprehensive summary, any comparisons to incompressible FPG flowfields may be inappropriate. The underlying mechanisms that govern the response of supersonic boundary layers to FPGs, such as expansion fans and bulk dilatation, are not found within their incompressible counterparts. Indeed, even the change in boundary layer thickness is strongly dependent upon the compressible nature of the flow. For these reasons, only compressible boundary layers will be reviewed below. Additionally, the discussion will focus upon the physical mechanisms governing the evolution of the turbulent structure through a favorable pressure gradient. For an overview of recent experimental studies into the effects of FPGs upon high-speed turbulent boundary layers, see §1.2.2.

Before addressing the physical mechanisms by which the pressure gradients affect the flowfield, it is important to discuss how the FPGs are characterized. In an effort to reconcile the discrepancies observed in the defect velocity plots when comparing boundary layers of varying pressure gradients, Clauser suggested that the effect of the pressure gradient be described as

$$\beta = \left(\frac{\delta^*}{\tau_w} \right) \left(\frac{dp}{dx} \right) \tag{2.1}$$

where δ^* is the displacement thickness, τ_w is the wall shear stress, and dp/dx is the streamwise pressure gradient. For boundary layers of similar β values, the defect scaling should show good agreement. An additional means of describing the pressure gradient strength was provided by Bradshaw (1974), who suggested that the ratio of the "extra strain rates" generated by the distortion and the "primary strain rate" of the boundary layer (i.e. dU/dy) be described as the distortion parameter $d = e / (dU/dy)$, where e comprises the extra strain rates. For values $d < 0.01$, the distortion is considered mild, while strong distortions exist when $d \geq 0.1$.

Smits & Wood (1985) noted that if the extra strain rates of the flow distortion are imposed over a time frame comparable to the lifetime of the large eddies, then the flow

will experience the distortion as an impulse. Thus, the effect of the distortion could best be described as the integral of the extra strain rates in time

$$I = \int e dt \tag{2.2}$$

In compressible flowfields, pressure gradient effects do not typically act in isolation, and are generally accompanied by wall curvature effects. If the extra strain rates generated by each of these distortion types is known, then it is possible to determine their relative contributions from Eqn. 2.2. Thomann (1968) showed that the effects of wall curvature upon the turbulent fluctuations are first-order, thus $I = \Delta\varphi$ for wall curvature, where $\Delta\varphi$ is the local turning angle in radians. For bulk dilatation, $I = (1/\gamma)(p_2/p_1)$, where γ is the ratio of specific heats (= 1.4 in air), and p_2/p_1 is the ratio between the downstream and undistorted surface pressures [Hayakawa, Smits & Bogdonoff (1984)]. Unfortunately, the interaction between wall curvature and bulk dilatation is likely non-linear, and thus a direct comparison of the relevant impulse parameters may not fully describe the behavior of the flowfield

For both incompressible and compressible boundary layers, the stabilizing effects of FPGs are well-known. However, the exact mechanisms by which the turbulence is reduced remains an active area of research. For a compressible boundary layer subjected to a convex curvature, the flow is subjected to several processes not present within the undistorted boundary layer: streamline curvature ($\partial V/\partial X < 0$), favorable streamwise pressure gradient ($\partial p/\partial X < 0$), wall-normal pressure gradient ($\partial p/\partial Y < 0$), and bulk dilatation ($\nabla \cdot \vec{V} > 0$), where the positions {X,Y} are in wind tunnel coordinates.

The majority of the insight into compressible FPG effects originates with the work of Bradshaw (1974), who noted that modification of the Reynolds stresses is an order of magnitude higher than predicted by the terms in the Reynolds stress transport equation that explicitly contain the extra strain rates. Bradshaw (1974) developed a simple physical model to describe the flow stabilization, attributing the majority of the FPG effects to bulk dilatation. When a supersonic boundary layer is subjected to a favorable

pressure gradient, the decreased density of the flowfield leads to an increased boundary layer thickness, due to the conservation of mass within the boundary layer [Spina, Smits & Robinson (1994)]. Bradshaw (1974) suggested that if the turbulent fluctuations within the turbulent boundary layer are represented by large rotating "eddies", then the bulk dilatation within the expanding boundary layer would necessarily lead to an increase in scale for these structures. Conservation of angular momentum would cause the now-larger eddies to rotate more slowly, hence decreasing the turbulent fluctuations within the boundary layer (see Fig. 2.4). Therefore, Bradshaw (1974) suggested that bulk dilatation is the primary mechanism by which the turbulence is reduced in expanding compressible boundary layers. This view has been supported by the rapid distortion analysis of Dussauge & Gaviglio (1987). Additionally, Arnette *et al.* (1998) used the vorticity transport equation to show that in the absence of baroclinic torque (which is generally negligible in the outer region of a compressible boundary layer), the Reynolds stress reduction can be attributed to the stabilizing influence of bulk dilatation.

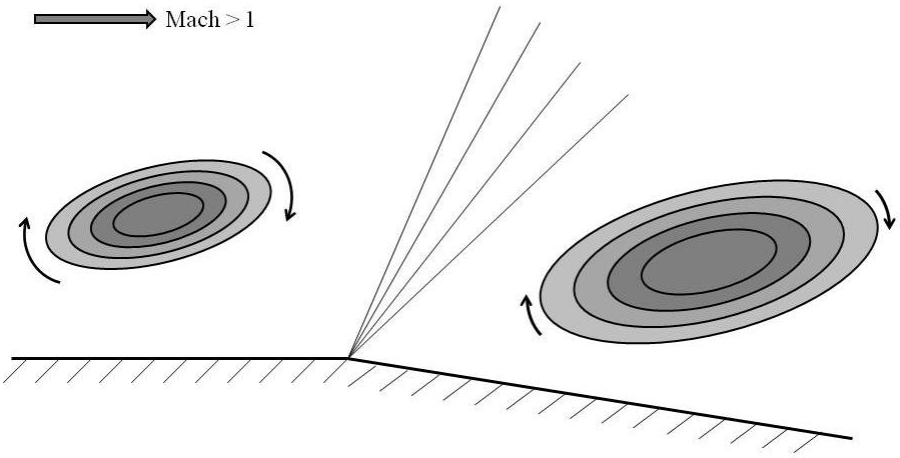

Figure 2.4 Graphical representation of the effect of bulk dilatation upon the large-scale structures

While the physical model of Bradshaw (1974) is logical and intuitive, recent experimental evidence suggests that bulk dilatation may not be the primary mechanism governing the stress reduction. Two-point correlations by Tichenor *et al.* (2013) have shown that the large-scale motions do not necessarily increase in scale with the boundary layer thickness. A similar behavior was observed by Arnette *et al.* (1995), though this is not explicitly stated in their conclusions. More recently, Humble, Peltier & Bowersox (2012) visualized the outer layer of an expanding flow using condensate-enhanced Rayleigh scattering. Correlations of the outer region structures suggested that the dimensional size of the eddies was unchanged by the FPG, while the non-dimensional size decreased. Additionally, they used fractal analysis to suggest that the stress reduction in the outer layer is due to a quenching of the small-scale structures (Fig. 2.5).

At present, there is no existing physical model that definitively describes the evolution of a compressible boundary layer through a favorable pressure gradient. This gap in the scientific literature will be addressed by the analyses in §7.

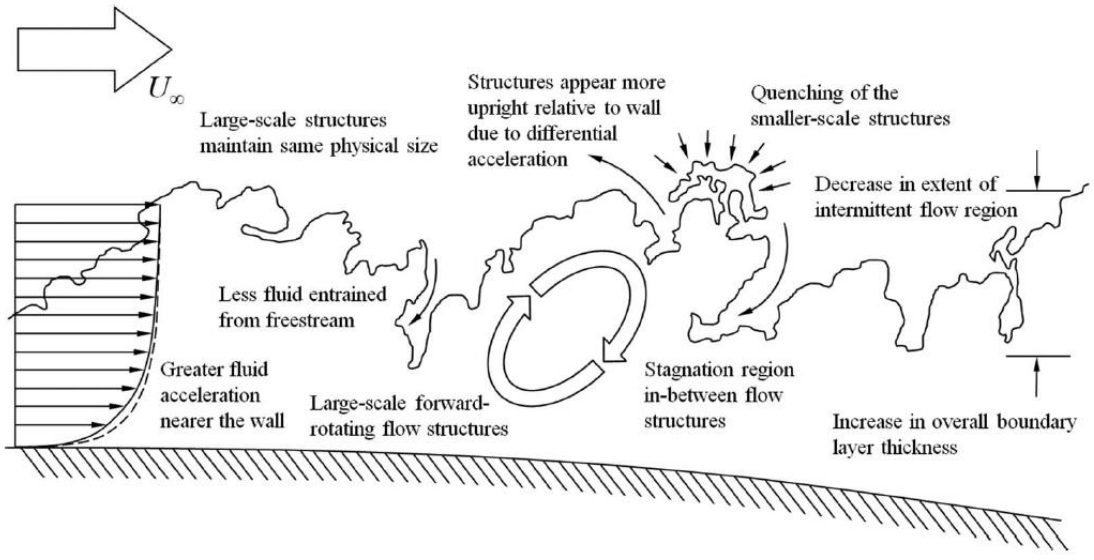

Figure 2.5 Summary of the effects of favorable pressure gradient and convex curvature upon the turbulence structure. *Note the quenching of the small-scale structures at the boundary layer edge.* Taken from Humble *et al.* (2012).

2.3. Surface Roughness Effects

Given the large number of parameters describing a rough-wall boundary layer (roughness height, roughness Reynolds number, solidity, flow compressibility), it is difficult to present a generic model of the relevant boundary layer motions over an arbitrarily rough surface. Instead, the following summary will highlight key findings of past studies, emphasizing the general trends observed within rough-wall flows. Where possible, the discussion will be confined to the effects of surface roughness within compressible boundary layers. For a discussion of recent experimental studies into roughness effects in high-speed boundary layers, the reader is directed to §1.2.1.

2.3.1. Classical Scaling Laws

Beginning with the work of Nikuradse (1933), incompressible rough-wall boundary layers have been the subject of numerous studies [see Perry *et al.* (1987); Perry *et al.* (1969); Grass (1971); Raupach (1991); Krogstad & Antonia (1994); Jiménez (2004)]. However, high-speed rough-wall flows have received considerably less attention [see Bowersox (2007) for a recent review], due to the associated technical challenges of probing highly compressible flowfields. The available database of rough-wall experimental data in high-speed turbulent boundary layers is shown in Table 2.1, covering a Mach number range of 0.7 to 8.1. Unfortunately, only four studies (including this dissertation) exist that have addressed the turbulent response of the boundary layer. It is this lack of experimental data that has prompted the current study.

The effects of roughness on the boundary layer can be described by the roughness Reynolds number

$$k^+ = \frac{k u_\tau}{\upsilon_w} \tag{2.3}$$

where k is the roughness height, u_τ is the friction velocity, and ν_w is the dynamic viscosity at the wall. High values of k^+ are considered to have a large effect upon the buffer layer, potentially disrupting the near-wall turbulence production cycle [Jiménez (2004)]. Therefore, classification of the roughness effect is determined by the value of k^+. For $k^+ < 5$, the roughness elements reside wholly within the viscous sublayer, and have no appreciable effect upon the boundary layer. This case is described as *hydraulically smooth*. Conversely, the frictional losses due to the roughness are independent of viscosity when $k^+ > 70$; this region is labeled *fully rough*. The flows that fall within the range $5 < k^+ < 70$ are considered *transitionally rough*, in that the flow properties are a function of both the viscosity and roughness height.

Table 2.1 Representative sample of available high-speed rough-wall data [adapted from Bowersox (2007)]

Authors (date)	*Mach*	k_s^+	k/δ	*Topology*	*Meas.*
Wade (1955)[a]	**2.5**	**10–40**	**NA[b]**	**v-Groove**	**Mean**
Goddard (1959)	**0.7–4.5**	**10–1000**	**0.02 – 0.07[b]**	**Sand**	**Mean**
Young (1965)[a]	**4.9**	**7–40**	**NA[b]**	**v-Groove**	**Mean**
Mann (1967)[a]	**4.9**	**10–150**	**NA[b]**	**v-Groove**	**Mean**
Reda, Fan & Ketter (1975)	**2.9**	**10–200**	**0.01 – 0.04[c]**	**Sand/Grooves**	**Mean**
Berg (1979)	**6.0**	**10–45**	**0.02 – 0.06[c]**	**Bars**	**Mean**
Hill, Voisinet & Wagner (1980)	**8.1[d]**	**163**	**0.06[e]**	**Sand Grain**	**Surface**
Holden (1984); Holden (1989)	**2.0–8.0[d]**	**20-1800**	**NA**	**Sand/Spheres**	**Surface**
Latin & Bowersox (2000, 2002)	**2.7**	**100–570**	**0.03 – 0.05**	**Sand/Bars/Squares**	**Mean/Turb**
Ekoto et al (2009)	**2.87**	**50-100**	**0.05 – 0.07**	**Squares/Diamonds**	**Mean/Turb**
Sahoo et al (2010)	**7.3**	**37 – 154[f]**	**0.06 – 0.16**	**Squares/Diamonds**	**Mean/Turb**
Present	**4.9**	**600**	**0.07**	**Diamond**	**Mean/Turb**

[a]As reported in Reda *et al*; [b]Original Reports were not available at the time of this writing; [c]Estimated from available plots in the original reports; [d]These are the local Mach numbers. The free stream Mach numbers were higher. For both studies, $T_w/T_{t\infty} \approx$ 0.2-0.3.[e]Only test condition with tabulated data. [f]Values given for k^+.

Nikuradse (1933) found that the only effect of roughness on the mean velocity is a vertical downward shift of the logarithmic region, and that this shift is a function of k^+. The resulting velocity profile for a rough-wall flow is

$$u^+ = \frac{1}{\kappa}\ln(y^+) + B - \Delta U^+(k^+) \tag{2.4}$$

where κ is the von Karman constant (= 0.41), B is the intercept of the profile (≈ 5.1 – 5.5), and ΔU^+ is the Clauser roughness function. In an effort to compare to Nikuradse's experimental data over sand-grain roughness, Schlichting (1955) formulated the equivalent sand-grain roughness, k_s. This parameter is intended to relate any surface roughness topology to the equivalent Nikuradse sand-grain roughness. The procedure for determining k_s is described below.

Nikuradse (1933) found that the roughness function ΔU^+ followed a logarithmic trend, given as

$$\Delta U^+ = \frac{1}{\kappa}\ln(k^+) + C \tag{2.5}$$

Substituting Eqn. 2.5 into Eqn. 2.4 yields

$$u^+ = \frac{1}{\kappa}\ln\left(\frac{y}{k}\right) + B - C \tag{2.6}$$

From his sand-grain roughness experiments, Nikuradse (1933) found that

$$u^+ = \frac{1}{\kappa}\ln\left(\frac{y}{k_s}\right) + 8.5 \tag{2.7}$$

Subtracting Eqn. 2.6 from Eqn. 2.7 yields

$$\frac{1}{\kappa}\ln\left(\frac{k_s}{k}\right) = 8.5 - B + C \tag{2.8}$$

Therefore, k_s can be solved as

$$k_s = k \cdot \exp\left[\kappa\left(8.5 - B + C\right)\right] \tag{2.9}$$

Unfortunately, Eqn. 2.9 shows that k_s can not be calculated *a priori*. It is necessary to first find C, which requires that the velocity profile be known, in order to estimate ΔU^+. Additionally, it has been suggested that k_s is inadequate for fully characterizing the effects of a given roughness geometry [Perry *et al.* (1969)]. This objection seems logical, considering that we are attempting to consolidate a large number of geometric factors (roughness height, orientation, frontal area, solidity, spacing) into a single numerical value.

In response to the difficulty of using k_s^+ as the sole description for a given roughness geometry, Perry *et al.* (1969) defined two canonical roughness topologies: '*d*-type' and '*k*-type.' Roughness patterns exhibiting 'd-type' behavior generally have a roughness spacing of $w/k < 3$, where w is the spacing between the roughness elements and k is the roughness height. A densely packed topology will trap vortices in the cavities, effectively 'shielding' the elements from the flow. The equivalent sand-grain roughness of a 'd-type' pattern is proportional to the boundary layer height δ. In contrast, a '*k*-type' topology has a roughness spacing of $w/k > 3$, allowing any vortices formed in the cavity to be shed downstream. This exposes the elements to the bulk of the flow; the equivalent sand-grain roughness is proportional to the roughness height k.

2.3.2. Compressibility Effects

The effects of compressibility on the turbulent boundary layer's response to surface roughness introduce additional complicating factors, due to the existence of nonisentropic features, such as shock waves and expansion fans. Despite these features, it has been shown by Goddard (1959) that the vertical shift of the streamwise velocity profile follows the incompressible form, when the van Driest II transformation is used. Additionally, Liepmann & Goddard (1957) suggested that the skin friction over a rough surface at high Mach numbers is primarily due to the form drag on the roughness elements. Therefore, they were able to show that the ratio between the incompressible

and compressible skin friction coefficients is due to the density ratio across the boundary layer.

The availability of experimental turbulence data in a rough-wall compressible boundary layer is extremely limited, as seen in Table 2.1. Additionally, the presence of roughness-generated shock waves greatly complicates any comparisons with incompressible data. Indeed, if the waves produced by the elements play a pivotal role in determining the turbulent response, then this naturally suggests that compressible flowfields may be more sensitive than their incompressible counterparts to the roughness geometry, further invalidating the use of k_s. An example of this response was seen by Ekoto *et al.* (2009) at Mach 2.87. Schlieren imaging showed that square roughness elements produced only weak waves, most likely due to the 'd-type' nature of the roughness. Consequently, the turbulence levels showed good agreement with the smooth-wall values, when Morkovin scaling was applied. In contrast, a repeating pattern of diamond roughness elements generated significant distortions across the entire boundary layer thickness, and did not collapse onto the smooth-wall data, even though the roughness height was equal for the square and diamond elements..

Given the dramatic changes observed in the presence of surface roughness, it would seem intuitive to suggest that the near-wall cycle of turbulence production (i.e. sweeps, ejections, bursting, etc.) is completely disrupted in a fully rough flow. However, Grass (1971) showed that in an incompressible rough-wall boundary layer, the effects of roughness on the Reynolds stress-producing motions is primarily confined to the physical mechanisms governing the sweeps and ejections, and that these motions still exist in a rough-wall flow. Grass (1971) suggested that the similar motions between smooth and rough surfaces may be due to the near-wall behavior, in which "the smooth boundary viscous sublayer fluid and the fluid trapped between the roughness elements simply forms a 'passive' reservoir of low momentum fluid which is drawn on during ejection phases." Therefore, while the fluid very near the wall may be disrupted, the motions that draw upon this fluid to generate the Reynolds stresses are likely unaffected.

In the current study, we wish to determine if this similarity holds true in the presence of a mean density gradient (i.e. a compressible boundary layer).

3. EXPERIMENTAL FACILITIES & HARDWARE

All experiments in the current study were performed in a Mach 5 blow-down wind tunnel, located within the National Aerothermochemistry Laboratory (NAL) at Texas A&M University. This section will begin with a brief description of the NAL complex, emphasizing the laboratory mission and capabilities. Following this overview, the supersonic wind tunnel used in the current study will be described. Lastly, the design and installation of the experimental models will be discussed.

3.1. NAL Laboratory Complex

The NAL is an interdisciplinary facility, jointly operated by the Departments of Aerospace Engineering and Chemistry. The mission of the laboratory is to investigate the behavior of high-speed (Mach > 3) shear layers and boundary layers, with a particular focus upon the effects of mechanical and thermal non-equilibrium. A secondary objective of the NAL is the development of novel supersonic and hypersonic experimental facilities, as evidenced by the wide array of wind tunnels available to the research staff. A summary of the facilities is given below, excepting the wind tunnel used in this study, which will be discussed in §3.2.

1) **Actively Controlled Expansion (ACE) Tunnel** (Semper *et al.* 2009; Tichenor *et al.* 2010) **:** The ACE tunnel is a hypersonic blow-down facility, capable of producing Mach 5 – 7 flow during a 50-second runtime. This Mach number-variability is achieved by actuating the two-dimensional nozzle planes at the throat contraction, while maintaining a constant exit area. The resulting flow is uniform (to within 0.5% of the exit Mach number) across the majority of the exit plane (Semper, Pruski & Bowersox 2012). Current experiments within this facility aim to probe the boundary layer structure behind three-dimensional trips.

2) **Mach 6 Quiet Tunnel (M6QT)** (Hofferth, Bowersox & Saric 2010)**:** The M6QT is a low-disturbance hypersonic wind tunnel. The facility, formerly located at

NASA Langley, is a key component of the National Center for Hypersonic Laminar-Turbulent Transition Research. Recent tests by Hofferth *et al.* (2013) have utilized high-bandwidth optical measurements to investigate the second-mode instabilities over a flared cone.

3) **Repetitively Pulse Hypersonic Test Facility** (Sanchez-Gonzales *et al.* 2012)**:** In order to support the mission of the laboratory, a hypersonic test facility was established for diagnostic development. The test cell has been instrumental in the development of the VENOM (vibrationally excited NO monitoring) technique, which is capable of simultaneous two-dimensional measurements of both velocity and static temperature (Sanchez-Gonzales *et al.* 2011).

4) **Hypersonic Shock Tunnel:** A hypersonic shock tunnel is currently being installed within the Impulse Lab wing of the NAL. While most facilities within the laboratory operate under "cold" conditions, the shock tunnel is able to achieve the high enthalpies (0.5 – 4.5 MJ/kg) encountered by hypersonic vehicles. Future tests will use molecular tagging velocimetry (MTV) for characterization of the freestream turbulence levels.

3.2. Experimental Facility

The facility used in this study is a supersonic blow-down wind tunnel, currently configured for Mach 5 flow (see Fig. 3.1). Interchangeable nozzles allow for experiments at Mach 2.2 and Mach 3, but were not used in this study. The wind tunnel was constructed in 2003-2004 by Isaac Ekoto, and was the first facility established within the NAL. The purpose of this wind tunnel is to enable high-fidelity nonintrusive measurements of compressible turbulent boundary layers at moderate Reynolds numbers ($Re/m \approx 5 \times 10^7$). An overview of the tunnel components and infrastructure is given below. For a detailed description of the tunnel design and construction, see Ekoto (2006).

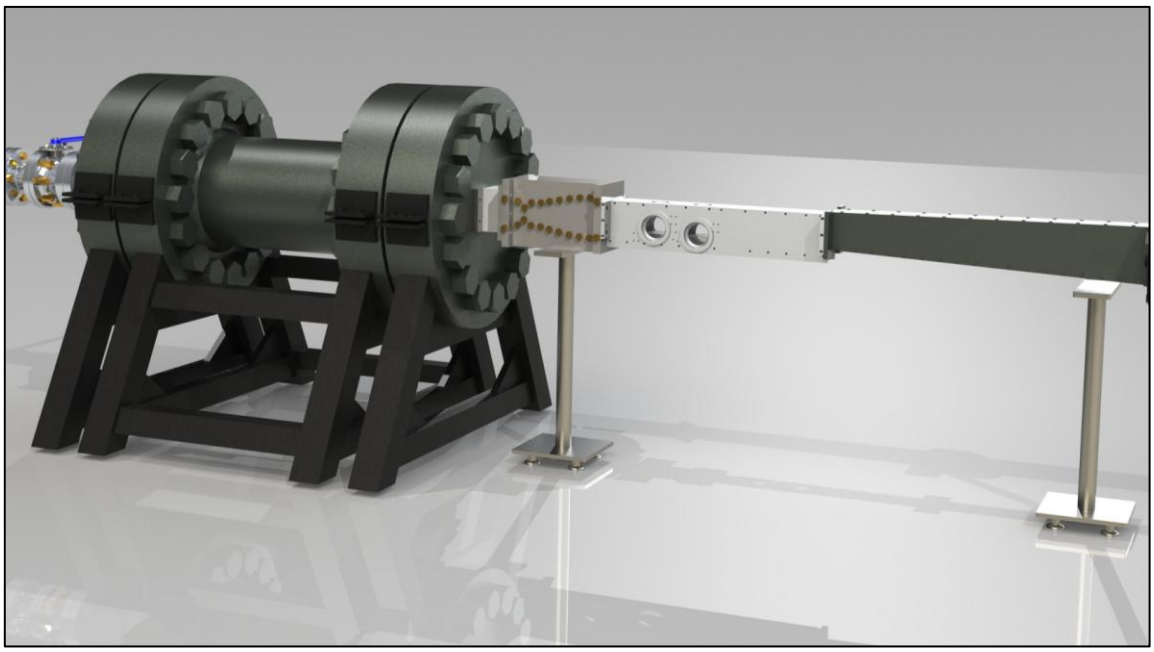

Figure 3.1 Supersonic wind tunnel used in the current study, *depicting the settling chamber, nozzle, test section, and diffuser (from left to right). Flow enters from the left.*

3.2.1. Air Supply

All facilities within the NAL complex share a common air supply infrastructure. High-pressure air was provided by two Chicago Pneumatic reciprocating compressors, supplying a combined mass flow rate of 0.25 kg/s at 15.5 MPa. Before the fluid was stored for future use, it was necessary to remove moisture and particulates from the air stream. An after-cooler downstream of the compressors was used to reduce the air temperature by approximately 10 – 15 degrees Celsius. The resulting water condensate, along with oil droplets from the compressors, was removed through an in-line cyclone separator. Two cartridge filters further reduced the contaminants within the air supply. The cleaned air was then passed through a Donaldson regenerative air dryer. Desiccant within the dryer absorbed a majority of the remaining water content, reducing the dew point to approximately 238 K at 1 atmosphere. This represents a volumetric water

concentration of ~ 200 parts per million. The processed air was then stored in a 23.3 m^3 air tank. During tunnel operation, air was passed through a 500 kW Chromalox in-line heater, before entering the laboratory. Heating the fluid is necessary to prevent oxygen condensation as the air is expanded through the supersonic nozzle.

3.2.2. Settling Chamber

The settling chamber is necessary to remove upstream perturbations induced by the infrastructure, thereby improving the flow uniformity within the wind tunnel. These disturbances include fluctuations created by the fluid negotiating through the heater and ball valves, along with the growth of the subsonic boundary layer within the upstream piping. The settling chamber is designed to dampen these perturbations, providing a uniform flow to the supersonic nozzle.

The shell of the settling chamber is constructed from 14" schedule 160 steel pipe, with a length of 36 inches (91.44 cm) and a wall thickness of 1.4 inches (3.57 cm). For the current operating conditions described in §3.7, this yielded a factor-of-safety greater than 10. Incoming air passed through a perforated 12.7 cm diameter cylinder, aligned coaxially with the vessel. This was designed to reduce the nonuniformities across the flow profile, such as those created by the presence of upstream boundary layers, by redistributing the fluid more evenly across the air stream. The flow was then straightened through a reverse cone, containing 225 holes evenly spaced along the surface. This design has the benefit of minimizing the pressure drop, while further spreading the flow (Pope & Goin 1965). Turbulent fluctuations, including those created by the perforated cylinder and reverse cone flow spreaders, are reduced by three wire mesh screens, each with a solidity of 45%. The resulting uniform flow exited the settling chamber through a 3 inch (7.62 cm) square port.

3.2.3. Supersonic Nozzle

The two-dimensional supersonic nozzle used in the current tunnel configuration was designed and constructed by Tilmann, Bowersox & Buter (1999), and is capable of producing a uniform Mach 4.9 flow. A welded contraction section was positioned between the settling chamber and nozzle, reducing the duct height from 7.62 cm to 3.81 cm over a distance of 22.9 cm (9 inches). This was necessary in order to correctly interface with the nozzle inlet, which was 7.62 cm wide by 3.81 cm high. The original design called for Mach 5.0 flow through an exit area measuring 7.62 cm by 7.62 cm, yielding a throat height of 0.305 cm (0.12 inches). The measured Mach 4.9 output was believed to be due to viscous losses along the nozzle sidewalls.

The symmetric nozzle contours, shown in Fig. 3.2, were designed by Tilmann *et al.* (1999) using the method of characteristics. The zero-radius throat required in a minimum length nozzle was replaced by a parabolic finite radius, reducing the probability of flow separation within the nozzle throat. Two centerline and wall expansion wave reflections were allowed, so that the turning angle was reduced directly downstream of the throat. Viscous losses were estimated by assuming turbulent boundary layers along the entire nozzle length, and calculating the displacement thickness δ^* as a function of local Reynolds number. However, Pitot pressure measurements by Tilmann *et al.* (1999) at the exit plane indicated a Mach number of 4.87 over a majority of the core flow. This discrepancy was believed to be due to viscous losses along the sidewalls, which were not included in the correction described previously.

The flow uniformity of the nozzle exit was evaluated by Tilmann *et al.* (1999), using a traversing Pitot probe. Measurements 3.8 cm downstream of the nozzle exit indicated approximately uniform flow across the center 80% of the exit plane, in agreement with three-dimensional simulations using the Baldwin-Lomax and k-ε turbulence models. The Pitot data suggested that a boundary layer approximately 8 – 10 mm thick had formed at the nozzle exit.

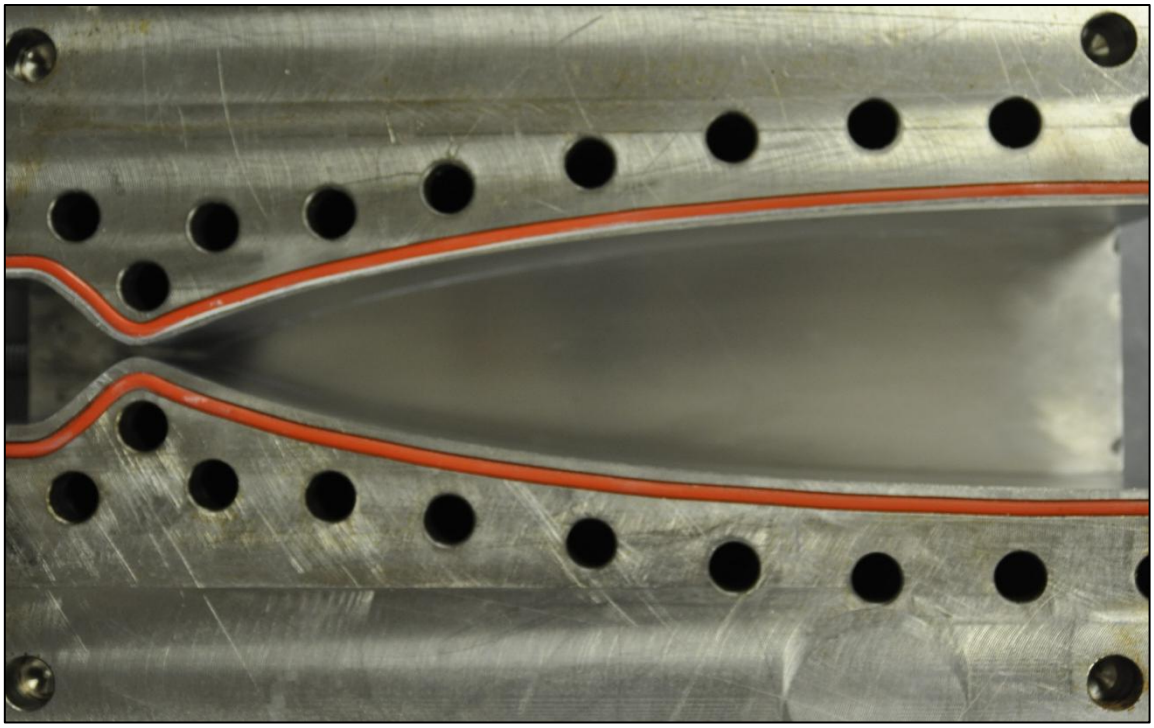

Figure 3.2 Contours of the Mach 4.9 nozzle used in the current study. *Flow is from left to right.*

3.2.4. Test Section

The test section used in the current study was designed to facilitate the use of nonintrusive optical diagnostics, by providing ample optical access to the 7.62 cm by 7.62 cm constant-area duct. The test section sidewalls and ceiling are machined from aluminum, with window ports placed 15.9 cm and 29.8 cm downstream of the nozzle exit (only the downstream measurement location is used in the current study). The top windows are 1.91 cm-thick fused silica, with 45 degree beveled edges to allow for flush alignment with the tunnel ceiling. Window ports are located in both sidewalls, providing a clear optical path across the span of the test section. The 7.62 cm-diameter side windows are contained within removable frames, and are flush with the interior of the test section. Figure 3.3 shows the test section, including an exploded view of the side window frame.

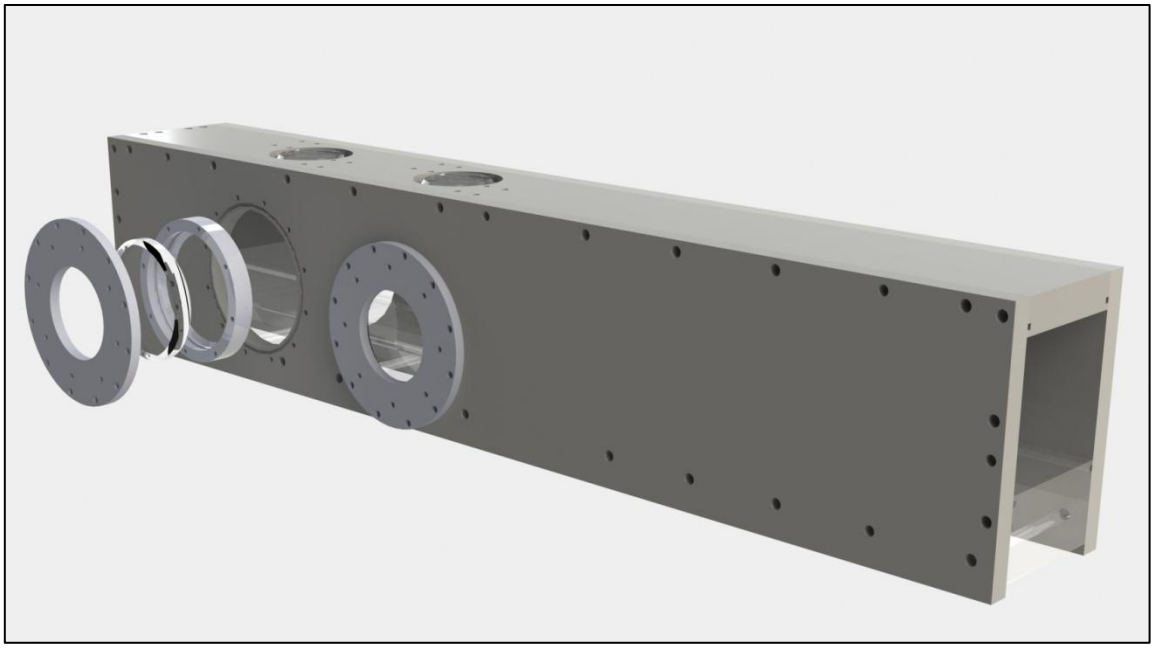

Figure 3.3 Test section assembly, with an exploded view of the side window frame. *Flow is from left to right.*

The floor of the test section is interchangeable between runs, allowing the experimental models (described further in §3.3) cover the entire 71.1 cm (28 inch) length of the test section. This enables the flow to establish a fully developed boundary layer over the prescribed surface topology, prior to the upstream measurement location. In order to ensure proper alignment with the nozzle floor during model installation, alignment pins are placed along the length of the test section.

3.2.5. Diffuser

In order to minimize the settling chamber pressure necessary to start the tunnel, a variable-area diffuser is attached to the downstream end of the test section. Shown in Fig. 3.4, the throat area is easily adjusted between runs, through the use of five threaded rods along the upper surface of the diffuser. This variability is necessary to account for

the increased Mach number caused by the flow acceleration over the pressure gradient models (described in §3.3.1). Static pressure ports are arrayed along the sidewall of the diffuser, allowing the tunnel operator to monitor the location of the shock system within the diffuser.

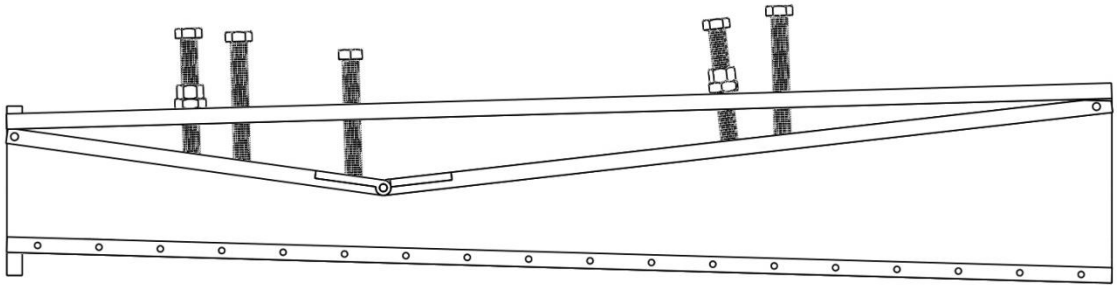

Figure 3.4 Cross-section of the diffuser geometry. *Flow is from left to right.*

3.2.6. Exhaust Muffler

During the initial tests of the wind tunnel, the test gas was exhausted directly to the atmosphere. However, sound measurements at the tunnel outlet showed noise levels of approximately 130 dB, decreasing to ~ 100 dB at distances of 20 – 30 feet from the exhaust pipe. By comparison, the noise from a commercial airliner is 125 dB at a distance of 100 meters. These noise levels were dangerously close to the peak sound level of 140 dB allowed by OSHA (Occupational Safety and Health Administration), and well above the 90 dB limit at which hearing protection is required (OSHA 1926.52). To ensure the safety of the research staff, an Allied Witan model M60 muffler was installed at the tunnel exhaust. The resultant noise level was approximately 90 – 100 dB at the exhaust, and dropped below the OSHA-regulated limit at a distance of only five feet. This was achieved by passing the exhaust air through a perforated steel plate, before exiting through four cylindrical cellulose filters. However, this geometry created

a large pressure drop within the system, requiring the tunnel operating pressure to be increased to unsafe levels in order to maintain choked flow.

The Allied Witan muffler was replaced with a high-flow, low pressure-drop muffler from Vanec. The new muffler subsonically expanded the flow through a plenum section lined with perforated steel plating and acoustically insulating material. The noise level was comparable to the previous model, but with a negligible manufacturer-quoted back-pressure of approximately 0.1 psi.

3.2.7. Tunnel Monitoring and Operating Conditions

Tunnel conditions were monitored in both the settling chamber and test section. The total temperature was measured using an Omega JQSS thermocouple inserted into the settling chamber, and amplified through an OMNI AMP-IV amplifier. An Endevco Model 8540 0-3048 kPa high-temperature pressure transducer (± 0.75% full-scale accuracy) was attached to a pitot probe in the settling chamber to monitor the total pressure. Static pressure within the test section was monitored using an MKS Series 902 0-101 kPa pressure transducer (± 1% full-scale accuracy), through a static port along the tunnel sidewall approximately 5 cm downstream of the nozzle exit plane. Signals from the thermocouple and pressure transducers were transmitted to a National Instruments SC-2345 signal conditioner block before being collected by a National Instruments 6036E data acquisition board. Tunnel conditions were recorded at 1 Hz through an in-house developed Labview program.

During all experiments, the Mach 4.9 nozzle designed by Tilmann *et al.* (1999) was installed in the tunnel, producing a uniform flow into the test section. At Mach 4.9, the compression ratio P_0 / P_s^e must be greater than approximately 18, where P_0 is the settling chamber total pressure and P_s^e is the static pressure at the tunnel exhaust (see Fig. 1.23 from Pope & Goin 1965). Since the facility exhausts to atmosphere, P_s^e is approximately equal to the atmospheric pressure, plus the back-pressure caused by the muffler. For all

test cases, the settling chamber pressure was set to approximately 340 psia (2.34 MPa). While this yielded a compression ratio of ~ 23, this was necessary to ensure the tunnel remained started during the favorable pressure gradient cases, due to the increased Mach number through the flow expansion.

As the air expands through the supersonic nozzle, both the static pressure and temperature drop dramatically. At the static pressure p_s = 4900 Pa in the test section, the components of air will liquefy at static temperatures below approximately 61 K (Fig. 1.40 of Pope & Goin 1965). Using the isentropic relation at the freestream Mach number of 4.9, this requires that the stagnation temperature be greater than ~ 354 K. The total temperature was maintained at approximately 365 K for all tests, as measured by the thermocouple mounted within the settling chamber. However, the overheat limit of the Chromalox heater forced the heating elements to cycle on and off, in order to prevent damage to the elements. This induced a long-wavelength (~ 120 seconds) oscillation in the total temperature, such that the actual value varied by ±5 K. Using the isentropic relation, this resulted in a static temperature T_s fluctuation of ±1 K. The resulting freestream velocity oscillation is ±6 m/s. It will be shown in §4.2 that this value is below the uncertainty of the mean velocity. Therefore, the heater oscillation was considered to have a negligible effect upon the measured data. In reality, the fluctuations described above were a worst-case scenario, since the PIV data was recorded only during intervals in which the temperature was stable. The actual oscillations are most likely much smaller than those reported here. The nominal operating conditions are listed in Table 3.1.

Table 3.1 Nominal tunnel operating conditions

Mach number	Total temperature (K)	Total pressure (MPa)	Static pressure (Pa)	Re/m [baseline case]
4.9	365	2.34	4900	~ 4.6×10^7

3.3. Experimental Models

The experimental models were machined from optical-grade acrylic, allowing a portion of the PIV laser sheet to pass through the test section floor, thereby decreasing reflections. Each model was designed as an interchangeable tunnel floor, completely replacing the bottom component of the test section. This allowed the working fluid to develop over a distance of approximately 28 cm, before reaching the downstream window location (see Fig. 3.3), where all measurements were collected. For all models, the x, y, and z coordinates describe the streamwise, wall-normal, and spanwise directions, respectively. The corresponding velocity components are given by u, v, and w. The coordinate system origin is arranged such that $(x, y) = (0, 0)$ is located at the upstream edge of the measurement window, which is centered 29.8 cm downstream of the nozzle.

Two types of models were used in the current study, corresponding to the two mechanical distortions under investigation, namely periodic surface roughness and curvature-driven favorable pressure gradients. Additionally, a flat-plate smooth-wall model was created as a baseline case. The model parameters for the rough-wall and FPGs topologies are given below in §3.3.1 and §3.3.2, respectively. The reader should note that the model geometries used in the current study are identical to those used by Ekoto *et al.* (2009), excepting their combined roughness-FPG models. The reasoning for using these same models is given below.

3.3.1. Periodic Roughness Model

As discussed in §2, turbulence stresses measured over sand-grain and *d-type* roughness topologies appear to collapse onto incompressible data, when scaled by the local density ratio (Latin & Bowersox 2000; Ekoto *et al.* 2009). However, this scaling does not hold when the roughness elements protrude above the local sonic line, generating distortions that penetrate through the entire thickness of the boundary layer. Figure 7b of Ekoto *et*

al. (2009) illustrates these distortions, through the use of schlieren photography. Their results suggest that the reduced kinematic shear stress over the diamond elements, compared to *d-type* square elements, is due to the localized pressure gradients induced by the shock waves and expansion fans. It is still unclear how the boundary layer structures respond to the rapid succession of localized pressure gradients, alternating in sign. The rough-wall models used in this study were designed to produce roughness-induced shock waves and expansions, corresponding to the distortions observed by Latin & Bowersox (2000) and Ekoto *et al.* (2009), so that these mechanisms may be studied in greater detail.

The periodic roughness array in this study is identical to that used by Ekoto *et al.* (2009), yielding a similar k/δ value of 0.07. This allows the current data to be more easily compared with known literature. The roughness topology consists of closely packed diamond elements, with the long axis aligned in the streamwise direction, and a 10° half-angle. The elements were machined from an acrylic block using a 1.59 mm (1/16 in.) diameter ball end mall, producing elements 1.59 mm wide by 9.0 mm long (measured at the crest of the elements). The ball end mill produced elements with filleted edges, such that the element width varies from 1.59 mm at the crest to 3.08 mm at the base. The resulting channels between the elements are therefore hemispherical. The element height k is 0.79 mm, measured from base to crest. A schematic of the geometry is given in Fig. 3.5. The orientation of the elements, including the hemispherical channels, is shown in Fig. 3.6.

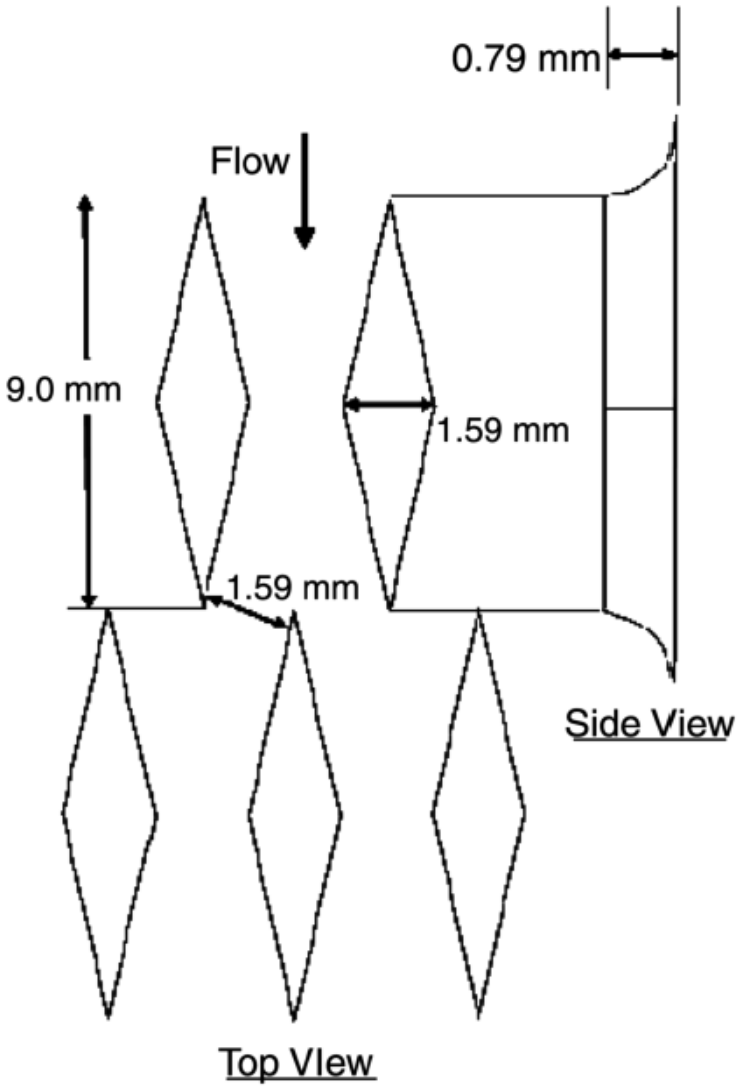

Figure 3.5 Schematic of diamond roughness topology (Ekoto *et al.* 2008)

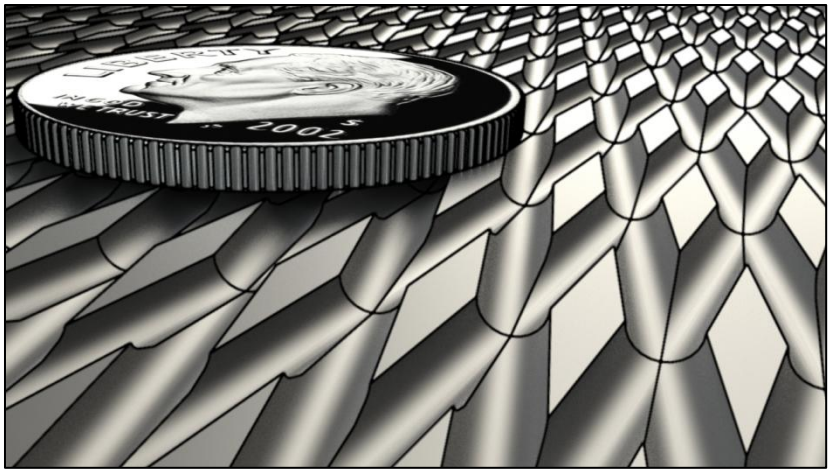

Figure 3.6 Perspective view of diamond roughness elements, looking downstream. *U.S. dime is included for scale comparison*

Upon first inspection of the roughness topology, it is expected that the flowfield will be highly three-dimensional. However, pressure sensitive paint measurements by Ekoto *et al.* (2009) have shown that the shocks and expansions generated by the elements merge near the wall, producing a periodically two-dimensional flowfield. This is supported by recent PIV data collected from the top-down viewpoint (not included in this study). In the current configuration, the PIV laser sheet is oriented along the center of the element crest (see §4.3 for further explanation of the data collection procedure).

3.3.2. Curvature-Driven Pressure Gradient Models

Three smooth-wall pressure gradients models were examined in this study: a nominally zero pressure gradient (ZPG), weak favorable pressure gradient (WPG), and strong favorable pressure gradient (SPG). These models are identical to the smooth-wall cases of Ekoto *et al.* (2009) and Tichenor *et al.* (2013). The subjective descriptors "weak" and "strong" are justified by the magnitude of the Reynolds shear stress response. Tichenor *et al.* (2013) have shown that the SPG model induces a sign reversal in the kinematic

shear stress *u'v'*, suggesting a possible reversal of the turbulent energy cascade. Indeed, it is this response that is a chief motivator for the current study.

The convex-curvature models were machined from acrylic and designed as interchangeable tunnel floors, similar to the rough-wall model. The curvature of the models was generated by the following polynomial: $Y = A(X - X_1)^3 + B(X - X_1)^2$, where Y is the transverse direction, X is the axial position measured from the nozzle exit plane, and X_1 and X_2 are the streamwise positions where the curvature begins and ends, respectively. This polynomial was applied over the domain $X_1 \leq X \leq X_2$. The polynomial constants are given in Table 3.2, and the geometry is shown in Fig. 3.7. At the measurement location X = 29.8 cm downstream of the nozzle, this results in a local wall angle of 1.7 degrees and 9.7 degrees for the WPG and SPG models, respectively. These angles were measured using a digital level, with a measurement accuracy of 0.1 degree. The corresponding radii of curvature are 183 cm and 69 cm for the WPG and SPG cases, respectively.

Table 3.2 Parameters for convex curvature

Model	A	B	X_1 (cm)	X_2 (cm)
WPG	6.423×10^{-5}	-3.757×10^{-3}	24.54	63.54
SPG	1.107×10^{-5}	-2.507×10^{-2}	24.54	39.64

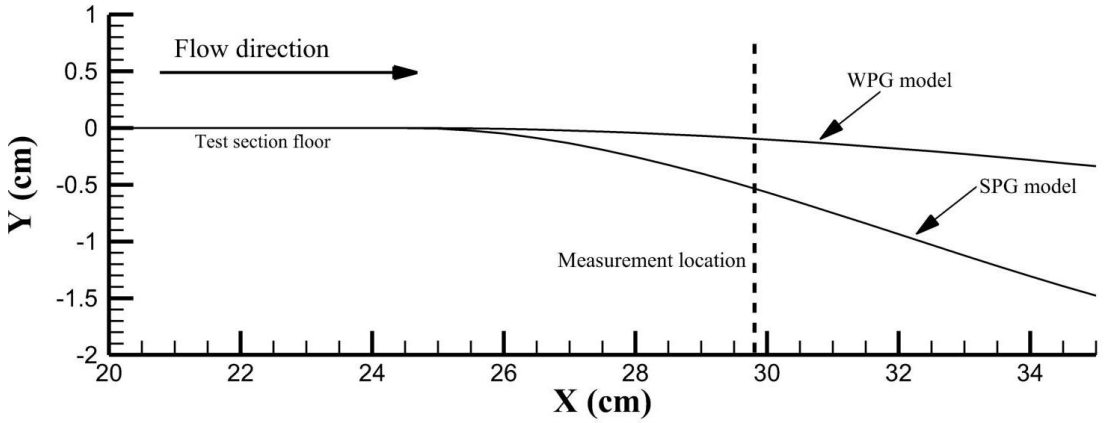

Figure 3.7 Convex curvature of favorable pressure gradient models. ZPG model not shown here

Six static pressure ports were arrayed along the length of the smooth-wall models, in order to measure the local pressure gradient (this was not possible for the rough-wall model due to the dense packing of the roughness elements). At the downstream measurement location used in this study, the pressure gradient *dp/dx* was calculated from two adjacent taps, separated by 2.9 cm. This was necessary in order to determine the Clauser pressure gradient parameter $\beta = (\delta^*/\tau_w)(dp/dx)$, described previously in §2.2. It should be noted that despite sharing the same wall curvature (and hence I_φ), only a general comparison can be made between the current smooth-wall data and the Mach 2.87 results of Ekoto *et al.* (2009). The different flow characteristics lead to different values of I_p and β, signifying a change in the contribution due to bulk dilatation.

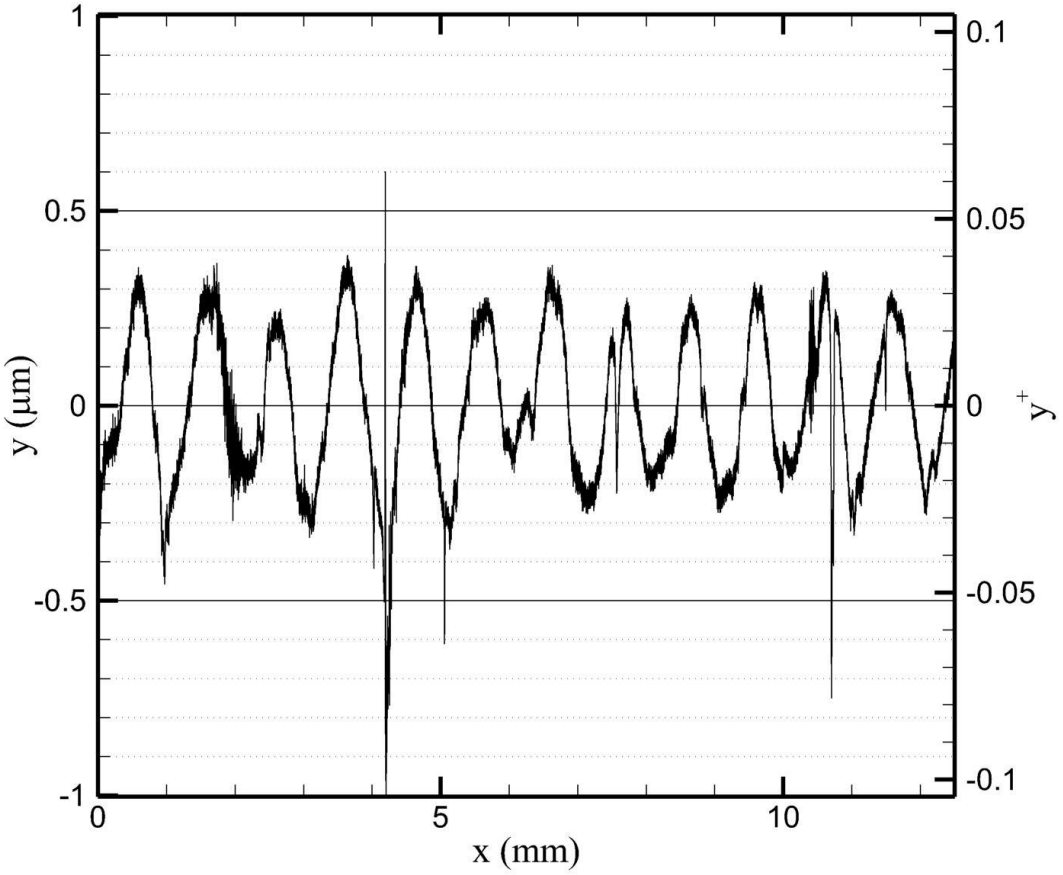

Figure 3.8 Surface roughness of smooth-wall models, *indicating that the models are hydraulically smooth. Note that* x *is measured from the upstream edge of the measurement location.*

In contrast to the periodic roughness, the convex curvature models were designed to be hydraulically smooth. This was verified through the use of a Mitutoyo Surftest SJ-400 profilometer. The measured surface profile was collected over a distance of 15 mm at the measurement location X = 29.8 cm, with a stylus tip radius of 2 μm. Figure 3.8 shows the surface roughness for the baseline ZPG case, indicating an oscillating roughness pattern with a 0.3 μm amplitude and ~ 1 mm wavelength. Scaling by viscous units, it is

clear that $k^+ << 1$, verifying that the model is indeed hydraulically smooth. This surface topology is considered representative of all smooth-wall models used in this study.

4. EXPERIMENTAL DIAGNOSTICS & ANALYSIS METHODS

Recalling the discussion of the research framework given in §1.3, a key technical contribution of this study is the creation of a database of archival-quality experimental data within distorted Mach 4.9 turbulent boundary layers. These data not only support the development and validation of high-fidelity predictive models, but also enable the higher-order analysis methods that are central to the research approach of this study. This section describes the diagnostics used in acquiring these data, focusing upon the particle image velocimetry (PIV) technique. First, a brief overview of schlieren photography is given in §4.1. The fundamental principles of PIV, including tracer particle response and vector reconstruction, are reviewed in §4.2. Section 4.3 describes the PIV experimental arrangement used in the current study, followed by a discussion of the data analysis methods in §4.4.

4.1. Schlieren Imaging

4.1.1. Schlieren Principles

The underlying principles for detecting striations (or *schliere*) in a medium were originally discovered by Robert Hooke in the mid-17th century, using his experience in optics to study the effects of density gradients upon light refraction. His early experiments lead to the first schlieren method, and provided a suitable diagnostic for studying fluid mixing and convection. Nearly 200 years later, Toepler developed the first *practical* schlieren arrangement. Using a knife-edge filter and incandescent light source, he demonstrated how temperatures differences of only 1° C could be visualized through a careful adjustment of the cut-off filter.

The physical principles underpinning these early experiments stem from the behavior of light rays as they transit a transparent medium. Within a vacuum, light travels at a constant speed of 2.99792 x 10^8 m/s, represented here by c_0. When photons encounter a transparent object, they decelerate to c, where $c < c_0$. The ratio of these speeds is the

index of refraction, $n = c_0/c$. Fortunately, the index of refraction within a gas can be calculated from a simple linear equation [Settles (2001)]

$$n - 1 = k\rho \tag{4.1}$$

where k is the Gladstone-Dale coefficient and ρ is the fluid density. Thus, the index of refraction of a test gas, and therefore the refraction of light rays through that gas, is linearly related to the density of the fluid along the light ray path. If the deflection of the light rays through the medium can be observed, then it is possible to infer the distribution of the density field within the test gas. This relation is at the core of the schlieren method.

In a typical schlieren system, a point light source is collimated into a beam and passed through the test gas. Due to the high cost of large high-quality lenses, parabolic mirrors are typically used to collimate the beam, producing a "z-type" configuration. On the far side of the test section, a second parabolic mirror re-focuses the light back to a point, before being projected onto a recording device (typically a CCD sensor in modern-day experiments). At the focal point, a knife-edge is positioned to partially intersect the light path. For a homogeneous density field within the test gas, the resulting image is uniformly darkened. However, if a density gradient exists within the fluid, then the local change in n will deflect the light rays passing through that point. If the deflection is normal to the edge of the cut-off filter, then the density gradient will appear as either a light or dark region within the image, depending upon the sign of the density gradient. This process is shown schematically in Fig. 4.1.

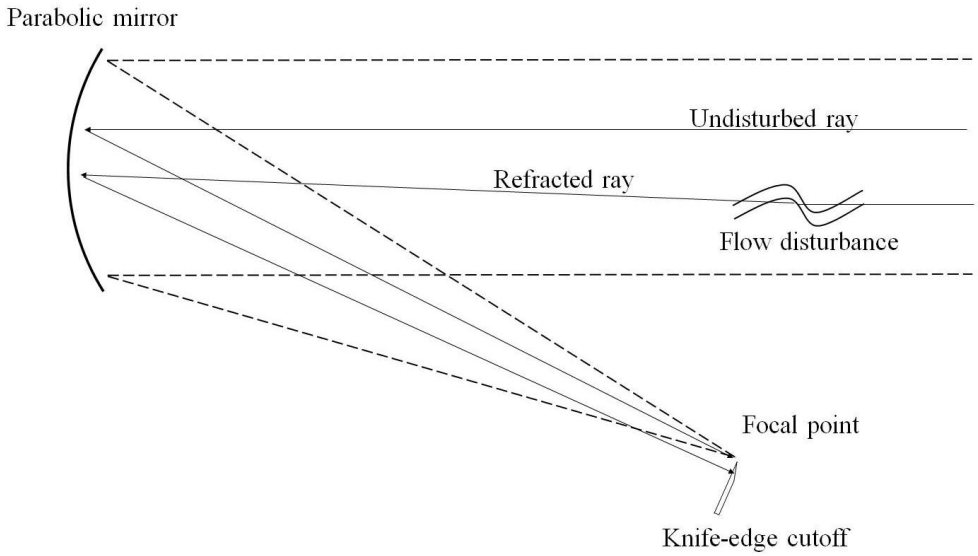

Figure 4.1 A schematic of a typical schlieren arrangement, showing the effects of light ray deflection. ***Note that the magnitude of the deflection is exaggerated in this figure.***

The relation between the light ray deflection and the index of refraction is given below in Eqn. 4.2, where *x* and *y* are the axial and wall-normal directions, respectively, and *z* is aligned along the optical axis of the schlieren system.

$$\frac{\partial^2 y}{\partial z^2} = \frac{1}{n}\frac{\partial n}{\partial y} \tag{4.2}$$

Integrating Eqn. 4.2 and defining $\varepsilon_y \equiv \frac{\partial y}{\partial z}$ as the ray deflection in the wall-normal direction, the deflection is given as

$$\varepsilon_y = \frac{1}{n}\int \frac{\partial n}{\partial y} dz \tag{4.3}$$

If the length of the downstream leg of the schlieren arrangement (i.e. from the test section to the knife-edge) is L, then ε_y is

$$\varepsilon_y = \frac{L}{n_0}\frac{\partial n}{\partial y} \tag{4.4}$$

where n_0 is the refractive index of the fluid outside the test section [Settles (2001)]. Combining Eqns. 4.1 and 4.4, it is obvious that the ray deflection visualized by the schlieren diagnostic is proportional to the wall-normal density gradient $\partial\rho / \partial y$. Note that Eqns. 4.2 – 4.4 describe a schlieren arrangement in which the knife-edge filter is arranged horizontally. If the cut-off is rotated by 90 degrees, then Eqns. 4.2 – 4.4 would describe the deflection ε_x, proportional to the axial density gradient $\partial\rho / \partial x$.

The design of a schlieren system is most often guided by the desire to achieve the highest possible resolution, though this is often tempered by the requisite cost and size of the optical arrangement. As the incident light rays pass through the flow disturbance, they are deflected according to Eqn. 4.3. Because the focal point is spatially finite, small deflections may go unnoticed, limiting the dynamic range of the measurement. However, according to Eqn. 4.4, it is possible to amplify the deflections by increasing the distance L, which is linearly proportional to ε_y. By choosing long-focal length optics and positioning the mirrors far from the test section, it is possible to detect very small disturbances.

The application of these principles to the current experiment is described in §4.1.2 – 4.1.3, including a discussion of the available light sources.

4.1.2. Continuous-Source Arrangement

The optical arrangement used in the current schlieren measurements was a "traditional" z-type configuration, sketched in Fig. 4.2. The light source (described below) was collimated using a 91.44 cm-focal length first-surface parabolic mirror, with a $\lambda/10$ surface flatness at 633 nm. After passing through the test section, the collimated beam was re-focused onto the filter cut-off using a second parabolic mirror.

Precise alignment of the mirrors was necessary to prevent any irregularities in the re-focused image plane. The angles of the mirrors with respect to the test section (shown in Fig. 4.2) were equal and opposite, in order to minimize *coma* aberrations. These errors arise when the mirror angles are dissimilar, causing the focal point to become stretched into a streak. In practice, the focal point resembles a comet with a short tail, hence the term *coma*. This inhomogeneous focus can greatly complicate the positioning of the knife-edge cut-off, leading to a nonuniformly lit background. Additionally, the mirror angles were minimized, to avoid *astigmatism*. This occurs when the angle is too large (usually > 15 degrees), and causes a point source to refocus as two right-angled lines, labeled the *sagittal* and *tangential* foci [Settles (2001)]. These foci are typically separated in the *z*-direction, preventing the use of a single cut-off filter. In the current experiment, the mirror angles were maintained at approximately 10 degrees, minimizing any aberrations due to *astigmatism*.

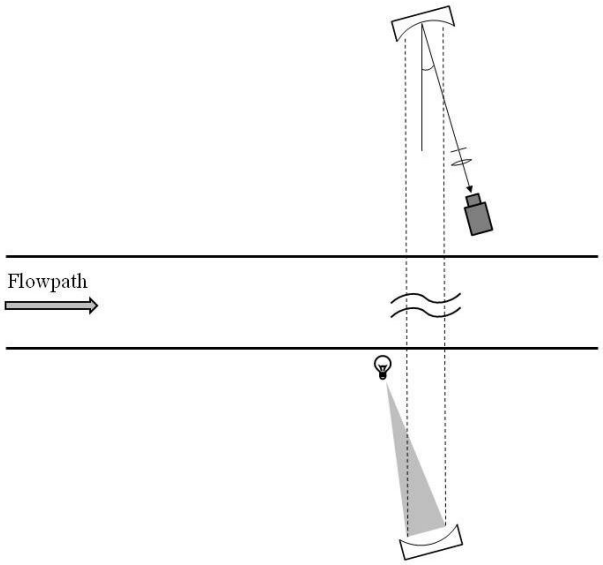

Figure 4.2 "Z-type" schlieren arrangement used in current experiment

During initial tests, a continuous incandescent light-source was used to illuminate the flow. A 50W bulb was focused onto a horizontal aperture, producing a 0.8 mm-thick horizontal line source. The cut-off used was a three-color filter, printed onto a 24 mm x 36 mm film strip (Fig. 4.3). The line source was focused onto the center strip of the filter, causing undisturbed flow features to be imaged in green, while density gradients appeared as red or blue. The resulting image was projected directly onto the sensor of a Nikon D5000 SLR digital camera, which recorded the images over an exposure time of 2.5 ms. This exposure was sufficient to provide adequate illumination of the flow features, showing steady-state phenomena such as shocks/expansions and the boundary layer edge. However, the relatively long exposure time caused intermittent features to be "smeared out", preventing the visualization of coherent turbulent structures. Sample images of the smooth ZPG and rough-wall cases are shown in Fig. 4.4. While the density gradients in the images are easily visualized due to the chosen cut-off filter, the finite thickness of the center green strip (Fig. 4.3) resulted in poor angular resolution, as small deflections would cause the light rays to pass through the "undisturbed" green region. This was remedied by using a knife-edge filter, as described in §4.1.3.

Figure 4.3 Color schlieren filter, used with continuous incandescent light-source.

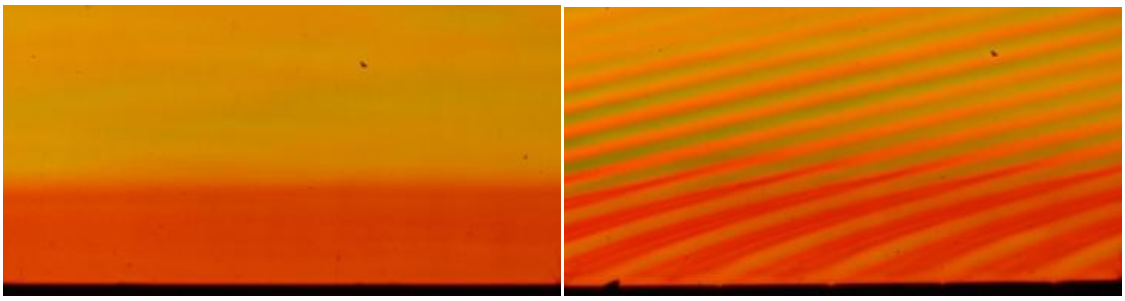

Figure 4.4 Sample schlieren photographs, using a color cut-off filter oriented in the wall-normal direction. ***Left: Smooth ZPG case. Right: Diamond roughness model. Note: Images are not on equal axes.***

4.1.3. Spark-Source Arrangement

In order to visualize the turbulent structures convecting through the boundary layer, a shorter camera exposure time was necessary, to prevent the "smearing" caused by long exposures. While a 5 – 10 ns exposure was needed to "freeze" the turbulent structures, it was not possible to gate the camera to such a short exposure, while maintaining sufficient illumination. Instead, the continuous incandescent light source was replaced by a short-duration, broadband "spark-source." Beutner, Adelgren & Elliott (2006) found that laser-induced gas breakdown can generate a high-intensity broadband source, suitable for use in schlieren photography. Following their technique, a Lab 150 Nd:YAG laser, emitting a 532 nm beam at 10 Hz, was focused into a gas calibration cell. The pulse width was approximately 5 ns, at a maximum energy of 360 mJ/pulse. As shown by Beutner *et al.* (2006), the resulting light generated by the gas breakdown is more intense when using argon, possibly due to the lower ionization energy. For this reason, the gas calibration cell in the current experiment was continually purged with argon gas. Additionally, it was found that the light intensity from the gas breakdown was largest when the pressure within the gas cell was maintained at 36 kPa. A 60 mm Nikon lens focused the spark onto a 0.75 mm diameter pinhole, providing a suitable point source for

the schlieren measurements. A Cooke PCO 1600 CCD camera was used to record the images, with an exposure time of 1 μs. This arrangement is shown in Fig. 4.5.

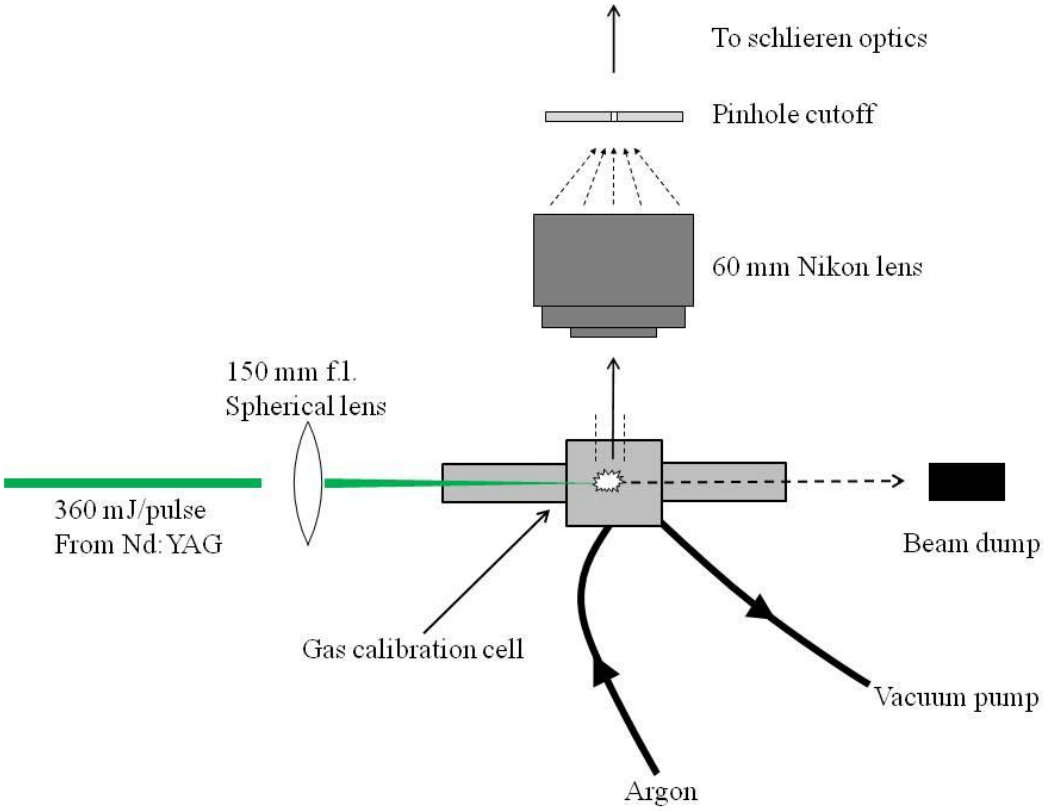

Figure 4.5 Schematic of gas breakdown "spark-source", for use in schlieren imaging

The duration of the breakdown-induced spark was estimated as less than 500 ns, found by varying the delay between the camera exposure and the laser. During this time period, the turbulent flow structures would convect a distance of 10 – 30 pixels. This had the effect of blurring the visualized structures, though a coarse approximation of their size and orientation is still possible. In order to maximize the angular resolution, the color filter cut-off was replaced by a knife-edge filter. The orientation of the knife-edge was

rotated by 90 degrees between runs, allowing the axial and wall-normal density gradients to be visualized. Sample images are shown in Fig. 4.6, for both orientations.

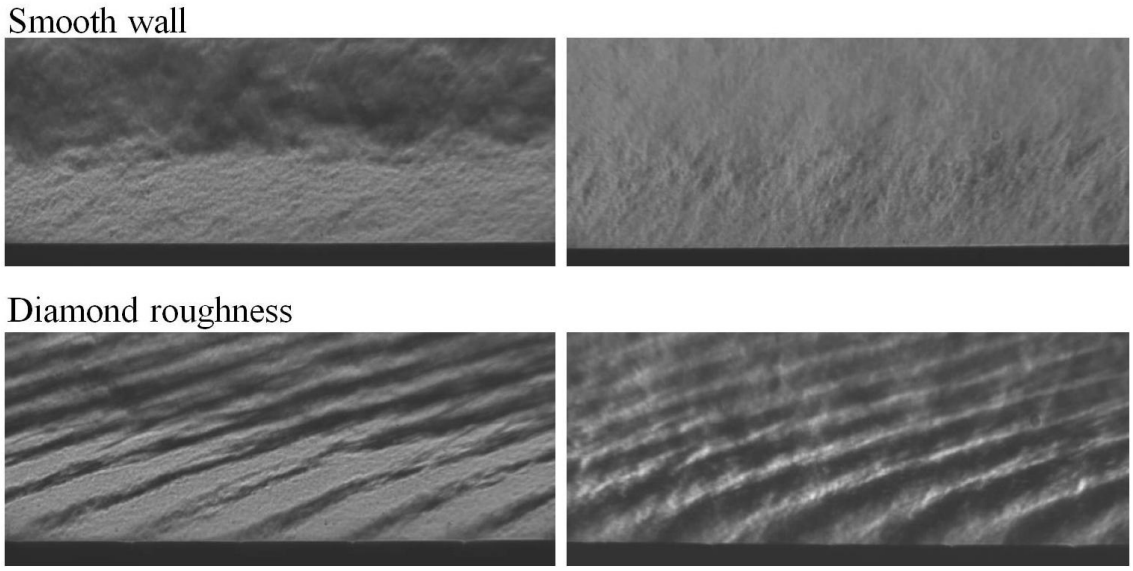

Figure 4.6 Sample schlieren images, using a gas breakdown-generated spark source. ***Left column: wall-normal gradient. Right column: streamwise gradient.***

In the left column of Fig. 4.6, the wall-normal mean density gradient of this compressible boundary layer is clearly visible, for both the rough and smooth cases. By rotating the knife-edge filter, it is possible to qualitatively observe the boundary layer structures. For the smooth-wall images in Fig. 4.6, the fine-grained nature of the turbulent boundary layer is apparent. The structure of the boundary layer is difficult to ascertain from the streamwise density gradient, showing small-scale structures that appear spatially compact. In contrast, the wall-normal gradient indicates the existence of streamwise-elongated streaks, present within the lower half of the boundary layer. These observations are consistent with the known structure of a turbulent boundary layer (§2.1), though further analysis of these images is warranted.

4.2. PIV Principles

Particle image velocimetry (PIV) is an optical nonintrusive diagnostic for measuring the velocity of a fluid within a plane (a discussion of volumetric PIV is not included in this dissertation), yielding a two-dimensional representation of the instantaneous kinematic state of the flowfield. The core principle of PIV is the imaging of suspended "seed" particles within the fluid medium, such that the flow velocity is determined from the displacements of the tracers. At time t_1, the seeded flow is illuminated by a short-duration light source, and the positions of the seed particles are recorded by a CCD camera. After a period of time $\Delta t = t_2 - t_1$, the flow is re-imaged onto a second exposure. By discretizing the images into interrogation windows, cross-correlation can be used to statistically determine the displacement Δd at each point within the flowfield. The reader should note that the displacement is merely the difference $\Delta d = \mathbf{x}(t_2) - \mathbf{x}(t_2)$, and hence any particle motions on a timescale shorter than Δt are removed through temporal filtering. Since the time step Δt is known *a priori*, the velocity at each point is computed as $v = \Delta d / \Delta t$, with the assumption that the chosen seed particles exactly follow the path of the fluid molecules, such that v is equal to the flow velocity. This procedure is described graphically in Fig. 4.7.

The above description provides a coarse overview of the PIV technique, including the two primary advantages of this diagnostic. Firstly, the measurements are nonintrusive, allowing the interrogation of complex geometries and sensitive flow regions. Secondly, PIV provides multiple simultaneous velocity measurements within a plane, allowing a quantitative description of the two-dimensional flow structure. While this technique may appear simple in principle, the application of PIV to practical flows (e.g. compressible flows, shear layers, cavity flows, reacting mixtures) can present significant challenges. The key components of this technique are discussed more thoroughly in §4.2.1 – 4.2.3, emphasizing the practical considerations necessary in designing a successful experiment. For a detailed summary of PIV, the reader is referred to Adrian (1991), Westerweel (1997), and Raffel *et al.* (2007).

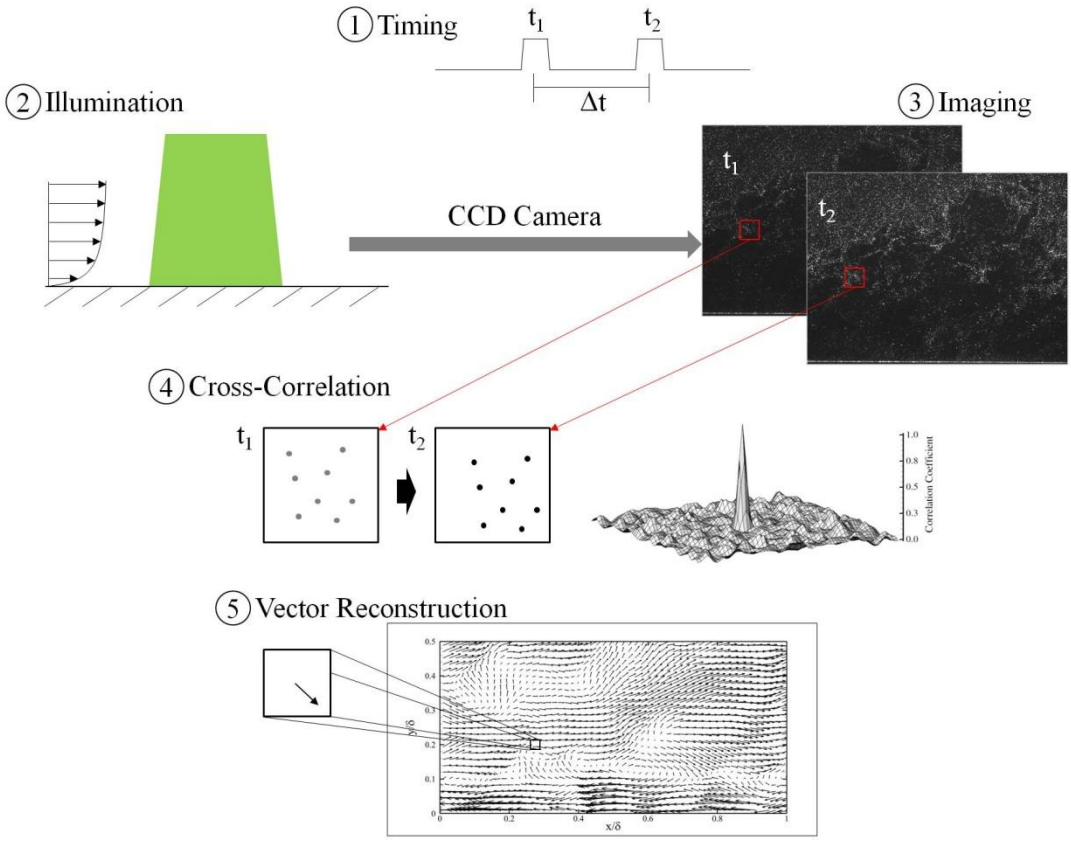

Figure 4.7 Overview of PIV technique, describing the five key steps in data collection and processing. *1) Timing, 2) Illumination, 3) Imaging, 4) Cross-correlation, and 5) Vector reconstruction*

4.2.1. Tracer Particles

The fundamental aspect of the PIV technique is the determination of the seed particle displacement (see §4.2.3), allowing the velocity of the fluid to be computed. This necessarily assumes that the seed particles faithfully track the fluid. While this criteria may be easily met in weakly disturbed flows (e.g. laminar incompressible boundary layers), complex flowfields may pose a greater challenge. In order to select the appropriate particle material and size for a given flow condition, it is necessary to first examine the dynamics of seed particles suspended within a viscous fluid.

The motion of a spherical particle (either liquid or solid) within a continuous medium is determined by the forces on that particle, given by [see Melling (1997)]

$$\frac{\pi d_p^3}{6}\rho_p\frac{d\overrightarrow{U_p}}{dt} = -3\pi\mu_f d_p\left(\overrightarrow{U_p}-\overrightarrow{U_f}\right)+\frac{\pi d_p^3}{6}\rho_f\frac{d\overrightarrow{U_f}}{dt} - \frac{1}{2}\frac{\pi d_p^3}{6}\rho_f\frac{d\left(\overrightarrow{U_p}-\overrightarrow{U_f}\right)}{dt} - \frac{3}{2}d_p^2\left(\pi\mu_f\rho_f\right)^{1/2}\int_{t_0}^{t}\frac{d\left(\overrightarrow{U_p}-\overrightarrow{U_f}\right)}{d\xi}\frac{d\xi}{\left(t-\xi\right)^{1/2}} \tag{4.5}$$

where d_p is the particle diameter, ρ_p is the particle density, μ_f is the fluid viscosity, ρ_f is the fluid density, U_p is the particle velocity, and U_f is the fluid velocity. The left-hand term in Eqn. 4.5 describes the acceleration force on a spherical particle, while the second term accounts for viscous drag from Stokes' law. As the fluid accelerates, a local pressure gradient is produced near the particle, leading to the force described in the third term. The resistance of an inviscid fluid to the particle motion is contained within the fourth term. Flow unsteadiness poses an additional obstacle to the particle motion, given by the fifth term, which is known as the *Basset history integral*.

For a solid particle in a gaseous flow, $\rho_f / \rho_p \ll 1$, allowing Eqn. 4.5 to be simplified as

$$\frac{d\overrightarrow{U_p}}{dt} = \frac{\left(\overrightarrow{U_f}-\overrightarrow{U_p}\right)}{\tau_p} \tag{4.6}$$

where τ_p is the time response of the particle, defined as

$$\tau_p = \frac{\rho_p d_p^2}{18\mu_f} \tag{4.7}$$

In order to determine the appropriate range for τ_p, it is instructive to examine the Stokes number, defined as $St = \tau_p/\tau_f$, where τ_f is the time response of the fluid. In the strictest sense, $St \leq 1$ would ensure that the particles track the motion of the fluid. However, Samimy & Lele (1991) suggested that a criterion of $St \leq 0.2$ is necessary to reproduce the velocity field. For high Mach numbers, the decreasing flow response time τ_f

necessarily requires ever-smaller values of τ_p in order to satisfy the Stokes number criterion. As shown in Eqn. 4.7, a smaller particle response time is most easily achieved by decreasing the particle diameter d_p. For this reason, it is common for supersonic PIV experiments to use seed particles with nominal diameters $d_p < 1$ μm.

In principle, the particle diameter d_p should be minimized, to ensure that the particles are accurately following the fluid motion. However, this leads to a corresponding decrease in the scattering cross-section C_s. When the seed particles intersect a laser sheet of intensity I_0, the total scattered power P_s is given by [see Raffel *et al.* (2007)]

$$P_s = C_s I_0 \tag{4.8}$$

Since the seed particle locations are recorded by imaging the scattered laser light, a decreased particle diameter will necessarily result in a lower signal to noise ratio (SNR). Therefore, a larger d_p is desirable, in order to ensure an adequate SNR.

The competing requirements of C_s and τ_p are the guiding factors in selecting the appropriate tracer particles for a PIV experiment. Given that a small scattering cross-section can be overcome by increasing the laser intensity (see Eqn. 4.8), the particle response time usually becomes the dominant concern when designing the experiment. In practice, most supersonic studies use particles with $d_p < 1$ μm.

4.2.2. Imaging

Given the small diameter of the PIV particles ($d_p < 1$ μm), most practical imaging systems are unable to directly visualize the particles. Instead, the particle image forms an Airy disk, consisting of concentric rings formed by the diffraction of the scattered light. The diameter of this disk d_{diff} is the smallest feature that can be detected by the imaging system, and is often referred to as the *diffraction spot size*, given by

$$d_{diff} = 2.44 f_{\#} (M + 1) \lambda \tag{4.9}$$

where $f_\#$ is the f-number, λ is the wavelength of the incident light, and M is the magnification, defined as

$$M = \frac{z_0}{Z_0} \tag{4.10}$$

Z_0 is the distance between the object and the lens, and z_0 is the distance between the imaging plane and the lens. In order to minimize bias errors, d_{diff} should be greater than 2 pixels. If the particle image diameter is smaller than this value, then the subpixel interpolation (see §4.2.3) will bias the resulting displacements to integer values, a phenomenon known as *peak-locking* [Westerweel (1997); Raffel *et al.* (2007)]. Generally, this error will manifest as "striping" in one of the mean velocity components. Since the magnification M is generally chosen to provide a desired field of view (FOV), the $f_\#$ is the only term that can be varied to increase the diffraction spot size. However, this leads to a smaller aperture (for a fixed focal length lens), therefore decreasing the amount of light impacting the camera sensor. For high $f_\#$ values, the scattered light from smaller particles may be similar in intensity to the system noise, leading to an apparent decrease in the effective particle concentration. Additionally, an increased $f_\#$ will result in a larger focal depth δ_z, given by

$$\delta_z = 4.88\lambda \left[\frac{f_\# (M+1)}{M} \right]^2 \tag{4.11}$$

It is generally desirable to ensure that the focal depth is no less than the laser sheet thickness. Otherwise, poorly focused particle images will be present in the raw data, potentially introducing errors into the correlation map.

4.2.3. Vector Reconstruction

The scattered light from the seed particles is recorded by two separate exposures, yielding an image pair describing the instantaneous particle locations at times t_1 and t_2.

For low seeding concentrations (i.e. the separation between the tracers is larger than the displacement), the displacements of the individual tracers can be measured, resulting in a technique known as particle tracking velocimetry (PTV). However, if the mean particle separation is less than the average displacement, "it is not possible to identify matching particle pairs unambiguously" [Westerweel (1997)]. Instead, a statistical measure of the displacement field is required.

In PIV, the images at t_1 and t_2 are partitioned into *interrogation windows* of size M×N, which are (usually) square subregions arrayed on an orthogonal grid. The light intensity distribution for each image is given by $I_1(i,j)$ and $I_2(i,j)$, respectively, where i and j describe the pixel locations. Using the interrogation window at t_1 as a template, the product of the intensity distributions is computed after shifting $I_1(i,j)$ by (dx,dy). Formally, this is described by the cross-correlation

$$C(dx, dy) = \sum_{i=0}^{M} \sum_{j=0}^{N} \left[I_1(i, j) - \mu_1 \right] \left[I_2(i + dx, j + dy) - \mu_2 \right] \tag{4.12}$$

where μ_1 and μ_2 are the averages of I_1 and I_2, respectively. The resulting correlation map C is repeated for all interrogation windows. The maximum peak in each map corresponds to the most probable displacement of the particles from t_1 to t_2. To account for variations in particle intensity, Eqn. 4.12 can be normalized by the standard deviations of the respective images, yielding a scaled correlation coefficient.

Using Eqn. 4.12, the displacement of the particles in each interrogation window is computed, generating a two-dimensional displacement map over the entire domain. However, these displacements are integer values, with the accuracy limited to 1 pixel. To improve the fidelity of the measurement and increase the dynamic range, it is possible to interpolate the correlation peak to subpixel accuracy. The most common method used is the Gaussian peak fit, which assumes that the correlation function resembles a Gaussian curve at the peak [Westerweel (1997)]. By fitting a known

function to the correlation map, the displacement can be interpolated to subpixel accuracy.

Using the above techniques, it is possible to calculate a two-dimensional displacement field to an accuracy of 0.1 pixel. However, the resulting velocity field will suffer from poor spatial resolution, as the velocity vector spacing is dictated by the size of the interrogation windows. By iteratively computing the particle displacement using successively decreasing interrogation window sizes, it is possible to generate a velocity field of much higher resolution. The first (largest) interrogation window size is chosen such that the mean particle displacement is no more than 25% of the window width [Raffel *et al.* (2007)]. Once the correlations have been calculated for this coarsest grid, the interrogation window dimensions are reduced by 50%, leading to a four-fold increase in the velocity vector density. The displacements calculated on the coarse grid are used as an "initial guess", allowing the smaller interrogation windows to refine the previous estimate. This procedure is repeated for successively smaller windows, producing a finer grid of velocity vectors. The final vector spacing is ultimately determined by the final interrogation window size, which in turn is constrained by the seed particle concentration. In order to compute a correlation peak that is significantly stronger than the background noise, it is necessary that the interrogation windows contain at least 10 particles [Keane & Adrian (1992)]. Obviously, this criteria is difficult to satisfy within the near-wall region of a compressible boundary layer, as the tracer concentration generally scales with the local fluid density.

4.3. PIV Experimental Arrangement

In this study, PIV was employed to measure the instantaneous velocity field of the boundary layer, within the streamwise wall-normal (x-y) plane. For each data set, 1035 image pairs were collected at a location 29.8 cm downstream of the nozzle exit, with the laser sheet oriented along the tunnel centerline $z = 0$. The PIV arrangement is shown in

Fig. 4.8, with the experimental parameters listed in Table 4.1. A detailed description of the relevant components is discussed in §4.3.1 – 4.3.3, including flow seeding, illumination and imaging, and vector processing, respectively.

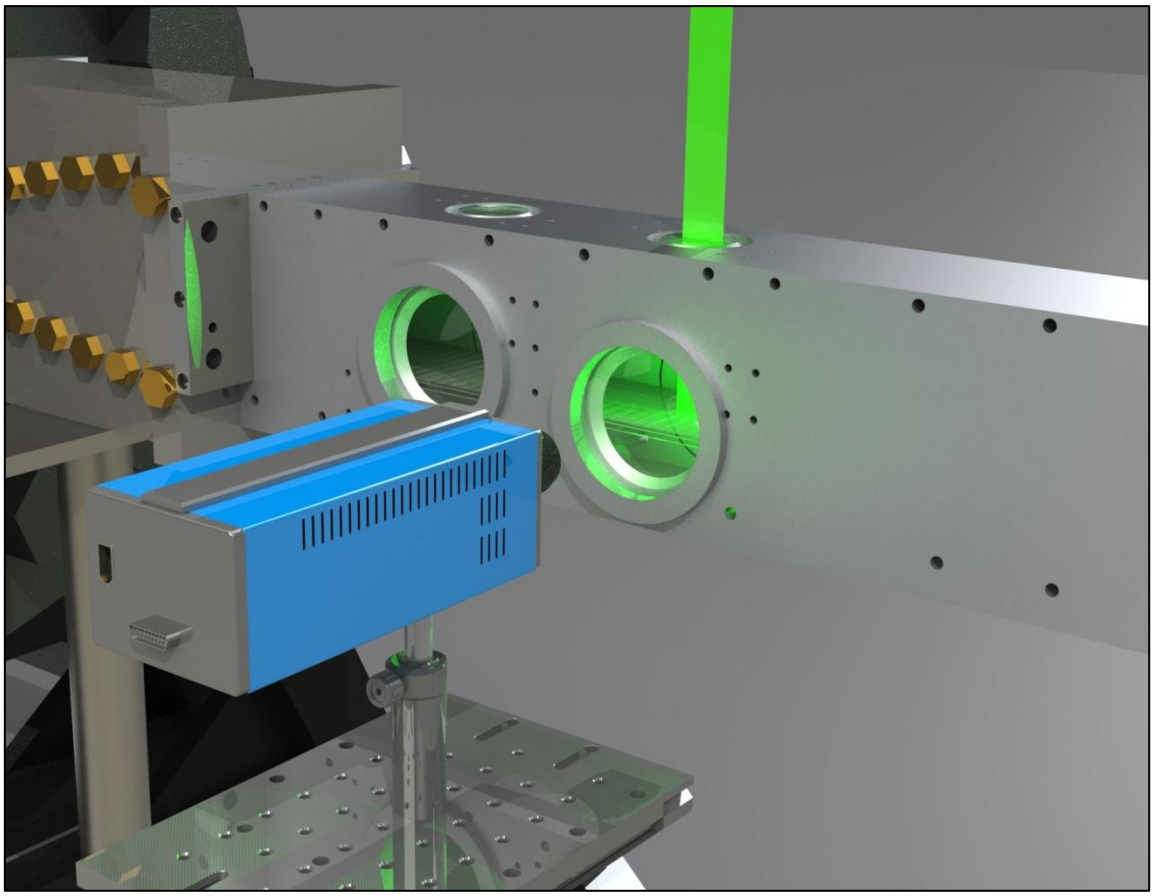

Figure 4.8 Drawing of PIV experimental arrangement, showing the camera system, laser sheet, and test section. *Flow is from left to right.*

Table 4.1 PIV experimental parameters

Test Section	Height	7.62 cm
	Width	7.62 cm
	Measurement location[1]	29.8 cm
Flow	Fluid	Air
	Re/m	~ 5.0×10^7
Seeding	Particle	TiO_2
	Nominal diameter	200 nm
	Stokes number	0.17
Laser Sheet	Laser type	Nd:YAG
	Energy	25 mJ/pulse
	Wavelength	532 nm
	Pulse duration	5 ns
	Sheet thickness	~ 1 mm
	Repetition rate	10 Hz
Camera	Camera type	CCD
	Resolution	1600 × 1200 pix
	Pixel size	7.4 μm
	Discretization	8 bit
	Lens focal length f	60 mm
	f-number	11
	Image exposure (Δt)	500 ns
	Number of image pairs	1035

[1] *Measured from nozzle exit plane*

4.3.1. Flow Seeding

As described in §4.2.1, the seed particles must possess a small time response τ_p so that they faithfully track the flow, while still generating a sufficiently large signal (i.e. scattered laser light). For this experiment, titanium dioxide (TiO_2) nano-particles were selected, with a manufacturer's quoted diameter of 200 nm. Titanium dioxide particles are highly reflective, and are easily cleaned from the model surfaces, making them ideal for fluid dynamic studies. Based upon the experiments of Ragni *et al.* (2011) within a supersonic flow, the time response of these particles was estimated as 2.5 μs. Computing the flow response time as $\tau_f = \delta/U_e$, the Stokes number was 0.17 for the smooth ZPG flowfield (a similar value was calculated for each of the mechanically distorted boundary layers), satisfying the requirement suggested by Samimy & Lele (1991) that $St \leq 0.2$. While it is possible to compute τ_p from Eqn. 4.7, this equation was believed to under-predict the time response of the particles. This is primarily due to the particle diameter

d_p, which is nominally 200 nm for the current experiment. It is common for agglomeration to increase this value by 200% – 300%, leading to a corresponding increase in τ_p [Raffel *et al.* (2007)]. Additionally, the agglomeration is unlikely to occur uniformly throughout the particle cloud, leading to a polydisperse distribution of particle diameters. For this reason, estimating τ_p from empirical data provides the most reliable measurement of the response time.

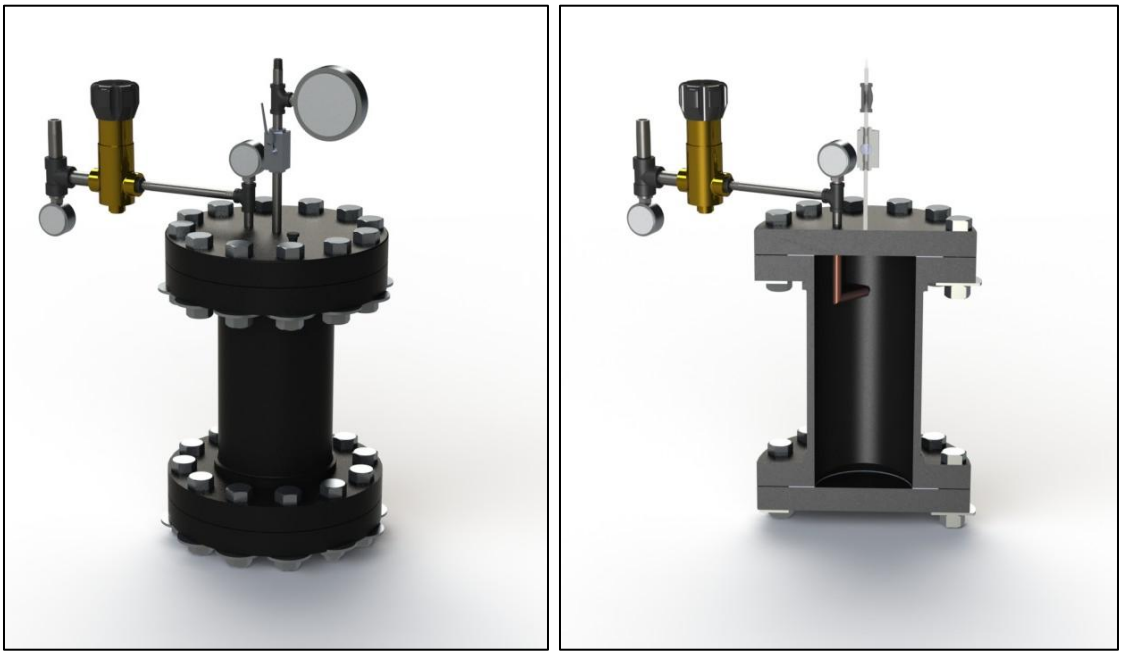

Figure 4.9 PIV seeder used in current experiment. *Left: Full seeder, showing outer shell. Right: Section view, showing copper tubing at 90 degree angle.*

Agglomeration of metal oxide powders such as TiO_2 may lead to larger effective particle diameters, ultimately reducing the fidelity of the tracer response. To mitigate this effect, a solid particle seeder was constructed that would prevent the entrainment of large particles, while allowing the passage of smaller tracers. This design was based upon the seeder used by Glass & Kennedy (1977), and is shown in Fig. 4.9. The outer shell was constructed of 6" Schedule 80 pipe, capped at both ends by blind flanges. The seeder

was filled to approximately 10% capacity with titanium dioxide powder. Dry, high-pressure air was injected through the copper tubing at the top of the seeder. The tubing entered the vessel and turned 90 degrees, creating a tangential jet of air. As the particles were entrained by this flow, the centrifugal force of the rotating flowfield would push the larger and more massive particles toward the seeder wall. Lighter particles remained within the seeder core, and were free to exit through the pipe located at the top center of the vessel. In this manner, the seeder is capable of filtering out larger agglomerated particles, similar to a cyclone separator. A more detailed description of the seeder construction, along with the suggested operating procedures, is given in Appendix D.

Arguably the most difficult step in PIV is seeding the flowfield, which must satisfy two criteria: 1) the particle injection must not introduce significant perturbations to the flow, and 2) the seeding concentration should be sufficiently high to achieve the desired resolution. In order to satisfy the first requirement, the seed particles were injected into the semi-quiescent fluid at the downstream end of the settling chamber. This location is approximately 30 cm upstream of the nozzle throat, allowing sufficient time for any flow perturbations to dissipate. The particles were injected through an aluminum strut, which was crimped to reduced blockage effects. A notch measuring 5 mm x 10 mm was cut into the strut, positioned flush with the bottom surface of the duct. It was hoped that the positioning of the strut along the duct floor would concentrate the particles within the near-wall region of the boundary layer. However, turbulent mixing was sufficiently strong that the particles were distributed throughout the test section by the time the tracers reached the measurement location.

The second requirement, that the seeding concentration be sufficiently high, is complicated by the density stratification of the Mach 4.9 boundary layer. In general, the tracer population scales with the flow density, leading to a nearly six-fold decrease in particle concentration at the wall. This is clearly seen in Fig. 4.10, which shows a raw image collected over the smooth ZPG model. To increase this concentration, it was necessary to inject the particles at a pressure 20% higher than P_0. While this over-

pressure also increased the population density throughout the boundary, the improvement in the near-wall concentration was sufficient to allow for a final interrogation window size of 32 x 32 pixels.

Figure 4.10 Sample raw image collected over smooth ZPG model, showing instantaneous seed particle concentration. *Note the lower concentration within the near-wall region, consistent with the density stratification of a compressible boundary layer.*

4.3.2. Illumination & Imaging

In order to visualize the seed particles, a light source was needed with a high intensity to generate a sufficient reflection from the particles. Additionally, this source must have a duration of less than 10 ns, in order to prevent blurring of the particles. These requirements necessitate the use of a pulsed laser. In this experiment, the particles were illuminated by a dual-head New Wave Solo 120 laser, operating at 10 Hz. Note that the low repetition rate of this laser prevented the collection of time-resolved data. The

attenuator was set to provide a beam of 532 nm wavelength at approximately 25 mJ/pulse. The pulse width of the beam was 5 ns, allowing the particles at the boundary layer edge to travel only 0.3 – 0.5 pixels during the pulse duration, effectively "freezing" the flow. This beam passed through a -25.4 mm focal length cylindrical optic, resulting in a sheet thickness of approximately 1 mm. The laser sheet was aligned at the tunnel centerline, passing through the top window of the test section. Before entering the tunnel, the fringes of the beam were clipped using a knife-edge cut-off, producing a nearly top-hat distribution of laser light.

The resulting scatter from the seeded flow was imaged using a Cooke PCO 1600 interline transfer CCD camera with a 1600 × 1200 pixel-sized sensor. A Nikon *f*/4 60 mm lens was used with an *f*-number of $f_{\#} = 11$. In addition, a circular polarizer was used in order to attenuate the laser light reflections from the wall while still maintaining sufficient particle light scattering behavior. Synchronization between the camera and laser was accomplished using a Quantum Composer model 9618 pulse generator, which triggered both the laser and camera. Images were recorded using the Camware V2.19 software package. The camera was operated in double-shutter mode, with an exposure time-separation of $\Delta t = 500$ ns. At the boundary layer edge, this produced a mean particle displacement of 30 – 35 pixels, providing a sufficiently large dynamic range between the large and small displacements.

At this point, an uninitiated reader may ask: How can the time-separation Δt be less than the particle response τ_p? This is best addressed by recasting these time constants as waveforms, shown in Fig. 4.11. In the current experiment, the particles are unable to resolve motions with a wavelength less than 2.5 μs. Any waveforms with a higher frequency are biased to longer wavelengths, due to aliasing effects. Essentially, τ_p represents the highest frequency content that can be detected within the boundary layer. However, it is still possible to detect *displacements* on a timescale less than τ_p, but only if the wavelength of that motion is greater than τ_p.

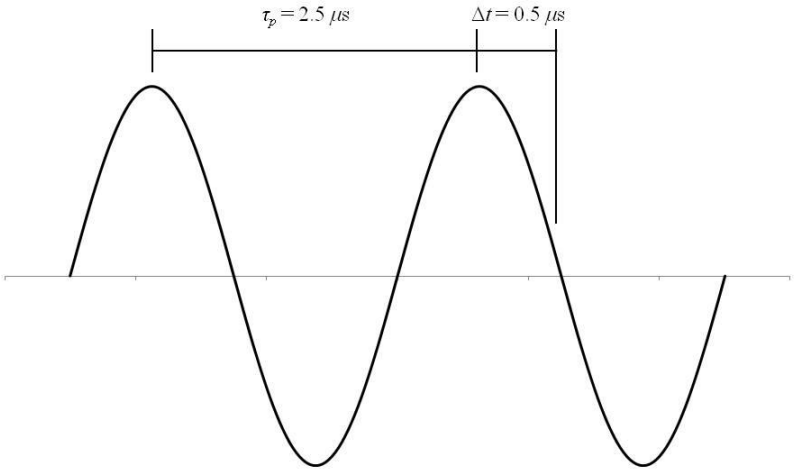

Figure 4.11 Waveform of the particle response time τ_p, compared to a displacement over the timescale Δt.

4.3.3. Vector Processing & Validation

Prior to processing the image pairs, it was necessary to perform several pre-processing steps, in order to mitigate the effects of tunnel movement and peak locking. The first issue, tunnel movement, was due to thermal expansion of the test section, leading to possible misalignment of the FOV. While the experimental models described in §3.3 maintained a nearly constant temperature throughout the tunnel operation (see Appendix A) due to the low thermal conductivity of acrylic, the aluminum sidewalls and ceiling were expected to experience a more significant temperature change. For Mach 4.9 and T_0 = 365 K, the adiabatic wall temperature T_{aw} is approximately 332 K. This represents a 40 K increase in temperature from ambient conditions. Assuming that the linear coefficient of thermal expansion α is 22.1 x 10^{-6} m*K/m for aluminum, we can compute the expected shift in the tunnel during a run as $\Delta L = L*\alpha*\Delta T$, where ΔL is the change in length, L is the original length, and ΔT is the temperature change. For L = 71.1 cm and ΔT = 40 K, the downstream shift is approximately 0.6 mm, or 48 pixels for the baseline

case. Since the aluminum tunnel ceiling underwent thermal expansion while the tunnel floor remained fixed, a bending moment was also exerted on the test section, causing the floor to bend downward. It was necessary to correct this shift during pre-processing, prior to the calculation of the velocity vectors.

For the $f_{\#}$ used in this experiment ($f_{\#}$ = 11), peak locking was not expected to be a significant source of error. However, the "striping" that is indicative of this phenomenon was partially visible in the mean wall-normal velocity component *V*. To mitigate this effect further, a Gaussian smoothing filter was applied to the images prior to processing. This filter broadens the particle images along a Gaussian curve, over a kernel size of 3 x 3 pixels. The net result is the effective increase in the particle image diameter d_{diff}, leading to reduced peak locking effects.

Processing of the vector fields was performed using DaVis 8.0.2, following the settings shown in Table 4.2. Starting at an initial window size of 128 x 128 pixels, the velocity vectors were computed using an adaptive weighting scheme, with four passes performed for each window size. This multi-pass technique improved the convergence of the displacements, leading to a better "initial guess" for the smaller window sizes. Additionally, the interrogation windows were overlapped by 50%, improving the vector density. It should be noted that a higher overlap factor does not equate to an increased resolution, since the raw data (i.e. particle location) has already been used in adjacent interrogation windows. This process was repeated until the final window size of 32 x 32 pixels was reached.

Despite the high seeding concentration and multi-pass vector processing, regions of spurious vectors were still observed in small regions of the flow, most likely due to inhomogeneous seeding. To remove these outliers, a combination of filters was applied to each instantaneous vector field. First, a median filter was performed at each point. In this technique, consider the velocity vector computed at position $\mathbf{x}(i, j)$. If the velocity $\boldsymbol{u}(i, j)$ is significantly different from the neighboring vectors, then $\boldsymbol{u}(i, j)$ is likely erroneous and can be removed. To perform this algorithmically, the 8 neighboring points

surrounding $\mathbf{x}(i, j)$ are considered, and are used to compute a local mean U_m, standard deviation (i.e. rms of $\boldsymbol{u}$), and median U_{med}. The difference between $\boldsymbol{u}(i, j)$ and U_{med} is computed, and the vector is removed if the difference is greater than a chosen threshold. In this experiment, the threshold was chosen as two times the standard deviation of the neighboring points, or $2\mathbf{u}_{\text{rms}}$. This filter was repeated twice at each point, in order to verify that all spurious vectors had been removed. The percentage of vectors removed by this filter, defined as the *vector dropout*, varied from 3% for the baseline case to 8% for the diamond roughness. Given the relatively low number of spurious vectors removed during the filtering process, it was possible to use bilinear interpolation to replace the missing vectors.

The final filter applied to the instantaneous fields was intended to alleviate sharp gradients within the flowfield. While the purpose of PIV is to measure the local velocity of the fluid, experimental considerations (particle time response, low-pass spatial filtering due to finite interrogation windows, wall reflections, etc.) may contribute to increased noise, possibly leading to slightly altered velocity gradients. In principle, this deviation from the "true" gradients is of little concern, and can be quantified by calculating the uncertainty of the differentiated velocity field. However, many post-processing techniques rely upon an accurate calculation of the velocity gradient tensor (see §5). An inspection of several finite difference schemes shows that the calculated gradient is particularly sensitive to experimental noise, leading to extremely high uncertainty levels (see Appendix B.4 for a detailed uncertainty analysis). In order to prevent the experimental noise from contaminating the differentiated data, a smoothing filter was passed over the instantaneous vector fields, reducing the coarse distribution of the local gradients. The use of a 3 x 3 pixel-sized kernel prevented further low-pass filtering of the data, since the kernel is smaller than the final interrogation window [Raffel *et al.* (2007)]. It should be noted that the velocity fields were very sensitive to the smoothing filter settings, and great care was taken to ensure that the filter process did not fundamentally alter the measured data. A comparison of these filter settings is given in Appendix C.

Table 4.2 PIV processing and filter settings, used in DaVis 8.0.2

Pre-Processing	Gaussian smoothing	3 x 3 pixel kernel
Vector Processing	Initial window size	128 x 128 pixels
	# of passes for initial window	4
	Final window size	32 x 32 pixels
	# of passes for final window	3
	Window weighting	Adaptive
	Overlap factor	50%
Vector Post-Processing	Median filter	2 passes; 2 rms
	Smoothing	1 pass; 3 x 3 kernel
	Interpolation	Yes
	Vector dropout	5% - 8%
	Digital resolution [px/mm]	79.6[1]; 70.3[2]; 57.5[3]; 68.7[4]
	Final vector spacing[5]	0.02δ
Ensemble-Averaging	Median filter	3 rms

[1]*Smooth ZPG*; [2]*Smooth WPG*; [3]*Smooth SPG*; [4]*Diamond roughness*
[5]*Includes 50% overlap factor*

In order to calculate the mean flow behavior, ensemble-averaging was performed at each point within the flow, generating a two-dimensional description of the mean and fluctuating statistics. An averaging filter was applied to the ensemble-averaged data, such that outliers were not included in the final statistics. At each spatial point, the combined instantaneous fields produced a data vector containing 1035 elements. A median filter was applied over these elements, using a $3\mathbf{u}_{rms}$ (or "3-sigma") threshold. This tolerance was chosen to eliminate the largest outliers, while still retaining a bulk of the flow energy. For a normal distribution, a 3-sigma cut-off includes approximately 99% of area under the curve. The uncertainty of these statistics was calculated based upon a 95% confidence interval, and are listed in Table 4.3 for the baseline boundary layer (the distorted flowfields exhibited similar uncertainty levels, and are not shown here). The variance of each statistic was estimated by assuming a normal distribution, following the technique of Benedict & Gould (1996). For additional information on the uncertainty computations, see Appendix B.

Table 4.3 Statistical uncertainty for the baseline flowfield, *based upon a 95% confidence interval*

Variable	Uncertainty
U, V	0.5 %
$\langle u'u' \rangle, \langle v'v' \rangle$	8.6 %
$\langle u'v' \rangle$	14.4 %

The procedures listed above produced highly-resolved instantaneous and mean displacement fields. However, the measurements were still in units of pixels/Δt. A calibration step was necessary to convert these displacements into velocity vectors of units m/s. After collecting the raw data and halting the wind tunnel, a calibration card was placed in the test section and aligned with the laser sheet. This calibration card contained a grid of known dimensions, allowing the digital resolution of each data set to be measured. These resolutions are listed in Table 4.2, in units of px/mm. For a final interrogation window size of 32 x 32 pixels, including a 50% overlap factor, the final vector spacing for each data set was approximately 0.02δ, where δ is the boundary layer thickness. It should be noted that to this author's knowledge, the spatial resolution of the current study is significantly higher than any other experiment performed at this Mach number. The high fidelity and low vector dropout of the instantaneous vector fields are the principal factors enabling many of the analyses included in this dissertation.

4.4. Post-Processing and Analysis Methods

The high-fidelity data collected during this study, consisting of high-resolution two-dimensional velocity fields (see §4.3), have the potential to reveal the instantaneous and statistical nature of the turbulent boundary layer structures. Recalling §1, the objective of this study is to elucidate the relationship between these boundary layer structures and the turbulence stresses. This requires analysis methods that are capable of both identifying

and characterizing these turbulent structures, along with their induced motions. The following sub-sections describe in detail these analysis methods, excepting vortex identification techniques, which are discussed more thoroughly in §5.

4.4.1. Ensemble-Averaged Profiles

Profiles of ensemble-averaged mean and fluctuating quantities are given as a function of y/δ (and x/δ for the diamond roughness). Mean velocities are denoted by a capital letter (U, V), while fluctuating velocities are the corresponding lower-case letter (u', v'). Instantaneous velocities are described by (u, v). The velocity components are ensemble-averaged over all 1035 images for each measurement location. In order to ease visualization and improve convergence, wall-normal profiles are spatially averaged over a streamwise distance of 0.5δ, unless otherwise noted. This spatial averaging has no appreciable effect upon the profile, other than removing small-scale noise. The only exception is for the rough-wall boundary layer, though this is discussed more thoroughly in §8.

4.4.2. Spectral Analysis

Taylor (1938) first suggested that the size of structures passing a fixed probe may be deduced by decomposing the velocity into "harmonic components." In this study, the distribution of energy among the flow scales is investigated through the Fourier transform of the fluctuating velocities u' and v'. For each instantaneous velocity field, the one-dimensional discrete Fourier transform is applied at a given height y/δ along the streamwise direction, computed as

$$u_n^i = \sum_{j=1}^{N} u_n^i e^{2\pi jn\sqrt{-1}/N} \tag{4.13}$$

where u^i_n is the fluctuating velocity data at height y/δ, N is the number of points in the streamwise direction, and u^i_n are the Fourier coefficients. The superscript $i = \{1,2\}$ denotes the velocity components u' and v', respectively. The power spectral density (PSD) Φ_{ii} is then computed as

$$\Phi_{ii} = \frac{1}{N}\left|u^i_n\right|^2 \tag{4.14}$$

where the term i denotes the velocity component. The cross-spectral density follows as

$$\Phi_{uv} = \frac{1}{N}\left|x^u_n\right|\left|x^v_n\right| \tag{4.15}$$

The resulting PSDs are ensemble-averaged over all ~ 1000 velocity fields, yielding a mean PSD as a function of y/δ. Scaling by $1/N$ in Eqns. 4.14 and 4.15 is necessary to ensure that Parseval's theorem is satisfied

$$\int_0^\infty \Phi_{ii} dk_1 = \overline{u_i' u_i'} \tag{4.16}$$

which states that the square of a function is equal to the square of its transform. In this application, this means that the energy described by the function Φ_{ii} is equal to the associated turbulent stress $\overline{u_i' u_i'}$, where the over-bar indicates ensemble-averaging. An additional scaling factor of $1/(2\pi)$ (not shown) is included in Eqns. 4.14 and 4.15, so that Eqn. 4.16 is true when the wavenumber $k_1 = \frac{2\pi}{\Lambda}$ is the variable of integration, where Λ is the wavelength.

The spectra are non-dimensionalized by the local mean Reynolds stress at the given y/δ location, such that the area under the curve k_1 vs $\Phi_{ii}/u_i'u_i'$ is unity. This scaling de-emphasizes the change in turbulent kinetic energy at each wall-normal position, allowing for inspection of the relative distribution of energy among the flow scales.

Additionally, the spectra may be premultiplied with the wavenumber, such that equal areas under the spectral curve correspond to equal energy content (Kim & Adrian 1999). This is done to aid visualization of the spectra when plotted on logarithmic axes. When the abscissa is plotted in logarithmic form, the energy content for a region $a < k_1 < b$ is defined as $\int_a^b \Phi_{ii} dk_1$, while the physical area of the graph is $\int_a^b \Phi_{ii} d(\log k_1)$. For the latter formula, changing the variable of integration to dk_1 introduces a $1/k_1$ scaling, since $d(\log k_1) = (1/k_1)dk_1$. Premultiplying by k_1 is performed to compensate for this scaling, such that equal areas contain equal energy, when plotted on a logarithmic scale. The reader is cautioned that premultiplication is done only to aid in interpretation of the data.

4.4.3. Quadrant Decomposition

Townsend (1976) initially proposed that the turbulent motions in the near-wall region may be separated into two distinct groups, labeled *active* and *inactive*. The inactive motions are outer-scaled structures, contributing very little to the shear stress $u'v'$. The motion from these large eddies can be characterized as "sweeping", affecting only the $u'u'$ and $w'w'$ stresses. This is due to the large scale of these motions, along with the large distance from the wall, such that the induced flow is "mostly parallel to the wall on the scale of the local distance from the wall" (Nickels *et al.* 2007). Conversely, the active motions are considered the primary contributors to the shear stress $u'v'$, and responsible for a majority of the near-wall momentum transport. These structures are localized within the near-wall region, and are scaled by wall parameters. Townsend's description of the active motions is consistent with the behavior described by the hairpin vortex model.

Given the central role that active motions play in the near-wall production of Reynolds shear stress, it is instructive to decompose their contributions based upon the sign of the fluctuating velocity components u' and v'. Combining this decomposition with the

current hairpin vortex model, it is possible to infer the behavior of the turbulent structures based upon the magnitude of the decomposed shear stress contributions.

First suggested separately by Willmarth & Lu (1972) and Wallace, Eckelmann & Brodkey (1972), quadrant decomposition separates the instantaneous shear stress contributions $u'v'$ into four separate bins, shown in Fig. 4.12. By ensemble-averaging the separate quadrants, the fractional contribution of the respective motions can be analyzed. In essence, this technique is akin to a conditional average, based upon the sign of u' and v'. Additionally, it is possible to compute the quadrant decomposition for various magnitudes of $u'v'$, by introducing a hyperbolic hole filter H, such that points are excluded for $|u'v'| < H\left|\overline{u'v'}\right|$. However, no filter was applied to the quadrant decomposition in the current study (i.e. $H = 0$), meaning that all shear stress contributions were considered, regardless of their magnitude.

The analysis of the quadrant decomposition results is greatly aided by the current hairpin vortex model. Considering the quadrants I – IV in Fig. 4.12 (hereafter referred to as Q1 – Q4), it is apparent that $u'v' < 0$ for Q2 and Q4. Indeed, the largest magnitude $u'v'$ motions are located within these quadrants. Furthermore, the relative signs of the components suggest that Q2 events consist of low-momentum fluid being ejected away from the wall, since $u' < 0$ and $v' > 0$. Conversely, Q4 events contain fluid that is "swept" toward the wall. Willmarth & Lu (1972) used this interpretation to suggest that Q2 events are responsible for the bursting phenomenon, and that these *ejections* are much stronger than the *sweeps* at $y^+ = 30$. Invoking the hairpin vortex model, the ejections are likely the result of induced fluid between the hairpin legs, being "squirted" away from the wall. The mutual induction of the vortices would lead to a particularly strong event, compared to the sweeps. The Q4 events are similar to the flowfield expected outboard of the vortex loops, as the hairpins draw the high-momentum fluid toward the wall. The sign of these sweep events is expected to be relatively weaker. Providing a physical explanation for the Q1 and Q3 events is more difficult, though it is possible that these motions are influence by spanwise vortices within the boundary layer.

It should be noted that each instantaneous shear stress contribution within the quadrants Q1 – Q4 is not necessarily associated with a coherent structure, and that these structural models merely provide a probable explanation for the relative magnitudes of these motions.

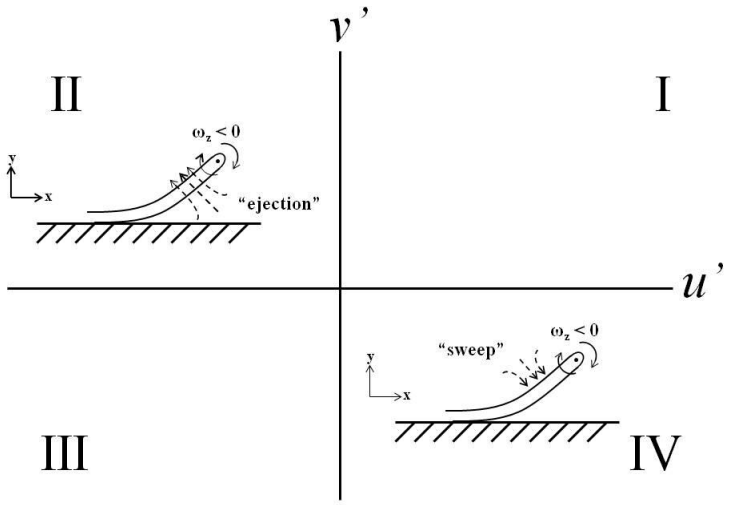

Figure 4.12 Sketch of quadrants used in quadrant decomposition, *including the probable relation with hairpin vortices.*

4.4.4. Length-Scale Estimation

The integral length scale is characteristic of the largest eddies within the flow, and can be computed from the one-dimensional auto-correlation R_i as:

$$L_{ii} \equiv \int_0^\infty R_i dx_i \tag{4.17}$$

where the subscript i denotes the velocity component (i.e. $R_{ii} \equiv R_{uu}$ for $i = 1$). Graphically, L_{uu} is the area under the longitudinal auto-correlation of *u'* (Pope 2000), shown in Fig. 4.13. Accurate calculation of the integral length scale requires data over a sufficient distance in the longitudinal direction, such that $R_1 \rightarrow 0$. Such fields of view are rarely available in experimental data. Instead, a representative streamwise length scale λ_x^u is chosen, approximating the area under the two-sided auto-correlation.

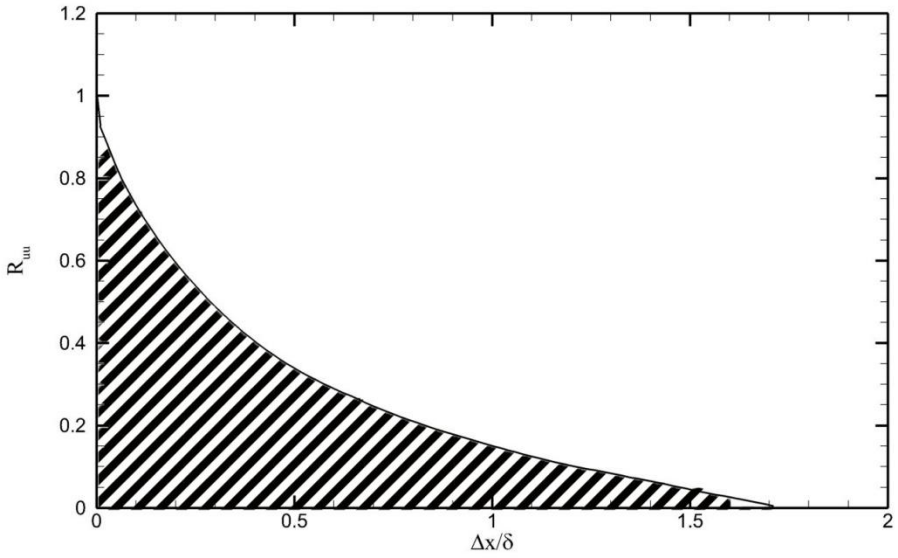

Figure 4.13 Depiction of the integral length scale L_{11}, calculated by Eqn. 4.17. *Graphically,* L_{11} *is equal to the shaded area under the curved.*

Figure 4.14 shows the two-sided longitudinal auto-correlation of *u'* for the smooth ZPG case, plotted at $y/\delta = 0.5$. The area under the given curve is numerically integrated, yielding $\int_{-\infty}^{\infty} R_1 dx_1 = 0.91$. Therefore, the streamwise length scale λ_x^u is 0.91 for this data. Because not every case in the current study has a sufficient field of view to directly compute this integral, a correlation threshold value is selected, describing a rectangular region with an area equal to the computed length scale. This is seen in Fig. 4.14, as the

area under the correlation curve is equal to the width of the cross-hatched rectangular region. The intersection between the correlation curve and the rectangular region is approximately $1/e$ (≈0.37), where e is the base of the natural logarithm. This threshold will be used for the determination of the streamwise length scale for all cases in the current study.

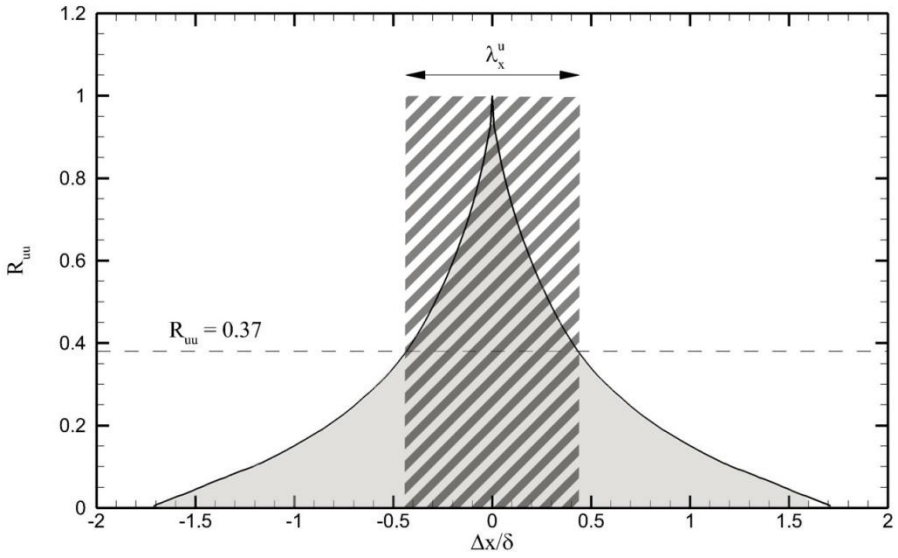

Figure 4.14 Longitudinal auto-correlation of *u'* at *y*/*δ* = 0.5, for the smooth ZPG case. *The streamwise length scale corresponds to an area equivalent to the region under the auto-correlation curve.*

4.4.5. Conditional Averaging

Conditional averaging is used in this study to statistically describe the localized flowfield around the hairpin vortex signatures, which are identified by the swirling strength λ_{ci} criterion (see §5 for a comparison of vortex identification techniques). The simplest method of determining the conditional average (denoted as $\langle u', v' | \lambda_{ci} \rangle$) is to tag each velocity vector that meets the chosen criteria, and compute the average velocity from this subset of the data. However, this method is impractical, as it requires accurate knowledge of the vortex core locations. It is possible to estimate these locations from the

contours of λ_{ci}, but sample data suggest that λ_{ci} is not distributed evenly within the detected vortex cores, most likely due to the misalignment of the vortex axes with the spanwise direction *z*. Any determination of the vortex core location by examining the centroid of the λ_{ci} contours would contain errors equal to several times the vector spacing. Given these limitations, it is necessary to estimate the conditionally averaged velocity.

Stochastic estimation allows the conditionally averaged velocity field to be estimated from unconditional data [Adrian (1975)]. Consider the velocity fluctuation u_i', where the velocity component is determined by the subscript $i = \{1,2\}$. For a given event E_j, the stochastic estimate becomes

$$\left\langle u_i' \mid E \right\rangle = A_{ij} E_j + B_{ijk} E_j E_k + \cdots \tag{4.18}$$

The conditional average $\left\langle u_i' \mid E \right\rangle$ is the "the best mean square estimate of u_i' given the data E_j" [Adrian (1994)]. Therefore, the mean square error $\left\langle \left[u_i' - F(E) \right]^2 \right\rangle$ is minimized when $F = \left\langle u_i' \mid E \right\rangle$. Applying this principle to Eqn. 4.18, it is possible to solve for the coefficients A_{ij} and B_{ijk}.

If the higher-order terms in Eqn. 4.18 are discarded, then the *linear stochastic estimate* of u_i' becomes

$$\left\langle u_i' \mid E \right\rangle = \sum_{j=1}^{M} A_{ij} E_j \tag{4.19}$$

where M is the number of conditional events in the vector E_j. The minimization of the mean square error can now be repeated for the linear estimate, yielding

$$\left\langle \left[\left\langle u_i' \mid E \right\rangle - \sum_j A_{ij} E_j \right]^2 \right\rangle = \text{minimum} \tag{4.20}$$

In order to minimize the error $\langle u_i' \mid E \rangle - \sum_j A_{ij} E_j$, the data must be statistically orthogonal to the error, such that

$$\left\langle \left[\langle u_i' \mid E \rangle - \sum_j A_{ij} E_j \right] E_k \right\rangle = 0 \tag{4.21}$$

for $j,k = 1, \ldots, M$. By manipulating Eqn. 4.21 further, a system of linear equations known as the *Yule-Walker* equations is formed, describing the coefficients A_{ij} [Adrian (1994)]. If the event vector **E** contains a single element (i.e. $j = 1$), then the coefficients A_{i1} are given by

$$A_{i1} = \frac{\langle E(\mathbf{x}) u_i'(\mathbf{x} + \Delta\mathbf{x}) \rangle}{\langle E^2(\mathbf{x}) \rangle} \tag{4.22}$$

As seen in Eqn. 4.22, the coefficients A_{i1} for the linear estimate of the conditional average are generated by computing the unconditional correlation between the event E and the data u_i'. By choosing the event E as the swirling strength λ_{ci}, and substituting Eqn. 4.22 into Eqn. 4.19, the estimate of the conditional average becomes

$$\langle u_i'(\mathbf{x} + \Delta\mathbf{x}) \mid \lambda_{ci}(\mathbf{x}) \rangle = \frac{\langle \lambda_{ci}(\mathbf{x}) u_i'(\mathbf{x} + \Delta\mathbf{x}) \rangle}{\langle \lambda_{ci}(\mathbf{x}) \lambda_{ci}(\mathbf{x}) \rangle} \lambda_{ci}(\mathbf{x}) \tag{4.23}$$

It is seen from Eqn. 4.23 that the nature of the conditional average is not affected by the value of λ_{ci}. Choosing a larger value for the conditional event merely scales the resulting vectors, while the overall structure remains unchanged. This is a critical observation, as it limits the analysis of the conditionally averaged velocity fields to the organization and relative magnitudes of the vectors.

5. VORTEX IDENTIFICATION TECHNIQUES

The widely-accepted hairpin vortex packet model (Adrian, Meinhart & Tomkins 2000) has proven successful in describing the observed motions within a turbulent boundary layer, such as bursting, sweeps/ejections, and high/low-speed streaks. Adrian *et al.* (2000) found in their incompressible channel flow data that "the hairpin vortex signature is the single most readily observed flow pattern in the (x,y)-plane." Given the central role that vortices play in determining the boundary layer motions, it is therefore essential that these coherent structures are accurately detected and characterized. The identification of a vortex is a challenging task, complicated by the lack of an objective definition [Haller (2005); Jeong & Hussain (1995)]. Most classical definitions describe a vortex as a region of concentrated vorticity, though this description may be inadequate in regions of high shear. Other researchers have proposed the presence of locally spiraling streamlines (Chong et *al*. 1990), or the existence of a pressure minimum (Jeong & Hussain 1995). The numerous descriptions of a vortex have spawned a correspondingly extensive list of detection methods. Unfortunately, no single definition/method is appropriate for all turbulent flows. A brief description of several successful structure identification schemes is given below, emphasizing only the most common methods used in two-dimensional data. For a thorough listing of vortex ID techniques over the past 30 years, see Table 1 of Kolář (2011).

5.1. Vortex Identification Methods

Several common vortex identification methods are described in the following sub-sections, with special emphasis upon the inherent assumptions and limitations of each technique. Note that the two-dimensional nature of the current data prevents the direct detection of three-dimensional coherent structures (for a three-dimensional view of a turbulent boundary layer, see the Mach 2 PIV data of Elsinga *et al.* (2010) and the Mach 5 visualizations of Humble *et al.* (2012)). Therefore, the current methods rely upon

detection of a "vortex signature." The nature of this signature is dependent upon the identification technique being employed, but is consistent with the presence of a hairpin vortex (or detached vortex, if in the outer layer).

5.1.1. Vorticity

Vorticity is the simplest, and most intuitive, means of detecting vortices. The concept of a rotating fluid structure naturally suggests a concentrated region of vorticity, consistent with the "tangle of vortex filaments" described by Hussain (1986). For two-dimensional data, only the spanwise vorticity ω_z is available, defined as

$$\omega_z = \frac{\partial V}{\partial x} - \frac{\partial U}{\partial y} \tag{5.1}$$

Streamwise-aligned structures, such as hairpin legs, are not detectable in this orientation. The vortex signature detected by this method corresponds to the hairpin "head", aligned roughly perpendicular to the *x*-*y* plane.

It is evident from Eqn. 5.1 that the bulk of ω_z is due to the primary shear *dU/dy*. Since vorticity is a measure of both the shear and rotation, the large strain rates near the wall may obscure any rotational motions corresponding to vortices. As an example, see the vorticity contours shown in Fig. 5.1 for the smooth ZPG case. The near-wall shear creates a large band of vorticity below $y/\delta = 0.2$. While the subtraction of a convective velocity $U_c = 0.85U_e$ shows that some of these features are indeed vortices, the large gradients in this region have the effect of "smearing out" the vortex signature, instead of displaying discrete coherent structures.

However, the reasoning given above, along with the example in Fig. 5.1, does not suggest that vorticity is ill-suited for vortex identification in *all* experiments. Humble *et al.* (2009) noted that vorticity magnitude is "an appropriate quantity for the visualization of vortical structures in this flow", referring to their Mach 2 tomographic PIV images of

a shock wave/boundary layer interaction. It is possible, and indeed likely, that the "smeared out" near-wall regions in Fig. 5.1 would gain structural significance if visualized as part of a three-dimensional data set. Therefore, the limitations of vorticity in this experiment may simply be due to the two-dimensional nature of the data.

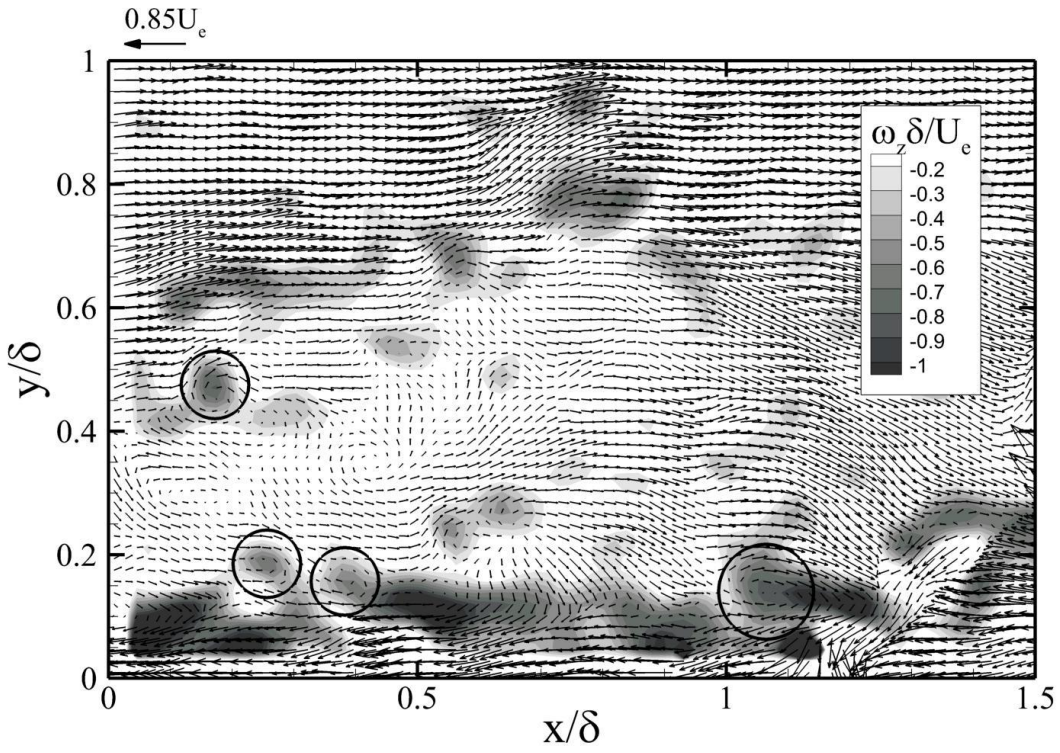

Figure 5.1 Vorticity contour of an instantaneous velocity field, for the smooth ZPG case. *The vorticity has been scaled by the boundary layer thickness and freestream velocity. A convective velocity of 0.85Ue has been subtracted from the streamwise component. Circles indicate locally spiraling fluid.*

5.1.2. Galilean Decomposition

In the past few decades, turbulent boundary layer research has increasingly focused upon the interaction between the near-wall vortex structures, as well as their locally induced flowfields. In doing so, many researchers have come to adopt the definition stated by Robinson (1991): "A vortex exists when instantaneous streamlines mapped onto a plane

normal to the vortex core exhibit a roughly circular or spiral pattern, when viewed from a reference frame moving with the center of the vortex core." This definition is central to the method of Galilean decomposition, which exposes vortices by presenting them in a convective reference frame. The resulting coherent structures are easily recognized (see the circled vortices in Fig. 5.1).

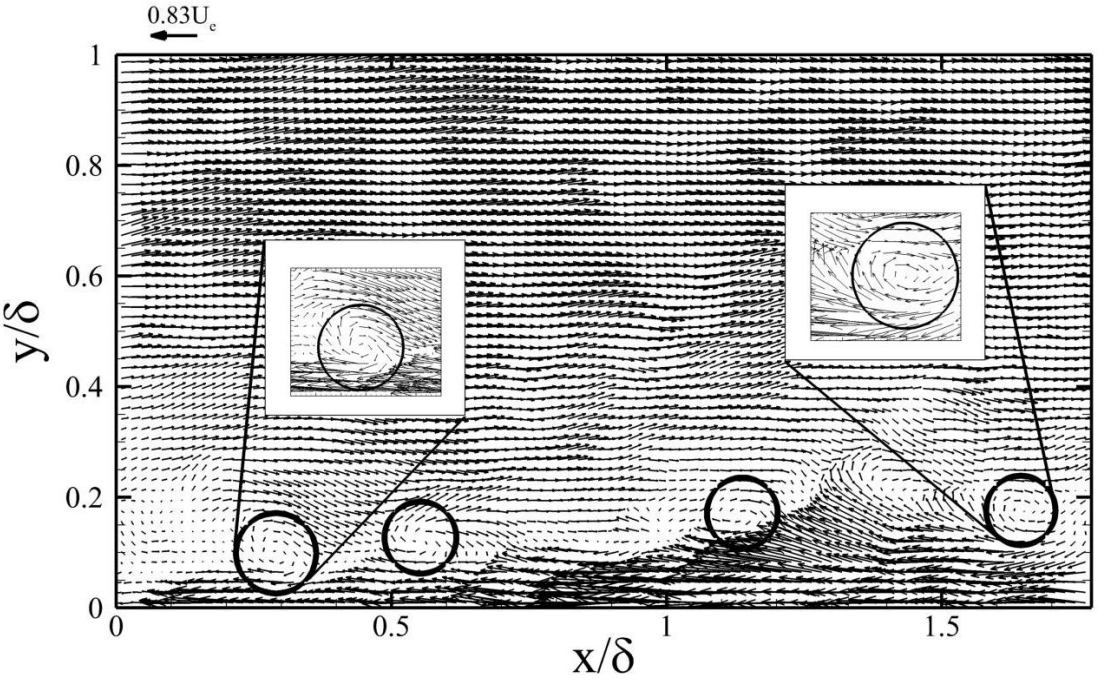

Figure 5.2 Galilean decomposition of an instantaneous velocity field, after subtracting a convective velocity $U_c = 0.83U_e$. *Detected vortices are circled, and examples of the locally spiraling flowfield are magnified.*

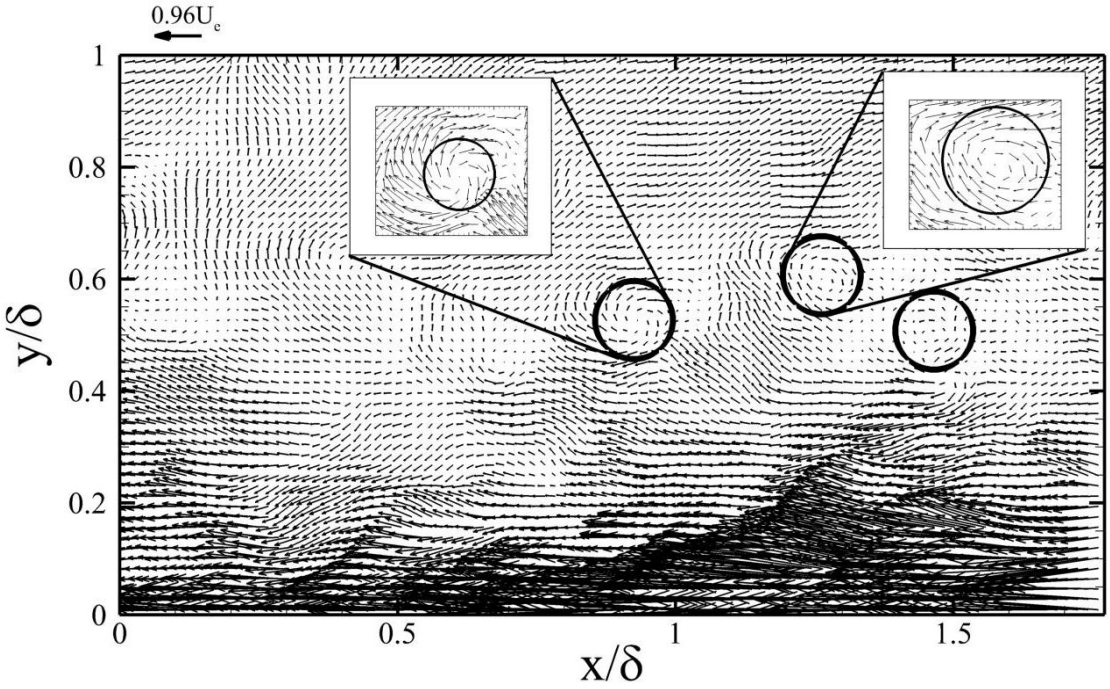

Figure 5.3 Galilean decomposition of an instantaneous velocity field, after subtracting a convective velocity U_c = 0.96U_e. *Detected vortices are circled, and examples of the locally spiraling flowfield are magnified. This flowfield is the same as that shown in Fig. 5.2, showing the effect of U_c.*

However, Robinson (1991) goes on to explain that choosing the correct reference frame is an iterative process. This is illustrated in Figs. 5.2 – 5.3, in which convective velocities equal to 83% and 96% of the freestream value, respectively, are subtracted from the instantaneous streamwise velocity of the same image. When the subtracted convective velocity is equal to the velocity at the center of a vortex core, the resulting velocity vectors resemble a circular or spiraling motion. As the subtracted velocity is increased, the previously uncovered vortices are lost, and new structures are revealed. The weakness of this method is that the convective velocity is not known *a priori*, and that any vortices revealed through this technique must be visually identified. These limitations have relegated Galilean decomposition to the role of validating vortices that have been detected through other methods (e.g. swirling strength, Q-criterion). In fact,

the circled vortices in Figs. 5.2 – 5.3 were originally detected through the swirling strength.

5.1.3. Local Pressure Minimum (λ_2 criterion)

Hunt, Wray & Moin (1988) initially proposed that the presence of a pressure minimum is a necessary, but not sufficient, condition for the existence of a vortex. Physically, the centrifugal force generated by the spiraling fluid within a coherent structure must be balanced by a pressure minimum at the vortex core, though this requirement is only true for steady inviscid flow. Jeong & Hussain (1995) showed that pressure minima may arise in unsteady irrotational motion absent any spiraling motion, due to the unsteady strain rate. Additionally, viscous effects in Stokes flow will prevent the creation of pressure minima, even in the presence of a vortex. They concluded that the use of pressure as the sole indicator of a vortex will fail in regions of unsteady strain and viscous effects.

Based upon these limitations, Jeong & Hussain (1995) formulated a new criterion using the pressure Hessian, which can describe local pressure extrema. Taking the gradient of the incompressible Navier-Stokes equation results in

$$a_{i,j} = -\frac{1}{\rho} p_{,ij} + \nu u_{i,jkk} \tag{5.2}$$

where $a_{i,j}$ is the acceleration term, $p_{,ij}$ is the pressure Hessian, and ν is the viscosity. Equation 5.2 is presented in indicial notation, with a subscript "," denoting differentiation. The acceleration can be decomposed into symmetric and antisymmetric components:

$$a_{i,j} = \underbrace{\left[\frac{DS_{ij}}{Dt} + \Omega_{ik}\Omega_{kj} + S_{ik}S_{kj}\right]}_{symmetric} + \underbrace{\left[\frac{D\Omega_{ij}}{Dt} + \Omega_{ik}S_{kj} + S_{ik}\Omega_{kj}\right]}_{antisymmetric} \tag{5.3}$$

The strain S_{ij} and rotation (vorticity) Ω_{ij} tensors are given by

$$S_{ij} = \frac{1}{2}\left(\frac{\delta u_i}{\delta x_j} + \frac{\delta u_j}{\delta x_i} \right)$$
$$\Omega_{ij} = \frac{1}{2}\left(\frac{\delta u_i}{\delta x_j} - \frac{\delta u_j}{\delta x_i} \right) \tag{5.4}$$

By neglecting the antisymmetric part of the acceleration in Eqn. 5.3, which constitutes the vorticity transport equation, Eqn. 5.2 can be rewritten as

$$\cancel{\frac{DS_{ij}}{Dt}} - \cancel{\nu S_{ij,kk}} + \boldsymbol{\Omega}^2 + \mathbf{S}^2 = -\frac{1}{\rho} p_{,ij} \tag{5.5}$$

(irrotational strain; viscous effects)

Since irrotational strain and viscous effects are negligible within a vortex core, the first two terms on the left side of Eqn. 5.5 can be neglected. Jeong & Hussain (1995) stated that "the occurrence of a local pressure minimum in a plane requires two positive eigenvalues" of the pressure Hessian $p_{,ij}$. Using Eqn. 5.5, this definition can be reformulated to require that $\boldsymbol{S^2+\Omega^2}$ have two negative eigenvalues. When the three eigenvalues of $\boldsymbol{S^2+\Omega^2}$ are ordered as $\lambda_1 \geq \lambda_2 \geq \lambda_3$, a vortex core can be said to exist when $\lambda_2 < 0$. Thus, the λ_2-criterion utilizes the concept of a pressure minimum to identify a vortex in an incompressible fluid, while compensating for viscous effects and unsteady motion.

The extension of this technique to compressible flows introduces additional terms, due to the non-zero divergence and non-zero density gradients. Following the steps described by Cucitore, Quadrio & Baron (1999), the previous derivation can be repeated for the compressible Navier-Stokes equation:

$$\rho\left(u_{i,t} + u_k u_{i,k}\right) = -p_{,i} + \mu u_{i,kk} + \left(\lambda + \mu\right) u_{k,ik} \tag{5.6}$$

where λ is the bulk viscosity, and the terms in the parentheses on the left side are the total derivative Du_i/Dt. Taking the gradient $(\,)_{,j}$ of Eqn. 5.6 yields

$$\rho\left(u_{i,jt}+u_{k,j}u_{i,k}+u_k u_{i,jk}\right)=-p_{,ij}+\mu u_{i,jkk}+(\lambda+\mu)u_{k,ijk}-\rho_{,j}\left(u_{i,t}+u_k u_{i,k}\right) \qquad (5.7)$$

Isolating the symmetric component of Eqn. 5.7 and substituting in S_{ij} and Ω_{ij} gives

$$\begin{aligned}\rho\frac{DS_{ij}}{Dt}+\rho\left(S_{ik}S_{kj}+\Omega_{ik}\Omega_{kj}\right)-\mu S_{ij,kk}-(\lambda+\mu)u_{k,ijk}+\\ +\frac{1}{2}\left(\rho_{,j}\frac{Du_i}{Dt}+\rho_{,i}\frac{Du_j}{Dt}\right)=-p_{,ij}\end{aligned} \qquad (5.8)$$

Compared to the incompressible form given in Eqn. 5.5, the equation for the pressure Hessian in Eqn. 5.8 contains additional terms, due to the non-zero divergence and density gradients present in a compressible flow. Even if the irrotational strain and viscous terms are discarded, Eqn. 5.8 does not directly relate the pressure Hessian $p_{,ij}$ to $\mathbf{S}^2+\mathbf{\Omega}^2$. Therefore, Kolár (2009) has concluded that "the λ_2 criterion is not extendable to compressible flows."

5.1.4. Q-Criterion

Hunt *et al.* (1988) suggested that a vortex (or "eddy zone" in their terminology) can be identified by two criteria: 1) the irrotational strain is much smaller than the vorticity, and 2) there is a pressure minimum within the vortex. The second criterion is necessary for rotational flow to ensure that the streamlines are curved. However, this pressure criterion is often neglected in practice, and its utility in detecting vortices has been questioned (see §5.1.3 and Jeong & Hussain (1995)).

The first criterion, that the irrotational strain be much smaller than the vorticity, can be further explored by examining the velocity gradient, or "deformation", tensor $\nabla\vec{V}$. For a

three-dimensional flow, eigenvalue decomposition of the deformation tensor yields the characteristic equation

$$\lambda^3 + P\lambda^2 + Q\lambda + R = 0 \tag{5.9}$$

where λ are the eigenvalues, and the principal invariants of $\nabla\vec{V}$ are given by

$$P = \nabla \cdot \vec{V} \tag{5.10}$$

$$Q = \frac{1}{2}\left(\left(\nabla \cdot \vec{V}\right)^2 - \mathrm{tr}\left(\nabla \vec{V}^2\right)\right) \tag{5.11}$$

$$R = -\mathrm{Det}\left[\frac{\delta u_i}{\delta x_j}\right] \tag{5.12}$$

The operator "Det" in Eqn. 5.12 refers to the determinant. The *Q* invariant in Eqn. 5.11 can be rewritten as

$$Q = \frac{1}{2}\left(P^2 + \|\Omega\|^2 - \|S\|^2\right) \tag{5.13}$$

where $\|\Omega\| = \mathrm{tr}\left[\Omega\Omega^t\right]^{1/2}$ and $\|S\| = \mathrm{tr}\left[SS^t\right]^{1/2}$. Recall from previous discussions that **S** and **Ω** are the strain and rotation (vorticity) tensors, and comprise the symmetric and antisymmetric parts of $\nabla\vec{V}$, respectively. Expressions for these terms are given in Eqn. 5.4.

For an incompressible flow, *P*=0, and Eqn. 5.13 is a measure of the relative contributions of vorticity and strain. If Q > 0, then the strain is smaller than the vorticity, thus satisfying the first criterion set by Hunt *et al.* (1988). This method is independent of the choice of reference frame, due to the use of the principal invariants. While the invariants in Eqns. 5.10 – 5.12 were originally derived for a three-dimensional flow, Eqn. 5.13 has been successfully applied to many incompressible two-dimensional

flowfields. Along with the swirling strength (described below in §5.1.5), the Q-criterion is one of the most widely used vortex identification schemes.

5.1.5. Swirling Strength

Returning to the vortex definition given by Robinson (1991), vortices can be identified by circular instantaneous streamlines, spiraling about a point in the convective reference frame. The basic premise of the swirling strength λ_{ci} originates with the work of Chong, Perry & Cantwell (1990), who analyzed the critical points of the surface defined by the characteristic equation of the velocity gradient tensor $\nabla\vec{V}$. They found that locally spiraling streamlines exist when two eigenvalues of $\nabla\vec{V}$ are complex. It should be noted that this criteria was binary: the presence of a vortex was merely identified by the existence of complex eigenvalues. No additional information on the coherent structures was provided by this scheme.

Zhou *et al.* (1999) extended this concept by examining the magnitude of the eigenvalues of $\nabla\vec{V}$. If a vortex is present, then the analysis of Chong *et al.* (1990) would require that $\lambda = \{\lambda_r, \lambda_{cr} \pm i\lambda_{ci}\}$, where $\lambda_{cr} \pm i\lambda_{ci}$ is the conjugate pair of complex eigenvalues. The corresponding eigenvectors are given by $v = \{v_r, v_{cr}, v_{ci}\}$. Note that the subscripts of λ and v are not indicial notation. In three dimensions, the flow is stretched along the vortex axis v_r, while v_{cr} and v_{ci} describe the plane of local swirling flow. Zhou *et al.* (1999) showed that the swirling rate is contained in λ_{ci}, which is labeled as the *swirling strength*. Specifically, λ_{ci} describes the period necessary to complete one revolution about the vortex core, given by $2\pi/\lambda_{ci}$. The degree of stretching or contraction along the vortex axis v_r is described by λ_r. In a steady field, the resulting streamlines can be represented in the curvilinear coordinate system (y_1, y_2, y_3) defined by $\{v_r, v_{cr}, v_{ci}\}$ as (Zhou *et al.* 1999)

$$y_1(t) = C_r \exp(\lambda_r t) \tag{5.14}$$

$$y_2(t) = \exp\left(\lambda_{cr} t\right)\left[C_c^{(1)} \cos\left(\lambda_{ci} t\right) + C_c^{(2)} \sin\left(\lambda_{ci} t\right)\right] \tag{5.15}$$

$$y_3(t) = \exp\left(\lambda_{cr} t\right)\left[C_c^{(2)} \cos\left(\lambda_{ci} t\right) - C_c^{(1)} \sin\left(\lambda_{ci} t\right)\right] \tag{5.16}$$

where C_r, $C_c^{(1)}$, and $C_c^{(2)}$ are constants. When this technique is applied to two-dimensional data, the computed λ_{ci} represents the component of swirling within the plane of the data.

Applying this technique to the same image used in Figs. 5.2 – 5.3 shows good agreement with the locally spiraling velocity identified through Galilean decomposition (§5.1.2). The resulting contours of λ_{ci} are given in Figs. 5.4 – 5.5. Note that no assumptions of incompressibility were made during the derivation, suggesting that this method is applicable for compressible flows. Indeed, it is the reliance solely upon the flow kinematics that makes this technique so attractive.

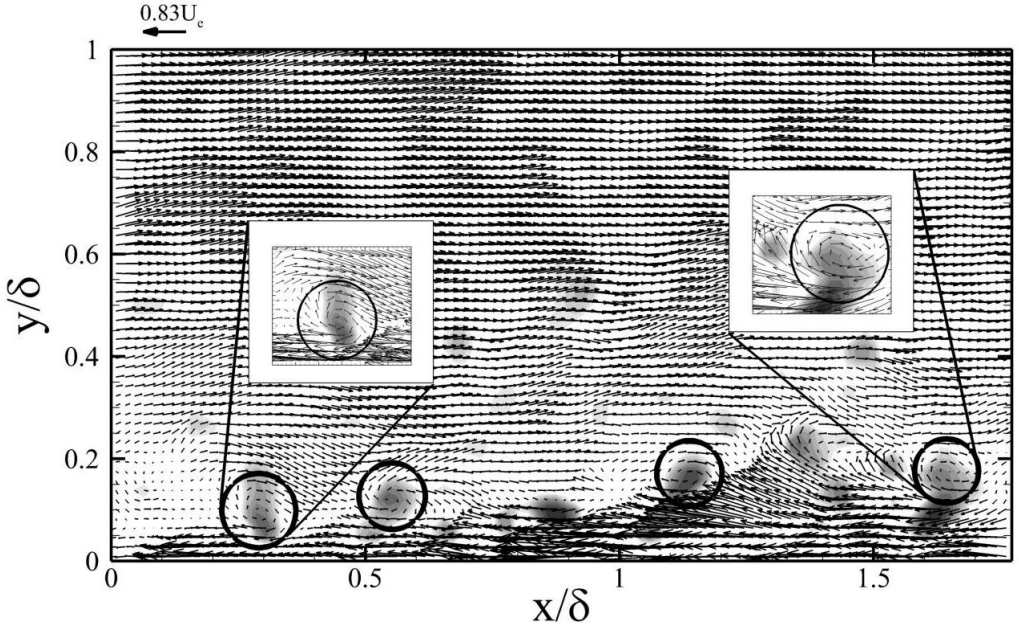

Figure 5.4 Contours of swirling strength λ_{ci}, after subtracting a convective velocity $U_c = 0.83U_e$.
Detected vortices are circled, and examples of the locally spiraling flowfield are magnified. This flowfield is the same as that shown in Fig. 5.2.

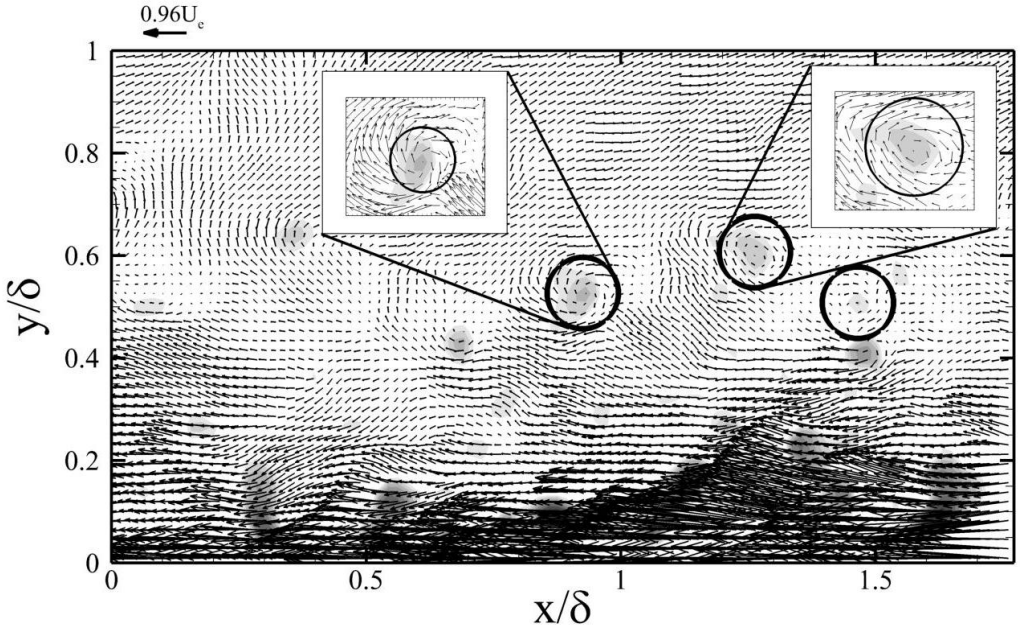

Figure 5.5 Contours of swirling strength λ_{ci}, after subtracting a convective velocity $U_c = 0.96U_e$. *Detected vortices are circled, and examples of the locally spiraling flowfield are magnified. This flowfield is the same as that shown in Fig. 5.3.*

5.2. Vortex ID Methods in Current Study

Many of the previously described detection schemes have proven effective in incompressible flowfields, and were instrumental in verifying many long-standing theories on the behavior of coherent structures. However, these same techniques have seen limited use in supersonic flows, and generally only for LES and DNS simulations [Marusic *et al.* (2000); Taylor, Martin & Smits (2005); Ringuette, Wu & Martin (2007); Pirozzoli, Bernardini & Grasso (2008); von Terzi, Sandberg & Fasel (2009)]. These numerical studies are inherently three-dimensional, and do not suffer from the measurement uncertainty associated with experimental data. Additionally, the simulated nature of these data allows the researchers to validate the applied vortex detection scheme by comparing the educed eddies with local pressure minima (recall from §5.1.4 that a local pressure minimum is a necessary condition for the Q-criterion). Knowledge

of the instantaneous static pressure field is generally not available in experimental data. Given these factors, it should come as no surprise that the application of vortex identification techniques to compressible experimental data is extremely rare. The author is aware of only two experiments that have employed these techniques: the Mach 2 flat-plate study of Elsinga *et al.* (2010), and the Mach 2.1 shock wave/turbulent boundary layer interaction (SWTBLI) data of Humble *et al.* (2009). Both of these studies used tomographic PIV to visualize the instantaneous three-dimensional velocity fields.

Highly compressible boundary layers pose a considerable challenge for many of the vortex identification techniques described in §5.1, whether due to boundary conditions (i.e. wall-bounded flow) or compressibility effects. Contours of vorticity (§5.1.1) are obscured by high shear near the wall, which is the most intriguing region in this study. Galilean decomposition (§5.1.2) is capable of rendering structures with locally spiraling streamlines, but only if the convective velocity of each structure is known *a priori*. Detecting pressure minima through the λ_2-criterion (§5.1.3) is unsuited for compressible flow, due to the argument given by Cucitore *et al.* (1999) . For the current study, both the Q-criterion and swirling strength λ_{ci} were tested as possible candidates for the eduction of turbulent vortices. Due to the fact that these analysis methods have never been applied to experimental data in this Mach number regime, it was necessary to investigate two methods, in order to determine the best choice for these data. It will be shown in §5.2.2 that while the Q-criterion is an appropriate choice for weakly compressible flows, the compressibility corrections necessary to detect coherent structures in a Mach 4.9 boundary layer have cast doubt upon the suitability of this technique for the current study. The following sub-sections will discuss the implementation of these algorithms (§5.2.1), as well as compressibility effects and corrections (§5.2.2), scaling and thresholds (§5.2.3), filtering of detected vortices (§5.2.4), and mechanical distortion effects (§5.2.5).

5.2.1. Implementation of Vortex Detection Algorithms

Both the Q-criterion and swirling strength are computed from the velocity gradient tensor $\nabla\vec{V}$. The evenly spaced vectors of the velocity fields allows for easy implementation of a finite difference scheme. Several common finite difference operators are given in Table 6.2 of Raffel *et al.* (2007), including central difference and Richardson extrapolation. A researcher may be tempted to select a lower-order operator (e.g. forward/backward difference) in order to compute a more "localized" gradient, and avoid the smoothing associated with higher-order schemes. However, that reasoning does not consider the relatively large uncertainties and truncation errors associated with differentiating experimental data. Given that the largest uncertainty in the computed gradients is due to measurement uncertainty of the velocity, the "least squares" operator was chosen for this study, which "attempts to reduce the effects of the random errors, that is, the measurement uncertainty, ε_u" (Raffel *et al.* 2007). The formula for this scheme is given as

$$\left(\frac{du}{dx}\right)_i \approx \frac{2u_{i+2} + u_{i+1} - u_{i-1} - 2u_{i-2}}{10\Delta x} \tag{5.17}$$

where Δx is the vector spacing, u is the velocity, and the subscript i denotes the spatial position. In the current study, the finite difference scheme in Eqn. 5.17 is applied at every point, populating the velocity gradient tensor $\nabla\vec{V}(x, y)$ for each of the instantaneous velocity fields. The swirling strength is extracted from the imaginary part of the complex eigenvalue of $\nabla\vec{V}$, while the Q-criterion is computed directly from the tensor components.

5.2.2. Compressibility Effects

Recalling the overview of vortex detection schemes given in §5.1, it is clear that λ_{ci} is based solely upon the kinematics of the flow, without any requirement of

incompressibility. However, the derivation of the Q-criterion given in Eqns. 5.9 – 5.13 explicitly requires that $\nabla \cdot \vec{V} = 0$. The application of the Q-criterion to compressible flow is questionable, due to the non-zero divergence of the flow ($P \neq 0$). Therefore, the second invariant of the velocity gradient tensor does not indicate the balance between local rotation and strain, i.e. $Q \neq \frac{1}{2}(\|\Omega\|^2 - \|S\|^2)$. The Q-criterion can still be applied to compressible flow, but a sufficiently large threshold value must be selected, such that the rotation rate is larger than the strain rate. The selection of this threshold for highly-compressible flows (i.e. $M \geq 5$) is ambiguous at best, and relies upon visual inspection of the resulting structures. Regardless, this technique has been applied to the supersonic flat-plate flowfield of Elsinga *et al.* (2010). They justified this usage based upon the fact that "compressibility effects are expected not to be important" in their Mach 2 flowfield, which is not necessarily true for the current Mach 4.9 study. It should be noted that Elsinga *et al.* (2010) also used the swirling strength for identifying vortices, since they found that the Q-criterion had difficulty in distinguishing closely spaced vortical structures.

Based upon the above argument, it seems logical to discard the Q-criterion based upon the requirement of incompressibility, and to proceed solely with the swirling strength. This is further supported by the fact that the Q-criterion has the tendency to produce "false positives", i.e. vortices which meet the criteria of the detection scheme, but are clearly not eddies. Examples of these "false positives" are given in Fig. 5.6 for an instantaneous velocity field from the smooth ZPG case. When the local convection velocity is subtracted, the flowfields show negligible rotation. While it is possible for the swirling strength to also falsely detect such structures, they did not occur as often.

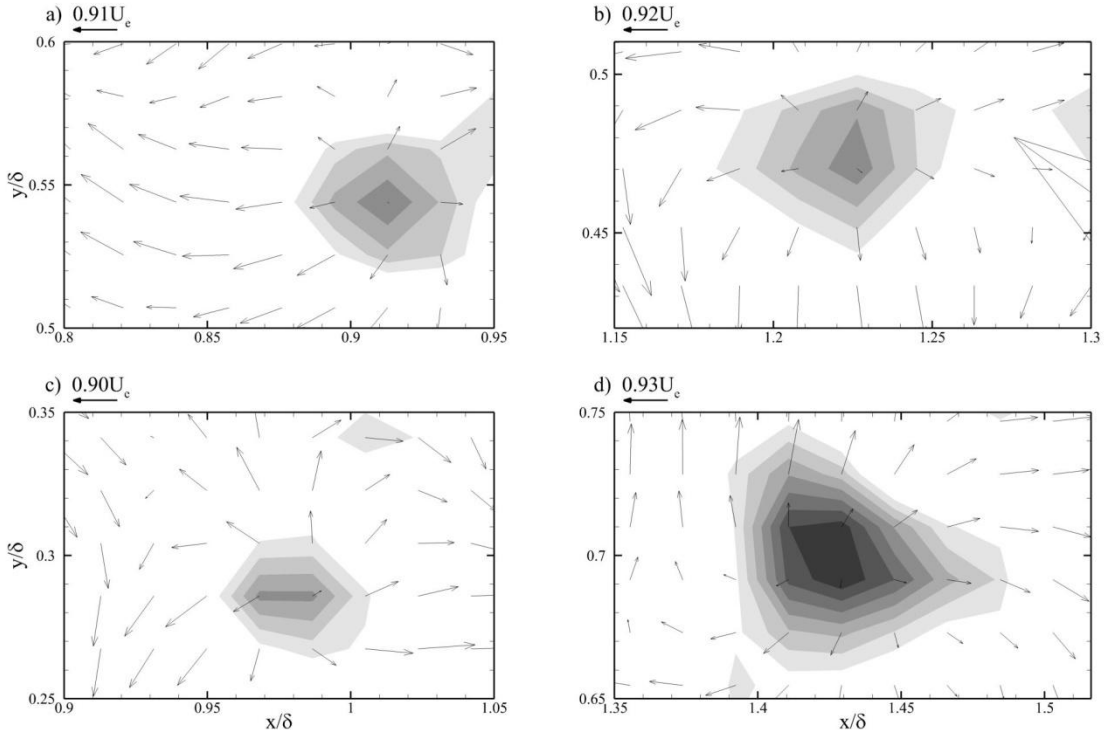

Figure 5.6 "False positive" vortices detected by the Q-criterion, after subtracting a local convective velocity. *Note that each of the detected "vortices" shows negligible rotation.*

Before the Q-criterion was discarded, a compressibility correction was applied to the algorithm, in order to remove the requirement that P=0. Since $Q = \frac{1}{2}(P^2 + \|\Omega\|^2 - \|S\|^2)$ for a compressible flow, it was possible to artificially set P=0 by modifying the diagonal components of the velocity gradient tensor as

$$\nabla \vec{V}_{inc} = \begin{pmatrix} \frac{du}{dx} & \frac{du}{dy} \\ \frac{dv}{dx} & \frac{dv}{dy} \end{pmatrix} - \frac{1}{2}\begin{pmatrix} \frac{du}{dx} + \frac{dv}{dy} & 0 \\ 0 & \frac{du}{dx} + \frac{dv}{dy} \end{pmatrix} \tag{5.18}$$

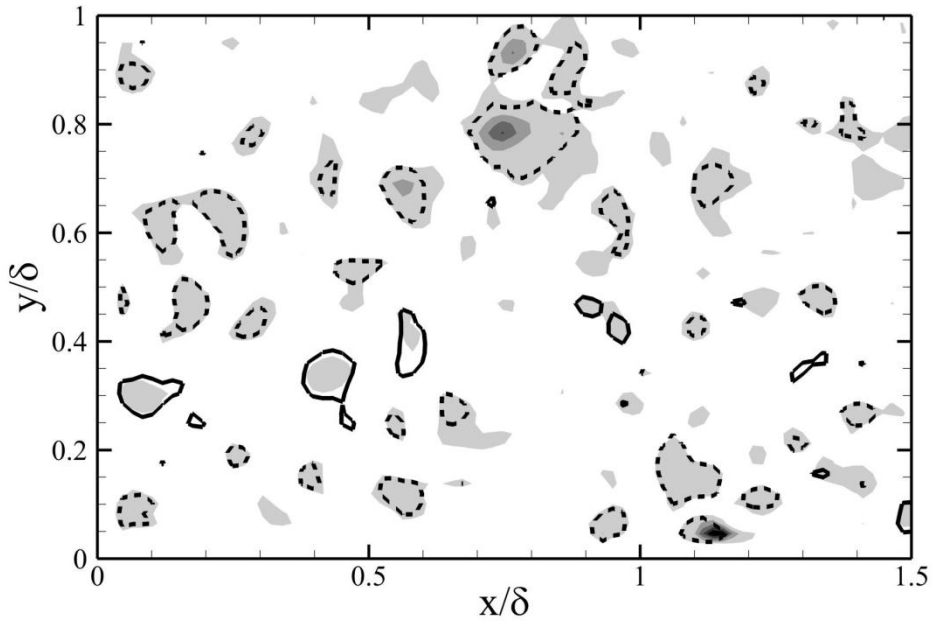

Figure 5.7 Comparison of the swirling strength (lines) and Q-criterion (contours). *Note that the Q-criterion over-predicts the presence of vortices.*

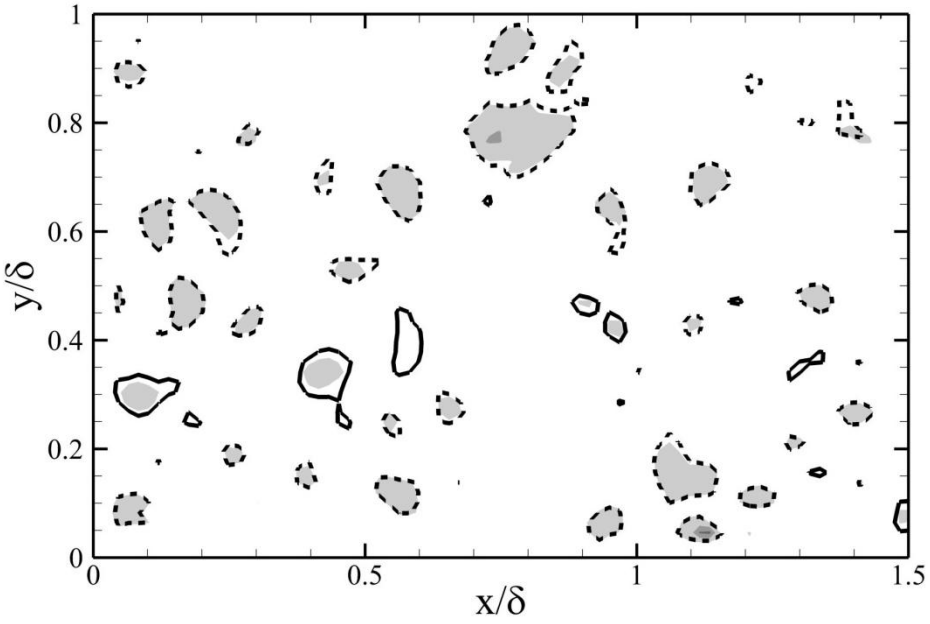

Figure 5.8 Comparison of the swirling strength (lines) and *corrected* Q-criterion (contours).

The trace of the resulting tensor $\nabla \vec{V}_{inc}$ is necessarily zero, and the requirement of $P = 0$ is satisfied, yielding $Q_{inc} = \frac{1}{2}(\|\Omega\|^2 - \|S\|^2)$. This correction drastically reduced the number of "false positive" vortices, and produced results consistent with the swirling strength. A comparison of the Q-criterion versus λ_{ci} is given in Fig. 5.7, followed by the corrected Q-criterion versus λ_{ci} in Fig. 5.8. These figures show that when compressibility corrections are applied, the Q-criterion and swirling strength produce reasonably consistent results, suggesting that both techniques are appropriate for high-Mach numbers flows. However, note that this comparison was only made for the baseline undistorted case. It was anticipated that the large bulk dilatation encountered through the expanding FPG flows, and periodically within the rough-wall flowfield, would render the Q-criterion unsuitable for mechanically distorted flows. Ultimately, the swirling strength was chosen for use in the current study, based upon its independence from the compressible state of the flow. The proceeding sub-sections will discuss implementation of only the swirling strength.

5.2.3. Scaling and Threshold

The two-dimensional swirling strength is a scalar quantity, indicating the relative "strength" of rotation about the vortex core. However, the value of λ_{ci} provides no additional information on the sense of rotation. Following Wu & Christensen (2006a), the swirling strength is weighted by the sign of the spanwise vorticity ω_z

$$\Lambda_{ci}(x,y) = \lambda_{ci}(x,y)\frac{\omega_z(x,y)}{|\omega_z(x,y)|} \tag{5.19}$$

The new formulation of the swirling strength Λ_{ci} in Eqn. 5.19 allows the detection method to distinguish between prograde and retrograde vortices. "Prograde" and "retrograde" refer to vortices rotating with and against the primary shear. Note that prograde vortices display a negative swirling strength Λ_{ci}, owing to the sign of the

vorticity. The importance of distinguishing between prograde and retrograde vortices is discussed in §7.5, when attempting to explain the reduced shear stress through a favorable pressure gradient.

The description of the swirling strength in §5.1.5 states that locally spiraling motion exists when $\lambda_{ci} \neq 0$. Given the measurement uncertainty inherent in the velocity gradients, a small non-zero threshold is necessary to distinguish between detected vortices and background noise (the sensitivity of the vortex detection technique to this filter is shown in Appendix E). However, the selection of a global threshold is hindered by the fact that the magnitude of the swirling strength varies throughout the boundary layer, due to the dependence upon the velocity gradient tensor. In the near-wall region where the strain rates are largest, a small threshold value may eliminate spurious vortices while retaining the detected coherent structures. However, this same value applied in the outer layer may inadvertently remove legitimate vortices, due to the diminishing strain rate magnitude at the boundary layer edge. Nagaosa & Handler (2003) and Wu & Christensen (2006a) found that dividing the swirling strength (or Q-criterion for Nagaosa & Handler (2003)) by the local rms value $\Lambda_{ci}^{rms}(y)$ produced a parameter that is insensitive to the distance from the wall. The rms value is used for normalization because the mean swirling strength is biased to a small value, due to non-zero Λ_{ci} existing only within vortex cores. This same procedure is applied to the current study, with reasonable success.

Figure 5.9 shows the probability density function (PDF) for $\Lambda_{ci}(x,y) = \Lambda_{ci}(x,y) / \Lambda_{ci}^{rms}(y)$ in the smooth ZPG case. The large PDF value at $\Lambda_{ci} = 0$ is due to the areas of the boundary layer not contained within a vortex core. The prograde structures ($\Lambda_{ci} < 0$) appear to collapse onto a single curve when scaled by the rms value, with some scatter visible for $0 > \Lambda_{ci}(x,y) > -2$. The population of vortices within this range of magnitudes appears to be stratified by wall-normal distances, suggesting a larger number of prograde vortices in the near-wall region. This observation is consistent with the currently accepted vortex packet model. The retrograde structures show

excellent agreement when scaled by $\Lambda_{ci}^{rms}(y)$, but only for $y/\delta > 0.2$. This behavior will be explained in §6 as being due to the lack of retrograde vortices in the lower region of the boundary layer. The PDF in Fig. 5.9 also shows that the intensity of the swirling strength for retrograde events is much weaker than prograde structures, requiring two filter thresholds to be implemented. The thresholds were initially selected based upon the location of the maximum PDF value, yielding values of -1 and 0.5 for the prograde and retrograde vortices, respectively. However, the detection of spurious vortices required that the thresholds be increased to minimize the contribution of measurement noise. The resulting range of accepted vortices is $\Lambda_{ci}(x,y) \le -1.5$ and $\Lambda_{ci}(x,y) \ge 1$.

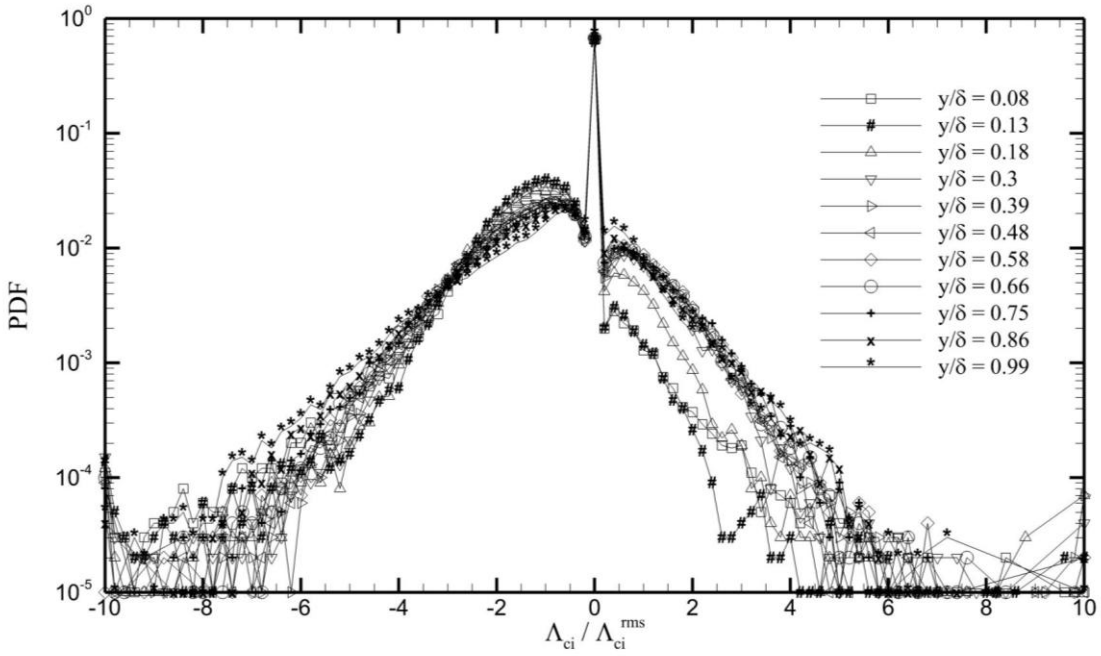

Figure 5.9 PDF of the swirling strength for the smooth ZPG case, scaled by $\Lambda_{ci}^{rms}(y)$ at each height.

5.2.4. Filtering of Detected Vortices

The vortices detected by these methods are thought to be representative of hairpin vortices in the near-wall region. The locally spiraling fluid, with the rotational axis aligned in the spanwise direction, is consistent with the presence of a hairpin "head." However, the spatial resolution of the current study, while higher than many of the previous studies at this Mach number, is still insufficient to capture the smallest and "youngest" developing vortices. The size of the detected vortices was calculated by counting the number of vectors within a detected vortex core, after applying the appropriate thresholds to the calculated values of $\Lambda_{ci}(x, y)$ at each point in the instantaneous flowfield. The spatial extent of a vortex core was determined based upon a four-connected neighborhood, where each point is considered the center of a square cell. A contiguous region is thus defined as including all cells which share a common edge. This differs from an eight-connected neighborhood, which also includes cells sharing only a single corner. Both of these templates are shown in Fig. 5.10. The four-connected template was used in the current study, providing a more conservative estimate of the vortex size. Using this method of estimating the vortex size, the total area A_v may be computed by multiplying the number of cells with Δx^2, where Δx is the vector spacing. For the current study, a minimum size limitation was enforced, such that structures spanning fewer than three vectors were rejected. A representative length scale can be computed as $L_v = \sqrt{A_v}$, yielding a minimum resolved vortex diameter of L_v = 36 viscous units for the smooth ZPG case.

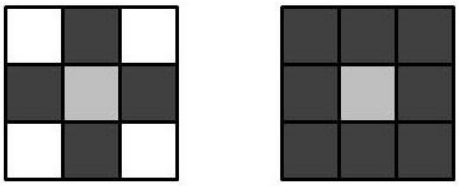

Figure 5.10 Templates used for determining the size of a vortex. *Left) Four-connected; Right) Eight-connected*

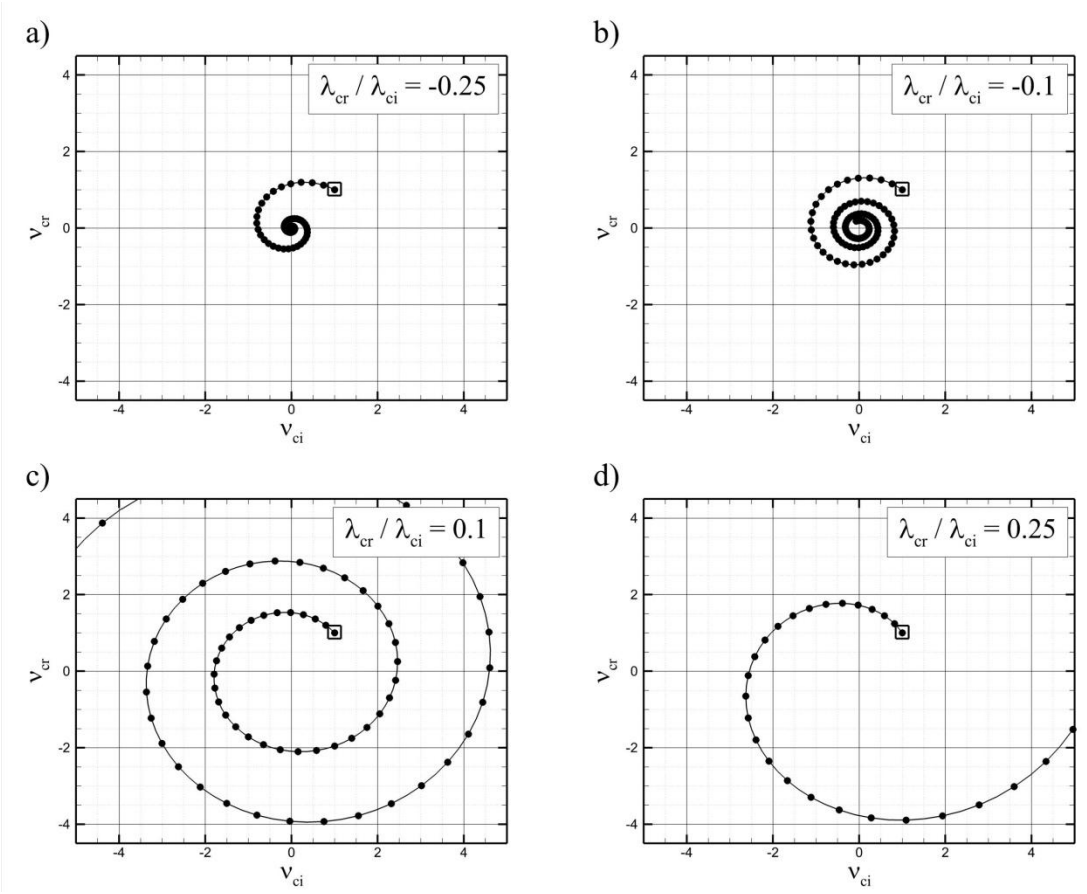

Figure 5.11 Examples of locally spiraling particles traces, showing the effects of $r = \lambda_{cr} / \lambda_{ci}$. *The particle motion is described by Eqns. 5.15 & 5.16, and the initial point is shown by an open box at (1,1).*

The final filter method applied to the detected vortices is based upon the notion of a vortex as a local region of spiraling fluid. Equations 5.15 and 5.16 describe the two-dimensional motion of a particle within a vortex, where the time necessary for one revolution about the vortex axis v_r is $2\pi/\lambda_{ci}$. Chakraborty *et al.* (2005) expanded upon this concept by determining the rate at which a particular vortex will converge/diverge. In their example, two particles are placed within a vortex, with an initial separation distance of r_0. The final distance r_f is a function of the eigenvalues λ_{cr} and λ_{ci}, and the number of revolutions n, computed as

$$\frac{r_f}{r_0} = \exp\left(2\pi n \frac{\lambda_{cr}}{\lambda_{ci}} \right) \tag{5.20}$$

Chakraborty *et al.* (2005) labeled the ratio $r = \lambda_{cr} / \lambda_{ci}$ the *inverse spiraling compactness*, as it describes the direction and magnitude of the spiraling motion. For values $r < 0$, a vortex spirals inward toward the origin, while $r > 0$ describes a diverging path that spirals outward. The case of $r = 0$ illustrates a circular orbit. Examples are given in Fig. 5.11, showing the effects of $\lambda_{cr} / \lambda_{ci}$.

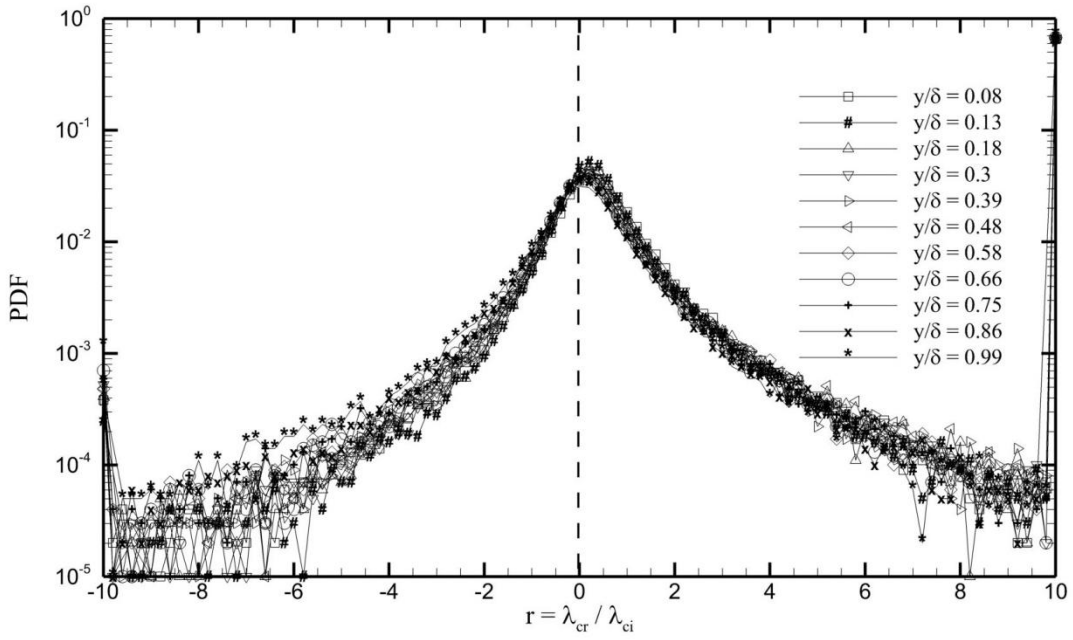

Figure 5.12 PDF of the inverse spiraling compactness, shown for the smooth ZPG case.

The ratio $r = \lambda_{cr} / \lambda_{ci}$ was implemented as a filter, such that any rapidly diverging motions are discarded. For large positive values of r, the particles within the vortex will quickly recede from each other, causing the structure to lose coherence. Additionally, the large separation distances after only one revolution (as described by Eqn. 5.20) will cause

particles at the vortex edge to experience a fluid environment that is non-local to the vortex core. It was therefore necessary to establish a positive upper bound on the allowable range of *r*. Following the method described above for selecting the $\Lambda_{ci}(x, y)$ threshold, a PDF was calculated for *r*, and shown in Fig. 5.12 for the smooth ZPG case. A clear peak is seen at $r = 0.25$, indicating that most of the vortices are spiraling slowly outward within the measurement plane. The threshold is set at $r = 0.5$, admitting a majority of the vortices while rejecting only the most rapidly diverging motions. This value is consistent with the upper bound computed by Chakraborty *et al.* (2005), who found that $r < 1/\sqrt{3}$ for incompressible flows.

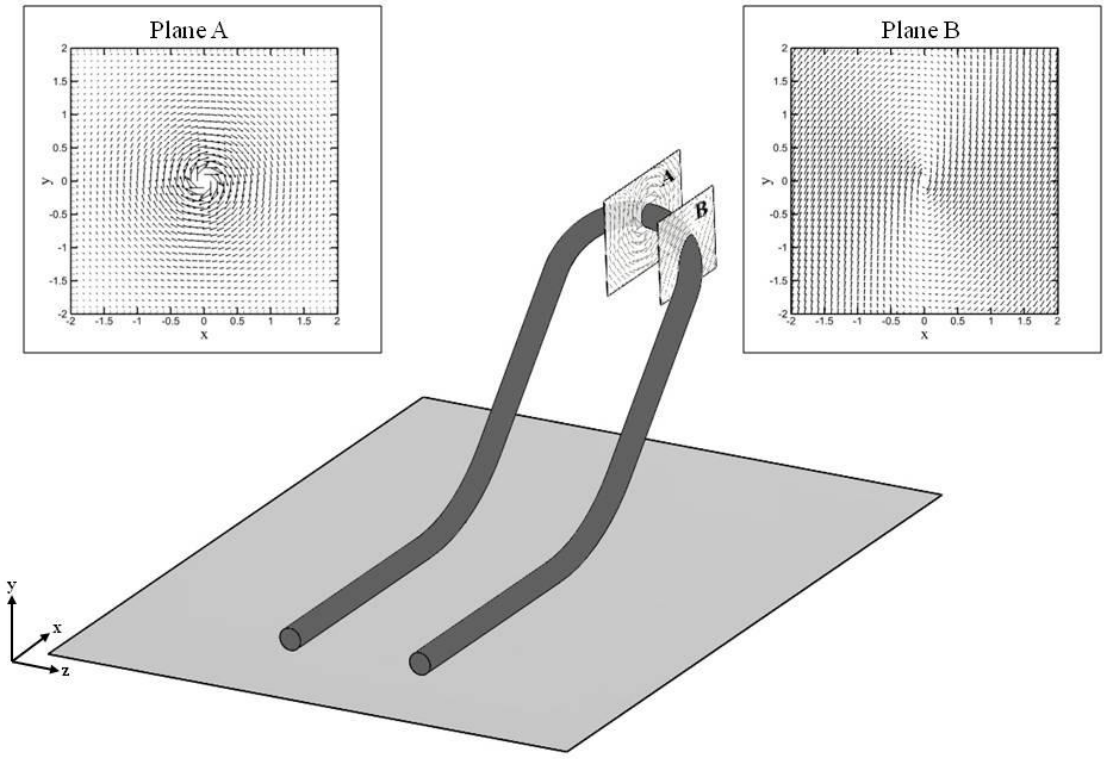

Figure 5.13 Examples of synthetic vortices, showing the effects of misalignment with the measurement plane.

Before continuing, it should be noted that the location of the maximum PDF in Fig. 5.12 does not necessarily mean that most coherent structures in the flowfield are diverging, only that their component of swirling motion in the *x*-*y* plane is spiraling outward. This may simply be a consequence of detecting three-dimensional rotational structures within a two-dimensional plane. If the vortex axis v_r is not aligned with the out-of-plane *z*-axis, the resulting vortex may appear distorted. An example of this is shown in Fig. 5.13 for synthetic vortices.

5.2.5. Mechanical Distortions Effects

The flowfields in this study pose a considerable challenge to the structure identification schemes reviewed above. The local gradients produced by the roughness elements impose extra strain rates upon the fluid, resulting in localized regions of dilatation and contraction. Additionally, the streamline curvature over the FPGs may result in deformation of any spiraling regions of fluid (i.e vortices). Before the response of the turbulent structures to mechanical distortions can be investigated, the effects of the imposed perturbations (i.e. surface curvature and roughness) upon the detection method must be explored.

The above examples utilized only the undistorted baseline flowfield. Before proceeding, it is necessary to determine if the selected thresholds are applicable to the distorted cases. PDFs of $\Lambda_{ci}(x,y) = \Lambda_{ci}(x,y) / \Lambda_{ci}^{rms}(y)$ are given in Figs. 5.14 – 5.16 for the smooth WPG, smooth SPG, and rough-wall cases, respectively. The trends appear to match those of the smooth ZPG case, including the location of the maximum PDF values and the reduction in the near-wall population of retrograde structures. The threshold values $\Lambda_{ci}(x,y) \le -1.5$ and $\Lambda_{ci}(x,y) \ge 1$ appear to be appropriate for the mechanically distorted cases. The same comparison is made for the *inverse spiraling compactness* in Figs. 5.17 – 5.19. For the smooth SPG case, the vortices above $y/\delta = 0.1$ show a stronger preference for positive *r* values, as compared to the smooth ZPG case, suggesting the

local flowfields near these vortices are more divergent in the outer layer. This may be due to the large dilatation in this region, and will be investigated further in §7. The distribution of r for the rough-wall case in Fig. 5.19 shows a more symmetric distribution around $r = 0$, with the peak PDF occurring near $r = 0.18$. The smooth WPG case appears qualitatively similar to the baseline model. While subtle differences may exist for the distorted cases, the choice of $r = 0.5$ as a threshold is still suitable.

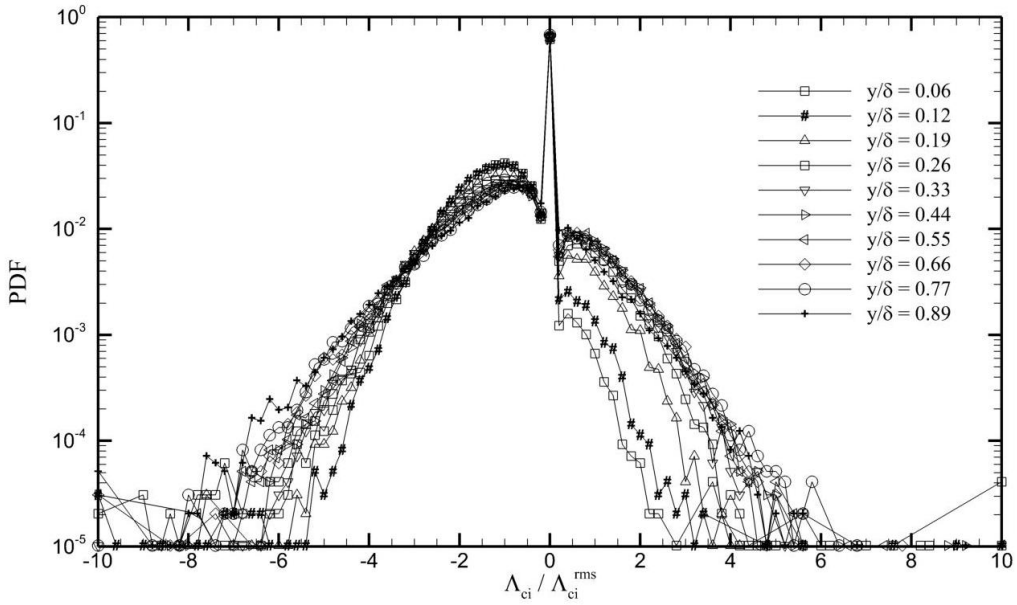

Figure 5.14 PDF of the swirling strength for the smooth WPG case, scaled by $\Lambda_{ci}^{rms}(y)$ at each height.

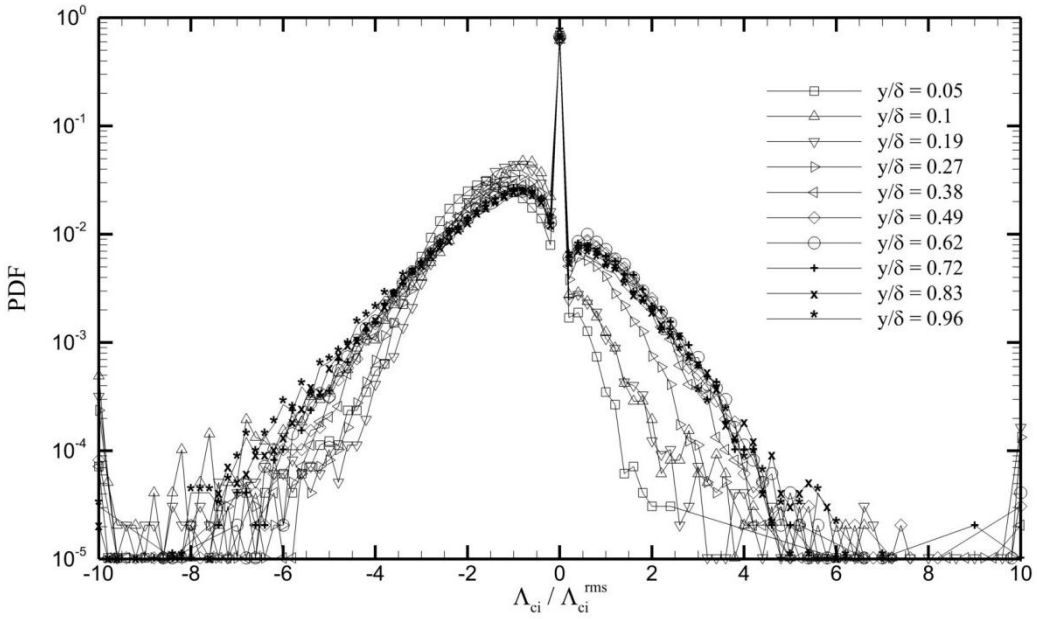

Figure 5.15 PDF of the swirling strength for the smooth SPG case, scaled by $\Lambda_{ci}^{rms}(y)$ at each height.

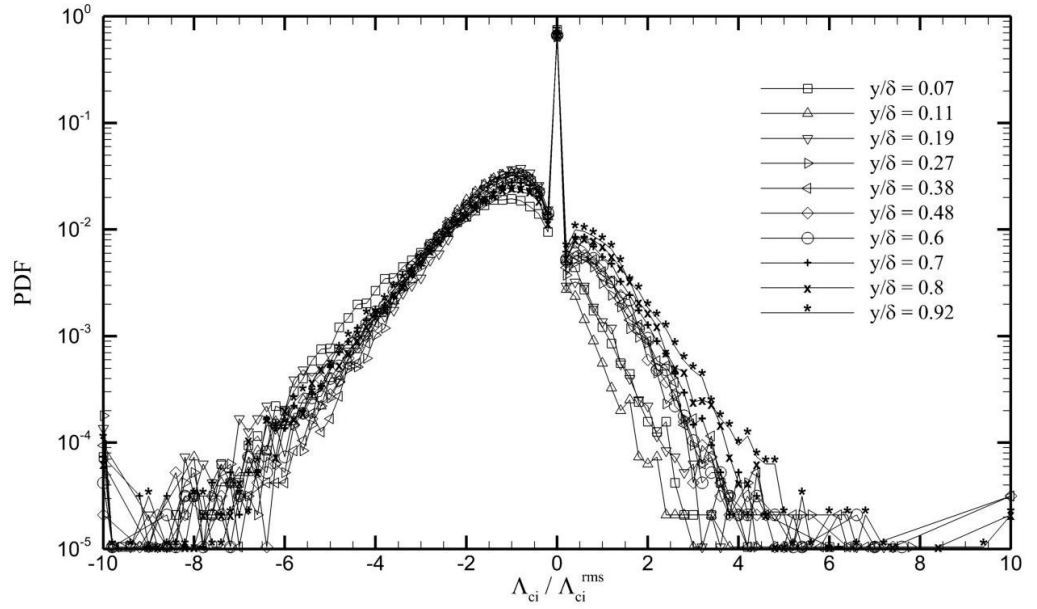

Figure 5.16 PDF of the swirling strength for the rough-wall case, scaled by $\Lambda_{ci}^{rms}(y)$ at each height.

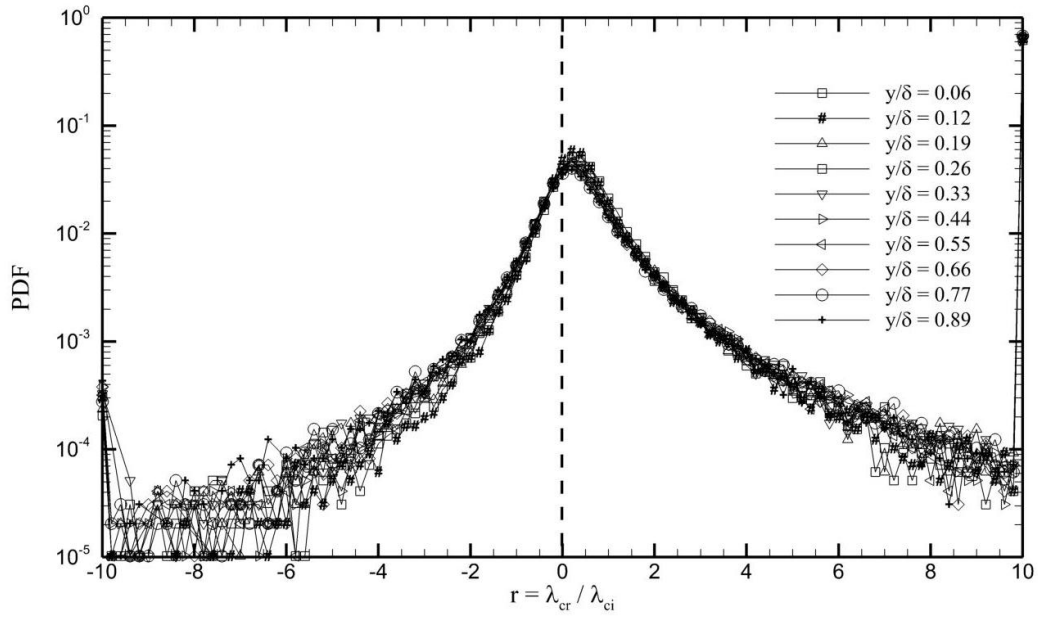

Figure 5.17 PDF of the inverse spiraling compactness, shown for the smooth WPG case.

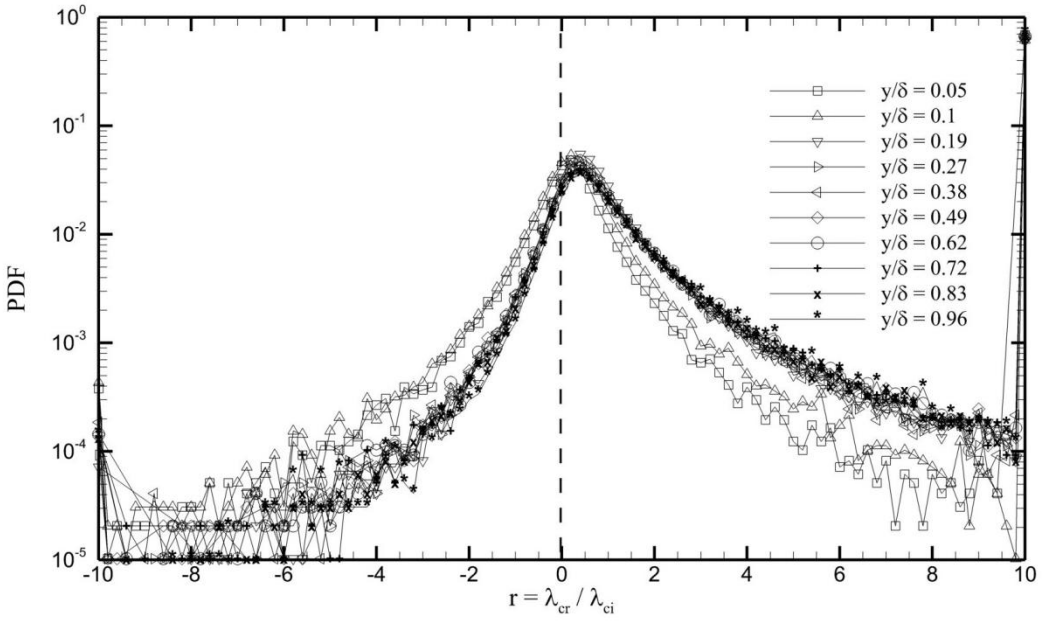

Figure 5.18 PDF of the inverse spiraling compactness, shown for the smooth SPG case.

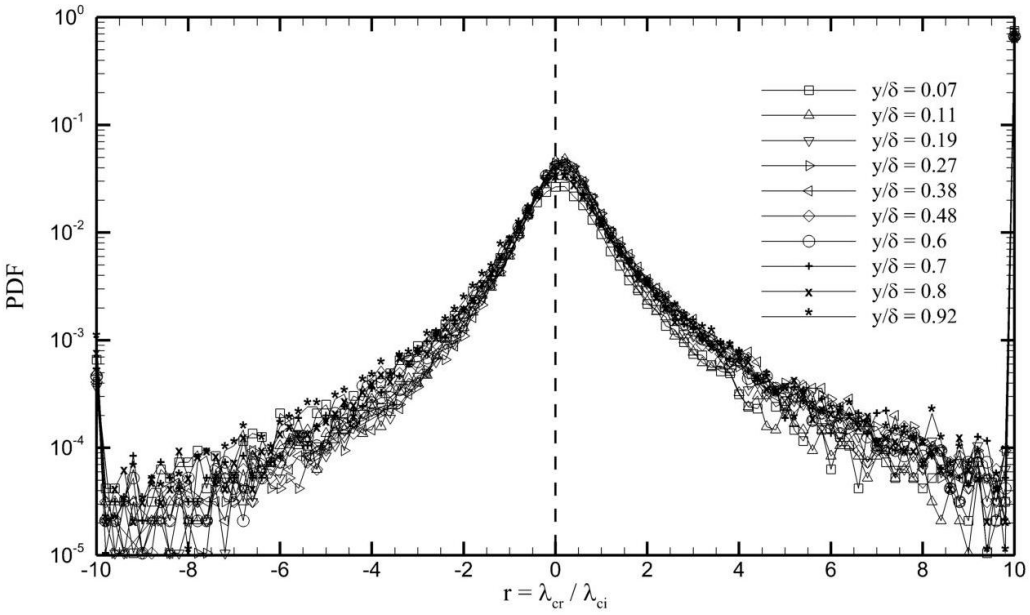

Figure 5.19 PDF of the inverse spiraling compactness, shown for the rough-wall case.

6. CHARACTERIZATION OF BASELINE FLAT-PLATE, SMOOTH-WALL BOUNDARY LAYER

Prior to discussing the mechanically distorted boundary layers in §7 and §8, it is important to thoroughly review the baseline state of the undistorted Mach 4.9 boundary layer. As stated in §1, the lack of highly resolved experimental data at this Mach number lends additional significance to the undistorted case, since the effects of highly compressible (M ≈ 5) conditions on the instantaneous boundary layer structure has not been thoroughly examined. Along with serving as a comparison case for the distorted flows, this baseline data set will yield valuable, and so-far absent, insight into the structural behavior of compressible boundary layers.

6.1. Flow Characteristics and Mean Velocity

The freestream and wall conditions for the baseline case are given in Table 6.1, determined at the measurement location 29.8 cm downstream of the nozzle exit. The boundary layer edge viscosity μ_e was calculated using Keyes' law, due to the low freestream temperature ($T_e \approx 63$ K). Sutherland's law was applied at the wall, yielding μ_w. The wall temperature T_w was measured using ISSI's UNT-01 temperature sensitive paint (TSP), yielding a value of 307 K. This wall temperature was approximately 93% of the adiabatic wall temperature T_{aw}, and was constant throughout the duration of the PIV measurement. Additional details of the TSP method are given in Appendix A. The friction velocity u_τ was determined through the Clauser chart method. In this study, the boundary layer thickness δ was defined as the height at which $U = 0.99U_e$.

Before discussing the baseline mean velocity, the effects of the constant-area duct on the boundary layer evolution should be mentioned. Since the test section maintained a constant cross-sectional area of 7.62 cm x 7.62 cm, the growing boundary layer thickness lead to a weakly adverse pressure gradient of $\beta = 0.1$. However, the boundary layer is still regarded as nominally zero pressure gradient, and the mean velocity and

Reynolds stress profiles given below show good agreement with other flat-plate, zero pressure gradient studies.

Table 6.1 Freestream and wall conditions of the baseline flowfield

Reynolds number	Re/m	~ 4.6 x 10^7
	Re_δ	5 x 10^5
	Re_θ (incompressible)	4.7 x 10^4
	Re_{δ_2} (= $\rho_e U_e \theta / \mu_w$) (incompressible)	1.1 x 10^4
	Re_θ	2.3 x 10^4
	Re_{δ_2} (= $\rho_e U_e \theta / \mu_w$)	5.3 x 10^3
	Re_τ (= $\rho_w u_\tau \delta / \mu_w$)	1120
Boundary layer parameter	δ [mm]	10.9
	δ^* [mm] (incompressible)	1.3
	θ [mm] (incompressible)	1.0
	δ^* [mm]	4.8
	θ [mm]	0.48
Pressure gradient	β	0.1
Wall conditions	ρ_w [kg/m^3]	0.0554
	T_w [K]	307
	T_w / T_{aw}	0.93
	u_τ [m/s]	35

The mean velocity profile U/U_e is shown in Fig. 6.1, compared with a $1/7^{th}$ power law and the Mach 4.97 DNS of Duan, Beekman & Martin (2010). The current study matches the power law at all but the closest point to the wall ($y/\delta \approx 0.01$), exhibiting the expected profile of a fully-developed turbulent boundary layer. A slight deviation is seen for $y/\delta <$ 0.4, in which the experimental profile is less full than the DNS of Duan *et al.* (2010). However, this may be explained by the slightly cold-wall condition (T_w / T_{aw} = 0.93) of the current study, while the DNS simulations were performed under adiabatic conditions. It is known that cold-wall conditions lead to a less-full mean velocity profile, as shown in Fig. 4a of Duan *et al.* (2010).

The mean velocity is shown again in Fig. 6.2, in inner-scaled coordinates. The van Driest II compressibility transformation was applied to the velocity, allowing comparison with lower-Mach number studies. Good agreement is seen with all studies plotted here, collapsing onto the logarithmic region for $50 < y^+ < 150$, and showing similar behavior within the wake region. The last usable data point for the current study is approximately $y^+ \approx 50$, which is within the upper portion of the buffer layer. This near-wall resolution, coupled with the high fidelity of the instantaneous images, is the key feature enabling the vortex identification discussed later in this section.

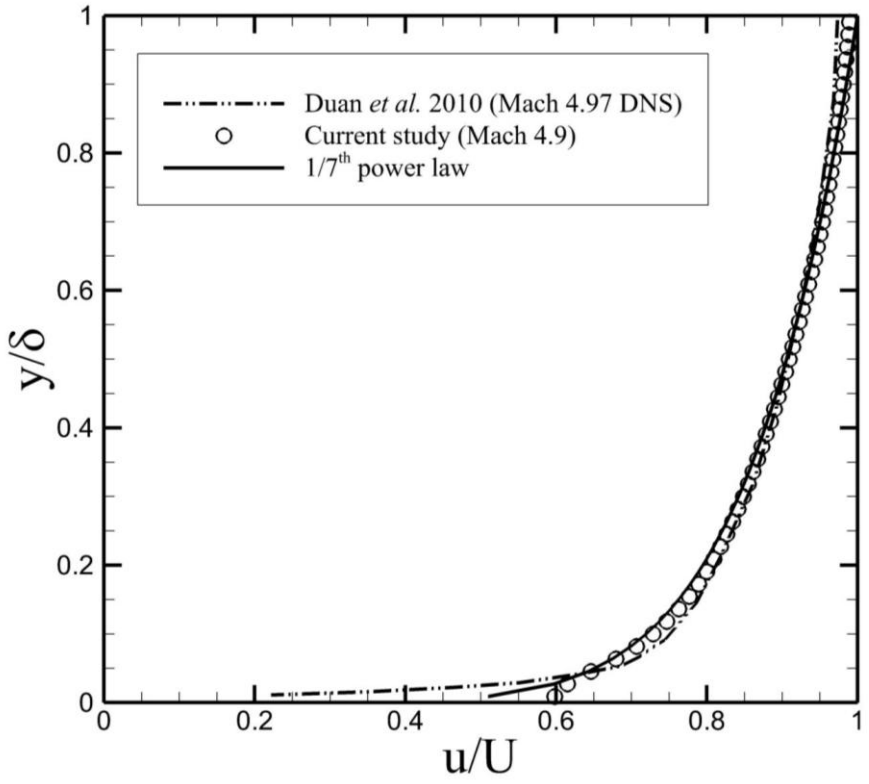

Figure 6.1 Mean velocity profile, *compared to a 1/7th power law and the Mach 4.97 DNS data of* Duan *et al.* (2010)*. The discrepancies seen in the near-wall region are most likely due to the slightly cold-wall (T_w / T_{aw} = 0.93) nature of the current study, leading to a less-full boundary layer profile.*

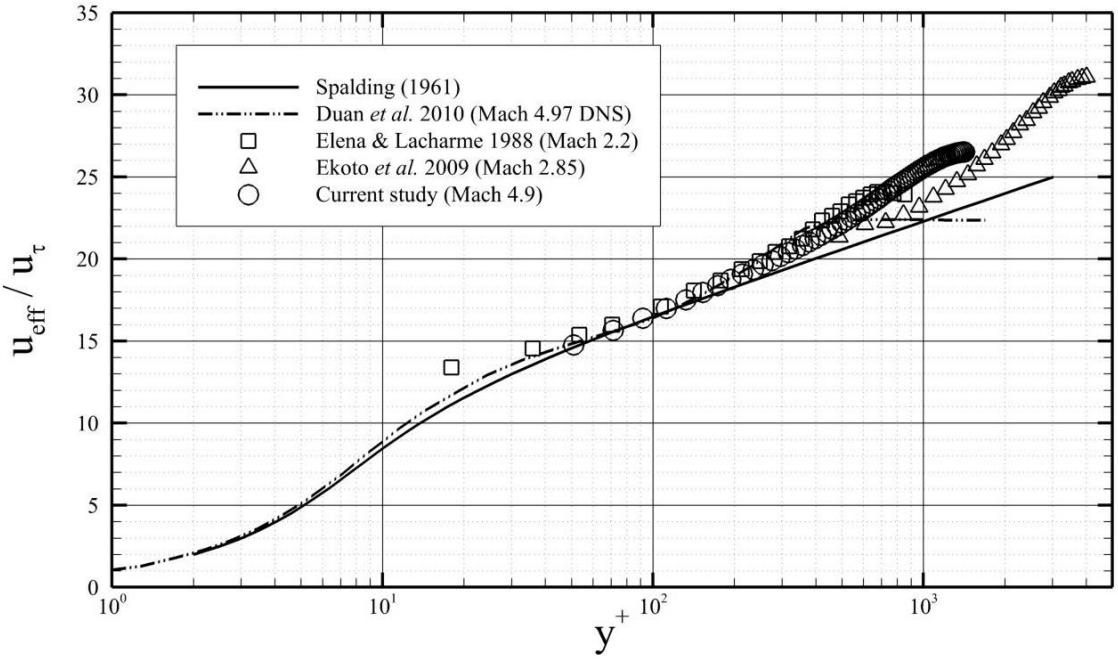

Figure 6.2 Inner-scaled mean velocity, using the van Driest II compressibility transformation.

6.2. Reynolds Stress Response

The responses of the axial and wall-normal stresses are investigated by viewing the rms velocity fluctuations *u'* and *v'*. When scaled by the friction velocity u_τ and the wall density ratio $(\rho/\rho_w)^{1/2}$ (calculated using the Crocco-Busemann relation), the current study shows reasonable agreement with existing supersonic studies in literature, as shown in Fig. 6.3. The Morkovin-scaled velocity fluctuations closely match the trends seen by Tichenor *et al.* (2013), excepting a small vertical shift. Since the data are normalized by u_τ, which was determined through the Clauser chart method, it is possible that the uncertainty on the friction velocity is responsible for the slight offset. Indeed, when the friction velocity of the current study is increased by 10% (not shown here), both data sets collapse onto each other. Therefore, it is reasonable to assume that the uncertainty on u_τ, estimated at ~ 5%, is responsible for any difference between the turbulent stress profiles of the current study and Tichenor *et al.* (2013).

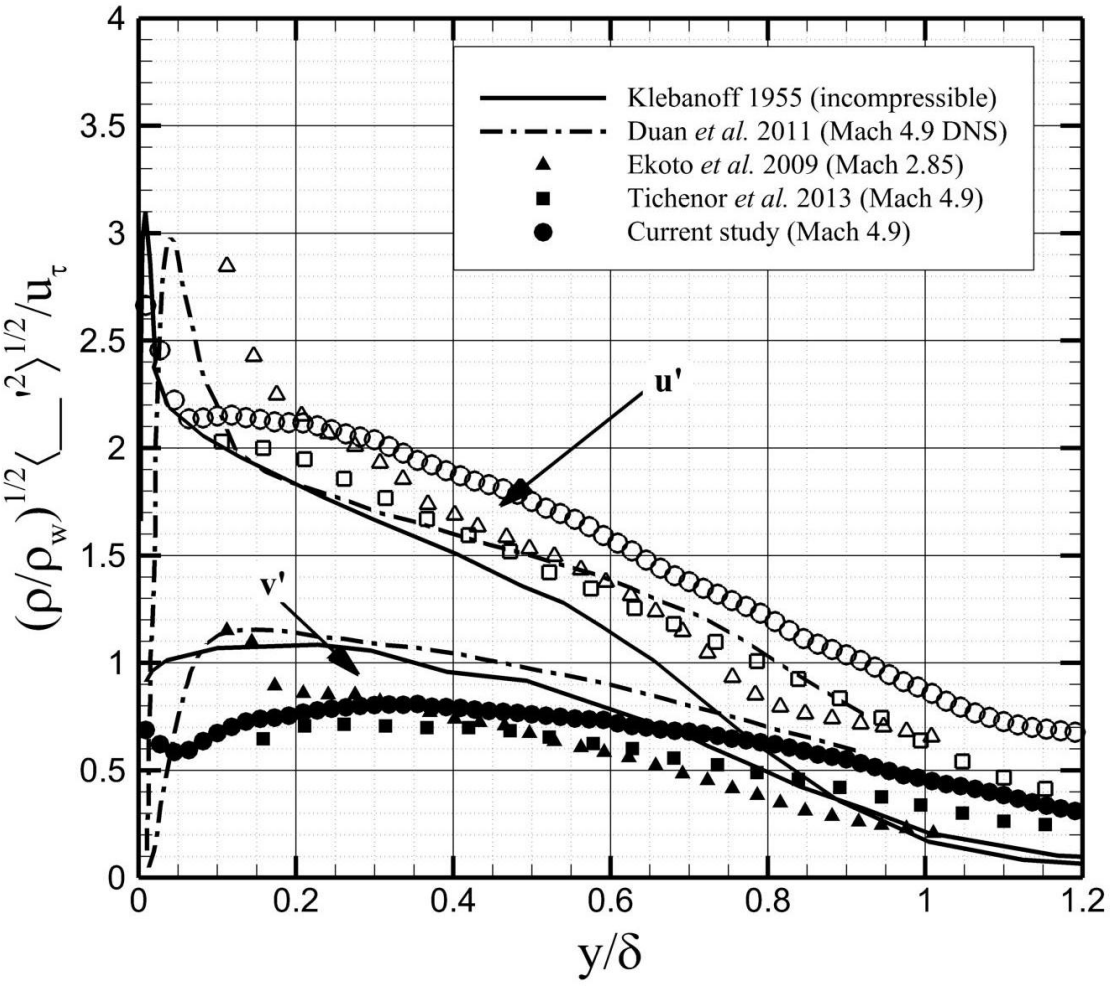

Figure 6.3 Morkovin-scaled velocity fluctuations, compared to existing supersonic studies in literature.

The Reynolds shear stress $-\rho\overline{u'v'}$, normalized by the wall shear stress τ_w, is shown in Fig. 6.4. Compared to the incompressible data of Klebanoff (1955), the current study exhibits a larger shear stress over most of the outer region of the boundary layer, which is consistent with the behavior of other supersonic experimental and numerical studies. The only exception is the Mach 2.8 LDV measurements of Luker, Hale & Bowersox (1998), who used the Couette flow assumption to determine $\tau_{xy}^T = \tau_w + (dp_w/dx)\,y$, whereas the Clauser chart method was applied in the current study. Despite the scatter

among the compressible data sets in Fig. 6.4, the profiles exhibit a similar slope over the range y/δ = 0.5 – 1.0, suggesting the difference in measured shear stress for the supersonic studies may be due to uncertainty on the outer scaling, i.e. the boundary layer thickness δ. In fact, the shear stress profiles of Ekoto *et al.* (2009) and Duan, Beekman & Martin (2011) collapse onto the current study above y/δ = 0.5 (shown in Fig. 6.5) when their boundary layer thicknesses are decreased and increased by 10%, respectively. Given the uncertainty in experimentally determining δ (see Appendix B.2), this variation is a likely contributor to the scatter observed in Fig. 6.4.

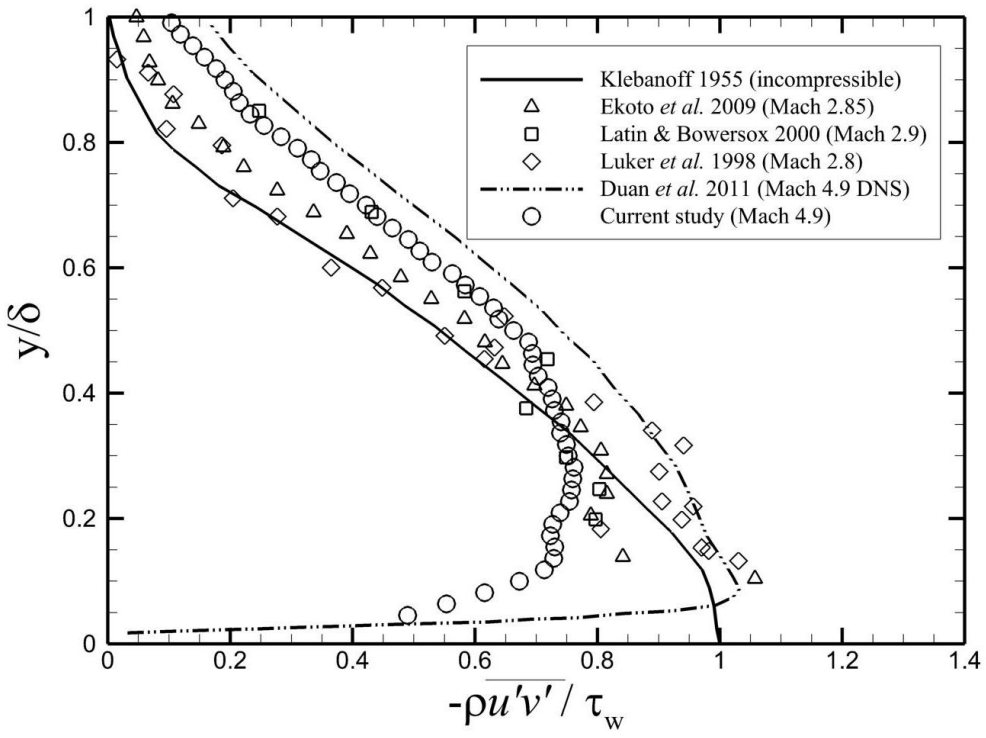

Figure 6.4 Reynolds shear stress profiles, scaled by wall shear stress τ_w.

In contrast to the outer region, the uncertainty on δ is insufficient to explain the behavior below y/δ = 0.5, where the three experimental studies in Fig. 6.5 show varying degrees of "roll-off", as the measured shear stress gradually decreases as the wall is approached.

This is a deviation from the expected trend, shown by the profile of Duan *et al.* (2011) in Fig. 6.5, in which the Reynolds shear stress approaches a peak value near the wall, before being attenuated by viscous forces. It is possible that the spatial filtering inherent to PIV is the primary cause of the reduced shear stress. Following Townsend's attached eddy hypothesis, the size distribution of the turbulent structures will approach smaller values as $y \rightarrow 0$. Accordingly, the number of *u'v'* fluctuations "captured" by the PIV interrogation window will be reduced in the near-wall region, contributing to the reduced shear stress. Using similar logic, Humble (2008) employed Prandtl's mixing length model to show that the Stokes number approaches unity near the wall, suggesting that particle slip is a dominant factor. Regardless of the cause, the shear stress behavior for the current baseline study is consistent with other experiments in this Mach number regime.

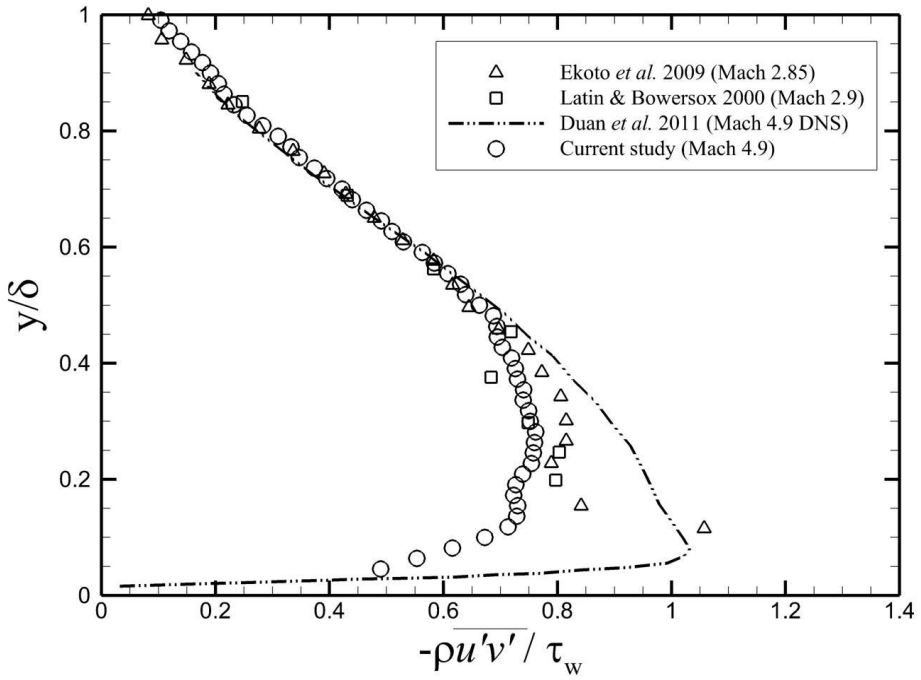

Figure 6.5 Reynolds shear stress profiles for supersonic studies. *Note that δ for* Ekoto *et al.* (2009) *and* Duan *et al.* (2011) *have been decreased and increased by 10%, respectively.*

6.3. Spectral Distribution of Turbulent Energy

The Reynolds stress profiles shown in §6.2 illustrate how the ensemble-averaged stresses are distributed throughout the boundary layer thickness. In order to view the energy content in the spectral domain, PSDs are computed along the streamwise direction at each height within the boundary layer. Figures 6.6 – 6.8 show the axial, wall-normal, and shear spectra, respectively. The PSDs are normalized by the local stress at each height, such that the resulting curves show the distribution of the *relative* energy content. The spectra are plotted for wall-normal positions down to $y^+ = 35$, which is marginally below the last usable data point from Fig. 6.2. This location is included only to show that the trends of the spectra extend into the buffer layer.

In the inertial subrange, both the axial and wall-normal components in Figs. 6.6 & 6.7 approach the $k^{-5/3}$ behavior expected for high Reynolds number flows. As anticipated, this behavior is only visible in the outer layer, due to the decreased local Reynolds number in the near-wall region. For the axial spectra in Fig. 6.6, each curve exhibits a logarithmic trend over the range $k_1\delta = 6 – 50$, with the slopes monotonically approaching -5/3 at the boundary layer edge. The two exceptions are the near-wall positions $y^+ = 35$ and 60, which most likely reside within the buffer layer. Both of these positions show increased relative energy content over the range $k_1\delta = 20 – 50$, suggesting energy is contained within smaller structures. At lower wavenumbers, the outer layer spectra show signs of a gradually decreasing slope, suggesting the existence of a k^{-1} region. Unfortunately, the FOV of the current study limits the low-wavenumber resolution, preventing confirmation of this behavior. However, a recent large-FOV study by English (2013) may provide sufficient resolution in this region. Note that the high-wavenumber resolution of the current study is limited by the finite size of the PIV interrogation window. The cut-off wavenumber k_c is computed as $k_c = 2.8/X$, where X is the interrogation window size [Foucaut, Carlier & Stanislas (2004)], yielding $k_c\delta \approx 75$. This value is close to the drop-off in the spectral content, suggesting that the signal above this wavenumber is dominated by noise.

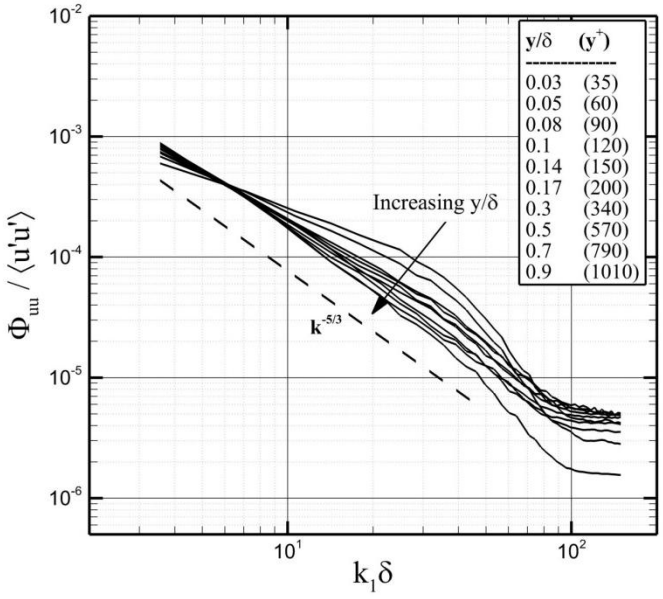

Figure 6.6 Normalized spectra of the axial stress component

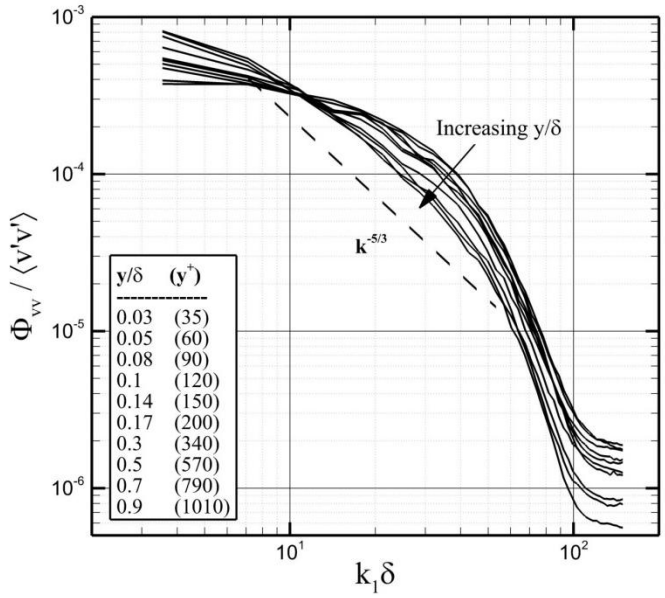

Figure 6.7 Normalized spectra of the wall-normal stress component

Unlike the axial component, the wall-normal PSD in Fig. 6.7 displays a more bimodal behavior. Above $y^+ = 200$, the spectra behave logarithmically, with an approximate slope of -5/3, though over a smaller wavenumber range ($k_1\delta$ = 10 – 40) than the axial component. Below this height, the spectra nearly collapse onto a single curve, showing elevated energy content for $k_1\delta$ = 20 – 50. The reader should note that this behavior is similar to the axial component at y^+ = 35 and 60 in Fig. 6.6. As observed for the axial spectra, the curves show increasing energy in the low-wavenumber range as y/δ increases, indicating more energy is transferred to the larger scales. However, the spectra at all heights within the boundary layer show a steeper slope for $k_1\delta$ = 50 – 100 than displayed by the axial component. This may be caused by energy being more confined to discrete ranges of wavenumbers, instead of the more uniform distribution observed in Fig. 6.6.

The shear spectra in Fig. 6.8 more closely resemble the axial component, in which the slope monotonically approaches -5/3 at the boundary layer edge. As expected, the relative energy content is transferred to lower wavenumbers with increasing distance from the wall. However, the outer layer spectra do not approach $k^{-7/3}$, instead displaying a shallower slope, possibly closer to $k^{-5/3}$. Given that Re_θ = 20,000 for the baseline case, the Reynolds number should be sufficiently high to display the -7/3 slope predicted by Lumley (1967). Instead, it is possible that the low friction Reynolds number may have an influence, since Re_τ = 1120 for the flat-plate model. Any further speculation as to the cause of this behavior is limited by the scarcity of shear spectra at these conditions in the scientific literature.

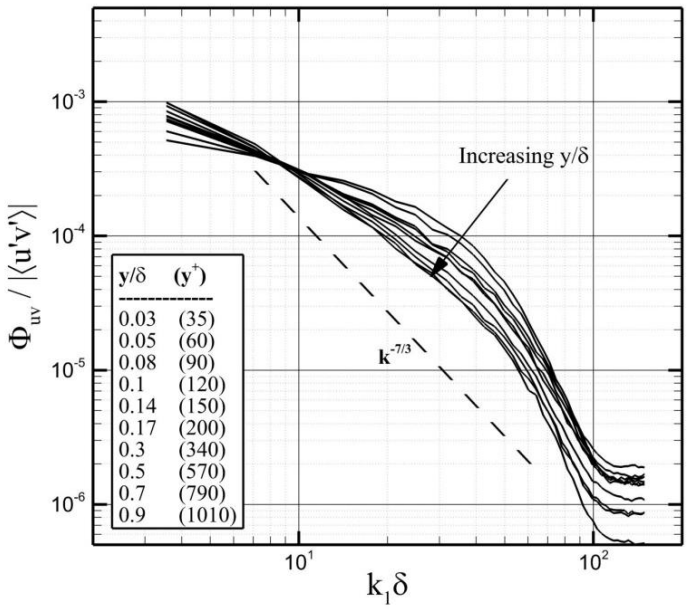

Figure 6.8 Normalized shear spectra

6.4. Spatial Distribution of Turbulent Energy

The spectra shown previously in §6.3 described the relative distribution of energy within the wavenumber domain. Observations of these spectra provided insight into the flow scales present at each height within the boundary layer, based upon the relative concentration of energy. To explore this behavior more fully, two-point correlations of the streamwise velocity R_{uu} are presented in Fig. 6.9, showing the energy distribution in the spatial domain. The inhomogeneity in the wall-normal direction requires the correlation to be computed at discrete reference points y_{ref}, such that

$$R_{uu}(\Delta x, y, y_{ref}) = \frac{u'(x, y_{ref})u'(x+\Delta x, y)}{\sqrt{\left\langle \left(u'(x, y_{ref})\right)^2 \right\rangle}\sqrt{\left\langle \left(u'(x+\Delta x, y)\right)^2 \right\rangle}} \tag{6.1}$$

The spatial two-point correlation in Eqn. 6.1 produces a statistical representation of the large-scale motion without the use of Taylor's hypothesis, calculated at each height y_{ref}. Since the PSD can be computed as the Fourier transform of the two-point correlation, the correlation length-scale is approximately equal to the wavelength at which the spectral energy content is largest. The equivalence between these two measured length scales, determined from the spectral and autocorrelation results, will be shown later in this section. Before continuing, it is important to describe the theoretical relation between the spectral length-scale Λ_x and the correlation length-scale λ_x^u. If the integral length-scale L_{uu} is computed from the autocorrelation as

$$L_{uu} \equiv \int_0^\infty R_{uu}\, dx \tag{6.2}$$

then L_{uu} will be exactly equal to the spectrally-derived wavelength of maximum energy (Note that Eqn. 6.2 is the definition of the integral length scale). However, the current study uses the threshold $1/e$ to estimate λ_x^u from the autocorrelation R_{uu} (see §4.4.4 for further details of this technique). This calculation method ensures that the two length-scales are only *approximately* equal.

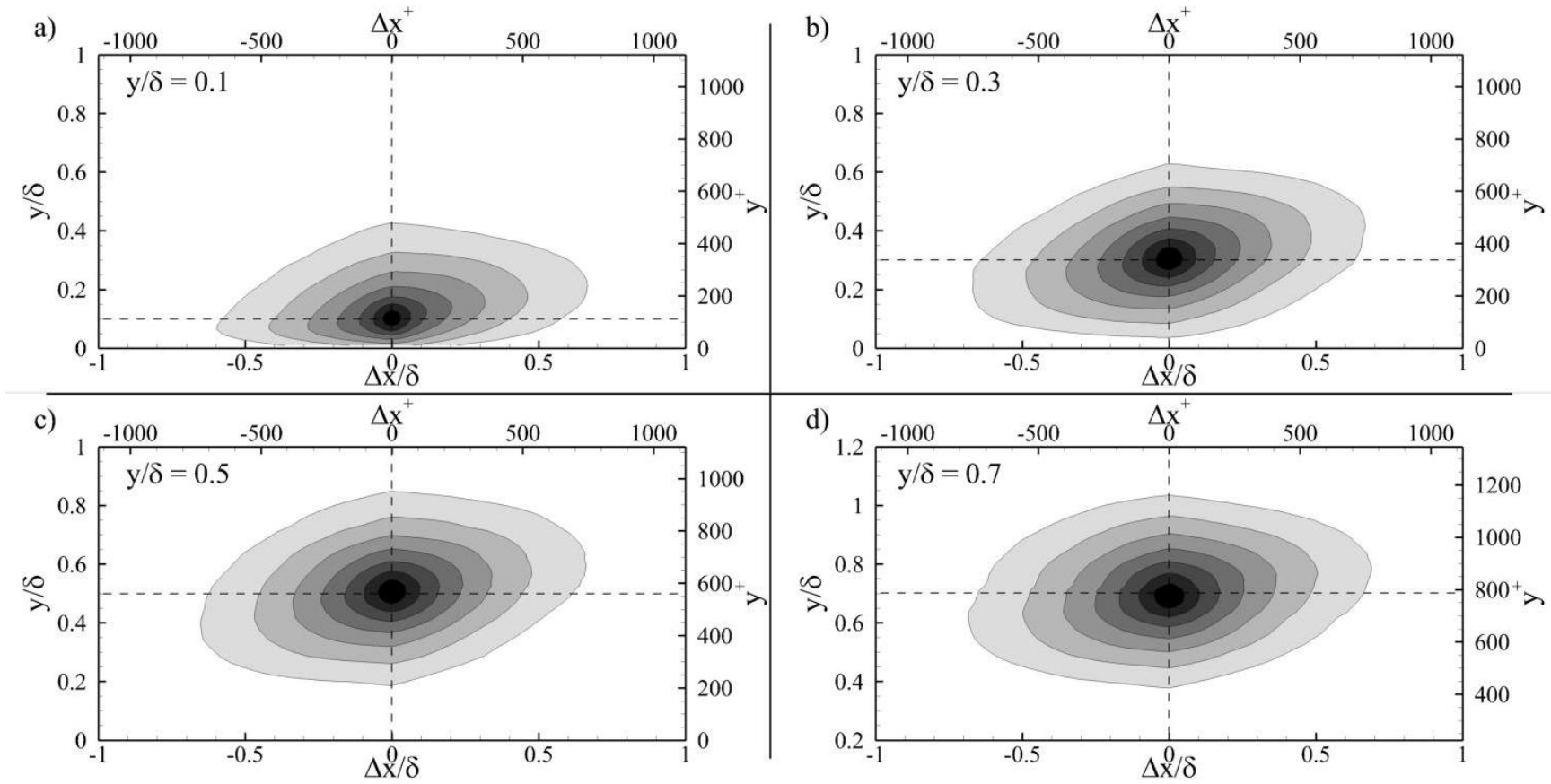

Figure 6.9 Two-point correlations of the u-velocity. *Isocontours are shown at 0.1 increments, with the outer level at 0.3*

The two-point correlation R_{uu} is shown in Fig. 6.9 for the baseline flat-plate model, at varying heights from the wall. Note the elliptical distribution of R_{uu} at each location, along with the small rotation angle with respect to the wall. Both the shape and orientation of the correlations are consistent with previous supersonic studies [Ganapathisubramani (2007); Tichenor *et al.* (2013)]. The streamwise extent of the correlations appears to increase slightly from y/δ = 0.1 to 0.3, consistent with Townsend's attached eddy hypothesis. The near-wall correlation can be considered representative of the hairpin vortex packet structure, since the vortices within the hairpin packets convect at a similar streamwise velocity U_c. Additionally, the high degree of correlation within the low-momentum streaks (which are associated with the presence of streamwise-aligned hairpin vortices) will result in a high correlation R_{uu} for these large-scale motions. It is possible to infer the size and orientation of these large-scale structures, by using the R_{uu} correlation at y/δ = 0.1. Viewing the R_{uu} = 0.4 isocontour in Fig. 6.9a, the hairpin packets most likely extend over a distance of ~ 1000 viscous units, at an angle of approximately 10 degrees. Both of these observations are consistent with previous studies [Adrian *et al.* (2000); Pirozzoli & Bernardini (2011)], and will be confirmed by inspecting instantaneous velocity fields in §6.5.

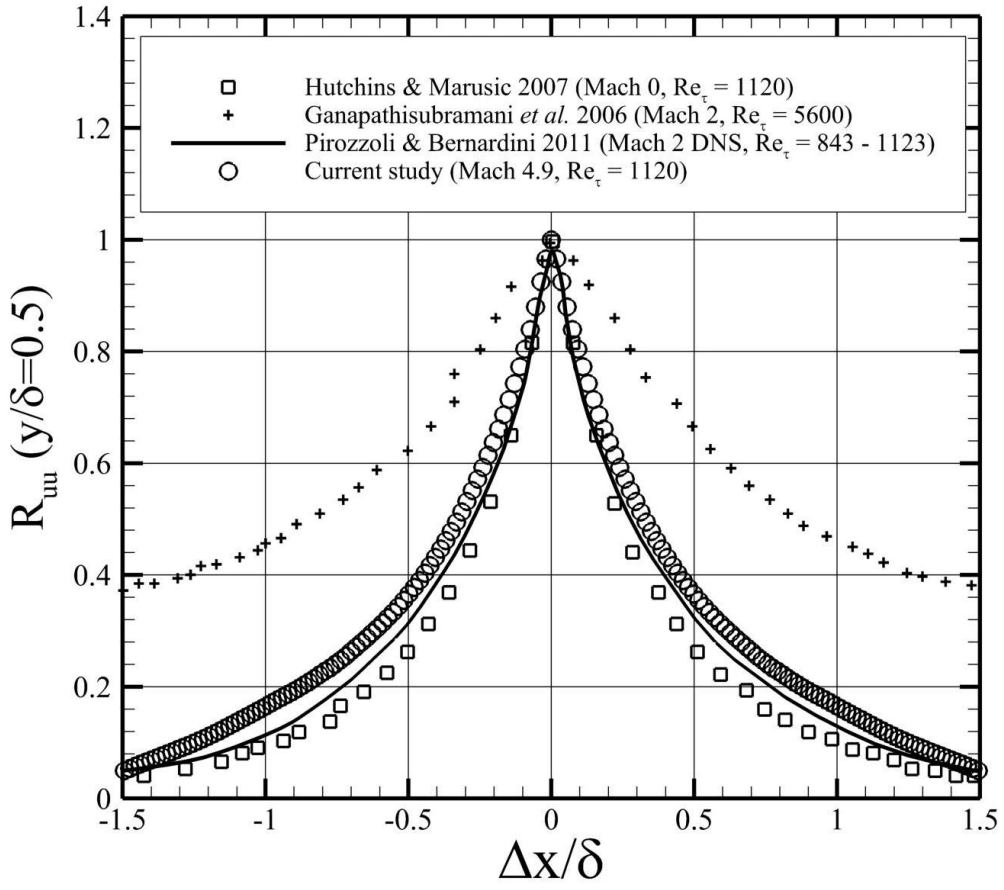

Figure 6.10 One-dimensional autocorrelation of R_{uu}, presented at $y/\delta = 0.5$. *Reasonable agreement is seen for all cases, except with the Mach 2 study of Ganapathisubramani, Clemens & Dolling (2006).*

By plotting the one-dimensional autocorrelation $R_{uu}(y_{ref})$, the two-point correlations in Fig. 6.9 can be compared to existing data in the literature (Fig. 6.10). At $y_{ref}/\delta = 0.5$, the autocorrelation in Fig. 6.10 shows good agreement with both the incompressible study of Hutchins & Marusic (2007a) and the Mach 2 DNS of Pirozzoli & Bernardini (2011). The Mach 2 PIV data of Ganapathisubramani *et al.* (2006) shows a much wider correlation, with a corresponding length scale that is approximately three times longer than the current study. Early analysis of these results attempted to explain the disparity by noting

the larger Re_τ for Ganapathisubramani *et al.* (2006). However, a recent large-FOV study by English (2013), performed for the same geometry and conditions as the current baseline case, shows good agreement with the autocorrelations of Ganapathisubramani *et al.* (2006) at both $y/\delta \approx 0.2$ and 0.5. It is possible that the reduced FOV of the current study has biased the autocorrelations to a narrower range, though more analysis is needed.

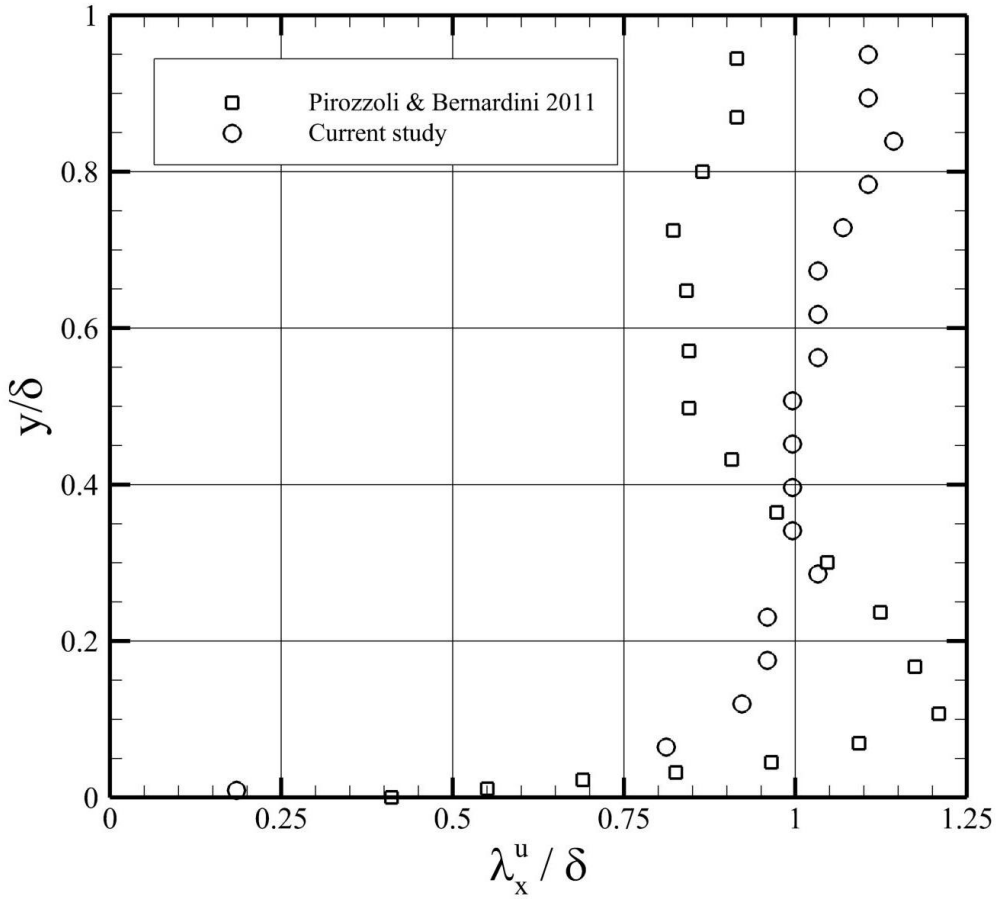

Figure 6.11 Streamwise length scale, plotted versus the Mach 2 DNS of Pirozzoli & Bernardini (2011)**.** *Every third point is shown for clarity. Note that the length scales of* Pirozzoli & Bernardini (2011) *are computed from the definition of the integral length scale, while the current study utilizes the threshold 1/e.*

Using a threshold of 1/*e* (see §4.4.4 for justification), it is possible to compute the streamwise length scale λ_x^u from the autocorrelation of the fluctuation streamwise velocity. Shown in Fig. 6.11, it is apparent that much of the boundary layer is populated by δ-scale motions, excepting points very near the wall. The current study exhibits a rapid increase in scale in the near-wall region, before attaining a nominal value of 1.0δ for the range $y/\delta = 0.3 - 0.7$. The length scales of Pirozzoli & Bernardini (2011) show a similar increase near the wall, though with a much steeper slope, with a peak forming at $y/\delta = 0.1$. Above this height, the length scale decreases to 0.8δ at $y/\delta = 0.5$. No explanation is available for the differing behavior between these studies, though it should be noted that Pirozzoli & Bernardini (2011) used the definition of the integral length scale (see Eqn. 6.2). It is possible that the different methods for computing the length scales in Fig. 6.11 (using the threshold 1/*e*, and computing the area under the autocorrelation) may account for any disparities in the results.

A notable feature of the two-point correlations in Fig. 6.9 is their orientation with respect to the wall. In order to analyze this behavior more fully, the structure angles are shown in Fig. 6.12. The orientations were computed by fitting an ellipse to the $R_{uu} = 0.4$ contour, and determining the local inclination of the fitted ellipse. The threshold $R_{uu} = 0.4$ was chosen since it is the nearest contour level to $1/e \approx 0.37$. Near the wall, the structure angle is considered representative of the orientation of the hairpin packets. As these large-scale structures mature and detach from the wall, their increased size, coupled with the large primary strain rate *dU/dy*, results in a more wall-normal orientation. This is because *dU/dy* is larger at the bottom of the structure, rotating the structure to larger angles. The small size of the near-wall structures (see Fig. 6.11) makes them less vulnerable to this reorientation. Above $y/\delta = 0.6$, the decreased shear *dU/dy* leads to a rapidly decreasing structure angle near the boundary layer edge. Good agreement is seen with Tichenor *et al.* (2013), especially above $y/\delta = 0.7$. Given the similar trends, the discrepancy for $y/\delta = 0.2 - 0.6$ may be due to the 2 degree uncertainty of θ, which was estimated by computing the structure angles for both $R_{uu} = 0.3$ and 0.5, and observing the difference in the resulting angles. The behavior for Pirozzoli &

Bernardini (2011) is qualitatively similar, though the peak angle is larger, with steeper slopes near the wall and at the boundary layer edge. Given the similar Reynolds numbers, this discrepancy may be due to a compressibility effect.

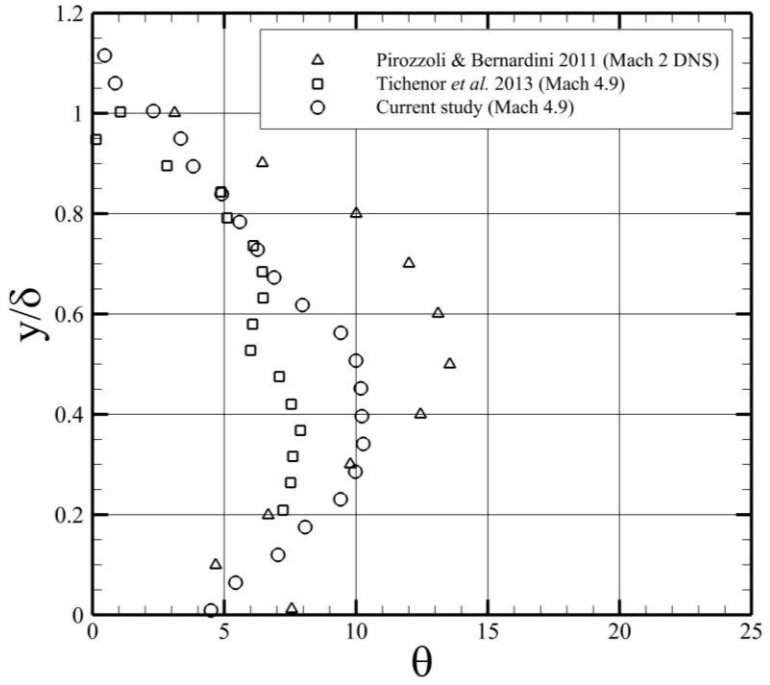

Figure 6.12 Structure angles of two-point correlations, computed for the current study at R_{uu} = 0.4.
Angle is given in units of degrees

6.5. Instantaneous Structure of Near-Wall Flow

In §6.4, two-point correlations were used to infer the behavior of the large-scale motions, including the orientation and streamwise length scales. By invoking the hairpin packet model of Adrian *et al.* (2000), the correlation length scale can be interpreted as representative of the average hairpin packet length (since the induced low-momentum fluid beneath a hairpin packet has a high degree of correlation), while the near-wall structure angle is comparable to the growth angle of the hairpin packet envelope [Adrian *et al.* (2000)]. However, the relation of these correlation-derived quantities to the actual

hairpin packet behavior is uncertain. This can be remedied by inspection of the instantaneous velocity fields, as shown below.

An instantaneous velocity field for the baseline case is shown in Fig. 6.13, with the hairpin packet envelope described by the dash-dotted line. The angle of the packet envelope, which is labeled the "characteristic growth angle" by Adrian *et al.* (2000), varies from nearly zero degrees to almost 25 degrees. The quasi-linear ramp-like orientation of the packet is consistent with the concept of hairpin "aging", as the vortices move away from the wall as they mature. The vortices are identified by subtracting a convective velocity equal to 83% of the freestream velocity. This particular packet contains four vortices, similar to the observations by Adrian *et al.* (2000). A comparison between Fig. 6.13 and the incompressible boundary layer of Adrian *et al.* (2000) in Fig. 6.14 shows excellent agreement, suggesting that a similar production mechanisms exists within these flowfields, despite the presence of a mean density gradient.

The most striking feature of the hairpin packet in Fig. 6.13, and the feature most likely to be detected by two-point correlations, is the long region (over 1.5δ in length) of relatively uniform low-momentum fluid beneath the packet. Assuming that the vortices A-D identify three-dimensional hairpin vortices, the structure in Fig. 6.13 can be envisaged as a low-momentum streak, straddled by multiple individual hairpin vortices (see Fig. 16 of Elsinga *et al.* (2010)). While the genesis of these structures remains an active area of research, Adrian *et al.* (2000) suggested that the low-momentum streak is related to the back-induction, or *ejection*, of fluid between the hairpin legs. This ejection is due to the concentrated vorticity within the hairpin legs and head. The sense of rotation in the hairpin head results in negative spanwise vorticity ($\omega_z < 0$), causing fluid between the hairpin legs to be ejected in the upstream direction. Conversely, fluid outboard of the hairpin legs is swept downstream. It is believe that these motions contribute to the high- and low-speed streaks visible within the near-wall region. The intensity of the ejections is generally stronger than the sweeps, due to the mutual induction of the hairpin legs. These phenomena are shown schematically in Fig. 6.15.

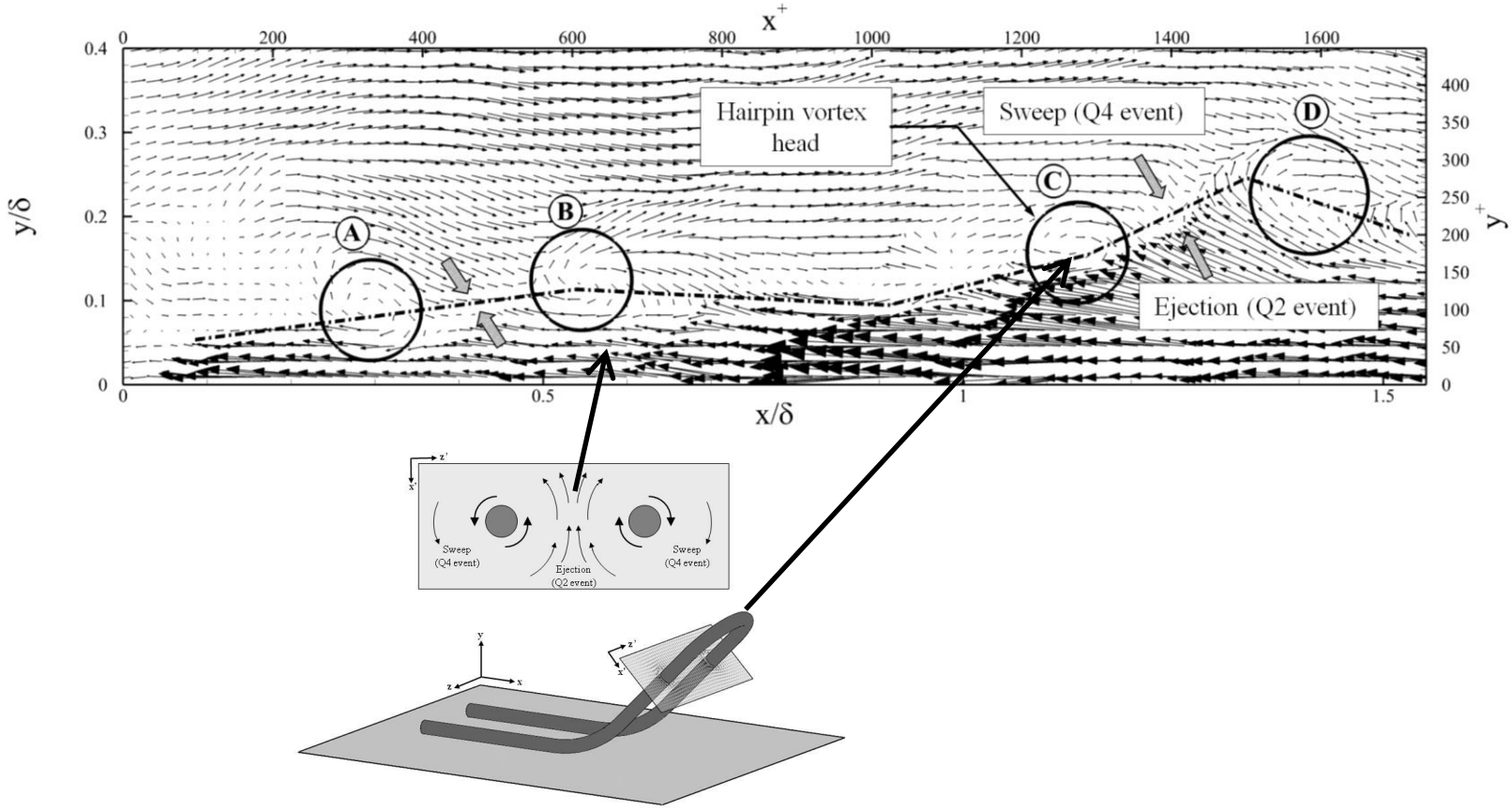

Figure 6.13 Instantaneous velocity field for baseline case, showing a hairpin vortex packet. *Individual vortices are identified by subtracting a convective velocity $U_c = 0.83U_e$. The relation to the sweep/ejection events is shown.*

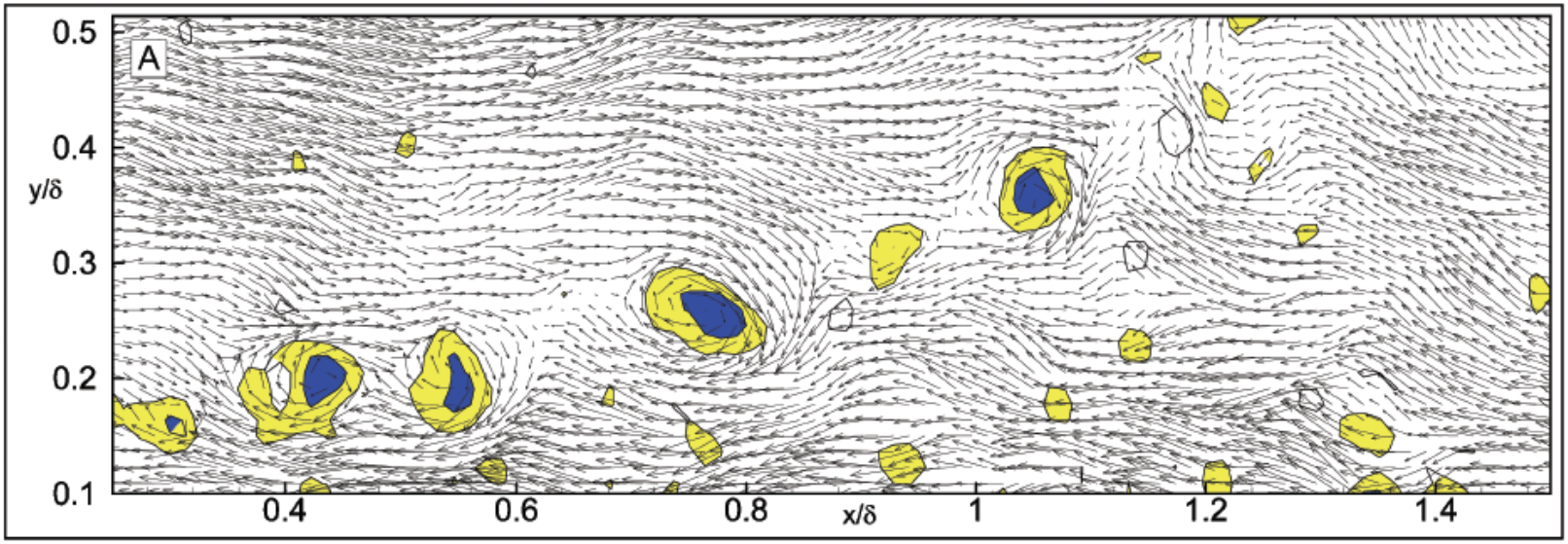

Figure 6.14 Instantaneous velocity field of incompressible boundary layer, taken from Adrian *et al.* (2000)**.** *Individual vortices are identified by subtracting a convective velocity* $U_c = 0.79U_e$

In Fig. 6.13, the contributions of the individual hairpins are not easily identified. While the zone of influence around the vortices can be estimated as approximately 150 – 200 viscous units wide (identified by examining the wall-normal component of the vectors), the individual ejections are indistinct. Indeed, it appears that the multiple ejection events have merged into a single zone of low-momentum fluid. Due to the streamwise alignment of the vortices, "the back-induced flows from the hairpins combine to produce stronger backflow than could be achieved by incoherently aligned individuals" [Adrian *et al.* (2000)]. Before continuing with the current analysis, a peculiarity of the hairpin packet in Fig. 6.13 should be discussed. Note the large spacing between vortices B and C, and the almost horizontal orientation of the growth angle. It is possible that Fig. 6.13 shows two hairpin packets, containing vortices A-B and C-D, that have become streamwise-aligned. This alignment is consistent with the formation of very large scale motions (VLSMs), as described by Kim & Adrian (1999).

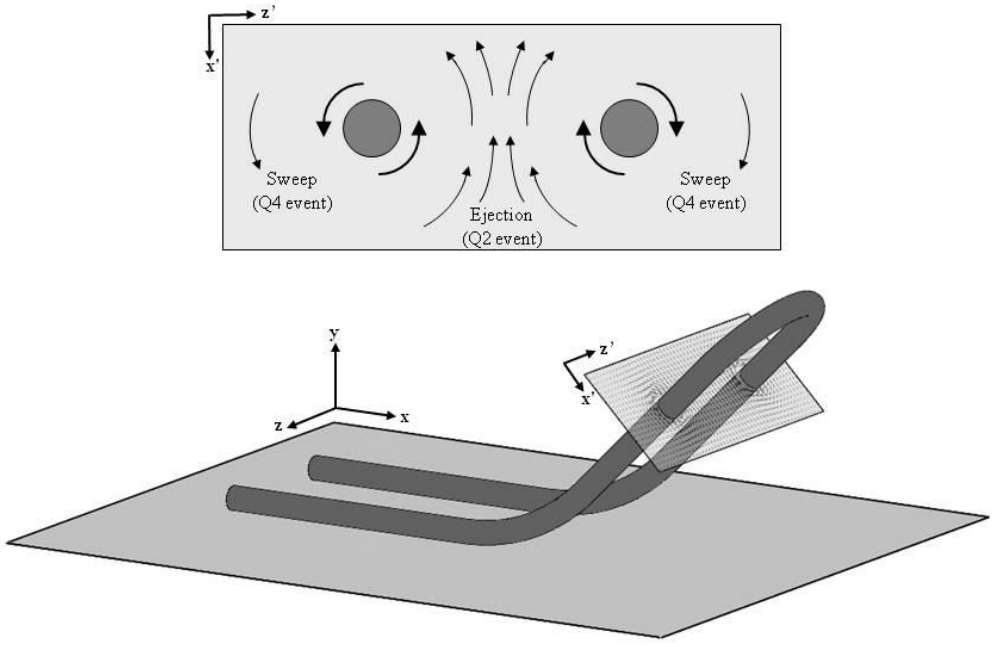

Figure 6.15 Schematic of an individual hairpin vortex, describing the sweep and ejection events. *Note that the ejection is larger in magnitude, due to the mutual induction between the hairpin legs.*

The hairpin packet shown in Fig. 6.13 provides a physical basis for the length scales measured in the flat-plate boundary layer, inevitably leading to the question: *How do the turbulent motions within the hairpin packets (sweeps/ejections, low-momentum streaks, etc.) manifest themselves in the turbulence statistics?* Addressing this question will lay the foundation for investigating the mechanically distorted boundary layers in §7 and §8.

It was shown in Fig. 6.13 that the hairpin packets and the resulting low-momentum streaks are due to the combined influence of multiple hairpin vortices, which is consistent with the existing hairpin vortex packet model. The width of an individual hairpin vortex, approximated as the zone of influence around the vortex core, is ~ 200 viscous units. The zone of influence was identified by examining the perturbation of the wall-normal velocity. This agrees with past studies, that have used two-point correlations and instantaneous visualizations to show that the motions associated with the wall-normal velocity are much more compact in the streamwise direction [Pirozzoli & Bernardini (2011)]. This naturally suggests that the *u'v'* motions will be similarly compact, since the shear stress is caused by (anti)correlation between the streamwise and wall-normal fluctuations. However, the corresponding *u*-motions extend to at least δ in the streamwise direction, as evidenced by the long tails present in the autocorrelation R_{uu} [Townsend (1976)], which correspond to the induced low-momentum flow beneath a hairpin packet in the near-wall region, as well as the corresponding high-momentum region outboard of the hairpin packet.

In order to probe the effects of these structures on the turbulence statistics, premultiplied spectra are shown in Figs. 6.16 – 6.18, for the streamwise, wall-normal, and shear spectra, respectively. Each component is plotted versus the streamwise wavelength Λ_x, indicating the relative energy content contained within each scale. While each plot incorporates data at $y^+ = 35$, which falls below the last usable data point shown in Fig. 6.2, this location is included only to show that the trends of the spectra extend into the buffer layer. For Figs. 6.16 – 6.18, this near-wall position is plotted as a dashed line, to indicate that the magnitude of these results may be subject to elevated uncertainty. As

such, this near-wall position is used only to support trends observed higher in the boundary layer. In Fig. 6.16, the normalized streamwise spectra at the nearest position to the wall (y^+ = 35) show a large "bulge" at a scale of 0.25δ – 0.3δ (250 – 300 viscous units), with negligible energy content at longer wavelengths, suggesting that the turbulent energy is confined to a relatively narrow range of scales. Note that this scale is several times smaller than the "inner peak" discovered by Hutchins & Marusic (2007b) at y^+ = 15, which they attributed to the near-wall turbulence regeneration cycle. Moving higher in the boundary layer to y^+ = 60, the local maximum has decreased in magnitude, as energy is transferred to longer wavelengths. However, this reduction may simply be due to the elevated uncertainty at y^+ = 35. Above this height, the "bulge" visible in the near-wall layers is now barely discernible, and has shifted to a slightly shorter wavelength of 0.2δ (~ 200 viscous units). Beyond y^+ = 200, the spectra are almost completely dominated by long-wavelength scales, extending beyond the FOV. Referring back to the inner-scaled velocity shown in Fig. 6.2, y^+ = 200 is near the upper edge of the logarithmic region for this flowfield, suggesting that the motions associated with the short wavelengths are relatively benign in the wake region. Also, note that the maximum energy content is located at wavelengths longer than the FOV for all distances from the wall, excepting the heights y^+ = 35 and 60, which reside within the buffer layer.

The wall-normal velocity spectra in Fig. 6.17 display a vastly different structure than the streamwise velocity spectra, with a majority of the energy content being concentrated at scales smaller than δ. Within the buffer layer, a narrow peak is observed at 0.2δ – 0.3δ. Moving up through the logarithmic region, the peak broadens to encompass 0.3δ – 0.4δ. In the outer region of the boundary layer, the spectra are more broadband, shifting to longer wavelengths ranging from 0.5δ to 1.0δ. A similar range of scales is observed for the shear spectra in Fig. 6.18, ranging from 0.2δ – 0.3δ in the buffer layer to 0.3δ – 0.4δ in the logarithmic region. However, the outer region shows increasing energy content at scales larger than δ, similar to the streamwise component in Fig. 6.16.

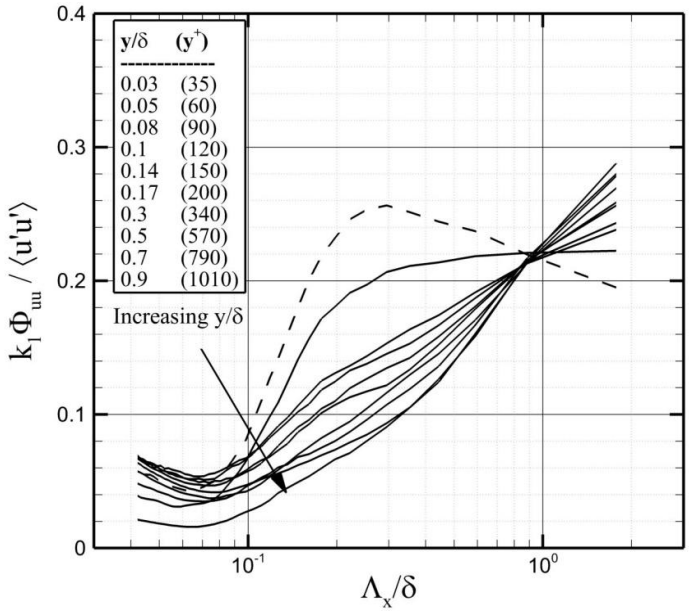

Figure 6.16 Premultiplied spectra of streamwise velocity component, plotted versus wavelength Λ_x

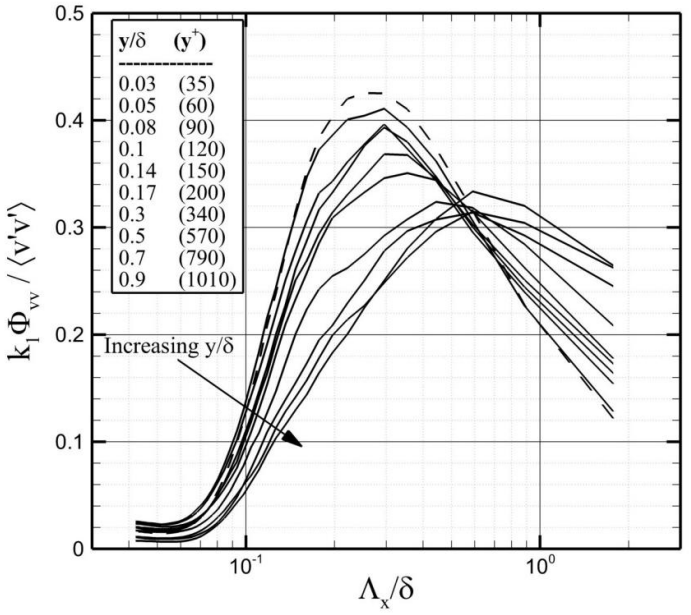

Figure 6.17 Premultiplied spectra of wall-normal velocity component, plotted versus wavelength Λ_x

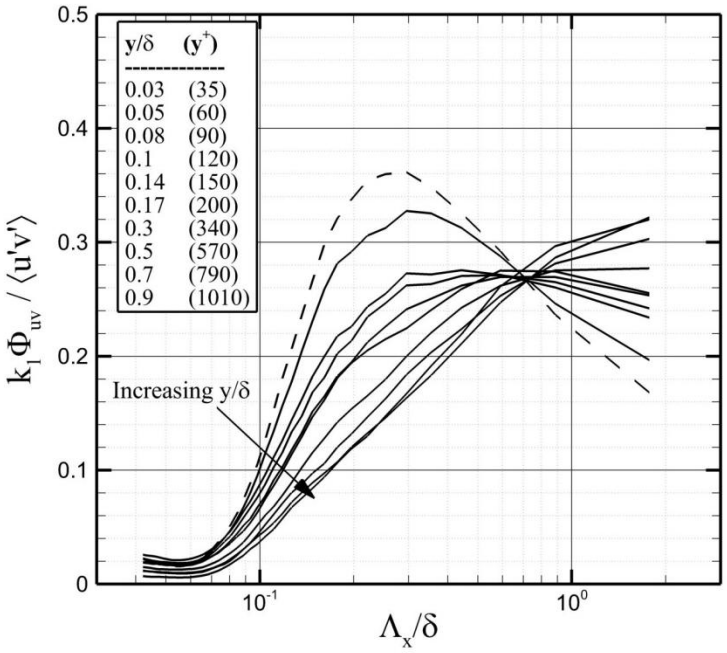

Figure 6.18 Premultiplied shear spectra, plotted versus wavelength Λ_x

Following the observations of the hairpin packet in Fig. 6.13, it is now possible to provide a physical basis for the spectral behavior in Fig. 6.16 – 6.18. Note that the streamwise velocity spectra in Fig. 6.16 show weak local maxima at 0.2δ throughout the logarithmic region, which coincides with the region of the boundary layer populated by inclined hairpin vortices [Robinson (1991); Adrian *et al.* (2000)]. This wavelength is most likely due to the signature of the individual ejection events from each hairpin vortex. Recall from Fig. 6.13 that the zone of influence around the vortices is approximately 0.2δ wide. The small spectral energy at these scales, while still sufficiently large to qualify as a local maximum, is due to the ejection events being subsumed within the large-scale low-momentum streak, which is responsible for the large energy content at wavelengths greater than δ. Moving higher in the boundary layer, the contributions from the individual vortices become weaker, such that the δ-scale motions are dominant. *In this manner, the spectral behavior of the streamwise velocity is likely due to long-wavelength motions stemming from the induced low-momentum*

*streaks beneath the hairpin packets, "punctuated" by 0.2*δ*-scale vortices within the logarithmic region.*

The link between the individual hairpin vortices and the spectral behavior is further supported by the wall-normal velocity spectra in Fig. 6.17. Since the *v*-velocity of each vortex does not streamwise-align like the streamwise component, the spectral peaks may be interpreted as estimates of the hairpin vortex scales. This is supported by the instantaneous visualizations of Adrian *et al.* (2000), who observed that "the individual vortex members contribute to the Reynolds stress and wall-normal turbulence locally, owing to the limited spatial coherence of the vertical component." Throughout the buffer layer and logarithmic region, the peak energy content ranges from 0.2δ to 0.4δ. While these scales are not exactly equal to those observed for the streamwise velocity component, the similarities are sufficient to suggest that the local maxima observed in Fig. 6.16 are indeed due to individual hairpin vortices. However, no explanation is readily available for the broad spectral peak within the outer region for the wall-normal component. Elsinga *et al.* (2010) suggested that this behavior is due to a combination of small- and large-scale structures, through this theory is unconfirmed at this time.

Before continuing with the analysis, it is prudent to briefly mention the behavior of the streamwise velocity spectra within the buffer layer (Fig. 6.16). For most of the boundary layer thickness, the majority of the energy content is concentrated at wavelengths greater than δ (excepting the small spectral "bumps" at 0.2δ, which been shown to coincide with the scale of individual hairpin vortices). However, negligible energy is contained within these δ-scales in the buffer layer. Since the long-wavelength motions have been theorized to represent the long low- and high-momentum streaks generated by the hairpin packets, it is reasonable to assume that these δ-scale streaks do not exist at this height within the boundary layer, or are severely weakened. Unfortunately, it is impossible to verify this speculation by inspecting instantaneous velocity fields, given the resolution of the current study. Additionally, it is known that the buffer lay is populated by pairs of quasi-streamwise vortices, which will form the legs of hairpin

vortices in the logarithmic region [Robinson (1991)]. Since low-speed streaks within the buffer layer are formed by induction of the near-wall fluid between these quasi-streamwise vortices, it is possible that the wavelength of the spectral peaks in the buffer layer (~ 0.3δ) is representative of the streamwise extent of these vortices. However, this length scale is several times smaller than the "inner peak" detected by Hutchins & Marusic (2007b) at $y^+ = 15$, which they measured as approximately 1000 viscous units. Additional data within the buffer layer is necessary to confirm this speculation.

6.6. Vortex Motions and Population Distribution

The previous sub-sections have utilized premultiplied spectra, two-point correlations, and instantaneous velocity fields to study the behavior of the turbulent structures, including their effect on the distribution of Reynolds stress among the flow scales. While the instantaneous velocity field shown in Fig. 6.13 is representative of the hairpin packet structure, the current discussion is limited by a lack of statistical results. This is remedied by using the swirling strength λ_{ci} to investigate the hairpin vortex statistics, including the vortex diameter, population distribution, and convective velocity.

Prior to discussing the statistical behavior of the hairpin vortices, it is prudent to review the swirling strength criterion, including its efficacy at detecting fluid structures rotating along a spanwise-oriented axis. Recall from the §5.1.5 that λ_{ci} is the imaginary part of the complex eigenvalue of the velocity gradient tensor, and is non-zero for locally spiraling pathlines. When weighted by the sign of the spanwise vorticity, the resulting contours are capable of distinguishing between prograde and retrograde vortices. This is illustrated in Fig. 6.19a, with filled contours of grey and black depicting the prograde and retrograde vortices, respectively. A local convective $U_c = 0.83U_e$ has been subtracted from the instantaneous velocity. The distribution of the vortices suggests that prograde structures dominate the boundary layer, with retrograde motions appearing outside the near-wall region. The occurrence rate of these structures will be investigated

more thoroughly later in this section. Figure 6.19b shows the same velocity field, but with a local convective velocity subtracted from each vortex. Combined with the sample velocity fields shown in §5.1.5, this example should be sufficient to demonstrate that λ_{ci} is a good indicator of vortical motions. However, the reader is reminded that the existence of a vortex does not necessarily indicate that a *hairpin vortex* is present. The two-dimensional velocity field can only detect the spanwise rotating fluid associated with a hairpin head. The existence of a hairpin vortex must be inferred from the location of the vortex (most likely in the logarithmic region), the presence of nearby vortices (suggesting streamwise-alignment in a hairpin packet), and a strong region of low-momentum fluid beneath the vortex (indicative of an ejection event between the hairpin legs). While hairpin heads (i.e. spanwise-oriented vortices) do exist in the outer region [Robinson (1991)], these structures have most likely detached from the wall, as suggested by the hairpin packet model [Adrian *et al.* (2000)].

Many of the example velocity fields shown previously in this dissertation have used Galilean decomposition to verify the existence of vortices, usually in conjunction with the swirling strength λ_{ci} (see Fig. 6.19). Recall from §5.1.2 that the primary weakness of this technique is the unknown convective velocity U_c and V_c of each vortex. However, by independently identifying the vortices through λ_{ci}, it is possible to conditionally average the streamwise and wall-normal velocities based upon the existence of a vortex, thereby producing the mean convective velocities. Profiles of U_c and V_c are shown below in Fig. 6.20. Above the height $y^+ = 100$, the streamwise component in Fig. 6.20a is seen to lag behind the mean velocity U by 1% of the freestream velocity. Over the same region, V_c is larger than the mean velocity V by approximately $0.005U_e$. The reader is cautioned that the differences between the mean and convective velocities are approximately equal to the mean velocity uncertainty ($\sim 0.01U_e$), though this does not necessarily invalidate the results in Fig. 6.20.

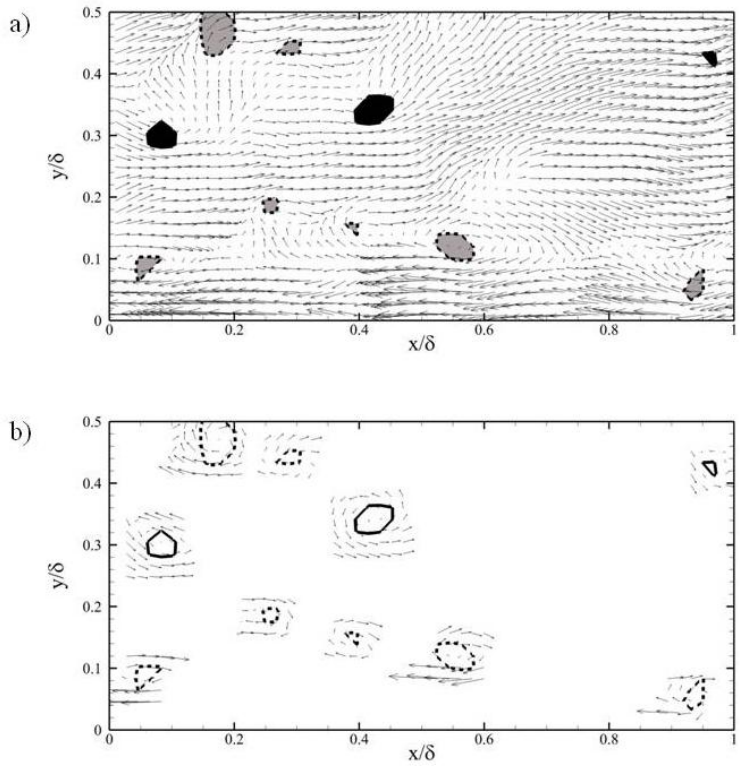

Figure 6.19 Instantaneous velocity field, showing vortices identified by the swirling strength criterion λ_{ci}. *Top)* *Grey contours indicate prograde vortices; black contours indicate retrograde vortices. A convective velocity $U_c = 0.83U_e$ has been subtracted.* ***Bottom)*** *Local convective velocity subtracted from each vortex. Prograde and retrograde structures are identified by dashed and solid lines, respectively.*

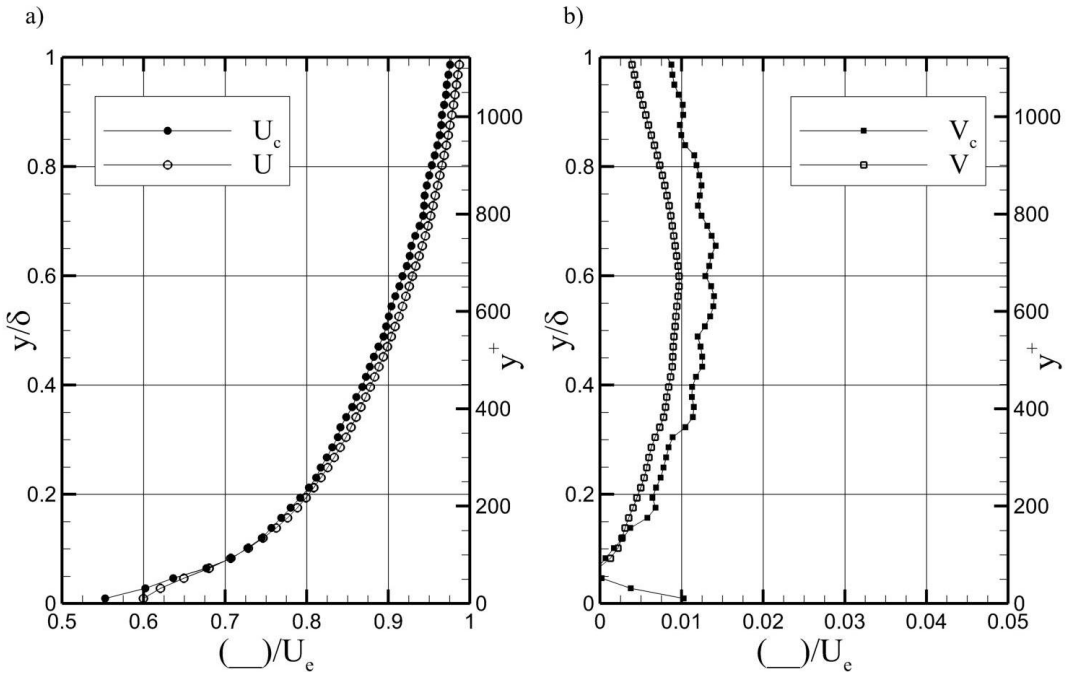

Figure 6.20 a) Streamwise and b) wall-normal convective velocity components, plotted versus the respective mean velocities.

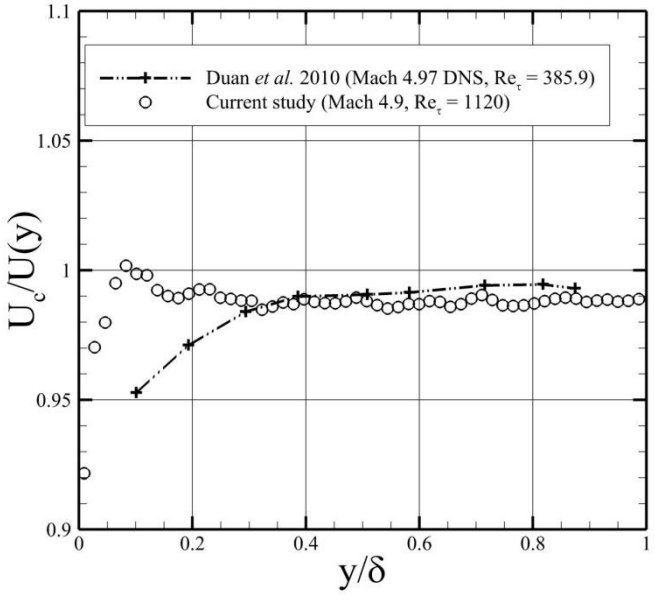

Figure 6.21 Streamwise convective velocity U_c, scaled by the local mean velocity U, plotted versus outer-scaled coordinates.

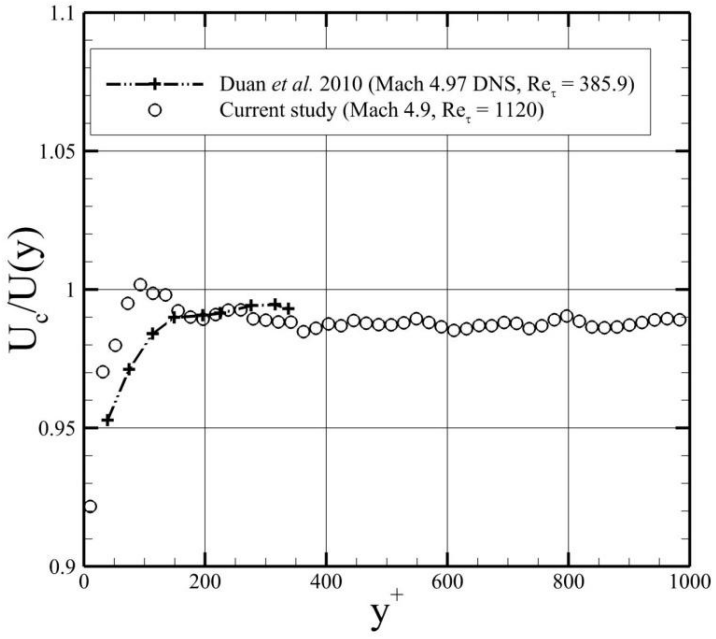

Figure 6.22 Streamwise convective velocity U_c, scaled by the local mean velocity U, plotted versus viscous-scaled coordinates.

The above profiles do not distinguish between prograde and retrograde vortices, though an analysis of the corresponding convective velocities (not shown here) suggests that there is no dependence upon the sign of the vortex for the upper 80% of the boundary layer thickness. All vortices in this region, regardless of the sense of rotation, appear to convect at similar velocities in both the streamwise and wall-normal directions. Below y/δ = 0.2, the convective velocity of the retrograde vortices shows a large degree of scatter, and does not agree with the mean velocity trend. This is most likely due to the low population of retrograde vortices in the near-wall region (discussed more thoroughly later in this section), such that the convective velocity is not statistically converged.

The streamwise convective velocity U_c is plotted in Fig. 6.21, and scaled by the local mean velocity U. For a majority of the boundary layer thickness, U_c is approximately 99% of the local mean value, showing excellent agreement with the Mach 4.97 DNS of

Duan *et al.* (2010). However, the two curves diverge below y/δ = 0.3, with the DNS results showing a larger disparity between the mean and convective velocities. When replotted versus viscous-scaled coordinates in Fig. 6.22, it is clear that the disparity occurs at the bottom of the logarithmic region. While the numerical and experimental results do not collapse onto each other below y^+ = 150, the slopes of the curves in the near-wall region are similar, neglecting the peak at y^+ = 100 for the current study.

The convective velocities shown in Figs. 6.20 – 6.22 show that the vortices in the boundary layer convect in the streamwise direction at a velocity $0.01U_e$ less than the local mean U, while the wall-normal component is approximately $0.005U_e$ greater than V. Adrian *et al.* (2000) suggested that the convective velocity of a vortex is influenced by its local environment, including both the surrounding fluid velocity and the "upstream component due to self-induction":

$$\vec{V}_c \approx \vec{V}_{mean} + \vec{V}_{induced} \tag{6.3}$$

Therefore, the upstream propagation of the induced fluid between the hairpin legs may result in a reduced convective velocity U_c, as shown in Fig. 6.20a and Figs. 6.21 – 6.22. This same self-induction may be responsible for the increased wall-normal convective velocity V_c in Fig. 6.20b. Individual hairpin vortices are typically angled at 45 degrees relative to the wall [Adrian *et al.* (2000)], causing a component of back-induced fluid to be oriented in the wall-normal direction. Consequently, the hairpin vortex may be "lifted" from the wall at a higher velocity than the surrounding fluid. Despite these physical mechanisms, previous studies have shown that the vortices convect at the mean velocity [Adrian *et al.* (2000); Elsinga *et al.* (2010); Carlier & Stanislas (2005); Wu & Christensen (2006a)]. Though the results of Adrian *et al.* (2000) show that the convective velocity is lower than the mean velocity above $y/\delta \approx 0.2 - 0.3$ ($y^+ \approx 400 - 600$) for Re_θ = 7705, the scatter due to the low sample size lead them to conclude that the convective and mean velocities are "remarkably close." Further analysis is needed to address the discrepancy between the convective velocities of the current study and previous experiments. It should be noted that the current study computes the convective

velocity based upon the instantaneous velocity at the hairpin heads, and does not distinguish between large- and small-scale structures (see LeHew, Guala & McKeon (2011) for an analysis of the scale-dependency of U_c at incompressible conditions).

The physical basis suggested above for U_c and V_c, in which the self-induction from the hairpin vortices produces a change in the convective velocity, should only apply to vortices comprising a hairpin head, i.e. prograde vortices. However, this study found that retrograde vortices experience a similar convective velocity in the outer region. For the above argument to be true, this would require that retrograde vortices are somehow related to the hairpin packet structure. This concept was suggested by Natrajan, Wu & Christensen (2007), based upon conditional averaging and two-point correlations of the prograde and retrograde structures. They observed that retrograde vortices often occur adjacent to their prograde counterparts, and theorized that this may be due to omega- or ring-like vortex loops. Additionally, Tomkins & Adrian (2003) suggested that a retrograde hairpin vortex may form from the merging of two hairpin loops. In order to probe the origin of the retrograde vortices in the current study, and their relation to the prograde vortex cores, probability density functions and two-point correlations are computed from the swirling strength contours.

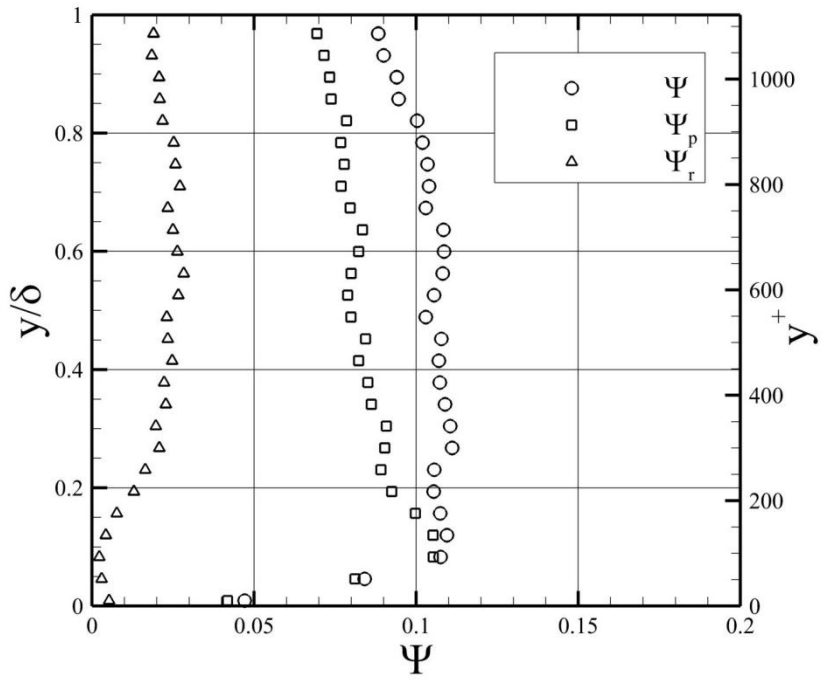

Figure 6.23 Population distribution of vortices, computed as a PDF. *The subscripts "p" and "r" denote prograde and retrograde, respectively*

First, the population distribution of the vortex cores is shown in Fig. 6.23, represented as Ψ. For each test case, 1035 velocity fields were processed. Within each instantaneous vector field, points residing inside a vortex core were tagged as "1", while the surrounding non-vortical fluid was set to "0." Ensemble-averaging these binary contour maps essentially produces a probability density function (PDF), defined as

$$\Psi = \frac{\#\text{ of vortices}}{N} \tag{6.4}$$

where N = 1035 is the total number of vector fields. The resulting two-dimensional contour of Ψ ranges from zero to one, and represents the probability of encountering a vortex at that point in the flowfield. The above process was repeated for the prograde and retrograde vortices, signified by Ψ_p and Ψ_r, respectively. Since Ψ is homogeneous in

the streamwise direction for the baseline case, spatially averaging over a streamwise distance of 0.5δ resulted in the profiles seen in Fig. 6.23.

The profile of Ψ in Fig. 6.23 shows that the total vortex population is relatively constant throughout the boundary layer thickness, excepting a slight decrease near the boundary layer edge and a sharp reduction below $y^+ = 100$. However, detection of vortices in the very near-wall region ($y^+ \leq 50$) should be considered suspect, due to the relatively limited resolution in this region. Decomposing the vortex population into prograde and retrograde components, a clear difference in the vortex distributions is visible. The prograde population Ψ_p achieves a peak of approximately 0.1 at $y^+ = 100$, and linearly decreases above this height. In contrast, the inner region of the flow contains almost no retrograde vortices, though a nearly constant population exists above $y/\delta = 0.25$. For much of the boundary layer, retrograde vortices represent approximately 20% of the total vortices. These findings are consistent with instantaneous snapshots of the velocity field, which have shown prograde vortices to be the dominant vortical structure, with a large concentration in the area of the flow corresponding to the logarithmic region. Conversely, instantaneous flowfields have revealed retrograde vortices only in the outer region, and in much smaller numbers.

The vortex population distributions in Fig. 6.23 agree qualitatively with Carlier & Stanislas (2005), who showed that the prograde vortices are roughly twice as populous as the retrograde vortices. Additionally, they showed that the prograde population achieves a peak at $y^+ \approx 120$, and decreases slowly above this location. Their retrograde vortex population is nearly constant above $y^+ = 100$. Below this height, both vortex populations decrease rapidly. Wu & Christensen (2006a) observed similar trends for their channel flow experiment at $Re_\tau = 1185$. Their measurements of the vortex density show that the retrograde structures achieve a nearly constant population above $y/\delta = 0.15$, and approach zero below this height. However, their prograde vortex density continues increasing near the wall, to a height of $y/\delta = 0.05$ ($y^+ \approx 60$). Despite this slight discrepancy in the near-wall behavior, the current study is consistent with the vortex

populations of Wu & Christensen (2006a), including their finding that the retrograde vortices constitute approximately 25% of the total vortex population. This agreement between the current study and past experiments was unexpected, given that the current resolution is poorer than the studies described above. For example, Carlier & Stanislas (2005) computed the average vortex radius as approximately 20 viscous units for Re_θ = 7500. Recall from §5.2.4 that the minimum resolvable vortex *diameter* for the current study, requiring a minimum of three vectors within a vortex, is approximately 36 viscous units for the baseline case. Therefore, the smallest vortices are undetected due to the spatial filtering of the PIV interrogation window.

Autocorrelations of the prograde and retrograde swirling strength, Λ_{ci}^{p} and Λ_{ci}^{r}, are shown in Figs. 6.24 – 6.25. Note that the estimated diameter of the prograde vortices, defined here at the R_{uu} = 0.2 isocontour, remains relatively constant at ~ 0.1δ (~ 100 viscous units) through the boundary layer thickness. The retrograde vortices exhibit similar behavior. While this method of determining the vortex cross-sectional diameter differs from the method employed by Carlier & Stanislas (2005), the qualitative trends agree quite well, indicating that the vortex diameter does not change with distance from the wall. Additionally, the similarity of the prograde and retrograde vortex diameters in Figs. 6.24 – 6.25 is useful in addressing a key limitation in the method for determining the vortex populations in Fig. 6.23. The current procedure for detecting vortices replies upon the contours of the swirling strength, since the centroid of the vortices is unknown (unlike the pattern recognition analysis employed by Carlier & Stanislas (2005)). When computing the vortex populations, the presence of a vortex was indicated by a vector coinciding with a region of non-zero swirling strength. Therefore, if the prograde vortices were larger, for example, then the resulting vortex population would be biased toward larger values of Ψ_p. The agreement between the cross-sectional vortex diameters in Figs. 6.24 – 6.25 alleviates this concern. Future analyses should also consider the variance in the respective vortex diameters, as the current results only address the mean diameter.

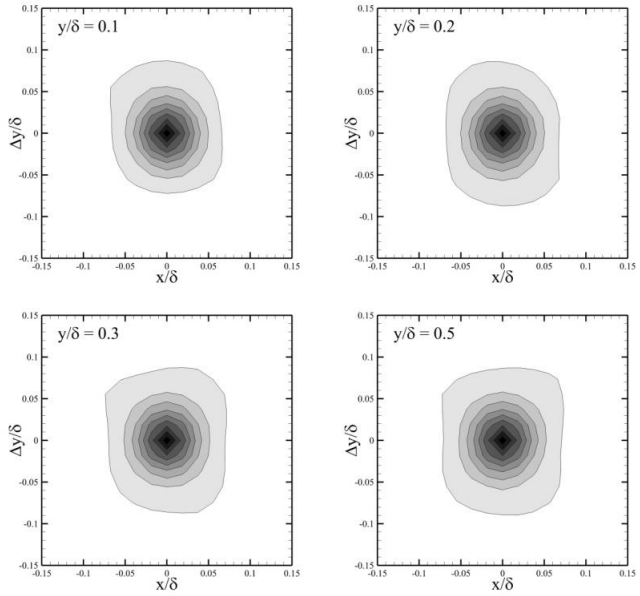

Figure 6.24 Autocorrelations of prograde swirling strength Λ_{ci}^{p} . *Outer contour is 0.1, in increments of 0.1*

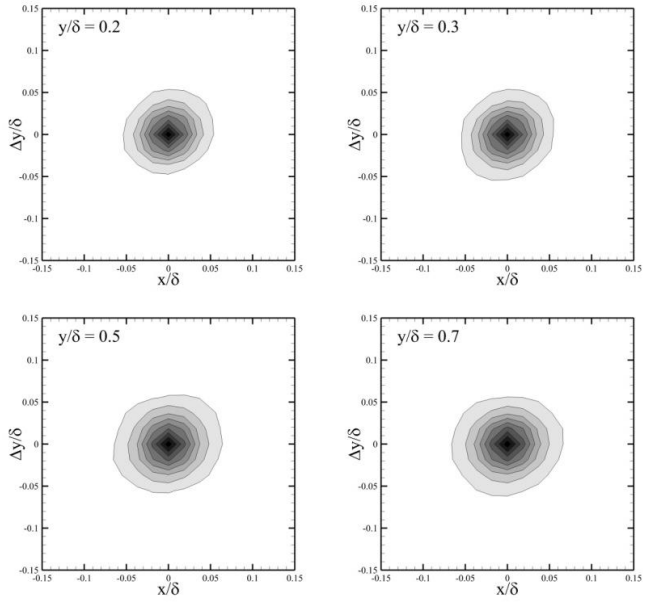

Figure 6.25 Autocorrelations of retrograde swirling strength Λ_{ci}^{r} . *Outer contour is 0.1, in increments of 0.1*

Finally, the cross-correlation between the prograde and retrograde swirling strength is shown in Fig. 6.26, computed as

$$R_{\Lambda_{ci}^{p}\Lambda_{ci}^{r}}(\Delta x, y, y_{ref}) = \frac{\Lambda_{ci}^{p}(x, y_{ref})\Lambda_{ci}^{r}(x+\Delta x, y)}{\sqrt{\left\langle\left(\Lambda_{ci}^{p}(x, y_{ref})\right)^{2}\right\rangle}\sqrt{\left\langle\left(\Lambda_{ci}^{r}(x+\Delta x, y)\right)^{2}\right\rangle}} \tag{6.5}$$

where Λ_{ci}^{p} and Λ_{ci}^{r} refer to the prograde and retrograde swirling strength components, respectively. The resulting correlation in Eqn. 6.5 describes the distribution of retrograde events around a prograde vortex, as shown in Fig. 6.26. Since the prograde swirling strength Λ_{ci}^{p} is weighted by the sign of the vorticity, the resulting cross-correlation is necessarily negative. The near-wall position $y/\delta = 0.2$ is rather noisy, possibly due to the scarcity of the retrograde structures in this region, and does not clearly indicate a clear structure. However, it is possible to observe that the correlation is negligibly small directly upstream and downstream of the prograde vortex, suggesting that any pairing between these vortices occurs in the wall-normal direction. At the three outer-most positions, local maxima in the correlation are observed at two general locations: 1) downstream and above the prograde vortex, and 2) upstream and below the prograde vortex. The downstream lobe forms an angle θ_{pr} that is 50 – 60 degrees relative to the horizontal plane, though this broadens to 40 – 70 degrees at $y/\delta = 0.7$. The upstream lobe shows similar variability, ranging from 220 to 270 degrees. These orientations are similar to those computed by Natrajan *et al.* (2007), though their correlations were computed for prograde events relative to a retrograde reference vortex. Unfortunately, no clear structure for the retrograde-prograde pairing can be discerned from these correlations. One can only observe that retrograde and prograde vortices appear to occur in pairs, angled in the downstream direction. However, if these events are due to omega- or ring-shaped vortices (as suggested by Natrajan *et al.* (2007) and others), and the prograde-retrograde pairing is due to the PIV plane slicing through the vortex shoulder,

then this may explain the similar convective velocities for the prograde and retrograde vortices.

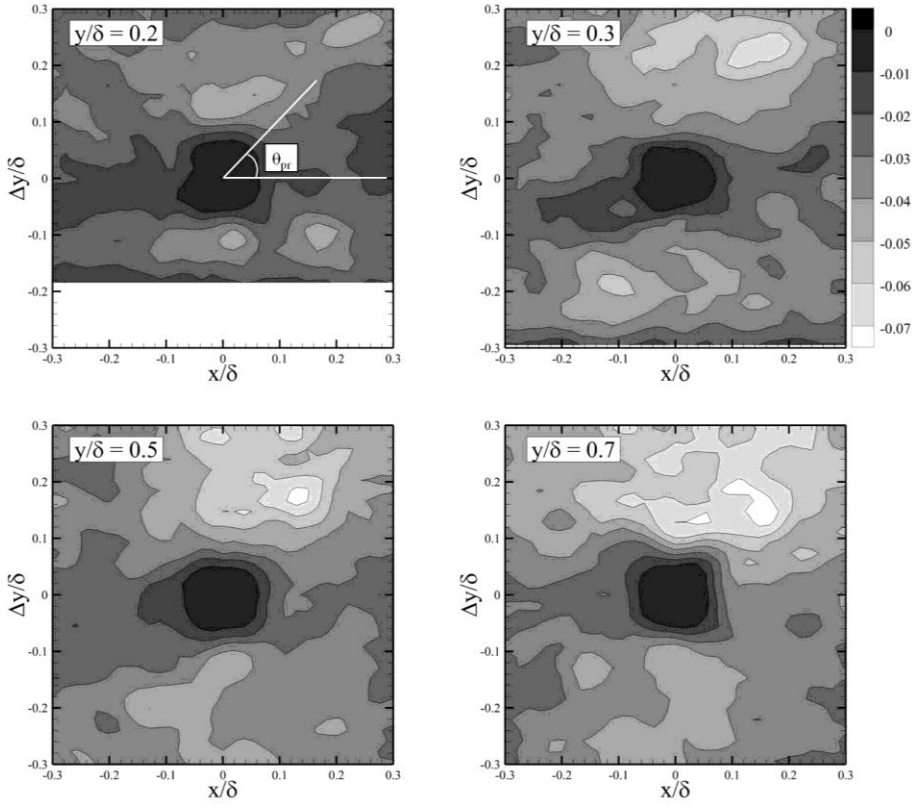

Figure 6.26 Cross-correlation of prograde and retrograde swirling strength, indicating the position of retrograde events relative to a reference prograde vortex

6.7. Conditional Structure of Near-Wall Flow

The instantaneous hairpin packet shown in Fig. 6.13 supports the theory that the low-momentum streaks in the logarithmic region are formed by the collective back-induction of fluid between the hairpin legs (see Fig. 6.15). Along with forming the low-momentum regions, the local flowfields induced by the individual hairpins (i.e. sweep and ejection events) are the prime contributors to the Reynolds shear stress. Given the central role

that individual hairpin vortices occupy in the turbulence production mechanism, it is essential to characterize the statistical behavior and contributions of these structures.

Figure 6.27 shows a triplet of spanwise vortices, aligned in the streamwise direction. The sweep and ejection events are labeled, indicating fluid being induced toward and away from the wall, respectively. As these regions of high- and low-momentum fluid collide, a local shear layer is formed downstream of the vortex. Due to the stronger intensity of the ejection events, caused by the mutual induction of the hairpin legs, the shear layer forms a shallow angle with respect to the wall.

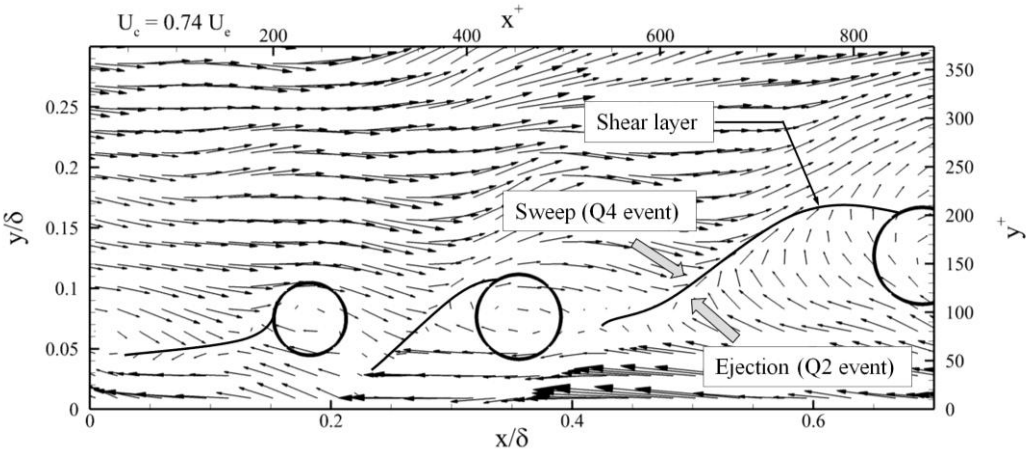

Figure 6.27 Instantaneous velocity field, showing shear layers forming downstream of the vortices.
Vortices are identified by subtracting a convective velocity $U_c = 0.74U_e$

While the visualization in Fig. 6.27 is useful for observing the local flowfield near a vortex, it is obvious that large variances exist in the ejection/sweep intensities and shear layer angles. Therefore, any further analysis of the contributions due to individual hairpin vortices must be conducted in a statistical manner. This is performed by computing the conditional average of the fluctuating velocity field, with a vortex signature as the conditional event. Because the exact centroid of each vortex is unknown, the conditional average must be estimated through linear stochastic estimation (LSE),

which is described more fully in §4.4.5. Recall that this method estimates the conditional velocity through the computation of unconditional correlations. The resulting conditionally-averaged velocity field is not necessarily equivalent to the instantaneous visualizations, owing to any variance in the vortex structure. The reader is also reminded that the conditional velocity only describes the *relative distribution* around a vortex, not the velocity magnitude. However, this is still sufficient to illustrate the locally induced vortex motions.

The conditionally-averaged velocity field for a prograde vortex is shown in Fig. 6.28. The region of spiraling flow is clearly seen at the event site, consistent with a prograde vortex signature. The $u' = 0$ isocontour is shown by a dashed line, identifying the local shear layer. At the near-wall $y/\delta = 0.1$ position, a strong region of back-induced flow is visible beneath and slightly upstream of the vortex, consistent with the motion produced by an ejection event. Additionally, a weaker region of fluid is observed above and downstream of the vortex, most likely due to the prograde vortex drawing fluid toward the wall. The shear layer extends to the wall upstream of the vortex, agreeing with the ramp-like orientations of hairpin packets observed by Adrian *et al.* (2000). The angle of this shear layer is ~ 12 degrees, similar to the 13 – 14 degree angle observed by Christensen & Adrian (2001), but smaller than the 18 degrees seen by Elsinga *et al.* (2010) at Mach 2. All of these observations are consistent with the hairpin packet structure discussed previously in this section.

The $y/\delta = 0.2$ and 0.3 locations in Fig. 6.28 continue to display the aforementioned the shear layer, though it no longer intersects the wall. This may suggest that the vortex packets above this height have detached from the wall, though this can not be corroborated by the current data. At all heights, a strong region of back-induced flow exists beneath the vortex. The existence of these hairpins near the boundary layer edge is consistent with the observations of Elsinga *et al.* (2010), who showed that large-scale hairpin vortices exist above the low-momentum streaks at points higher in the boundary layer ($y/\delta > 0.6$).

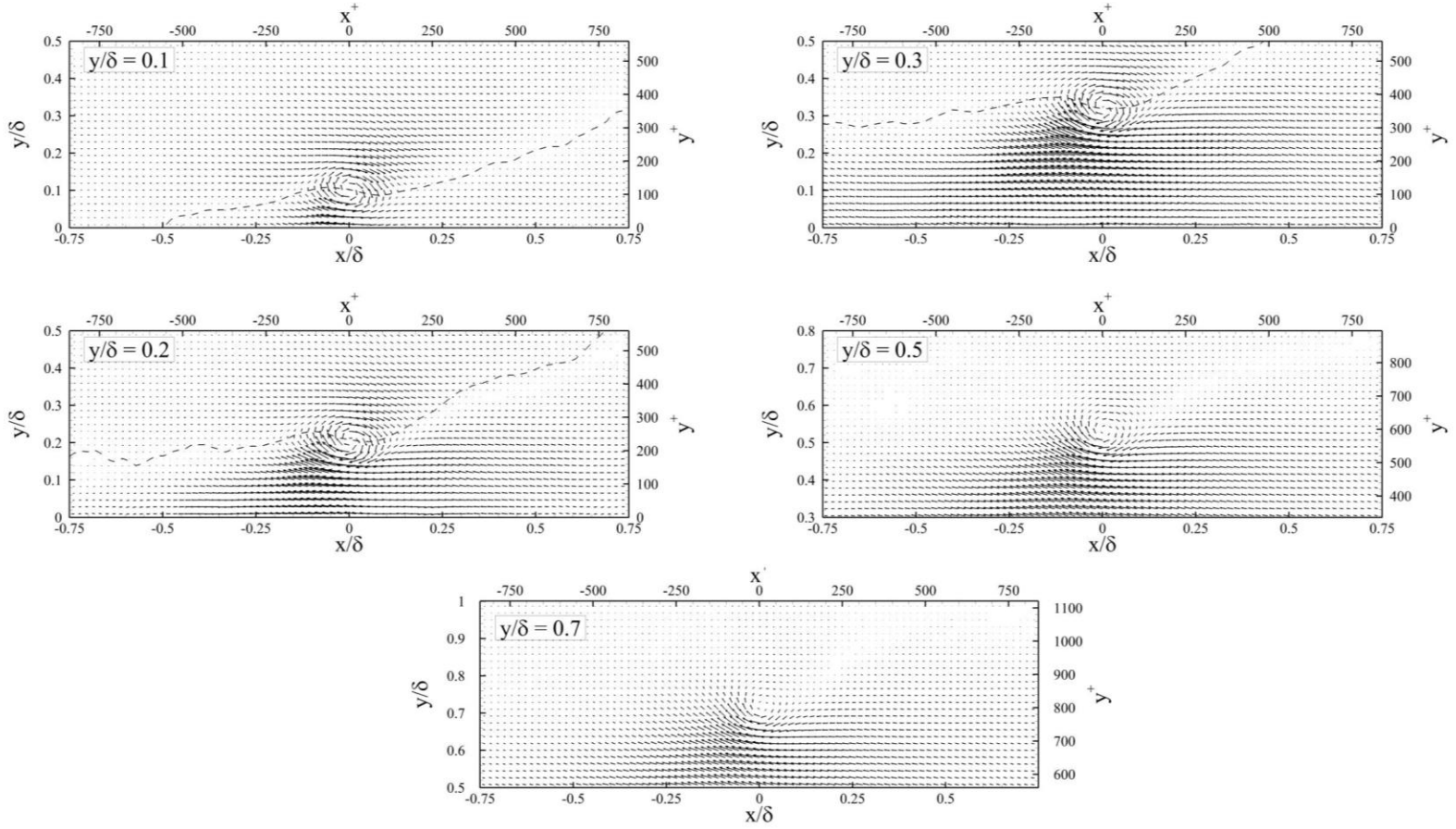

Figure 6.28 Conditionally averaged velocity field for prograde vortex event

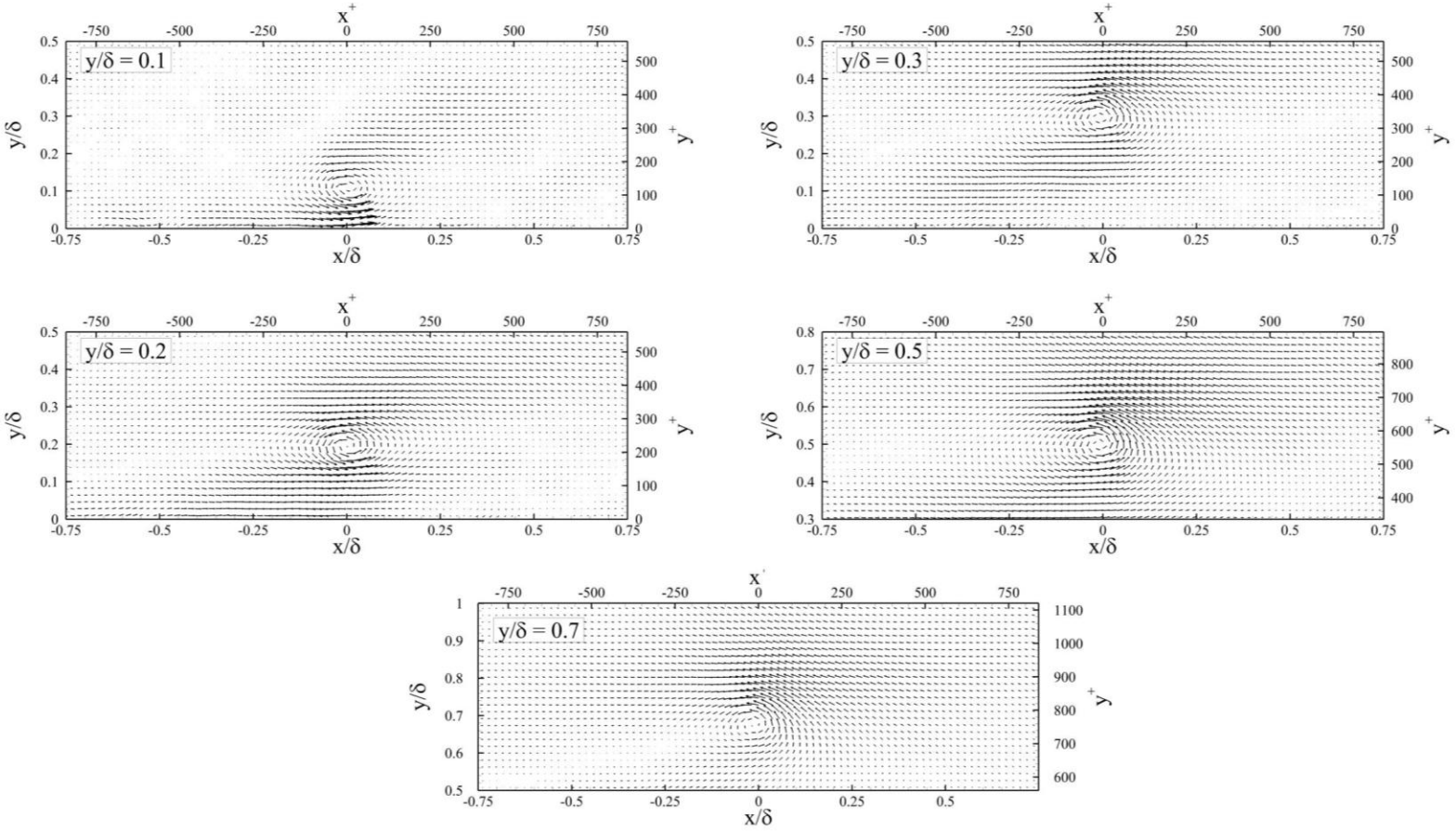

Figure 6.29 Conditionally averaged velocity field for retrograde vortex event

The conditional average is shown again in Fig. 6.29, but for a retrograde vortex event. The spiraling motion at the event site is still clearly visible, though the sense of rotation is in the opposite direction. At y/δ = 0.1, a strong region of forward-induced flow exists beneath the vortex, suggesting the fluid is being swept in the downstream direction. Above this height, at y/δ = 0.2, the locally induced flow is more isotropic, with the magnitude of the velocity above and below the vortex approximately equal. However, the locations y/δ = 0.3 – 0.7 show high-intensity ejections of fluid above and downstream the vortex core.

Figures 6.28 – 6.29 have illustrated the average behavior of the locally-induced flowfield near a vortex event. However, these results do not directly address the Reynolds stress contributions of the hairpin vortices. To investigate how the local flowfield influences the shear stress, the cross-correlation between the swirling strength and shear stress *u'v'* has been computed as

$$R_{\Lambda_{ci}^{p(r)}(u'v')}(\Delta x, y, y_{ref}) = \frac{\Lambda_{ci}^{p(r)}(x, y_{ref})u'v'(x+\Delta x, y)}{\sqrt{\left\langle \left(\Lambda_{ci}^{p(r)}(x, y_{ref})\right)^2 \right\rangle}\sqrt{\left\langle \left(u'v'(x+\Delta x, y)\right)^2 \right\rangle}} \tag{6.6}$$

where the superscripts "p" and "r" indicate the sign of the event vector (i.e. prograde or retrograde). The cross-correlation in Eqn. 6.6 describes the behavior of the local shear stress around a prograde or retrograde vortex. Before continuing, a brief explanation of the cross-correlation sign is needed. Note that the swirling strengths have been scaled by the sign of the local vorticity ω_z, yielding $\Lambda_{ci}^{p} < 0$ and $\Lambda_{ci}^{r} > 0$. Therefore, $R_{\Lambda_{ci}^{p}(u'v')} > 0$ when *u'v'* is negative, and $R_{\Lambda_{ci}^{r}(u'v')} < 0$ when *u'v'* is negative.

The cross-correlation $R_{\Lambda_{ci}^{p}(u'v')}$ is shown in Fig. 6.30, describing the distribution of *u'v'* near a prograde vortex. The corresponding conditionally-averaged velocity field has been overlaid. Two local maxima are observed at y/δ = 0.1: 1) above and downstream of the vortex core, and 2) below and upstream of the prograde vortex. Comparing to the conditional velocity, these locations are consistent with sweep and ejection events,

respectively. However, the downstream lobe is no longer visible for y/δ = 0.2 – 0.5, while the upstream lobe grows in magnitude and size. This suggests that the shear stress production is increasingly due to the ejection events, and that these events occupy a larger area of the flow away from the wall. The reader is reminded that Fig. 6.30 shows the correlation *coefficients*. The increasing magnitude at higher points in the boundary layer does not suggest that the intensity of these events (and therefore the magnitude of the shear stress *u'v'*) is larger, but that the *relative* contribution of the ejections is increasingly dominant.

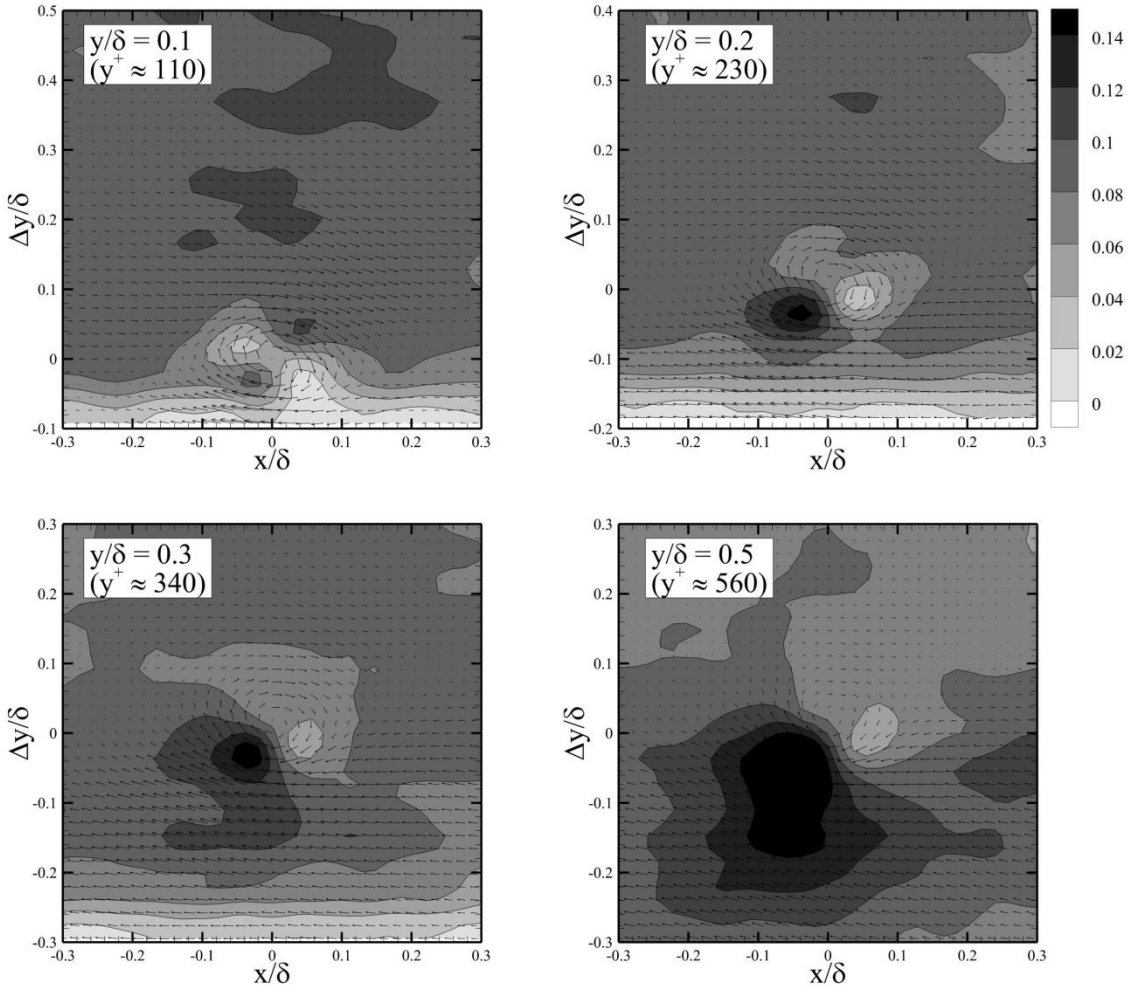

Figure 6.30 Cross-correlation of prograde swirling strength and shear stress

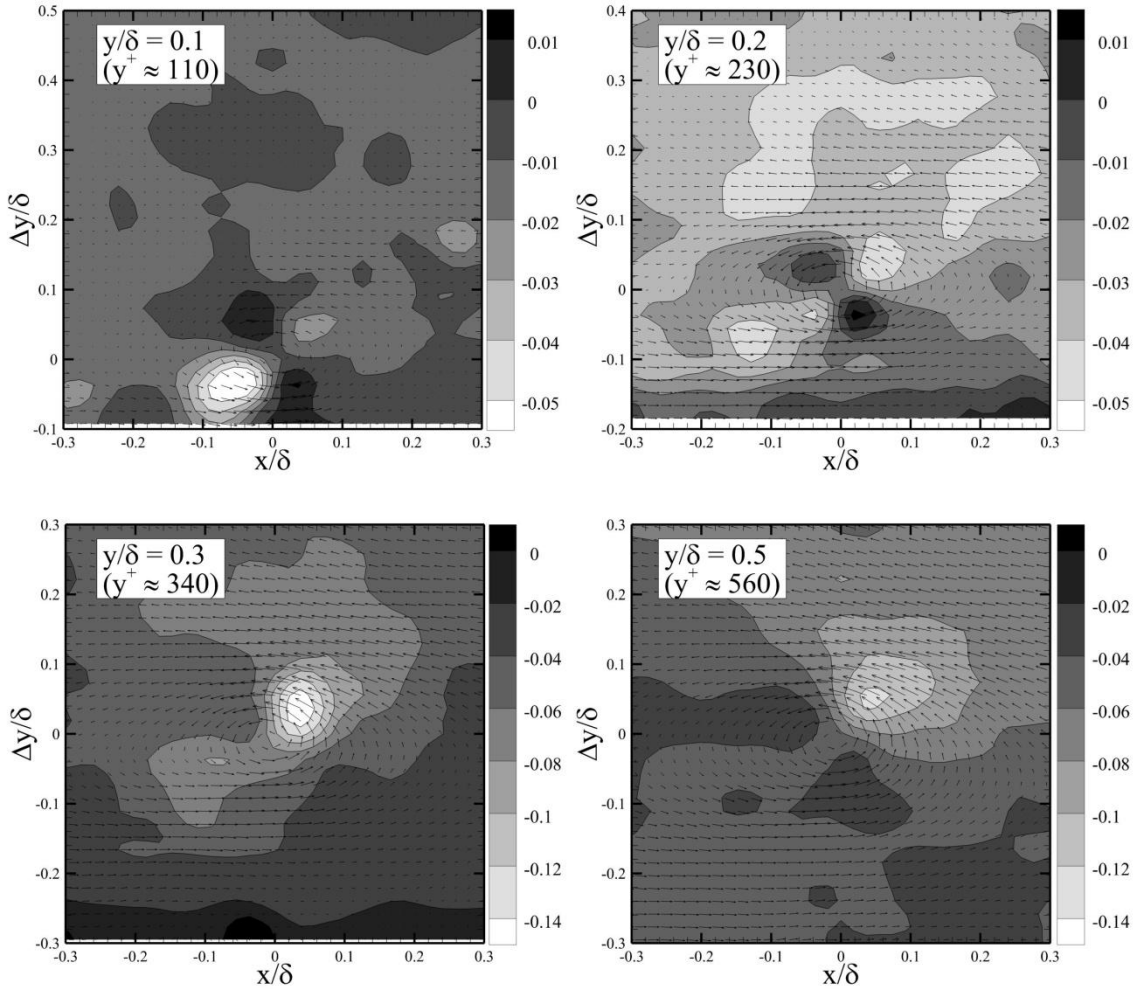

Figure 6.31 Cross-correlation of retrograde swirling strength and shear stress. *Note the different contour levels at each location*

The cross-correlation $R_{\Lambda_{ci}^{r}(u'v')}$ for retrograde vortices is shown in Fig. 6.31. At $y/\delta = 0.1$, a large lobe is observed below and upstream of the vortex, due to the forward-swept fluid beneath the retrograde event. An additional lobe appears downstream and above the vortex at $y/\delta = 0.2$, though the correlation coefficient of each area is much reduced. The two outer-most positions both show a local maximum above the vortex, as the fluid is drawn upstream by the retrograde vortex. However, the most interesting result is

observed at $y/\delta = 0.1 – 0.2$, in which *positive* correlations exist near the vortex core. For this correlation, a positive value indicates that $u'v' > 0$. Therefore, the retrograde vortices appear to be acting against the mean shear stress in this region, contributing to *negative production*, albeit weakly. While this concept was described by Hussain (1986) in terms of coherent structure orientation and pairing, retrograde vortices were not considered. Previous studies have shown that prograde and retrograde vortices both contribute to the mean shear stress [Wu & Christensen (2006a)], though no discussion has been made as to the *sign* of the shear stress due to the retrograde events. The near-wall results in Fig. 6.31 suggest that the presence of retrograde vortices is not merely a peculiarity of the turbulence structure, but that these vortices may somehow counterbalance the mean shear stress. Further analysis is needed for the shear stress magnitude produced by these retrograde events.

6.8. Origin of Retrograde Vortices

Given the results presented herein, sufficient evidence exists to comment upon the origin of the retrograde vortices within the boundary layer. First, a review of the existing theories is warranted. One possible origin of the retrograde structures stems from the spanwise growth of hairpin vortices. As the vortices mature, their increase in scale naturally leads to a decreased spanwise separation between adjacent vortices. When this separation distance decreases to a sufficiently small value, the vortices may undergo a merging process [Tomkins & Adrian (2003)]. While the exact details of this mechanism are unknown, several possible scenarios have been proposed by Tomkins & Adrian (2003). One scenario, depicted in Fig. 6.32, occurs when the original vortices break apart, subsequently re-connecting to form a large prograde hairpin and a smaller retrograde hairpin. The retrograde vortex is initially upstream and below from the prograde structure.

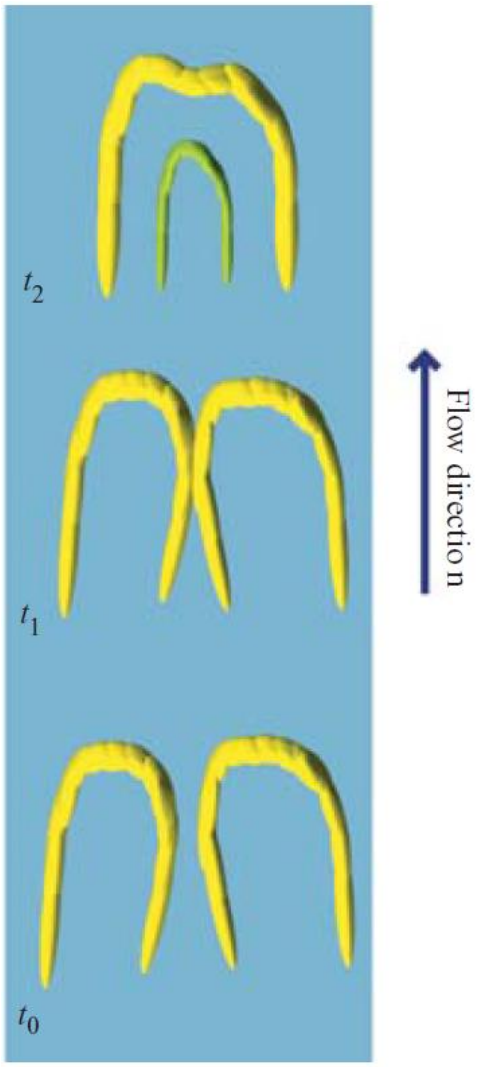

Figure 6.32 One of several possible merging scenarios for adjacent hairpin vortices, showing the creation of a large prograde vortex and a smaller retrograde vortex (shown in green). *Image is adapted from* Tomkins & Adrian (2003).

The second possible scenario describing the creation of retrograde vortices is merely due to the two-dimensional nature of the current data set. Consider the existence of omega- and ring-shaped vortex loops within turbulent boundary layer, as observed by Zhou *et al.* (1999), among others. When imaging the flow through PIV, a two-dimensional plane is passed through the test section. If this plane happens to bisect the "shoulder" of an omega-shaped vortex, then a retrograde/prograde vortex pair will be observed, with the

retrograde vortex positioned upstream and below its prograde counterpart. This mechanism was proposed by Natrajan *et al.* (2007), in order to explain the presence and orientation of retrograde vortices within incompressible boundary layers.

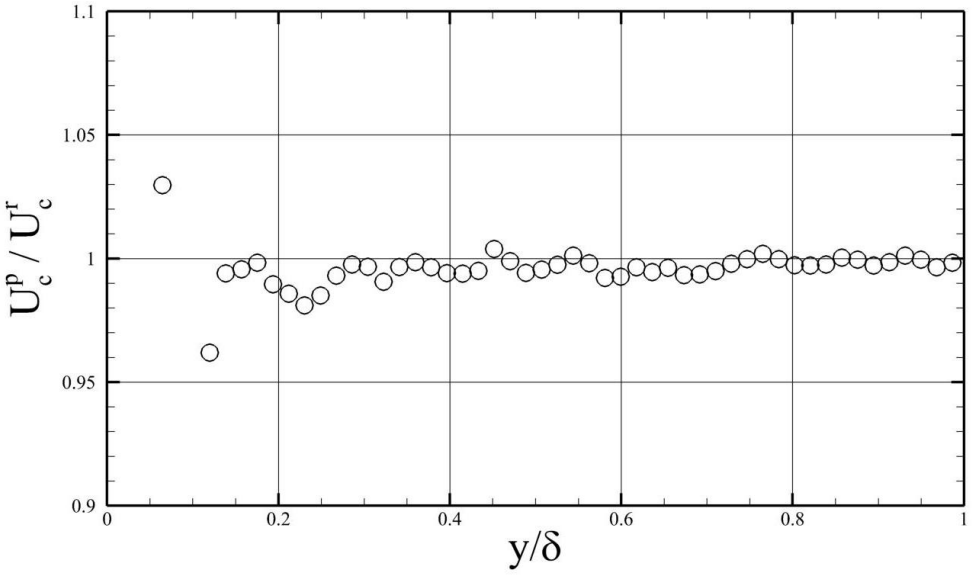

Figure 6.33 Ratio of streamwise convective velocities, for prograde and retrograde vortices

The analyses described previously in this section may now be applied to the current issue, namely the genesis of retrograde vortices. The convective velocities presented in §6.6 showed that the streamwise propagation of a vortex occurred at a velocity approximately 1% slower than the local mean velocity. This analysis made no distinction between prograde and retrograde vortices. However, if the convective velocities are now computed for each vortex population, then it is obvious that the convective velocity is insensitive to the sign of the vortex. This is shown in Fig. 6.33 as the ratio between the prograde and retrograde convective velocities, denoted by U_c^p / U_c^r. The significance of this finding can be seen by considering the analysis given in §6.6. Recall that the convective velocity of a structure is a function of both the local fluid velocity and the self-induced flowfield, approximated by Eqn. 6.3. As explained in §6.6, prograde hairpin

vortices are expected to convect more slowly than the mean velocity, due to the strength of the back-induced flow between the hairpin legs. Naturally, a hairpin with a reversed sense of rotation (i.e. a retrograde vortex) should convect at a velocity that is greater than the local mean, due to fluid being *swept forward* between the hairpin legs. Since Fig. 6.33 shows that the prograde and retrograde structures have similar streamwise convective velocities, this would appear to suggest that the retrograde vortices are not representative of separate hairpin structures.

The analysis given above indicates that the retrograde and prograde vortices may share a common structure, as shown by the nearly identical streamwise convective velocities. This is further supported by the cross-correlation between the prograde and swirling strengths, $R_{\Lambda_{ci}^{p}\Lambda_{ci}^{r}}$. Shown in Fig. 6.26, the correlation indicated a preferred orientation between the prograde and retrograde vortices, with the retrograde events arranged at two locations relative to the prograde reference event: 1) above and downstream, and 2) below and upstream. This description generally matches the theory advanced by Natrajan *et al.* (2007), who suggested that the vortex pairing is due to the presence of omega- or ring-shaped structures.

Further evidence of this phenomenon is presented in the shear stress-swirling strength correlations in Figs. 6.30 and 6.31. The correlation $R_{\Lambda_{ci}^{r}(u'v')}$ at y/δ = 0.3 and 0.5 in Fig. 6.31 shows large-magnitude lobes downstream and above the retrograde vortex core, suggesting a strong shear stress-producing events in this area of the flow, consistent with the ejection of low-momentum fluid away from the wall. Additionally, the correlation $R_{\Lambda_{ci}^{p}(u'v')}$ indicates a similarly strong ejection upstream and below a prograde event. If these vortices are part of a larger omega-shaped structure, then the mutual induction between the vortex legs would contribute to a flow structure similar to that seen in Figs. 6.30 and 6.31. This concept is illustrated in Fig. 6.34.

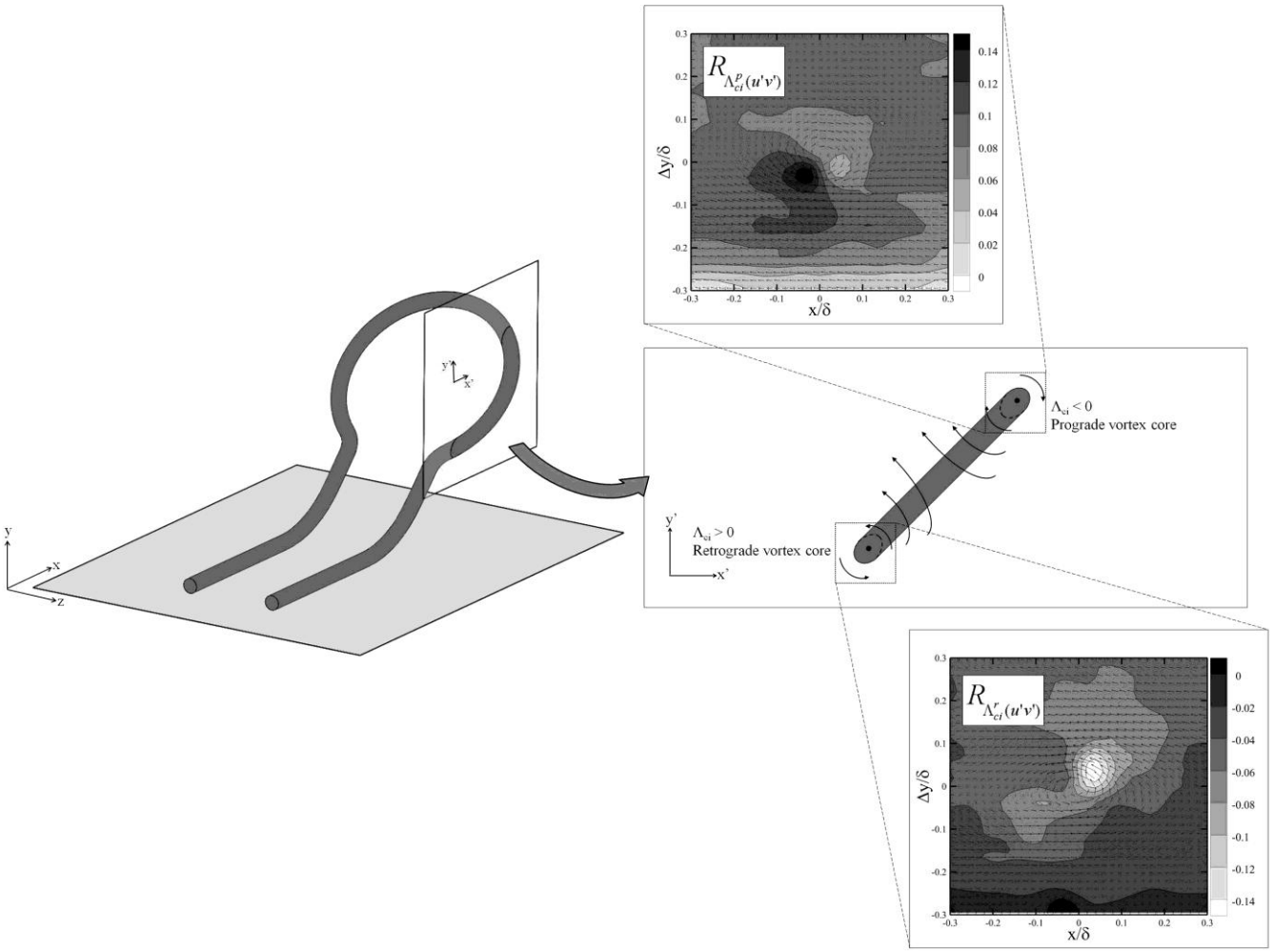

Figure 6.34 Conceptual diagram of omega-shaped vortex loop, showing the possible orientation of retrograde and prograde vortices. *Note the agreement between the shear stress-swirling strength correlations and the vortex structure.*

6.9. Summary and Discussion of Results

The turbulence structure of a Mach 4.9 flat-plate boundary layer was investigated using PIV in the *x*-*y* plane. Mean velocity and Reynolds stress profiles show excellent agreement with previous supersonic studies. Correlations of the streamwise velocity show that δ-scale motions exist throughout much of the boundary layer thickness, and are oriented at approximately 10 degrees relative to the wall. Instantaneous visualizations of the velocity suggest that the δ-scale structures are most likely packets of streamwise-aligned hairpin vortices, and that the correlated low-momentum streaks beneath them are due to mutual back-induction of fluid between the hairpin legs. These observations are consistent with previous studies at both incompressible and supersonic conditions [Adrian *et al.* (2000); Christensen & Adrian (2001); Elsinga *et al.* (2010) and many others]. Premultiplied spectra of the streamwise, wall-normal, and shear components show that the physical imprint of the individual hairpins and longer low/high-momentum streaks is visible within the Reynolds stresses at discrete wavelengths.

The population distribution of the vortex cores was shown to be heavily biased toward prograde vortices, though both prograde and retrograde events convect at approximately the same velocity. As anticipated, the largest concentration of prograde vortices is within the logarithmic region. The retrograde vortices, while comprising only 20% of the vortex population, are believed to be part of a larger omega- or ring-shaped vortex structure. Conditionally averaged velocity fields showed that the locally induced motions near a prograde vortex core agree well with previous experiments [Christensen & Adrian (2001); Elsinga *et al.* (2010)], illustrating both sweep and ejection events. However, the prograde sweep events were shown to be less dominant as the distance from the wall increases. Similar motions were observed around conditionally-averaged retrograde vortices, though at different orientations. Finally, the Reynolds stress contribution of the vortices was investigated by computing the swirling strength-shear stress correlation. Shear stress concentrations around the prograde vortex cores were shown to be

coincident with the sweep and ejection events identified through conditional averaging, supporting the theory that hairpin vortices are the primary contributors to the Reynolds shear stress. However, the near-wall retrograde vortices produced lobes of *positive* shear stress $\overline{u'v'}$, suggesting that these structures may contribute to negative production within this region. Further investigation into the contributions of the retrograde vortices, along with their relation to the prograde structures, is currently needed.

7. BOUNDARY LAYER RESPONSE TO STREAMLINE CURVATURE-INDUCED FAVORABLE PRESSURE GRADIENTS

Favorable pressure gradient and convex wall curvature effects in supersonic boundary layers have received modest attention in the past several decades [Bradshaw (1974); Arnette *et al.* (1998); Luker *et al.* (2000)], including the most recent study by Tichenor *et al.* (2013). While previous efforts have focused upon the response of the turbulence statistics, the physical mechanisms governing these motions remain poorly understood (see §2.2 for a summary of the current literature). This section investigates not only the ensemble-averaged behavior of the flow through the expansion regions, but also the response of the coherent structures. By examining the distortion of the large-scale motions and near-wall vortices, it is possible to provide a physical basis for the behavior of the turbulence statistics.

7.1. Mean Flow Response

Mean flow parameters are shown in Table 7.1 for all three pressure gradient cases. Recall from §3.3.2 that the zero pressure gradient, weak pressure gradient, and strong pressure gradient models are labeled as ZPG, WPG, and SPG, respectively. The subjective terms “weak” and “strong” refer to the magnitude of the response of the kinetmatic shear stress, which will be shown later in this section. The experimental data were collected over two curved-wall models and a flat-plate baseline model (see §3.3.2), at a distance 29.8 cm downstream of the nozzle exit. For all cases, the wall temperature T_w was approximately 307 K. While the expanding flow was expected to lead to a reduced wall temperature, the large thermal mass and low thermal conductivity of the acrylic models resulted in T_w remaining constant for each geometry. Flush-mounted pressure taps arrayed along the model floor yielded the wall pressure p_w within the measurement region, as well as upstream of the wall curvature. The impulse parameter $I_p = (1/\gamma)\ln(p_2/p_1)$ was calculated using p_1 from the undistorted region of the flow,

upstream from the wall curvature, whereas p_2 was measured within the FOV. The pressure gradient parameter $\beta = (\delta^*/\tau_w)\mathrm{d}p/\mathrm{dx}$ was calculated from the local pressure gradient dp/dx, which was determined from pressure taps adjacent to the measurement region. When calculating β, the incompressible form of δ^* was used, due to the lack of a mean density profile for the distorted flowfields [see Appendix F]. Note that β for the ZPG case is listed in Table 7.1 as a non-zero value. As described in §6, the constant area of the test section lead to a weakly adverse pressure gradient for the flat-plate model. However, it was shown that the resulting flowfield agrees well with other zero pressure gradient boundary layers in the scientific literature, and is therefore a suitable baseline case.

Before continuing with the experimental results, a comment must be made concerning the response of the boundary layer thickness. Table 7.1 shows that δ decreases by approximately 10% for the WPG case (compared to the ZPG case), where δ is measured at $U = 0.99U_e$. The authors had initially anticipated an increased boundary layer thickness for the favorable pressure gradient cases, consistent with the bulk dilatation encountered in an expanding flow. While no explanation is readily available for this behavior, it is possible to speculate that this behavior may be a result of the slight curvature (1.7 degrees) of the WPG model, producing wall curvature and pressure gradient effects that are of similar magnitude. This is illustrated by a comparison of I_p and I_φ for the WPG case. In contrast, the SPG impulse parameters imply that pressure gradient effects are dominant, leading to bulk dilatation being the primary mechanism affecting the evolution of δ. Unfortunately, the interaction between wall curvature and pressure gradient effects on the boundary layer thickness has not been explored in detail, due to the technical challenge of producing a ZPG curved-wall flow in supersonic conditions. Further investigation is needed to fully explain the observed reduction in boundary layer thickness.

Table 7.1 Mean flow parameters

Model	δ [mm]	U_e [m/s]	u_τ [m/s]	τ_w [Pa]	Re_τ	I_p	I_φ	β
ZPG	10.9	762	35	69	1120	0.04	0	0.1
WPG	10.0	766	37	71	1030	-0.08	0.03	-0.2
SPG	12.9	754	40	44	750	-0.49	0.17	-1.1

The ensemble-averaged streamwise and wall-normal velocity profiles are shown in Figs. 7.1 and 7.2, respectively. Note that for all cases, the coordinates $\{x,y,z\}$ are arranged in a body-fixed reference frame (unless otherwise noted). The streamwise component U/U_e in Fig. 7.1 exhibits the expected trend for a favorable pressure gradient boundary layer, with the near-wall fluid being accelerated beyond the ZPG case. The physical basis for this behavior stems from the lower velocity of the near-wall fluid (compared to the outer region of the boundary layer), which necessarily resides within the expansion region for a longer period of time, and therefore experiences a larger axial acceleration, leading to a fuller velocity profile. As anticipated, the degree of acceleration is proportional to the magnitude of the pressure gradient, with the SPG case showing the largest deviation from the baseline velocity profile. At a distance 0.2δ from the wall, the mean streamwise velocity of the WPG and SPG flows is approximately 3% and 8% larger than the undistorted boundary layer, respectively.

The wall-normal velocity profiles V/U_e in Fig. 7.2 exhibit a large sensitivity to the model geometry. For the FPG cases, the V-velocity linearly increases with y/δ, and the slopes of these profiles remain constant throughout the boundary layer thickness. The large magnitude of the FPG wall-normal velocity is most likely due to the rotation of the local coordinate system, leading to a 10x increase in v/U for the SPG case. While the increase for the WPG case is marginal compared to the SPG model, the wall-normal velocity still experiences a nearly 400% increase at the boundary layer edge.

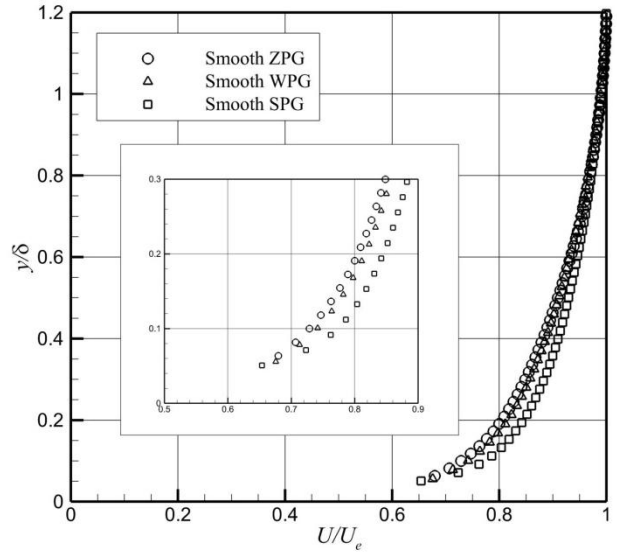

Figure 7.1 Mean streamwise velocity profile, *plotted versus* y/δ.

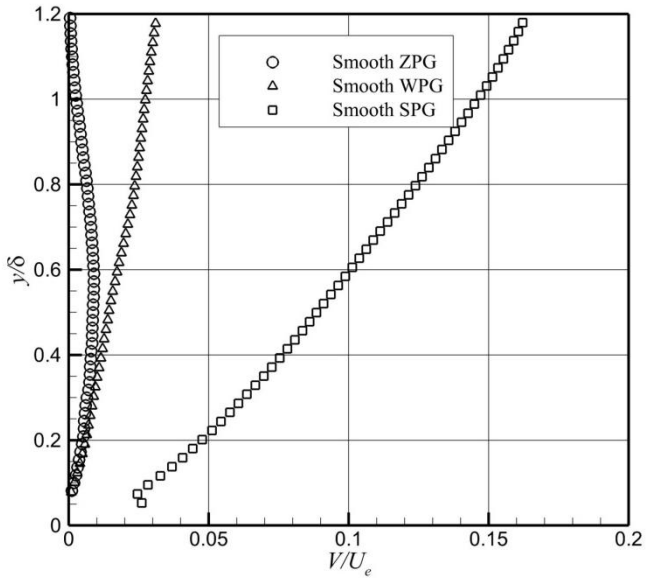

Figure 7.2 Mean wall-normal velocity profile, *plotted versus* y/δ

The streamwise velocity is transformed using the van Driest II compressibility transformation, and plotted versus inner-scaled coordinates in Fig. 7.3. An extended logarithmic region is observed for the SPG case, along with a severely depressed wake region relative to the ZPG and WPG boundary layers. In contrast, the WPG case is minimally perturbed from the baseline flowfield in the wake region, and collapses onto the ZPG data below $y^+ \approx 500$. It should be noted that the friction velocity u_τ, determined from the Clauser chart method, is relatively constant with respect to the pressure gradient (see Table 7.1). However, the decreasing wall density of the SPG case results in a 40% decrease in the wall shear stress τ_w, computed as $\tau_w = \rho_w u_\tau^2$. Due to the constant wall temperature for each case, and hence a constant wall viscosity μ_w, the near-wall strain rate dU/dy must necessarily decrease for the SPG model, since $\tau_w = \mu_w \left.\frac{\partial U}{\partial y}\right|_{y=0}$.

Given that the SPG velocity profile is fuller than the WPG and ZPG cases (Fig. 7.1), this suggests that an inflection point should exist in the region of fluid directly adjacent to the wall. It is unknown if this inflection would exist under adiabatic conditions, and what effect it may have on the turbulence production.

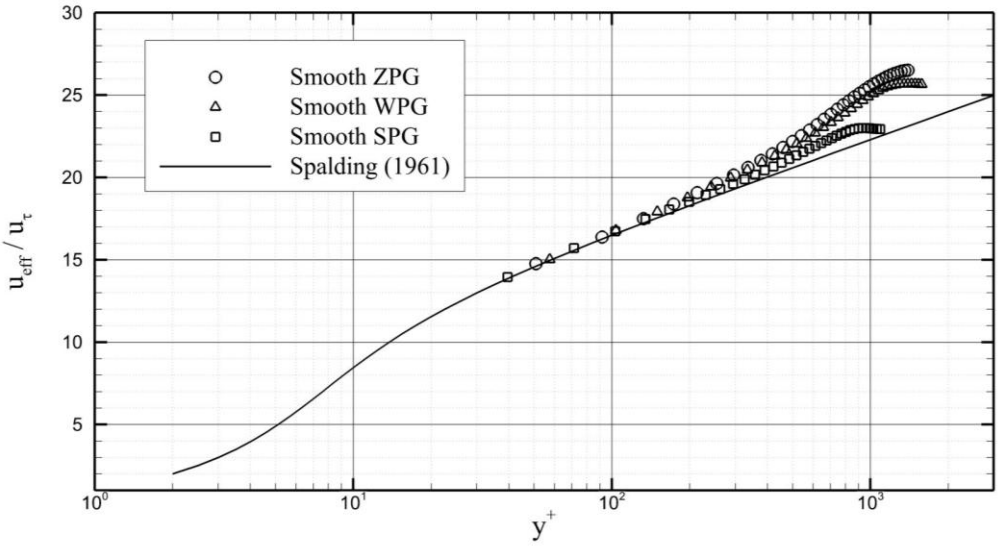

Figure 7.3 Inner-scaled mean velocity, using the van Driest II compressibility transformation

7.2. Reynolds Stress Response

The responses of the axial, wall-normal, and shear stresses are presented in Figs. 7.4 – 7.6, respectively, and scaled by the freestream velocity U_e. Due to the similarity of the boundary layer edge velocities (Table 7.1), Figs. 7.4 – 7.6 essentially provide a comparison of the dimensional stresses. Each profile is extracted from the center of the FOV, and averaged over a streamwise distance 0.5δ, in order to improve visualization. The observed reduction of the kinematic turbulent stresses is consistent with previous data from Luker *et al.* (2000) and Arnette *et al.* (1998), including the sign reversal of the shear stress *u'v'*. As described in §7.1 for the mean velocity, the deviation of the stresses from the baseline case is proportional to the magnitude of the pressure gradient.

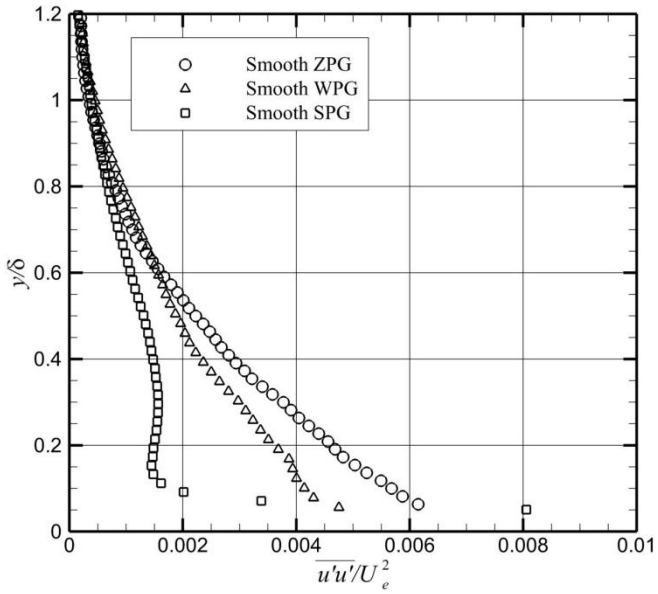

Figure 7.4 Axial kinematic stress over the FPG models, scaled by the freestream velocity

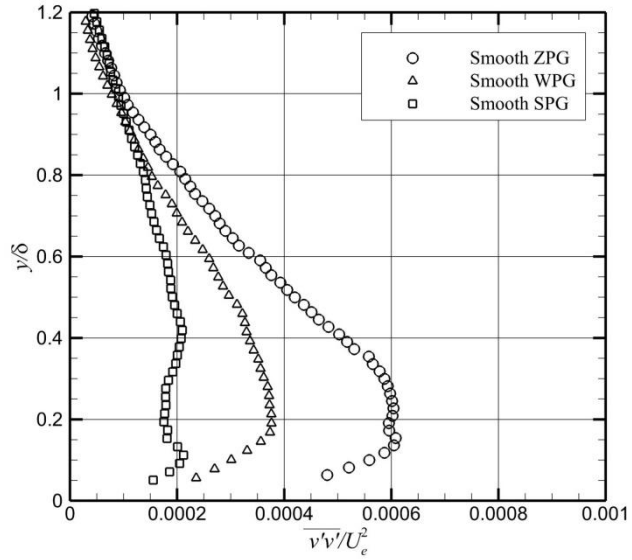

Figure 7.5 Wall-normal kinematic stress over the FPG models, scaled by the freestream velocity

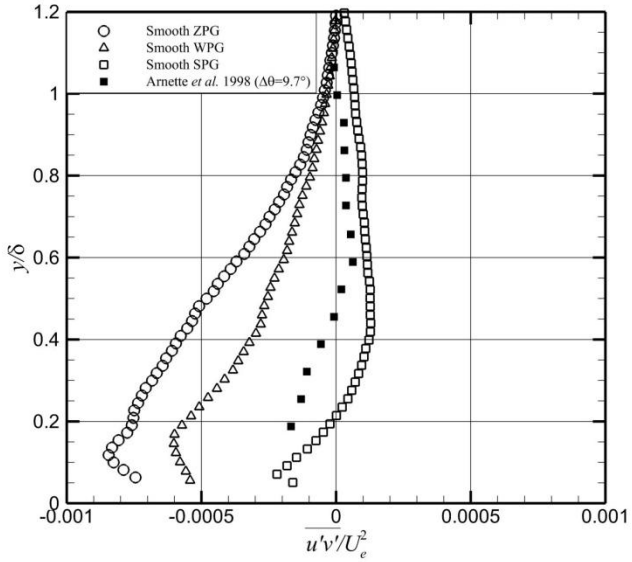

Figure 7.6 Kinematic shear stress over the FPG models, scaled by the freestream velocity. *The current study is compared to the supersonic data of* Arnette *et al.* (1998)*, measured over a 14 degree gradual expansion. The streamwise position was chosen to match the local curvature of the current study. Note that the data of* Arnette *et al.* (1998) *was scaled by the incoming velocity* U_0.

The axial kinematic stress in Fig. 7.4 illustrates the stabilization expected within a FPG boundary layer, with reductions of 20% and 60% for the WPG and SPG cases, respectively. Above y/δ = 0.6, the WPG flow exhibits a slightly larger axial stress, increasing by approximately 5% above the ZPG value. While the magnitude of this discrepancy is similar to the uncertainty of the turbulence stresses, the most likely explanation is the uncertainty of the boundary layer thickness δ (see §6.2 and Figs. 6.4 – 6.5 for an example of the sensitivity to δ). A similar reduction in turbulence stress is observed for the wall-normal component in Fig. 7.5, with the WPG and SPG values at y/δ = 0.2 decreasing by 40% and 60%, respectively. However, the most significant reduction is exhibited by the kinematic shear stress, plotted in Fig. 7.6. While the WPG model produces a 25% – 30% decrease in the magnitude of $u'v'$, the SPG flowfield experiences a reduction *greater than 100%*, yielding $u'v' > 0$ for the outer 80% of the boundary layer. This sign reversal has been observed previously over centered and gradual expansions [Luker *et al.* (2000); Arnette *et al.* (1998); Tichenor *et al.* (2013)], and agrees qualitatively with the Mach 3 data of Arnette *et al.* (1998), collected at a similar wall inclination over a 14 degree gradual expansion. The implications of the shear stress response are significant, indicating that kinetic energy is being transferred back into the mean flow. For a more thorough examination of the response of the turbulence stresses and strain rates, including implications for turbulence modeling, see Tichenor *et al.* (2013).

The sensitivity of the current data to the coordinate frame rotation has been mentioned previously, when discussing the behavior of the wall-normal mean velocity profile V/U_e (Fig. 7.2). Given the dramatic response of the kinematic shear stress in Fig. 7.6, it is necessary to determine if the observed behavior is due to the choice of coordinate system. Using the local wall angles, the WPG and SPG shear stresses are projected onto the wind tunnel axes (which is equivalent to the ZPG frame of reference), and shown in Fig. 7.7. Note that the coordinate transformation is only applied to $u'v'$, and that y/δ is still measured normal to the wall. The WPG case experiences a marginal change in magnitude when transformed, owing to the small rotation angle $\Delta\theta$ = 1.7 degrees.

However, the transformed SPG shear stress no longer experiences a sign reversal, and monotonically approaches zero at the boundary layer edge. The remaining difference between the ZPG and (transformed) SPG shear stress values is therefore due to the relaxation of the turbulent fluctuations. Indeed, the desire to explain this difference through physically-derived models has motivated much of the analysis in the remainder of this section.

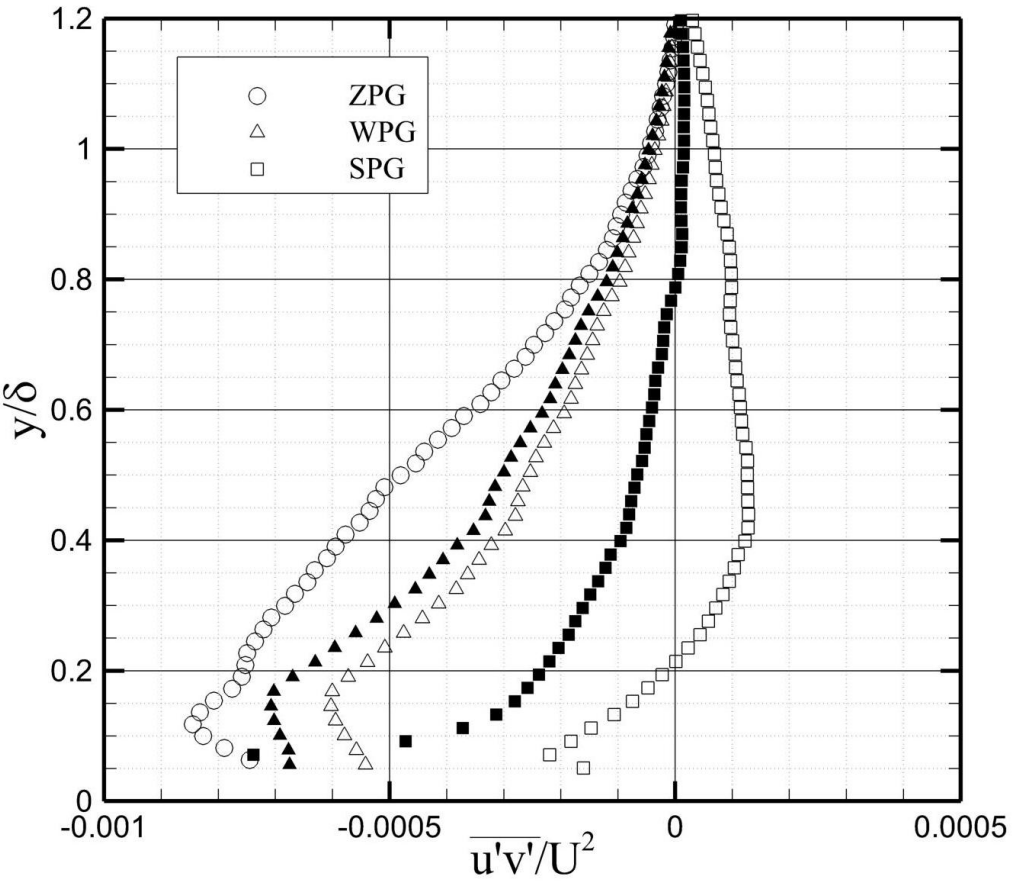

Figure 7.7 Transformed kinematic shear stress over the FPG models, scaled by the freestream velocity. *The filled symbols describe the shear stress after being rotated into the wind tunnel axes. Note that* y/δ *is still measured normal to the wall.*

The contributions of hairpin vortices to the mean shear stress was discussed at length in §6, using instantaneous visualizations, conditional averaging, and two-point correlations to illustrate the salient features. Given that the locally induced flowfields surrounding the vortices are the primary mechanism for generating the Reynolds shear stress [Adrian *et al.* (2000); Wu & Christensen (2006a)], the shear stress response observed in Fig. 7.6 naturally leads to the following question: *What structure/motions are responsible for the mean shear stress response within the FPG boundary layers?*

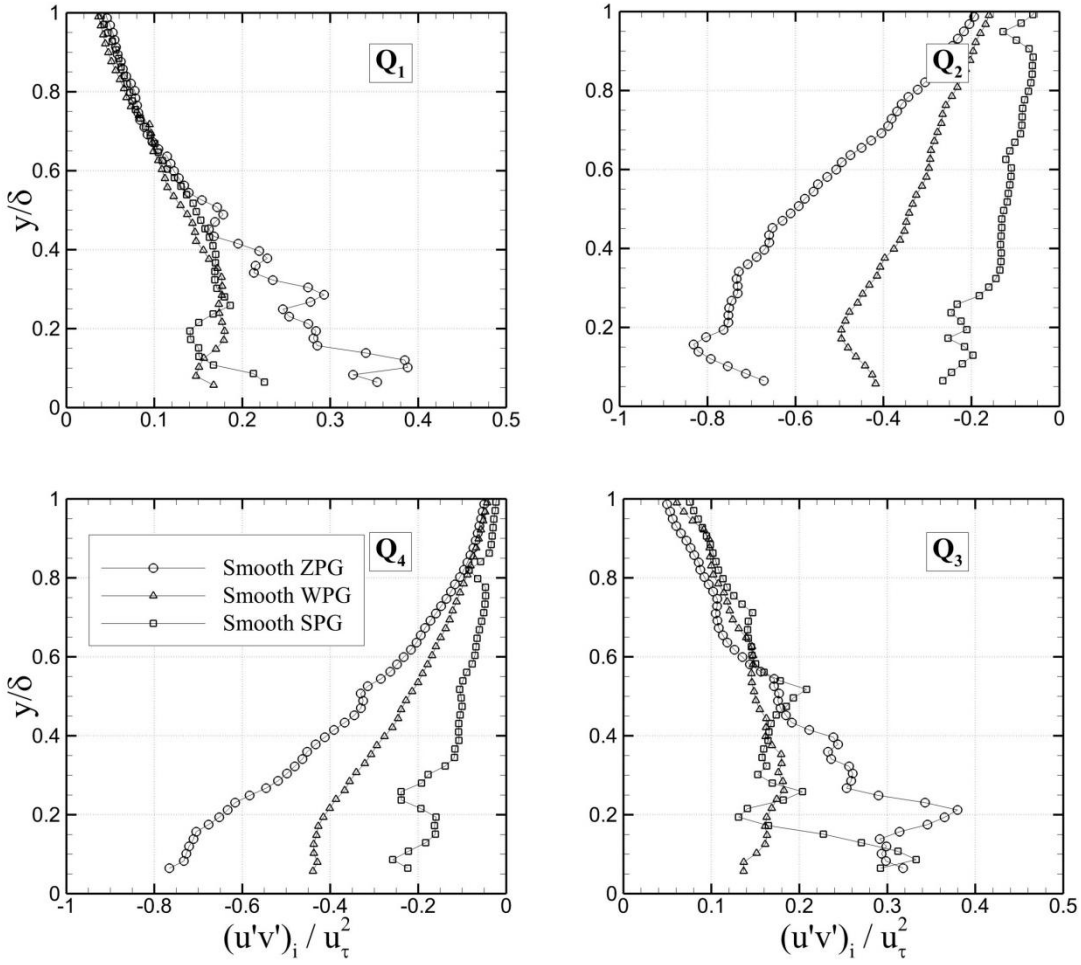

Figure 7.8 Quadrant decomposition of the FPG boundary layers, showing the contribution of each quadrant event.

Using quadrant decomposition, it is possible to infer the distortion of the vortex-induced flowfields, by examining the contributions to the mean kinematic shear stress [Willmarth & Lu (1972)]. At each height in the boundary layer, the instantaneous $u'v'$ signal is binned according to the sign of the axial and wall-normal fluctuations (see §4.4.3 for a more thorough description of this method). The contribution from each quadrant is shown in Fig. 7.8, without filtering the events based upon magnitude (i.e. H = 0). The Q2 and Q4 events (*ejections* and *sweeps*, respectively) follow the trend seen in Fig. 7.6, in which the fluctuations are attenuated in proportion to the strength of the pressure gradient. Projecting this result onto the hairpin packet model, this suggests that the entrainment and ejection of fluid around and between the hairpin legs has been suppressed. A similar trend is observed for the Q1 and Q3 events in Fig. 7.8 (*inward interactions* and *outward interactions*, respectively), in which the FPGs lead to a reduced shear stress magnitude. While the scatter in these components is larger (most likely due to a smaller population of these events [Tichenor *et al.* (2013)]), it is apparent that the reduced magnitude of the Q1 and Q3 motions is nearly identical for the WPG and SPG cases, excepting the Q3 events below $y/\delta = 0.2$. This suggests that the Q1 and Q3 motions may respond as a step function, with the magnitude of the reduction only weakly dependent upon the pressure gradient strength. Unfortunately, the physical basis of the Q1 and Q3 motions is not easily characterized, limiting our interpretation of these trends with respect to the hairpin packet model. It would be instructive to repeat this analysis for stronger distortions (i.e. larger pressure gradients), to determine the relation between the Q1 and Q3 motions and β. Regardless, Fig. 7.8 appears to confirm that the stabilizing influence of the FPGs is exerted upon all four quadrants of the shear stress. While this result may seem intuitive, prior to this analysis it was unknown whether the instantaneous shear stress events were lower in magnitude, or if the Q2 and Q4 events were being counteracted by a positive shear stress contribution (i.e. Q1 and Q3 motions).

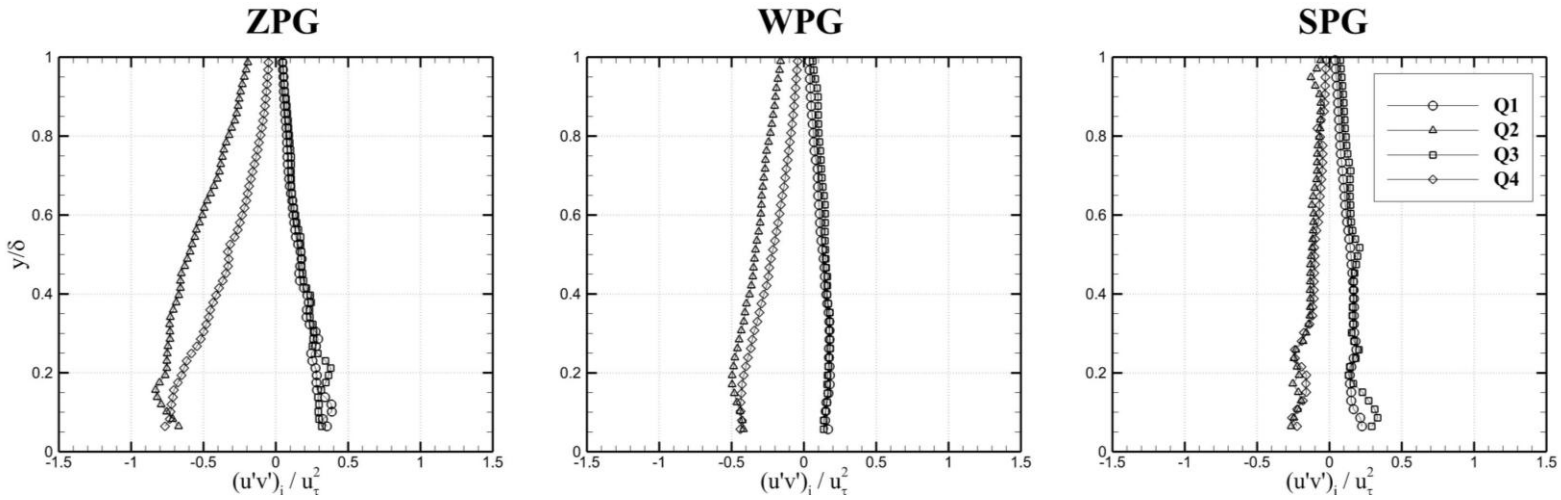

Figure 7.9 Distribution of quadrant events within each test case

The quadrant events are replotted in Fig. 7.9, showing the relative distribution of shear stress-producing motions within each boundary layer. As noted in §6.5, and shown in Fig. 6.15, the mutual induction of the hairpin legs results in a stronger ejection of fluid in the upstream direction, relative to the sweep events. This imbalance is visible in Fig. 7.9 for the ZPG case, in which the ejection event is "a dominant feature of the structure of the turbulent boundary layer" [Lu & Willmarth (1973)]. As the strength of the pressure gradient is increased, both the Q2 and Q4 magnitudes are reduced across the entire boundary layer thickness, though the ejection events are reduced by a larger margin, suggesting a particular sensitivity to the attenuation of the mean shear stress. For the SPG case, the magnitude of the shear stress events is distributed evenly among all four quadrants. By extension, this suggests that the strong favorable pressure gradient has deformed the hairpin vortex loops in such a way that the mutual induction between the hairpin legs no longer produces an ejection event that is stronger than the corresponding sweep.

Before continuing with the current analysis, it is necessary to qualify the observations made in the previous paragraphs. As stated above, the stress profiles in Figs. 7.4 – 7.6 were determined at the center of the FOV. However, given that the boundary layer evolves in the streamwise direction, it is prudent to determine whether these profiles are representative of the entire FOV. To determine the evolution of the Reynolds stresses across the measurement region, profiles are extracted at five streamwise locations, averaged over a distance of 0.2δ. The streamwise positions are described by s/δ, where s is the distance downstream from the start of the wall curvature. Additionally, the corresponding undistorted boundary layer is shown for comparison.

The ZPG and WPG cases showed negligible change across the FOV, as expected, and are not shown here. However, the flow over the SPG model continued to evolve in the streamwise direction, with the turbulence stresses reducing in magnitude as s/δ increased, similar to the behavior observed by Arnette *et al.* (1998). This evolution is shown in Figs. 7.10 – 7.12 for the axial, wall-normal, and shear stresses, respectively.

The attenuation of the axial stress is largest in the near-wall region, varying by 22% of the ZPG value across the FOV, and collapses onto the ZPG boundary layer above y/δ = 0.8. The evolution near the wall may be caused by the "quenching" of small-scale structures, while the large-scale structures near the boundary layer edge remain intact. Additionally, this response may be due to the time-scales of the near-wall structures, which are typically smaller due to the reduced length scales in this region. By this logic, the large-scale structures in the outer region have not had sufficient time to respond to the pressure gradient. However, given sufficient time (i.e. a sufficiently large s/δ), the departure point of the axial stress from the ZPG profile would be expected to approach y/δ = 1.0, due to the slow response of the large-scale motions. This argument is supported by the evolution of the wall-normal and shear stresses, which exhibit smaller variations of 11% and 9% across the FOV. The *u'*-bearing eddies are typically ~ δ in length, as shown by the R_{uu} correlations and premultiplied spectra in §6. In contrast, the near-wall scales associated with *v*' and *u'v'* motions are typically smaller, spanning 0.2 – 0.3δ and 0.3 – 0.4δ, respectively (see Figs. 6.17 – 6.18). Assuming that the pressure gradient dp_w/dx is relatively constant across the FOV (which is plausible, considering that the change in inclination angle is ~ 0.5 degrees within the measurement region), the smaller *v'*- and *u'v'*- scales would lead to a more rapid response/attenuation in these components. This is evidenced by the large reduction in the wall-normal and shear components (compared to the axial component), and the relatively small evolution within the FOV, suggesting that the *v'* and *u'v'* motions have already experienced a majority of the stabilization. In contrast, the larger length scale of the *u'*-bearing eddies, with a correspondingly longer timescale, causes the axial component to "fall behind" the other components, which results in the larger variation over the FOV seen in Fig. 7.10. Visualizations by Arnette *et al.* (1998) support this reasoning, showing that the large-scale structures survive the initial expansion, but are less evident in the post-expansion region, suggesting the "large-scale structures are much slower to respond." It should be restated that this argument is based upon the assumption that the forcing due to the model geometry is approximately constant across the FOV. Examination of the

streamwise variation of the d*V*/d*y* strain rate (not included here) supports this assumption.

It should also be noted that the SPG boundary layer experienced approximately 1 mm of growth across the entire FOV. The extracted stress profiles in Figs. 7.10 – 7.12 are plotted versus y/δ_{local}, where δ_{local} is the boundary layer thickness at each streamwise position. Extrapolating this turbulence reduction to the downstream edge of the curvature, it is possible that the SPG boundary layer is approaching "reverse transition" [Arnette *et al.* (1998)], though the current FOV is insufficient to view this behavior. Considering this flow evolution, it may be prudent for future analyses to repeat the quadrant decomposition described previously, as a function of streamwise position.

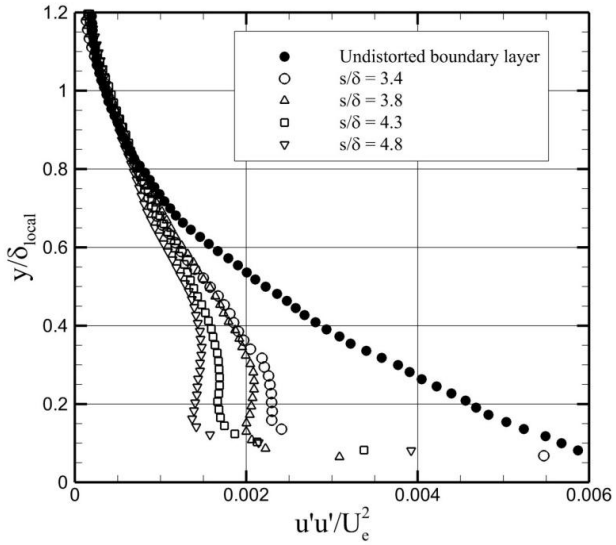

Figure 7.10 Streamwise evolution of the axial kinematic stress over the SPG model. δ_{local} *is the local boundary layer thickness*

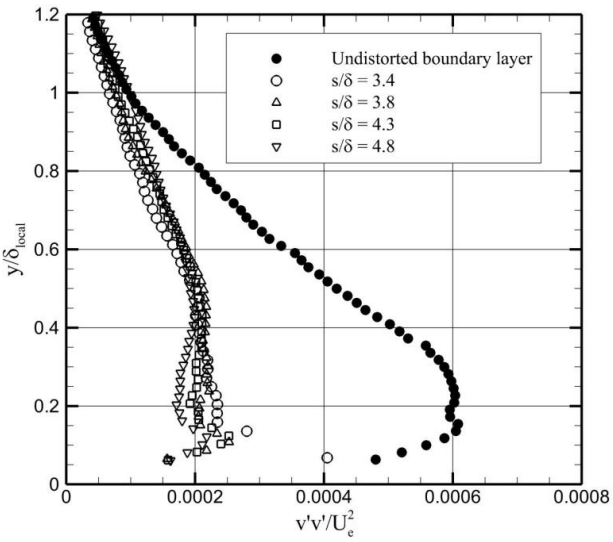

Figure 7.11 Streamwise evolution of the wall-normal kinematic stress over the SPG model. δ_{local} *is the local boundary layer thickness*

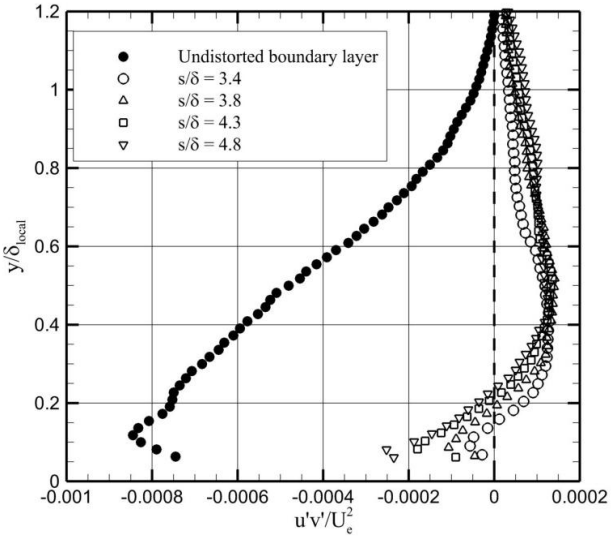

Figure 7.12 Streamwise evolution of the kinematic shear stress over the SPG model. δ_{local} *is the local boundary layer thickness*

7.3. Spatial Organization of Large-Scale Structures

As discussed in §6.4, the spatial organization and orientation of the large-scale motions can provide vital insight into the behavior of the turbulence-producing structures (i.e. hairpin vortices and packets). This behavior bears additional significance for the FPG boundary layers, since many previous studies have suggested that bulk dilatation is the primary mechanism for reducing the shear stress through the expansion region [Bradshaw (1974); Dussauge & Gaviglio (1987); Smith & Smits (1991); Arnette *et al.* (1998)], while Luker *et al.* (2000) speculated that the stabilization of the Reynolds stress is due to the disintegration of the large-scale structures. Given that the physical mechanisms governing the relaxation of turbulent fluctuations through an FPG boundary layer have not been directly measured, it may be possible to address existing theories within the scientific literature through an examination of the large-scale structures.

The two-point correlation of the streamwise velocity R_{uu} is shown in Fig. 7.13 for the outer region of the boundary layer, at heights y/δ = 0.3, 0.5, and 0.8. Minimal variation is observed between the ZPG and WPG motions, except for a broadening of the WPG correlation along the minor axis at y/δ = 0.8. The most visible change is seen in the SPG case, in which the spatial extent of the correlations is marginally reduced across the outer region of the boundary layer. This change in scale is more obvious when the one-dimensional autocorrelation $R_{uu}(y_{ref})$ is plotted in Fig. 7.14. For all three positions shown in Fig. 7.14, the SPG autocorrelation falls within the curves describing the ZPG and WPG cases, suggesting a shorter streamwise length. While the ZPG and WPG autocorrelations collapse onto each other for $R_{uu} > 0.2 – 0.3$, the WPG curve is broader at small correlation values. Following the logic employed by Latin & Bowersox (2000) in analyzing their temporal autocorrelations, it is possible to suggest that the large-scale structures are larger in the WPG flowfield, while the small-scale structures show good agreement with the ZPG case. Given the anomalous nature of the WPG case, as exemplified by the unexpected reduction in boundary layer thickness, the cause of this behavior is not immediately apparent. Returning to Fig. 7.13, the SPG correlations are

reoriented to a more wall-normal angle, which can be attributed to "differential acceleration" across the flow structure [Humble *et al.* (2012)], as the bottom of the fluid mass is accelerated more strongly than the top. This reorientation is qualitatively consistent with observations by Arnette *et al.* (1995) at Mach 3.

Correlations in the inner region (Fig. 7.15) exhibit trends at $y/\delta = 0.2$ that are similar to those observed in the outer region, including the reorientation of the SPG correlation. However, the most striking behavior occurs at $y/\delta = 0.1$ for the SPG flowfield, shown in Fig. 7.15c. The spatial extent of the correlation is approximately 50% of the corresponding ZPG correlation. Additionally, the correlation no longer exhibits the elliptical distribution observed at points higher in the boundary layer. Instead, the correlation is narrower at its base, with a large lobe extending in the downstream direction at a 45 degree angle. If the correlation R_{uu} is considered representative of the hairpin packet scale and orientation (see §6.4 for justification), then Fig. 7.15c suggests that the packet structure has been severely deformed by the strong favorable pressure gradient. While analyses given later in this section will present a physical model that explains the attenuation of the turbulent stress through an FPG, the results shown below in Fig. 7.15 appear to indicate that the SPG boundary layer structures experience a dramatic reduction in scale within the near-wall region.

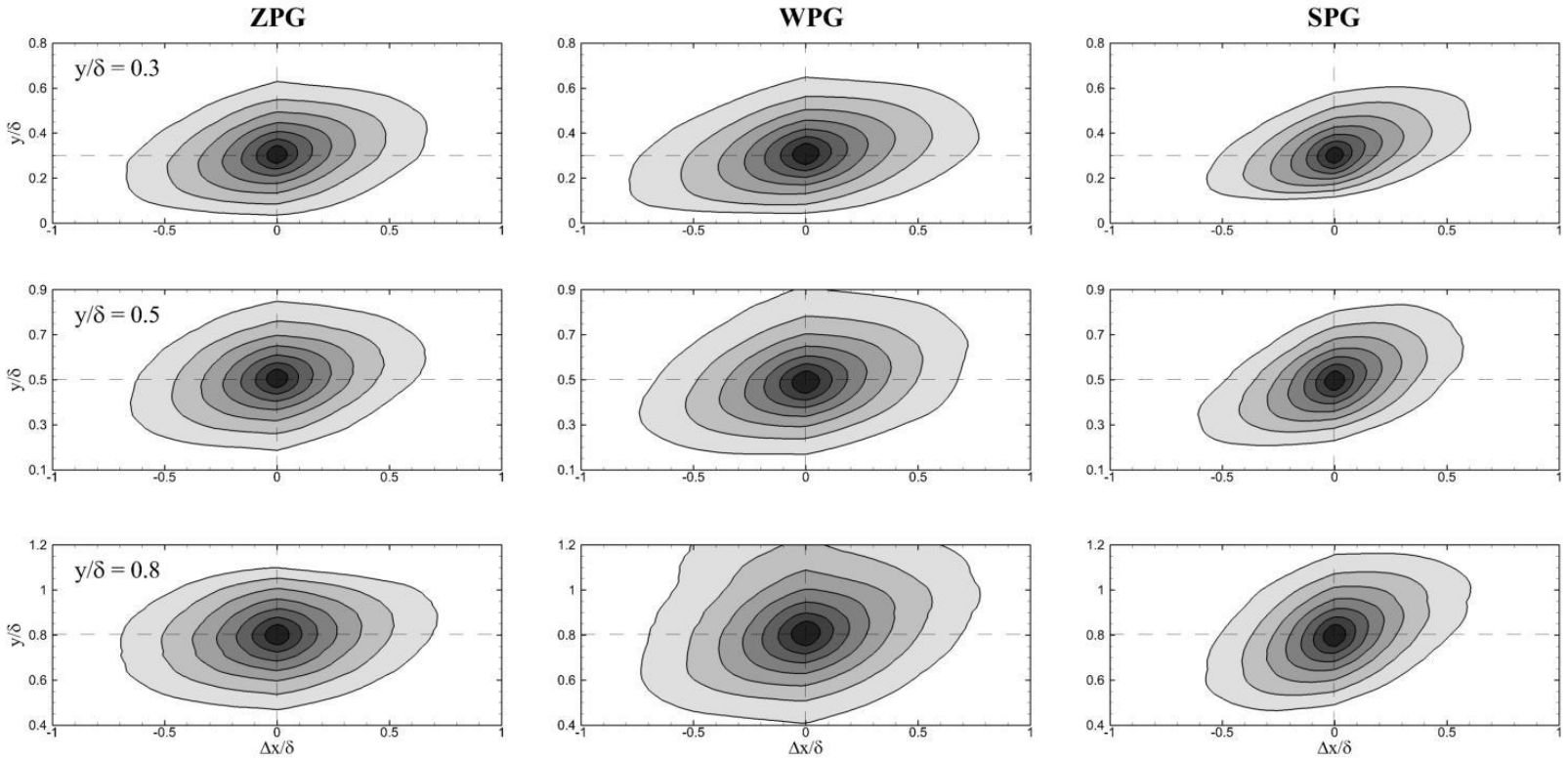

Figure 7.13 Two-point correlations R_{uu}, computed at wall-normal locations y/δ = 0.3 (top), 0.5 (middle), and 0.8 (bottom). *The outer isocontour is R_{uu} = 0.3, and proceeds in steps of 0.1.*

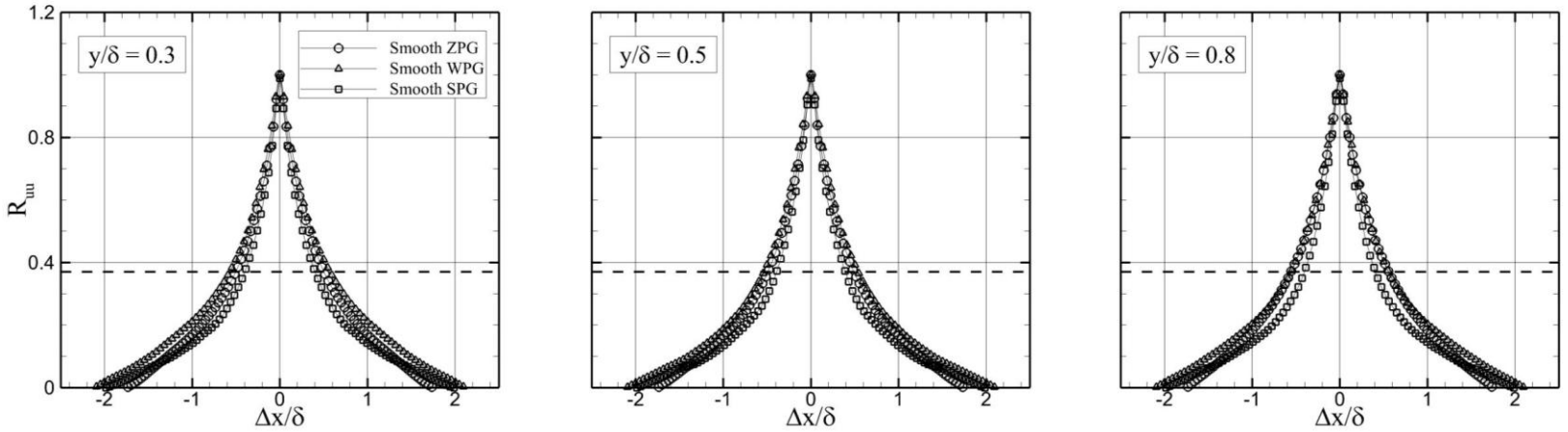

Figure 7.14 One-dimensional autocorrelations R_{uu}, shown at y/δ = 0.3 (left), 0.5 (center), and 0.8 (right). *The dashed line indicates R_{uu}= 1/*e*, which is used in calculating the streamwise length scale.*

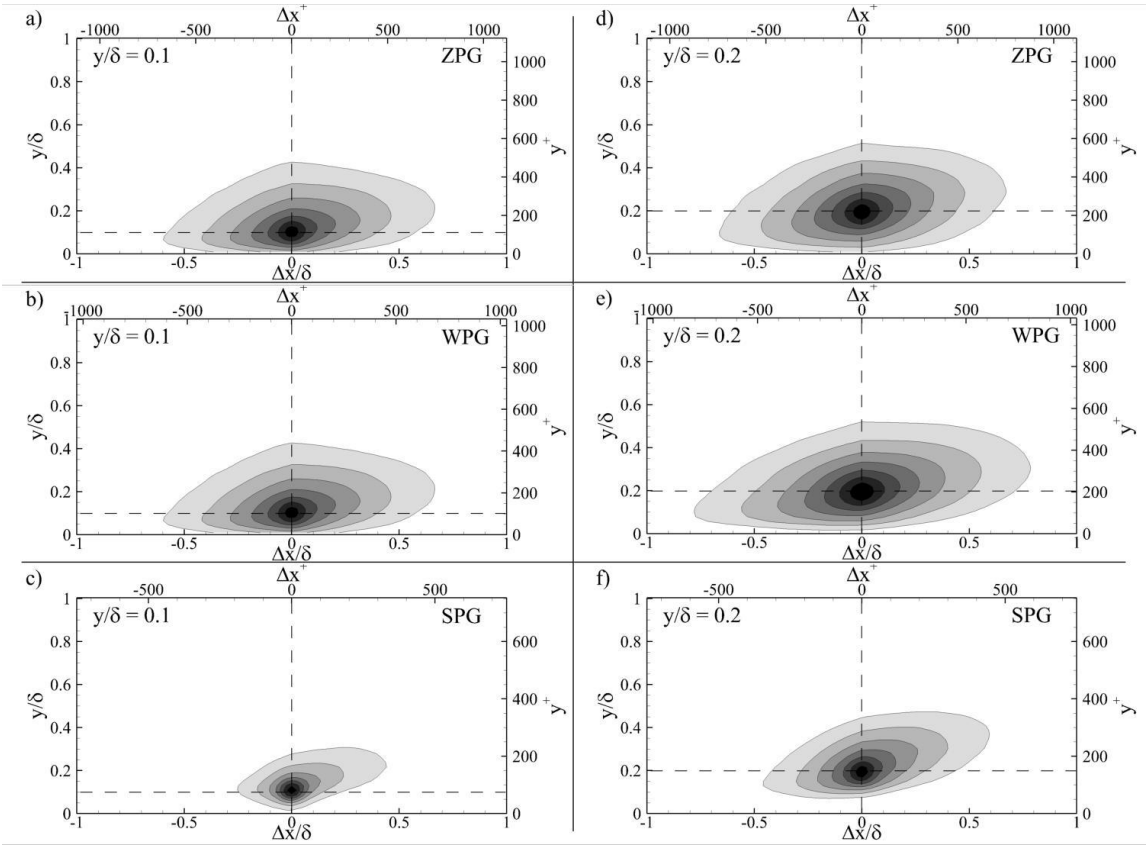

Figure 7.15 Two-point correlations R_{uu}, computed at wall-normal locations y/δ = 0.1 (left column) and 0.2 (right column). *The outer isocontour is R_{uu} = 0.3, and proceeds in steps of 0.1.*

The reduced spatial extent of the correlations is examined more fully by estimating the streamwise length λ_x^u from the autocorrelations in Fig. 7.14, using R_{uu}= 1/*e* as the threshold. Plotted in Fig. 7.16, the length scale λ_x^u confirms the trends seen in Fig. 7.14, suggesting that the SPG structures are more spatially compact in the streamwise direction. The sharp decrease below y/δ = 0.3 most likely suggests the onset of the structure deformation observed in Fig. 7.15c, culminating in a streamwise length scale of 0.35δ at y/δ = 0.1. The cause of this deformation is not readily apparent from these results. Above this height, the length scale is approximately constant at 0.8δ for the SPG case. The WPG length scales indicate a much different behavior, extending to 1.1δ for y/δ = 0.15 – 0.5, and collapsing onto the ZPG profile for y/δ = 0.6 – 0.9. While an

increased length scale was initially anticipated due to bulk dilatation, it is unknown why this behavior is confined to the lower half of the boundary layer for the WPG case, and why it isn't observed in the SPG case.

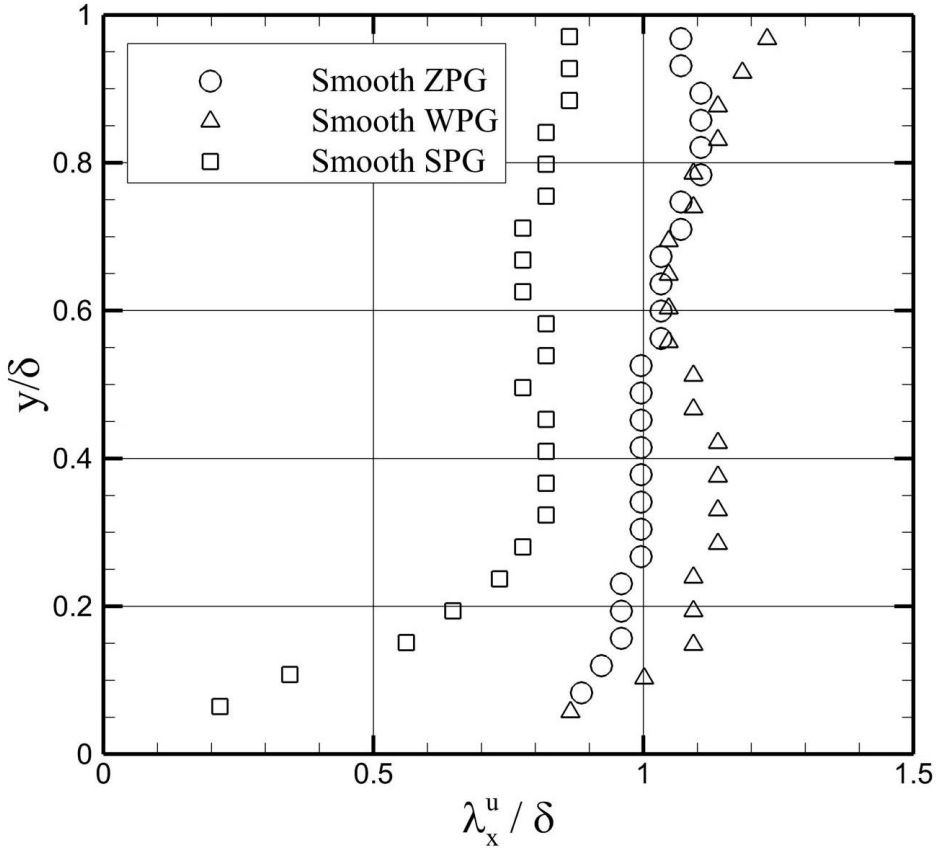

Figure 7.16 Streamwise length scales, estimated from the autocorrelations at $R_{uu} = 1/e$

Referring back to the two-point correlations shown in Fig. 7.13, note that the structure angles change at different rates for each case. As such, extracting a length scale that is computed solely from the streamwise extent may not accurately represent the true size of a structure. Instead, ellipses are fitted to the $R_{uu} = 0.4$ contour through a least-squares algorithm, allowing the major and minor axes and structure angle to be determined. This

contour level is chosen because it describes a well-formed ellipse for each height, whereas higher contour levels become too isotropic to uniquely describe the structure orientation. Furthermore, the R_{uu} = 0.4 contour is similar to the 1/*e* threshold used to compute λ_x^u from the one-dimensional correlations.

First, the structure angle θ is plotted in Fig. 7.17. Below y/δ = 0.4, the WPG angle collapses onto the ZPG data, suggesting that the large-scale motions respond quickly enough to follow the mild wall curvature. Above this height, the angle increases to approximately 15 degrees at y/δ = 0.7, possibly due to the *differential acceleration* described previously. In contrast, the SPG structure angle is increased for all wall-normal positions, ranging from 14 degrees in the inner region to 24 degrees near the boundary layer edge. While these angles are smaller than those observed by Arnette *et al.* (1995) and Humble *et al.* (2012), it should be noted that both studies used condensate Rayleigh scattering to visualize the flowfield.

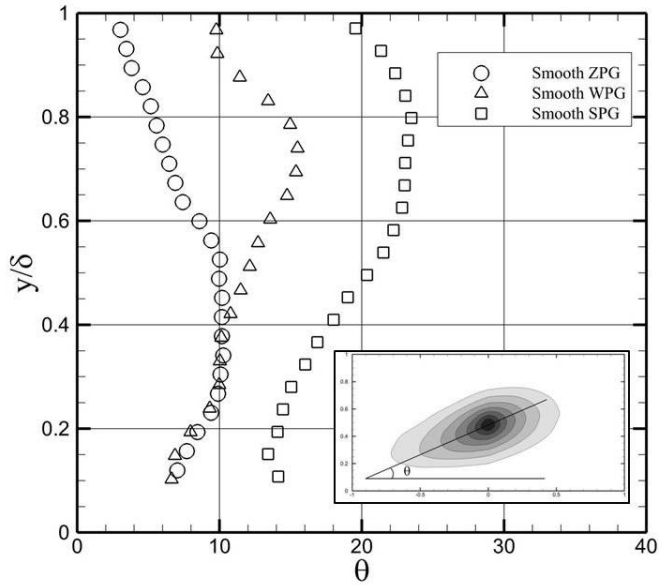

Figure 7.17 Structure angles of FPG boundary layers, computed from R_{uu} = 0.4 isocontour. *The inset figure describes the method for calculating θ. Every second point is shown for clarity. Angle is given in units of degrees.*

Given that the rotation of the reference frame has been shown to have a sizable impact upon the interpretation of the turbulent fluctuations (see Fig. 7.7), it is prudent to question whether a coordinate transformation into the wind tunnel axes will have a similar effect upon the structure orientation. The transformed structure angle $\theta_{w.t.}$ is plotted in Fig. 7.18. The subscript "w.t." signifies that the angle is shown for the wind tunnel axes. Below $y/\delta = 0.5$, the FPG angles fall below the ZPG curve, suggesting that the structures are rotating to follow the wall curvature. However, the interesting behavior occurs for the WPG and SPG cases above $y/\delta = 0.5$, showing that the curves collapse onto each other. While the agreement between these cases may be coincidental, the behavior in the outer half of the boundary layer does suggest that reorientation of the structures is dominant in this region.

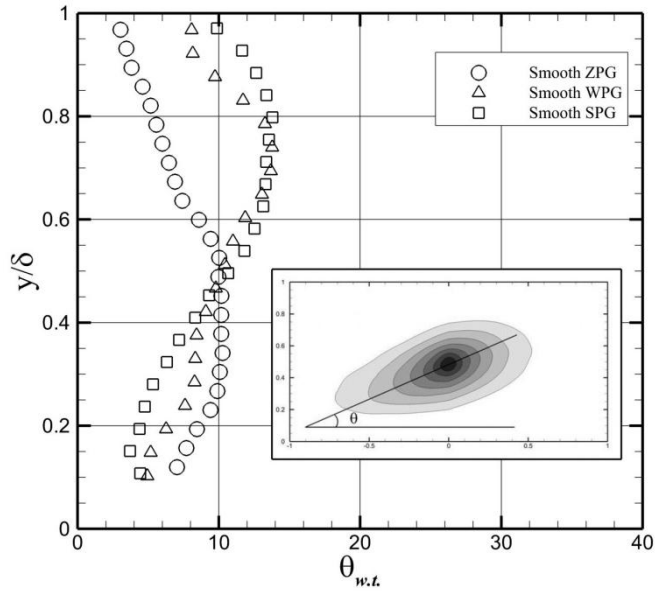

Figure 7.18 Structure angles of FPG boundary layers, transformed into wind tunnel axes. *The coorindate y is still measured normal to the wall. Every second point is shown for clarity. Angle is given in units of degrees.*

The increased structure angles observed in Fig. 7.17 reaffirm the need to account for the structure orientation when estimating the length scale. This is done by computing the major and minor axes of the R_{uu}= 0.4 isocontour, as shown in Fig. 7.19. Unlike the streamwise length scales shown in Fig. 7.16, the major axis of the WPG flowfield is larger everywhere in the boundary layer. However, the SPG case still exhibits the sharp decline at y/δ = 0.3, pertaining to the deformation of the R_{uu} correlation in Fig. 7.15c. The minor axes appear to follow a different trend, with the WPG structure becoming increasingly "stretched" in the transverse direction near the boundary layer edge.

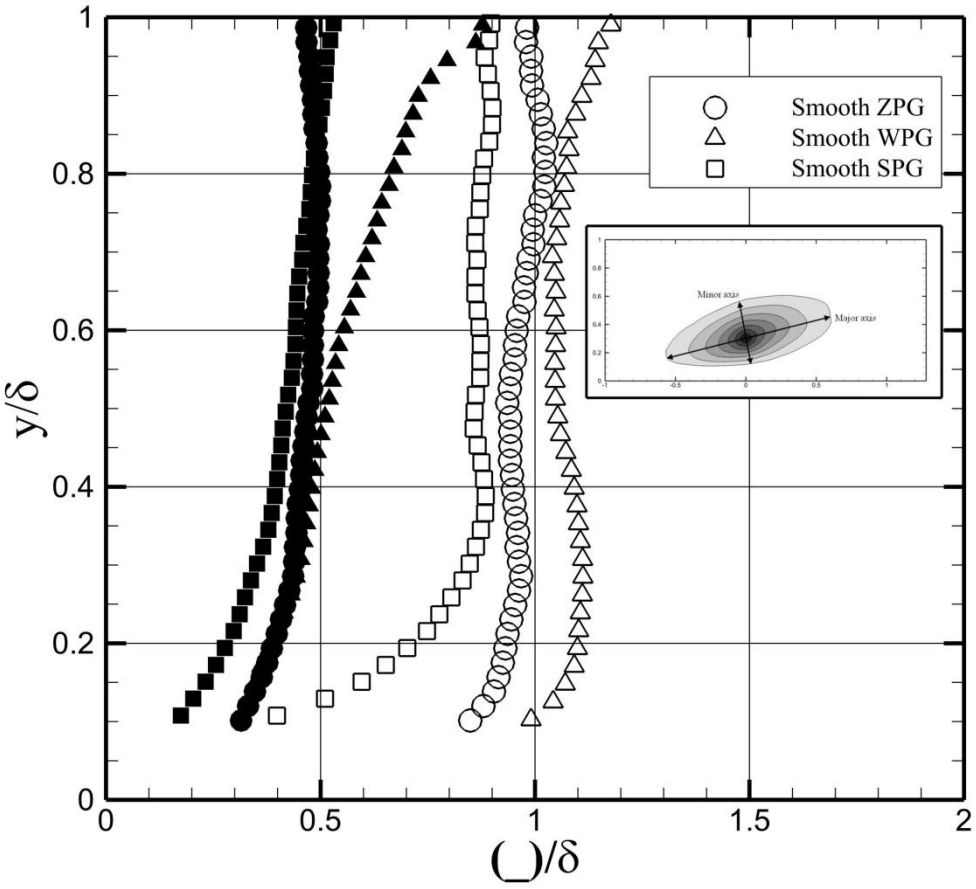

Figure 7.19 Major (hollow symbols) and minor (filled symbols) axes for the FPG boundary layers.
The orientation of the axes relative to the R_{uu} correlation is shown in the inset image.

Before any attempt is made to infer the distortion of the large-scale motions, and presumably the hairpin vortex packets, from the behavior observed in Fig. 7.19, it is instructive to revisit the scaling used when presenting the major and minor axes. Outer scaling is employed in Fig. 7.19, using the respective boundary layer thickness for each case. This scaling was selected to match previous flat-plate studies in the literature [English (2013); Ganapathisubramani *et al.* (2006); Hutchins & Marusic (2007a); Pirozzoli & Bernardini (2011)]. However, given the variations in δ between each FPG flowfield, along with the relative sizes of the major axes, it is possible that the observed trends are simply due to the change in the scaling parameter. In order to isolate the response of the large-scale motions from the boundary layer growth, the major and minor axes from Fig. 7.19 are rescaled by the ZPG boundary layer thickness, δ_{ZPG}. Figure 7.20 shows the rescaled major and minor axes, effectively yielding a comparison of the dimensional structure sizes. The major axes appear to collapse onto each other for $y/\delta > 0.3$, to within the estimated uncertainty ($\sim 0.1\delta$), while the shortened scale of the SPG structure remains for the near-wall region. The minor axes show excellent agreement over the distance $y/\delta = 0.3 – 0.65$, though the FPG structures are stretched in the transverse direction above this height. It is possible that the diverging streamlines in the outer edge of the SPG boundary layer have contributed to this deformation of the minor axes. However, the reduced thickness of the WPG boundary layer is not expected to produce any streamline divergence, though the structures still exhibit stretching in the transverse direction. Rescaling by δ_{ZPG} was also performed for the streamwise length scales, which were shown previously in Fig. 7.16. Figure 7.21 shows the rescaled length scales, which appear to follow the behavior of the rescaled major and minor axes in Fig. 7.20.

The trends observed in Figs. 7.20 – 7.21 for the rescaled structure dimensions appear to suggest that the large-scale motions do not increase in dimensional size through the favorable pressure gradient, and that any change in scale is most likely due to the evolution of the boundary layer thickness (excepting the near-wall region of $y/\delta < 0.3$). This observation holds great significance for modeling the Reynolds stress response, as

past studies have suggested that bulk dilatation would increase the dimensional extent of the large-scale structures, and that the conservation of angular momentum would necessarily lead to a reduction in the fluctuating quantities [Bradshaw (1974); Arnette *et al.* (1998)]. The current results suggest that an additional, and as yet unknown, mechanism may be responsible for the attenuation of the Reynolds stress through a favorable pressure gradient.

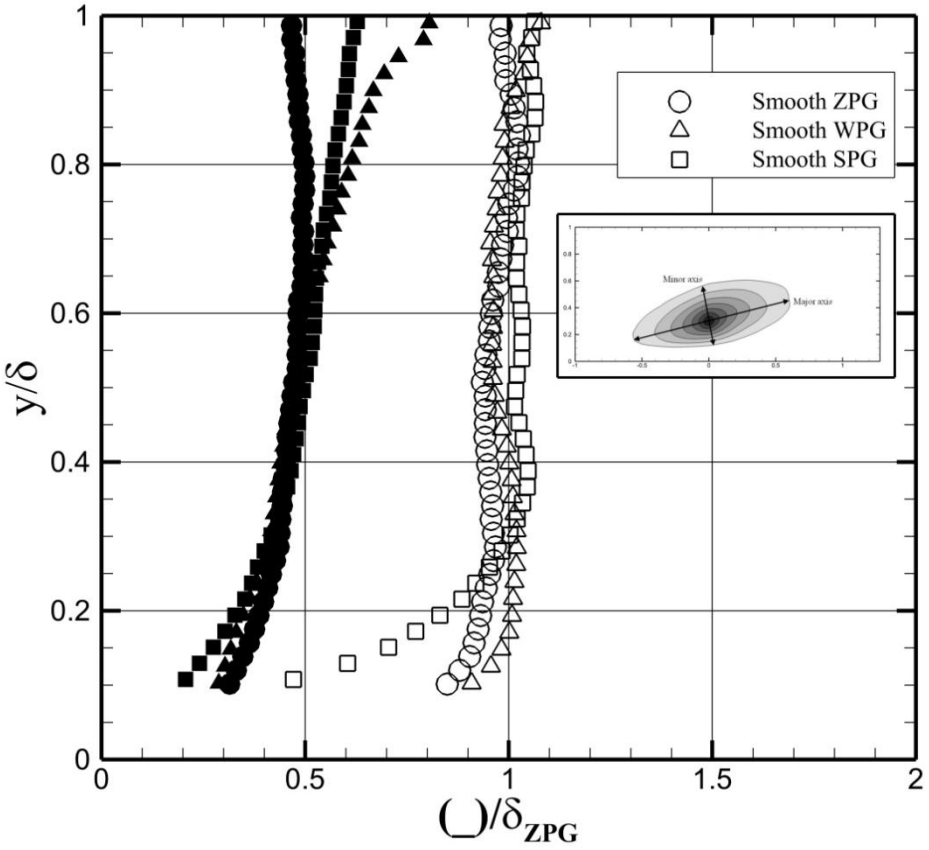

Figure 7.20 Major (hollow symbols) and minor (filled symbols) axes for the FPG boundary layers, scaled by the ZPG boundary layer thickness.

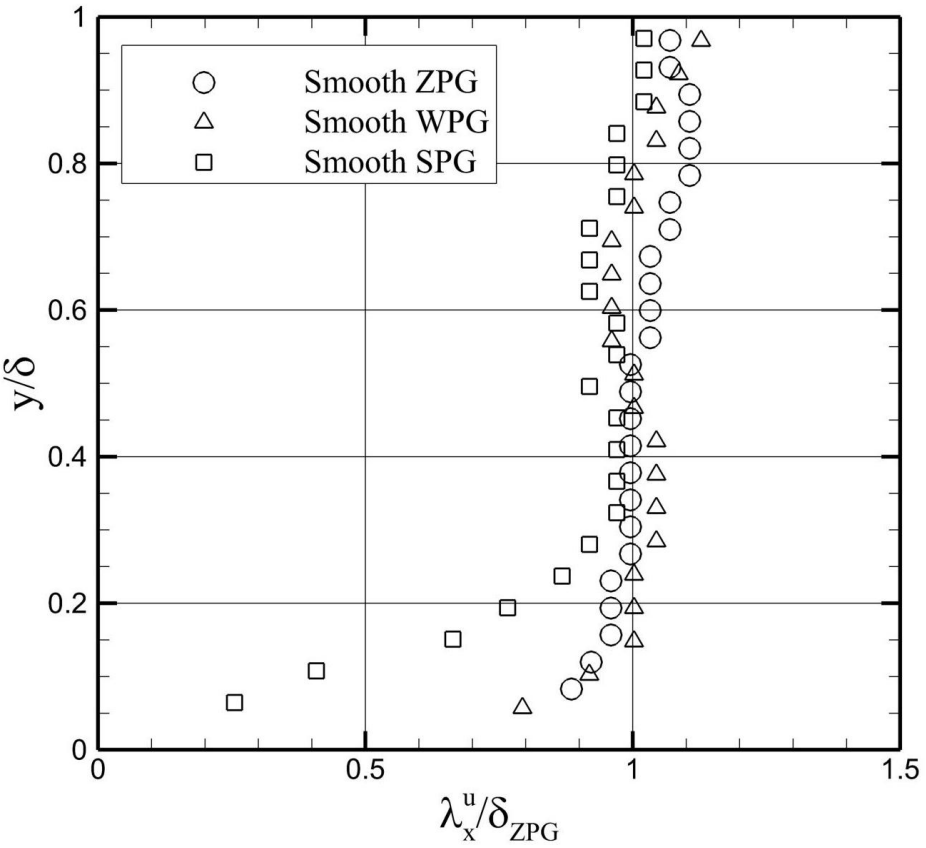

Figure 7.21 Streamwise length scales, estimated from the autocorrelations at $R_{uu} = 1/e$, and scaled by the ZPG boundary layer thickness.

7.4. Instantaneous and Statistical Structure of Near-Wall Boundary Layer

The correlations of the fluctuating velocity, and their respective length scales, suggest that the large-scale motions of the SPG boundary layer (which in §6 were suggested to be representative of the hairpin packet behavior) deviate from the ZPG trends in the region $y/\delta < 0.3$. Considering that the turbulent structures (and hence turbulent production) originate primarily in the buffer layer and logarithmic region [Robinson (1991)], it is plausible to assume that any change in the Reynolds stress distribution within the boundary layer may be traced back to the distortion/deformation of the structures in the near-wall region. [For a more complete review of the turbulent

structures and their origins, see Robinson (1991) and Adrian (2007)]. This speculation is supported by the observation that the Reynolds stress is attenuated across the entire boundary layer for the SPG case, while the length scales are only perturbed within the near-wall region. Following this framework, the subsequent analyses will focus upon the deformation of the near-wall structures in the SPG boundary layer.

An instantaneous velocity field is shown in Fig. 7.22 for the SPG boundary layer, showing the streamwise alignment of vortices in the near-wall region. The arrangement of the vortices is similar to the hairpin packet observed in the ZPG boundary layer (Fig. 6.13), including the observed vortex spacing of $0.2 - 0.4\delta$, though the low-momentum region beneath the vortices is much less coherent. Indeed, the back-induced fluid associated with ejection (Q2) events is only visible beneath vortices A and B. While the zone of influence around each vortex (identified by examining the perturbation of the wall-normal velocity component) is comparable in size to that observed for the ZPG boundary layer ($\sim 02 - 0.3\delta$), the strength of the ejections beneath the vortices is much weaker. This structure appears to suggest that the fluid within these packets, corresponding to the large-scale motions, is less correlated in the streamwise direction. The two-point correlations R_{uu} in the near-wall region (Fig. 7.15) and the instantaneous visualizations by English (2013) in the *x*-*z* plane both support this observation.

Higher in the boundary layer, a similar vortex organization is present, most likely corresponding to the "mature" vortex packets (Fig. 7.23). The 20-degree orientation of the structure is consistent with the structure angles shown in Fig. 7.17. Additionally, only the vortices lower in the boundary layer (Fig. 7.23a) show any degree of back-induced flow, corresponding to the region of the flow in which $u'v' < 0$ (Fig. 7.6). The local flowfield surrounding the two vortices at $y/\delta \approx 0.4$ in Fig. 7.23b appears nearly isotropic.

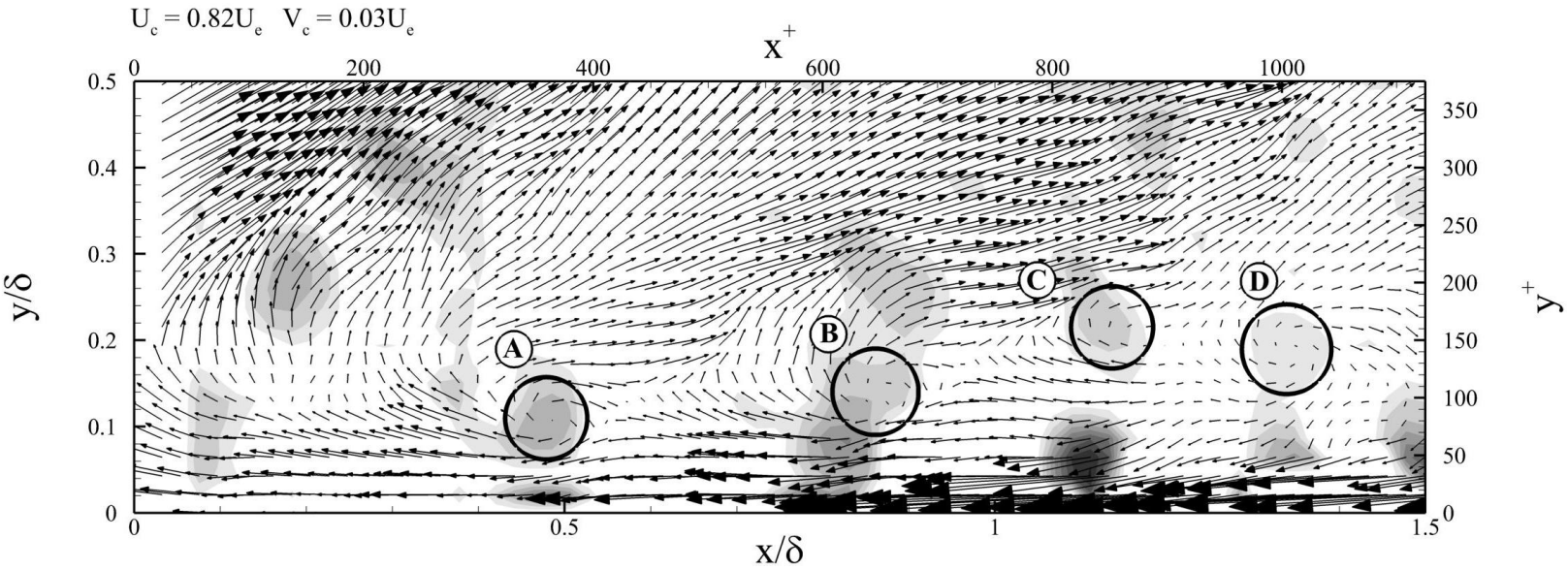

Figure 7.22 Instantaneous velocity field for the SPG boundary layer. *Convective velocities $U_c = 0.82U_e$ and $V_c = 0.03U_e$ have been subtracted, to show the locally spiraling fluid. The streamwise alignment of the vortices is similar to that observed for the ZPG flowfield, though the motion seen above is much less correlated in the streamwise direction.*

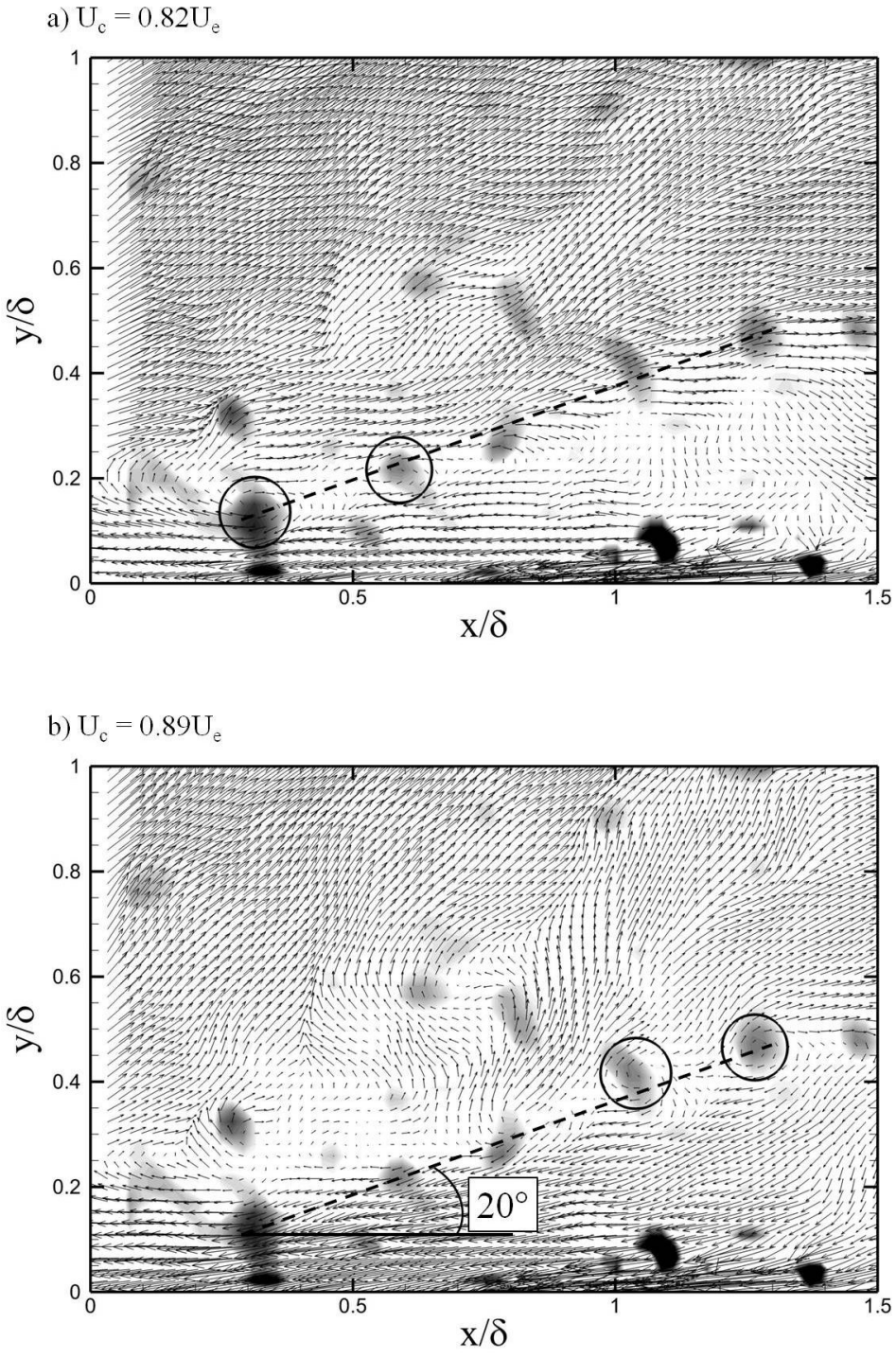

Figure 7.23 Instantaneous velocity field for the SPG boundary layer, showing the increased orientation angle of the structures. *Convective velocities of $0.82U_e$ and $0.89U_e$ have been subtracted from the top and bottom fields, respectively.*

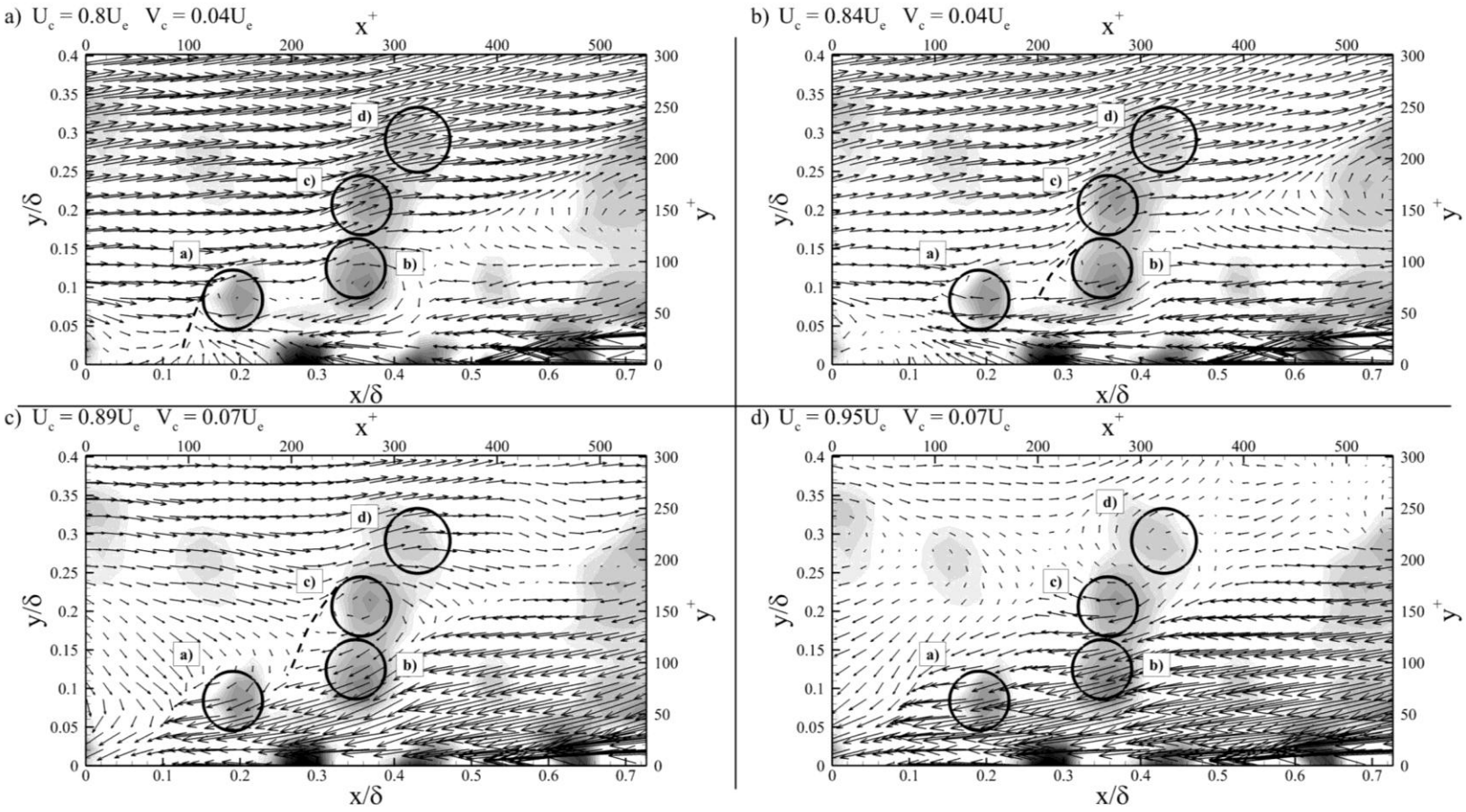

Figure 7.24 Instantaneous velocity field of the SPG boundary layer, showing a vertical "stack" of vortices. *The vortex labels a – d correspond to the listed convective velocities. Local shear layers are shown by dashed lines.*

The structures in Figs. 7.22 – 7.23 are qualitatively similar to those observed for the ZPG baseline case, excepting an increased orientation angle and weaker ejection events. However, the SPG flowfield also contains an additional arrangement of vortices that, while less common, may be sufficiently numerous to be considered a relevant flow structure. This configuration is seen in Fig. 7.24, depicting a near-vertical "stack" of vortices. While the severe angle of this structure may be ascribed to the differential acceleration described earlier, the orientation angle is much larger than shown in Fig. 7.17. An additional explanation may stem from the large wall-normal convective velocity V_c within the SPG boundary layer (discussed further in §7.5), which could "lift" the vortices away from the wall. While it is possible that this arrangement could lead to the shortened streamwise length scale observed previously in §7.3 for the near-wall SPG boundary layer, the statistical relevance of this vortex configuration is still unknown, and will be probed further through conditional averaging in §7.6.

Considering the instantaneous flow visualizations in Figs. 7.22 – 7.24, the authors propose several possible explanations for the reduced streamwise correlation. First, the acceleration in the SPG boundary layer may "delaminate" the hairpin vortex packets, increasing the vortex streamwise separation until the vortices are essentially discrete structures. Since it is known that the close spacing of hairpin vortices serves to amplify the magnitude of the ejection events through mutual induction [Adrian *et al.* (2000)], it is possible that the increased separation distance would result in a weaker region of back-induced flow beneath the vortices, and hence a weaker correlation. However, comparisons between Fig. 7.22 and the ZPG boundary layer suggest that the streamwise separation distance between the vortices has not changed appreciably. The second explanation for the reduced correlation, which is supported by the authors, is that the vortices have been "weakened" through a currently unknown mechanism (this is discussed more thoroughly in §7.7). The weaker ejections beneath these hairpin vortices persist over a shorter streamwise distance, causing the correlation to shift to shorter length scales. [This theory presupposes that the low-momentum streaks are caused by the back-induced flow from the hairpin vortices. More discussion of this causal relation

is given in §2.1.] The weaker ejections are consistent with the vortex behavior observed in Figs. 7.22 – 7.23, as well as the quadrant decomposition analysis in §7.2. An additional explanation for the reduced streamwise length scale stems from the vertical vortex arrangement seen in Fig. 7.24, though it is unknown whether this structure is sufficiently populous to effect the mean correlation. The statistical behavior of these structures, and their relevance to the theories proposed above, is examined more closely in §7.6 through conditional averaging.

Given the distortion of the large-scale motions visible in the two-point correlations and instantaneous visualizations, it is expected that the distribution of energy content among the flow scales will experience a similar response. This is investigated through the streamwise spectra of the fluctuating velocity components, premultiplied by the wavenumber k_1. Prior to discussing the spectral response of the FPGs, it is necessary to determine the correct scaling parameter of the associated length scales. Since the PSD is merely the Fourier transform of the two-point correlation, it follows that the length scales in the outer region should scale by δ. However, the scaling for the near-wall spectra is less certain, and will be discussed below.

The streamwise spectra of the fluctuating u-velocity component Φ_{uu}, premultiplied by the wavenumber k_1 and scaled by the axial stress $u'u'$, is shown in Figs. 7.25 and 7.26 for the FPG boundary layers at $y/\delta \leq 0.1$. The SPG spectrum is not plotted at $y/\delta = 0.03$, due to the slightly lower resolution for that data set. The wavelengths in Fig. 7.25 are scaled by δ, while inner scaling is applied to Fig. 7.26. Recall from §6.5 that the individual hairpin vortices were believed to produce small-scale ($\sim 0.2\delta$) peaks in the near-wall premultiplied spectra of Φ_{uu}, and that these peaks rapidly decreased in magnitude as the wall-normal distance was increased. These same features are observed in Figs. 7.25 and 7.26, and are identified by the small arrows in each figure. Note that for $y/\delta = 0.08$ and 0.1, these "vortex-related peaks" are nearly imperceptible, and would likely go unnoticed if viewed in isolation (i.e. without the spectra at $y/\delta = 0.03$ and 0.05).

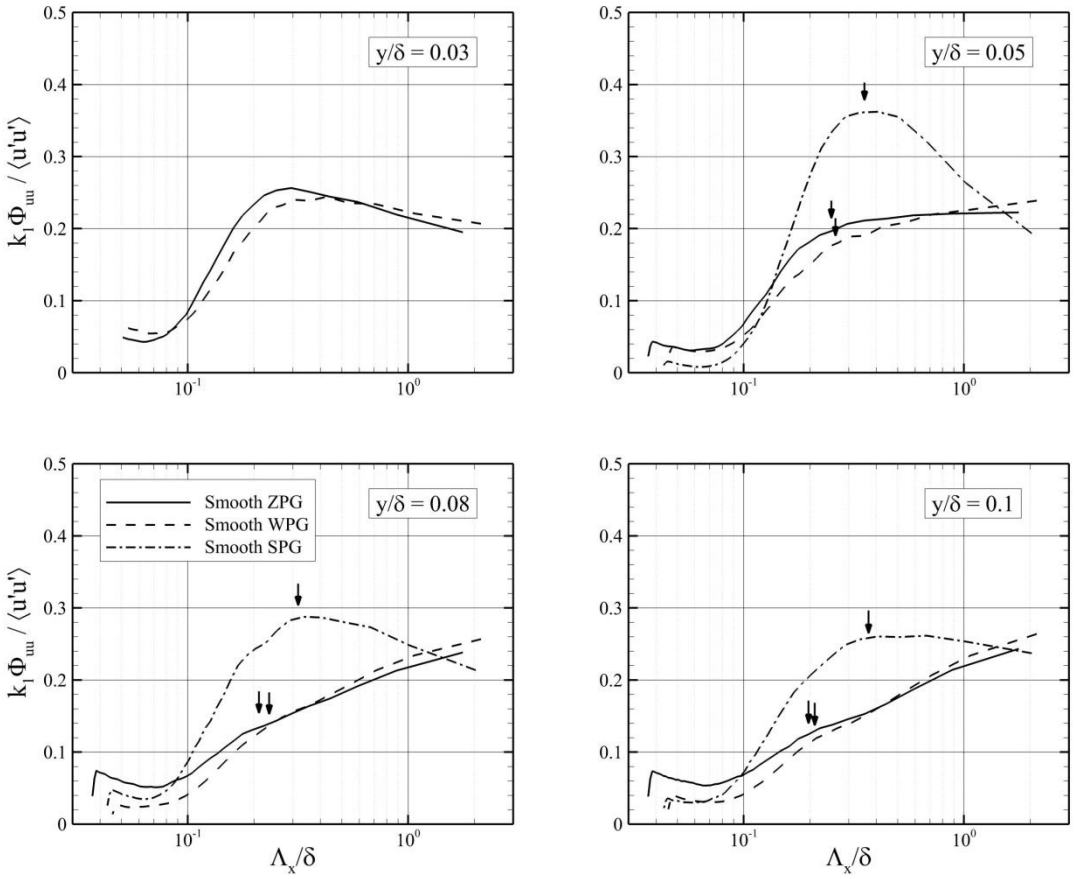

Figure 7.25 Premultiplied spectra of the fluctuating *u*-velocity component, for $y/\delta \leq 0.1$. *Outer scaling is applied to the wavelengths. Arrows indicate the local maxima, pertaining to the signature of the hairpin vortices.*

When scaled by δ, the spectra in Fig. 7.25 show excellent agreement between the ZPG and WPG scales, with the local maxima in the spectra occurring at $0.2 - 0.25\delta$. The length scale associated with the SPG boundary layer is slightly larger, at $0.3 - 0.35\delta$. In contrast, the inner-scaled length scales in Fig. 7.26 show good agreement between all three flowfields, with the near-wall peaks at approximately 250 viscous units. While the inner-scaling in Fig. 7.26 shows better agreement between the ZPG, WPG, and SPG boundary layers, it is logical to ask: "*Should* the near-wall length scales of the local maxima show good agreement between the ZPG and FPG boundary layers?" Recalling

the lessons learned in §6, the implication of this agreement is that the induced flowfields beneath the hairpin vortices persist over a similar streamwise distance. Unfortunately, there is no data available in the literature at these conditions to guide this scaling choice. However, given that the current vortex models in the scientific literature suggest that the hairpin vortices originate within the buffer layer [see Adrian (2007) for a concise overview of existing data], it is possible to speculate that inner-scaling may be applied to the near-wall spectra Φ_{uu}.

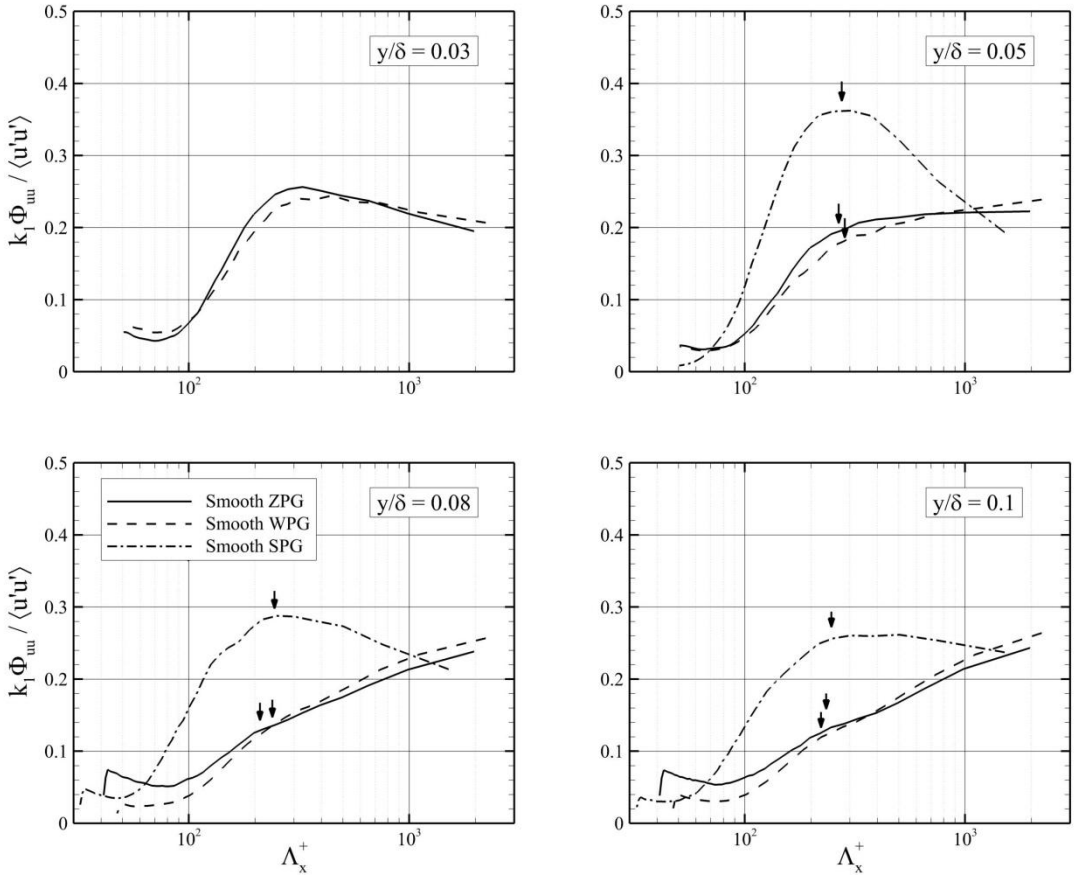

Figure 7.26 Premultiplied spectra of the fluctuating *u*-velocity component, for $y/\delta \leq 0.1$. *Inner scaling is applied to the wavelengths. Arrows indicate the local maxima, pertaining to the signature of the hairpin vortices.*

Considering the near-wall viscous-scaled spectra Φ_{uu} in Fig. 7.26, it is readily apparent that the SPG axial stress *u'u'* is confined to a relatively narrow range of scales for $y/\delta \leq 0.1$, centered at $\Lambda_x^+ \approx 250$ viscous units. While the ZPG and WPG flows experience similar behavior at $y/\delta = 0.03$ and 0.05, these spectra become increasingly broadband above this height. Assuming that this near-wall peak in the Φ_{uu} spectra is a signature of the individual vortices, and that the δ-scale motion is due to the low-momentum streak beneath the hairpin packet (see §6), Fig. 7.26 appears to suggest that the low-momentum back-induced fluid associated with the streamwise-aligned hairpin vortices is not present in the SPG boundary layer below $y/\delta = 0.1$. Instead, the individual vortices are more "discrete", indicating that the hairpin loops may not be streamwise-aligned into coherent vortex packets. This observation is consistent with the SPG instantaneous velocity field in Fig. 7.22.

The above analysis is repeated for the near-wall premultiplied spectra of the wall-normal velocity component, Φ_{vv}. Figures 7.27 and 7.28 show the spectra for all three FPG cases at $y/\delta \leq 0.1$, with outer and inner scaling applied to the wavelength Λ_x, respectively. Recall from §6.5 that the peak in the Φ_{vv} spectra was assumed to be an approximation of the "zone of influence" of a spanwise-oriented vortex. In contrast to the streamwise component, the Φ_{vv} spectra for each boundary layer in Fig. 7.27 collapse when scaled by δ. However, it was suggested above that the near-wall Φ_{uu} should be scaled by viscous coordinates. If this scaling is also applicable to the wall-normal component Φ_{vv}, then Fig. 7.28 would suggest that the region of fluid perturbed by a vortex is smaller in the SPG boundary layer (in viscous units). Considering that the vortices perturb the surrounding fluid primarily through the sweep (Q4) and ejection (Q2) events, the behavior in Fig. 7.28 supports the quadrant decomposition results in Figs. 7.8 and 7.9, which suggested that the shear-stress producing motions are attenuated within the SPG flowfield.

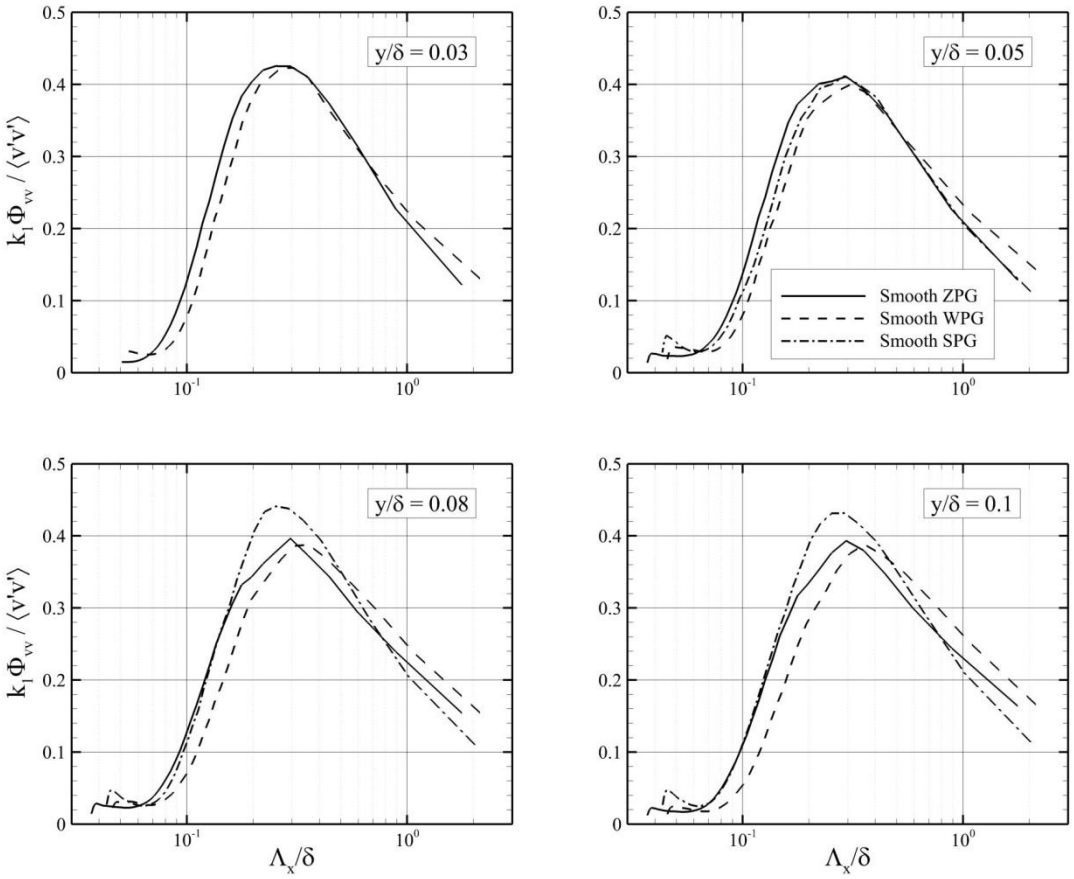

Figure 7.27 Premultiplied spectra of the fluctuating *v*-velocity component, for $y/\delta \leq 0.1$. *Outer scaling is applied to the wavelengths.*

Before proceeding with the analysis of the vortex motions and population distribution in §7.5, a brief mention of the spectral behavior in the outer region ($y/\delta \geq 0.3$) is warranted. The outer-scaled spectra Φ_{uu} in Fig. 7.29 show good agreement in the outer region, consistent with the two-point correlation results from §7.3. A similar trend is observed for the outer-scaled spectra Φ_{vv} in Fig. 7.30, in which the agreement between the ZPG and FPG boundary layers increases with y/δ. While the total energy content (i.e. Reynolds stress) is reduced for the FPG flowfields, Figs. 7.29 and 7.30 indicate that the distribution of the spectral energy is relatively unchanged near the boundary layer edge. Based upon this observation, it is possible to speculate that the associated physical

mechanisms governing the boundary layer behavior are also unchanged in this region of the flowfield. If true, this would support the theory that the reduction in Reynolds stress through the FPG boundary layer originates within the near-wall region.

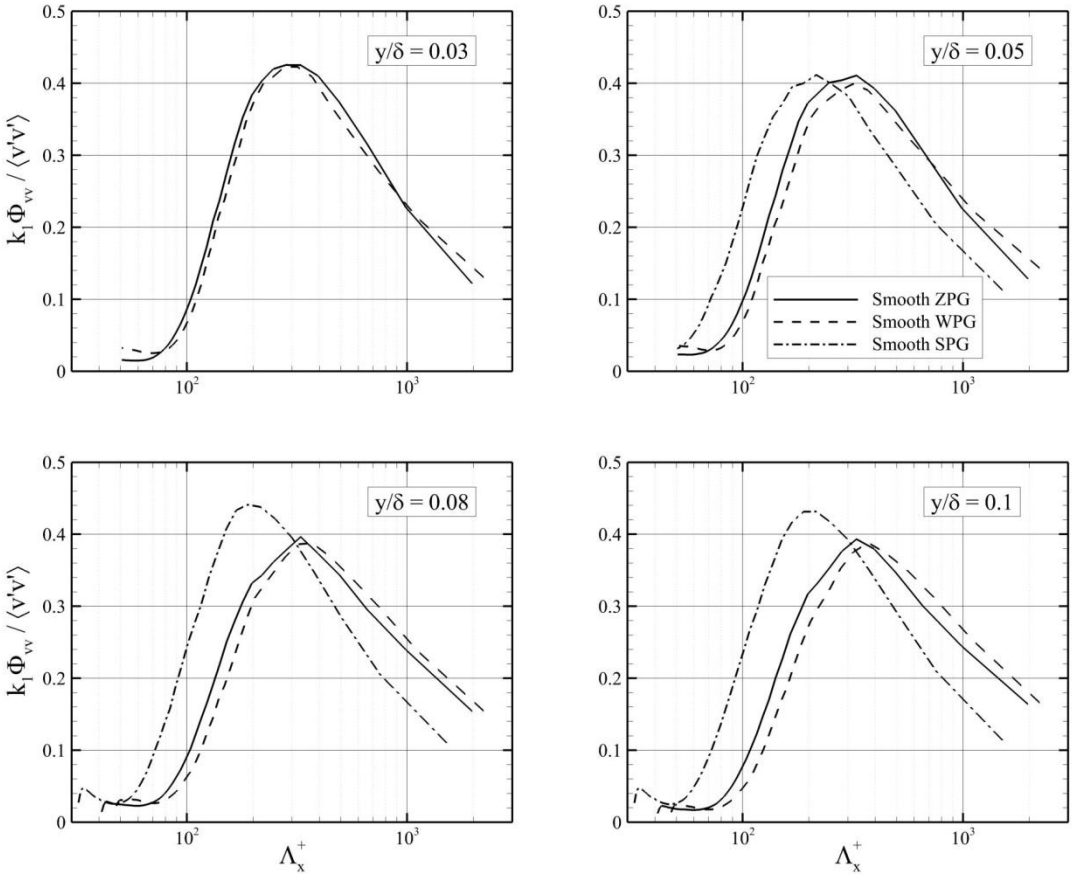

Figure 7.28 Premultiplied spectra of the fluctuating *v*-velocity component, for $y/\delta \leq 0.1$. *Inner scaling is applied to the wavelengths.*

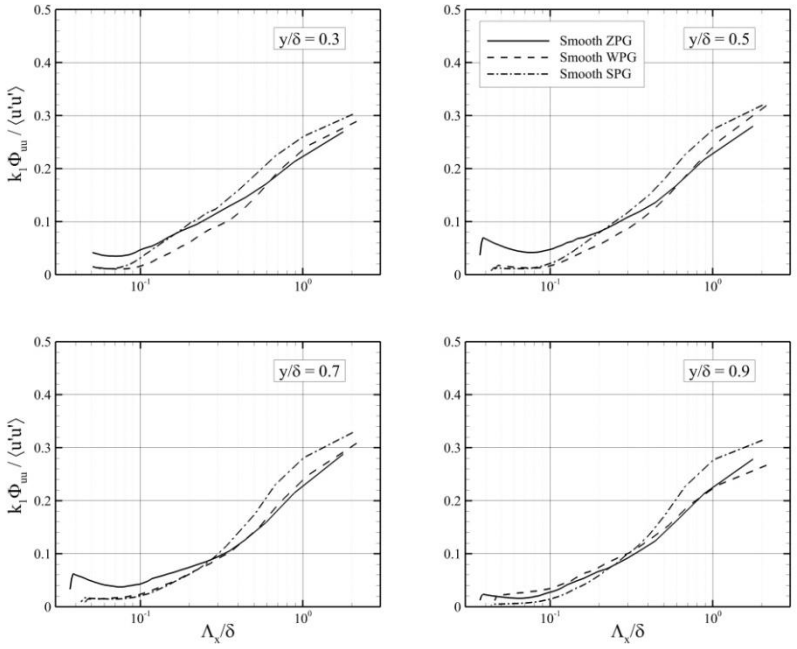

Figure 7.29 Premultiplied spectra of the fluctuating *u*-velocity component, for $y/\delta \geq 0.3$. *Outer scaling is applied to the wavelengths.*

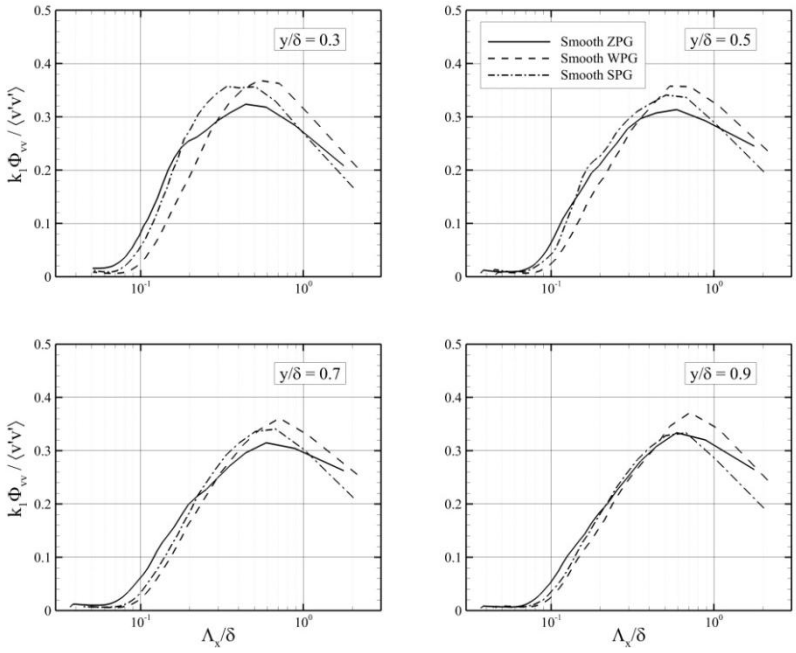

Figure 7.30 Premultiplied spectra of the fluctuating *v*-velocity component, for $y/\delta \geq 0.3$. *Outer scaling is applied to the wavelengths.*

Finally, the applicability of spectral analysis to the SPG flowfield must be briefly addressed. Given the evolving nature of the SPG boundary layer (Figs. 7.10 – 7.12), the reader would be justified in questioning whether the spectra described above are representative of the entire FOV, and if the length scales estimated from the premultiplied spectra are a function of the streamwise position. If we were to accept the theory proposed by Luker *et al.* (2000), that the reduction in Reynolds stress is due to the "breakdown of the turbulent structures", then the evolution of the turbulent stresses in Figs. 7.10 – 7.12 would be accompanied by an attendant decrease in the wavelength of the large-scale motions at the downstream edge of the FOV. However, a comparison of the premultiplied spectra Φ_{uu} computed over the upstream and downstream halves of the FOV indicate minimal change in the length scales throughout the boundary layer (Fig. 7.31).

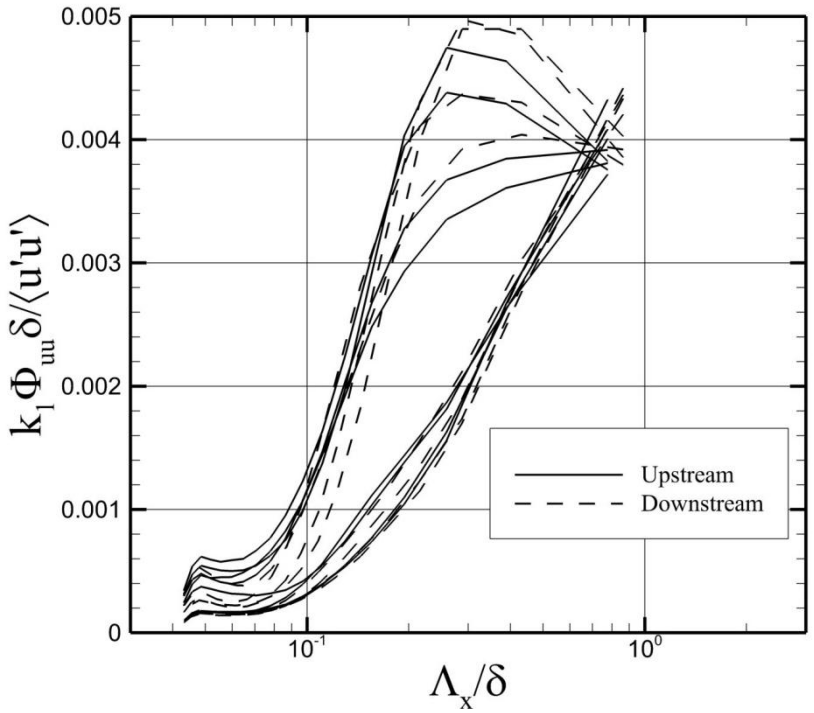

Figure 7.31 Premultiplied spectra of the fluctuating *u*-velocity component, computed over the upstream and downstream halves of the SPG boundary layer. *Outer scaling is applied to the wavelengths.*

7.5. Vortex Motions and Population Distribution

The quadrant decomposition analysis in §7.2 demonstrated that the magnitudes of the ejection (Q2) and sweep (Q4) events were dramatically reduced within the SPG boundary layer. This was supported by the instantaneous velocity field in Fig. 7.22, which suggested that the diminished intensity of the vortex-induced local velocity field contributed to the shortened length scale in the near-wall region. It has been suggested previously that the attenuation of these shear-stress contributions is due to a "weakening" of the hairpin vortices. Prior to investigating the statistical response of the motions surrounding the near-wall eddies through conditional averaging (§7.6), the effect of this "weakening" upon the vortex size, velocity, and distribution is examined.

The convective velocity of the vortices is calculated through conditional averaging of the streamwise and wall-normal velocity components, including only points that fall within a vortex (no distinction is made between prograde and retrograde vortices). The resulting velocity components U_c and V_c are normalized by the local mean velocity, and plotted in Figs. 7.32 – 7.33. The streamwise component U_c shows very similar behavior for the ZPG and WPG boundary layers at all points in the flow, with the vortices convecting at approximately 99% of the mean velocity U. It was stated in §6 that this is most likely due to the back-induced flow caused by the hairpin loops, which retards the forward motion of the vortices [Adrian *et al.* (2000)]. Following this same logic, it is expected that weaker ejection events would cause the vortices to convect at a velocity approximately equal to the mean flow. Indeed, this behavior is observed for the SPG boundary layer at $y/\delta \leq 0.3$ in Fig. 7.32. Above $y/\delta = 0.4$, the convective velocity for the SPG case shows good agreement with the ZPG and WPG flows. It should be noted that this behavior is similar to the streamwise length scales given in Fig. 7.21, which showed that the reduced scales of the SPG boundary layer occurred only for $y/\delta \leq 0.3$, and collapsed onto the ZPG and WPG trends for all points higher in the boundary layer.

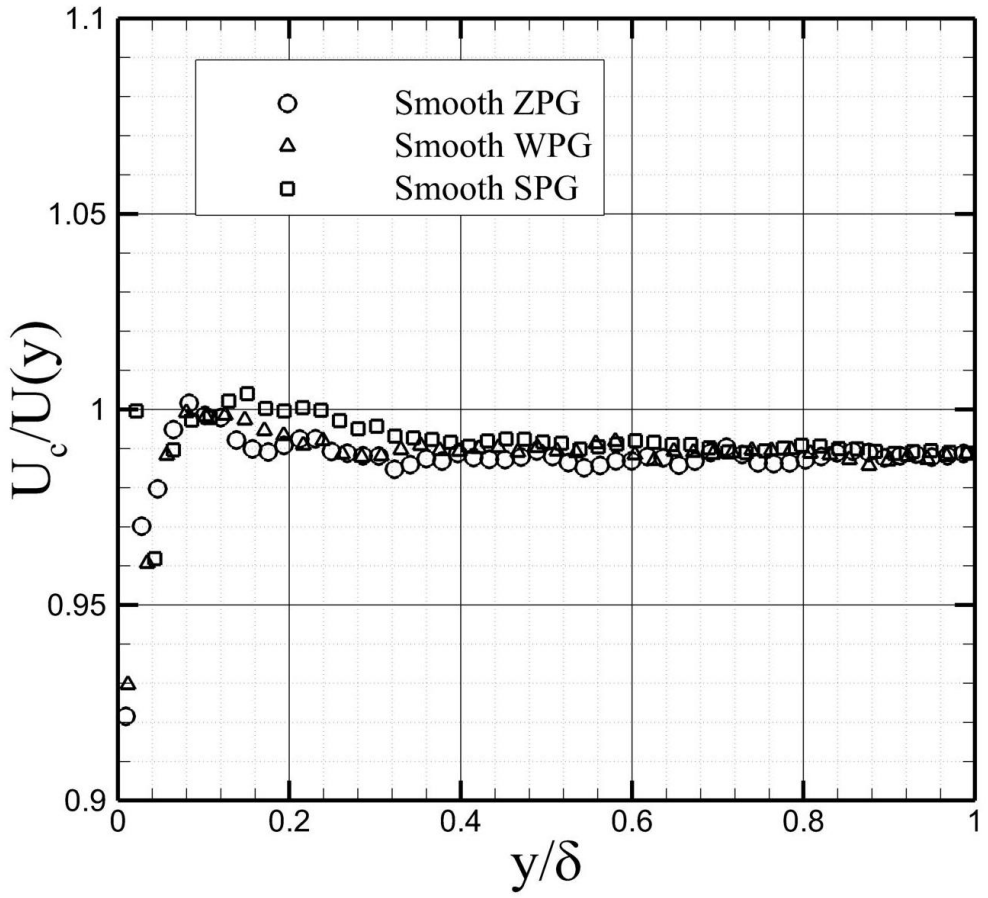

Figure 7.32 Streamwise convective velocity U_c, scaled by the local mean velocity

The wall-normal convective velocity V_c, scaled by the local mean velocity V, is given in Fig. 7.33. It was speculated in §6.6 that the approximately 45-degree angle of the hairpin legs [Adrian *et al.* (2000); Zhou *et al.* (1999); Robinson (1991)] would cause the ejection events to induce a wall-normal convective velocity that is greater than the local mean flow. This is observed in Fig. 7.33 for the ZPG and WPG boundary layers, though the effect in the WPG flow is less pronounced. The convective velocity ratio $Vc/V(y)$ increases approximately linearly with y/δ for the ZPG boundary layer above $y/\delta = 0.2$, with the wall-normal convective velocity at the boundary layer edge approaching 160% of the mean flow value. The WPG flow experiences an opposite trend, attaining a peak

value of 130% at y/δ = 0.3 before monotonically decreasing to 110% of the mean flow velocity for the outer half of the boundary layer. However, the vortices in the SPG case appear to be transported from the near-wall region at the same rate as the bulk flow. While this may also be a result of the weaker ejection events, the effect is experienced across the entire boundary layer thickness, whereas the streamwise convective velocity U_c was only affected in the near-wall region. At this time, the mechanism influencing the wall-normal convective velocity V_c remains unknown.

The wall-normal transport of the turbulent structures in the SPG boundary layer occurs at a rate similar to the mean velocity V_c. Therefore, it is reasonable to conjecture that the vortices in the SPG flow spend less time in the inner layer, inhibiting their ability to induce the low-speed fluid typically observed within hairpin packets. It is this fluid that contributes primarily to the Reynolds shear stress. While no temporally-resolved data is available for this flowfield, it is possible that the reduced residence time of the vortices may have an impact upon the mean Reynolds shear stress. Furthermore, the wall-normal convection of the coherent structures may provide insight into the vortex population distribution. While the exact mechanisms leading to the creation of a hairpin vortex are still under investigation, numerical studies by Zhou *et al.* (1999) have shown that the hairpin vortices are capable of autogeneration, as older structures trigger the creation of younger structures. The reduced residence time of a vortex packet within the near-wall region may diminish the likelihood of inducing the formation of these younger vortices. Fewer structures produced at the wall would reduce the population available to be convected outward, thereby reducing the population uniformly across the boundary layer.

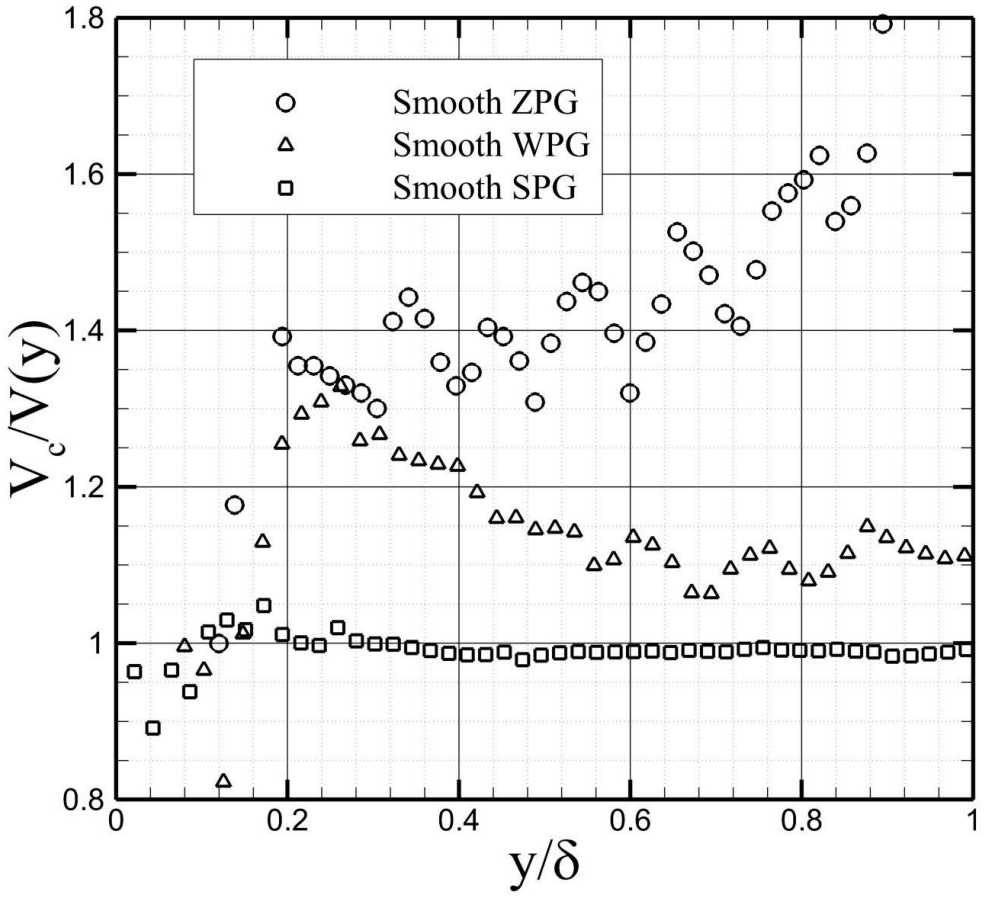

Figure 7.33 Wall-normal convective velocity V_c, scaled by the local mean velocity

The analyses performed within this section appear to support the currently proposed theory that the decreased Reynolds stress within the SPG boundary layer is ultimately due to weaker vortex-induced motions (i.e. sweeps and ejections). However, the actual structure of the hairpin vortex has remained unexplored. While the current orientation of the data set does not allow the hairpin legs to be identified, the spanwise-oriented vortices that form the heads of the hairpins have been detected through the swirling strength λ_{ci}. In order to examine their evolution through the expanding boundary layer, autocorrelations of the prograde swirling strength $R_{\Lambda^P\Lambda^P}$ are shown in Figs. 7.34 – 7.35

for the ZPG and SPG flowfields, respectively. The WPG vortices experienced minimal distortion, and are not shown here.

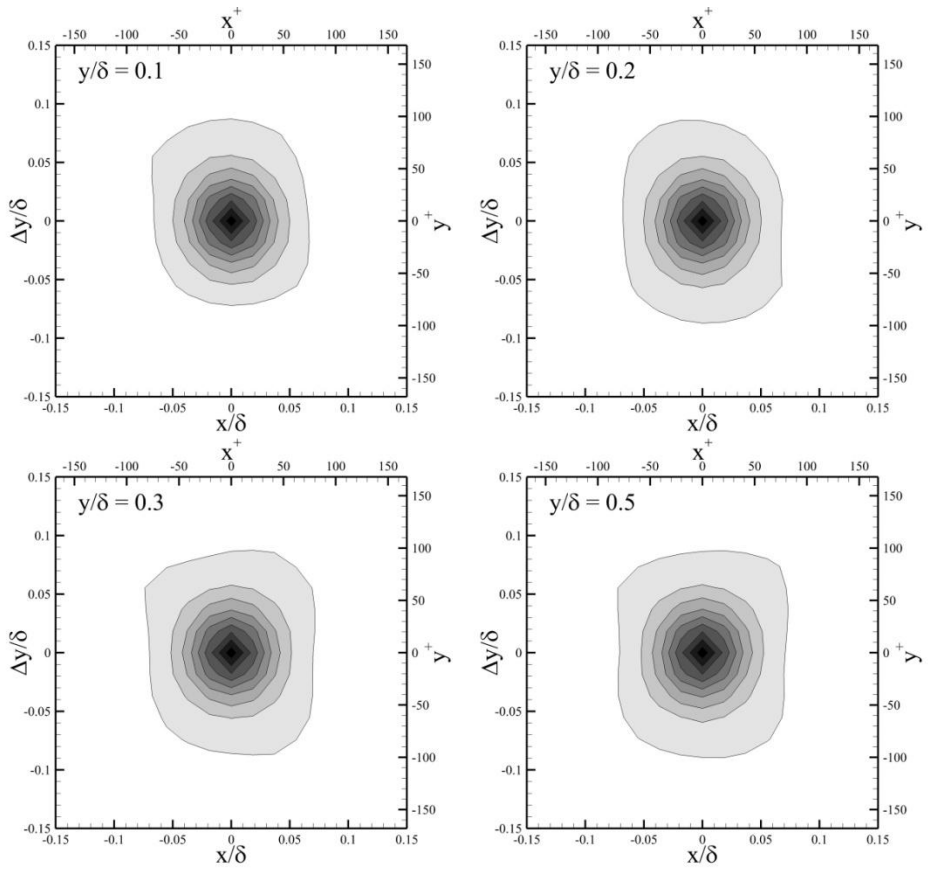

Figure 7.34 Autocorrelation of the prograde swirling strength, for the ZPG boundary layer

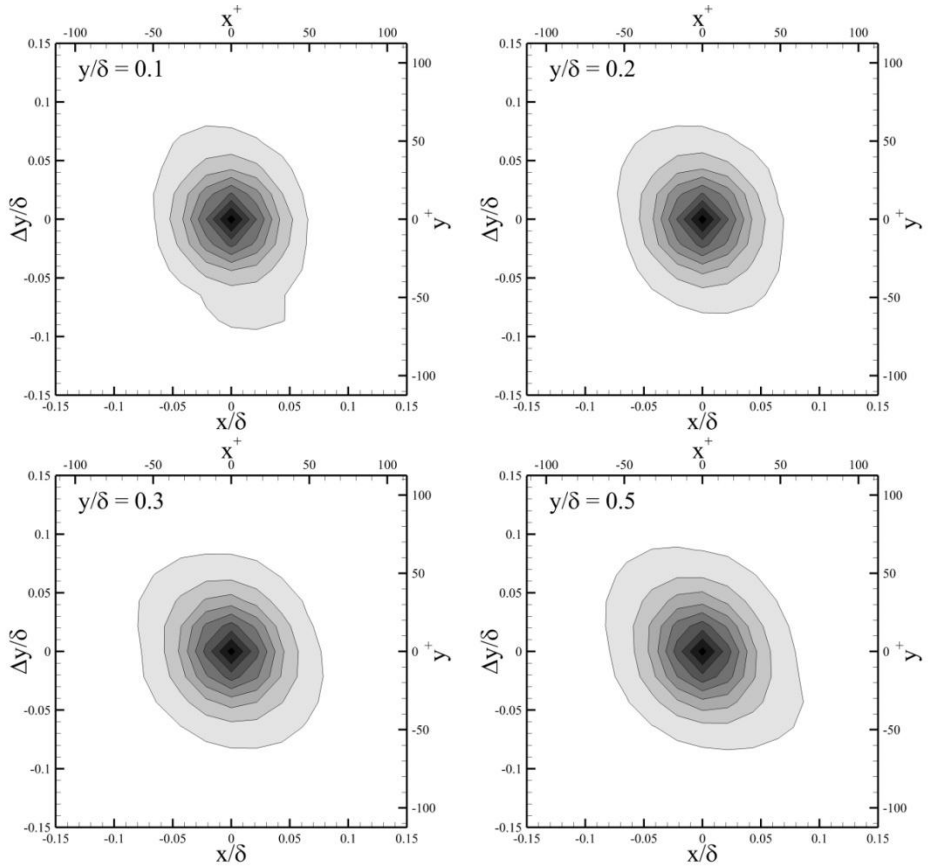

Figure 7.35 Autocorrelation of the prograde swirling strength, for the SPG boundary layer

The ZPG vortices in Fig. 7.34 are roughly isotropic at high correlation values, though appear stretched in the wall-normal direction at $R_{\Lambda^P\Lambda^P}$ = 0.1. The SPG boundary layer exhibits a similar structure in Fig. 7.35, though with obvious distortions. The vortex structure is clearly rotated in the upstream direction by 20 – 40 degrees, visible in the isocontour lines below $R_{\Lambda^P\Lambda^P}$ = 0.4. The angle appears to increase with distance from the wall, similar to the behavior of the large-scale motions in Fig. 7.17. This suggests that when the large-scale structures (corresponding to the high- and low-momentum streaks generated by the vortex packets) are rotated through the mechanism of *differential acceleration*, the heads (and most likely legs) of the hairpin vortices may experience a

similar reorientation. Such a reorganization may also serve to explain the behavior of the wall-normal convective velocity V_c in Fig. 7.33.

An additional observation from Figs. 7.34 – 7.35 pertains to the vortex diameters. Following the convention suggested in §6.6, the diameter of the vortices can be estimated from the 0.2 isocontour. For the ZPG flow, this yields a diameter of approximately 0.1δ (~ 100 viscous units), and is constant throughout the boundary layer thickness. The SPG boundary layer yields a comparable response, maintaining a similar constant cross-sectional diameter across the flowfield. The significance of this similarity will be discussed more thoroughly in §7.7.

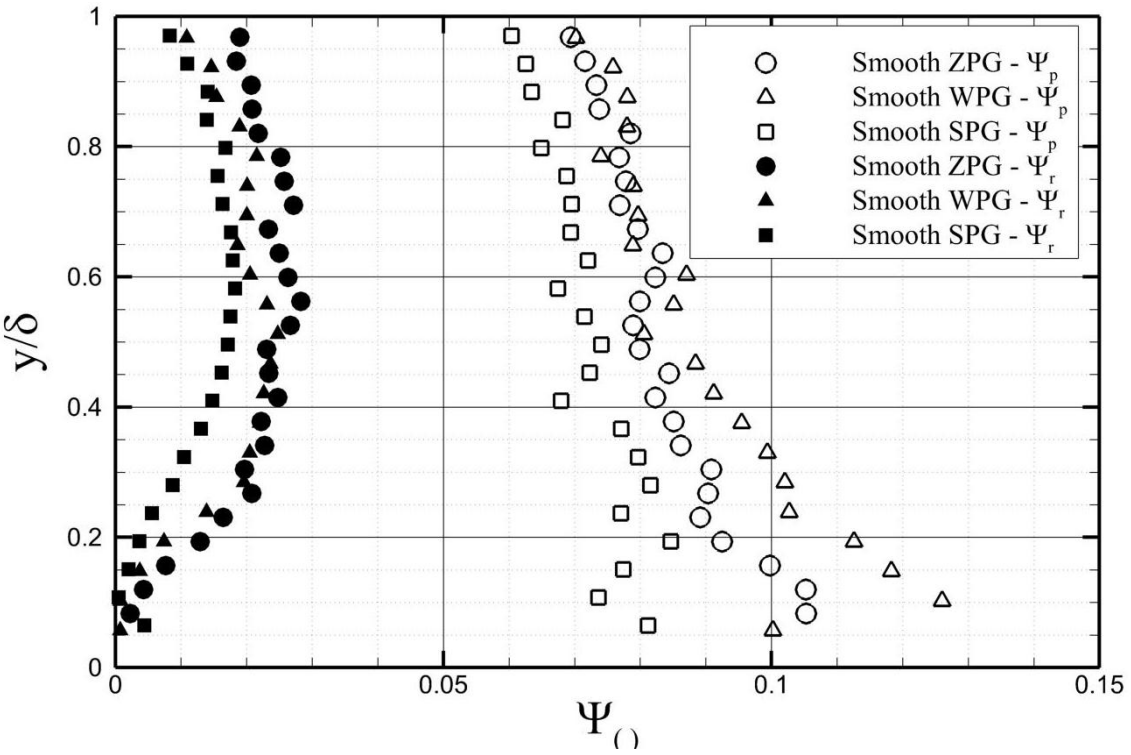

Figure 7.36 Vortex population distribution. *Subscripts "p" and "r" denote prograde and retrograde structures, respectively.*

Before proceeding with the analysis of the locally induced flowfields near the hairpin vortices in §7.6, it is useful to consider the population of the vortices throughout the boundary layer. Since the ejections and sweeps generated by these vortices are a primary mechanism for generating shear stress, any change in the population distribution may be reflected in the turbulence statistics. Indeed, the authors originally hypothesized that the reduced shear stress in the SPG boundary layer is due to a reduction in the vortex population, though that hypothesis has been shown to be false. The vortex population is shown in Fig. 7.36, for both prograde and retrograde vortices. The reduced occurrence of retrograde structures is observed for all flowfields, with a slightly smaller population in the SPG case. For all cases, the retrograde vortices appear to occupy approximately 20% of the total vortex population. However, the prograde structures are responsible for a larger fraction of the total shear stress (see Fig. 9 of Wu & Christensen (2006a)), and their distribution is of greater interest. Before discussing the SPG flowfield, the behavior of the WPG boundary layer should be noted. Above y/δ = 0.5, the ZPG and WPG populations of prograde structures show good agreement, as expected for small disturbances introduced by the weak pressure gradient. However, the *increased population* observed for the WPG case below y/δ = 0.5 was unanticipated. The cause of this behavior is currently unknown. In contrast, the SPG prograde vortices experience a 10% – 15% reduction in population across the boundary layer thickness. Due to the range of vortex strengths within the boundary layer (described by the PDF of the swirling strength λ_{ci} in Fig. 5.15), any attenuation of the vortices may result in a decreased population of the "weakest" structures (i.e. smallest λ_{ci} value), thereby decreasing the total shear stress. This suppression of the weakest vortices is analogous, but not equivalent, to the quenching of small-scale structures observed by Humble *et al.* (2012). However, it is possible that this population reduction is merely a result of the finite threshold used in detecting a vortex.

7.6. Conditional Structure of Near-Wall Boundary Layer

The instantaneous behavior of the vortices was examined in §7.4, showing the reduced magnitude of the ejection events within the SPG hairpin packet, possibly leading to a weakly correlated low-momentum region beneath the vortices. In order to provide a statistical measure of the locally induced flowfield, conditionally averaged velocity fields are presented in Figs. 7.37 – 7.39 for the ZPG, WPG, and SPG boundary layers, respectively. In each figure, a prograde vortex has been used as the conditional event. The WPG velocity fields in Fig. 7.38 are similar to the ZPG case, including the shear layer angle and the relative magnitude of the back-induced flow. This agreement is consistent with the structure angles shown in Fig. 7.17 near the wall, suggesting that the hairpin packets possess a similar characteristic growth angle. However, the SPG case in Fig. 7.39 shows a clear departure from the ZPG velocity field. At the three inner-most locations, the shear layer defined by $u' = 0$ is oriented at a larger angle with respect to the wall, consistent with the rotation of the large-scale motions. At $y/\delta = 0.2$ and 0.3, this angle is approximately 16 – 18 degrees. Nearest to the wall, the shear layer extends upstream only 0.2δ, suggesting that the vortices in the SPG boundary layer may not be streamwise-aligned in packets, and that the low-momentum streak is truncated to a shorter length scale. The most important result in Fig. 7.39 concerns the distribution of the velocity vectors around the vortex core. For $y/\delta = 0.1 – 0.3$, the local flowfield is more isotropic than the corresponding positions in the ZPG boundary layer, lacking the strong back-induced flow beneath the vortex that is visible for the ZPG case. A comparison of these motions is shown in Fig. 7.40, for the ZPG and SPG cases, clearly indicating that the induced flow beneath the vortex is smaller in magnitude. However, the ejection events appear to recover at $y/\delta = 0.5$ and 0.7, as the back-induced flow becomes more prominent. These observations confirm that the reduced magnitude of the ejection events, as detected by the quadrant decomposition, is due to the weaker induction of fluid by the hairpin vortices. This behavior is discussed more fully in §7.7.

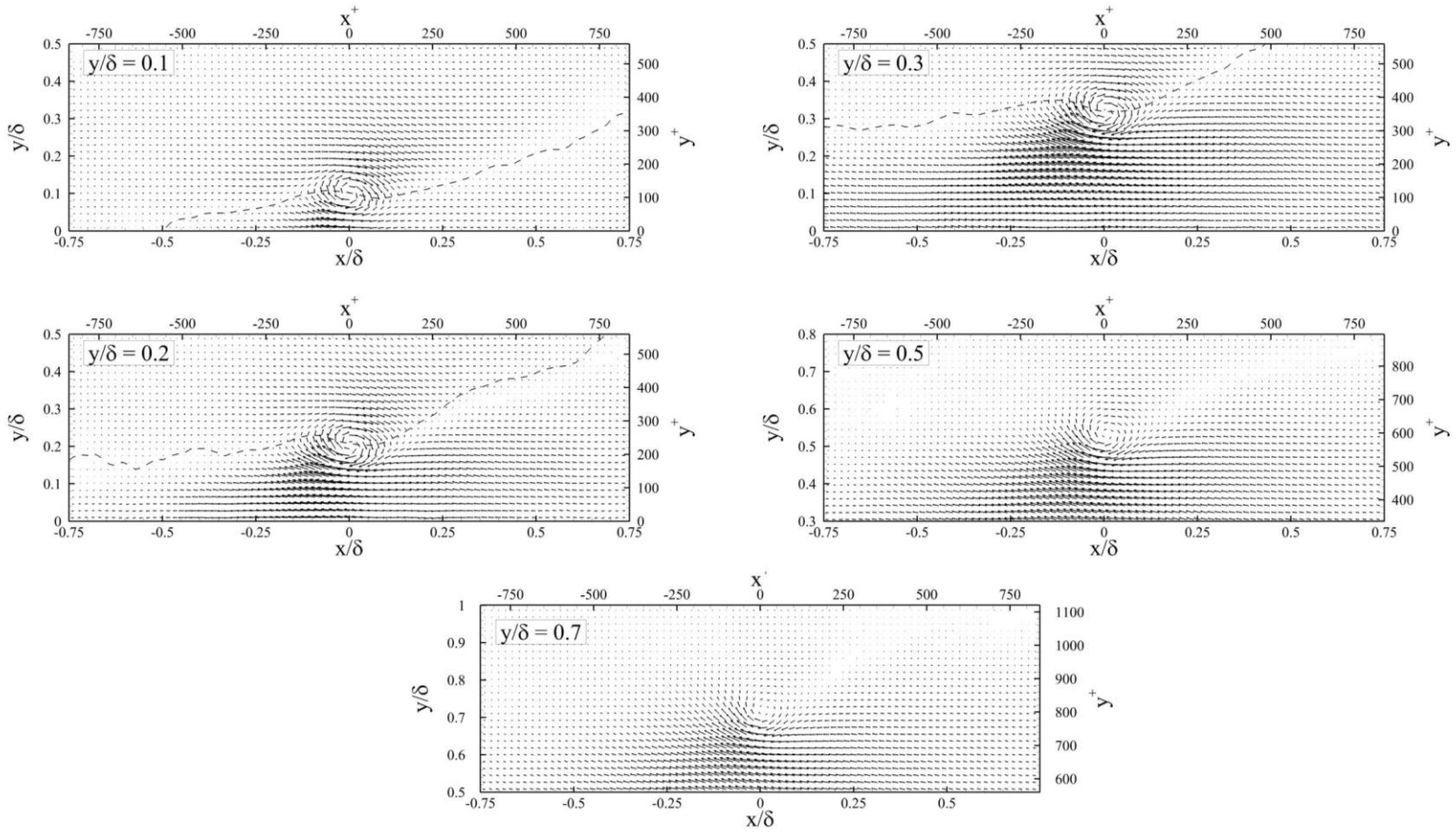

Figure 7.37 Conditional average of the ZPG velocity fields, using a prograde vortex as the conditional event. *The dashed line indicates the contour u' = 0.*

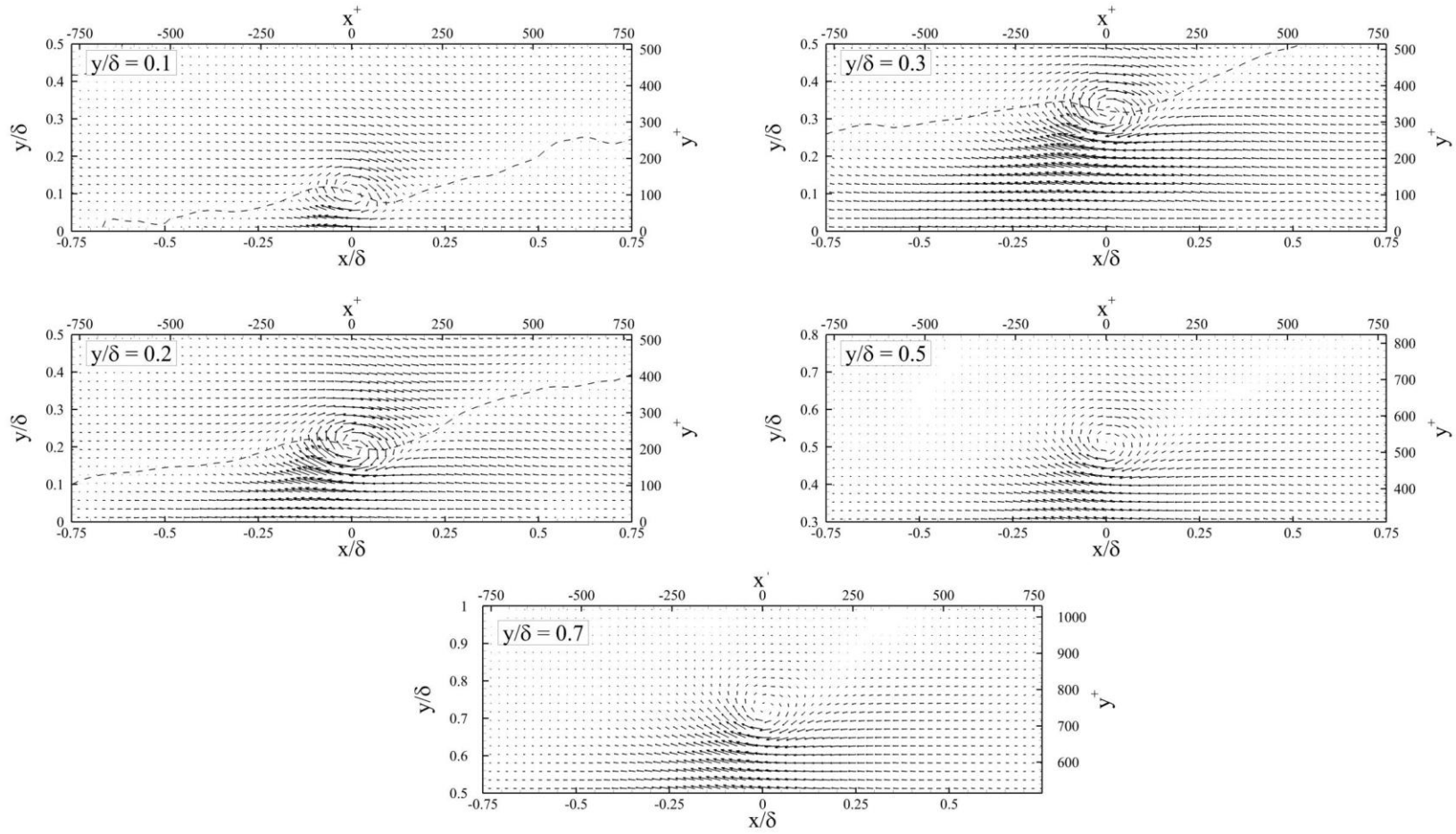

Figure 7.38 Conditional average of the WPG velocity fields, using a prograde vortex as the conditional event. *The dashed line indicates the contour u' = 0.*

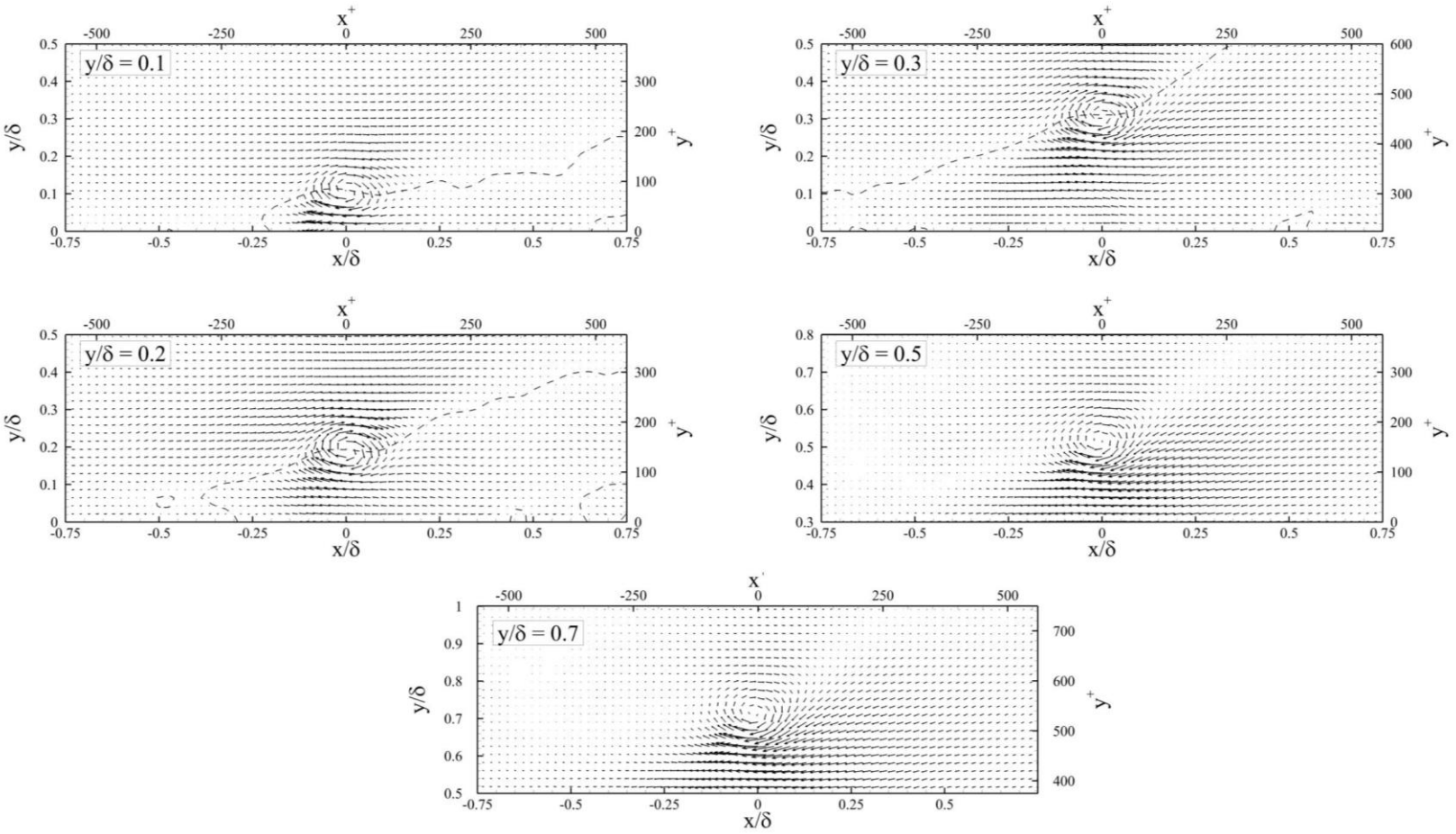

Figure 7.39 Conditional average of the SPG velocity fields, using a prograde vortex as the conditional event. *The dashed line indicates the contour u' = 0.*

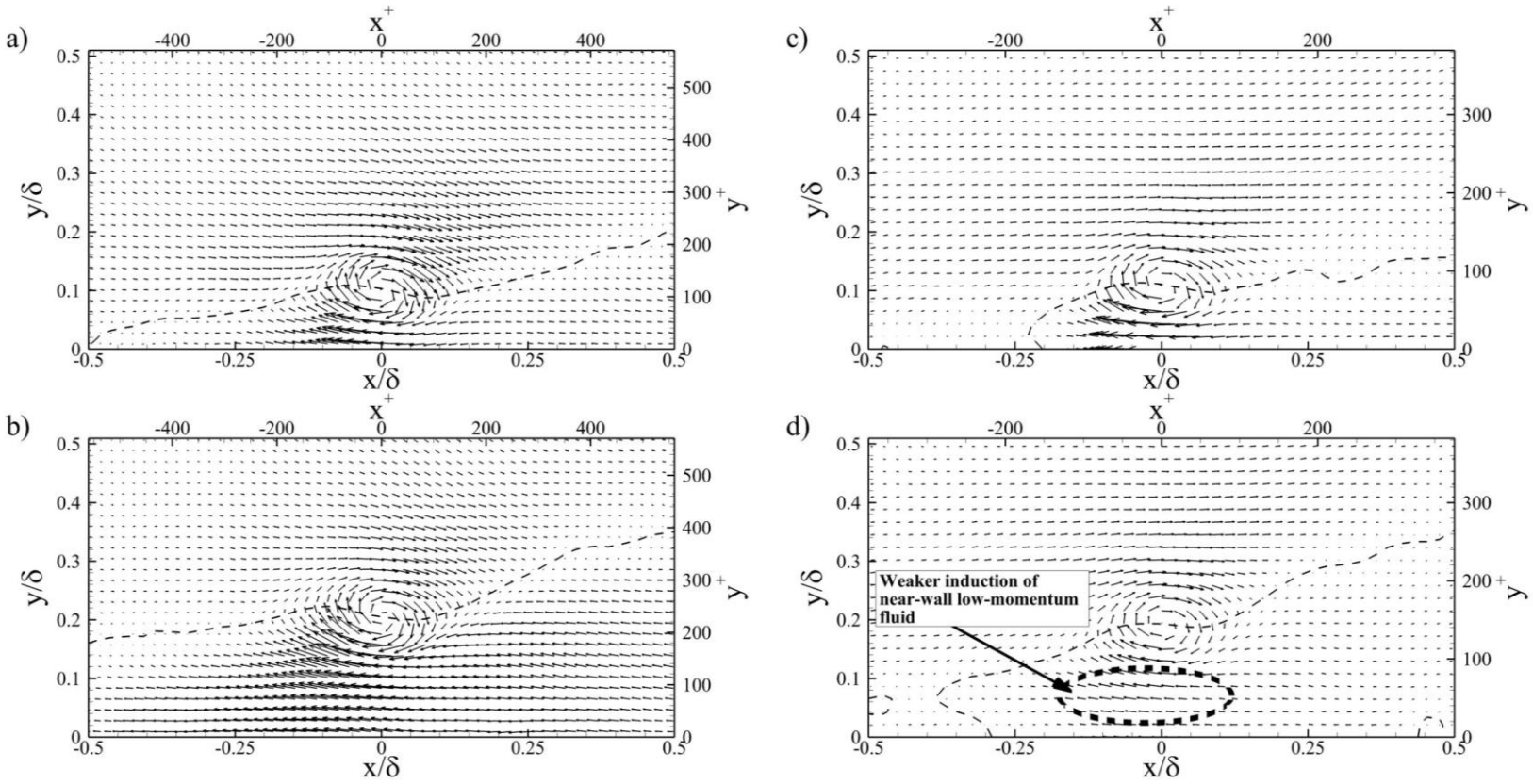

Figure 7.40 Comparison of the ZPG (left column) and SPG (right column) conditionally averaged velocity fields, at y/δ = 0.1 (top row) and y/δ = 0.2 (bottom row). *A prograde vortex is used as the conditional event. The dashed line indicates the contour u' = 0.*

The above results have shown that the decreased shear stress contributions of the SPG boundary layer, first indicated by the quadrant decomposition analysis, are due to the reduced magnitude of the vortex-induced flowfield. However, the direct relation between these motions and the shear stress production has not been thoroughly explored in this study. This is remedied by examining the cross-correlation between the prograde swirling strength and the instantaneous shear stress *u'v'*, computed as

$$R_{\Lambda_{ci}^{p}(u'v')}(\Delta x, y, y_{ref}) = \frac{\Lambda_{ci}^{p}(x, y_{ref})u'v'(x+\Delta x, y)}{\sqrt{\left\langle \left(\Lambda_{ci}^{p}(x, y_{ref})\right)^2 \right\rangle}\sqrt{\left\langle \left(u'v'(x+\Delta x, y)\right)^2 \right\rangle}} \tag{7.1}$$

In practice, the cross-correlation in Eqn. 7.1 describes the distribution of shear stress around a prograde vortex core. This is shown in Figs. 7.41 – 7.43 for the ZPG, WPG, and SPG boundary layers, respectively. Additionally, the conditionally averaged velocity vectors are overlaid onto each contour. Since the correlations are scaled by the rms of the swirling strength and shear stress for each case, a larger correlation value does not suggest that the intensity of the events (and therefore the magnitude of the shear stress *u'v'*) is larger, but that the *relative* contribution of the motions is dominant within that flowfield. The current analysis will be confined to the location, spatial extent, and size of the lobes within the correlation. Note that $\Lambda_{ci}^{p} < 0$ (since prograde vortices possess negative spanwise vorticity ω_z), so that a positive value of $R_{\Lambda_{ci}^{p}(u'v')}$ indicates that the shear stress *u'v'* is negative in that region.

The shear stress-prograde swirling strength cross-correlation is shown in Fig. 7.41 for the ZPG boundary layer. At the near-wall position of y/δ = 0.1, two local maxima are observed: 1) above and downstream of the vortex core, and 2) below and upstream of the prograde vortex. Comparing to the conditionally averaged velocity, these locations are consistent with sweep and ejection events, respectively. However, the downstream lobe is no longer visible for y/δ = 0.2 – 0.5, while the upstream lobe grows in magnitude and size. This suggests that the shear stress production is increasingly due to the ejection events as the wall-normal distance increases, and that these events occupy a larger area

of the flow in the outer region. The increased size of the correlation lobe at $y/\delta = 0.5$ may be related to the large-scale hairpins detected by Elsinga *et al.* (2010) above $y/\delta = 0.6$ in their Mach 2 boundary layer.

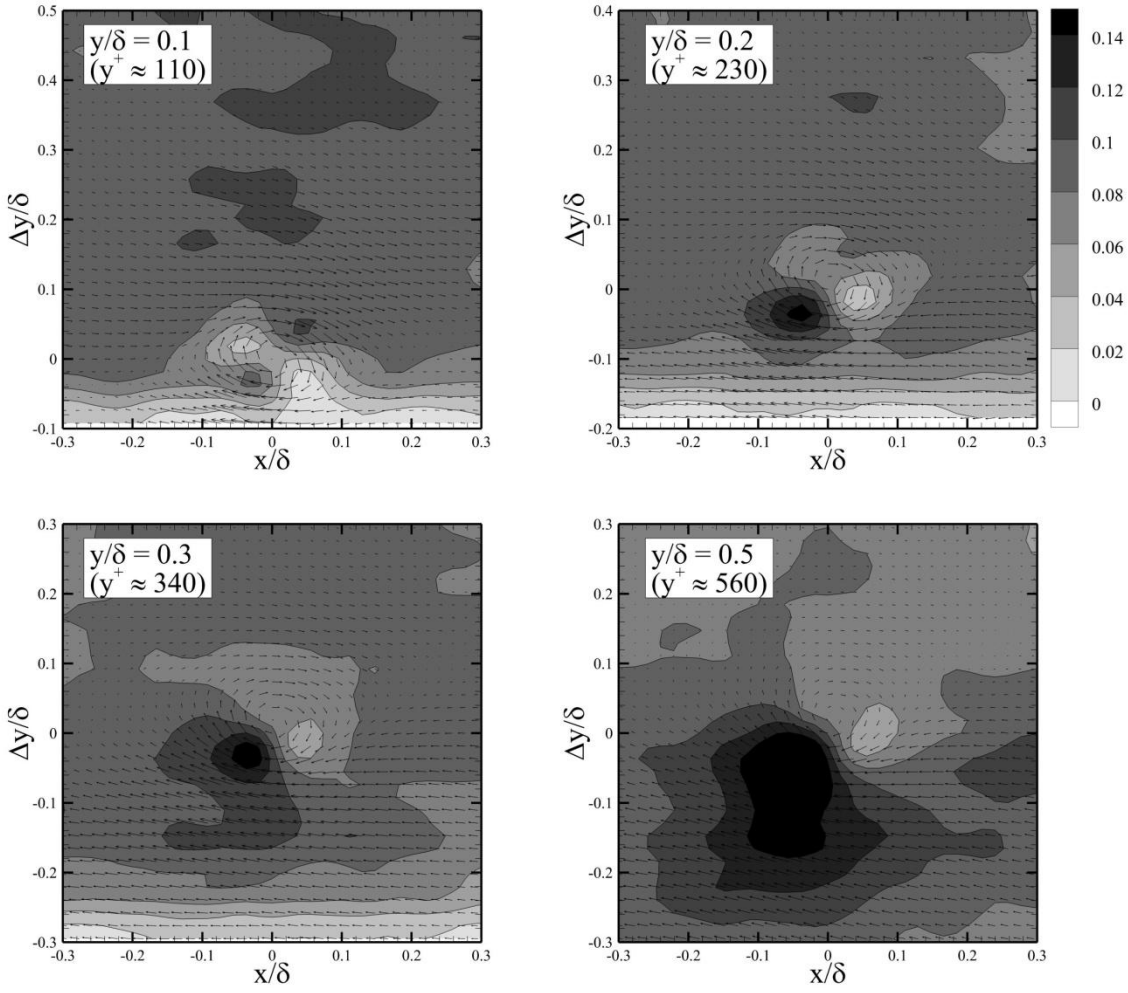

Figure 7.41 Cross-correlation of prograde swirling strength and shear stress, for the ZPG boundary layer. *Conditionally averaged velocity fields are overlaid onto each contour.*

The WPG boundary layer in Fig. 7.42 demonstrates similar behavior, producing correlation lobes at $y/\delta = 0.1$ corresponding to the sweep and ejection events around the prograde vortex core. Moving higher in the boundary layer, the ejection events become increasingly dominant. The only difference arises at $y/\delta = 0.5$, in which the spatial extent of the upstream lobe is markedly smaller than its ZPG counterpart.

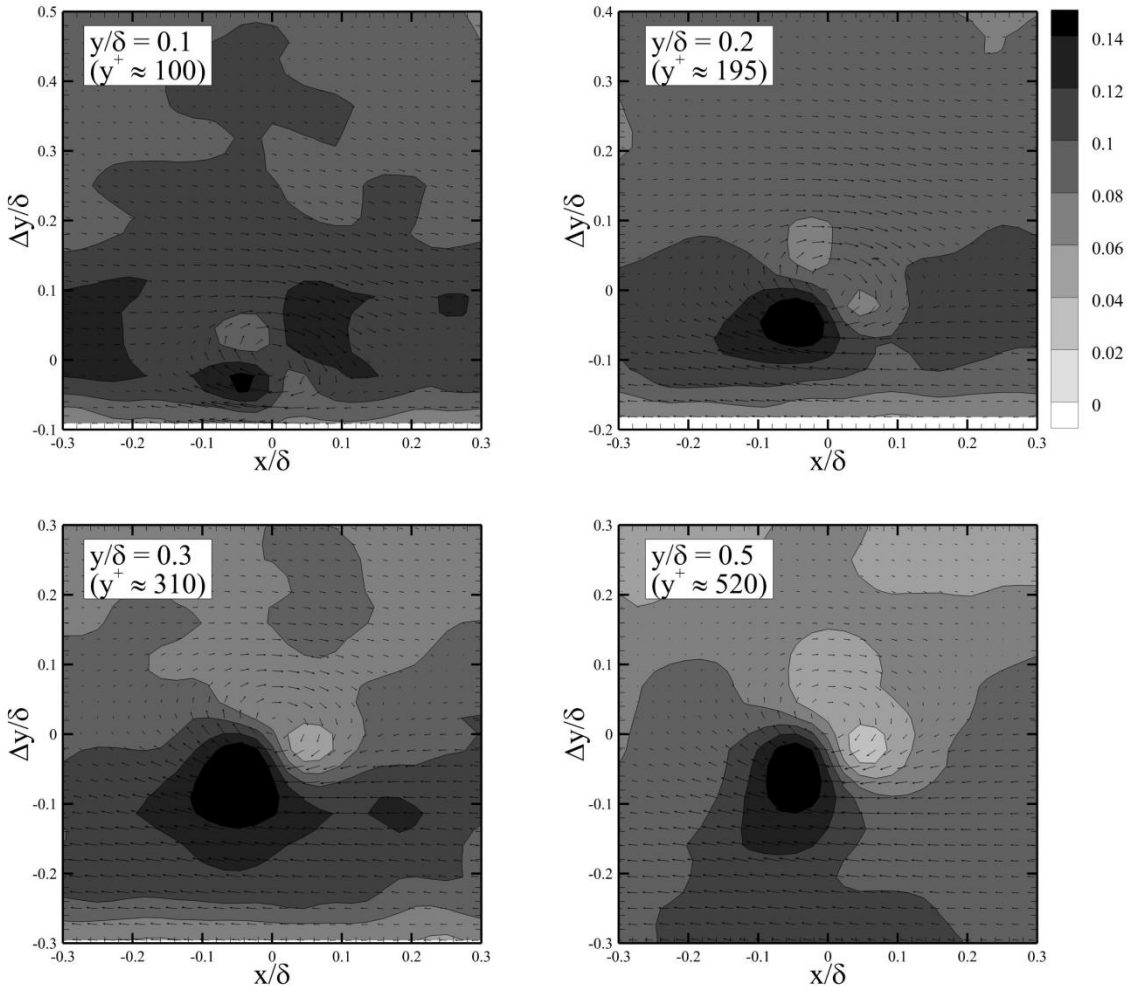

Figure 7.42 Cross-correlation of prograde swirling strength and shear stress, for the WPG boundary layer. *Conditionally averaged velocity fields are overlaid onto each contour.*

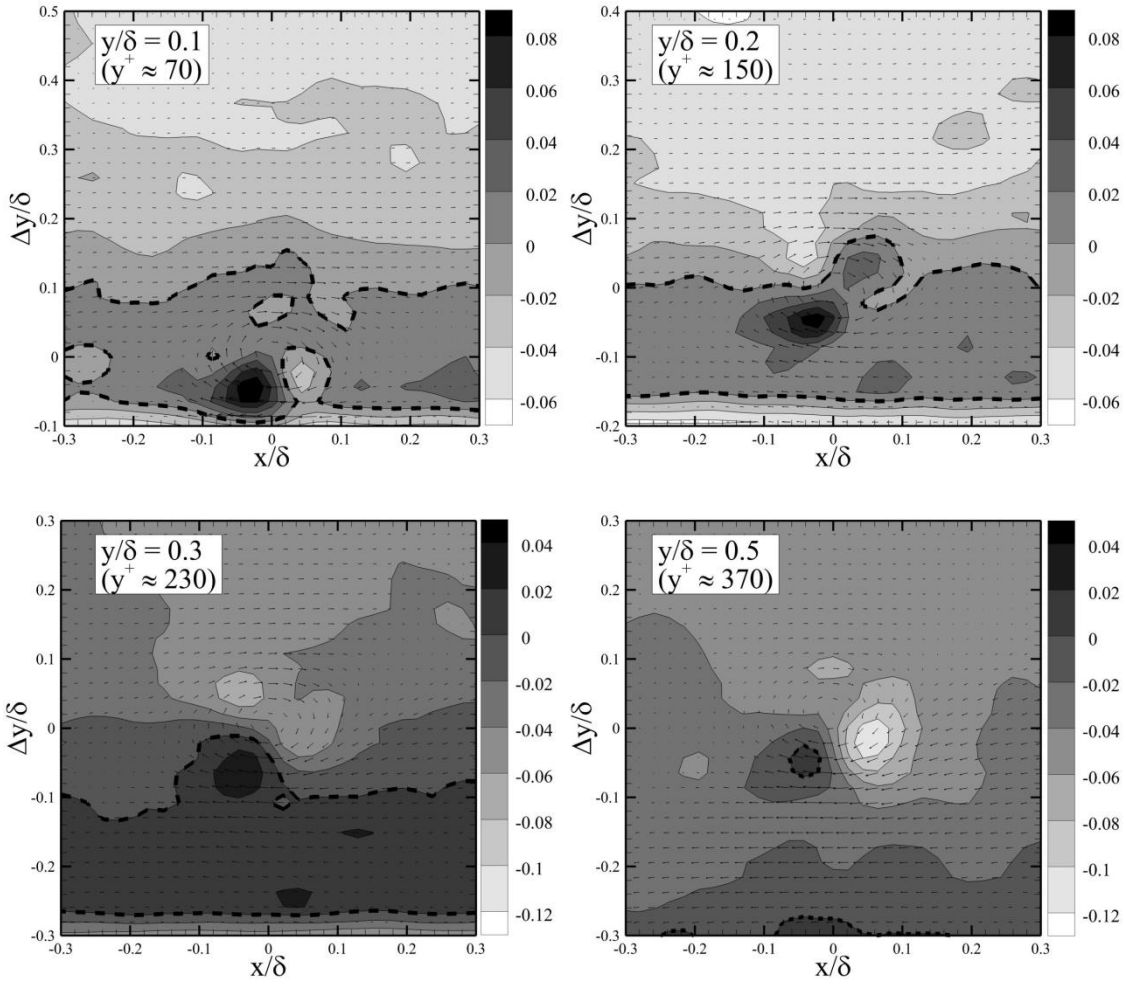

Figure 7.43 Cross-correlation of prograde swirling strength and shear stress, for the SPG boundary layer. *Conditionally averaged velocity fields are overlaid onto each contour. Dashed lines indicate the boundary between positive and negative correlation values. Note the different contour levels for each frame.*

In keeping with the previous analyses of this section, the largest deviation from the baseline case occurs within the SPG flowfield. Recall from §7.2 that the mean shear stress experiences a sign reversal in the outer 80% of the SPG boundary layer. This behavior is reflected in the distribution of the shear stress encircling the prograde vortex core in Fig. 7.43. Note that the dashed line delineates the border between the positive and negative correlation values. At y/δ = 0.1, the local shear stress distribution is

predominantly negative, with a large lobe corresponding to the ejected low-momentum fluid. Recall from Fig. 7.6 that the mean shear stress distribution is negative at this height in the boundary layer. However, this position still experiences small contributions of positive shear stress. Projecting the cardinal directions onto the correlations, the positive shear stress lobes occur at y/δ = 0.1 north and southeast of the vortex core, possibly corresponding to Q1 and Q3 events, respectively. At y/δ = 0.2, the negative shear stress events appear at positions northeast and southwest of the vortex, coincident with the sweep and ejection events, respectively. Above this height, the lobe associated with the sweep events is no longer visible. Instead, the negative shear stress contribution is confined within the ejection events for y/δ = 0.3 and 0.5, while a highly-correlated positive shear stress lobe appears at the southeast position for y/δ = 0.5, corresponding to a Q3 event. These correlations suggest that as the wall-normal distance increases, the negative shear stress contribution is increasingly due to the ejection of low-momentum fluid away from the wall. However, this contribution becomes less dominant, while the relative significance of the Q3 "inner interaction" increases in the outer region. Also, it should be noted that a wide band of positive correlation (i.e. negative shear stress) is visible over the range y/δ = 0 – 0.2, for the three inner-most correlation positions, corresponding to the region of negative mean shear stress from Fig. 7.6.

In §7.2, it was shown that the rotation of the coordinate frame is largely responsible for the sign reversal of the mean shear stress. This coordinate transformation was applied to the instantaneous velocity fields, and the correlation $R_{\Lambda_{ci}^{p}(u'v')}$ was repeated for the SPG case in Fig. 7.44. Qualitatively, the orientation of the correlation lobes is similar to those in Fig. 7.43. The ejection events appear to be the dominant contributors to the negative shear stress at y/δ = 0.1, 0.3, and 0.5, with a weak sweep event arising in y/δ = 0.1. The contributions of the sweep and ejection events are approximately equal for y/δ = 0.2. However, the most striking feature is the strong negatively correlated region at y/δ = 0.5, indicating a positive shear stress event from a Q3 "inner interaction." This suggests that while the sign reversal of the mean shear stress is due to the coordinate transformation, the positive shear stress contributions are not eliminated.

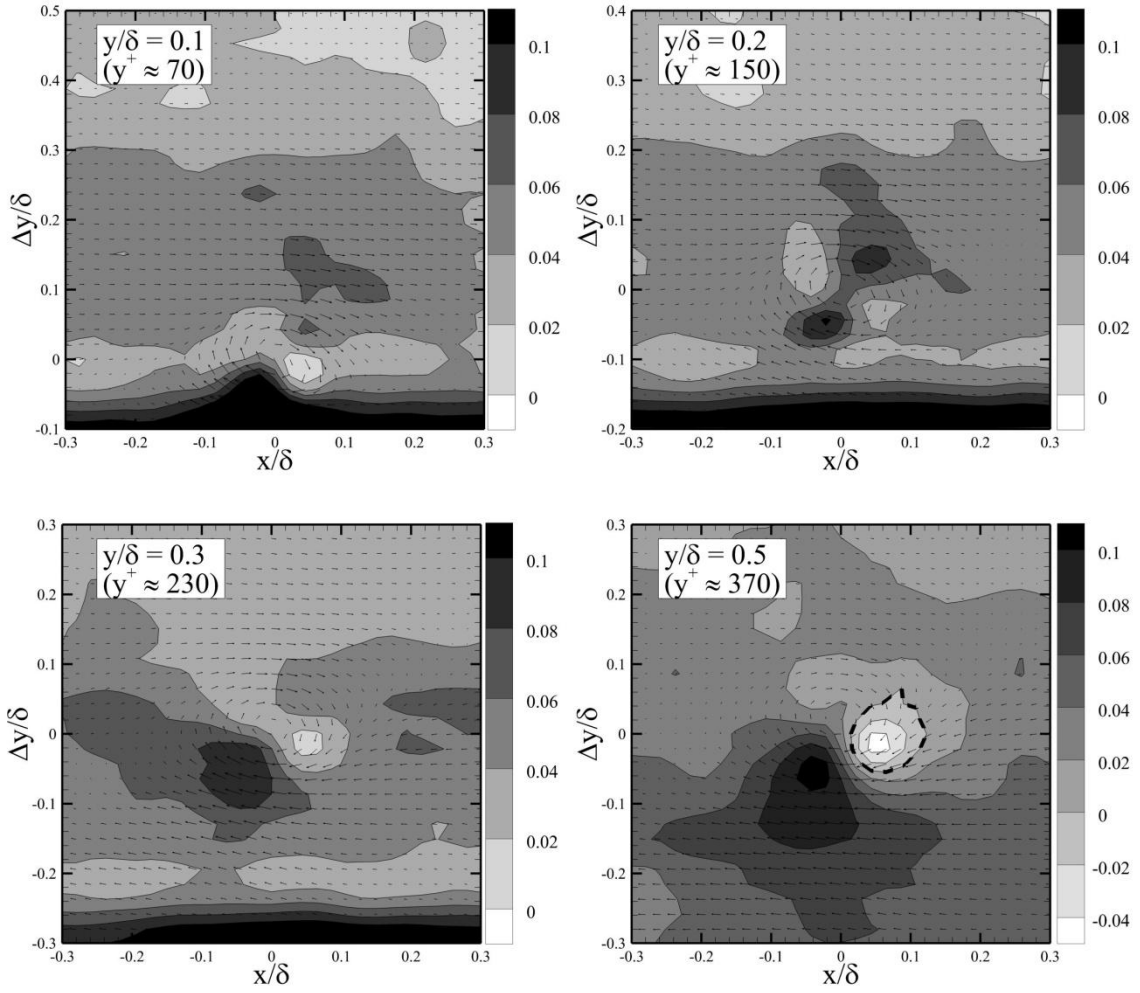

Figure 7.44 Cross-correlation of prograde swirling strength and shear stress, for the SPG boundary layer, after rotating the coordinate frame into the wind tunnel axes. *Conditionally averaged velocity fields are overlaid onto each contour. Dashed lines indicate the boundary between positive and negative correlation values. Note the different contour levels for each frame.*

Comparing between the ZPG and transformed SPG cases in Figs. 7.41 and 7.44 using inner coordinates, the shear stress distribution within the logarithmic region ($y^+ \approx 100 – 200$) shows good agreement, indicating that the sweep and ejection events both contribute to the mean shear stress. Above $y^+ = 200$, the sweep events are less significant, while the ejections become increasingly dominant. Neglecting the negative correlation lobe at $y/\delta = 0.5$ in Fig. 7.44, these correlations appear to suggest that the

structure of the individual hairpin vortices, and the associated shear stress-producing mechanisms, are relatively unchanged by the favorable pressure gradient. However, the reader is reminded that the above statement does not suggest that the *magnitudes* of the shear stress-producing contributions are unchanged. Additionally, the conditionally averaged velocity fields and $R_{\Lambda_{ci}^{p}(u'v')}$ correlations only describe the motions within a plane bisecting the hairpin vortex head. The induced motions outboard of the hairpin vortices are not described by these analyses.

7.7. Discussion of Results

The analyses performed within this section have yielded considerable insight into the physical mechanisms within a compressible turbulent boundary layer, and their response to streamline curvature-induced favorable pressure gradients. Using these results, conceptual models are synthesized in the following sub-sections, pertaining to the most salient features of the SPG boundary layer.

7.7.1. Length Scale Distribution

The reduction in the near-wall length scale for the SPG case was observed in both the two-point correlations and premultiplied spectra, indicating an approximately 50% decrease in the spatial extent of the large-scale motions. As noted in §7.4, two theories exist for the reduced length scale: 1) the acceleration within the boundary layer "delaminates" the hairpin packet, increasing the streamwise separation between the vortices, such that the low-momentum streak is "shredded" through the expansion, and 2) the ejections beneath the vortices are weaker (discussed more thoroughly in §7.7.2) and shorter in the streamwise direction, reducing the correlation within the low-momentum streak. The SPG instantaneous velocity field in Fig. 7.22 shows that the vortices are arranged at intervals of 200 – 300 viscous units, consistent with the

observations for a ZPG boundary layer in Fig. 6.13. This suggests that the vortex spacing is relatively constant, despite the favorable pressure gradient. The conditionally averaged velocity fields in Figs. 7.24 and 7.26 show that the ejection events are weaker for the SPG case, and extend over a shorter streamwise distance. Essentially, there is less overlap between the back-induced flow beneath each vortex, such that the correlation is biased toward the streamwise length of the ejection event ($\sim 0.2 - 0.3\delta$), as evidenced by the "bulge" in the near-wall premultiplied spectra of Φ_{uu}. From these observations, it is possible to conclude that *the shortened streamwise length scale in the near-wall region of the SPG boundary layer is a result of the weakened shear-stress producing motions induced by the hairpin vortices*. This differs from past studies, which have speculated that the length scale reduction is a cause of the shear stress attenuation [Luker *et al.* (2000)].

In the outer region of the boundary layer, Fig. 7.21 indicated that the dimensional streamwise length of the large-scale motions is approximately equal for all cases, suggesting that the spatial extent of the structures is relatively unperturbed by the favorable pressure gradient. This result was unanticipated, as past studies have shown that bulk dilatation is the primary mechanism within an expanding boundary layer [Bradshaw (1974); Arnette *et al.* (1995); Arnette *et al.* (1998)]. Initially, the authors speculated that this may be a function of the large timescale of the *u'*-bearing motions. However, this seems implausible, since the growth of the structures is attributed to dilatation, which is a response of the fluid, and not dependent upon the structure response. Therefore, the large-scale motions should expand along with the bulk flow. However, if we consider that the FPG diminishes the turbulence production in the outer layer [Luker *et al.* (2000); Ekoto *et al.* (2009); Tichenor *et al.* (2013)], then the evolution of the large-scale structures will be governed largely by dissipation. If the reduction in scale (from dissipation) is counter-balanced by the dilation of the structure, then it is possible that the δ-scale structures will remain constant in size, dimensionally. Currently, further investigation is necessary to confirm this conjecture.

7.7.2. Shear Stress Attenuation

The conditionally averaged velocity fields indicate that the SPG vortices induce a weaker back-induced flow (i.e. ejection), as evidenced by the quadrant decomposition. Due to the central role that the hairpin vortices occupy in generating the Reynolds shear stress [Adrian *et al.* (2000); Wu & Christensen (2006a)], this suggests that the reduced stresses within the SPG boundary layer are partly due to the weaker induction of near-wall fluid. However, the mechanism that leads to these weaker events is still unknown, and will be discussed below.

The quadrant decomposition results for the SPG case show that the strengths of the shear stress-producing events are dramatically reduced from the ZPG case, and that the magnitudes of the sweep and ejection motions are approximately equal (see Fig. 7.9). Two possible explanations for this behavior are available, relating to the deformation of the hairpin vortices. Recall that the sweeps and ejections are caused primarily by the induction of high- and low-speed fluid around and between the legs of a hairpin vortex, respectively. This motion is shown schematically in Fig. 7.45. Due to the sense of rotation, the collective induction between the hairpin legs should produce a relatively strong ejection of low-speed fluid, compared to the more diffuse sweep of high-speed fluid that occurs outboard of the hairpin. This is seen in the quadrant decomposition for the baseline case in Fig. 7.9, in which the Q2 events show a stronger intensity. For the sweep and ejection events to have similar magnitudes (as seen in Fig. 7.9 for the SPG case), it is possible that the favorable pressure gradient causes the hairpin to widen, such that the legs are spaced further apart. This would minimize the collective induction between the legs, and hence reduce the intensity of the ejection event. This process is shown in Fig. 7.46a. Unfortunately, the current data set is not able to determine the deformation of the vortices along the z-axis, being confined only to the x-y plane. However, a recent wide-field study by English (2013) in the x-z plane may provide more insight into this possible behavior. Outer-scaled auto-correlations in the streamwise-spanwise plane at $y/\delta = 0.2$ are shown for each pressure gradient case in Fig. 7.47, re-

plotted from English (2013). The spanwise correlation of the streamwise velocity, denoted as R_{uz} by English (2013), shows a relatively constant width for all pressure gradient cases when scaled by the local boundary layer thickness. This suggests that the statistical width of the ejected fluid does not change with the increasingly favorable pressure gradient. The reader is cautioned that this only indirectly supports the notion that the hairpin legs experience minimal "spreading" through the expansion region. A direct measurement of the hairpin width would require a higher-resolution study, utilizing conditional averaging to determine any spanwise deformation of the individual hairpin vortices. However, an approximation of this structure may be possible through low-pass filtering of the instantaneous velocity fields [Tomkins & Adrian (2003); Elsinga *et al.* (2010)], which emphasizes the large-scale motions within the boundary layer.

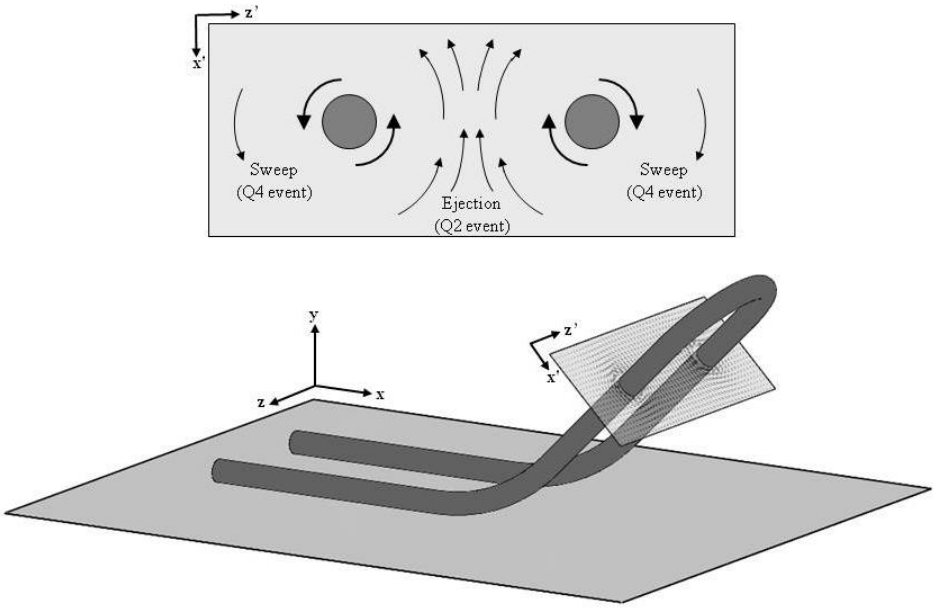

Figure 7.45 Schematic of a hairpin vortex, identifying the motions contributing to sweeps and ejections

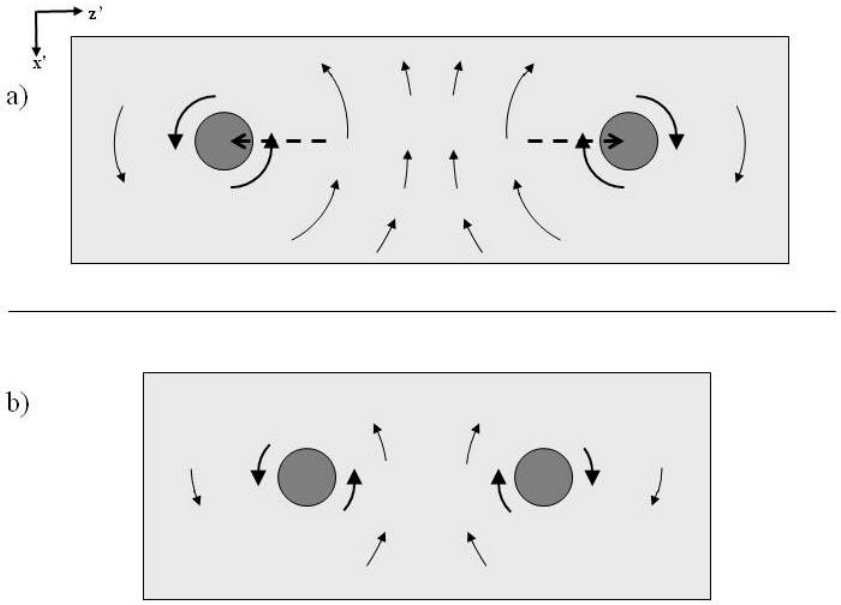

Figure 7.46 Illustrations of the possible mechanisms contributing to the reduced magnitude of the ejection events, including a) vortex spreading and b) reduced vorticity. *The axes* x' *and* z' *are identical to those presented in Fig. 7.45.*

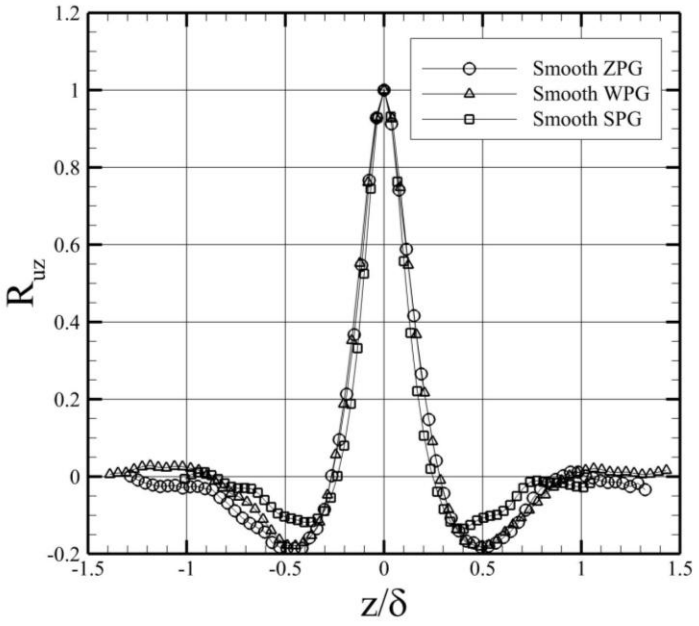

Figure 7.47 Outer-scaled autocorrelation of the u' velocity component, presented in the spanwise direction at y/δ = 0.2. *Data were provided by* English (2013)

The second possible explanation for the equivalence of the sweep and ejection magnitudes is related to the magnitude of the vorticity along the vortex axis. If the vorticity of the hairpin vortex is reduced through the favorable pressure gradient, the ability of the vortex to entrain and eject fluid would also be diminished, thereby reducing the magnitude of the sweeps and ejections. This would initially appear to reduce both the Q2 and Q4 events equally, and would not recreate the behavior seen in Fig. 7.9. However, the diminished vorticity may also reduce the "zone of influence" around the vortex, such that the collective induction between the hairpin legs is ultimately weakened (see Fig. 7.46b). Again, direct observation of this behavior requires data either in the *x*-*z* plane, or preferably in a plane oriented normal to the vortex axis of the hairpin legs (see Ganapathisubramani *et al.* (2005)). Fortunately, since the rotational rate of the vortex is constant along its length (otherwise the vortex would "twist up" and shear apart), it is possible to ascertain any reduction in the vorticity by viewing the hairpin head, which is visible in the current *x*-*y* orientation. Profiles of the mean prograde swirling strength are given in Fig. 7.48, averaged at each height in the boundary layer over a distance of 0.5δ, and non-dimensionalized by the baseline boundary layer thickness δ_{ZPG} and edge velocity U_{ZPG}. The swirling strength is plotted instead of the vorticity, since the high shear in the near-wall region may occlude any changes in the vorticity magnitude. Recall from §5.1.5 that the swirling strength is essentially the inverse of the period required for a particle to orbit the vortex axis, meaning that a large value of λ_{ci} indicates that the vortex is rotating rapidly. Non-dimensionalizing the prograde swirling strength by δ_{ZPG} and U_{ZPG} allows for a direct comparison of the angular velocity of the vortices.

The mean prograde swirling strength plotted in Fig. 7.48 shows a 30% - 40% reduction for the SPG case, suggesting that the vortices are rotating at a slower rate. This reduction matches the conceptual model described above, indicating that the reduced mean swirling strength may be responsible for the reduction in the magnitude of the shear stress-producing motions for the SPG case, leading to equivalent intensities of the sweep and ejection events. Finally, the reduction in swirling strength is consistent with the

observations of English (2013), who noted that the SPG *u*-velocity contours in the *x*-*z* plane at $y/\delta = 0.2$ "are much less intense relative to the average velocity." Since the low- and high-momentum streaks are related to the fluid entrained by the hairpin vortex packets, this supports the theory that the reduced rotational rate of the hairpin vortices (represented by the mean swirling strength in Fig. 7.48) is responsible for the lower-intensity sweeps and ejections, and hence the reduced shear stress. Additional data is necessary to ascertain whether the reduced swirling strength is present when the vortices are formed, or if these features develop as the hairpin "matures."

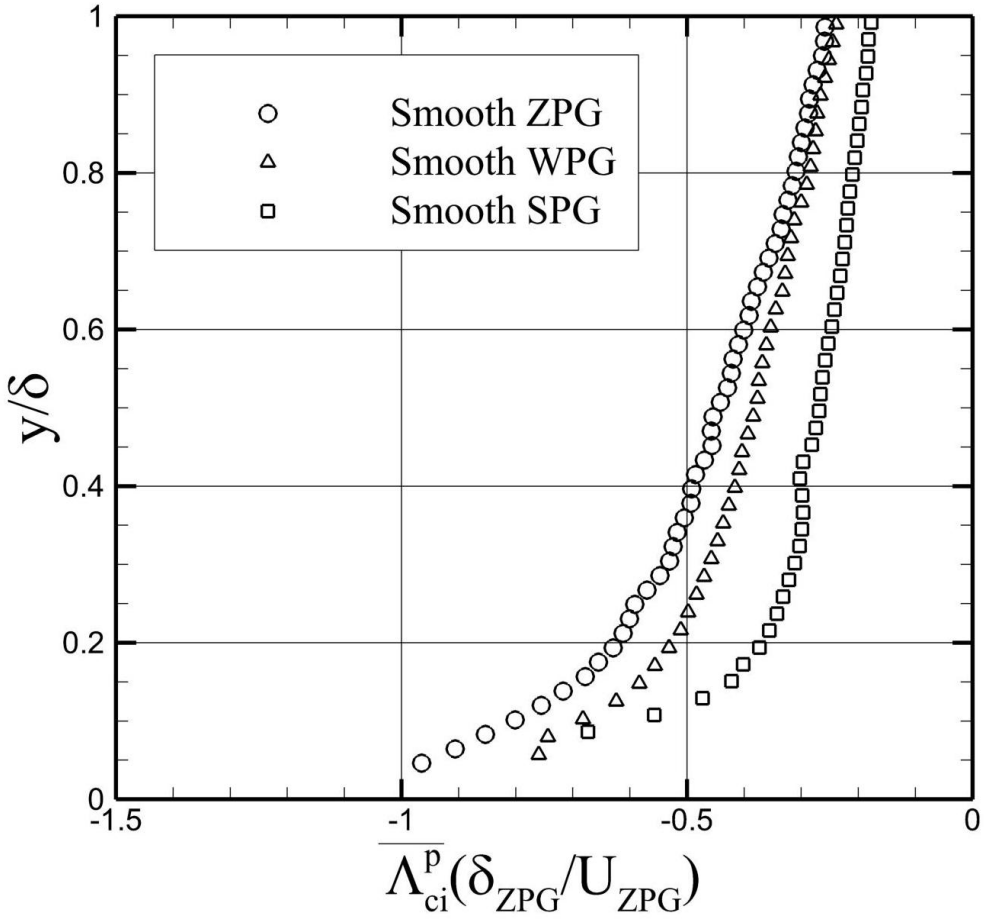

Figure 7.48 Mean prograde swirling strength, non-dimensionalized by the ZPG boundary layer thickness and freestream velocity

While the mechanism leading to the reduced swirling strength is currently unknown, it may be possible to draw insight from the behavior of incompressible boundary layers. Piomelli, Balaras & Pascarelli (2000) used LES to examine an accelerated incompressible boundary layer, showing that the coherent streamwise vortices are elongated in the acceleration region, while the magnitude of the dimensional vorticity is unchanged. They speculated that the vortices are stretched in the streamwise direction, such that the thinner structures are more susceptible to viscous dissipation. A similar mechanism was considered for the current supersonic study. While the acceleration *dU/dx* was negligible across the FOV [Tichenor *et al.* (2013)], it is possible that the wall-normal strain rate *dV/dy* exerted a similar influence upon the angled hairpin legs. Indeed, this very mechanism was proposed by Tichenor *et al.* (2013).

Initially, it would appear that vortex stretching may be a viable explanation for the weakened state of the hairpin vortices. Near the wall, the turbulent Mach number is approximately 0.2 – 0.3, calculated as

$$M' = \frac{u_{rms}}{a} \tag{7.2}$$

where a is the local speed of sound. Since M' is within the incompressible range, it seemed possible that the strain rate *dV/dy* could stretch the hairpin legs, leading to a smaller vortex diameter, and hence increased dissipation. Since this stretching occurs in the wall-normal direction, it isn't possible to resolve the diameter of the hairpin legs in the current orientation.

Upon further examination, the application of the *hairpin stretching* theory to the current flowfield seems less credible. Firstly, the turbulent Mach number may not be a suitable parameter for describing the hairpin vortex behavior. As seen in Eqn. 7.2, M' is calculated from the u_{rms} term. The fluctuations comprising u_{rms} are generally short-lived, and are not necessarily contained within an organized structure. In contrast, the hairpin vortices and subsequent packets possess a large degree of spatial and temporal coherence. Therefore, while the turbulent fluctuations may be characterized by M', the

coherent structures are more likely to be described by the Mach number of the local fluid. Since Fig. 7.32 showed that the vortices convect at almost the mean velocity, it is likely that their behavior is determined by the local Mach number, which is supersonic. Hence, any stretching of the vortices in the wall-normal direction would not necessarily result in a reduced cross-sectional diameter.

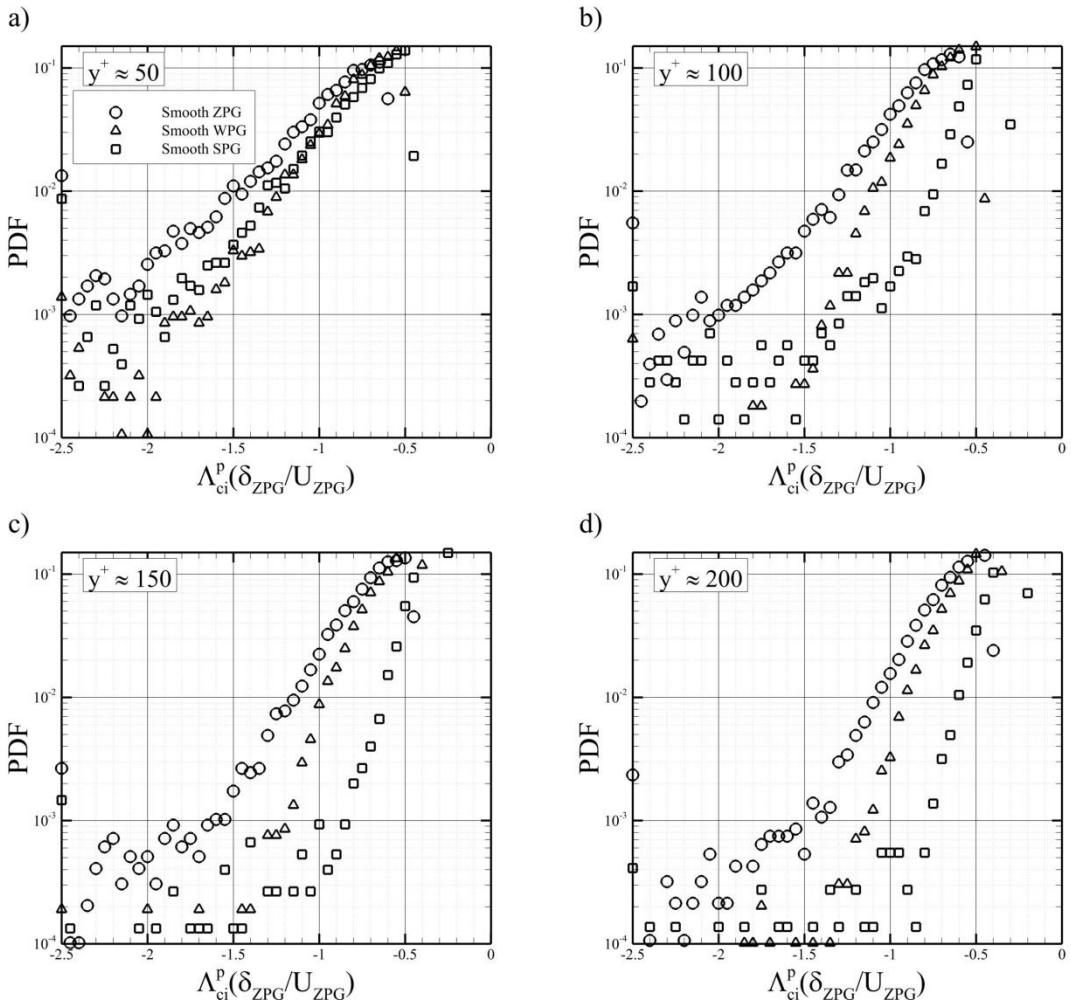

Figure 7.49 PDF of prograde swirling strength (after filtering for size/strength/orbital compactness; see §5). *Swirling strength is scaled by ZPG boundary layer thickness and edge velocity.*

An additional inconsistency arises when the attenuation of the vortices is examined. As stated previously, the rotational rate (i.e. swirling strength) should be constant along the length of the vortex. Therefore, any reduction in the rotation of the vortex will be visible in the hairpin head. It was shown in Fig. 7.48 that the mean rotation rate of the prograde vortices is reduced within the FPG boundary layers. However, if vortex stretching leads to a smaller cross-sectional diameter of the hairpin legs, then conservation of angular momentum would necessitate that the rotational rate *increases*. Piomelli *et al.* (2000) suggested that the viscous dissipation of the smaller structures counteracted the increased vorticity, leading to dimensional vorticity levels that were nearly unchanged from the upstream state in their study. Since viscous dissipation does not act instantaneously, some of the SPG vortices within the FOV should be rotating at a higher rate than their baseline counterparts, prior to their attenuation. A PDF of the prograde swirling strength in Fig. 7.49 does not reveal this behavior. Instead, all vortices have been weakened within the SPG case, regardless of their swirling strength. The only exception occurs at $y^+ \approx 50$, where a majority of the reduction occurs for the strongest vortices. These results suggest that the mechanism responsible for the reduced swirling strength, and therefore the reduced Reynolds stress, acts upon all vortices. This behavior is not consistent with the previously mentioned vortex stretching theory.

7.8. Summary

The effects of favorable pressure gradients upon a Mach 4.9 boundary layer were examined using high-resolution PIV. Three experimental models were investigated: a baseline ZPG case, and two convex curvature models. For the favorable pressure gradient flowfields, all three measured stress components (axial, wall-normal, and shear) were attenuated through the expansion region. However, the most dramatic response was observed in the shear stress for the SPG flowfield, which underwent a sign reversal over the outer 80% of the boundary layer. This observation served as the motivation for the remaining analyses, with the goal of providing a physical explanation for the response of

the Reynolds stresses, by examining the distortion, re-orientation, and attenuation of the turbulent structures.

The streamwise evolution of the turbulence stresses in §7.2 showed a large variation in the axial stress across the FOV of the SPG boundary layer, while the wall-normal and shear components experienced a considerably smaller variation. It was argued that the axial stress evolved at a slower rate, due to the larger timescale of the δ-scale u-bearing eddies. However, the flow scales associated with the wall-normal and shear stresses are 3-5 times smaller, suggesting that the attenuation of these fluctuations occurred more quickly. This suggests that the SPG boundary layer is in a state of non-equilibrium, as the stress components approach the post-expansion condition at different rates.

Quadrant decomposition of the shear-stress producing motions showed that the magnitudes of the sweeps and ejections were strongly suppressed in the SPG boundary layer. This analysis was confirmed through instantaneous visualizations of the boundary layer, as well as conditionally averaged velocity fields. Given that the hairpin vortices are the primary contributors to the mean shear stress, it was speculated that the reduced shear stress may be due to the deformation of these structures. Supported by data from English (2013), it was shown that the weaker ejection events are likely due to the reduced vorticity within the hairpin vortices, as suggested by profiles of the mean prograde swirling strength. A summary of these findings is given in Fig. 7.50. It should be noted that this model provides an additional mechanism by which favorable pressure gradients lead to the attenuation of the Reynolds shear stress, and does not necessarily address or refute any effects due to bulk dilatation.

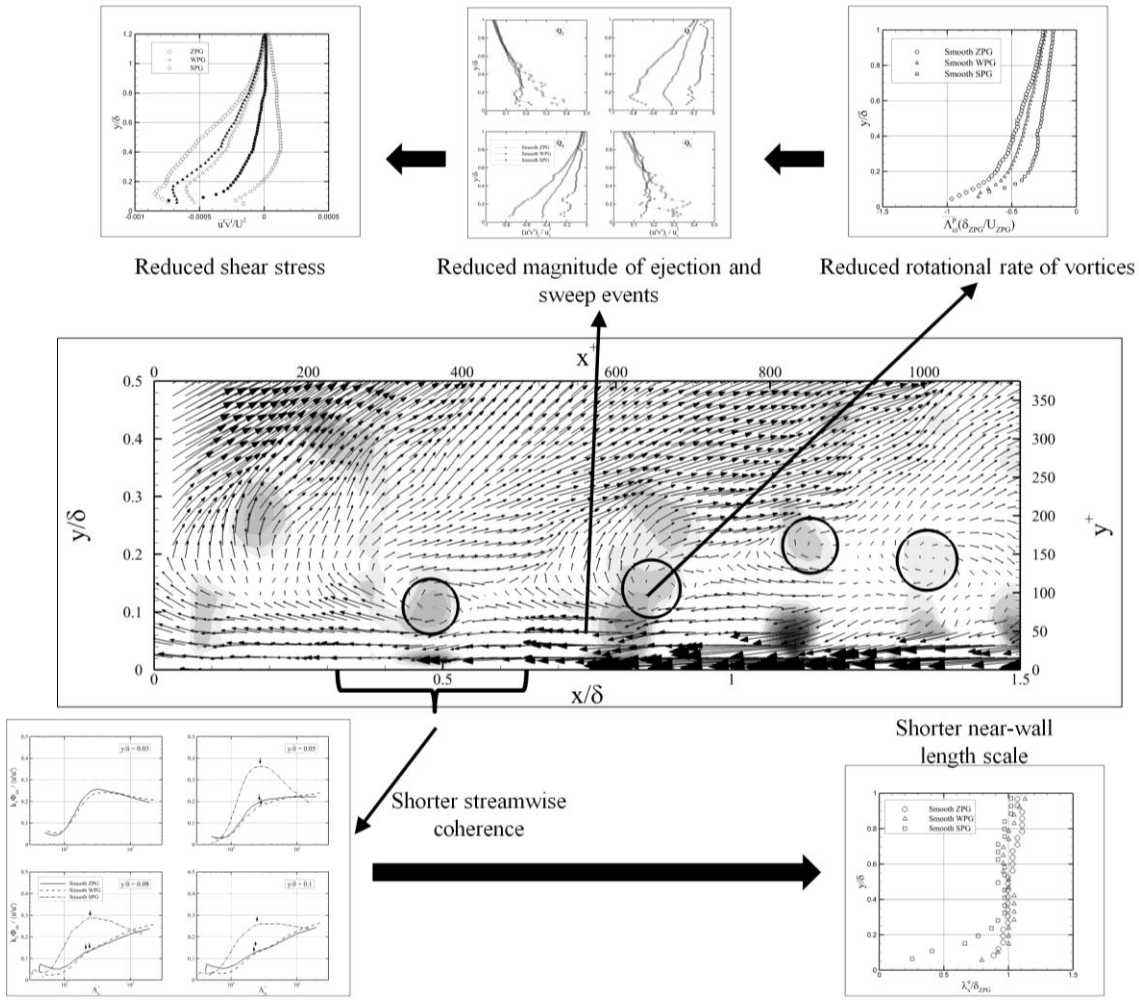

Figure 7.50 Summary of FPG results, showing the relation between the deformation of the turbulent structures and the measured Reynolds shear stress

8. BOUNDARY LAYER RESPONSE TO PERIODIC SURFACE ROUGHNESS

The previous sections have described the state of the undistorted boundary layer structures (§6), and how the deformation of these structures within a favorable pressure gradient (FPG) are manifested within the Reynolds stresses (§7). Using similar analysis techniques, the primary goal of the current section is to describe the response of the boundary layer structures to a diamond roughness topology, and to develop a framework linking the turbulent structure deformation to the Reynolds stress response. The insight gained in the previous chapters is instrumental to the analyses given below, as Ekoto *et al.* (2009) has shown that the shear stress response to a diamond roughness topology can be attributed to alternating favorable and adverse pressure gradients. Recall from §7 that the reduction in Reynolds shear stress through a favorable pressure gradient may be due to a "weakening" of the hairpin vortices, inhibiting their ability to contribute to the mean shear stress. Therefore, a secondary objective of this section is to assess the applicability of this theory to a local roughness-induced pressure gradient.

8.1. Flow Visualization

Prior to analyzing the mean flow and turbulent response of the rough-wall boundary layer, it was necessary to qualitatively describe the roughness-induced flow distortions. While the available experimental data for rough-wall supersonic boundary layers is severely limited (see §2.3 and Table 2.1), it has been shown that large roughness elements can generate periodic disturbances within the boundary layer [Latin & Bowersox (2000); Ekoto *et al.* (2009)]. Similar disturbances are seen in the current study, using schlieren photography shown in Figs. 8.1 and 8.2 for the baseline and rough-wall models (see §4.1.2 and 4.1.3 for details of the experimental setup). The data in Fig. 8.1 were collected using a three-color cut-off filter oriented in the wall-normal direction, showing a clear delineation between the boundary layer and freestream, where the boundary layer is the red region along the tunnel floor. The distortions generated by

the diamond roughness elements are clearly seen in Fig. 8.1b, indicating a cyclical response of the mean density field, which corresponds to the periodic roughness pattern. An interesting feature is that these waves extend across the boundary layer and into the freestream, suggesting that the entire boundary layer thickness is perturbed by the surface roughness. Naturally, this would imply that the rough-wall similarity hypothesis [Raupach (1991)] is not applicable to the current study, as the roughness-generated shock waves and expansions fans provide an additional means by which the outer layer turbulence field may be perturbed by the surface roughness. This will be shown quantitatively in §8.3.

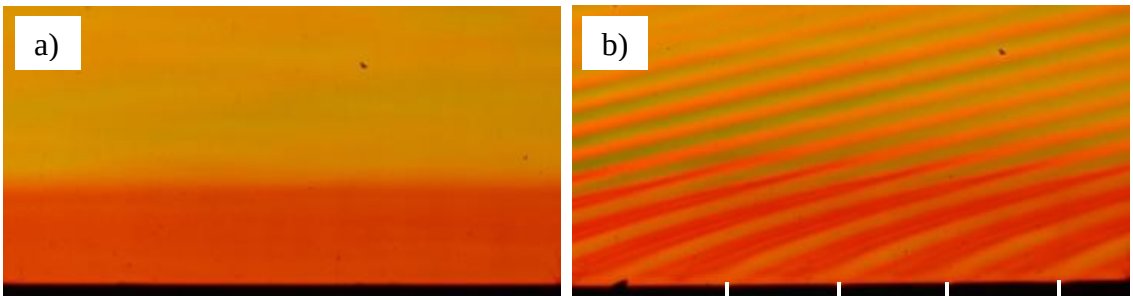

Figure 8.1 Schlieren images of smooth-wall (left) and diamond roughness (right) boundary layers. *A three-color filter was used as the cutoff. White lines in the diamond roughness image indicate the edges of the roughness elements. Flow is from left to right.*

The schlieren images in Fig. 8.1 indicate the response of the mean flow only, due to the use of a continuous light source (§4.1.2). By decreasing the duration of the illumination, it is possible to capture the instantaneous motions, providing a more accurate depiction of the boundary layer structure (§4.1.3). Additionally, the streamwise and wall-normal density gradients are viewed by rotating the cut-off filter by 90 degrees. These methods are applied to the smooth- and rough-wall boundary layers in Fig. 8.2.

The boundary layer edge is plainly visible through the wall-normal density gradient in Figs. 8.2a and 8.2c. In Fig. 8.2a, the fine-grained nature of the baseline turbulent

boundary layer is apparent, along with possible indications of structures oriented approximately 45 degrees relative to the wall, consistent with the observations by Poggie *et al.* (2004). This structure of the baseline flowfield appears markedly different when viewing the streamwise density gradient in Fig. 8.2b. The turbulent structures are more spatially compact, with no clear orientation angle. These trends are qualitatively similar to the length scales of the baseline flowfield, as seen in the premultiplied spectra of the axial and wall-normal fluctuating velocities (see §6.5).

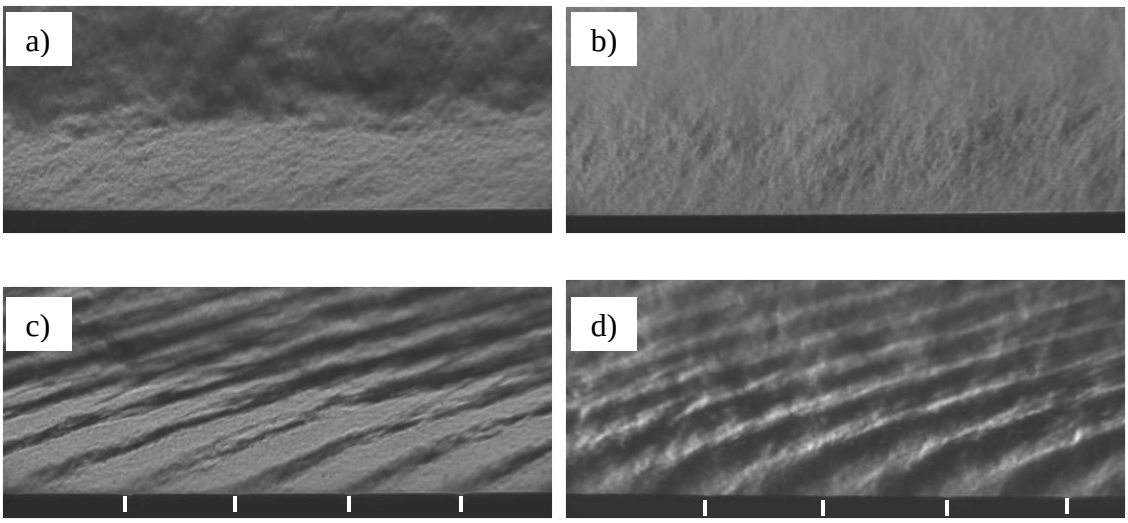

Figure 8.2 Schlieren images of smooth (top row) and diamond roughness (bottom row) boundary layers, using a short-duration spark-source. *Left column: wall-normal density gradient. Right column: streamwise density gradient. Flow is from left to right. White lines in the diamond roughness image indicate the edges of the roughness elements.*

The addition of surface roughness in Figs. 8.2c and 8.2d introduces significant distortions to the boundary layer, completely obscuring the orientation and spatial extent of any turbulent structures. This suggests that the roughness-induced waves are the dominant mechanisms for perturbing the flowfield. Indeed, the interaction between these distortions and the turbulent structures is a primary focus of this section. In Fig. 8.2c, the boundary layer edge is still discernible, though with a noticeably corrugated periphery.

Unlike the long-exposure schlieren data shown in Fig. 8.1b, the roughness-generated waves in Figs. 8.2c and 8.2d exhibit fluctuations in their instantaneous position and thickness, which is most likely related to the impact of turbulent structures advecting through the boundary layer (this is more clearly seen when the data are animated). The relation between the shock wave motion and the Reynolds stresses is not explored in this study, though future analyses may address this behavior.

8.2. Mean Flow Response

Schlieren imaging has qualitatively shown that the roughness-induced waves generate significant distortions within the boundary layer, consistent with the visualizations of Ekoto *et al.* (2009). The effects of these distortions upon the boundary layer parameters are seen in Table 8.1, showing increases in the boundary layer thickness δ, displacement thickness δ^*, and momentum thickness θ. Due to the lack of a known mean density field for the rough-wall case [see Appendix F], δ^* and θ are presented in Table 8.1 using the incompressible formulation. Note that the rough-wall boundary layer can be classified as "fully rough", as $k_s^+ > 70$. Correspondingly, the roughness elements are seen to occupy a large portion of the flow, with $k/\delta \approx 0.07$.

Table 8.1 Flow parameters for smooth and rough boundary layers

	Smooth	**Rough**
δ [mm]	10.9	11.3
δ^* [mm] (incompressible)	1.3	2.2
θ [mm] (incompressible)	1.0	1.4
u_τ [m/s]	35	69
Re_τ ($= \rho_w u_\tau \delta / \mu_w$)	1120	2330
ΔU^+	N/A	13
k_s [mm]	N/A	3.0
k^+	N/A	161
k_s^+	N/A	602
ε [mm]	N/A	0.3

8.2.1. Wall-Normal Profiles

Following the procedure used in §6 and §7, velocity profiles are extracted in the wall-normal direction, and averaged over a distance of 0.5δ to improve visualization. The boundary layer profile of the streamwise velocity component is given in Fig. 8.3, showing reduced velocity in the near-wall region, which can be attributed to the increased drag caused by the roughness elements. This effect can be clearly seen when the streamwise velocity is re-plotted in inner-scaled coordinates, using the van Driest II transformation (Fig. 8.4). The vertical shift of the rough-wall data ΔU^+ is approximately 13, suggesting that the roughness has a relatively large impact upon the buffer layer [Jiménez (2004)]. This differs from the value of 4.8 reported by Ekoto *et al.* (2009) at Mach 2.87 over an identical roughness topology, indicating a possible Reynolds number or compressibility effect. Additionally, the wake region of the rough-wall boundary layer is less pronounced than the baseline flowfield, with the rough-wall logarithmic region extending over a range $y^+ \approx 100 - 800$. The friction velocity was estimated by implementing the Clauser chart method. However, it has been shown that this method is imprecise when applied to rough-wall boundary layers [Perry *et al* (1969)], due to the multiple parameters necessary for a correct curve fit: effective origin ε, roughness function ΔU^+, and friction velocity u_τ. Attempting to determine these three parameters from a single plot results in an under-defined system, in which a range of combinations may yield a seemingly "correct" result. This range of acceptable values provides an estimate of the uncertainty of the friction velocity of ~15% for the rough-wall case. In contrast, the estimated smooth-wall friction velocity uncertainty was ~ 5%. For this study, the friction velocity is used as a "coarse adjustment" to match the $1/\kappa$ slope of the log-law, where κ is the von Karman constant. The effective origin ε is used to "fine-tune" the fit. Finally, the roughness function ΔU^+ was determined from the offset of the inner-scaled mean velocity.

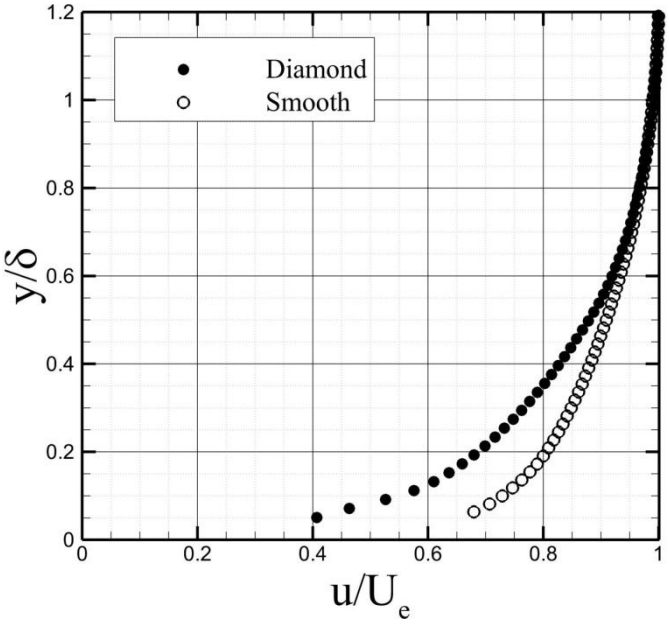

Figure 8.3 Streamwise velocity profiles of the smooth and rough flowfields. *Data were averaged over a distance of 0.5δ, to improve visualization.*

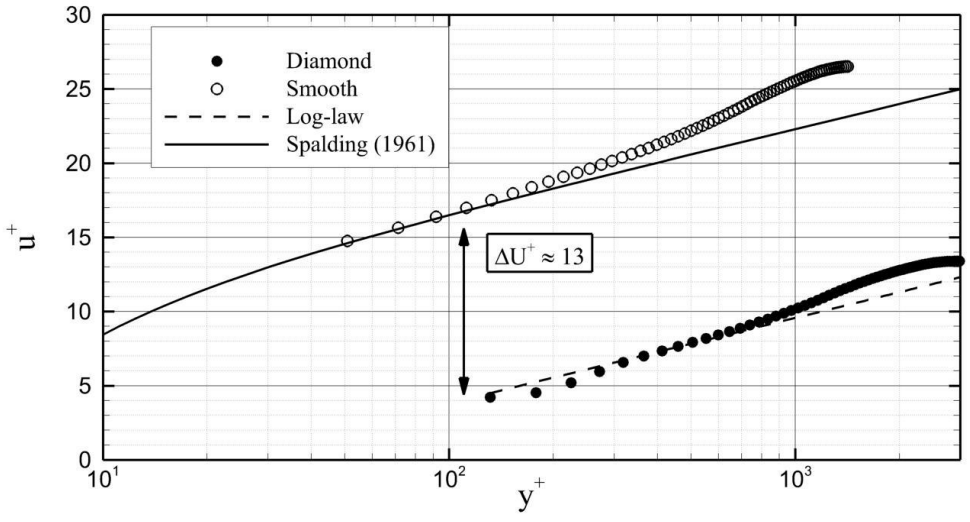

Figure 8.4 Inner-scaled streamwise velocity, presented using the van Driest II transformation. *Note the vertical displacement of the rough-wall profile, yielding a Clauser roughness function $\Delta U^+ \approx 13$. The friction velocity was estimated using the Clauser chart method.*

The boundary layer profiles presented in Figs. 8.3 and 8.4 were extracted over a streamwise distance of 0.5δ. However, it was shown in §3.3.1 that the roughness topology consists of a periodic array of diamond roughness elements, producing a three-dimensional pattern of repeating elements. This would appear to suggest that the flow evolution should be dependent upon the "phase" of the roughness pattern. In order to assess the sensitivity of the streamwise velocity to the spatial location, the inner-scaled velocity in Fig. 8.4 is re-plotted, with profiles averaged over three positions: over the element crest, over the element trough, and over the entire element. These positions are shown in Fig. 8.5, indicating minimal variation of the mean streamwise velocity. As such, the "element" position provides a suitable representation of the mean flow response.

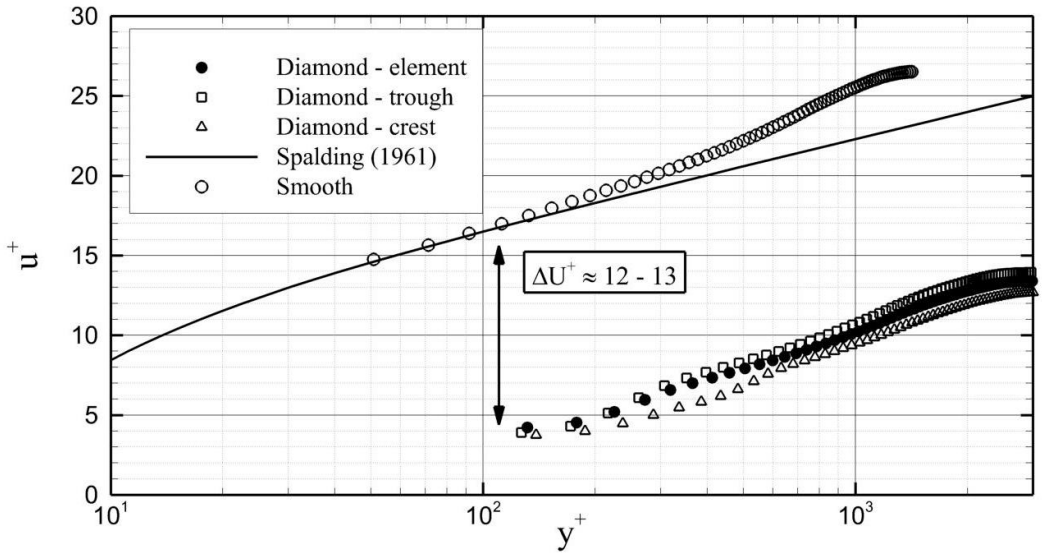

Figure 8.5 Comparison of the inner-scaled streamwise velocity, extracted from multiple positions over the roughness element. *Minimal variation of the streamwise velocity is observed over the roughness element, and is comparable to the uncertainty on the friction velocity.*

8.2.2. Streamwise Evolution

The PIV laser sheet was positioned over the center of the roughness elements (Fig. 8.6), capturing two full periods of the roughness pattern within the field of view (FOV). Initially, it was believed that the roughness topology would generate significant three-dimensional effects. However, pressure sensitive paint (PSP) experiments by Ekoto *et al.* (2009) and unpublished DES simulations by Dr. R. Srinivasan suggested that the shock waves and expansion fans generated by the roughness elements merged into a quasi-two-dimensional structure at a small distance above the roughness elements. Recent PIV measurement by English (2013) in the *x*-*z* plane at $y/\delta = 0.2$ support these conclusions, suggesting that the rough-wall boundary layer can be viewed as a two-dimensional flowfield.

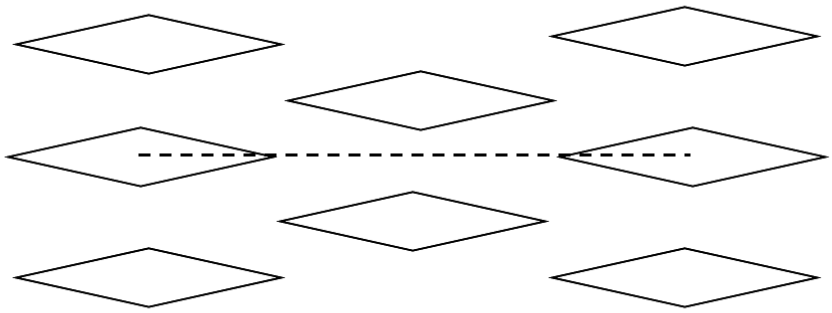

Figure 8.6 Positioning of PIV laser sheet over the roughness topology. *Flow is from left to right. The thickness of the sheet is under-exaggerated in the current figure. The actual sheet thickness is comparable to the spanwise width of the roughness elements.*

The FOV of the current experiment illustrates the streamwise evolution of the mean flow, over two periods of the roughness topology. The streamwise velocity is extracted at multiple heights and shown in Fig. 8.7, following the cyclical behavior indicated by

the schlieren images in §8.1. Note that the velocity amplitude response is approximately 0.02u/U at y/δ = 0.24, decreasing to less than 0.01u/U in the outer region. This diminishing response is most likely attributable to the shock angles seen in Fig. 8.1b, which are more wall-normal in the near-wall region. A similar comparison of the wall-normal velocity evolution in Fig. 8.8 shows a comparable oscillatory behavior, with a variation of approximately 0.01v/U. However, unlike the profiles of u/U in Fig. 8.7, the wall-normal velocity experiences a sign change across the FOV. This behavior is discussed more thoroughly in Appendix G.

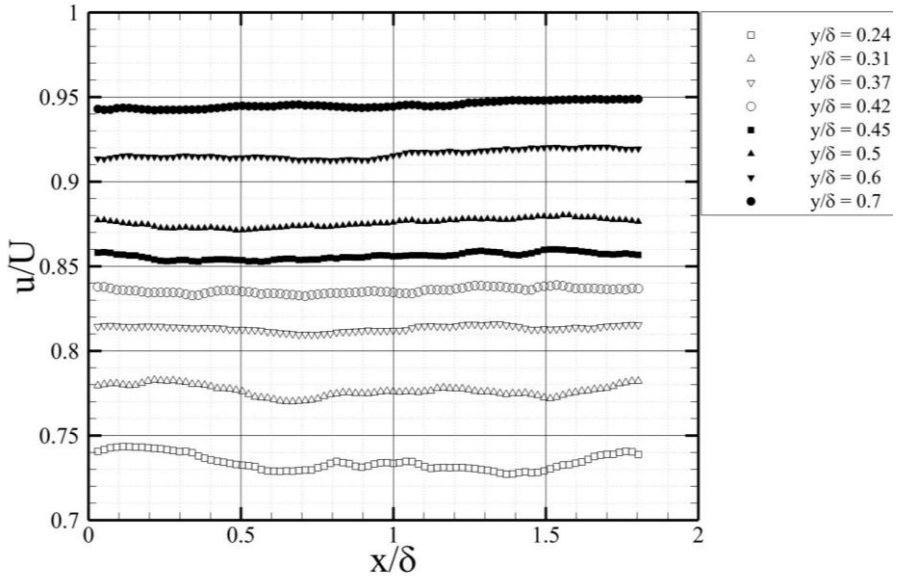

Figure 8.7 Streamwise evolution of rough-wall velocity *u/U*, plotted versus *x/δ*. *Note the increased oscillation amplitude in the near-wall region.*

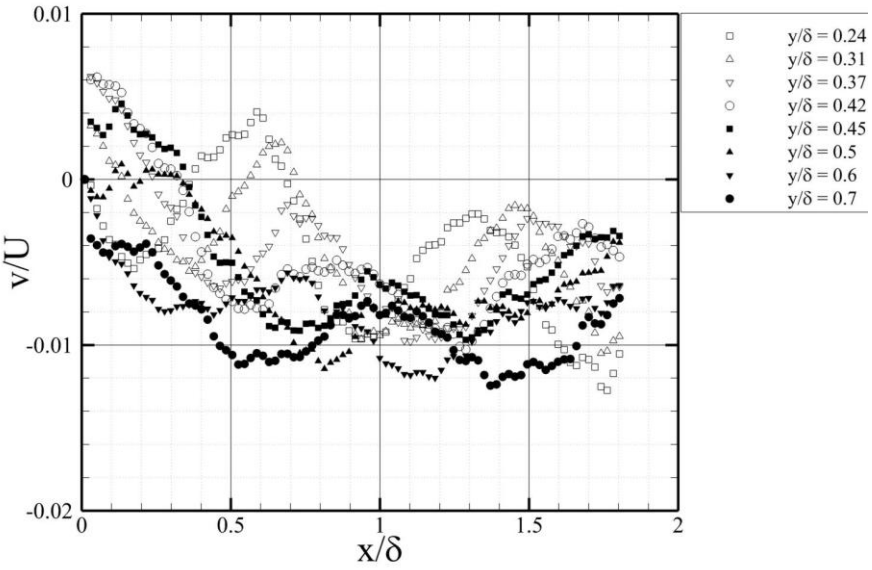

Figure 8.8 Streamwise evolution of rough-wall velocity *v/U*, plotted versus *x/δ*. *The sign reversal of the wall-normal velocity is addressed in Appendix G.*

8.3. Reynolds Stress Response

8.3.1. Streamwise Evolution

Prior to examining the wall-normal distribution of the Reynolds stress components, it is imperative that the streamwise evolution be fully characterized. As shown in Fig. 8.5, the wall-normal profile of the inner-scaled streamwise velocity experiences minimal evolution over a roughness element. Streamwise averaging over a roughness element provides a suitable representation of the boundary layer response. A similar comparison is made for the axial, wall-normal, and shear stress components in Figs. 8.9 – 8.11, respectively.

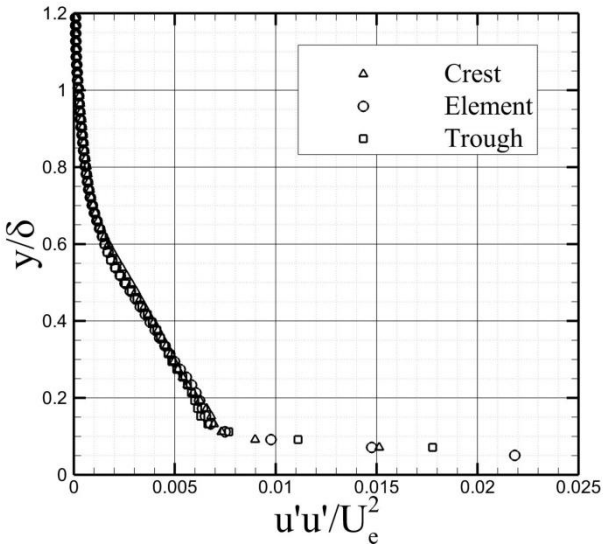

Figure 8.9 Rough-wall axial stress, extracted from multiple positions over a roughness element. *Negligible variation is observed between the profile locations.*

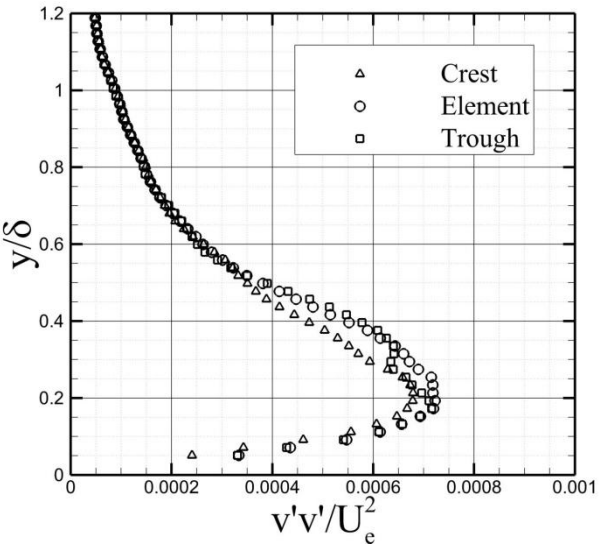

Figure 8.10 Rough-wall wall-normal stress, extracted from multiple positions over a roughness element. *A 7% variation is observed between the profile locations, below $y/\delta = 0.5$.*

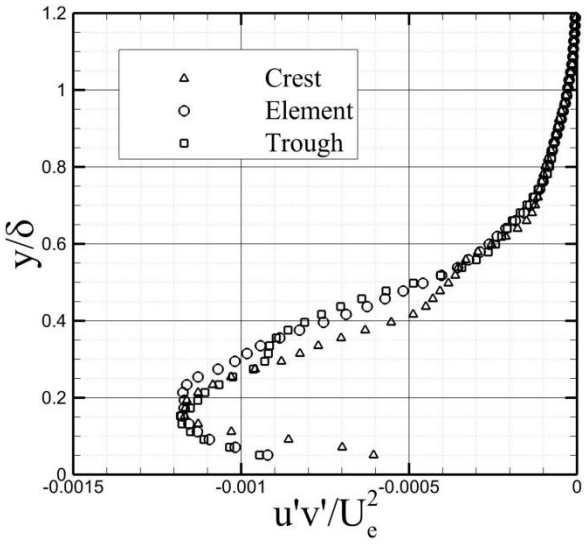

Figure 8.11 Rough-wall shear stress, extracted from multiple positions over a roughness element. *A 7% variation is observed between the profile locations, below y/δ = 0.5.*

The axial stress component is relatively insensitive to the streamwise position, varying by less than 2% (recall from §4 that the uncertainty on $\langle u'u' \rangle$ is approximately 5%). In contrast, the wall-normal and shear stresses in Figs. 8.10 and 8.11 vary by approximately ± 7% about the "element" value below y/δ = 0.5. Above this height, all positions collapse onto a single curve for each stress component. Initially, this behavior appears counterintuitive, given the schlieren imagery described in §8.1. Logically, the reader may expect the axial and wall-normal stress components to oscillate in a similar fashion. A possible explanation for this response may be drawn from the small-disturbance equations for hypersonic flow. For high Mach number flowfields over a slender body, the Euler equations may be simplified to show that the majority of the flow disturbance occurs in the wall-normal direction. See Ch. 4 of Anderson (2006) for the complete derivation. While the current study is neither hypersonic nor inviscid, an analogous phenomenon may be responsible for the negligible axial stress variation.

The mean shear stress *u'v'* is extracted at multiple heights within the boundary layer, and plotted versus *x/δ* in Fig. 8.12. As seen in Fig. 8.7 for the mean streamwise velocity, the amplitude response of the shear stress decreases with increasing distance from the wall. This response was originally attributed by Ekoto *et al.* (2009) to alternating adverse and favorable pressure gradients, which were generated by the wave pattern visible in Figs. 8.1 – 8.2. Note that the favorable pressure gradient effect is not sufficiently strong enough to produce a sign reversal of the shear stress, as was seen in §7. Additionally, the magnitude of the shear stress in the current study remains greater than the corresponding smooth-wall value, despite the stabilizing effect of the favorable pressure gradient, for $y/\delta < 0.4$. Above this height, the shear stress magnitude within the roughness-generated expansion fans is less than the corresponding smooth-wall value at that height. The significance of this behavior is seen more clearly in the following sub-section.

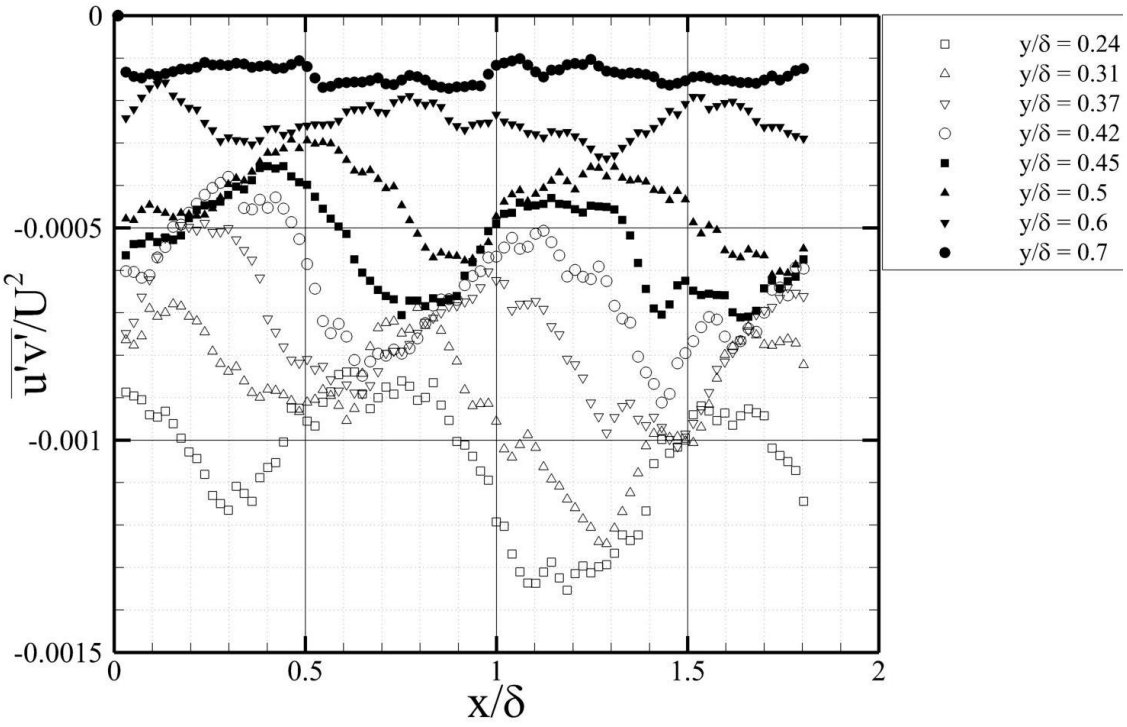

Figure 8.12 Streamwise evolution of rough-wall shear stress, plotted versus *x/δ*. *Note the increased oscillation amplitude in the near-wall region.*

8.3.2. Wall-Normal Profiles

Given the moderate spatial variation of the Reynolds stress components in Figs. 8.9 – 8.11, all wall-normal profiles presented hereafter will be averaged over a full roughness element. This is performed for the Reynolds stresses in Figs. 8.13 – 8.15, and compared to the corresponding smooth-wall profiles. When scaled by the respective friction velocities, it is immediately apparent that the rough-wall stresses are severely reduced below the baseline case, with magnitudes ranging from 25% to 40% of the smooth-wall values. Prior to inspecting these profiles, it was anticipated that the rough-wall axial stress would be slightly attenuated in the near-wall region, due to the increased form drag of the roughness elements [Grass (1971)]. However, the magnitude of the observed attenuation was unprecedented, and is far greater than that seen in any incompressible study. Typically, the inner-scaled Reynolds stresses are equal to or greater than the smooth-wall values [Krogstad, Antonia & Browne (1992); Antonia & Krogstad (2001); Latin & Bowersox (2000)]. Small decreases have been observed over varying roughness geometries [Flack, Schultz & Connelly (2007); Amir & Castro (2011)], though in some cases these reductions may be attributed to measurement uncertainty. The only known study to have observed a similar reduction in rough-wall stresses was the Mach 7.3 experimental work of Sahoo *et al.* (2010), performed over diamond mesh and *d*-type square bars.

In an effort to explain the reduced stresses observed in Figs. 8.13 – 8.15, note that all Reynolds stresses were scaled by the square of their respective friction velocities. Since the rough-wall friction velocity is approximately 100% larger than the smooth-wall value (Table 8.1), it is possible that the observed discrepancies in Figs. 8.13 – 8.15 were simply due to the choice of scaling parameter. To better assess the relative changes in the turbulence, the data were re-plotted in Figs. 8.16 – 8.18 with a common scaling, which in this case was the smooth wall friction velocity $u_{\tau(sm)}$. This has the added benefit of reducing the uncertainty of the inner-scaled stresses, which is worsened by the

increased uncertainty of the rough-wall friction velocity. Note that the re-scaled stresses show considerably better agreement between the rough-wall and baseline flowfields.

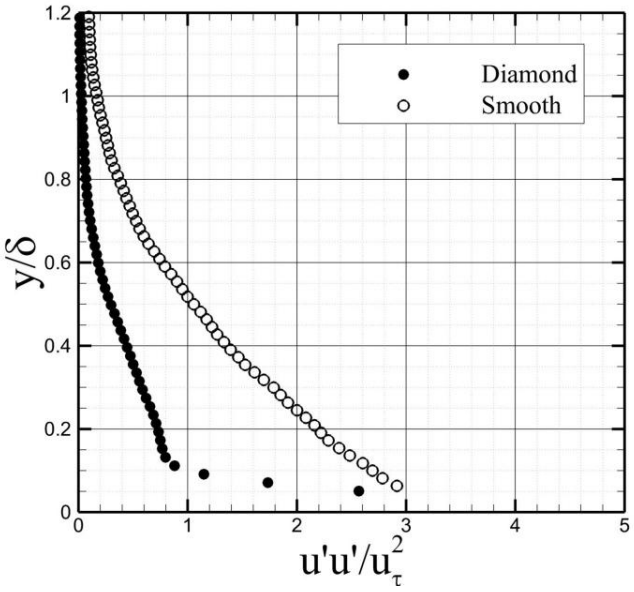

Figure 8.13 Inner-scaled axial stress. *Data are scaled by the respective friction velocities.*

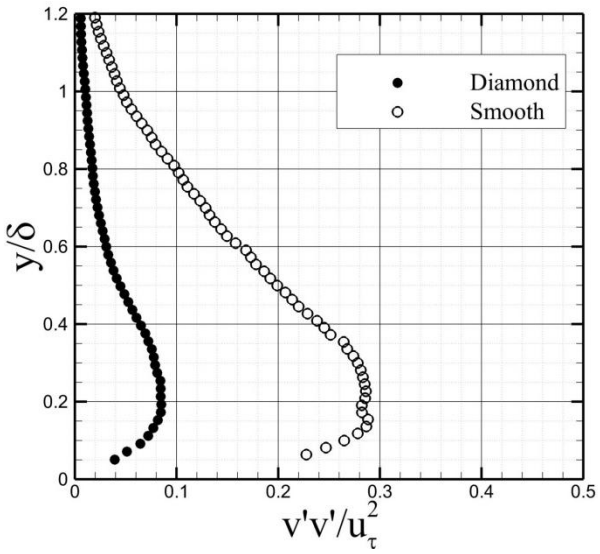

Figure 8.14 Inner-scaled wall-normal stress. *Data are scaled by the respective friction velocities.*

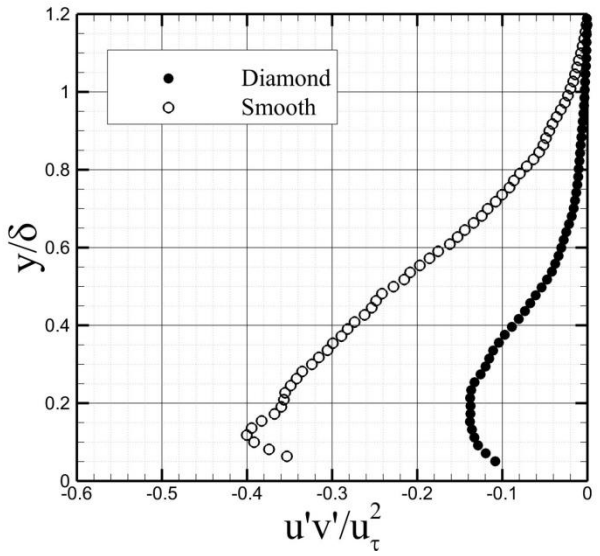

Figure 8.15 Inner-scaled shear stress. *Data are scaled by the respective friction velocities.*

All three stress components in Figs. 8.16 – 8.18 exhibit a bimodal behavior, with the outer-region rough-wall stresses decreasing by approximately 7%, 35%, and 50% for the

axial, transverse, and shear components, respectively. Near y/δ = 0.2, the rough-wall Reynolds stresses increased by 25%, 20%, and 35% over the smooth-wall values. For all components, the "crossover point" at which the rough- and smooth-wall stresses are equal is approximately y/δ = 0.45 – 0.5. A similar response was observed by Ekoto *et al.* (2009) at Mach 2.87. Their data showed that the diamond roughness pattern produced a larger shear stress than the smooth wall below y/δ = 0.4, when both cases are scaled by the same reference conditions [see Fig. 12a of Ekoto *et al.* (2009)]. Above this height, the shear stress dropped below the baseline values.

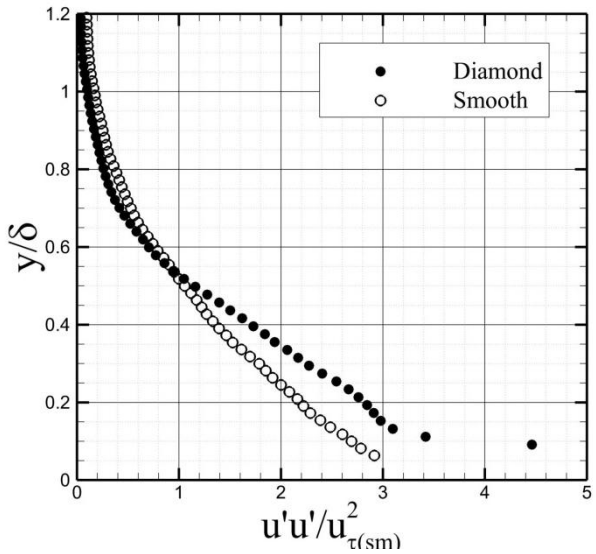

Figure 8.16 Inner-scaled axial stress. *Data are scaled by the smooth-wall friction velocity.*

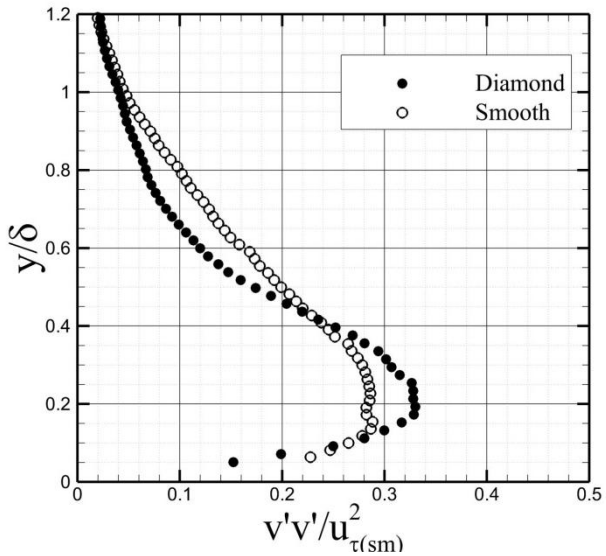

Figure 8.17 Inner-scaled wall-normal stress. *Data are scaled by the smooth-wall friction velocity.*

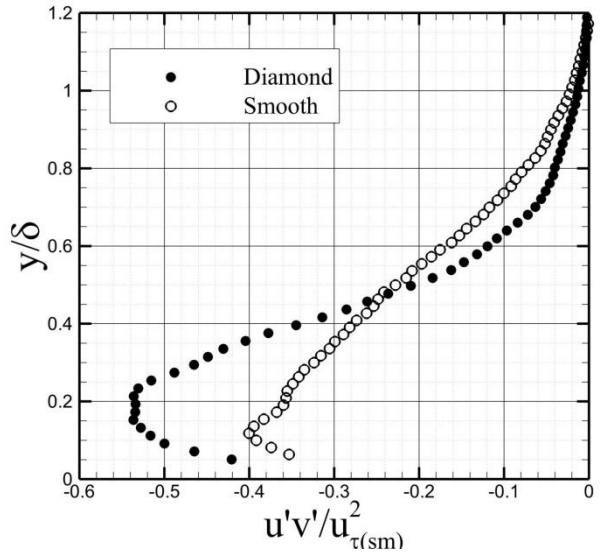

Figure 8.18 Inner-scaled shear stress. *Data are scaled by the smooth-wall friction velocity.*

As stated previously, the inner-scaled Reynolds stresses of Sahoo *et al.* (2010) indicated a dramatic decrease in the rough-wall values, similar to the current study. In order to support the common scaling used in Figs. 8.16 – 8.18, the 0.75 mm diamond mesh roughness (k/δ = 0.06) of Sahoo *et al.* (2010) is re-scaled in a similar fashion. The axial and transverse stresses are presented in Figs. 8.19 – 8.20, comparing the effects of the scaling parameter. Remarkably, the re-scaled data of Sahoo *et al.* (2010) follow a comparable trend to the current study, with increased stresses below y/δ = 0.4 – 0.5. It is interesting to note that the observed stress reductions have only occurred in high-Mach number studies, suggesting that the roughness-generated wave patterns may be a key phenomenon in the Reynolds stress evolution. This also complicates any comparisons with incompressible data, as these features are not present in subsonic flowfields.

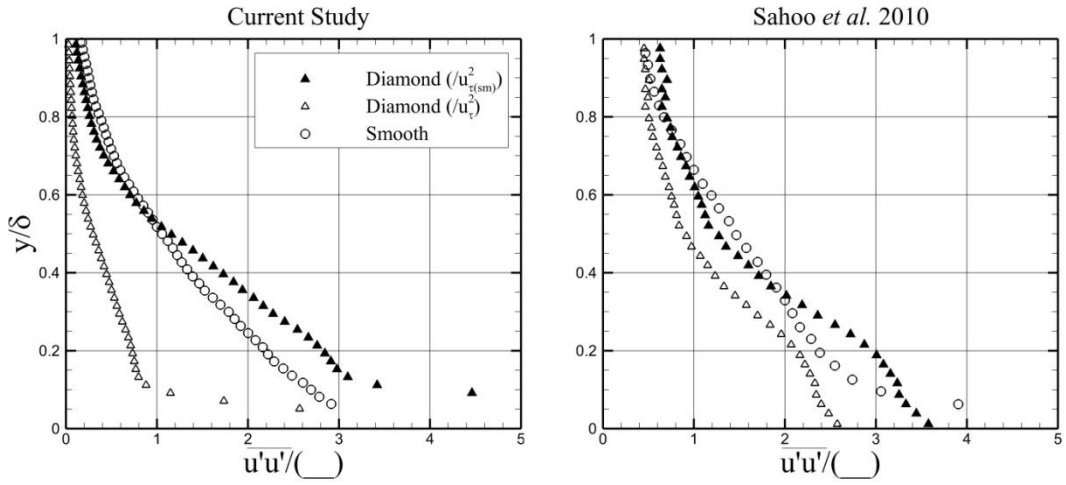

Figure 8.19 Comparisons of scaling effects upon the axial stress. Left: current study. Right: Sahoo *et al.* (2010)

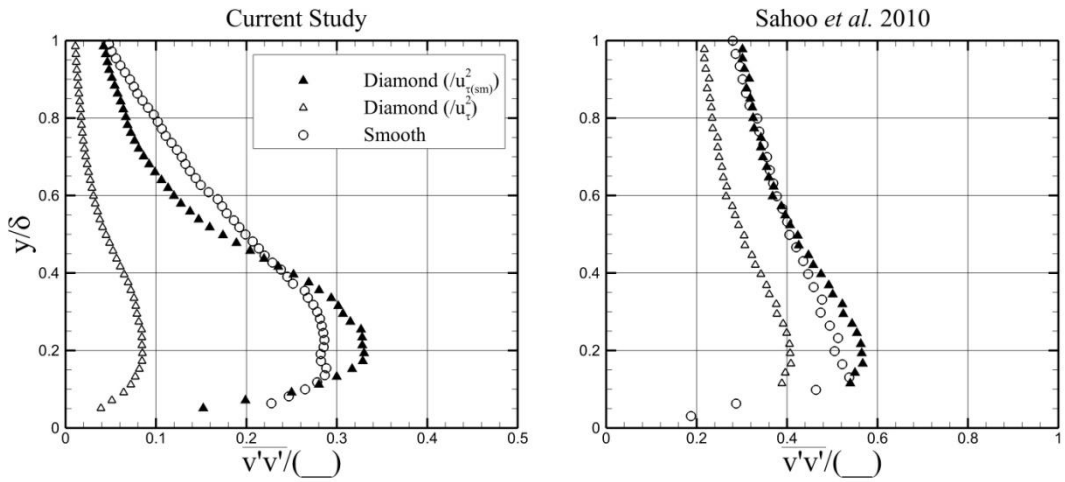

Figure 8.20 Comparisons of scaling effects upon the wall-normal stress. Left: current study. Right: Sahoo *et al.* (2010)

Before continuing with the current analyses, a brief comment upon the Reynolds stresses in Figs. 8.16 – 8.18 is necessary. Recall that the cyclical response of the rough-wall boundary layer is attributed to alternating adverse and favorable pressure gradients, due to the shock waves and expansion fans generated by the roughness elements [Ekoto *et al.* (2009)]. The bimodal response of the re-scaled stresses suggests that the roughness-induced pressure gradients may also affect the stress distribution in the wall-normal direction. The decreased stress in the outer half of the boundary layer is consistent with the influence of a favorable pressure gradient [Spina *et al.* (1994); Bradshaw (1974); Dussauge & Gaviglio (1987)], while the near-wall response may be due to an adverse pressure gradient. However, the reader is cautioned that this speculation is predicated upon the notion that the smooth-wall friction velocity $u_{\tau(sm)}$ is the correct scaling parameter. This choice of scaling is discussed further in §8.7, using additional experimental evidence as justification.

8.3.3. Shear Stress-Producing Events

The re-scaled stresses in Figs. 8.16 – 8.18 show that the roughness primarily affects the wall-normal and shear stress components, consistent with existing literature [Krogstad *et al.* (1992); Krogstad & Antonia (1999)]. This suggests a particular sensitivity of the "active motions" [Townsend (1976)] to the surface condition. In order to characterize these motions, probability density functions (PDFs) of the instantaneous shear stress $u'v'$ are computed at multiple heights within the boundary layer, and compared to the baseline flowfield in Fig. 8.21. The instantaneous motions are scaled by the smooth-wall friction velocity, such that $u'v'/u^2_{\tau(sm)} = (u'v')^+_{(sm)}$.

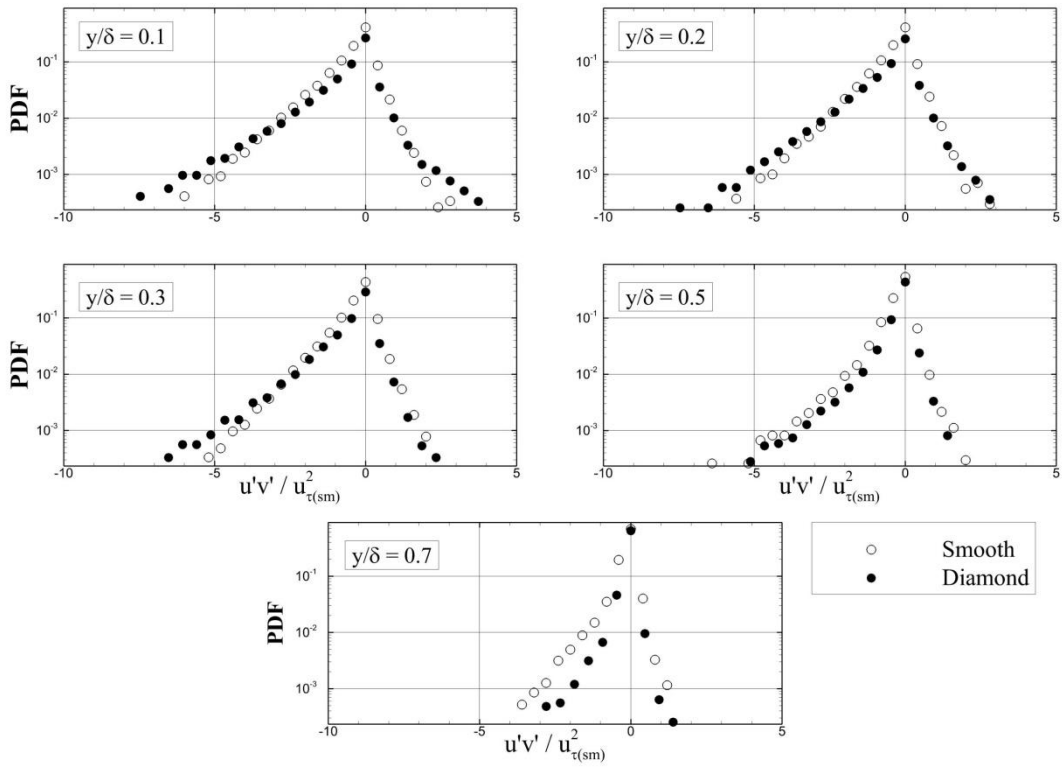

Figure 8.21 PDFs of the instantaneous shear stress events, scaled by the smooth-wall friction velocity.

The skewed nature of the PDFs in Fig. 8.21 is consistent with the negative mean shear stress in Fig. 8.18. Excepting the large-magnitude events at $y/\delta = 0.1$, the positive shear stress events in Fig. 8.21 appear unaffected by the surface roughness. The evolution of the mean shear stress in Fig. 8.18 is therefore primarily due to the negative shear stress events. At all heights within the boundary layer, the population of low-magnitude negative $u'v'$ events ($|u'v'| < 2.5u^2_{\tau(sm)}$) is reduced for the rough-wall case. This is counter-balanced by an attendant increase in the number of large-magnitude events, for the near-wall region $y/\delta \leq 0.3$ over the diamond roughness. As the distance from the wall increases, the population of the large-magnitude shear stress events decreases below the smooth-wall value. The wall-normal evolution of the rough-wall shear stress is thus solely a function of the significant negative $u'v'$ events. This behavior is similar to that observed by Wu & Christensen (2006b) over a short fetch of "real roughness", replicated from a damaged turbine blade. They observed that the roughness primarily increased the population of large-magnitude negative $u'v'$ events in the near-wall region, though no change in the small-magnitude motions was observed.

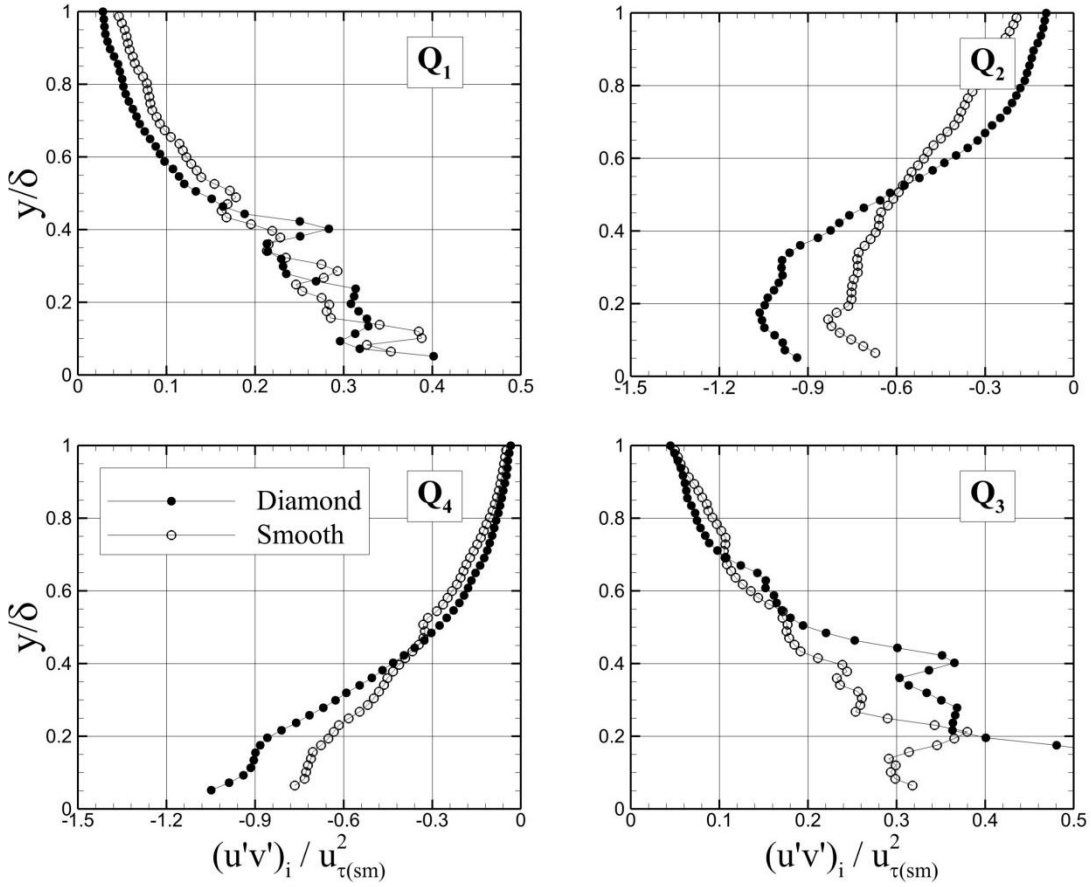

Figure 8.22 Stress contributions of quadrant events, as determined by quadrant decomposition. *Note the different axis limits for the Q1 and Q3 events.*

The shear stress events described in Fig. 8.21 indicate that the roughness is responsible for suppressing the low-magnitude negative *u'v'* motions throughout the boundary layer, while the population of large-magnitude events is a function of *y/δ*. The physical significance of these events is best characterized through quadrant decomposition, in which the shear stress-producing motions are binned according to the sign of the *u'* and *v'* fluctuations (see §4.4.3 for a description of this technique). The shear stress contributions of the respective quadrants are shown in Fig. 8.22, for a hole size H = 0. The rough-wall Q1 and Q3 events are attenuated by approximately 10% in the outer region, though the increased noise in the near-wall region prevents any reliable

observation in this portion of the flow. The most significant changes are seen for the Q2 and Q4 events. Qualitatively, these rough-wall profiles match the mean shear stress trend, increasing in magnitude below $y/\delta \approx 0.5$. The magnitudes of the rough-wall Q4 events, which describe the entrainment of high-momentum fluid, are 10% lower than the smooth-wall values in the outer region. Near the wall, the Q4 events have increased to approximately 140% of the baseline magnitude. Krogstad *et al.* (1992) attributed this difference to the "open nature of the rough surface." However, the largest sensitivity to the surface condition is observed in the ejection (Q2) events. Below $y/\delta = 0.5$, the rough-wall ejections are 30% to 40% more intense than the baseline flow, though these roles are reversed in the outer region.

8.4. Spatial Organization of Large-Scale Structures

8.4.1. Two-Point Correlations

The rough-wall dimensional stresses in Figs. 8.16 – 8.18 follow a bimodal behavior, increasing beyond the smooth-wall magnitude in the near-wall region, while being attenuated below the baseline values in the outer region. In an effort to explain this distribution, autocorrelations of the streamwise fluctuating velocity are computed as

$$R_{uu}(\Delta x, y, y_{ref}) = \frac{u'(x, y_{ref})u'(x+\Delta x, y)}{\sqrt{\left\langle \left(u'(x, y_{ref})\right)^2 \right\rangle}\sqrt{\left\langle \left(u'(x+\Delta x, y)\right)^2 \right\rangle}} \tag{8.1}$$

and plotted for the outer region in Fig. 8.23. Recall from §2.1.2 that the *large-scale structures* are identified as "correlated mass(es) of fluid" [Arnette *et al.* (1995)]. Hence, the correlations in Fig. 8.23 describe the orientation and distribution of the large-scale motions in the outer region. These structures are significant in characterizing the Reynolds stress distribution, since a majority of the boundary layer turbulent kinetic energy (TKE) is contained the within long-wavelength motions.

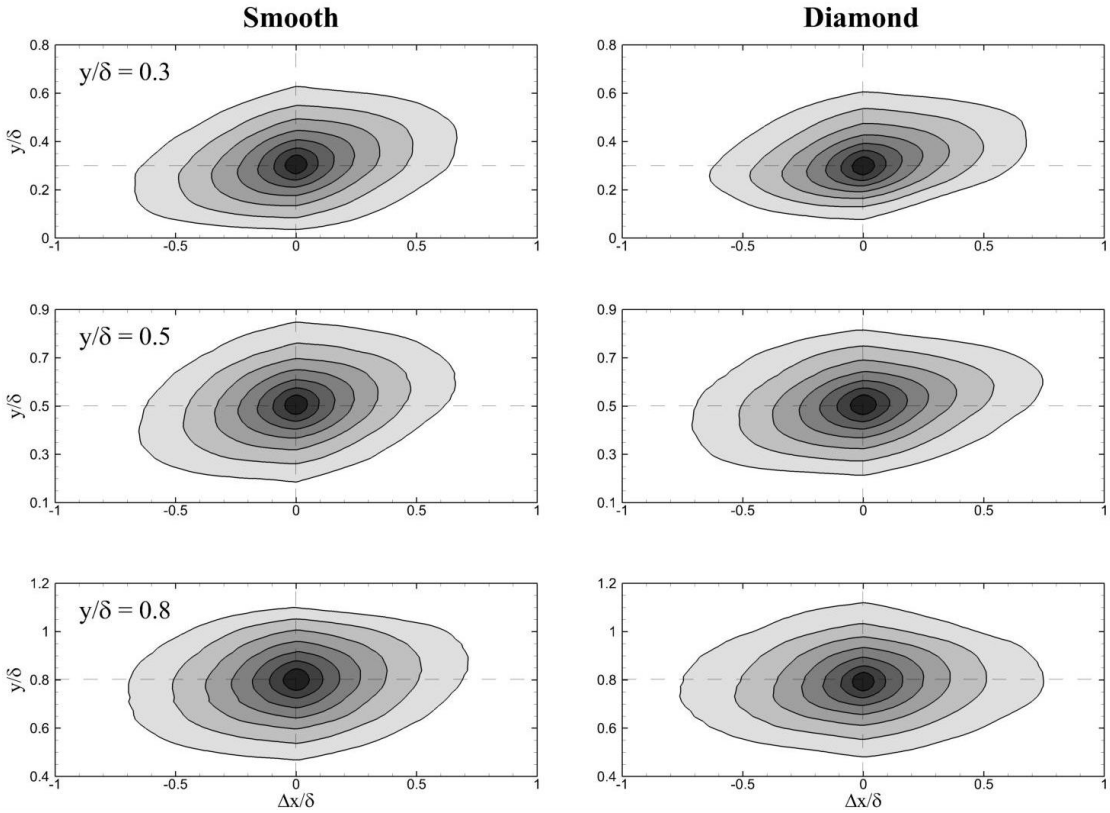

Figure 8.23 Two-point correlations of the fluctuating streamwise velocity, R_{uu}, plotted in the outer region $y/\delta \geq 0.3$

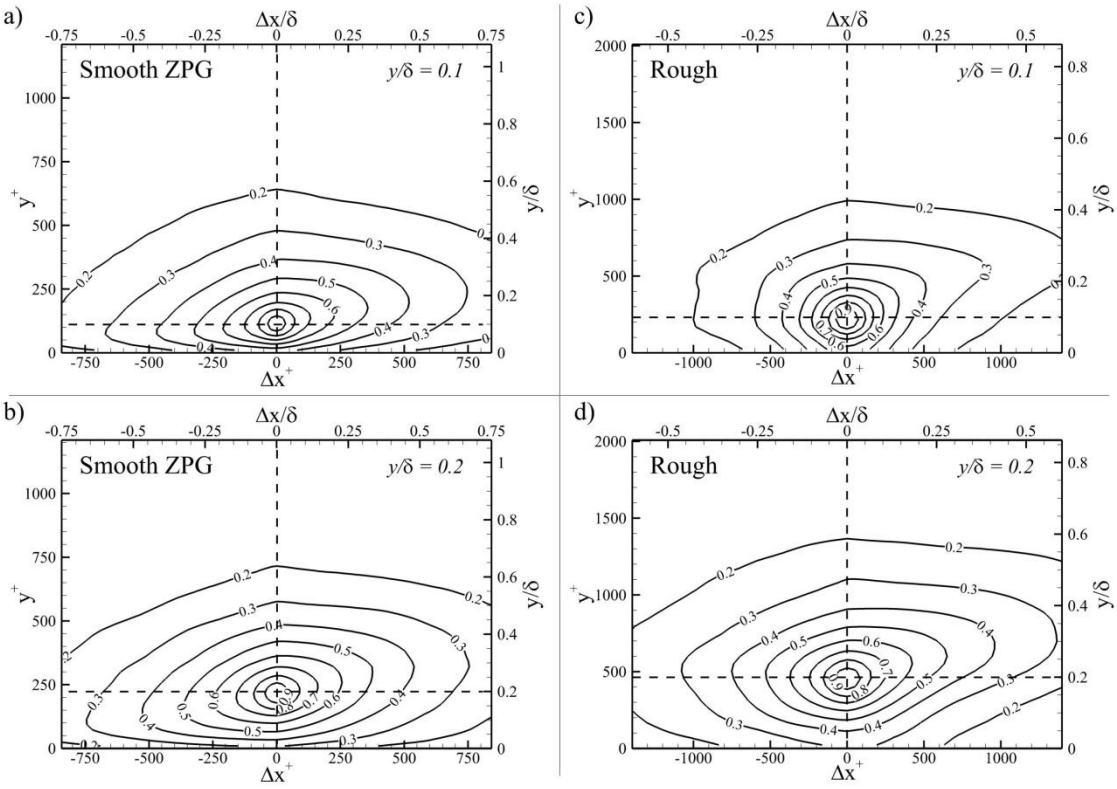

Figure 8.24 Two-point correlations of the fluctuating streamwise velocity, R_{uu}, plotted in the near-wall region. *Remarkable agreement is observed between the rough-wall correlations in panes* c) *and* d), *and the correlations of* Guala *et al.* (2012).

The rough-wall correlations in Fig. 8.23 closely follow the trends of the baseline flow, exhibiting an elliptical distribution rotated in the downstream direction. Additionally, the streamwise length scales appear qualitatively similar. This agreement between the large-scale motions was unanticipated, given that the rough-wall structures are traversing alternating shock waves and expansions fans. However, this similarity does not persist in the near-wall region $y/\delta \leq 0.2$, as shown in Fig. 8.24. While the baseline correlation maintains an elliptical shape, the rough-wall structure is increasingly distorted as y/δ decreases. At $y/\delta = 0.1$, the correlation over the diamond roughness is approximately 50% shorter in the streamwise direction, compared to the smooth-wall boundary layer. This reduced length scale, coupled with the asymmetric "lobe" on the upper downstream corner of the correlation, is remarkably similar to the near-wall correlation of the smooth

SPG flowfield in Fig. 7.15c. While this does not necessarily indicate a common mechanism for these effects, it is interesting that a global favorable pressure gradient and a periodic roughness topology (which produces alternating favorable and adverse pressure gradients) both experience an equivalent response of the near-wall large-scale structures. A similar correlation was also seen by Guala *et al.* (2012) over a sparse array of hemispherical roughness elements in an incompressible boundary layer [see Fig. 2b of Guala *et al.* (2012)]. They noted that the R_{uu} = 0.2 isocontour followed the smooth-wall trend, and attributed the correlation shape to a "superposition of existing large-scale motions away from the wall and small-scale structures shed from the upstream hemisphere." This explanation is inadequate for the current study, as even the lower correlation values deviate from the smooth-wall structure.

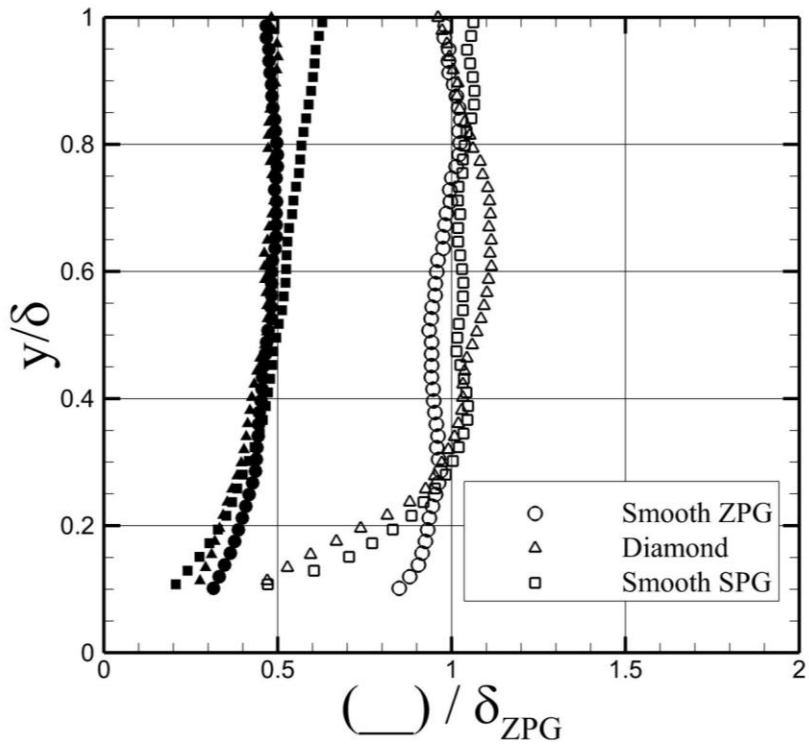

Figure 8.25 Major and minor axes of the two-point correlations, determined from the R_{uu} = 0.4 isocontour. *Dimensions are scaled by the smooth-wall boundary layer thickness. The response of the favorable pressure gradient is overlaid onto the graph, showing a similar scale reduction in the near-wall region, when compared to the rough-wall flow.*

Following the procedure used in §7.3, the $R_{uu} = 0.4$ isocontours in Fig. 8.23 – 8.24 are approximated as ellipses through a least-squares fit. At each height, the inclination and dimensions are extracted, and compared between the baseline and rough-wall cases. The dimensional major and minor axes are compared in Fig. 8.25, scaled by the smooth-wall boundary layer thickness (though recall from Table 8.1 that the rough-wall δ is only 4% larger than the baseline value). There is excellent agreement between the smooth- and rough-wall boundary layers for the minor axis length, suggesting that the only deformation of the large-scale structures occurs along the longitudinal axis. Over the range $y/\delta = 0.3 – 0.8$, the rough-wall major axis is approximately 10% – 15% larger than the smooth-wall curve, though both flowfields may be described as possessing δ-scale motions. Below this range, the surface roughness contributes to a rapidly decreasing length scale, nearing 0.5δ at $y/\delta = 0.1$, which is consistent with behavior of the two-dimensional correlation in Fig. 8.24. While the decreased length scale of a rough-wall boundary layer is consistent with existing literature [Grass (1971)], the length scale reduction of the current study is confined to only the near-wall region. Both Guala *et al.* (2012) and Krogstad & Antonia (1994) have observed shortened structures throughout the boundary layer thickness, though it should be noted that these studies were conducted under incompressible conditions, and thus lacked the roughness-generated waves present over the current geometry. This difference may be significant, since the reduced longitudinal extent of the rough-wall structures has been attributed to the form drag of the roughness elements [Grass (1971)]. If the authors are correct in speculating that the near-wall region is dominated by adverse pressure gradient effects (see §8.3.2), then the increased wave drag would contribute to shorter length scales in that region of the flow. This hypothesis is discussed further in §8.8.

As stated above for the two-dimensional correlation, the response of the rough-wall boundary layer is remarkably similar to the behavior of the smooth SPG flow in §7. This similarity is illustrated by overlaying the major and minor axes of the smooth SPG boundary layer onto Fig. 8.25. For the lower 40% of the boundary layer, the major axes of the distorted flows nearly collapse onto a single curve. Grass (1971) suggested that

the shortened rough-wall length scales may be related to the increased magnitude of the ejection events. Interestingly, a comparable length scale trend is seen for the smooth SPG boundary layer, yet the quadrant events of the FPG flow have been dramatically reduced below the baseline values (see Fig. 7.8). At present, no explanation is available for this agreement between the surface roughness and FPG effects.

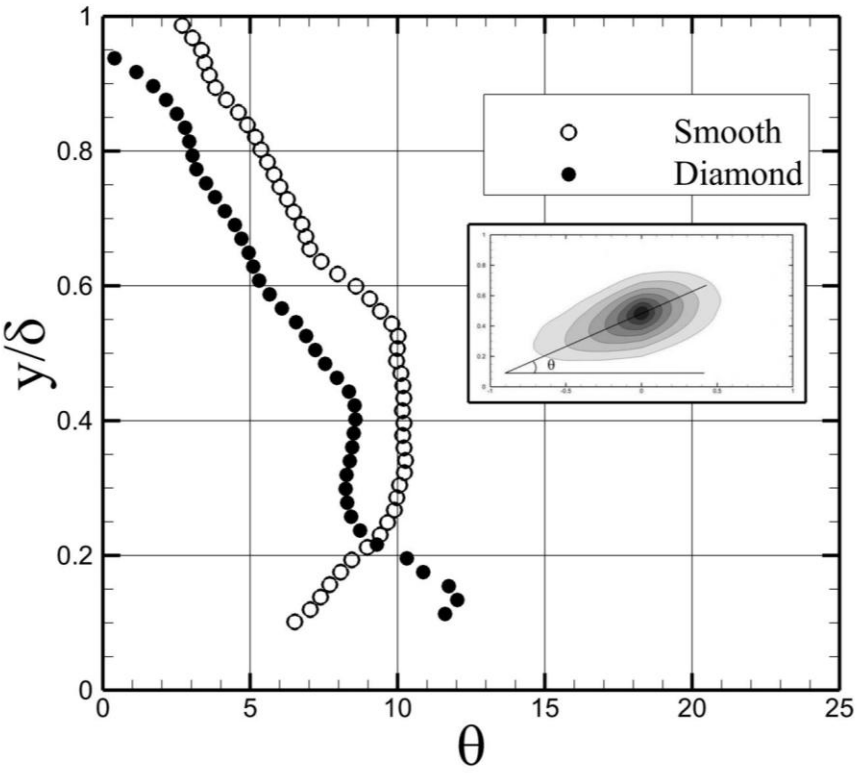

Figure 8.26 Orientation angle of the large-scale motions, determined from the R_{uu} = 0.4 isocontour.
Angle is given in units of degrees.

The orientation angles of the smooth- and rough-wall structures are presented in Fig. 8.26. Above y/δ = 0.2, the surface roughness contributes to a decreased structure inclination, approximately 2 degrees lower than the baseline boundary layer. In the near-wall region, the smooth-wall angle decreases in a linear fashion, from 10 degrees at y/δ =

0.3 to 6 degrees at y/δ = 0.1. In contrast, the rough-wall angle increases from 8 degrees to 12 degrees over a similar range. For both cases, the uncertainty of the orientation angle is approximately 2 – 3 degrees, which was estimated by comparing the scatter in the angles computed at R_{uu} = {0.3; 0.4; 0.5}. The increased rough-wall structure angle in the inner region qualitatively agrees with the findings of Krogstad and Antonia (1994), who showed that mesh roughness increases the angle of the coherent motions to approximately 38 degrees at y/δ = 0.16. However, the magnitude of their rough-wall structure angle is approximately four times the smooth-wall value, while the current study experiences an increase of approximately 100% at a similar height. They explained this trend by noting the increased wall-normal fluctuations over a rough surface, which may rotate the structures away from the wall. Wu & Christensen (2010) observed that the structure angles are relatively insensitive to the presence of irregular roughness, over the range y/δ < 0.4. Unfortunately, no additional data exists for the structure angle reorientation over a rough wall at supersonic conditions.

8.4.2. Streamwise Dependency

Before continuing, it is prudent to discuss the sensitivity of the two-point correlations to the streamwise position. As the large-scale motions traverse the shock waves and expansion fans, the fluid within the structure experiences alternating favorable and adverse pressure gradients. Therefore, it is reasonable to suggest that the state of these structures should be dependent upon the position relative to a roughness element. However, the following analysis shows this to be untrue.

The correlations discussed previously in this sub-section are repeated at three streamwise positions, centered over an element crest and trough. The third position is equidistant between the ends of a roughness element. The major axes and structure angles are extracted for each position, and compared in Figs. 8.27 – 8.28. Excepting outliers at y/δ = 0.1 and 0.3, the correlation parameters appear to be invariant with streamwise location,

to within experimental uncertainty. This result initially seemed counter-intuitive, given the previously observed effects of FPGs from §7. However, a logical argument can be made for this agreement, by examining the relevant length scales of the boundary layer.

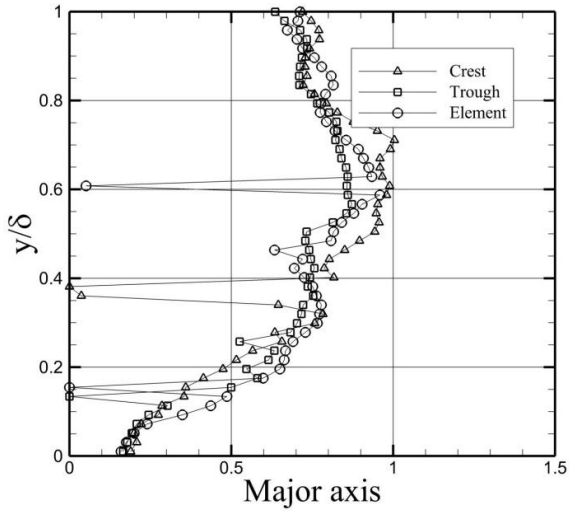

Figure 8.27 Streamwise dependency of major axis of large-scale motions, for rough-wall boundary layer. *Major axis is scaled by* δ.

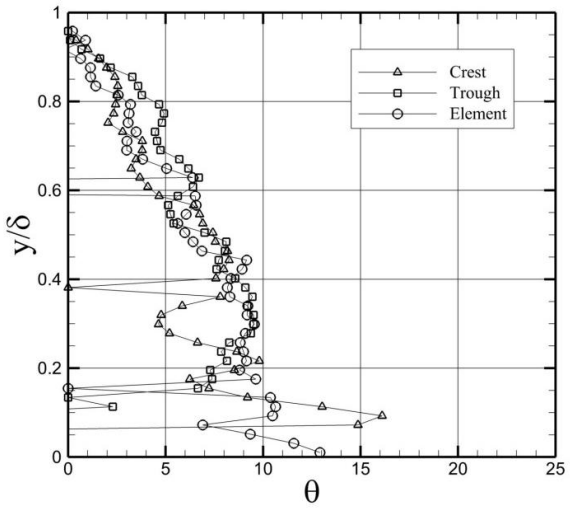

Figure 8.28 Streamwise dependency of the orientation angle of the large-scale motions. *The orientation angle is measured in degrees.*

Given that the coherent motions are primarily δ-scale (Fig. 8.25) and that the shock spacing is less than δ (as suggested by the geometry, and confirmed from the schlieren images), the coherent structures detected by the two-point correlations cannot wholly reside between two consecutive wave structures. The length of a single coherent structure will experience alternating compressions and dilatations along its length, corresponding to the adverse and favorable pressure gradients created by the shocks and expansions, respectively. As opposed to the reorientation produced by a single pressure gradient (Fig. 7.17), these oscillating distortions will produce a "crinkling" effect within the large δ-scale structures, without any net rotation of the fluid element. The reader should note that this sequence provides a possible explanation for the absent cyclical response of the coherent structure orientation, but does not suggest that these structures are unperturbed by the roughness elements. This sequence may also explain the lack of streamwise variation of the structure length scale, though Fig. 7.21 suggests that λ_x^u does not change appreciably through a favorable pressure gradient.

It should be noted that the pressure gradients within the rough-wall flow are not merely a periodic superposition of APGs and FPGs. The close proximity of these regions may in fact constrain their effect upon the fluid elements. For example, consider a single favorable pressure gradient region within the rough-wall flow. Reorientation in FPGs is partially due to streamline divergence through the expansion region [Humble *et al.* (2012)], leading to a larger structure angle. However, this region in the rough-wall flowfield is bounded by a shock wave, limiting the area through which the streamlines can diverge. This can be restated as a function of the integrated (in time) flow distortion, by invoking the impulse parameter $I = \int_{t_1}^{t_2} e \, dt$ [Spina *et al.* (1994)]. As the spacing between the waves is decreased, the difference in the limits of integration will also decrease, curtailing the total impulse I. Therefore, it is possible that the close spacing of the roughness-induced distortions may dampen their effect on the coherent structures, thereby mitigating the cyclical response of the fluid elements.

8.4.3. Spectral Content

In order to provide a more complete view of the large-scale motions, the energy content within the streamwise length scales is examined through comparisons of the power spectral density (PSD). The premultiplied spectra of the fluctuating streamwise velocity Φ_{uu} are presented in Figs. 8.29 – 8.30. Recall from §4.4.2 that premultiplication is performed in order to aid visualization, such that equal areas of the graph describe equal energy content. Normalizing by the mean stress at each height allows the *relative* energy content within each flow scale to be described. All wavelengths are presented as outer-scaled, which is similar to comparing the dimensional scales, given that the rough- and smooth-wall boundary layer thicknesses vary by only 4%. While it was argued in §7.4 that the near-wall wavelengths should be inner-scaled, §8.3 showed that the Reynolds stresses are best viewed in dimensional form.

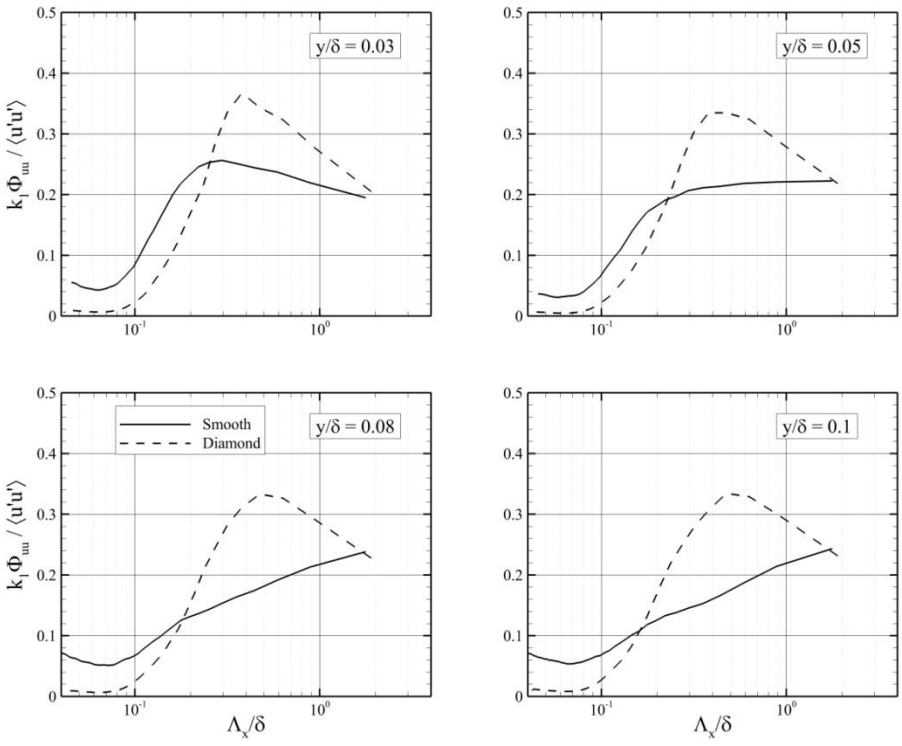

Figure 8.29 Premultiplied spectra of the fluctuating streamwise velocity, normalized by the mean axial stress at each height. *Spectra are shown for heights $y/\delta \leq 0.1$. The streamwise wavelengths are presented in outer-scaled format.*

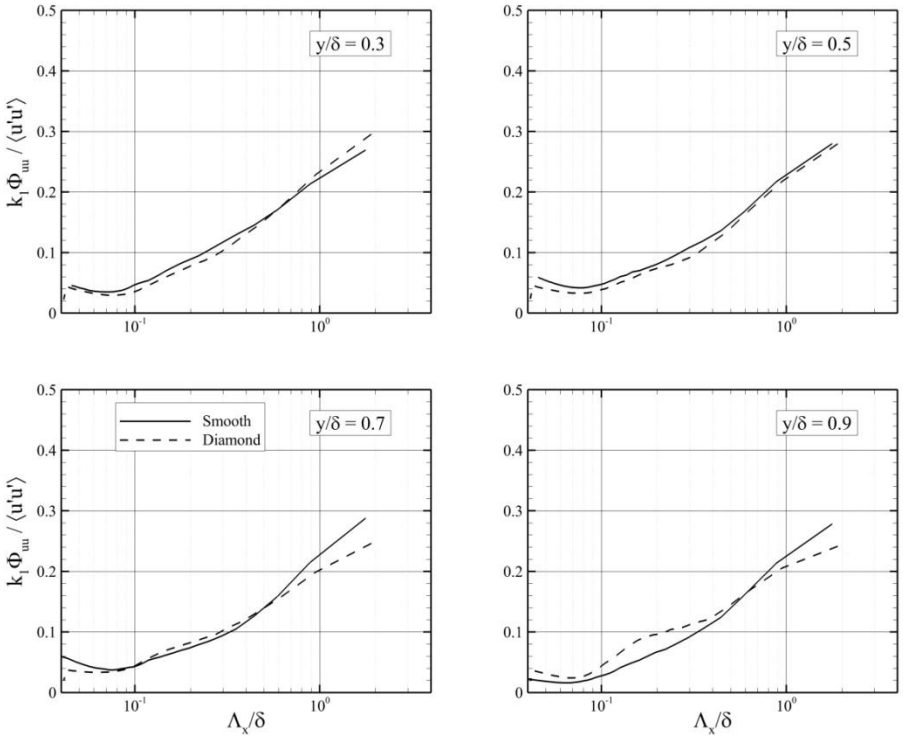

Figure 8.30 Premultiplied spectra of the fluctuating streamwise velocity, normalized by the mean axial stress at each height. *Spectra are shown for heights $y/\delta \geq 0.3$. The streamwise wavelengths are presented in outer-scaled format.*

The near-wall spectral content of the streamwise component is shown in Fig. 8.29. A spectral peak is clearly evident for the rough-wall case at all heights $y/\delta \leq 0.1$, corresponding to a wavelength of approximately $0.5 - 0.6\delta$. Note that this length scale is approximately 2 to 3 times larger than the smooth-wall local maximum, which was shown in §6 to describe the streamwise extent of individual hairpin vortices. Unlike the baseline flowfield, no δ-scale motions are present at $y/\delta \leq 0.1$. This supports the two-point correlation results in §8.4.1, which showed that the near-wall roughness scales are reduced below the baseline values. The length scale of the rough-wall peak appears qualitatively similar to the shock/expansion spacing seen in §8.1, initially indicating that the PSD may be dominated by the roughness-generated waves. However, the outer region PSDs in Fig. 8.30 do not show a spectral peak at $0.5 - 0.6\delta$, despite the fact that

the Reynolds stresses still experience a periodic response at these heights in the boundary layer (see Fig. 8.12). Therefore, the near-wall wavelength over the surface roughness must be due to the physical size of a relevant flow structure. Above $y/\delta = 0.1$, the spectral content of the streamwise component shows good agreement between the rough and smooth boundary layers, excepting a slightly increased contribution from the short-wavelength motions ($0.1 - 0.2\delta$) near the boundary layer edge.

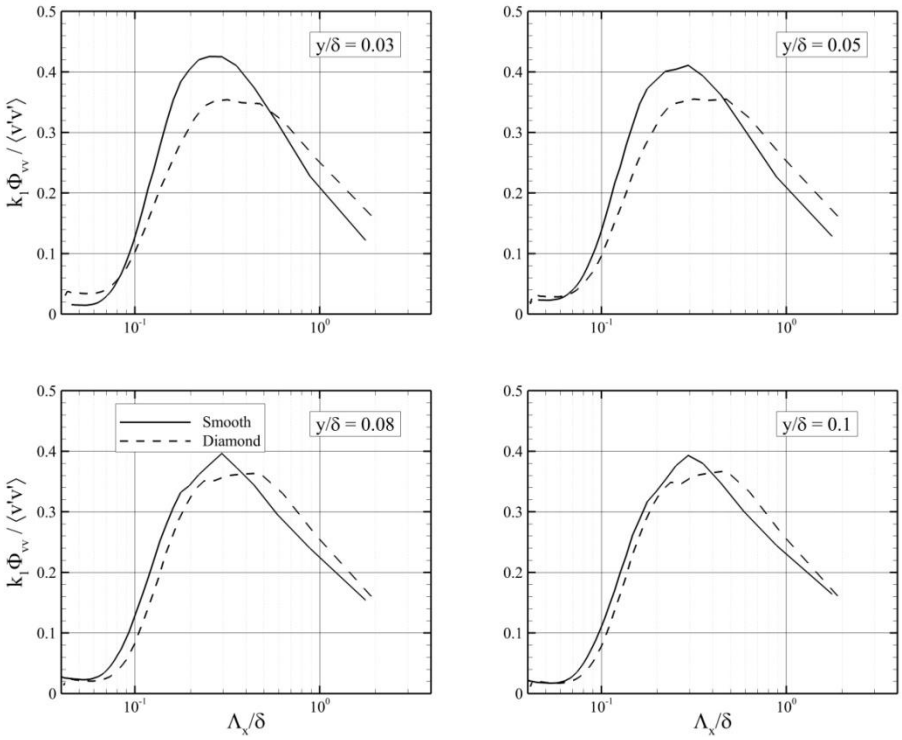

Figure 8.31 Premultiplied spectra of the fluctuating wall-normal velocity, normalized by the mean transverse stress at each height. *Spectra are shown for heights $y/\delta \leq 0.1$. The streamwise wavelengths are presented in outer-scaled format.*

Unlike the axial component, the rough-wall spectra Φ_{vv} in Figs. 8.31 – 8.32 follow a similar trend as the baseline case for the majority of the boundary layer height, with deviations occurring only at the near- and far-wall locations. At the boundary layer edge,

the rough-wall spectrum experiences a slight increase in width, including additional contributions from the small-scale motions. Nearer the wall, at $y/\delta < 0.08$, the roughness has shifted the Φ_{vv} spectra to a longer wavelength by approximately 0.1δ, though the shape of the curve remains unchanged. The increased contribution from scales spanning the range $0.5 – 1.0\delta$ would be consistent with the wavelength of the roughness spacing.

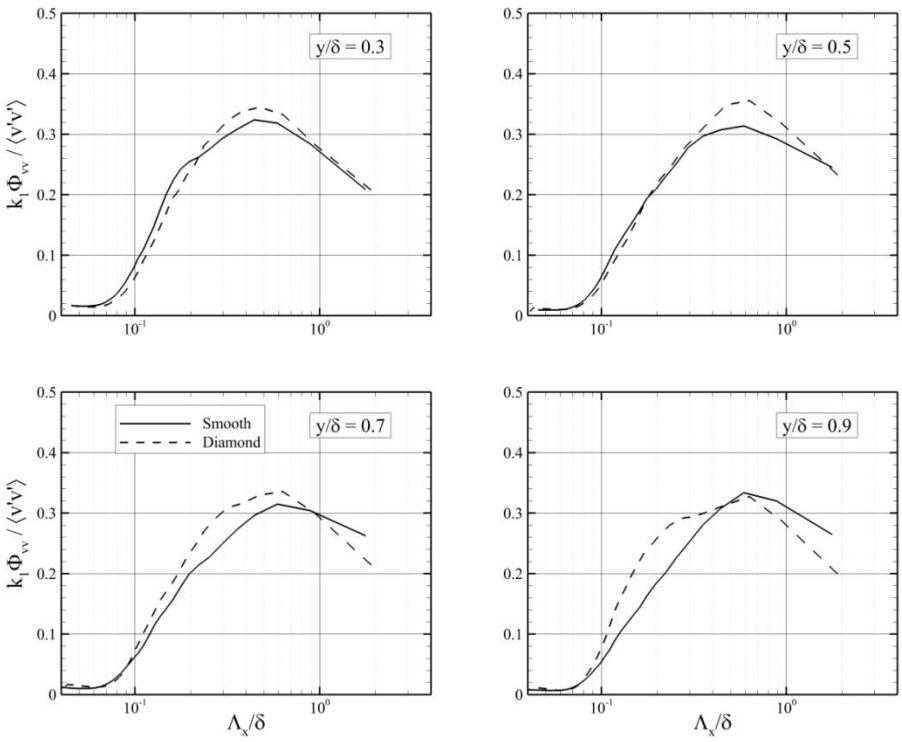

Figure 8.32 Premultiplied spectra of the fluctuating wall-normal velocity, normalized by the mean transverse stress at each height. *Spectra are shown for heights $y/\delta \geq 0.3$. The streamwise wavelengths are presented in outer-scaled format.*

The changes in the spectral content observed in Figs. 8.29 – 8.32 suggest that the *u'*-bearing motions are more strongly perturbed by the roughness topology. This finding appears to contradict the behavior of the axial stress in Fig. 8.16, which showed only a marginal change in the streamwise fluctuations due to surface roughness. Additionally,

Krogstad & Antonia (1999) showed that the streamwise spectra Φ_{uu} is shifted to higher wavenumbers (i.e. shorter wavelengths) in the near-wall region, which is counter to the observations made in the current study. Unfortunately, no definitive evidence of vortex shedding was observed in the spectral content, though increased energy content was seen in the near-wall Φ_{uu} and Φ_{vv} spectra for the range of scales 0.5 – 1.0δ. Recall from §3 that the streamwise length of the element crest is 9.0 mm (0.8δ), suggesting a possible link between the dimensions of the surface roughness and the shape of the spectra.

8.5. Vortex Motions and Population Distribution

The analyses prior to this sub-section have focused upon the behavior of the large-scale structures. Given that the coherent motions are strongly correlated to the induced flowfields generated by the hairpin vortex packets [Adrian *et al.* (2000)], it may be possible to address the contraction and reorientation of the rough-wall structures by examining the motions of the hairpin vortices.

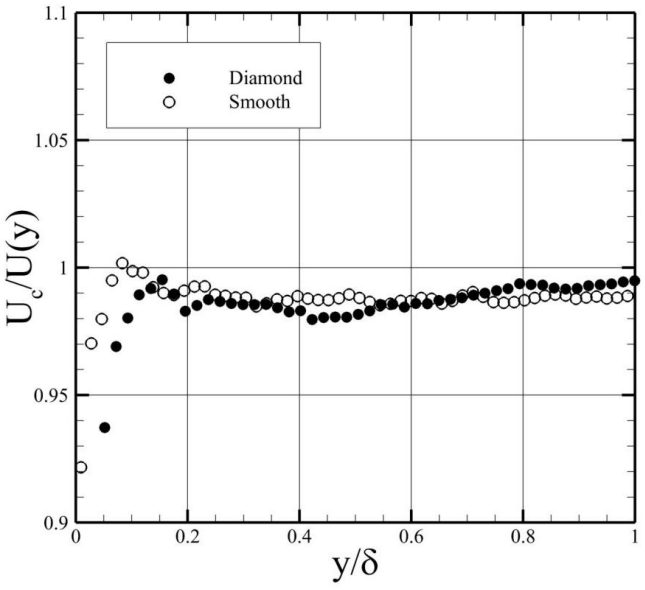

Figure 8.33 Streamwise convective velocity, divided by the local mean velocity.

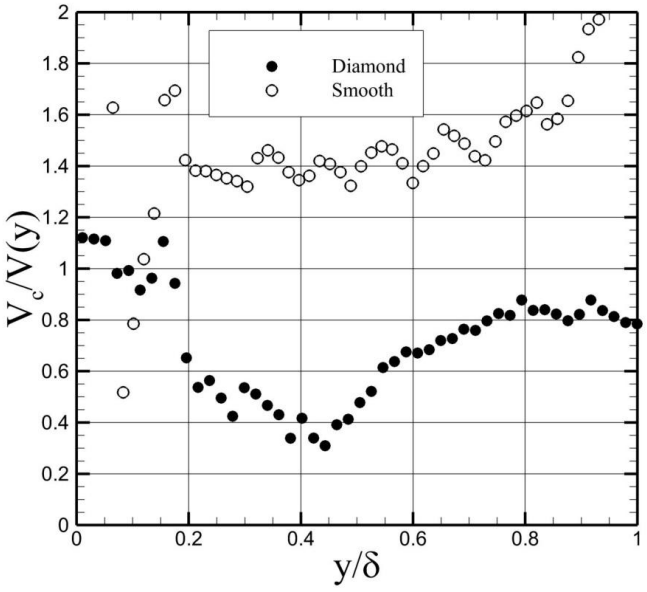

Figure 8.34 Wall-normal convective velocity, divided by the local mean velocity.

The streamwise convective velocity U_c of the individual vortices is computed by conditionally averaging the instantaneous velocity u, based upon the presence of a hairpin vortex. When divided by the local mean velocity $U(y)$, the resulting convective velocity ratio describes the motion of the vortices relative to the surrounding fluid. Plotted in Fig. 8.33, qualitative agreement is seen between the smooth and rough convective velocity ratios. However, closer inspection indicates that the rough-wall vortices convect at a velocity 98% - 99% of the mean flow, for $y/\delta < 0.6$. Above this height, the convective velocity ratio increases to approximately 99.5%. In comparison, the smooth-wall vortices travel at approximately 99% of the mean velocity, for the entire boundary layer thickness. The behavior of the rough-wall vortices can be attributed to the self-induced flowfield generated by the eddies, as described in §6.6 and Eqn. 6.3. As shown in Fig. 8.22, the rough-wall ejection events (Q2) are stronger than the baseline flowfield below $y/\delta = 0.5$. The increased magnitude of the back-induced flow leads to a

smaller streamwise convective velocity. As the Q2 intensity decreases in the outer region, the convective velocity increases toward the mean flow value.

Following a similar procedure, the wall-normal convective velocity ratio is computed, and presented in Fig. 8.34. Recall from §6.6 that the increased wall-normal convective velocity V_c, compared to the surrounding mean flow, is due to "self-induction" by the individual hairpin vortices. However, Fig. 8.34 shows that the rough-wall hairpin vortices are convected away from the wall at a velocity lower than the surrounding fluid, though the velocity ratio varies with the wall-normal distance y/δ. For $y/\delta < 0.2$, the rough-wall vortices follow the mean flow velocity, as $V_c/V(y) \approx 1$. When a similar behavior was observed for the smooth SPG boundary layer in §7.5, it was speculated that this was due to the weaker ejection events within the FPG, as evidenced by the quadrant decomposition in Fig. 7.8. Unfortunately, a similar argument is not applicable to the rough-wall flow, as the Q2 events are clearly more intense in the near-wall region of the distorted boundary layer. The convective velocity ratio of the rough-wall vortices decreases to approximately 0.4 at $y/\delta = 0.4$, before increasing to 0.8 in the outer region. It is not evidently clear why $V_c/V(y) < 1$ for a majority of the boundary layer. The authors can only speculate that an additional external mechanism is retarding the upward movement of the hairpin structures. It is possible that the shock/expansion wave pattern acts as a hindrance to the vertical motion of the vortices, though the influence of these waves upon the transiting structures remains unclear. Any insight into the wall-normal motion of the vortices may also address the reorientation of the large-scale motions.

It was suggested in §8.4.3 that the distortions of the near-wall spectra may be attributed to vortex shedding from the roughness elements. In order to investigate this further, the population distribution of the individual vortices is examined for the smooth- and rough-wall boundary layers. The total population of the vortices is presented in Fig. 8.35, irrespective of the sign of rotation. Recall from §6.6 that Ψ is the PDF of the vortex occurrence, essentially describing the probability of encountering a vortex at a specific wall-normal distance. Excepting outliers at $y/\delta = 0.1$ and 0.2 (which are believed to be

the result of reflections from the roughness elements), the vortex population appears unperturbed by the surface roughness condition. However, this observation no longer holds when the populations are segregated into prograde and retrograde structures (Fig. 8.36). The number of retrograde vortices in the rough-wall flow is reduced by up to 75% across the entire boundary layer, compared to the baseline case. Since the presence of these structures was attributed to omega- and ring-shaped vortex loops in §6, Fig. 8.36 appears to suggest that these vortex topologies are less prominent over a rough wall. The population of prograde vortices is increased by 10% to 15% for the rough-wall flow over the range y/δ = 0.3 – 0.6, which would be consistent with increased vortex shedding from the roughness elements, although it is unknown why this increased population is only visible over a narrow range of wall-normal distances.

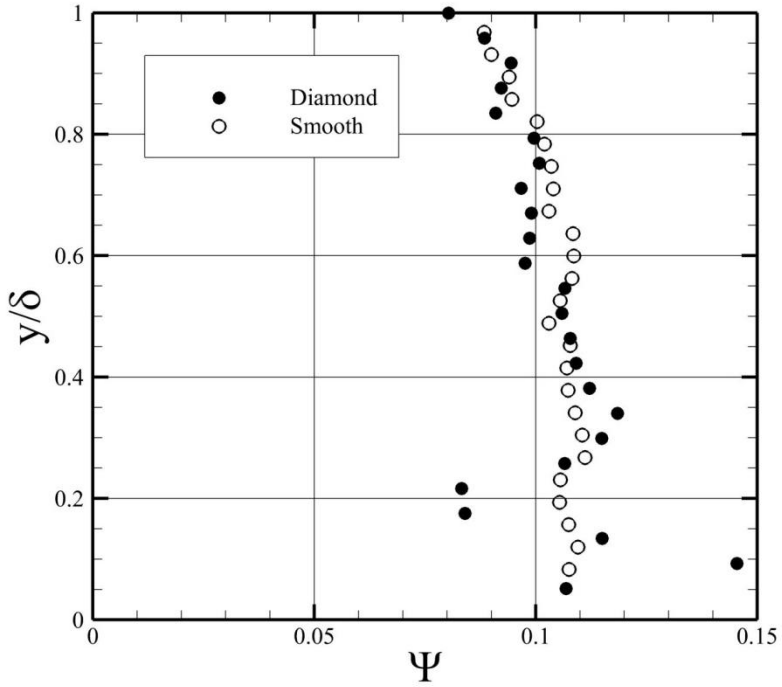

Figure 8.35 Population distribution of spanwise vortices, as detected by the swirling strength λ_{ci}

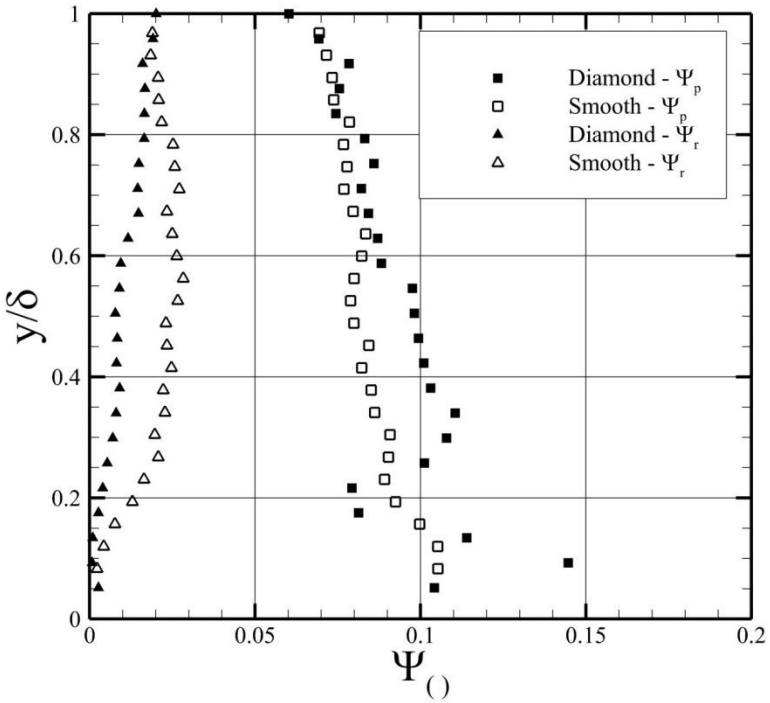

Figure 8.36 Comparison of prograde and retrograde vortex populations

8.6. Conditional Structure of Near-Wall Boundary Layer

The spectral content discussed in §8.4.3 showed that the *u'*-bearing motions are strongly distorted in the rough-wall boundary layer, with the majority of the energy content confined to a narrow range of scales 0.5 – 0.6δ. Conversely, the wall-normal spectra underwent only marginal evolution. Unfortunately, the experimental evidence presented prior to this discussion is insufficient to provide a physical basis for the observed changes in the streamwise and wall-normal spectra. To address this, the instantaneous organization of the rough-wall boundary layer is presented in Fig. 8.37.

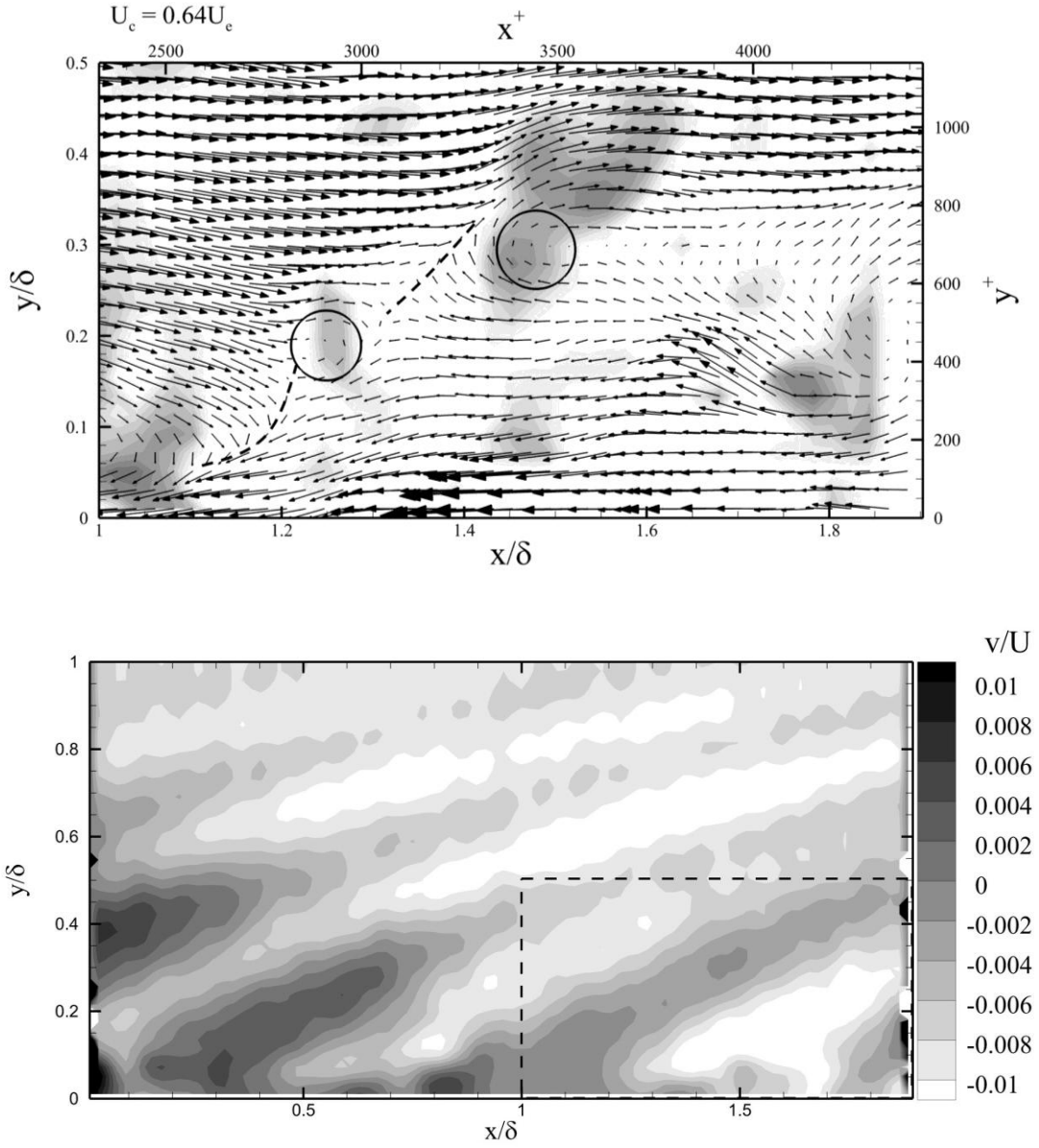

Figure 8.37 Top: Instantaneous realization of rough-wall vector field, showing steeply angled vortex alignments. Bottom: Portion of rough-wall flowfield examined in top image.

Inspections of the instantaneous boundary layer structure did not reveal the expected hairpin packet organization, as was seen in §6. Overall, it was difficult to visually recognize a vortex packet structure that agreed with the baseline flowfield. It is unknown whether this was simply due to the selected instantaneous flowfields, or if this represented a disruption of the vortex packet structure in the rough-wall boundary layer. However, a preferential organization was observed in several instantaneous images, showing the alignment of vortices at a 45-degree angle relative to the wall (Fig. 8.37). Comparisons to the v/U_e contour in Fig. 8.37b suggest that this vortex structure may be attributed to the wave structure generated by the roughness elements.

Given the difficulty in recognizing the hairpin vortex structure from the instantaneous velocity fields, no definitive observations can be made regarding the organization of the near-wall vortices. Instead, a statistical representation of the vortices is provided through conditional averaging in Fig. 8.38. Using a prograde vortex as the conditional event, the surrounding velocity field is estimated through linear stochastic estimation (LSE). Beginning at $y/\delta = 0.1$, the sweep and ejection events surrounding the prograde vortex are clearly visible. As the wall-normal distance increases, the ejection events below the vortex becomes increasingly dominant, as observed in the baseline flowfield in §6.7. Initially, evolution of the ejection event would appear to dispute the quadrant decomposition results of Fig. 8.22, which showed that Q2 events are weaker in the outer half of the boundary layer (compared to the baseline case). However, the reader is reminded that LSE does not indicate the absolute magnitude of the conditional velocity, only the organization and relative magnitude. Therefore, while the ejection events in the outer region of the rough-wall flow are more dominant than the Q4 events, their magnitude is still lower than the corresponding baseline events.

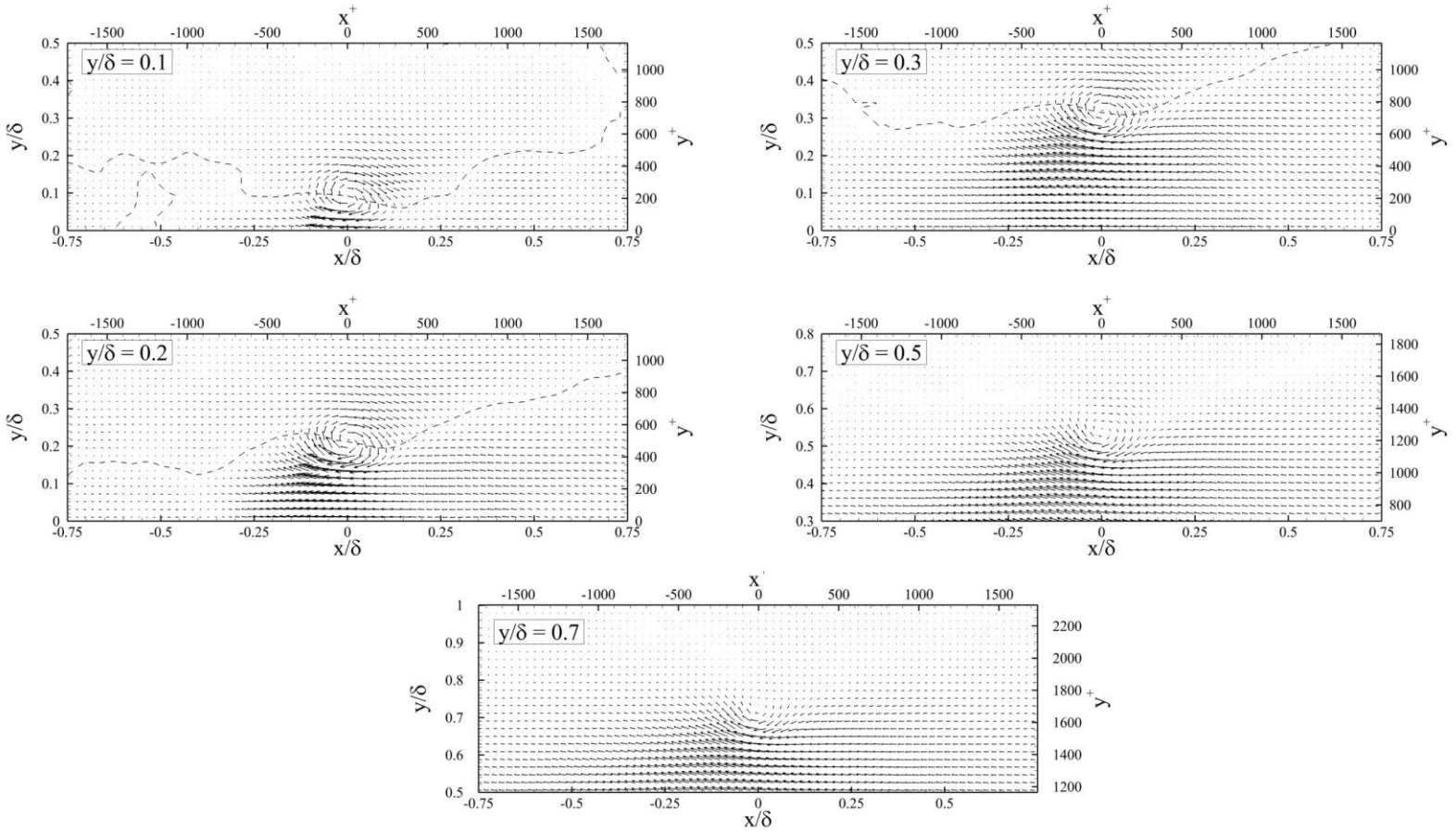

Figure 8.38 Conditionally averaged velocity field of the rough-wall boundary layer, based upon the presence of a prograde vortex event. *The u' = 0 contour is denoted by a dashed line.*

The characteristic growth angle of the hairpin packets can be interpreted from the $u' = 0$ contour in the conditional averages, as was done in §6.7 for the baseline flowfield. In Fig. 8.38, the near-wall growth angle is highly convoluted, casting doubt that the vortices are organized into streamwise-aligned packets. This disorganization is reduced for $y/\delta = 0.2 - 0.3$, though it is difficult to determine conclusively whether the vortices are organized in the streamwise direction.

8.7. Discussion of Results

8.7.1. Reynolds Stress Scaling

It was shown in §8.3 that the rough-wall Reynolds stresses were approximately 25% - 40% of the smooth-wall values (Fig. 8.13 – 8.15), when scaled by the respective friction velocities. Due to the increased skin friction of the rough surface (caused by the contributions of form drag and wave drag), the rough-wall friction velocity was approximately 100% larger than the smooth-wall friction velocity. Therefore, it was speculated that the discrepancy in the inner-scaled Reynolds stresses was merely due to the choice of scaling parameter. When both cases were scaled by the smooth-wall friction velocity $u_{\tau(sm)}$ (effectively comparing the dimensional stresses), better agreement was observed between the rough and smooth cases (Fig. 8.16 – 8.18). Applying this scaling to the Mach 7.3 mesh roughness of Sahoo *et al.* (2010), a similar response was seen, with the rough- and smooth-wall stresses collapsing onto a single curve for the wall-normal component (Figs. 8.19 – 8.20).

This choice of scaling was justified by claiming that it improved the agreement between the rough- and smooth-wall stresses, and that the discrepancy in Figs. 8.13 – 8.15 was merely due to the increased wall shear stress of the roughness topology. However, this prompts the necessary question: *Should* the stresses agree between the rough and smooth cases? Currently, the risk is that the stresses have been *forced* to agree by selecting the

desired scaling parameter. In order to justify this choice, external confirmation of the Reynolds stress behavior is necessary.

In §7, it was ultimately shown that the reduced shear stress within the smooth SPG flowfield was due to the reduced rotational rate of the hairpin vortices, leading to weaker shear stress contributions (i.e. Q2 and Q4 events). This was shown by comparing the mean prograde swirling strength between the baseline and FPG boundary layers. A similar analysis can be performed for the rough-wall boundary layer.

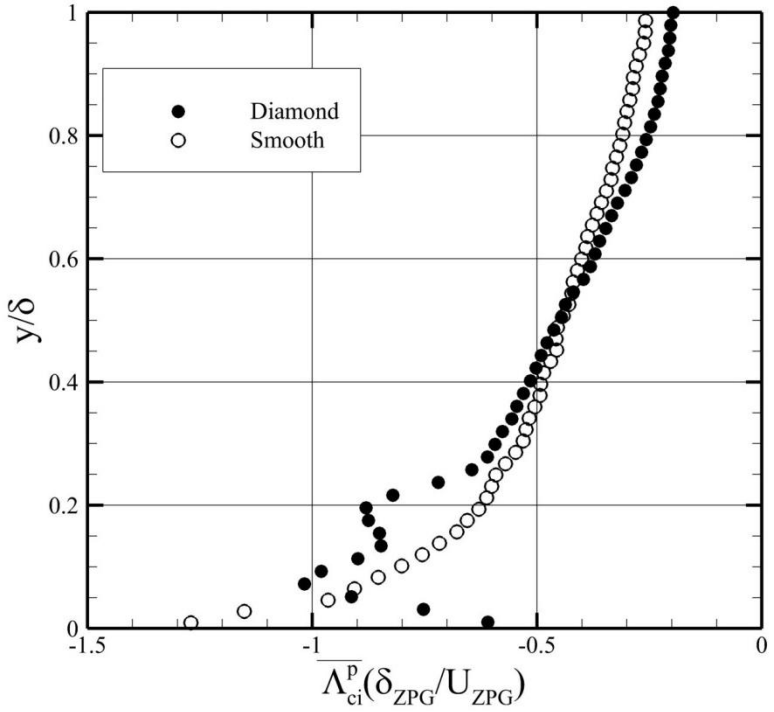

Figure 8.39 Mean prograde swirling strength, describing the rotational rate of the spanwise vortices

In §8.3, it was speculated that the increased dimensional stresses in the near-wall region were due to the action of a roughness-generated adverse pressure gradient, while the stress reduction above $y/\delta = 0.5$ was consistent with the behavior of a favorable pressure gradient. Thus, it was suggested that not only are the roughness-generated pressure

gradients responsible for the streamwise evolution of the Reynolds stresses, but that these pressure gradients affect the wall-normal distribution, yielding a bimodal behavior. If the favorable pressure gradient effects are dominant in the outer region, then it is reasonable to expect that the prograde swirling strength should be depressed below the smooth-wall value, following the analysis given in §7. This is shown in Fig. 8.39, indicating that the hairpin vortices are rotating more slowly in the outer half of the boundary layer, consistent with the findings of §7. Additionally, the "crossover point" of the mean swirling strength matches the behavior of the re-scaled Reynolds stresses.

These findings confirm the use of $u_{\tau(sm)}$ as the appropriate scaling parameter, and show that the Reynolds stress behavior can be attributed to the distribution of pressure gradient effects within the boundary layer. The implications for this finding are significant, suggesting that the roughness effects may be captured by simply reproducing the pressure field, without modeling the full roughness topology.

8.7.2. Reynolds Stress Redistribution

The effects of the roughness appear to occur in two spatially distinct regions, separated at y/δ = 0.4-0.5. In §8.3, it was shown that the dimensional magnitudes of the rough-wall Reynolds stresses are reduced below the smooth-wall value in the outer half of the boundary layer, and are increased in the lower half. While an increased Reynolds stress is consistent with most roughness studies, the observed bimodal behavior appears unique to high-Mach number studies. Ekoto *et al* (2009) and Sahoo *et al.* (2010) observed similar Reynolds stress responses, when using a common scaling parameter. The mechanism by which the roughness modifies the turbulent field must therefore be strongly influence by the compressibility of the flow, as to this author's knowledge, no incompressible roughness study has seen the Reynolds stress reductions observed in Figs. 8.13 – 8.15.

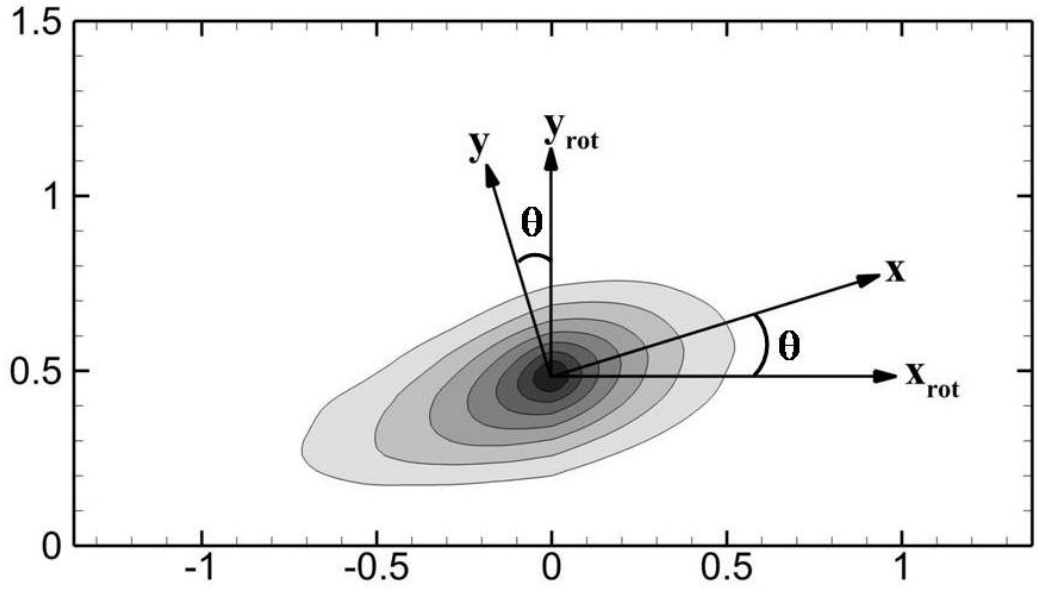

Figure 8.40 Axes of coordinate transformation, described in Eqns. 8.2 – 8.4

The schlieren photographs in Figs. 8.1 and 8.2 illustrate the periodic shock waves and expansion fans generated by the roughness. As the coherent motions traverse these features, it is possible that local coordinate rotations may be in part responsible for the observed turbulence stress response in Fig. 8.16 – 8.18. This is consistent with Luker *et al* (2000), who showed that the Reynolds shear stress response over a convex curvature model may be partially described by accounting for the local coordinate frame rotation. To test this theory, a coordinate transformation is applied to the Reynolds stresses for the smooth and rough data. The transformation angle θ is set equal to the structure angle computed from the two-point correlation R_{uu}, shown in Fig. 8.26. The selection of the R_{uu} correlation was motivated by the fact that the majority of the boundary layer TKE is contained within the large-scale structures. Figure 8.40 shows the relation between the existing and rotated coordinates. The coordinate transformations of the rotated turbulent stresses are given by:

$$u'_{rot}u'_{rot} = u'u'\left(\cos^2(\theta)\right) + v'v'\left(\sin^2(\theta)\right) - 2u'v'\sin(\theta)\cos(\theta) \quad (8.2)$$

$$v'_{rot}v'_{rot} = v'v'\left(\cos^2(\theta)\right) + u'u'\left(\sin^2(\theta)\right) + 2u'v'\sin(\theta)\cos(\theta) \quad (8.3)$$

$$u'_{rot}v'_{rot} = u'v'\left(\cos^2(\theta) - \sin^2(\theta)\right) + u'u'\sin(\theta)\cos(\theta) - v'v'\sin(\theta)\cos(\theta) \quad (8.4)$$

where u' and v' are the measured fluctuating components, and u'_{rot} and v'_{rot} are the transformed components. The resulting stresses in both the original and structure angle coordinate systems are shown in Figs. 8.41 – 8.43.The axial stresses in Fig. 8.41 show minimal change after undergoing the coordinate transformation. This is a reflection of the relatively small structure angles shown in Fig. 8.26. Specifically, for small angles, Eqn. 8.2 reduces to $u'_{rot}u'_{rot} \approx u'u'$. However, the transformed wall-normal and shear stresses were significantly reduced when transformed by the structure angle coordinate; see Figs. 8.42 and 8.43. The reader should exercise caution when interpreting the rotated shear stress component in Fig. 8.43, as an uncertainty analysis showed that the shear stress equation in Eqn. 8.4 is highly sensitive to the uncertainty of the structure angle θ. When the 2 – 3 degree structure angle variance is included, the resulting uncertainty is approximately equal to the magnitude of the shear stress. An interesting observation from the data in Fig. 8.42 is that when rotated, the rough and smooth wall data nearly overlap. This suggests that Reynolds stress redistribution is a dominant mechanism that should be included when modeling these classes of flows.

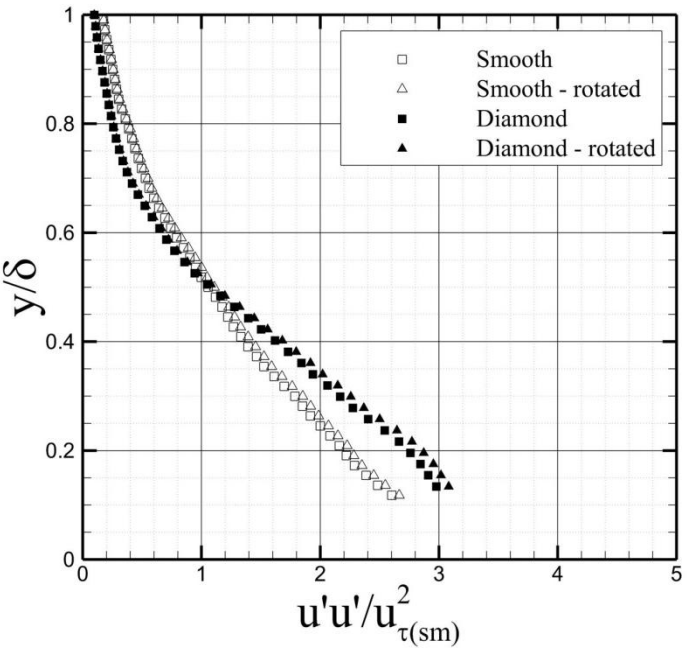

Figure 8.41 Transformed axial stress, following the coordinate transformation in Eqn. 8.2

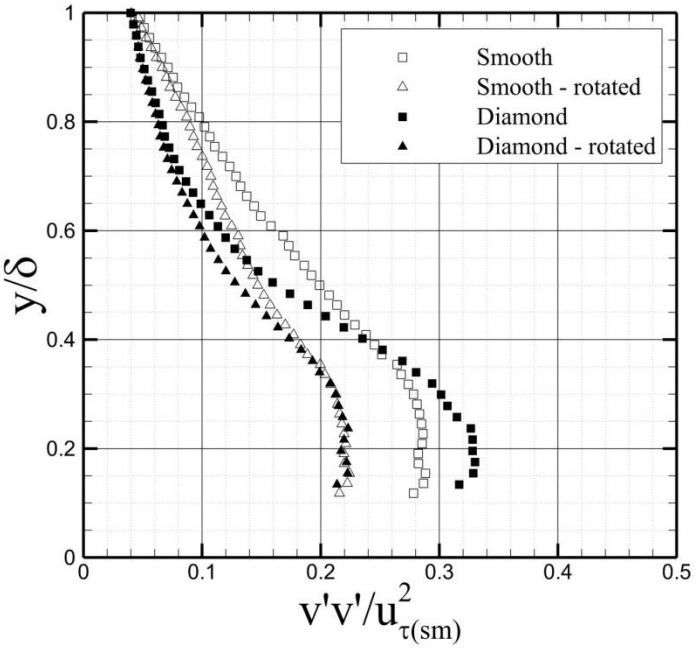

Figure 8.42 Transformed wall-normal stress, following the coordinate transformation in Eqn. 4.3

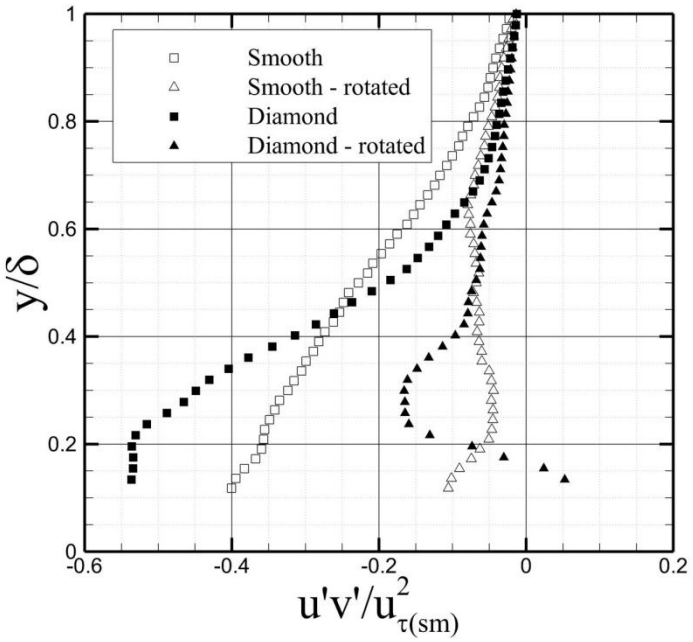

Figure 8.43 Transformed shear stress, following the coordinate transformation in Eqn. 8.4

8.7.3. Reorientation of Large-Scale Motions

The coordinate transformation in §8.7.2 suggests that the evolution of the wall-normal stress component can be described by the reorientation of the large-scale motions. However, the physical mechanism governing the rotation of the rough-wall structures remains unknown. In §8.4.1, structure angles derived from the two-point correlations R_{uu} showed that the rough-wall coherent structures are inclined more wall-parallel for $y/\delta >$ 0.2, compared to the baseline flow. Currently, no general theory exists to explain the reorientation of large-scale structures in the presence of roughness. However, the inclination can be attributed to two phenomena: 1) the increased drag of the roughness elements, rotating the structures toward the wall, and 2) the increased "open-ness" of the rough-wall decreases the damping of the wall-normal fluctuations (i.e. *v'v'*), rotating the structures more wall-normal. The contribution of the second mechanism is explored below.

In order to determine the cause of the reorientation observed in Fig. 8.26, ratios are formed between the rough- and smooth-wall flows, for both the structure angle and wall-normal stress $v'v'$ (i.e. $(v'v')_{rough} / (v'v')_{smooth}$ and $\theta_{rough} / \theta_{smooth}$). These ratios are shown in Fig. 8.44. Qualitatively, the ratios follow similar trends, with the best agreement occurring above $y/\delta = 0.4$. Unfortunately, there is insufficient information to suggest a causal relationship. Figure 8.44 merely suggests that the wall-normal fluctuations are related to the reorientation of the large-scale motions, supporting the coordinate transformation results in §8.7.2.

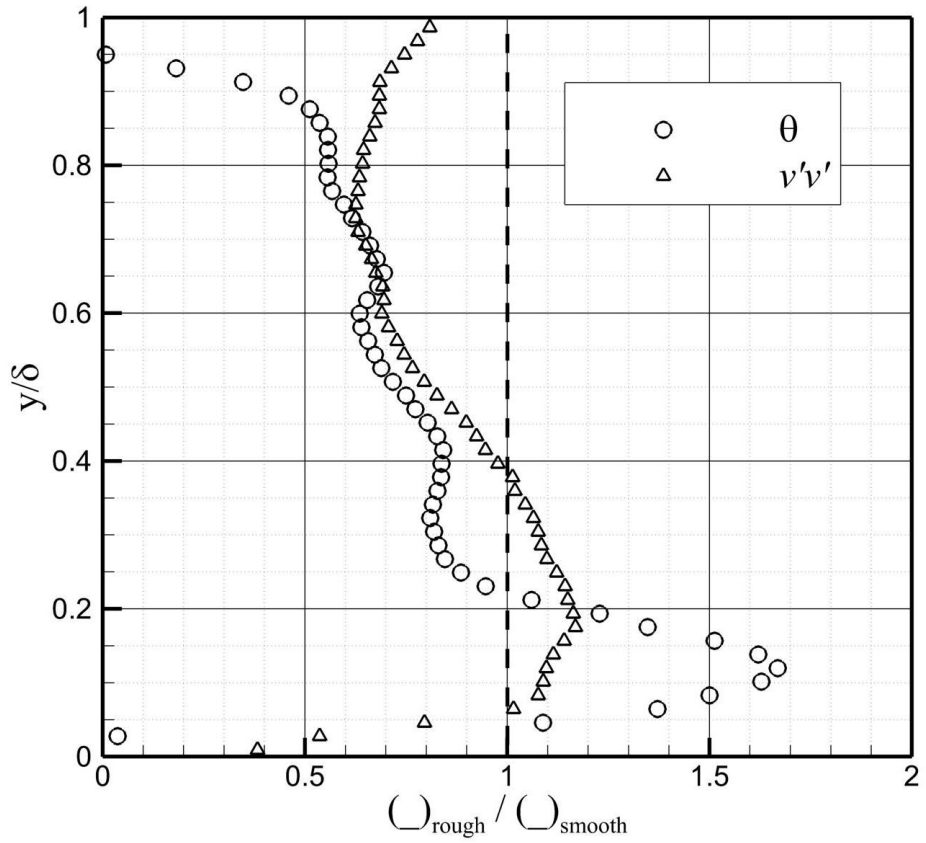

Figure 8.44 Ratios of the structure angle and wall-normal stress, where the rough-wall value is scaled by the associated smooth-wall value at each height.

8.8. Summary

The effects of periodic diamond roughness (k/δ = 0.07) upon a Mach 4.9 turbulent boundary layer were examined using particle image velocimetry. The mean flow exhibited an oscillatory response due to the shock waves and expansion fans generated by the roughness elements. This process is consistent with the measurements at Mach 2.87 by Ekoto *et al* (2009). Profiles of dimensional kinematic stresses show that the roughness is responsible for increased turbulent fluctuations in the lower half of the boundary layer (compared to a smooth baseline model), while leading to decreased turbulent stresses above $y/\delta \sim 0.5$. Following the observed behavior of favorable pressure gradients in §7, it was found that the stress reduction in the outer region of the rough-wall flow is likely due to favorable pressure gradient effects. This was determined by comparing the mean prograde swirling strength of the smooth and rough flowfields. Therefore, the dimensional stresses (supported by the prograde swirling strength) suggest that the roughness-induced pressure gradients affect both streamwise evolution of the flowfield, along with the stress distribution in the wall-normal direction. The implications for this finding are significant, suggesting that the roughness effects may be captured by simply reproducing the pressure field, without modeling the full roughness topology.

In order to provide a physical link between the flow structure and stress distribution, the coherent motions within the flow were examined through spatial two-point correlations. The structure angles of the rough-wall boundary layer were increased for $y/\delta < 0.2$, but then decreased below the smooth wall values for $y/\delta > 0.2$. It was suggested here that re-organization of these coherent motions within the rough-wall flow was partly due to the shock waves and expansion fans generated by the roughness elements. Furthermore, an attempt to explain the Reynolds stress behavior through the re-orientation of the coherent structures has shown initial success, where it was observed that the rough and smooth Reynolds transverse stress, when rotated to the local structure angle, show

excellent agreement. This finding suggests that Reynolds stress redistribution is a predominant mechanism that should be included when modeling this class of flow.

Along with the findings listed above, two key questions remain from this study:

1) How does the shock/expansion angle affect the evolution of the hairpin vortex packets, including the wall-normal convective velocity of the individual vortices?
2) Why do the Q2 (ejection) events show an increased sensitivity to the surface roughness, compared to the Q4 (sweep) events?

It is hoped that additional experimental studies at various Mach numbers can illustrate the effect of the wave angle upon the structure evolution. The work of Sahoo *et al.* (2010) shows promise in this area. Addressing the second question, concerning the quadrant events, may require repeating the quadrant decomposition using various hole size filters $H \neq 0$.

9. SUMMARY

The effects of mechanical distortions on a Mach 4.9 turbulent boundary layer were experimentally investigated, through the application of high-resolution PIV. Baseline (undistorted) boundary layer measurements were conducted over a flat-plate acrylic model. The distorted boundary layers were separately generated using convex curvature and periodic surface roughness. Due to the technical challenge of experimentally probing high-Mach number boundary layers, very little experimental data is available for mechanically distorted flows in this Mach number regime. The existing studies are limited to statistical measurements, e.g. turbulent stresses *u'u' and u'v'*, which are instrumental in determining the shear stress response of the boundary layer, as well as validating RANS simulations. However, these measurements do not directly address the physical mechanisms that govern the boundary layer evolution within a distorted flowfield. This limitation served as the motivation for the current study, with the goal of experimentally determining the principal physical processes governing the behavior of a high-Mach number, mechanically distorted turbulent boundary layer. To address this objective, the author formulated two scientific questions that have guided the data collection and analysis:

3) How do mechanical distortions modify the turbulent structures in a Mach 5 turbulent boundary layer?
4) How does the modification of these structures manifest itself in the turbulence statistics?

In order to address these questions, archival-quality PIV data were collected over the flat-plate, curved-wall, and rough-wall models. Initial analysis efforts focused upon the Reynolds stress responses, in order to compare this study to any relevant data in the literature. Quadrant decomposition provided insight into the shear-stress producing motions, and guided the higher-order analyses to the most interesting aspects of the flowfields. Additionally, two-point correlations and spectral analysis served to elucidate the reorientation and reorganization of the coherent structures. The most compelling

results were uncovered by detecting the instantaneous vortices within the boundary layer, achieved by computing the swirling strength λ_{ci} for every velocity field. Examinations of the instantaneous velocity fields, guided by the vortex detection algorithm, provided clues as to the physical processes responsible for the changing length scales and Reynolds stress levels. However, the most significant observations came from the statistical analysis of the vortex motions and distributions. Conditionally averaged velocity fields, employing a spanwise-oriented vortex as the conditional events, revealed the distortion of the locally-induced motions (i.e. ejections and sweeps), which are primary sources of the shear stress production. Finally, correlations between the swirling strength and instantaneous shear stress provided a direct link between the locally spiraling fluid and the Reynolds shear stress. These results provided a phenomenological framework in which to analyze the turbulent stress response of the distorted boundary layers.

Given the large number of analyses employed in this study, the resulting representations of the distorted boundary layers provided multiple viewpoints through which to interpret the flow response. The results summarized below in §9.1 - §9.3 are limited to addressing the questions listed above, concerning the response of the turbulent structures. However, the richness of this study provides the opportunity to also approach the analysis from a turbulence modeling or flow control background. In other words, the depth of this study has generated considerably more opportunities than originally conceived when designing the experiment.

9.1. Undistorted (ZPG) Boundary Layer

Measurements in a Mach 4.9 undistorted boundary layer showed that the relevant motions are very similar to those encountered in incompressible flowfields. While the determination of the streamwise length scale was limited by the FOV (a common problem in PIV experiments), the large-scale motions appeared to follow the

incompressible trends. This was determined through two-point correlations and spectral analysis. Additionally, instantaneous visualization of the boundary layer provided a physical basis for the spectral behavior, suggesting that the long-wavelength motions stem from the induced low-momentum streaks beneath the hairpin packets, which are "punctuated" by 0.2δ-scale vortices within the logarithmic region.

Conditionally-averaged velocity fields showed that the locally induced motions near a prograde vortex core agree well with previous experiments [Christensen & Adrian (2001); Elsinga *et al.* (2010)], illustrating both sweep and ejection events. However, the prograde sweep events were shown to be less dominant as the distance from the wall increases. Finally, the Reynolds stress contribution of the vortices was investigated by computing the swirling strength-shear stress correlation. Shear stress concentrations around the prograde vortex cores were shown to be coincident with the sweep and ejection events identified through conditional averaging, supporting the theory that hairpin vortices are the primary contributors to the Reynolds shear stress. However, the near-wall retrograde vortices produced lobes of *positive* shear stress, suggesting that these structures may contribute to negative production within this region.

9.2. Effects of Wall Curvature and Favorable Pressure Gradients

The effects of favorable pressure gradients upon a Mach 4.9 boundary layer were examined using three experimental models: a baseline ZPG case, and two convex curvature models. For the favorable pressure gradient flowfields, all three measured stress components (axial, wall-normal, and shear) were attenuated through the expansion region. However, the most dramatic response was observed in the shear stress for the SPG flowfield, which underwent a sign reversal over the outer 80% of the boundary layer. This observation served as the motivation for the remaining analyses, with the goal of providing a physical explanation for the response of the Reynolds stresses, by examining the distortion, re-orientation, and attenuation of the turbulent structures.

Quadrant decomposition of the shear-stress producing motions showed that the magnitudes of the sweeps and ejections were strongly suppressed in the SPG boundary layer. This analysis was confirmed through instantaneous visualizations of the boundary layer, as well as conditionally averaged velocity fields. Given that the hairpin vortices are the primary contributors to the mean shear stress, it was speculated that the reduced shear stress may be due to the deformation of these structures. Supported by data from English (2013), it was shown that the weaker ejection events are likely due to the reduced vorticity within the hairpin vortices, as suggested by profiles of the mean prograde swirling strength. It should be noted that this model provides an additional mechanism by which favorable pressure gradients lead to the attenuation of the Reynolds shear stress, and does not necessarily address any effects due to bulk dilatation.

9.3. Effects of Periodic Surface Roughness

The effects of periodic diamond roughness (k/δ = 0.07) upon a Mach 4.9 turbulent boundary layer were examined using particle image velocimetry. The mean flow exhibited an oscillatory response due to the shock waves and expansion fans generated by the roughness elements. This process is consistent with the measurements at Mach 2.87 by Ekoto *et al* (2009). Profiles of dimensional kinematic stresses show that the roughness is responsible for increased turbulent fluctuations in the lower half of the boundary layer (compared to a smooth baseline model), while leading to decreased turbulent stresses above $y/\delta \sim 0.5$. Following the observed behavior of favorable pressure gradients in §7, it was found that the stress reduction in the outer region of the rough-wall flow is likely due to favorable pressure gradient effects. This was determined by comparing the mean prograde swirling strength of the smooth and rough flowfields. Therefore, the dimensional stresses (supported by the prograde swirling strength) suggest that the roughness-induced pressure gradients affect both streamwise evolution of the flowfield, along with the stress distribution in the wall-normal direction. The

implications for this finding are significant, suggesting that the roughness effects may be captured by simply reproducing the pressure field, without modeling the full roughness topology.

In order to provide a physical link between the flow structure and stress distribution, the coherent motions within the flow were examined through spatial two-point correlations. The structure angles of the rough-wall boundary layer were increased for $y/\delta < 0.2$, but then decreased below the smooth wall values for $y/\delta > 0.2$. It was suggested here that re-organization of these coherent motions within the rough-wall flow was partly due to the shock waves and expansion fans generated by the roughness elements. Furthermore, an attempt to explain the Reynolds stress behavior through the re-orientation of the coherent structures has shown initial success, where it was observed that the rough and smooth Reynolds transverse stress, when rotated to the local structure angle, show excellent agreement. This finding suggests that Reynolds stress redistribution is a predominant mechanism that should be included when modeling this class of flow.

9.4. Contributions of the Current Study

The contributions of the current study to the scientific literature are listed below:

1) High-fidelity, archival quality data was collected for a Mach 4.9 turbulent boundary layer, under distorted and undistorted conditions. The resolution of this data set is comparable to incompressible studies, and is suitable for validation of higher-order simulations (e.g. LES).
2) Instantaneous visualizations and conditional averaging of the undistorted flowfield have suggested that the hairpin packet model is applicable to a Mach 4.9 boundary layer. While studies at lower Mach numbers have confirmed this behavior (see the Mach 2 tomographic PIV of Elsinga *et al.* (2010)), the author is aware of no such observations at this Mach number. (Note: The current study

only *implies* that hairpin packets are present, based upon the vortex distribution and alignment. Confirmation of this behavior requires three-dimensional data.)

3) A physical model has been created for the FPG boundary layer, showing that pressure gradient effects may be responsible for the weakening of the hairpin vortices in the near-wall region, leading to lower-intensity sweeps/ejections and a reduced mean shear stress $u'v'$.
4) The effects of periodic roughness have been partially captured by accounting for the reorientation of the transverse stress, with potential implications for modeling this behavior.

9.5. Recommendations

Recommendations for future analysis methods and experiments are described below, including possible improvements upon the current analyses.

9.5.1. Vortex Detection

The detection of vortical structures is a key component of the current analysis, allowing the response of the turbulence statistics to be explained within a phenomenological framework. Therefore, a robust and reliable detection scheme is necessary, in order to capture the instantaneous flow structures while minimizing the number of "false positives." This algorithm must be applicable to distorted flows, and insensitive to compressibility effects.

The existing detection schemes reviewed in §5.1 are expected to produce similar results (see Chakraborty, Balachandar & Adrian 2005). However, comparisons of the swirling strength and unmodified Q-criterion for the current study show clear discrepancies in the resulting vortices (see §5.2.2 for a detailed comparison). The non-zero dilatation present within the smooth SPG case requires the compressible form to be employed. Conversely, the swirling strength does not require any modification for compressibility effects, being

based solely on the kinematics of the flow. In fact, the compressibility correction employed in §5.2.2 only affects the real part of the eigenvalues of the velocity gradient tensor, such that the swirling strength is unchanged.

Alongside the difficulty of applying the afore-mentioned schemes to compressible flow, an additional weakness is present for all of the methods discussed: the vortex identification is based upon the velocity gradient tensor. The differentiation of experimental data results in increased noise, which is quantified by the relatively high uncertainty for the velocity gradients (Appendix B). Future analyses should employ a technique that makes no assumptions of incompressibility, and does not rely upon the differentiation of experimental data. *Pattern recognition analysis* may satisfy both of these criteria.

Pattern recognition analysis utilizes the convolution product between the instantaneous velocity field and an idealized vortex structure. In practice, this is achieved by computing the discrete wavelet transform, where the mother wavelet is a prototypical vortex. The resulting map shows peaks where the local flowfield is similar to the model vortex. Carlier & Stanislas (2005) improved upon this technique by fitting an Oseen vortex to the peaks in the detection function, providing a direct measure of both the radius and circulation for each detected vortex. This allows the distribution of the vortex size and strength to be computed for the flowfield. An additional advantage of this technique is that it yields the centroid of each vortex, such that the conditional average can be directly computed. It is also possible to compute the center of each eddy in the current study, by using the distribution of the swirling strength within a vortex core. However, inspection of the instantaneous velocity fields shows that λ_{ci} is often distributed asymmetrically within the vortex, limiting the current analysis to only an estimate of the conditional average, i.e. LSE..

The author strongly recommends that future analyses of this data set employ *pattern recognition analysis* for identifying vortices.

9.5.2. POD Analysis

The conditional average of the fluctuating velocity field, using the swirling strength λ_{ci} as the event vector, is defined as $(u'v'|\lambda_{ci})$. This allows the researcher to specify which event to investigate, regardless of its overall significance to the flow (i.e. energy content). In contrast, methods such as proper orthogonal decomposition (POD) produce multiple basis functions, ranked by the contribution to the overall mean (or turbulent) kinetic energy. This has the benefit of allowing the researcher to identify the most significant flow structures present within the flowfield, though identifying a specific topology (e.g. a vortex) may prove difficult, depending upon the energy content associated with that structure.

In the current study, the conditional event is chosen *a priori*, based upon the sign and magnitude of the swirling strength, i.e. $u'v'|\lambda_{ci}$. This choice was justified by considering the primary role that hairpin vortices play in producing the near-wall Reynolds shear stress in undistorted flows. Due to the severe lack of experimental data for mechanically distorted turbulent boundary layers, it was necessary to confirm (or at least support) the existence of hairpin vortex packets within the FPG and rough-wall boundary layers of the current study, prior to estimating the conditional average. This was performed by visually investigating sample instantaneous flowfields, after subtracting an appropriate convective velocity. The instantaneous vector fields showed that hairpin packets are present in the distorted boundary layers, though they have been deformed by the near-wall acceleration/deceleration (and possibly by the wall-normal convective velocity V_c present within the SPG case). The statistical behavior of the vortices was then probed using conditional averaging, showing that sweeps and ejections are indeed associated with the hairpin vortex signature, even in a distorted boundary layer.

Recall that a region of spanwise rotating fluid, identified by the swirling strength, was chosen as the event vector for the conditional average. The resulting conditionally averaged vector fields provided insight into how the local flowfield is perturbed by the mechanical distortions. This dissertation has shown that the behavior of the Reynolds

stresses in a mechanically distorted boundary layer may be explained by examining the response of the turbulent structures. However, the assumption is made that the hairpin vortices, including their associated sweep and ejection events, remain the *primary* mechanisms for producing Reynolds shear stress. Unfortunately, neither the conditional average nor the shear stress-swirling strength correlation $R_{\lambda(u'v')}$ can confirm this, only verifying that these structures still exist within the distorted flowfields. These methods show the relative velocity of the surrounding fluid, and the relative distribution of the instantaneous shear stress *u'v'* around a vortex, respectively.

Future analyses should employ POD to complement the conditionally averaged velocity fields. The resulting basis functions may reveal whether any unexpected flow topologies are present within the distorted boundary layers, and will allow the relative energy content of the existing structures to be quantified.

9.5.3. Form Drag of Roughness Elements

In Section 8, it was shown that the rough-wall stresses show good agreement with the smooth-wall values, when scaled by the smooth-wall friction velocity $u_{\tau(sm)}$. The resultant stress profiles showed a bimodal behavior, in which the **dimensional** rough-wall stresses are higher near the wall, and lower in the outer region. When scaled by $u_{\tau(sm)}$, the crossover point at which the smooth- and rough-wall stresses are equal is $y/\delta \approx 0.4 - 0.5$. It was suggested that the increased friction velocity over the diamond roughness is due to the increased pressure drag caused by the roughness elements, though the current study has insufficient data to support that theory. However, by measuring the distribution of the temperature and pressure at the wall, it may be possible to determine the cause of the increased friction velocity, and perhaps uncover the appropriate scaling parameter for the rough-wall Reynolds stresses.

Using the Clauser chart method, the rough-wall friction velocity has been estimated, accounting for the effective origin ε. Recall that the friction velocity is a function of both the wall shear stress τ_w and the wall density ρ_w:

$$u_\tau = \sqrt{\frac{\tau_w}{\rho_w}} \tag{9.1}$$

For a smooth wall, τ_w is due solely to the viscous forces along the surface. However, rough walls add an additional component to the wall shear stress, namely the *form drag* caused by the pressure differential across the roughness element. Therefore, it may be possible to decompose τ_w as

$$\tau_w = \tau_w^s + \tau_w^p \tag{9.2}$$

where the superscripts "s" and "p" describe the surface/viscous and form drag components, respectively. This is shown schematically in Fig. 9.1 below, for an isolated roughness element.

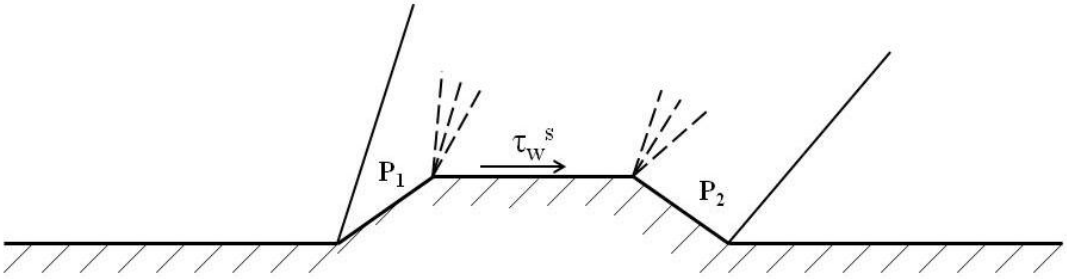

Figure 9.1 Isolated roughness element in a supersonic flow, showing the contributions of surface/viscous and form drag

Assuming the form drag component τ_w^p can be computed as

$$\tau_w^p \propto p_1 - p_2 \tag{9.3}$$

it may be possible to estimate τ_w^s for the current rough-wall boundary layer. The importance of this parameter is described below.

In incompressible rough-wall boundary layers, the Reynolds stresses generally show good agreement with the smooth-wall case when scaled by $(u_\tau)^2$ [Schultz & Flack (2007); Volino, Schultz & Flack (2011)], though some researchers have observed large amplifications of the wall-normal stress $\overline{v'v'}^+$ (Antonia & Krogstad (2001)). To this author's knowledge, no incompressible study has observed the large (50% - 75%) *decrease* present in the Reynolds stresses for the current study. Since the stresses are presented in inner-scaled form, it is possible that the reduced stress is primarily due to the altered skin friction, and therefore friction velocity. Liepmann & Goddard (1957) suggested that for high Reynolds number boundary layers, the skin friction of a rough wall is due to the form drag of each roughness element. Goddard (1959) extended this concept, showing that the reduced skin friction over rough surfaces is due to the lower wall density ρ_w. However, the roughness elements in these referenced studies were relatively small, residing below the sonic line. For the current study, the crests of the elements protrude into the supersonic portion of the flow, generating strong distortions. By measuring the local pressure fields produced by these distortions, it may be possible to show that the viscous component of the wall shear stress is unchanged, and that the increased friction velocity is due to the roughness-induced pressure gradients.

The following procedure may be used to decompose τ_w into the viscous and form drag components:

1) Measure u_τ from the mean velocity profile, using the Clauser chart method.
2) Use pressure sensitive paint (PSP) and temperature sensitive paint (TSP) to determine T_w and p_w, and therefore ρ_w.
3) Use ρ_w (averaged over a single element) to compute τ_w, knowing u_τ (from Step 1).
4) Knowing the pressure distribution across the roughness element, and assuming $\tau_w^p = p_1 - p_2$, solve $\tau_w = \tau_w^s + \tau_w^p$ for τ_w^s.

5) Renormalize Reynolds stresses by $u_\tau^s = \sqrt{\frac{\tau_w^s}{\rho_w}}$.

If the resulting stress profiles, normalized by u_τ^s, show good agreement with the smooth-wall values, then this would indicate that the wave drag generated by the roughness elements is the likely explanation for the observed decrease in the rough-wall Reynolds stresses.

9.5.4. Vortex Stretching within Favorable Pressure Gradients

It was shown in §7 that the reduced shear stress of the smooth SPG flowfield is due to the lower rotational rate (i.e. smaller swirling strength) of the prograde vortices. In an attempt to provide a physical explanation for this behavior, the effects of vortex stretching in the wall-normal direction were explored. Piomelli *et al.* (2000) suggested that the reduced vorticity within an accelerated incompressible boundary layer may be due to streamwise stretching of the near-wall vortices. As the vortices are stretched, continuity would require that their cross-sectional diameter decrease. It was suggested that the thinner vortices would be more susceptible to viscous dissipation. An analogous behavior was discussed in §7.7.2, examining whether the elevated dV/dy strain rate may result in the near-wall hairpin vortices being stretched vertically. While the turbulent Mach number M' lies within the incompressible regime, it was argued that the coherent structures are likely to behave similarly to the surrounding compressible flow. Thus, any vortex stretching in the vertical direction would not necessarily decrease the diameter of the vortices.

While the above argument is logical, it is not a definitive refutation of the vortex stretching theory. In order to address this concept fully, a direct measure of the vortex diameter is necessary. The diameter of the spanwise vortices was estimated by computing the autocorrelation of the prograde swirling strength in the *x-y* plane. If data

of a similar resolution were collected in the *x*-*z* plane, it would be feasible to estimate any reduction in the diameter of the hairpin legs. It may be possible to test this theory using the top-down PIV of English (2013).

REFERENCES

ACARLAR, M.S. & SMITH, C.R. 1987a. A Study of Hairpin Vortices in a Laminar Boundary Layer. Part 1. Hairpin Vortices Generated by a Hemisphere Protuberance. *Journal of Fluid Mechanics* **175**, 1-41.

ACARLAR, M.S. & SMITH, C.R. 1987b. A Study of Hairpin Vortices in a Laminar Boundary Layer. Part 2. Hairpin Vortices Generated by Fluid Injection. *Journal of Fluid Mechanics* **175**, 43-83.

ADRIAN, R.J. 2007. Hairpin Vortex Organization in Wall Turbulence. *Physics of Fluids* **19**(4).

ADRIAN, R.J. 1975. On the Role of Conditional Averages in Turbulence Theory. In *Turbulence in Liquids*, pp. 323-332. , Rolla, Missouri: University of Missouri.

ADRIAN, R.J. 1991. Particle-Imaging Techniques For Experimental Fluid-Mechanics. *Annual Review of Fluid Mechanics* **23**(1), 261-304.

ADRIAN, R.J. 1994. Stochastic Estimation of Conditional Structure : A Review. *Applied Scientific Research* **53**, 291-303.

ADRIAN, R.J. & MARUSIC, I. 2012. Coherent Structures in Flow Over Hydraulic Engineering Surfaces. *Journal of Hydraulic Research* **50**(5), 451-464.

ADRIAN, R.J., MEINHART, C.D. & TOMKINS, C.D. 2000. Vortex Organization in the Outer Region of the Turbulent Boundary Layer. *Journal of Fluid Mechanics* **422**, 1-54.

AKOMAH, A., HANGAN, H. & NAUGHTON, J. 2011. Very High Reynolds Number Boundary Layers over 3D Sparse Roughness and Obstacles: The Mean Flow. *Experiments in Fluids* **51**(3), 743-752.

AMIR, M. & CASTRO, I.P. 2011. Turbulence in Rough-Wall Boundary Layers: Universality Issues. *Experiments in Fluids* **51**(2), 313-326.

ANDERSON, J.D. 2006. *Hypersonic and High-Temperature Gas Dynamics* 2nd ed., Reston, VA: American Institute of Aeronautics and Astronautics.

ANTONIA, R.A. & KROGSTAD, P.-Å. 2001. Turbulence Structure in Boundary Layers over Different Types of Surface Roughness. *Fluid Dynamics Research* **28**(2), 139-157.

ARNETTE, S., SAMIMY, M. & ELLIOTT, G. 1998. The Effects of Expansion on the Turbulence Structure of Compressible Boundary Layers. *Journal of Fluid Mechanics* **367**, 67-105.

ARNETTE, S.A., SAMIMY, M. & ELLIOTT, G.S. 1995. Structure of Supersonic Turbulent Boundary Layer after Expansion Regions. *AIAA Journal* **33**(3).

BENEDICT, L.H. & GOULD, R.D. 1996. Towards Better Uncertainty Estimates for Turbulence Statistics. *Experiments in Fluids* **22**(2), 129-136.

BERG, D.E. 1979. Surface Roughness Effects on a Mach 6 Turbulent Boundary Layer. *AIAA Journal* **17**(9), 929-930.

BERRY, S.A., HORVATH, T.J., HOLLIS, B.R., THOMPSON, R.A. & HAMILTON, H.H. 1999. X-33 Hypersonic Boundary Layer Transition. *AIAA 1999-3560*.

BEUTNER, T., ADELGREN, R. & ELLIOTT, G. 2006. Characterization of Schlieren Light Source Using Laser -Induced Optical Breakdown in Argon. *AIAA Journal* **44**(2), 399-402.

BOWERSOX, R.D.W. 2007. Survey of High-Speed Rough Wall Boundary Layers : Invited Presentation. *AIAA 2007-3998*.

BRADSHAW, P. 1974. The Effect of Mean Compression or Dilatation on the Turbulence Structure of Supersonic Boundary Layers. *Journal of Fluid Mechanics* **63**, 449-464.

CANTWELL, B.J. 1981. Organized Motion in Turbulent Flow. *Annual Review of Fluid Mechanics* **13**, 457-515.

CARLIER, J. & STANISLAS, M. 2005. Experimental Study of Eddy Structures in a Turbulent Boundary Layer using Particle Image Velocimetry. *Journal of Fluid Mechanics* **535**, 143-188.

CHAKRABORTY, P., BALACHANDAR, S. & ADRIAN, R.J. 2005. On the Relationships between Local Vortex Identification Schemes. *Journal of Fluid Mechanics* **535**, 189-214.

CHONG, M.S., PERRY, A.E. & CANTWELL, B.J. 1990. A General Classification of Three-Dimensional Flow Fields. *Physics of Fluids* **2**(5), 765-777.

CHRISTENSEN, K.T. & ADRIAN, R.J. 2001. Statistical Evidence of Hairpin Vortex Packets in Wall Turbulence. *Journal of Fluid Mechanics* **431**, 433-443.

CLAUSER, F.H. 1956. The Turbulent Boundary Layer. *Advances in Applied Mechanics* **4**, 1-51.

CUCITORE, R., QUADRIO, M. & BARON, A. 1999. On the Effectiveness and Limitations of Local Criteria for the Identification of a Vortex. *European Journal of Mechanics - B/Fluids* **18**(2), 261-282.

VAN DRIEST, E.R. 1951. Turbulent Boundary Layer in Compressible Fluids. *Journal Of The Aeronautical Sciences* **18**(3), 145-160.

DUAN, L., BEEKMAN, I. & MARTIN, P. 2010. Direct Numerical Simulation of Hypersonic Turbulent Boundary Layers. Part 2. Effect of Wall Temperature. *Journal of Fluid Mechanics* **655**, 419-445.

DUAN, L., BEEKMAN, I. & MARTIN, P. 2011. Direct Numerical Simulation of Hypersonic Turbulent Boundary Layers. Part 3. Effect of Mach Number. *Journal of Fluid Mechanics* **672**, 245-267.

DUSSAUGE, J.P. & GAVIGLIO, J. 1987. The Rapid Expansion of a Supersonic Turbulent Flow : Role of Bulk Dilatation. *Journal of Fluid Mechanics* **174**, 81-112.

EKOTO, I.W. 2006. *Supersonic Turbulent Boundary Layers with Periodic Mechanical Non-Equilibrium*. Ph.D. Dissertation. Texas A&M University.

EKOTO, I.W., BOWERSOX, R.D.W., BEUTNER, T. & GOSS, L. 2009. Response of Supersonic Turbulent Boundary Layers to Local and Global Mechanical Distortions. *Journal of Fluid Mechanics* **630**, 225-265.

EKOTO, I.W., BOWERSOX, R.D.W., BEUTNER, T. & GOSS, L. 2008. Supersonic Boundary Layers with Periodic Surface Roughness. *AIAA Journal* **46**(2), 486-497.

ELSINGA, G.E., ADRIAN, R.J., VAN OUDHEUSDEN, B.W. & SCARANO, F. 2010. Three-dimensional vortex organization in a high-Reynolds-number supersonic turbulent boundary layer. *Journal of Fluid Mechanics* **644**, 35-60.

ENGLISH, B.L. 2013. *Large-Scale Streamwise Turbulent Structures in Hypersonic Boundary Layers*. M.S. Thesis. Texas A&M University.

FLACK, K. A., SCHULTZ, M.P. & CONNELLY, J.S. 2007. Examination of a Critical Roughness Height for Outer Layer Similarity. *Physics of Fluids* **19**(9).

FOUCAUT, J.M., CARLIER, J. & STANISLAS, M. 2004. PIV Optimization for the Study of Turbulent Flow using Spectral Analysis. *Measurement Science and Technology* **15**(6), 1046-1058.

FRY, R.S. 2004. A Century of Ramjet Propulsion Technology Evolution. *Journal of Propulsion and Power* **20**(1), 27-58.

GANAPATHISUBRAMANI, B. 2007. Statistical Properties of Streamwise Velocity in a Supersonic Turbulent Boundary Layer. *Physics of Fluids* **19**(9).

GANAPATHISUBRAMANI, B., CLEMENS, N.T. & DOLLING, D.S. 2006. Large-Scale Motions in a Supersonic Turbulent Boundary Layer. *Journal of Fluid Mechanics* **556**, 271-282.

GANAPATHISUBRAMANI, B., HUTCHINS, N., HAMBLETON, W.T., LONGMIRE, E.K. & MARUSIC, I. 2005. Investigation of Large-Scale Coherence in a Turbulent Boundary Layer using Two-Point Correlations. *Journal of Fluid Mechanics* **524**, 57-80.

GLASS, M. & KENNEDY, I.M. 1977. An Improved Seeding Method for High Temperature Laser Doppler Velocimetry. *Combustion and Flame* **29**, 333-335.

GODDARD, F.E. 1959. Effect of Uniformly Distributed Roughness on Turbulent Skin-Friction Drag at Supersonic Speeds. *Journal of the Aerospace Sciences* **26**(1), 1-24.

GOLD, H. & PROBSTEIN, R.F. 1970. Inelastic Deformation and Crosshatching. *AIAA Paper 70-768*.

GRASS, A.J. 1971. Structural Features of Turbulent Flow over Smooth and Rough Boundaries. *Journal of Fluid Mechanics* **50**, 233-261.

GUALA, M., TOMKINS, C.D., CHRISTENSEN, K.T. & ADRIAN, R.J. 2012. Vortex Organization in a Turbulent Boundary Layer Overlying Sparse Roughness Elements. *Journal of Hydraulic Research* **50**(5), 465-481.

HALLER, G. 2005. An Objective Definition of a Vortex. *Journal of Fluid Mechanics* **525**, 1-26.

HAYAKAWA, K., SMITS, A.J. & BOGDONOFF, S.M. 1984. Hot-Wire Investigation of an Unseparated Shock-Wave/Turbulent Boundary-Layer Interaction. *AIAA Journal* **22**(5), 579-585.

HEAD, M.R. & BANDYOPADHYAY, P. 1981. New Aspects of Turbulent Boundary-Layer Structure. *Journal of Fluid Mechanics* **107**, 297-338.

HILL, J.A.F., VOISINET, R.L.P. & WAGNER, D.A. 1980. Measurements of Surface Roughness Effects on the Heat Transfer to Slender Cones at Mach 10. *AIAA 80-0345*.

HOFFERTH, J.W., BOWERSOX, R.D.W. & SARIC, W.S. 2010. The Mach 6 Quiet Tunnel at Texas A & M : Quiet Flow Performance. *AIAA 2010-4794*.

HOFFERTH, J.W., HUMBLE, R.A., FLORYAN, D.C. & SARIC, W.S. 2013. High-Bandwidth Optical Measurements of the Second-Mode Instability in a Mach 6 Quiet Tunnel. *AIAA 2013-0378*.

HOLDEN, M.S. 1984. Experimental Studies of Surface Roughness Shape and Spacing Effects on Heat Transfer and Skin Friction in Supersonic and Hypersonic flows. *AIAA 84-0016*.

HOLDEN, M.S. 1989. Studies of Surface Roughness and Blowing Effects on Hypersonic Turbulent Boundary Layers Over Slender Cones. *AIAA Paper 1989-0458*.

HUMBLE, R.A. 2008. *Unsteady Flow Organization of a Shock Wave / Boundary Layer Interaction*. Ph.D. Dissertation. TU Delft.

HUMBLE, R.A., ELSINGA, G.E., SCARANO, F. & VAN OUDHEUSDEN, B.W. 2009. Three-Dimensional Instantaneous Structure of a Shock Wave/Turbulent Boundary Layer Interaction. *Journal of Fluid Mechanics* **622**, 33-62.

HUMBLE, R.A., PELTIER, S.J. & BOWERSOX, R.D.W. 2012. Visualization of the Structural Response of a Hypersonic Turbulent Boundary Layer to Convex Curvature. *Physics of Fluids* **24**(10).

HUNT, J.C.R., WRAY, A.A. & MOIN, P. 1988. Eddies, Streams, and Convergence Zones in Turbulent Flows. In *Center for Turbulence Research*, pp. 193-208.

HUSSAIN, F. 1986. Coherent Structures and Turbulence. *Journal of Fluid Mechanics* **173**, 303-356.

HUTCHINS, N. & MARUSIC, I. 2007a. Evidence of Very Long Meandering Features in the Logarithmic Region of Turbulent Boundary Layers. *Journal of Fluid Mechanics* **579**, 1-28.

HUTCHINS, N. & MARUSIC, I. 2007b. Large-Scale Influences in Near-Wall Turbulence. *Philosophical Transactions of the Royal Society A: Mathematical, Physical and Engineering Sciences* **365**(1852), 647-64.

JEONG, J. & HUSSAIN, F. 1995. On the Identification of a Vortex. *Journal of Fluid Mechanics* **285**, 69-94.

JIMÉNEZ, J. 2004. Turbulent Flows Over Rough Walls. *Annual Review of Fluid Mechanics* **36**(1), 173-196.

JOHNSON, B. & BUSHNELL, D.M. 1970. Power-Law Velocity-Profile-Exponent Variations with Reynolds Number, Wall Cooling, and Mach Number in a Turbulent Boundary Layer. *NASA TN D-5753*.

KEANE, R.D. & ADRIAN, R.J. 1992. Theory of Cross-Correlation Analysis of PIV Images. *Applied Scientific Research* **49**, 191-215.

KIM, J. & MOIN, P. 1986. The Structure of the Vorticity Field in Turbulent Channel Flow . Part 2 . Study of Ensemble-Averaged Fields. *Journal of Fluid Mechanics* **162**, 339-363.

KIM, K.C. & ADRIAN, R.J. 1999. Very Large-Scale Motion in the Outer Layer. *Physics of Fluids* **11**(2), 417-422.

KLEBANOFF, P.S. 1955. Characteristics of Turbulence in a Boundary Layer with Zero Pressure Gradient. *NACA 1247*.

KLINE, S.J. & MCCLINTOCK, F.A. 1953. Describing Uncertainties in Single Sample Experiments. *Mechanical Engineering* **75**, 3-8.

KLINE, S.J., REYNOLDS, W.C., SCHRAUBT, F.A. & RUNSTADLER, P.W. 1967. The Structure of Turbulent Boundary Layers. *Journal of Fluid Mechanics* **30**(4), 741-773.

KOLÁR, V. 2009. Compressibility Effect in Vortex Identification. *AIAA Journal* **47**(2), 473-475.

KOLÁŘ, V. 2011. Brief Notes on Vortex Identification. In *8th WSEAS International Conference on Fluid Mechanics, 8th WSEAS International Conference on Heat and Mass Transfer*, pp. 23-28. Puerto Morelos, Mexico.

KROGSTAD, P.-Å. & ANTONIA, R. A. 1994. Structure of Turbulent Boundary Layers on Smooth and Rough Walls. *Journal of Fluid Mechanics* **277**, 1-21.

KROGSTAD, P.-Å. & ANTONIA, R.A. 1999. Surface Roughness Effects in Turbulent Boundary Layers. *Experiments in Fluids* **27**(5), 450-460.

KROGSTAD, P.-Å., ANTONIA, R.A. & BROWNE, L.W.B. 1992. Comparison Between Rough- and Smooth-Wall Turbulent Boundary Layers. *Journal of Fluid Mechanics* **245**, 599-617.

LAGANELLI, A. L. & NESTLER, D.E. 1969. Surface Ablation Patterns - A Phenomenology study. *AIAA Journal* **7**(7), 1319-1325.

LARSON, H.E. & MATEER, G. 1968. Cross-Hatching: A Coupling of Gas Dynamics with the Ablation Process. *AIAA Paper 68-670*.

LATIN, R.M. & BOWERSOX, R.D.W. 2000. Flow Properties of a Supersonic Turbulent Boundary Layer with Wall Roughness. *AIAA Journal* **38**(10), 1804-1821.

LATIN, R.M. & BOWERSOX, R.D.W. 2002. Temporal Turbulent Flow Structure for Supersonic Rough-Wall Boundary Layers. *AIAA Journal* **40**(5), 832-841.

LAUNDER, B., REECE, G. & RODI, W. 1975. Progress in the Development of a Reynolds-Stress Turbulence Closure. *Journal of Fluid Mechanics* **68**(3), 537-566.

LEHEW, J., GUALA, M. & MCKEON, B.J. 2011. A Study of the Three-Dimensional Spectral Energy Distribution in a Zero Pressure Gradient Turbulent Boundary Layer. *Experiments in Fluids* **51**(4), 997-1012.

LIEPMANN, H.W. & GODDARD, F.E. 1957. Note on the Mach Number Effect upon the Skin Friction of Rough Surfaces. *Journal of the Aeronautical Sciences* **24**(10), 784.

LIU, T. & SULLIVAN, J.P. 2005. *Pressure and Temperature Sensitive Paints*, Berlin, Germany: Springer.

LU, S.S. & WILLMARTH, W.W. 1973. Measurements of the Structure of the Reynolds Stress in a Turbulent Boundary Layer. *Journal of Fluid Mechanics* **60**(03), 481-511.

LUKER, J.J., BOWERSOX, R.D.W. & BUTER, T.A. 2000. Influence of Curvature-Driven Favorable Pressure Gradient on Supersonic Turbulent Boundary Layer. *AIAA Journal* **38**(8), 1351-1359.

LUKER, J.J., HALE, C.S. & BOWERSOX, R.D.W. 1998. Experimental Analysis of the Turbulent Shear Stresses for Distorted Supersonic Boundary Layers. *Journal of Propulsion and Power* **14**(1), 110-118.

LUMLEY, J.L. 1967. Similarity and the Turbulent Energy Spectrum. *Physics of Fluids* **10**(4), 855.

MANN, H. 1967. *Experimental Study of the Compressible Turbulent Boundary Layer Skin Friction and Heat Transfer in the Fully Rough Regime*, University of Texas, Austin, Texas. DRL-554, Defense Research Laboratory.

MARUSIC, I., CANDLER, G.V., INTERRANTE, V., MARTIN, P., SUBBAREDDY, P.K. & MOSS, A. 2000. Detection and Tracking of Coherent Features in a Mach 4 Turbulent Boundary Layer. *AIAA 2000-2414*.

MELLING, A. 1997. Tracer Particles and Seeding for Particle Image Velocimetry. *Measurement Science Technology* **8**, 1406-1416.

MOIN, P. & KIM, J. 1982. Numerical Investigation of Turbulent Channel Flow. *Journal of Fluid Mechanics* **118**, 341-377.

MOIN, P. & KIM, J. 1985. The Structure of the Vorticity Field in Turbulent Channel Flow . Part 1 . Analysis of Instantaneous Fields and Statistical Correlations. *Journal of Fluid Mechanics* **155**, 441-464.

MORKOVIN, M. 1961. Effects of Compressibility on Turbulent Flows. *Mecanique de la Turbulence*, 367-380.

NAGAOSA, R. & HANDLER, R. A. 2003. Statistical Analysis of Coherent Vortices near a Free Surface in a Fully Developed Turbulence. *Physics of Fluids* **15**(2), 375-394.

NARASIMHA, R. & SREENIVASAN, K.R. 1973. Relaminarization in Highly Accelerated Turbulent Boundary Layers. *Journal of Fluid Mechanics* **61**(3), 417-447.

NATRAJAN, V.K., WU, Y. & CHRISTENSEN, K.T. 2007. Spatial Signatures of Retrograde Spanwise Vortices in Wall Turbulence. *Journal of Fluid Mechanics* **574**, 155-167.

NICKELS, T.B., MARUSIC, I., HAFEZ, S., HUTCHINS, N. & CHONG, M.S. 2007. Some Predictions of the Attached Eddy Model for a High Reynolds Number Boundary Layer. *Philosophical transactions. Series A, Mathematical, physical, and engineering sciences* **365**(1852), 807-22.

NIKURADSE, J. 1933. Laws of Flow in Rough Pipes. *NACA 1292*.

PANTON, R.L. 2001. Overview of the Self-Sustaining Mechanisms of Wall Turbulence. *Progress in Aerospace Sciences* **37**(4), 341-383.

PERRY, A.E. & CHONG, M.S. 1982. On the Mechanism of Wall Turbulence. *Journal of Fluid Mechanics* **119**, 173-217.

PERRY, A.E., LIM, K.L. & HENBEST, M. 1987. An Experimental Study of the Turbulence Structure in Smooth- and Rough-Wall Boundary Layers. *Journal of Fluid Mechanics* **177**, 437-466.

PERRY, A.E., SCHOFIELD, W.H. & JOUBERT, P.N. 1969. Rough Wall Turbulent Boundary Layers. *Journal of Fluid Mechanics* **37**(02), 383-413.

PIOMELLI, U., BALARAS, E. & PASCARELLI, A. 2000. Turbulent Structures in Accelerating Boundary Layers. *Journal of Turbulence* **1**(1), 1-16.

PIROZZOLI, S. & BERNARDINI, M. 2011. Turbulence in Supersonic Boundary Layers at Moderate Reynolds Number. *Journal of Fluid Mechanics* **688**, 120-168.

PIROZZOLI, S., BERNARDINI, M. & GRASSO, F. 2008. Characterization of Coherent Vortical Structures in a Supersonic Turbulent Boundary Layer. *Journal of Fluid Mechanics* **613**, 205-231.

POGGIE, J., ERBLAND, P.J., SMITS, A.J. & MILES, R.B. 2004. Quantitative Visualization of Compressible Turbulent Shear Flows using Condensate-Enhanced Rayleigh Scattering. *Experiments in Fluids* **37**(3), 438-454.

POPE, A. & GOIN, K.L. 1965. *High-Speed Wind Tunnel Testing*, Malabar, FL: Krieger Publishing Company.

POPE, S.B. 2000. *Turbulent Flows*, New York, NY: Cambridge University Press.

RAFFEL, M., WILLERT, C.E., WERELEY, S.T. & KOMPENHANS, J. 2007. *Particle Image Velocimetry: A Practical Guide* 2nd ed., Berlin: Springer.

RAGNI, D., SCHRIJER, F., OUDHEUSDEN, B.W.V. & SCARANO, F. 2011. Particle Tracer Response across Shocks Measured by PIV. *Experiments in Fluids* **50**(1), 53-64.

RAUPACH, M.R. 1991. Rough-Wall Turbulent Boundary Layers. *Applied Mechanics Reviews* **44**(1), 1-25.

REDA, D.C., FAN, C. & KETTER, F.C. 1975. Compressible Turbulent Skin Friction on Rough and Rough/ Wavy Walls. *AIAA Journal* **13**(5), 553-554.

REYNOLDS, O. 1895. On the Dynamical Theory of Incrompessible Viscous Fluids and the Determination of the Criterion. *Philosophical Transactions of the Royal Society A: Mathematical, Physical and Engineering Sciences* **186**.

RICHARDSON, L.F. 1922. *Weather Prediction by Numerical Process*, Cambridge: Cambridge University Press.

RINGUETTE, M.J., WU, M. & MARTIN, P. 2007. Coherent Structures in Direct Numerical Simulation of Turbulent Boundary Layers at Mach 3. *Journal of Fluid Mechanics* **594**, 59-69.

ROBINSON, S.K. 1991. Coherent Motions in the Turbulent Boundary Layer. *Annual Review of Fluid Mechanics* **23**(1), 601-639.

SAHOO, D., PAPAGEORGE, M. & SMITS, A.J. 2010. PIV Experiments on a Rough-wall Hypersonic Turbulent Boundary Layer. *AIAA 2010-4471*.

SAMIMY, M. & LELE, S.K. 1991. Motion of Particles with Inertia in a Compressible Free Shear Layer. *Physics of Fluids A: Fluid Dynamics* **3**(8), 1915.

SANCHEZ-GONZALES, R., SRINIVASAN, R., BOWERSOX, R.D.W. & NORTH, S.W. 2011. Simultaneous Velocity and Temperature Measurements in Gaseous Flow Fields using the VENOM Technique. *Optics Letters* **36**(2), 196-198.

SANCHEZ-GONZALES, R., SRINIVASAN, R., HOFFERTH, J.W., KIM, D.Y., TINDALL, A., BOWERSOX, R.D.W. & NORTH, S.W. 2012. Repetitively Pulsed Hypersonic Flow Apparatus for Diagnostic Development. *AIAA Journal* **50**(3).

SCHLICHTING, H. 1955. *Boundary Layer Theory*, McGraw-Hill.

SCHRIJER, F.F.J. & SCARANO, F. 2007. Particle Slip Compensation in Steady Compressible Flows. In *7th International Symposium on Particle Image Velocimetry*.

SCHULTZ, M.P. & FLACK, K. A. 2007. The Rough-Wall Turbulent Boundary Layer from the Hydraulically Smooth to the Fully Rough Regime. *Journal of Fluid Mechanics* **580**, 381-405.

SEMPER, M.T., PRUSKI, B.J. & BOWERSOX, R.D.W. 2012. Freestream Turbulence Measurements in a Continuously Variable Hypersonic Wind Tunnel. *AIAA 2012-0732*.

SEMPER, M.T., TICHENOR, N.R., BOWERSOX, R.D.W., SRINIVASAN, R. & NORTH, S.W. 2009. On the Design and Calibration of an Actively Controlled Expansion Hypersonic Wind Tunnel. *AIAA 2009-799*.

SETTLES, G.S. 2001. *Schlieren and Shadowgraph Techniques: Visualizing Phenomena in Transparent Media*, Berlin: Springer-Verlag.

SMITH, D.R. & SMITS, A.J. 1994. The Effects of Streamline Curvature and Pressure Gradient on the Behavior of Turbulent Boundary Layers in Supersonic Flow. *AIAA 1991-2227*.

SMITH, D.R. & SMITS, A.J. 1991. The Rapid Expansion of a Turbulent Boundary Layer in a Supersonic Flow. *Theoretical and Computational Fluid Dynamics* **2**, 319-328.

SMITS, A.J. & WOOD, D.H. 1985. The Response of Turbulent Boundary Layers to Sudden Perturbations. *Annual Review of Fluid Mechanics* **17**(1), 321-358.

SPINA, E.F., SMITS, A.J. & ROBINSON, S.K. 1994. The Physics of Supersonic Turbulent Boundary Layers. *Annual Review of Fluid Mechanics* **26**(1), 287-319.

STOCK, H.W. 1975. Surface Patterns on Subliming and Liquefying Ablation Materials. *AIAA Journal* **13**(9), 1217-1223.

TAYLOR, E.M., MARTIN, M.P. & SMITS, A.J. 2005. Preliminary Study of the Turbulence Structure in Supersonic Boundary Layers using DNS Data. *AIAA Paper 2005-5290*.

TAYLOR, G.I. 1938. The Spectrum of Turbulence. *Proceedings of the Royal Society A: Mathematical, Physical and Engineering Sciences* **164**(919), 476-490.

VON TERZI, D. A., SANDBERG, R.D. & FASEL, H.F. 2009. Identification of Large Coherent Structures in Supersonic Axisymmetric Wakes. *Computers & Fluids* **38**(8), 1638-1650.

THEODORSEN, T. 1952. Mechanism of Turbulence. In *Proc. Second Midwestern Conf. of Fluid Mechanics*, pp. 1-19. Columbus, OH: Ohio State University.

THOMANN, H. 1968. Effect of Streamwise Wall Curvature on Heat Transfer in a Turbulent Boundary Layer. *Journal of Fluid Mechanics* **33**(2), 283-292.

TICHENOR, N.R., HUMBLE, R.A. & BOWERSOX, R.D.W. 2013. Response of a Hypersonic Turbulent Boundary Layer to Favourable Pressure Gradients. *Journal of Fluid Mechanics* **722**, 187-213.

TICHENOR, N.R., SEMPER, M.T., BOWERSOX, R.D.W., SRINIVASAN, R. & NORTH, S.W. 2010. Calibration of an Actively Controlled Expansion Hypersonic Wind Tunnel. *AIAA 2010-4793*.

TILMANN, C.P., BOWERSOX, R.D.W. & BUTER, T.A. 1999. On the Design and Construction of an Academic Mach 5 Wind Tunnel. *AIAA 1999-0800*.

TOMKINS, C.D. & ADRIAN, R.J. 2003. Spanwise Structure and Scale Growth in Turbulent Boundary Layers. *Journal of Fluid Mechanics* **490**, 37-74.

TOWNSEND, A.A. 1976. *The Structure of Turbulent Shear Flow* 2nd ed., Cambridge University Press.

VOLINO, R.J., SCHULTZ, M.P. & FLACK, K. A. 2011. Turbulence Structure in Boundary Layers over Periodic Two- and Three-Dimensional Roughness. *Journal of Fluid Mechanics* **676**, 172-190.

WADE, J. 1955. *An Experimental Investigation of the Effects of Surface Roughness on the Drag of a Cone- Cylinder Model at a Mach Number of 2.48*, University of Toronto, Toronto, Canada. Report 34, Institute of Aerophysics.

WALLACE, J.M., ECKELMANN, H. & BRODKEY, R.S. 1972. The Wall Region in Turbulent Shear Flow. *Journal of Fluid Mechanics* **54**(01), 39-48.

WESTERWEEL, J. 1997. Fundamentals of Digital Particle Image Velocimetry. *Measurement Science and Technology* **8**, 1379-1392.

WHITE, C.O. & GRABOW, R.M. 1973. Crosshatch Surface Patterns-Comparison of Experiment with Theory. *AIAA Journal* **11**(9), 1316-1322.

WHITE, F.M. 2006. *Viscous Fluid Flow* 3rd ed., McGraw-Hill.

WILLMARTH, W.W. & LU, S.S. 1972. Structure of the Reynolds Stress near the Wall. *Journal of Fluid Mechanics* **55**(01), 65-92.

WU, Y. & CHRISTENSEN, K.T. 2006a. Population Trends of Spanwise Vortices in Wall Turbulence. *Journal of Fluid Mechanics* **568**, 55-76.

WU, Y. & CHRISTENSEN, K.T. 2006b. Reynolds-Stress Enhancement Associated with a Short Fetch of Roughness in Wall Turbulence. *AIAA Journal* **44**(12), 3098-3106.

WU, Y. & CHRISTENSEN, K.T. 2010. Spatial Structure of a Turbulent Boundary Layer with Irregular Surface Roughness. *Journal of Fluid Mechanics* **655**, 380-418.

YOUNG, F. 1965. *Experimental Investigation of the Effects of Surface Roughness on Compressible Turbulent Boundary Layer Skin Friction and Heat Transfer*, University of Texas, Austin, Texas. DRL-532, Defense Research Laboratory.

ZHOU, J., ADRIAN, R.J., BALACHANDAR, S. & KENDALL, T.M. 1999. Mechanisms for Generating Coherent Packets of Hairpin Vortices in Channel Flow. *Journal of Fluid Mechanics* **387**, 353-396.

APPENDIX A

WALL TEMPERATURE MEASUREMENT

For turbulent boundary layers, a key scaling parameter for the near-wall inner-scaled motions is the kinematic viscosity at the wall, defined as $\nu_w = \mu_w/\rho_w$. If the pressure field p_w is known, then only the wall temperature T_w is required to compute ν_w. Additionally, measurements of T_w can reveal whether the flow is non-adiabatic (i.e. $T_w \neq T_{aw}$), which may affect the boundary layer profile and stress distribution [White (2006)]. Other applications of temperature measurements include determining the heat flux in high-enthalpy flows, or monitoring the transition location within transitional boundary layers.

The traditional method of measuring T_w relies upon integrated thermocouples, either surface- or flush-mounted. However, these devices suffer from several weaknesses. Firstly, the thermocouples provide only single-point measurements. While this may be suitable for determining the heat flux, other experiments (such as determining the transition location) may require a whole-field measurement. In addition, improper mounting of the thermocouples may lead to perturbations within the flowfield. This can be exacerbated if the thermocouple material and the model have different coefficients of thermal expansion.

Many of these limitations can be overcome through the use of infrared (IR) thermography. Using an IR-sensitive camera, whole-field non-intrusive measurements of the surface can be collected. This technique is commonly used in high-enthalpy flows, or in cases where the test model can not be altered. Indeed, these advantages are the foremost reasons that IR thermography is used in major facilities.

Temperature sensitive paint (TSP) provides another method for the measurement of T_w, yielding full-field non-intrusive measurements of the surface temperature, at a lower cost and higher spatial resolution than other systems [Liu & Sullivan (2005)]. In TSP, a two-part mixture containing luminescent molecules suspended in an oxygen-impermeable polymer binder is applied to the model surface. When the paint is illuminated by an

excitation source of the correct wavelength, the luminescent molecules are excited to higher energy levels. As these molecules relax back to their ground state, light is emitted at a longer wavelength, which is imaged by a CCD camera. The intensity of the emission is a function of the local temperature, due to thermal quenching. This intensity can then be related to the surface temperature, through the application of a known calibration. For a more thorough discussion of TSP, the reader is directed to Liu & Sullivan (2005).

A.1. TSP Principles

When the photons from the excitation source impact the TSP, the luminescent molecules are excited from a ground singlet state S_0 to an excited singlet state S_1 or S_2. Relaxation occurs through both radiative and non-radiative processes. Emission is due to the transition from the single S_1 or triplet T_1 state to the ground state S_0, producing either fluorescence or phosphorescence, respectively. The triplet state T_1 is populated by a non-radiative transition from S_1 to T_1, a process known as intersystem crossing. An additional non-radiative process is external conversion, which involves transfer between the excited luminophores and the environment. This interaction with external factors is also referred to as "quenching", and is the primary mechanism governing the behavior of TSP [Liu & Sullivan (2005)].

At elevated temperatures, the increased frequency of collisions leads to a greater degree of relaxation through external conversion. This "thermal quenching" results in a lower emission intensity as the temperature increases, providing a suitable metric for determining the surface temperature. The dependency of the emission intensity I upon the temperature T is contained within the Arrhenius equation [Liu & Sullivan (2005)]:

$$\ln \frac{I(T)}{I(T_{ref})} = \frac{E_{nr}}{R}\left(\frac{1}{T} - \frac{1}{T_{ref}}\right) \tag{A.1}$$

where T_{ref} and R describe the reference temperature and gas constant, respectively. The activation energy for the non-radiative quenching is given by E_{nr}. The inverse relation between T and $I(T)$ is clearly seen in Eqn. A.1.

A.2. Experimental Arrangement

For all measurements, the surface temperature was determined using UNT-01 temperature sensitive paint, provided by ISSI. The paint was excited by an LED array, which provided a uniform output at a wavelength of 400 nm. During relaxation of the luminophores, the light emission from the paint occurred in the 500 nm – 720 nm wavelength range, which was imaged using a Cooke PCO 1600 CCD camera. A 450 nm long-pass filter was used when viewing the paint surface, to remove any reflections from the excitation source.

A.2.1. Calibration

Calibration of the TSP was performed in a dedicated bench-top calibration cell, shown in Fig. A.1. The paint was applied to an aluminum target, measuring approximately 30 mm x 30 mm x 40 mm. Initial tests had used a thin aluminum plate, but temperature nonuniformities along the surface prevented a suitable calibration. The CCD camera was oriented normal to the target surface, with the LED arrays positioned on either side. For all images, the camera exposure was 500 ms. The target was heated using a surface-mounted electric heater, attached on the external face of the calibration cell. Surface temperatures were monitored by a thermocouple mounted on the painted face of the target.

Equation A.1 is presented as a function of the temperature and emission *ratios*. Therefore, the calibration must be performed using these ratios, and not merely the measured values I and T. The reference temperature was equal to the ambient

temperature, T_{ref} = 294 K. During the calibration process, the reference emission I_{ref} was measured prior to heating the target. The temperature was then increased in increments of approximately 5 K, allowing sufficient time between tests for the surface temperature to stabilize.

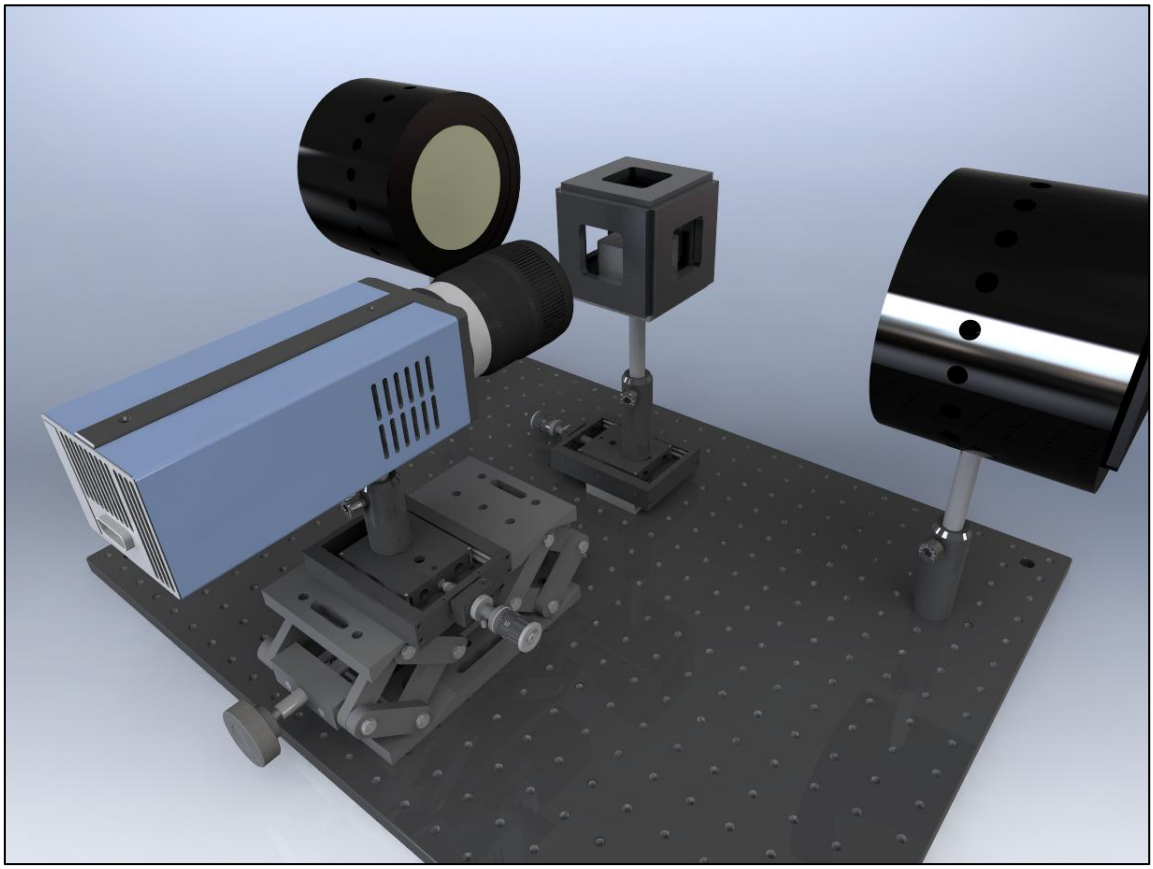

Figure A.1 TSP calibration cell, showing CCD camera and LED arrays (thermocouple and electric heater are not shown)

It was discovered that dark noise within the camera contributed to small fluctuations within the measured intensity I, which resulted in small-scale surface temperature fluctuations of 2 – 3 K. To mitigate this effect, multiple images were collected at each calibration condition, and ensemble-averaged to form a mean intensity field. The number

of images was selected so that the uncertainty of the measured intensity ε_I was less than 1%, where the uncertainty was computed as

$$\varepsilon_I = \frac{I_{rms}}{\sqrt{N}} \tag{A.2}$$

I_{rms} is the rms fluctuation of the measured intensity, and N is the number of sampled images. It was found that N = 25 images was sufficient to force ε_I to less than 1% of the mean value. Additionally, a background image was subtracted for each calibration point, to prevent external light sources from contaminating the calibration data. The measured intensities of the resulting mean images were scaled by the reference mean image, producing M two-dimensional fields of the ratio I_{ref} / I, where M is the number of calibration conditions. In order to yield a single value of I_{ref} / I for each condition, the intensity ratios were spatially averaged over the center of each image, which was allowable due to the uniformity of the intensity ratio for each image.

The pre-processing steps described above yielded M values of I_{ref} / I and T/T_{ref}. The calibration curve was generated by a second-order least squares polynomial fit of the plotted data.

A.2.2. Experimental Procedure

Surface temperature measurements were performed for the acrylic baseline and smooth SPG models. Initial tests using the diamond roughness geometry did not yield usable data, since it was not possible to uniformly illuminate the rough surface through the available optical access.

The TSP was applied to a 25 mm x 25 mm square section of the acrylic model, using 3 – 5 light coats of paint, allowing 30 – 60 seconds of drying time between coats. In order to ensure that the painted surface did not perturb the flowfield, the surface profile was measured using a Mitutoyo Surftest SJ-400 profilometer, and shown in Fig. A.2. The

transition from unpainted to painted surface introduces a small roughness peak, though the disturbance is less than 0.5 mm in length, and is mostly contained within the viscous sublayer ($y^+ < 5$). Therefore, the painted surface was not expected to introduce any significant distortions to the boundary layer.

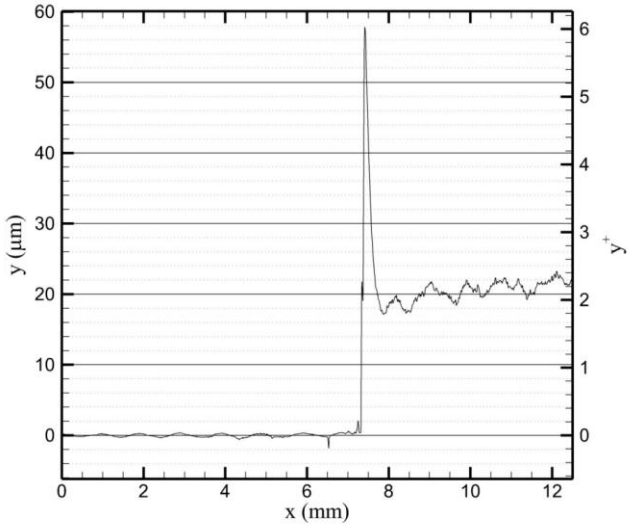

Figure A.2 Surface roughness of TSP, measured using a Mitutoyo SJ-400 profilometer. *The peak seen at x = 7.5 mm is due to the transition from unpainted to painted surface*

Prior to testing, the painted models were stored in complete darkness, to prevent photo-degradation of the TSP. During installation and testing, the room lights were darkened, to ensure a longer lifetime of the paint. Reference images were collected prior to the tunnel operation, along with a background image. The test images were collected throughout the operation of the tunnel, showing the evolution of the surface temperature.

A.3. Measured Surface Temperature

The measured surface temperatures for the baseline and smooth SPG models are shown in Figs. A.3 and A.4, respectively. For each case, the model surface maintains a nearly

constant surface temperature, varying by less than 5 K during the tunnel operation. The PIV measurements were typically performed at t = 250 – 350 seconds, during which the model experienced only a 1 – 2 K increase. Also, note that the surface temperature was approximately 84% - 85% of the total temperature T_0. For the test conditions used during the PIV collection, this yields a surface temperature of 307 K, with a variance of 1 – 2 K.

It was initially expected that the surface temperature of the smooth SPG model would decrease dramatically, due to the flow expansion through the favorable pressure gradient. Figure A.4 shows that the surface temperature was relatively unaffected by the FPG. Instead, it is more likely that the large thermal mass of the model, combined with the low thermal conductivity of acrylic, allowed for a nearly constant surface temperature.

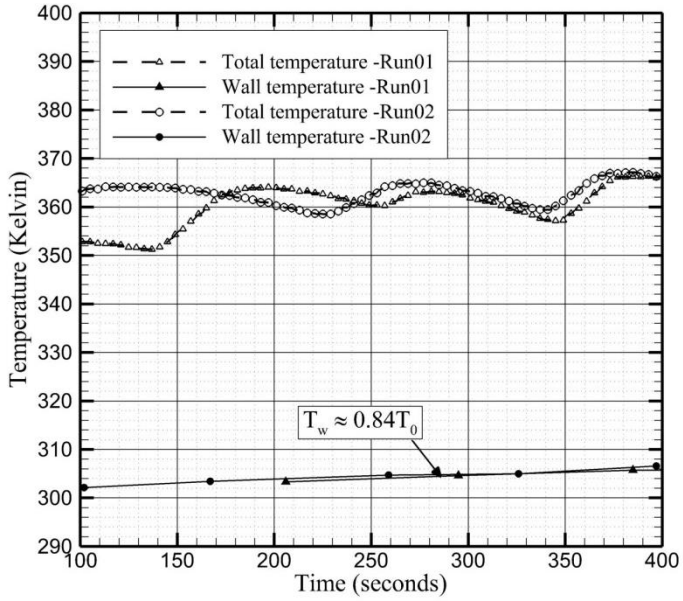

Figure A.3 Wall temperature of the baseline model, measured with ISSI UNT temperature sensitive paint. *The wall temperature wall approximately 84% of the total temperature*

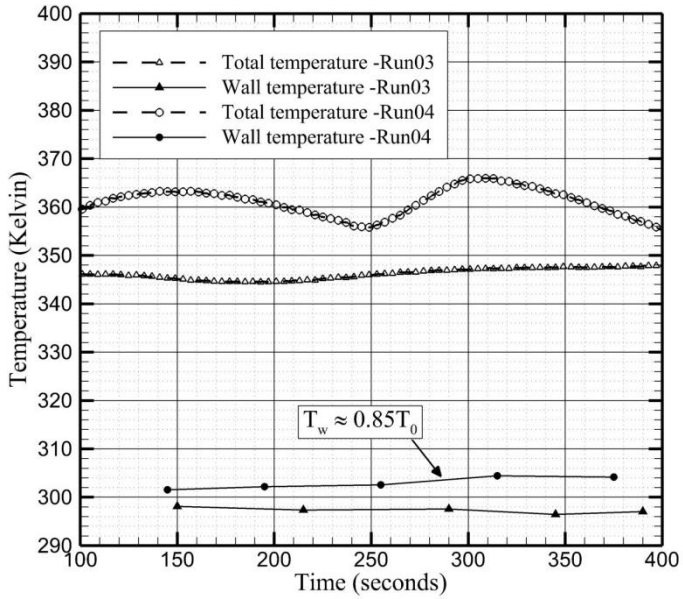

Figure A.4 Wall temperature of the smooth SPG model, measured with ISSI UNT temperature sensitive paint. *The wall temperature wall approximately 85% of the total temperature*

APPENDIX B

UNCERTAINTY ANALYSIS

Experimental uncertainty is inherent to any measured quantity, due to the combined effects of both systematic (bias) and random errors. No experiment is complete without a full and thorough reporting of the uncertainty levels of the data. This section will detail the factors influencing the measured values and computed statistics, accounting for uncertainties due to data collection and finite sample size. Knowledge of the relative uncertainty levels will allow for a more informed discussion of the experimental results.

The measurement uncertainty of any quantity can be expressed as the combined effects of the contributing uncertainties, multiplied by their respective sensitivity coefficients [Kline & McClintock (1953)]. This approach is known as *linear error/uncertainty propagation*, estimating the uncertainty as

$$\varepsilon_y = \sqrt{\left(\frac{df}{dx_1}\varepsilon_{x_1}\right)^2 + \left(\frac{df}{dx_2}\varepsilon_{x_2}\right)^2 + \ldots} \tag{B.1}$$

where ε_y is the total dimensional uncertainty, ε_x is the uncertainty of the contributing factors, and $\frac{df}{dx}$ is the sensitivity coefficient. The linear nature of this estimation requires that the measurement uncertainties ε_x be uncorrelated. While this assumption is not strictly true for every measurement, it is a reasonable approximation. Furthermore, in order to calculate the sensitivity coefficients, a model equation must exist for the measured value

$$y = f(x_1, x_2, x_3, \ldots) \tag{B.2}$$

where y is the measured value, dependent upon variables x_n.

B.1. Instantaneous Velocity

PIV has been employed in this study to produce a two-dimensional grid of velocity vectors. The uncertainty analysis described below follows the procedure given by Humble (2008). While the imaging and processing of the PIV data can be quite complex (see §4.2), the core principle of this technique is embodied in the simple relation:

$$u = \frac{\partial s}{\partial t} \tag{B.3}$$

where u is the calculated velocity, and ∂s and ∂t are the measured particle displacement and time step, respectively. Necessarily, any uncertainty in calculating the velocity u will be due to both random and bias errors in the determination of the particle positions. Recasting Eqn. B.3 in discrete terms, and applying Eqn. B.1 yields

$$\varepsilon_u = \sqrt{\left(\frac{1}{\Delta t}\varepsilon_{\Delta s}\right)^2 + \left(\frac{\Delta s}{\Delta t^2}\varepsilon_{\Delta t}\right)^2} \tag{B.4}$$

In Eqn. B.4, Δs is the maximum particle displacement (in physical dimensions) and Δt is the time separation between exposures. The uncertainty $\varepsilon_{\Delta s}$ is a function of the spatial resolution $\kappa = l_c/n_c$, where l_c is the calibration dot spacing (in physical coordinates) and n_c is the pixel spacing between the calibration does. The uncertainty of the spatial resolution, ε_κ, can be formulated as

$$\varepsilon_\kappa = \sqrt{\left(\frac{\partial \kappa}{\partial l_c}\varepsilon_{l_c}\right)^2 + \left(\frac{\partial \kappa}{\partial n_c}\varepsilon_{n_c}\right)^2} = \sqrt{\left(\frac{1}{n_c}\varepsilon_{l_c}\right)^2 + \left(\frac{l_c}{n_c^2}\varepsilon_{n_c}\right)^2} \tag{B.5}$$

Additionally, a small error is present in the cross-correlation, represented as ε_{cc}. Combining these components yields

$$\varepsilon_{\Delta s} = \sqrt{\left(\kappa\varepsilon_{cc}\right)^2 + \left(\frac{\Delta s}{\kappa}\varepsilon_\kappa\right)^2} \tag{B.6}$$

The resulting elemental and total uncertainties are listed in Table B.1, for the baseline boundary layer case.

Table B.1 Uncertainty parameters of PIV calculations

Parameter	Baseline boundary layer
U_e	760 m/s
Δt	500 ns
Δs	0.44 mm
$\varepsilon_{\Delta t}$	1 ns
n_c	252.7 pixels
l_c	3.175 mm
κ	0.0126 mm/px
ε_{l_c}	0.06 mm
ε_{n_c}	5 pixels
ε_{cc}	0.1 pixels
$\varepsilon_{\Delta s}$	0.012 mm
ε_u / U_e	3.14%

B.2. Boundary Layer Thickness

The boundary layer thicknesses quoted in this dissertation were evaluated by determining the height at which $u/U = 0.99$. This is the most common method by which δ is measured. However, the gradual slope of the velocity profile at the boundary layer edge (i.e. $dU/dy \approx 0$) can lead to an imprecise estimate of the boundary layer thickness. The uncertainty of δ is generally quoted as approximately 5% - 10%, though this value is often only estimated through a visual inspection. Given the importance of the boundary layer thickness in outer scaling, it is necessary to compute a more quantitative measure of the boundary layer thickness uncertainty ε_δ.

One approach to computing ε_δ is by comparing the measured profile with a known velocity distribution. However, since there is no closed-form solution to the turbulent boundary layer profile (unlike the laminar case, in which Blasius' solution can be

employed), an empirical solution is often selected. This profile takes the form of a power law, computed as

$$\frac{u}{U} = \left(\frac{y}{\delta} \right)^{1/n} \tag{B.7}$$

The term n is the velocity profile exponent, and is determined empirically. For most cases, $n = 7$. However, Johnson & Bushnell (1970) showed that $n \approx 7 - 9$ for boundary layers in conditions similar to those in this study (Mach 3 – 5, Re_θ = 20,000 – 70,000), making the velocity profile in Eqn. B.7 unsuitable for computing the uncertainty ε_δ.

In order to establish a robust method for computing ε_δ, let us first consider the factors that contribute to the uncertainty. Since the boundary layer edge is currently defined as the height at which $u/U = 0.99$, it is natural to assume that ε_δ is dependent upon the mean velocity uncertainty ε_U. Upon first inspection, it may seem reasonable to also include the spatial uncertainty ε_y, though that approach is incorrect. It is important to remember that the spatial location (i.e. δ) is a function of the velocity distribution. The position is an *output*, and therefore ε_δ is not explicitly dependent upon ε_y.

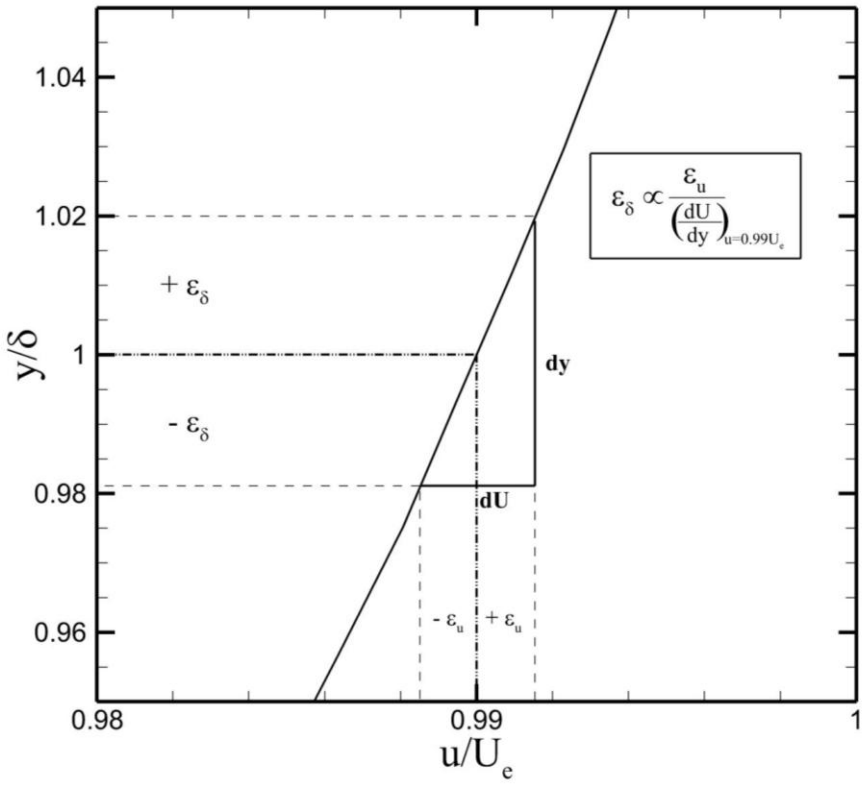

Figure B.1 Velocity profile, showing the relation between ε_δ and dU/dy. *Note: The uncertainties ε shown in the figure are meant to show the relation with dU/dy, and are not representative of the magnitude of the actual uncertainties in this study.*

The final, and primary, contributor to ε_δ is the velocity gradient dU/dy. As stated previously, the decreasing magnitude $dU/dy \ll 1$ at the boundary layer edge is the chief impediment to obtaining a precise measure of δ. Naturally, if one were to construct an expression for ε_δ, it should be inversely proportional to dU/dy. For a given ε_U, the magnitude $|dU/dy|$ will scale the resulting boundary layer thickness uncertainty, as shown in Fig. B.1 and computed as

$$\varepsilon_\delta \propto \frac{\varepsilon_U}{\left(\frac{\partial U}{\partial y}\right)_{u=0.99U_e}} \tag{B.8}$$

Note that Eqn. B.8 is a proportionality, as there may be additional coefficients on the right-hand side. The form of the expression in Eqn. B.8 can be explained logically, by considering the two extreme (and unrealistic) cases, a) $dU/dy \approx 1$, and b) $dU/dy \rightarrow 0$. For the first case, the velocity profile exhibits a gradual slope at $y/\delta = 1$, shown in Fig. B.2. For a known ε_U, the large dU/dy leads to a small projection onto the vertical axis, and hence a small uncertainty ε_δ. In contrast, a small value of dU/dy produces a nearly vertical slope. Using the same value for ε_U as in Fig. B.2, the projection onto the vertical axis is much larger in Fig. B.3, owing to the vanishingly small gradient dU/dy.

Using the computed uncertainty ε_U and gradient dU/dy for the smooth ZPG case, it is possible to estimate an uncertainty for the boundary layer thickness. The resulting value is $\delta = 10.9 \pm 0.66$ mm, or 6.1% when nondimensionalized by δ.

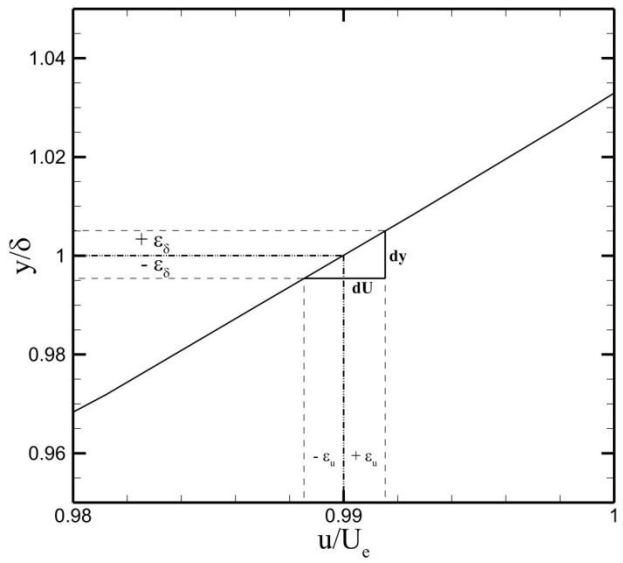

Figure B.2 Mean velocity profile, showing the effect of $dU/dy \approx 1$ on the uncertainty ε_δ. *Note: The uncertainties ε shown in the figure are meant to show the relation with dU/dy, and are not representative of the magnitude of the actual uncertainties in this study.*

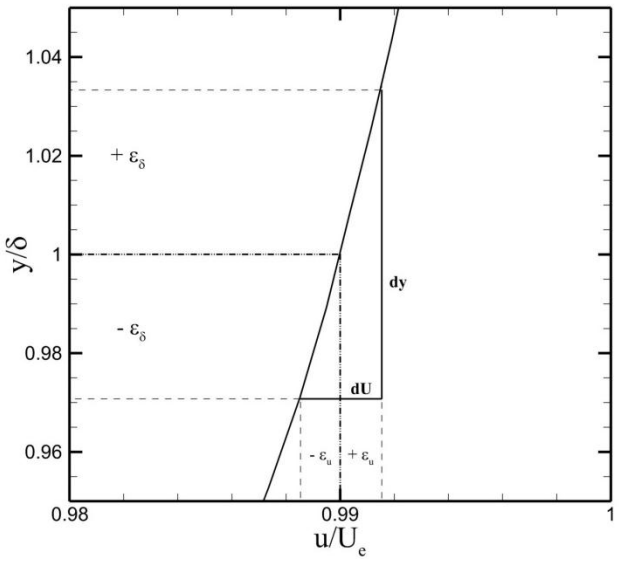

Figure B.3 Mean velocity profile, showing the effect of $dU/dy \rightarrow 0$ on the uncertainty ε_δ. *Note: The uncertainties ε shown in the figure are meant to show the relation with dU/dy, and are not representative of the magnitude of the actual uncertainties in this study.*

B.3. Particle Slip Estimation

In §4.2.1, the selection of seeding particles for PIV is described, emphasizing the competing demands of a sufficiently large scattering cross-section and a necessarily small particle response time τ_p. Considering only the parameter τ_p, the suitability of a particular seeding material can be assessed by computing the Stokes number, defined as $St = \tau_p/\tau_f$. If $St \leq 0.2$, then the particle is assumed to reliably track the flowfield [Samimy & Lele (1991)]. Conversely, the particle slip, defined as the difference between the (measured) particle velocity U_p and the flow velocity U_f, is deemed prohibitively large for $St > 0.2$. While this assumption may be reasonable, there are two main drawbacks in relying upon this criterion as the primary determination in selecting a seeding particle. 1) The requirement $St \leq 0.2$ condenses the boundary layer response into a single time constant $\tau_f = \delta/U_e$, which is compared with τ_p to yield a single value for the Stokes number. This allows a relatively simple assessment of the suitability of a particle (in terms of response time), but completely ignores localized distortions which may violate

the criterion placed upon *St*. 2) The inequality in $St \leq 0.2$ suggests that the suitability of a particle does not behave as a step function with *St*, where $St = 0.2$ is the threshold. Instead, as the particle response time τ_p is reduced with respect to the flow response time τ_f, the error due to particle slip will decrease monotonically. Samimy & Lele (1991) found that $St = 0.2$ produced an error of 2% in the measured velocity, though this result is dependent upon the features contained within the flowfield.

The criterion $St \leq 0.2$ was employed in selecting the TiO_2 particles used in the current study. However, in order to address the concerns listed above, the effects of τ_p on both the distribution and magnitude of the slip velocity U_{slip} must be determined. The equation describing the motion of a particle suspended in a medium (Melling 1997) is given below, after simplifying for $\rho_f / \rho_p << 1$

$$\frac{\pi d_p^3}{6} \rho_p \frac{d\vec{U}_p}{dt} = 3\pi \mu_f d_p (\vec{U}_f - \vec{U}_p) \tag{B.9}$$

where d_p is the particle diameter. Defining the slip velocity $U_{slip} = U_f - U_p$ and grouping the coefficients into a single term τ_p, Eqn. B.9 can be rewritten as

$$\frac{d\vec{U}_p}{dt} = \frac{\vec{U}_{slip}}{\tau_p} \tag{B.10}$$

From this formulation, it is clear that the particle response time τ_p can be computed as

$$\tau_p = \frac{\rho_p d_p^2}{18 \mu_f} \tag{B.11}$$

Equation B.11 clearly shows the dependence of τ_p on the particle size and density, explaining the search for ever-smaller seeding particles for use in high-speed flows.

By determining a value for τ_p (whether experimentally or through Eqn. B.11), Eqn. B.10 can directly yield the slip velocity for a known flowfield. Assuming a two-dimensional flow, the time derivative in Eqn. B.10 can be decomposed as

$$\frac{d\overrightarrow{U_p}}{dt} = \frac{d\overrightarrow{U_p}}{dx}\frac{dx}{dt} + \frac{d\overrightarrow{U_p}}{dy}\frac{dy}{dt} \tag{B.12}$$

Substituting $u_p = dx/dt$ and $v_p = dy/dt$, Eqns. B.10 and B.12 can be combined to produce an equation for the slip velocity

$$\overrightarrow{U_{slip}} = \tau_p \left(\frac{d\overrightarrow{U_p}}{dx} u_p + \frac{d\overrightarrow{U_p}}{dy} v_p \right) \tag{B.13}$$

Equation B.13 allows the velocity bias to be computed as a function of τ_p, providing a method for assessing the ability of a seeding particle to reliably track the flowfield in question. A further advantage stems from the local nature of Eqn. B.13, allowing an experimenter to determine both the magnitude and location of the velocity bias. This procedure was used by Schrijer & Scarano (2007) in order to correct the flow through an oblique shock, though no such correction method is employed in the current study. It should be noted that this procedure cannot be used *a priori*, as it requires knowledge of the measured particle velocity, and is only suitable for determining the error inherent in a given data set.

The method described above was applied to the rough-wall model in the current study. This case was considered to provide the greatest challenge to the dynamic response of the particles, given the shock waves and expansion fans evident in the schlieren images. Figure B.4 shows both components of the slip velocity at three heights within the boundary layer. Negative values suggest that the particles are traveling faster than the fluid, and indicate the presence of a compression. Comparisons with Figs. 8.7 and 8.12 confirm this observation, showing negative values of U_{slip} corresponding to regions of increased Reynolds stresses. The magnitude of the slip velocity increases near the wall, though the maximum velocity for each component does not exceed $0.007U_e$, which is comparable to the statistical uncertainty of the mean streamwise velocity. The median value of the slip velocity is much lower, approximately 0.2% - 0.4% of the edge velocity U_e. These values suggest that the particle lag through the distortions is negligible. While

this analysis was performed for the mean flow only, it is reasonable to also extend this conclusion to the instantaneous flow, though further analysis is needed.

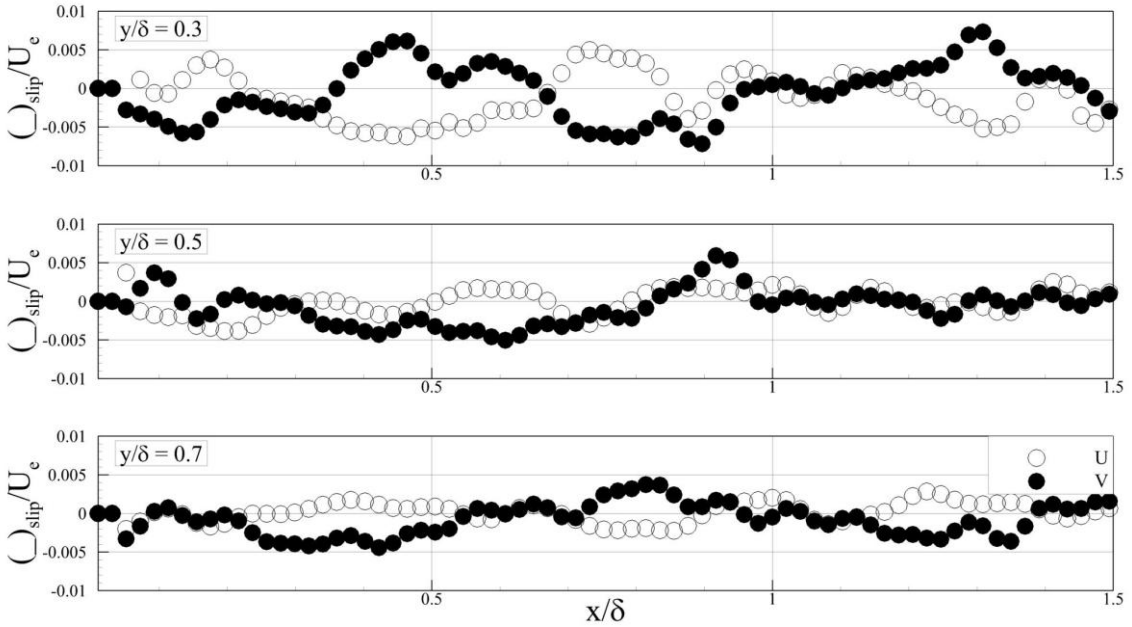

Figure B.4 Calculated particle slip, for rough-wall boundary layer

B.4. Velocity Gradients

The least-squares finite difference operator for the first derivative is given in Table 6.2 of Raffel *et al.* (2007) as

$$\left(\frac{du}{dx}\right)_i \approx \frac{2u_{i+2} + u_{i+1} - u_{i-1} - 2u_{i-2}}{10\Delta x} \tag{B.14}$$

where Δx is the vector spacing, u is the velocity, and the subscript i denotes the spatial position. Assuming that the spatial uncertainty of Δx is negligible, and representing the first derivative operator as the function f, the L_2-norm of the uncertainty can be computed by

$$\varepsilon_{\left(\frac{du}{dx}\right)_i} = \sqrt{\left(\frac{\partial f}{\partial u_{i+2}}\varepsilon_{u_{i+2}}\right)^2 + \left(\frac{\partial f}{\partial u_{i+1}}\varepsilon_{u_{i+1}}\right)^2 + \cancel{\left(\frac{\partial f}{\partial u_i}\varepsilon_{u_i}\right)^2} + \left(\frac{\partial f}{\partial u_{i-1}}\varepsilon_{u_{i-1}}\right)^2 + \left(\frac{\partial f}{\partial u_{i-2}}\varepsilon_{u_{i-2}}\right)^2} \quad \text{(B.15)}$$

The measurement uncertainty of the velocity is given as ε_u, and computed in §B.1 as 24 m/s. Assuming that this measurement uncertainty ε_u is valid for all points within the flow (i.e. $\varepsilon_u = \varepsilon_{u_i} = \varepsilon_{u_{i+1}} = \ldots$), Eqn. B.15 can be simplified as

$$\begin{aligned} \varepsilon_{\left(\frac{du}{dx}\right)_i} &= \sqrt{(\varepsilon_u)^2\left[\left(\frac{\delta f}{\delta u_{i+2}}\right)^2 + \left(\frac{\delta f}{\delta u_{i+1}}\right)^2 + \left(\frac{\delta f}{\delta u_{i-1}}\right)^2 + \left(\frac{\delta f}{\delta u_{i-2}}\right)^2\right]} \\ &= \sqrt{(\varepsilon_u)^2\left[\left(\frac{1}{5\Delta x}\right)^2 + \left(\frac{1}{10\Delta x}\right)^2 + \left(\frac{-1}{10\Delta x}\right)^2 + \left(\frac{-1}{5\Delta x}\right)^2\right]} \end{aligned} \quad \text{(B.16)}$$

Scaling the resulting uncertainty by δ/U_e yields a non-dimensional value of 0.54 for the instantaneous strain rate. The uncertainty of the mean strain rate can be computed by replacing ε_u with the mean uncertainty ε_U, yielding 0.17. The high level of uncertainty serves to emphasize the difficulty of applying gradient-based vortex identification methods, which is discussed below in further detail.

B.5. Swirling Strength λ_{ci}

Using the uncertainty calculated for the instantaneous strain rates in §B.4, it is possible to estimate the resulting uncertainty levels for the swirling strength λ_{ci}. As described in §5.1.5, the swirling strength is the imaginary component of the complex eigenvalue of the velocity gradient tensor $\nabla\vec{V}$. In a two-dimensional space, the resulting characteristic equation is given by

$$\lambda^2 - \lambda\left(\frac{\delta u}{\delta x} + \frac{\delta v}{\delta y}\right) + \frac{\delta u}{\delta x}\frac{\delta v}{\delta y} - \frac{\delta v}{\delta x}\frac{\delta u}{\delta y} = 0 \quad \text{(B.17)}$$

where $\lambda = \{\lambda_1, \lambda_2\}$ are the two eigenvalues. Solving for λ yields

$$\lambda_1, \lambda_2 = \frac{\overbrace{\left(\frac{\delta u}{\delta x} + \frac{\delta v}{\delta y}\right)}^{\lambda_{cr}} \pm \overbrace{\sqrt{\left(\frac{\delta u}{\delta x} + \frac{\delta v}{\delta y}\right)^2 - 4\left(\frac{\delta u}{\delta x}\frac{\delta v}{\delta y} - \frac{\delta v}{\delta x}\frac{\delta u}{\delta y}\right)}}^{\lambda_{ci}}}{2} \tag{B.18}$$

If the fluid is locally spiraling, then the eigenvalues will be complex conjugates, such that $\{\lambda_1,\lambda_2\} = \lambda_{cr} \pm \lambda_{ci}$. Therefore, the swirling strength λ_{ci} is described by

$$\begin{aligned} \lambda_{ci} &= \frac{1}{2}\sqrt{\left(\frac{\delta u}{\delta x} + \frac{\delta v}{\delta y}\right)^2 - 4\left(\frac{\delta u}{\delta x}\frac{\delta v}{\delta y} - \frac{\delta v}{\delta x}\frac{\delta u}{\delta y}\right)} \\ &= \frac{1}{2}\sqrt{\left(\frac{\delta u}{\delta x}\right)^2 + \left(\frac{\delta v}{\delta y}\right)^2 - 2\frac{\delta u}{\delta x}\frac{\delta v}{\delta y} + 4\frac{\delta v}{\delta x}\frac{\delta u}{\delta y}} \end{aligned} \tag{B.19}$$

Prior to estimating the uncertainty $\varepsilon_{\lambda_{ci}}$, the sensitivity coefficients are computed as

$$\frac{\delta\lambda_{ci}}{\delta\left(\frac{\delta u}{\delta x}\right)} = \frac{1}{2}\left[\frac{1}{2}\frac{2\frac{\delta u}{\delta x} - 2\frac{\delta v}{\delta y}}{\sqrt{\left(\frac{\delta u}{\delta x}\right)^2 + \left(\frac{\delta v}{\delta y}\right)^2 - 2\frac{\delta u}{\delta x}\frac{\delta v}{\delta y} + 4\frac{\delta v}{\delta x}\frac{\delta u}{\delta y}}}\right] \tag{B.20}$$

$$\frac{\delta\lambda_{ci}}{\delta\left(\frac{\delta u}{\delta y}\right)} = \frac{1}{2}\left[\frac{1}{2}\frac{4\frac{\delta v}{\delta x}}{\sqrt{\left(\frac{\delta u}{\delta x}\right)^2 + \left(\frac{\delta v}{\delta y}\right)^2 - 2\frac{\delta u}{\delta x}\frac{\delta v}{\delta y} + 4\frac{\delta v}{\delta x}\frac{\delta u}{\delta y}}}\right] \tag{B.21}$$

$$\frac{\delta\lambda_{ci}}{\delta\left(\frac{\delta v}{\delta x}\right)} = \frac{1}{2}\left[\frac{1}{2}\frac{4\frac{\delta u}{\delta y}}{\sqrt{\left(\frac{\delta u}{\delta x}\right)^2 + \left(\frac{\delta v}{\delta y}\right)^2 - 2\frac{\delta u}{\delta x}\frac{\delta v}{\delta y} + 4\frac{\delta v}{\delta x}\frac{\delta u}{\delta y}}}\right] \tag{B.22}$$

$$\frac{\delta\lambda_{ci}}{\delta\left(\frac{\delta v}{\delta y}\right)} = \frac{1}{2}\left[\frac{1}{2}\frac{2\frac{\delta v}{\delta y} - 2\frac{\delta u}{\delta x}}{\sqrt{\left(\frac{\delta u}{\delta x}\right)^2 + \left(\frac{\delta v}{\delta y}\right)^2 - 2\frac{\delta u}{\delta x}\frac{\delta v}{\delta y} + 4\frac{\delta v}{\delta x}\frac{\delta u}{\delta y}}}\right] \tag{B.23}$$

The sensitivity coefficients were evaluated at $y/\delta = 0.1$ for the smooth ZPG model. This wall-normal location was chosen because it provides a "worst-case" scenario estimate, owing to the large gradients near the wall, and because the vortex detection method identified the largest population of coherent structures in the near-wall region. Using the sensitivity coefficients in Eqns. B.20-23, along with the uncertainty estimate for the non-dimensional instantaneous strain rate (see §B.4), the swirling strength uncertainty can be calculated through Eqn. B.1. When scaled by $\Lambda_{ci}^{rms}(y/\delta = 0.1)$, the uncertainty is comparable to the values observed in Fig. 5.9. The reader is cautioned that this does not necessarily invalidate any results based upon λ_{ci}. Recall that in §5, two vortex detection methods were tested, giving similar results for the smooth ZPG case. Instead, this merely provides additional impetus to implement a vortex identification technique that is not gradient-based, such as pattern recognition analysis. These techniques are briefly discussed in §9.5.1.

APPENDIX C

SENSITIVITY OF PIV SETTINGS

The sensitivity of the ensemble-averaged turbulence statistics to the PIV settings is described below. The processing settings, post-processing filters, and averaging filters of the DaVis PIV software package are compared. A description of these filters is provided in §4.3.3. All comparisons are made for the baseline boundary layer case, though this is considered representative of all geometries studied in this dissertation.

C.1. Processing & Post-Processing Settings

The settings used during the computation of the individual vector fields, along with the post-processing filters, are considered below. Table C.1 lists the settings used in this study, for each comparison case. The sensitivity of the ensemble-averaged shear stress $u'v'$ is shown in Fig. C.1. For all cases, a 3 sigma averaging filter was applied to generate the ensemble-averaged data plotted in Fig. C.1 (see §C.2 for a discussion of the averaging filter). Elevated shear stress levels were observed when using a 16 x 16 pixel final window size. This is most likely due to an insufficient seeding level in the near-wall region, since fewer than 10 particles were observed in a 16 x 16 pixel region in the instantaneous particle images. Keane & Adrian (1992) suggested that 10 – 12 particles are necessary to generate a sufficiently strong correlation peak. Considerable noise was observed for the shear stress from Case 2, due to the lack of smoothing applied to the instantaneous fields. However, 2 passes of smoothing (Case 3) caused the fluctuation levels to decrease below $y/\delta = 0.4$. From these observations, a final window size of 32 x 32 pixels was chosen, and only 1 smoothing pass was applied. The remainder of the settings did not affect the ensemble-averaged statistics. Inspection of the instantaneous vector fields (not included here) indicated that Case 8 yielded the best representation of the boundary layer flowfield.

Table C.1 Comparison cases, for determining sensitivity of PIV settings in DaVis v8

	Processing					Multi-pass filters				Post-processing filters		
Case	**Initial window size**	**Final window size**	**Median filter type**	**Remove if >**	**Replace if <**	**# passes - median filter**	**Median filter type**	**Remove if >**	**Replace if <**	**Peak Q ratio <**	**# passes smoothing**	**Interpolation**
Baseline	128	32	Strongly remove	2	3	1x	strongly remove	2	3	off	1	Yes
Case 1	128	32	Strongly remove	2	3	1x	strongly remove	2	3	off	1	No
Case 2	128	32	Strongly remove	2	3	1x	strongly remove	2	3	off	Off	Yes
Case 3	128	32	Strongly remove	2	3	1x	strongly remove	2	3	off	2	Yes
Case 4	128	32	Strongly remove	2	3	1x	strongly remove	2	3	1.1	1	Yes
Case 5	128	32	Strongly remove	2	3	1x	strongly remove	2	3	1.3	1	Yes
Case 6	128	32	Strongly remove	2	3	2x	strongly remove	2	3	off	1	Yes
Case 7	128	32	Strongly remove	2	3	1x	remove/replace		2	off	1	Yes
Case 8	128	32	Strongly remove	2	3	2x	remove/replace		2	off	1	Yes
Case 9	128	32	remove/replace		2	1x	strongly remove	2	3	off	1	Yes
Baseline - 16	128	16	Strongly remove	2	3	1x	strongly remove	2	3	off	1	Yes
Case 6 - 16	128	16	Strongly remove	2	3	2x	strongly remove	2	3	off	1	Yes

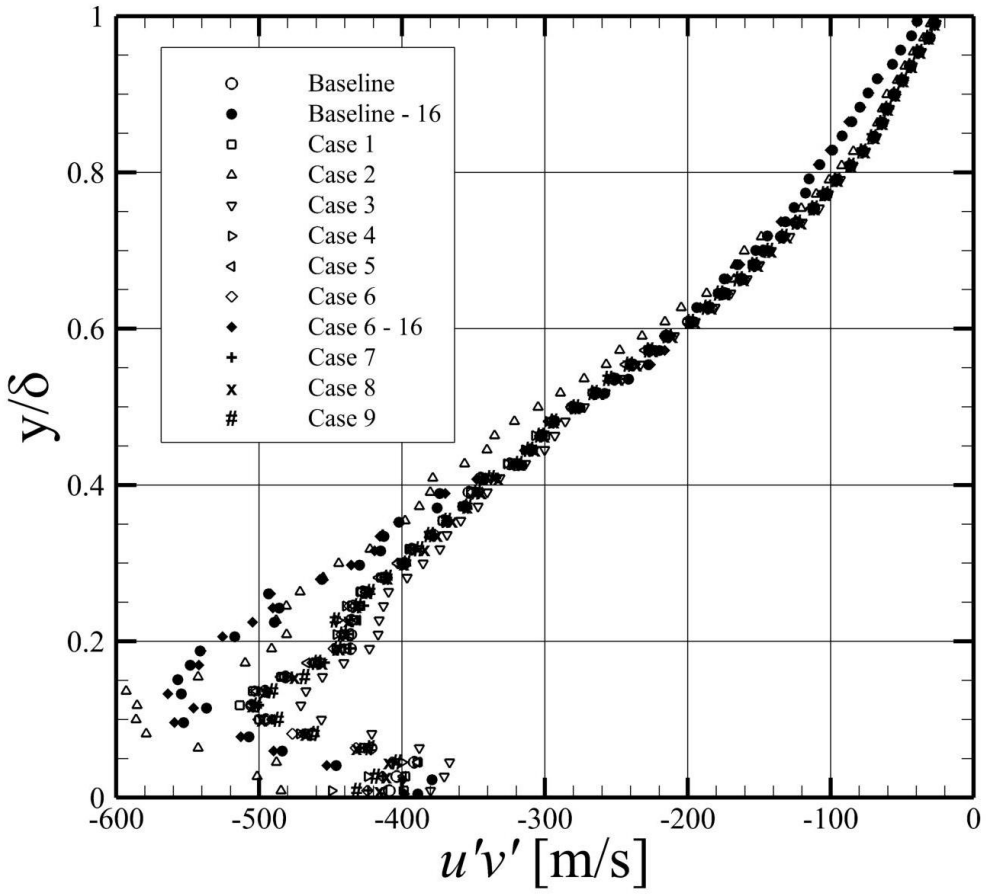

Figure C.1 Comparison of ensemble-averaged shear stress for all cases listed in Table C.1. *A 3 sigma averaging filter was used to compute the plotted statistics*

C.2. Averaging Filter

When computing the ensemble-averaged statistics, an averaging filter was applied to remove outliers present in the instantaneous flowfields. The range of allowable values is based upon the standard deviation of the velocity components, computed at each point in the flowfield. The filter settings are generally referred to as "2 sigma" or "3 sigma", removing vectors that are more than 2 or 3 standard deviations from the mean, respectively. The effects of these settings on Case 8 are shown below in Fig. C.2.

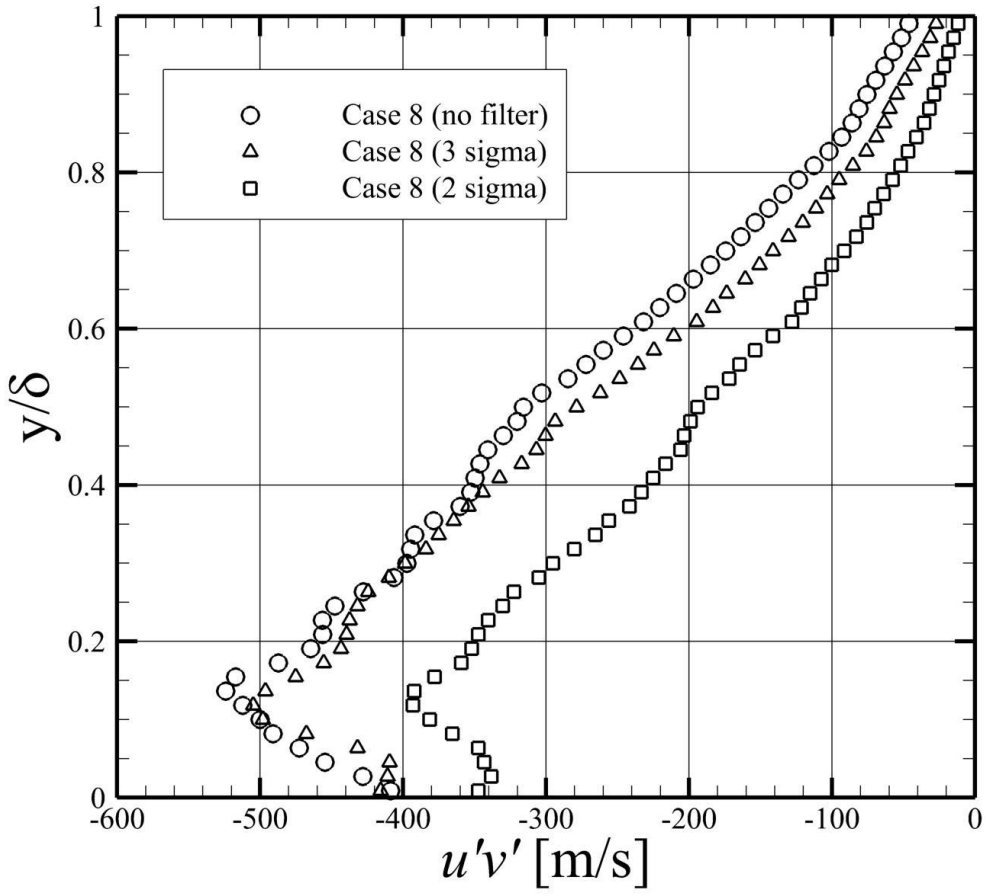

Figure C.2 Comparison of averaging filters for Case 8

Minor oscillations are visible in the "no filter" case, since all vectors are included in the statistic. In contrast, the "2 sigma" case is much smoother, but the peak shear stress has been reduced by 20%. The "3 sigma" filter provides a suitable compromise, as it removes the small-scale fluctuations while maintaining the approximate magnitude of the unfiltered shear stress. For a Gaussian distribution, a "3 sigma" filter would retain 99% of the energy.

APPENDIX D

SEEDER OPERATION MANUAL

This document has been prepared in order to instruct new users in the safe operation of the HSWT High-Pressure Seeder (hereafter referred to as the "seeder"). This equipment is used to inject solid seed particles into a high-pressure facility (> 50 psia) for performing particle-based laser diagnostics (PIV, LDV, etc.).

D.1. Construction & Design

The seeder was constructed from a 12" length of 6" Sch 80 pipe, capped at each end by a 300# blind flange. The vessel has been pressure-tested to 600 psi for 4 hours, though the **maximum safe operating pressure is 450-500 psi**. High-pressure air is currently supplied by a 3/8" stainless steel pipe [A], which connects to the 2" stainless line in the heater room. **Only dry air should be used with this seeder.** The inlet air is controlled by a Tescom regulator (C_v = 2.0) [B], which enters the seeder through a ½" OD copper tube [C]. The tube is bent at a 90° angle, and is oriented tangentially to the curved wall. A ½" pipe is located at the top center of the vessel [D], through which air and seed particles are exhausted. Ball valves are located on the 3/8" inlet pipe (upstream of the regulator) [not shown], and downstream of the vessel on the ½" exit pipe [E]. The pressure can be monitored from three locations: upstream of the regulator [F], at the seeder inlet [G], and in the seeder exit pipe [H]. Additional seeding can be added to the vessel through a ½" fill port on the top surface [I].

The design for the seeder is replicated from equipment in use by the Aerospace Engineering Department at Delft University of Technology. **Only solid seeding particles should be used in this vessel (no liquid seeding).** When the high-pressure air enters the seeding vessel, it is diverted 90° by the copper tube. This acts as a cyclone separator, spinning the larger/heavier particles to the outer wall of the vessel. The lighter particles are free to exit at the top center of the seeder through the ½" pipe.

Care should be taken to prevent moist air from entering the seeder. However, this may occur during tunnel unstart, or when seeding at ambient conditions. Do not be alarmed if you open the seeder and find that the particles are "clumpy." Using dry air (dew point ≤ −40° F) during operation will help remove moisture from the particles. **Never use air supplied by the shop compressor.**

A – Inlet pipe, 3/8" stainless steel

B – Tescom regulator (C_v = 2.0)

C – ½" copper tube (90° angle)

D – ½" exhaust pipe

E – downstream ball valve

F – upstream pressure gauge (0 – 2500 psi)

G – seeder inlet pressure gauge (0 – 500 psi)

H – exit pressure gauge (0 – 500 psi)

I – fill port

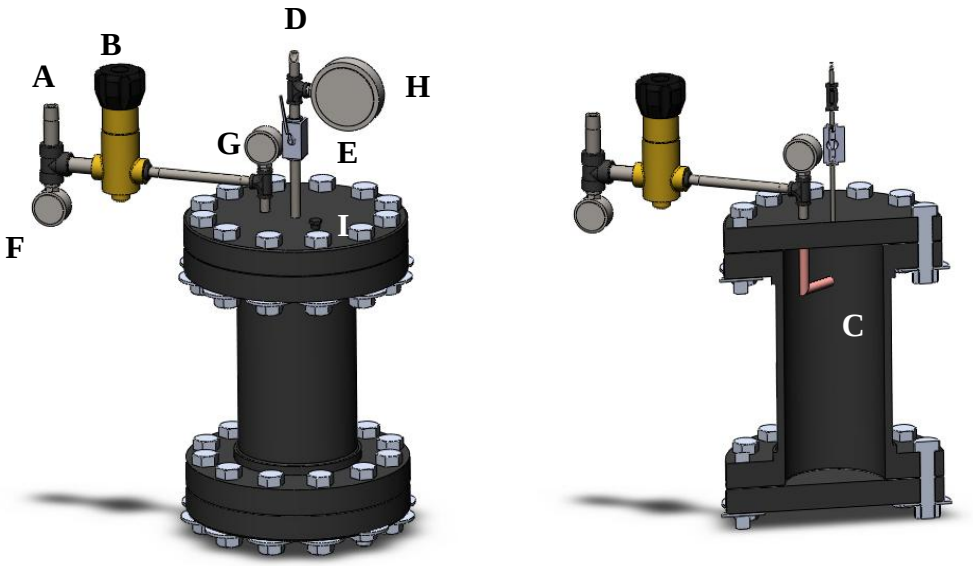

Figure D.1 High-pressure seeder. Left: full view, showing critical components and flowpath. Right: cross-section, showing angled copper tubing

D.2. Procedures

D.2.1. Prior to Operation

1. Ensure that seeder is filled with solid particles (no more than 1/4 - 1/3 full).
2. Check that seeder fill port is tight.
3. Turn regulator handle counter-clockwise until stopped (i.e. turn regulator to zero).
4. Close upstream and downstream ball valves.

D.2.2. After Tunnel has Started

1. Slowly open downstream ball valve (located on ½" pipe). Monitor pressure gauges as vessel fills with high-pressure air.
2. Ensure that regulator is set to zero, and slowly open upstream ball valve.
3. To begin seeding, increase pressure through regulator. Keep seeder vessel pressure below 500 psi.

Note: Never open upstream ball valve when downstream valve is closed. Even if regulator is set to zero, air will still leak into vessel, potentially pressurizing it to a dangerous level. Remember, regulator ≠ ball valve (i.e. a closed regulator will still pass air).

D.2.3. Prior to Shutdown

1. Reduce seeder regulator pressure to zero.
2. Close upstream ball valve.
3. Leave downstream ball valve open.

Note: Never close downstream ball valve when regulator is still open.

D.2.4. After Tunnel Shutdown

1. Ensure that tunnel static pressure has returned to ambient.
2. Ensure that seeder vessel pressure is zero.

3. Close downstream ball valve.

For safe operation, procedures must be followed in the order given. Any deviation may result in dangerous conditions.

APPENDIX E

SENSITIVITY OF VORTEX IDENTIFICATION TECHNIQUE

The use of the swirling strength criterion to detect spanwise vortices was thoroughly described in §5.2. In order to reduce the noise inherent in the vortex detection technique, several filters and thresholds were applied. The figures shown below describe the sensitivity of the convective velocity and vortex populations to the prescribed filters. Table E.1 lists the various filters used in this comparison. All comparisons shown are for the baseline boundary layer case, though comparable trends were observed in the mechanically distorted flowfields (not shown here).

Table E.1 Vortex ID filter settings

	Prograde swirling strength (__ Λ_{rms})	***Retrograde swirling strength (__ Λ_{rms})***	***Vortex size (# vectors)***
Baseline	-1.5	1	3
Case 1	-1.5	1	5
Case 2	-1.5	1	8
Case 3	-1.5	1	12
Case 4	-1.5	1	20
Case 5	-2.5	2	3
Case 6	-2	1.5	3

The streamwise and wall-normal convective velocities are plotted in Figs. E.1 and E.2, respectively. The vortex size threshold had a negligible impact upon U_c, though V_c did increase by approximately $0.002U_e$ as the smaller vortices were removed. The swirling strength thresholds, both prograde and retrograde, had almost no effect upon the convective velocities.

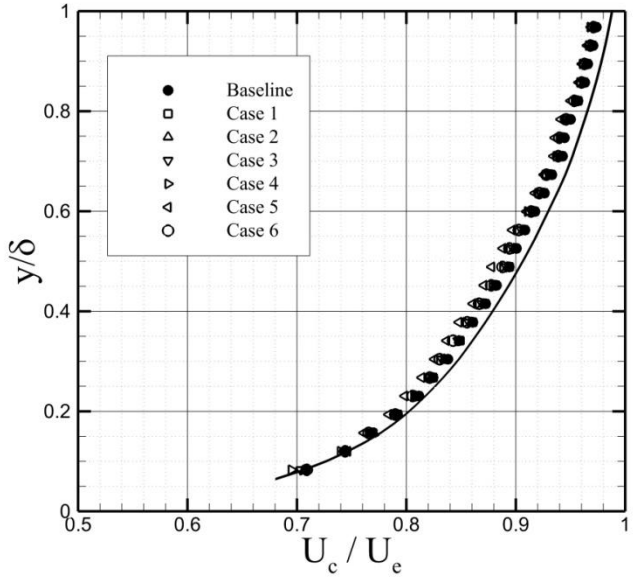

Figure E.1 Sensitivity of streamwise convective velocity to vortex ID filters. *Mean velocity u/U_e is shown as a solid line*

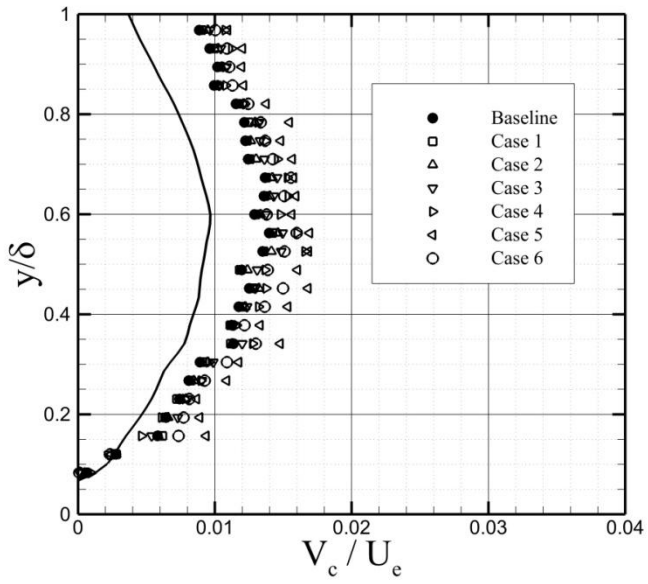

Figure E.2 Sensitivity of wall-normal convective velocity to vortex ID filters. *Mean velocity v/U_e is shown as a solid line*

The vortex populations plotted in Figs. E.3 – E.5 were much more sensitive to the filter settings. The increased swirling strength thresholds in Cases 5 and 6 resulted in decreased vortex populations of 60% and 30%, respectively (Fig. E.3). Similar responses were seen for the vortex size filter. Comparisons of the prograde and retrograde vortex populations in Figs. E.4 and E.5 showed that both populations were equally affected by the threshold settings in Table E.1. Therefore, the population ratio between the prograde and retrograde vortices was unaffected by the filter settings. Since the total population (Fig. E.3) is likely to be affected by the parameters of the PIV diagnostic (resolution, FOV, etc.), the population ratio was deemed a better metric for determining the correct filter settings. Given that the population ratio is relatively insensitive, the choice of filter settings for the vortex identification did not greatly affect the interpretation of the data.

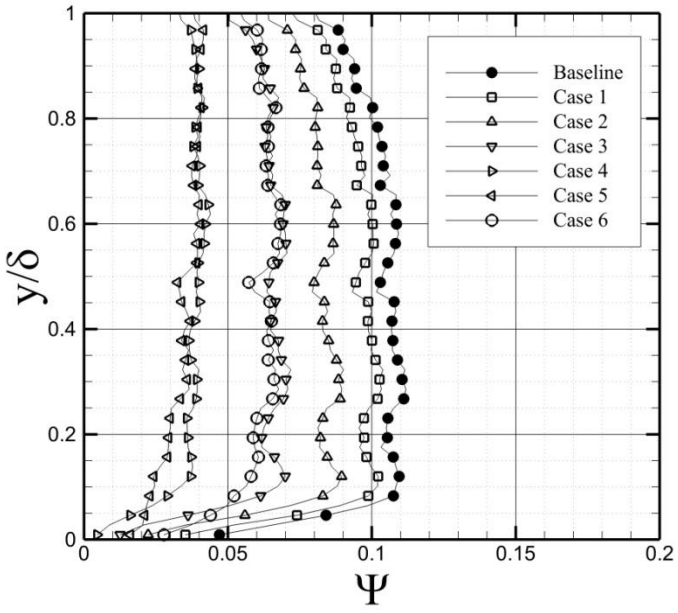

Figure E.3 Sensitivity of total vortex population to vortex ID filters

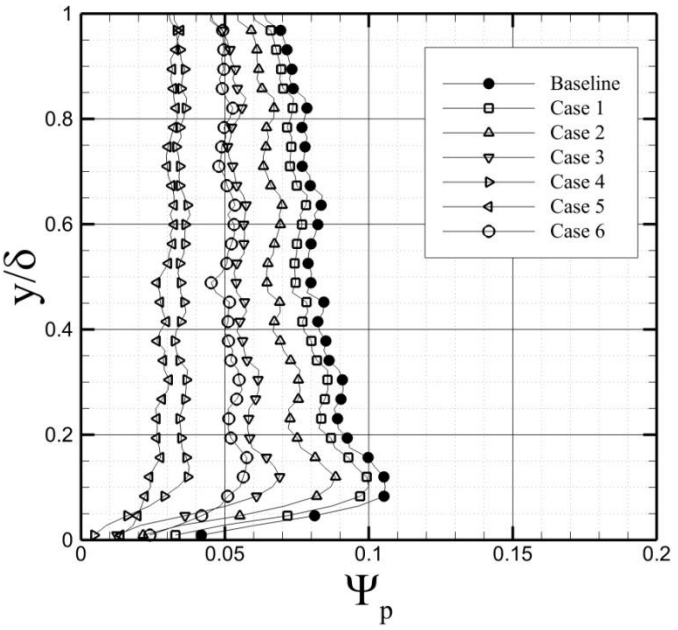

Figure E.4 Sensitivity of prograde vortex population to vortex ID filters

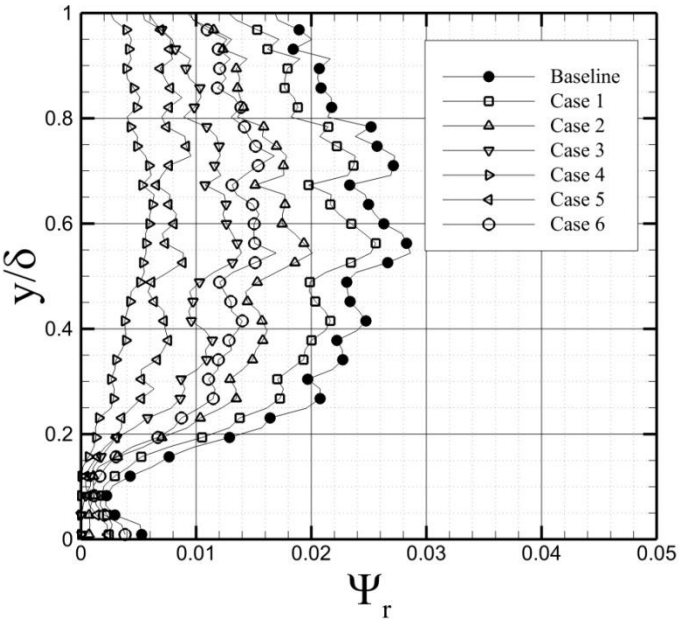

Figure E.5 Sensitivity of retrograde vortex population to vortex ID filters

APPENDIX F

APPLICABILITY OF CROCCO-BUSEMANN RELATION TO NON-ZERO PRESSURE GRADIENTS

Computation of the displacement thickness δ^* and momentum thickness θ for the distorted boundary layers was not possible, due to the unknown pressure and temperature field (and hence an unknown density profile). Therefore, the values for δ^* used in computing β for the FPG flowfields (§7) were determined by using the incompressible formulation for δ^*.

To illustrate the difficulty in determining the temperature profile for a compressible FPG boundary layer, the derivation of the Crocco-Busemann relation is repeated below, assuming $dp/dx \neq 0$. The following arguments are adapted from the derivation given in White (2006).

Starting from the energy equation, and assuming steady flow

$$\rho u \frac{\delta h}{\delta x} + \rho v \frac{\delta h}{\delta y} = u \frac{dp_e}{dx} + \frac{\delta}{\delta y}\left(\frac{\mu}{\mathrm{Pr}} \frac{\delta h}{\delta y} \right) + \mu \left(\frac{\delta u}{\delta y} \right)^2 \tag{F.1}$$

we can relate the gradient of the enthalpy h to the velocity u by $\frac{\delta h}{\delta s} = \frac{\delta h}{\delta u}\frac{\delta u}{\delta s}$, where s is a spatial coordinate. Setting Pr = 1, the energy equation now becomes

$$\rho u \frac{\delta h}{\delta u}\frac{\delta u}{\delta x} + \rho v \frac{\delta h}{\delta u}\frac{\delta u}{\delta y} = u \frac{dp_e}{dx} + \frac{\delta}{\delta y}\left(\mu \frac{\delta h}{\delta u}\frac{\delta u}{\delta y} \right) + \mu \left(\frac{\delta u}{\delta y} \right)^2$$

$$= u \frac{dp_e}{dx} + \frac{\delta h}{\delta u}\frac{\delta}{\delta y}\left(\mu \frac{\delta u}{\delta y} \right) + \mu \left(\frac{\delta u}{\delta y} \right)^2 \frac{\partial^2 h}{\partial u^2} + \mu \left(\frac{\delta u}{\delta y} \right)^2$$

$$\frac{\delta h}{\delta u}\left[\rho u \frac{\delta u}{\delta x} + \rho v \frac{\delta u}{\delta y} - \frac{\delta}{\delta y}\left(\mu \frac{\delta u}{\delta y} \right) \right] = u \frac{dp_e}{dx} + \left(1 + \frac{\partial^2 h}{\partial u^2} \right) \mu \left(\frac{\delta u}{\delta y} \right)^2 \tag{F.2}$$

Substituting the momentum equation

$$\rho u \frac{\delta u}{\delta x} + \rho v \frac{\delta u}{\delta y} - \frac{\delta}{\delta y}\left(\mu \frac{\delta u}{\delta y} \right) = - \frac{dp_e}{dx} \tag{F.3}$$

into the left-hand bracket of the energy equation yields

$$\frac{\delta h}{\delta u}\left[- \frac{dp_e}{dx} \right] - u \frac{dp_e}{dx} = \left(1 + \frac{\partial^2 h}{\partial u^2} \right) \mu \left(\frac{\delta u}{\delta y} \right)^2 \tag{F.4}$$

If $dp_e/dx = 0$, then a solution can be found from $\frac{\partial^2 h}{\partial u^2} = -1$. Integrating, and using boundary conditions at $y = 0$ and $y = \delta$, will yield the Crocco-Busemann relation for temperature. However, if dp_e/dx is non-zero, then the equation can be re-arranged as

$$\frac{\partial^2 h}{\partial u^2} \mu \left(\frac{\delta u}{\delta y} \right)^2 + \frac{dp_e}{dx} \frac{\delta h}{\delta u} = - \mu \left(\frac{\delta u}{\delta y} \right)^2 - \frac{dp_e}{dx} u \tag{F.5}$$

This is a 2nd-order nonlinear elliptic PDE, and does not present a theoretical solution. Furthermore, this is complicated by the fact that our assumption of $\frac{\delta h}{\delta s} = \frac{\delta h}{\delta u} \frac{\delta u}{\delta s}$ may not be strictly true for pressure-gradient flows. This relation assumes that u is the primary velocity component, and that v is negligible. However, it is possible for v to become significant through expanding flows. For example, the SPG case in the current study demonstrates a ratio of $u/v \approx$ 6-7 at the boundary layer edge.

APPENDIX G

DECREASING BOUNDARY LAYER THICKNESS OVER SURFACE ROUGHNESS

The streamwise evolution of the rough-wall mean velocity shows a periodic oscillation, consistent with the expected response to a periodic roughness pattern (Fig. G.1). However, the wall-normal velocity (Fig. G.2), while maintaining this periodic response, also shows an offset bias toward the upstream third of the FOV, ultimately undergoing a sign change across the FOV. This behavior is also observed in the streamwise velocity u/U in Fig. G.1, though without the sign change, showing a slight increase in the streamwise velocity across the FOV. The linearly decreasing wall-normal velocity, coupled with the relatively small acceleration ($0.01u/U$ in 2δ), initially suggested that this behavior is due to a minor misalignment of the PIV camera.

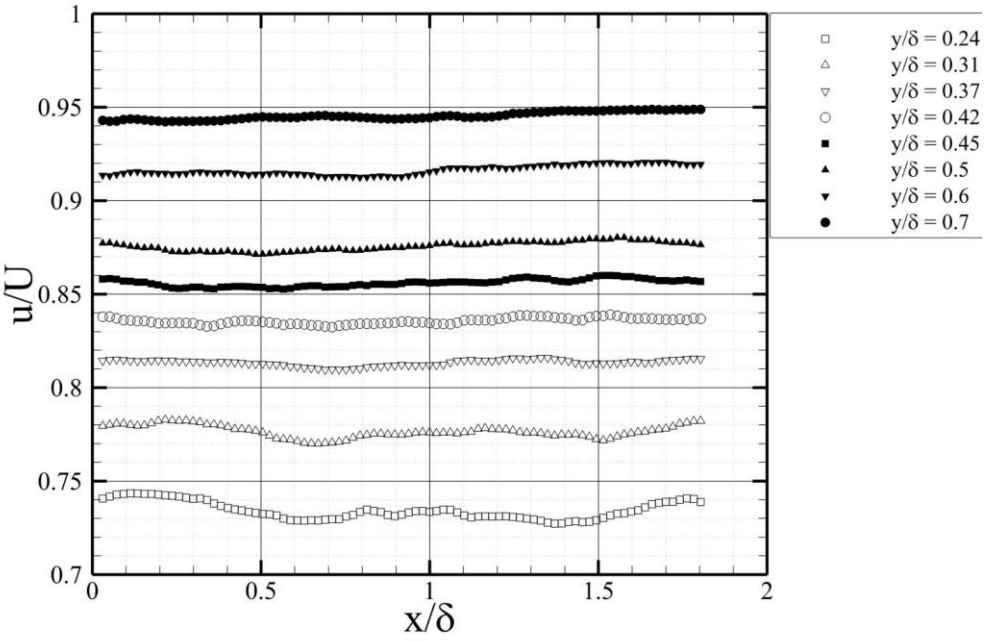

Figure G.1 Streamwise evolution of u-velocity versus *x/δ*. *Note that the velocity increases with x/δ at the boundary layer edge.*

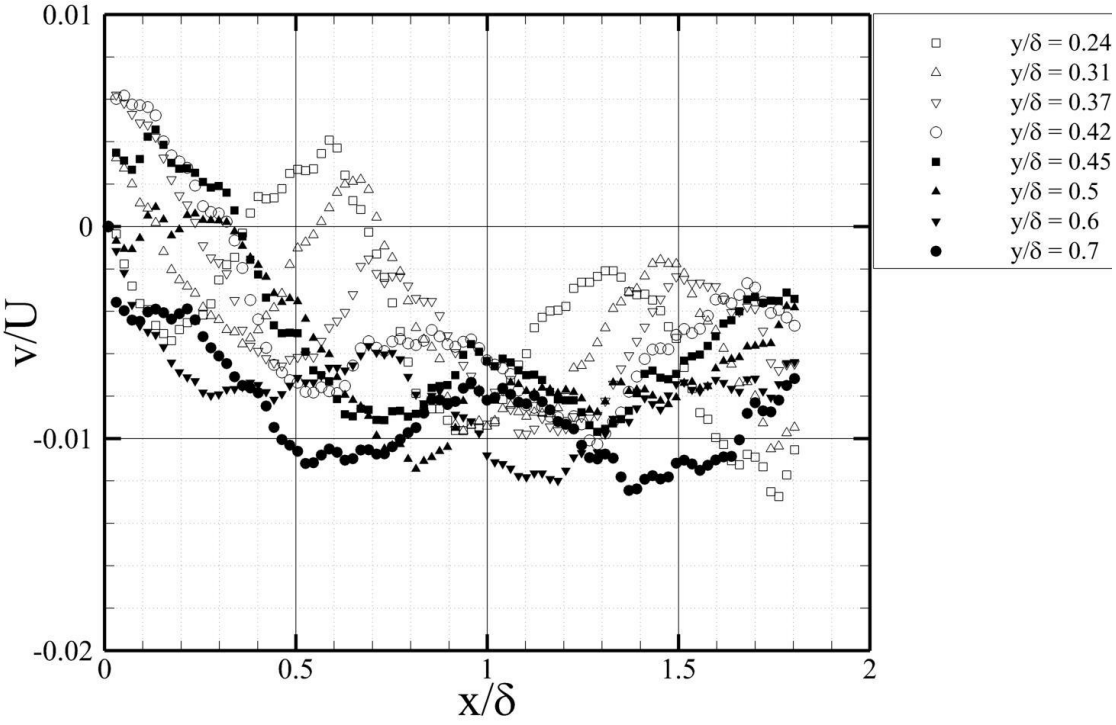

Figure G.2 Streamwise evolution of v-velocity versus *x/δ*. *Note the sign reversal of the velocity*

In order to determine the degree of camera misalignment, the (reasonable) assumption was made that the boundary layer thickness does not evolve appreciably within the FOV. The misalignment can then be determined by extracting isocontours of velocity near the boundary layer edge, and computing the resultant angles with respect to the $y = 0$ line. This yielded a misalignment angle of approximately 1°, which is an order of magnitude larger than anticipated. Prior to correlating the particle images, the PIV data were pre-processed to account for camera rotation. These corrections were accurate to 0.1-0.2°. The calculated angle of 1° is too large to be ignored during pre-processing. This was confirmed through inspection of the original data, which exhibited a misalignment of only 0.8°, before pre-processing was performed. Therefore, the trends seen in Figs. G.1 and G.2 cannot be explained simply through a rotation of the PIV camera.

If the behavior in Figs. G.1 and G.2 is due to the flow response (as opposed to a measurement error), only two possible explanations exist: 1) the mean flow is accelerating, or 2) the boundary layer height is decreasing. It is implausible for the flow to accelerate through the FOV, given that the constant area of the test section will limit the flow to a nominally zero or slightly adverse pressure gradient. However, if the boundary layer growth is sufficiently rapid upstream of the measurement location, then it is conceivable that the increasingly adverse pressure gradient will lead to a *decrease* in the boundary layer thickness. While this behavior is not observed for the smooth-wall flow, it is possible that this mechanism becomes important over the roughness geometry, due to the rapid boundary layer growth associated with rough-wall flows, and exacerbated by the increasing contribution of the displacement thickness δ^*/δ with roughness height k (for a recent example of the dependence of δ^* upon k, see Akomah, Hangan & Naughton 2011).

The dense packing of the roughness elements prevented this theory from being verified through the direct measurement of the pressure gradient dp_w/dx. However, the trend of the boundary layer height can be examined by extracting wall-normal velocity profiles at the extreme upstream and downstream edges of the FOV. For the smooth ZPG flowfield, the boundary layer grows by approximately 0.2 mm across the FOV. In contrast, the rough-wall boundary layer experiences a 0.2 mm *reduction* in height, producing a 0.5° downward slope along the boundary layer edge. For a fixed wall-normal position y_1, moving downstream would lead to an increasing y/δ position, leading to the increased u/U observed in Fig. G.1. As the boundary layer decreases in height, the wall-normal velocity V will re-orient toward the wall, leading to the sign change in Fig. G.2. The small region of positive v/U for $x/\delta < 0.25$ suggests that the measurement location is near the inflection point of the boundary layer evolution. Despite the trends discussed in Figs. G.1 and G.2, this gradual decrease in boundary layer thickness is not expected to have an appreciable effect upon the dynamics of the boundary layer, especially the near-wall motions. For affirmation, the reader should note the small magnitude (~ 0.5% - 1% of U_e) of the anomalies discussed herein.